Springer Proceedings in Materials

Ivan A. Parinov
Shun-Hsyung Chang
Banh Tien Long *Editors*

Advanced Materials

Proceedings of the International Conference on "Physics and Mechanics of New Materials and Their Applications", PHENMA 2019

Springer

Springer Proceedings in Materials

Volume 6

Springer Proceedings in Materials publishes the latest research in Materials Science and Engineering presented at high standard academic conferences and scientific meetings. It provides a platform for researchers, professionals and students to present their scientific findings and stay up-to-date with the development in Materials Science and Engineering. The scope is multidisciplinary and ranges from fundamental to applied research, including, but not limited to:

- Structural Materials
- Metallic Materials
- Magnetic, Optical and Electronic Materials
- Ceramics, Glass, Composites, Natural Materials
- Biomaterials
- Nanotechnology
- Characterization and Evaluation of Materials
- Energy Materials
- Materials Processing

To submit a proposal or request further information, please contact one of our Springer Publishing Editors according to your affiliation:

European countries: **Mayra Castro** (mayra.castro@springer.com)
India, South Asia and Middle East: **Priya Vyas** (priya.vyas@springer.com)
South Korea: **Smith Chae** (smith.chae@springer.com)
Southeast Asia, Australia and New Zealand: **Ramesh Nath Premnat** (ramesh.premnath@springernature.com)
The Americas: **Michael Luby** (michael.luby@springer.com)
China and all the other countries or regions: **Mengchu Huang** (mengchu.huang@springer.com)

More information about this series at http://www.springer.com/series/16157

Ivan A. Parinov · Shun-Hsyung Chang ·
Banh Tien Long
Editors

Advanced Materials

Proceedings of the International Conference on "Physics and Mechanics of New Materials and Their Applications", PHENMA 2019

Springer

Editors
Ivan A. Parinov
I. I. Vorovich Mathematics, Mechanics and Computer Sciences Institute
Southern Federal University
Rostov-on-Don, Russia

Shun-Hsyung Chang
Department of Microelectronics Engineering
National Kaohsiung University of Science and Technology
Kaohsiung, Taiwan

Banh Tien Long
School of Mechanical Engineering
Hanoi University of Science and Technology
Hanoi, Vietnam

ISSN 2662-3161 ISSN 2662-317X (electronic)
Springer Proceedings in Materials
ISBN 978-3-030-45119-6 ISBN 978-3-030-45120-2 (eBook)
https://doi.org/10.1007/978-3-030-45120-2

This Springer imprint is published by the registered company Springer Nature Switzerland AG
The registered company address is: Gewerbestrasse 11, 6330 Cham, Switzerland

Preface

Materials science is a very quickly developing area of modern science, techniques and technologies. It requires corresponding development of theoretical, experimental and numerical methods, directed on researching and designing numerous advanced materials, composites and structures. Industrial needs are aimed on the manufacture of devices, demonstrating very high accuracy of measurement, reliability and durability. These goods must operate under temperatures and pressures changing into broad limits, as well as in aggressive media. Besides pure scientific and technical problems, they should decide sharp social tasks of modern life (ecology, medicine, rehabilitation, etc.). At the same time, the quality of these devices and technologies is directly caused by the structure-sensitive properties, physical and mechanical characteristics of used materials. The investigation of modern physical, technical and technological processes also requires the manufacture of materials and devices demonstrating optimal and outstanding properties.

This collection of 50 chapters presents selected reports of the 2019 International Conference on "Physics, Mechanics of New Materials and Their Applications" (PHENMA-2019), which has been taken place in Hanoi, Vietnam, November 7–10, 2019 (http://phenma2019.math.sfedu.ru). The conference was sponsored by the National Foundation for Science and Technology Development (Vietnam), Vietnam Union of Science and Technology Associations (VUSTA), Ministry of Education and Science of Russian Federation, Russian Foundation for Basic Research, South Scientific Center of Russian Academy of Science, Ministry of Science and Technology of Taiwan, The Korean Society of Ocean Engineering (South Korea), New Century Education Foundation (Taiwan), Ocean and Underwater Technology Association (Taiwan), Unity Opto Technology Co. (Taiwan), Fair Well Fishery Co. (Taiwan), Woen Jinn Harbor Engineering Co. (Taiwan), Lorom Group (Taiwan), Longwell Co. (Taiwan), Vietnam Maritime University (Vietnam), Vinh Long University of Technology Education (Vietnam), Hanoi University of Industry (Vietnam), Vietnamese-German University (Vietnam), Ho Chi Minh City University of Agriculture and Forestry (Vietnam), Research Institute of Agriculture Machinery (Vietnam), Don State Technical University (Russia), University of 17 Agustus 1945 Surabaya (Indonesia),

University of 45, Surabaya (Indonesia), University of Islam Kadiri (Indonesia), University of Darul Ulum, Jombang (Indonesia), University of Maarif Hasyim Latif, Sidoarjo (Indonesia), PDPM Indian Institute of Information Technology, Design and Manufacturing (India), Korea Maritime and Ocean University (South Korea) and South Russian Regional Centre for Preparation and Implementation of International Projects.

The thematic of the PHENMA-2019 continued ideas of previous international symposia and conferences: PMNM-2012 (http://pmnm.math.rsu.ru), PHENMA-2013 (http://phenma.math.sfedu.ru), PHENMA-2014 (http://phenma2014.math.sfedu.ru), PHENMA-2015 (http://phenma2015.math.sfedu.ru), PHENMA-2016 (http://phenma2016.math.sfedu.ru), PHENMA-2017 (http://phenma2017.math.sfedu.ru) and PHENMA-2018 (http://phenma2018.math.sfedu.ru), whose results have been published in the following edited books *Physics and Mechanics of New Materials and Their Applications*, Ivan A. Parinov, Shun-Hsyung Chang (Eds.), Nova Science Publishers, New York, 2013, 444 p. ISBN: 978-1-626-18535-7; *Advanced Materials—Physics, Mechanics and Applications*, Springer Proceedings in Physics. Vol. 152. Shun-Hsyung Chang, Ivan A. Parinov, Vitaly Yu. Topolov (Eds.), Springer, Heidelberg, New York, Dordrecht, London, 2014, 380 p. ISBN: 978-3-319-03748-6; *Advanced Materials—Studies and Applications*, Ivan A. Parinov, Shun-Hsyung Chang, Somnuk Theerakulpisut (Eds.), Nova Science Publishers, New York, 2015, 527 p. ISBN: 978-1-634-63749-7; *Advanced Materials—Manufacturing, Physics, Mechanics and Applications*, Springer Proceedings in Physics, Vol. 175, Ivan A. Parinov, Shun-Hsyung Chang, Vitaly Yu. Topolov (Eds.). Heidelberg, New York, Dordrecht, London: Springer Cham. 2016, 707 p. ISBN: 978-3-319-26322-9; *Advanced Materials—Techniques, Physics, Mechanics and Applications*, Springer Proceedings in Physics, Vol. 193, Ivan A. Parinov, Shun-Hsyung Chang, Muaffaq A. Jani (Eds.). Springer Nature, Cham, Switzerland. 2017, 627 p. ISBN: 978-3-319-56062-5; *Advanced Materials—Proceedings of the International Conference on "Physics and Mechanics of New Materials and Their Applications,"* PHENMA-2017, Springer Proceedings in Physics, V. 207, Ivan A. Parinov, Shun-Hsyung Chang, Vijay K. Gupta (Eds.). Springer Nature, Cham, Switzerland. 2018, 640 p. ISBN: 978-3-319-78918-7; *Advanced Materials—Proceedings of the International Conference on "Physics and Mechanics of New Materials and Their Applications,"* PHENMA-2018, Springer Proceedings in Physics, V. 224, Ivan A. Parinov, Shun-Hsyung Chang, Yun-Hae Kim (Eds.). Springer Nature, Cham, Switzerland. 2019, 666 p. ISBN: 978-3-030-19893-0, respectively.

The papers of the PHENMA-2019 are divided into four scientific directions: (i) Processing Techniques of Advanced Materials, (ii) Physics of Advanced Materials, (iii) Mechanics of Advanced Materials and (iv) Applications of Advanced Materials.

Into the framework of the first direction, it is considered the influence of composition and structure of Pt-based electrocatalysts on their durability. Then, there are investigations of the effect of organic additives on morphology and electrocatalytic activity of platinum nanomaterials and X-ray spectroscopy study of the

atomic and electronic structures of polyacrylonitrile-based nanocomposites. Moreover, morphology and structure of carbon nanoparticles, generated from graphite nitrate, are studied also as the formation of surface micro-, nanostructures and wear in nanocomposite coatings with passing to TiN coating deposited by a method combining magnetron sputtering and arc evaporation. Buckling folded composite plate subjected to in-plane loading condition with the cutting process in metallic alloys continues the studies of this part. The first part is finished by considering the optimal technology for processing sport wears from waterproof fabric.

The physical topic is opened by the theoretical investigation of the equation for density matrix systems of identical particles. Then, crystal structure and dielectric properties of solid solutions $Bi_{3-x}Lu_xTiNbO_9$ with high Curie temperature are studied also as an investigation of InSb thin films for IR SAW photodetectors. Experimental investigations of optical and dielectric properties of ferroelectric BSN ceramics doped with rare-earth elements and the developed universal technique to determine the intensity of the optical fields are present in the next chapters. Moreover, the strength of interatomic high-angular bonds in iron and properties of bottom ash particle polymer composites are studied by modern physical methods. Effects of process parameters on surface roughness and methods of its optimization in metallic samples are studied by different theoretical and experimental approaches. Finally, the investigation of technogenic materials, applied for road constructions, finishes the physical part.

In the part of mechanics are present new mathematical and finite element modeling of active composite materials in original ACELAN-COMPOS package and FEM investigation of effective moduli of transversely isotropic thermoelastic materials with nanoscale porosity. Surface waves in the metallic glass layer with initial stresses and surface wave propagation in anisotropic elastic half-space are investigated in the next chapters also as the problem of re-reflections of ultrasonic waves from obstacles in 2D elastic material. Timoshenko model is used to analyze wave processes in wedge-shaped waveguides, and the mechanical model of a keratoprosthesis of the ocular cornea is developed. Then, the shell with auxetic properties in the model of transverse shear is studied also as the coupled problem of thermoviscoelasticity for composite polymer shell of revolution. The FEM study of the stratification of multilayer structures is developed based on neural network technologies. Finally, the structural correlation and mechanical properties in amorphous hafnium oxide under pressure are stated.

An analytical model for AlGaN/GaN MOS-HEMT for high-power applications opens the fourth part. The structural scheme of electroelastic actuator for nanomechatronics and the process of extraction of energy from rotating objects are studied. Computer modeling and experimental research of the centrifugal-rotary equipment and also compliant parallel mechanism for vibration-assisted milling are developed. Then, the design and analysis of a compliant constant-torque mechanism for rehabilitation devices are present. Moreover, some actual experimental and theoretical problems are decided on machines with bearings. Combining the Kalman filter and particle filter in object tracking is considered, and the artificial neural network model for visualization of internal defects in structural elements is

developed. Finally, some approaches and methods for processing the vibration signals in underwater applications and stomatology are discussed.

The book will be very useful for students of different levels of education, scientists and engineers, whose research interests are devoted to the development and manufacture of nanomaterials, nanostructures, piezoelectrics and other promising materials and composites with special properties. The book also discusses theoretical and experimental problems, directed to R&D of modern devices based on advanced materials, which are available for a broad spectrum of scientific and technical applications. The book includes new research results in the fields of materials science, condensed matter physics, chemistry, mechanics, computational and physical modeling and experiment, manufacture of advanced materials and composites, mathematical processing test results, computational methods and various applications.

This edited book was partially supported by Southern Federal University, grant No. VnGr/2020-04-IM (Ministry of Science and Higher Education of the Russian Federation).

Rostov-on-Don, Russia — Ivan A. Parinov
Kaohsiung, Taiwan — Shun-Hsyung Chang
Hanoi, Vietnam — Banh Tien Long
February 2020

Contents

Contributors

K. G. Abdulvakhidov Southern Federal University, Rostov-on-Don, Russia

Sergey M. Afonin Institute of Microdevices and Control Systems, National Research University of Electronic Technology (MIET), Moscow, Russia

Anastasia Alekseenko Chemistry Department, Southern Federal University, Rostov-on-Don, Russia

Sergey V. Belenov Chemistry Faculty, Southern Federal University, Rostov-on-Don, Russia

T. I. Belyankova Southern Scientific Center of Russian Academy of Sciences, Rostov-on-Don, Russia;
I. I. Vorovich Institute of Mathematics, Mechanics and Computer Science, Southern Federal University, Rostov-on-Don, Russia

P. Yu Belyavskiy ETU "LETI", St. Petersburg, Russia

Yu. V. Berestneva Biotechnology Laboratory, Federal State Budget Scientific Institution "Federal Scientific Centre of Agroecology, Complex Melioration and Protective Afforestation of the Russian Academy of Sciences", Volgograd, Russia

Bui Van Binh University of Power Electric, Hanoi, Viet Nam

Boris V. Bondarev Moscow Aviation Institute, Moscow, Russia

Nikolay V. Boyev Southern Federal University, Rostov-on-Don, Russia

Natalia I. Bronnikova Material Science Department, Don State Technical University, Rostov-on-Don, Russia

Tuan-Anh Bui School of Mechanical Engineering, Hanoi University of Science and Technology, Hanoi, Vietnam

N. I. Buravchuk I. I. Vorovich Mathematics, Mechanics and Computer Sciences Institute, Southern Federal University, Rostov-on-Don, Russia

Shun-Hsyung Chang Department of Microelectronic Engineering, National Kaohsiung University of Science and Technology, Kaohsiung, Taiwan, ROC

M. I. Chebakov Southern Federal University, Rostov-on-Don, Russia;
Rostov State Transport University, Rostov-on-Don, Russia

Ssu-Wei Chen Department of Electrical Engineering, National Kaohsiung University of Science and Technology, Kaohsiung, Taiwan, ROC

A. V. Cherpakov Department of Theoretical and Applied Mechanics, Don State Technical University, Rostov-on-Don, Russia;
Institute of Mathematics, Mechanics and Computer Sciences, Southern Federal University, Rostov-on-Don, Russia

Quang-Khoa Dang Faculty of Mechanical Engineering, Ho Chi Minh City University of Technology and Education, Ho Chi Minh City, Vietnam

S. A. Danilchenko Southern Federal University, Rostov-on-Don, Russia;
Rostov State Transport University, Rostov-on-Don, Russia

Maria Danilenko Chemistry Department, Southern Federal University, Rostov-on-Don, Russia

A. A. Davydova Supramolecular Chemistry Department, L.M. Litvinenko Institute of Physical-Organic and Coal Chemistry, Donetsk, Ukraine

Ngoc-Duc Do School of Mechanical Engineering, Hanoi University of Science and Technology, Hai Ba Trung District, Hanoi City, Vietnam

Nguyen-Trung Do School of Engineering Physics, Hanoi University of Science and Technology, Hanoi, Vietnam

Nguyen Duc-Toan School of Mechanical Engineering, Hanoi University of Technology and Science, Hanoi, Vietnam

Alexander Epikhin Don State Medical University, Rostov-on-Don, Russia

V. A. Glazunova Department of High-Pressure Physics and Advanced Technologies, Donetsk Institute for Physics and Engineering named after A.A. Galkin, Donetsk, Ukraine

Nadegda Glushko Department of Theoretical and Applied Mechanics, Don State Technical University, Rostov-on-Don, Russia

V. V. Gnatovskaya Supramolecular Chemistry Department, L.M. Litvinenko Institute of Physical-Organic and Coal Chemistry, Donetsk, Ukraine

L. V. Grigoryev ITMO University, St. Petersburg, Russia;
ETU "LETI", St. Petersburg, Russia

Vijay K. Gupta PDPM IIITDM Jabalpur, Jabalpur, India

O. V. Guryanova I. I. Vorovich Mathematics, Mechanics and Computer Sciences Institute, Southern Federal University, Rostov-on-Don, Russia

F. A. Hermawati Department of Informatics, Universitas 17 Agustus 1945, Surabaya, Indonesia

Le Thuong Hien University of Power Electric, Hanoi, Viet Nam

Pham Thi Hoa Hung Yen University of Technology and Education, Hung Yen, Viet Nam

Pham Trong Hoa University of Transport and Communications (UTC), Hanoi, Vietnam

Trung-Kien Hoang Faculty of Mechanical Engineering, Ho Chi Minh City University of Technology and Education, Ho Chi Minh City, Vietnam

Jin H. Huang Department of Mechanical and Computer-Aided Engineering, Feng Chia University, Taichung, Taiwan, ROC

Doan Thi Huong Hung Yen University of Technology and Education, Hung Yen, Viet Nam

Leonid Igumnov Research Institute for Mechanics, National Research Lobachevsky State University of Nizhny Novgorod, Nizhny Novgorod, Russia

Niharika Jain Department of Conservative Dentistry and Endodontics, Triveni Institute of Dental Science, Hospital and Research Centre, Bilaspur, Chhattisgarh, India

Prashant K. Jain CAD/CAM Lab, Mechanical Engineering Discipline, PDPM, Indian Institute of Information Technology, Design and Manufacturing Jabalpur, Jabalpur, Madhya Pradesh, India

M. A. Jani University of 17 Agustus 1945, Surabaya, Indonesia

E. M. Kaidashev Southern Federal University, Rostov-on-Don, Russia

V. V. Kalinchuk Southern Scientific Center of Russian Academy of Sciences, Rostov-on-Don, Russia;
I. I. Vorovich Institute of Mathematics, Mechanics and Computer Science, Southern Federal University, Rostov-on-Don, Russia

P. K. Kankar Discipline of Mechanical Engineering, Indian Institute of Technology Indore, Indore, Madhya Pradesh, India

G. Y. Karapetyan Southern Federal University, Rostov-on-Don, Russia

Roman Karotkiyan Research and Education Center “Materials”, Don State Technical University, Rostov-on-Don, Russia

I. M. Kastiawan Department of Mechanical Engineering, Universitas 17 Agustus 1945, Surabaya, Indonesia

V. E. Kaydashev Southern Federal University, Rostov-on-Don, Russia;
Moscow Institute of Physics and Technology, Dolgoprudny, Russia

Vladislav Khomich Institute for Electrophysics and Electric Power RAS, Saint-Petersburg, Russia

Yury Khomich Institute for Electrophysics and Electric Power RAS, Saint Petersburg, Russia

Evgeniy Kislyakov Research and Education Center "Materials", Don State Technical University, Rostov-on-Don, Russia

E. M. Kolosova Southern Federal University, Rostov-on-Don, Russia

K. D. Kosolapova Faculty of Physics, Southern Federal University, Rostov-on-Don, Russia

M. A. Kremennaya Faculty of Physics, Southern Federal University, Rostov-on-Don, Russia

Oleg V. Kudryakov Material Science Department, Don State Technical University, Rostov-on-Don, Russia

M. E. Kutepov Southern Federal University, Rostov-on-Don, Russia

Jen-Hong Lan Medical Physics & Informatics Lab., Department of Electronics Engineering, National Kaohsiung University of Science and Technology, Kaohsiung, Taiwan, ROC;
Medical Physics and Research Department, Hong Kong Sanatorium & Hospital, Hong Kong, China

Tsair-Fwu Lee Medical Physics & Informatics Lab., Department of Electronics Engineering, Department of Electrical Engineering, National Kaohsiung University of Science and Technology, Kaohsiung, Taiwan, ROC;
Biomedical Engineering, Kaohsiung Medical University, Kaohsiung, Taiwan, ROC

Chih-Hsueh Lin Medical Physics & Informatics Lab., Department of Electronics Engineering, National Kaohsiung University of Science and Technology, Kaohsiung, Taiwan, ROC;
Biomedical Engineering, Kaohsiung Medical University, Kaohsiung, Taiwan, ROC

Chin-Feng Lin Department of Electrical Engineering, National Taiwan Ocean University, Kaohsiung, Taiwan, ROC

Alexander Litvinenko Research and Education Center "Materials", Don State Technical University, Rostov-on-Don, Russia

Chao-Hong Liu Medical Physics & Informatics Lab., Department of Electronics Engineering, National Kaohsiung University of Science and Technology, Kaohsiung, Taiwan, ROC

Banh Tien Long School of Mechanical Engineering, Hanoi University of Science and Technology, Hanoi, Viet Nam

Nikolay V. Lyanguzov Physical Faculty, Southern Federal University, Rostov-on-Don, Russia;
Southern Research Center RAS, Rostov-on-Don, Russia

Thi-Bich Mac Department of Mechanical Engineering, Hung Yen University of Technology and Education, Hung Yen, Vietnam

Ivan Markov Research Institute for Mechanics, National Research Lobachevsky State University of Nizhny Novgorod, Nizhny Novgorod, Russia

Yuri F. Migal Southern Scientific Center of Russian Academy of Sciences, Rostov-on-Don, Russian Federation

T. A. Mikhailova Faculty of Physics, Southern Federal University, Rostov-on-Don, Russia

Sergey Mikolutskiy Institute for Electrophysics and Electric Power RAS, Saint-Petersburg, Russia

T. A. Minasyan Southern Federal University, Rostov-on-Don, Russia

I. P. Miroshnichenko Don State Technical University, Rostov-on-Don, Russia

Elizaveta Moguchikh Chemistry Department, Southern Federal University, Rostov-on-Don, Russia

Muhyin Department of Mechanical Engineering, Universitas 17 Agustus 1945, Surabaya, Indonesia

Tejkaran Narolia PDPM IIITDM Jabalpur, Jabalpur, India

Andrey Nasedkin Institute of Mathematics, Mechanics and Computer Science, Southern Federal University, Rostov-on-Don, Russia

Anna Nasedkina Institute of Mathematics, Mechanics and Computer Science, Southern Federal University, Rostov-on-Don, Russia

Ankit Nayak CAD/CAM Lab, Mechanical Engineering Discipline, PDPM, Indian Institute of Information Technology, Design and Manufacturing Jabalpur, Jabalpur, Madhya Pradesh, India

Loc P. Ngo Department of Global Production Engineering and Management, Vietnamese-German University, Thu Dau Mot City, Binh Duong, Vietnam

Thi-Thao Ngo Faculty of Mechanical Engineering, Hung Yen University of Technology and Education, Khoai Chau, Hung Yen, Vietnam

Duc-Toan Nguyen School of Mechanical Engineering, Hanoi University of Science and Technology, Hai Ba Trung District, Hanoi City, Vietnam

Dung Thi Quoc Nguyen Faculty International Training, Thai Nguyen University of Technology, Thai Nguyen, Viet Nam

Khac-Huy Nguyen Faculty of Mechanical Engineering, Ho Chi Minh City University of Technology and Education, Ho Chi Minh City, Vietnam

Manh-Toan Nguyen School of Mechanical Engineering, Hanoi University of Science and Technology, Hanoi, Vietnam

Tai P. Nguyen Department of Global Production Engineering and Management, Vietnamese-German University, Thu Dau Mot City, Binh Duong, Vietnam

Thi-Hong-Minh Nguyen School of Mechanical Engineering, Hanoi University of Science and Technology, Hanoi City, Viet Nam

Van-Khien Nguyen Faculty of Mechanical Engineering, Ho Chi Minh City University of Technology and Education, Ho Chi Minh City, Vietnam

Van-Thuong Nguyen School of Mechanical Engineering, Hanoi University of Science and Technology, Hai Ba Trung District, Hanoi City, Vietnam

Aleksey Nikulin Chemistry Department, Southern Federal University, Rostov-on-Don, Russia

O. N. Oskolkova Supramolecular Chemistry Department, L.M. Litvinenko Institute of Physical-Organic and Coal Chemistry, Donetsk, Ukraine

I. A. Panfilov Department of Theoretical and Applied Mechanics, Don State Technical University, Rostov-on-Don, Russia

Kirill Paperj Chemistry Department, Southern Federal University, Rostov-on-Don, Russia

I. A. Parinov Institute of Mathematics, Mechanics and Computer Sciences, Southern Federal University, Rostov-on-Don, Russia

Ivan A. Parinov I. I. Vorovich Mathematics, Mechanics, and Computer Science Institute, Southern Federal University, Rostov-on-Don, Russia

Lyubov Parinova I. I. Vorovich Mathematics, Mechanics and Computer Sciences Institute, Southern Federal University, Rostov-on-Don, Russia

Angelina Pavlets Chemistry Department, Southern Federal University, Rostov-on-Don, Russia

Huy-Tuan Pham Faculty of Mechanical Engineering, Ho Chi Minh City University of Technology and Education, Ho Chi Minh City, Vietnam

Son-Minh Pham Faculty of Mechanical Engineering, Ho Chi Minh City University of Technology and Education, Ho Chi Minh City, Vietnam

Van-Hung Pham School of Mechanical Engineering, Hanoi University of Science and Technology, Hanoi, Vietnam

Thanh-Vu Phan Faculty of Mechanical Engineering, HCMC University of Technology and Education, Ho Chi Minh City, Vietnam

E. V. Pronina Faculty of Physics, Southern Federal University, Rostov-on-Don, Russia

E. P. Putri University of 17 Agustus 1945, Surabaya, Indonesia

Tran Minh Quang School of Engineering Physics, Hanoi University of Science and Technology, Hanoi, Vietnam

Amirtham Rajagopal Department of Civil Engineering, Indian Institute of Technology, Hyderabad, India

E. V. Raksha Supramolecular Chemistry Department, L.M. Litvinenko Institute of Physical-Organic and Coal Chemistry, Donetsk, Ukraine

Evgeniy Sadyrin Research and Education Center "Materials", Don State Technical University, Rostov-on-Don, Russia

V. G. Safronenko I. I. Vorovich Mathematics, Mechanics and Computer Sciences Institute, Southern Federal University, Rostov-on-Don, Russia

M. V. Savoskin Supramolecular Chemistry Department, L.M. Litvinenko Institute of Physical-Organic and Coal Chemistry, Donetsk, Ukraine

A. A. Semenov ETU "LETI", St. Petersburg, Russia

Alexander Senichev Department of Information Technologies, Don State Technical University, Rostov-on-Don, Russia

Sergey N. Shevtsov South Center of Russian Academy of Science, Rostov-on-Don, Russia

S. I. Shevtsova Institute of Earth Science, Southern Federal University, Rostov-on-Don, Russia

Chin-Shiuh Shieh Medical Physics & Informatics Lab., Department of Electronics Engineering, National Kaohsiung University of Science and Technology, Kaohsiung, Taiwan, ROC;
Biomedical Engineering, Kaohsiung Medical University, Kaohsiung, Taiwan, ROC

V. A. Shmatko Faculty of Physics, Southern Federal University, Rostov-on-Don, Russia

V. P. Sizov Southern Federal University, Rostov-on-Don, Russia

B. V. Sobol Department of Information Technologies, Don State Technical University, Rostov-on-Don, Russia

Boris Sobol Department of Information Technologies, Don State Technical University, Rostov-on-Don, Russia

Arcady Soloviev Department of Theoretical and Applied Mechanics, Don State Technical University, Rostov-on-Don, Russia;
Institute of Mathematics, Mechanics and Computer Sciences, Southern Federal University, Rostov-on-Don, Russia

Arkadiy Soloviev Department of Theoretical and Applied Mechanics, Don State Technical University, Rostov-on-Don, Russia

A. N. Soloviev Department of Theoretical and Applied Mechanics, Don State Technical University, Rostov-on-Don, Russia;
Institute of Mathematics, Mechanics and Computer Sciences, Southern Federal University, Rostov-on-Don, Russia

Sergey Stepanov Volga State University of Technology, Yoshkar-Ola, Russia

Tsung-Jen Su Department of Electrical Engineering, National Taiwan Ocean University, Kaohsiung, Taiwan, ROC

P. V. Sukhov Supramolecular Chemistry Department, L.M. Litvinenko Institute of Physical-Organic and Coal Chemistry, Donetsk, Ukraine

Nikolay Sushentsov Volga State University of Technology, Yoshkar-Ola, Russia

Michael Swain Sydney University, Sydney, Australia

M. A. Tamarkin Department of Mechanical Engineering, Don State Technical University, Rostov-on-Don, Russia

Van-The Than Faculty of Mechanical Engineering, Hung Yen University of Technology and Education, Khoai Chau, Hung Yen, Vietnam

Pham Duc Thanh Hanoi University of Transport and Communications, Hanoi, Viet Nam

Phan Thanh Thao Hanoi University of Science and Technology, Hanoi, Vietnam

Nguyen Van Tho Department of Theoretical and Applied Mechanics, Department of Mechanical Engineering, Don State Technical University, Rostov-on-Don, Russia;
Faculty of Mechanical Engineering, Hai Phong University, Hai Phong City, Vietnam

Nguyen-Hoang Thoan School of Engineering Physics, Hanoi University of Science and Technology, Hanoi, Vietnam

Nguyen Duc Toan School of Mechanical Engineering, Hanoi University of Science and Technology, Hanoi, Viet Nam

Thanh T. Tran Department of Global Production Engineering and Management, Vietnamese-German University, Thu Dau Mot City, Binh Duong, Vietnam

Tran Thuy Trang Hanoi University of Science and Technology, Hanoi, Vietnam

Nguyen-Ngoc Trung School of Engineering Physics, Hanoi University of Science and Technology, Hanoi, Vietnam

Cong-Nam Truong Faculty of Mechanical Engineering, HCMC University of Technology and Education, Ho Chi Minh City, Vietnam

I-Hsing Tsai Medical Physics & Informatics Lab., Department of Electronics Engineering, National Kaohsiung University of Science and Technology, Kaohsiung, Taiwan, ROC

Chin-Dar Tseng Medical Physics & Informatics Lab., Department of Electronics Engineering, National Kaohsiung University of Science and Technology, Kaohsiung, Taiwan, ROC

Dao Anh Tuan School of Engineering Physics, Hanoi University of Science and Technology, Hanoi, Vietnam

O. M. Tukodova Don State Technical University, Rostov-on-Don, Russia

Bui Van-Bien Department of Mechanical Engineering, Haiphong University, Haiphong, Vietnam

Valery N. Varavka Material Science Department, Don State Technical University, Rostov-on-Don, Russia

P. V. Vasiliev Department of Information Technologies, Don State Technical University, Rostov-on-Don, Russia

Pavel Vasiliev Department of Information Technologies, Don State Technical University, Rostov-on-Don, Russia

Aleksandr Vatulyan I. I. Vorovich Mathematics, Mechanics and Computer Sciences Institute, Southern Federal University, Rostov-on-Don, Russia

A. N. Vdovichenko Supramolecular Chemistry Department, L.M. Litvinenko Institute of Physical-Organic and Coal Chemistry, Donetsk, Ukraine

I. A. Verbenko Research Institute of Physics, Southern Federal University, Rostov-on-Don, Russia

Le-Van Vinh Phenikaa University, Hanoi, Vietnam

Vadim A. Volochaev Chemistry Faculty, Southern Federal University, Rostov-on-Don, Russia

E. I. Vorovich Don State Technical University, Rostov-on-Don, Russia

Gia-Hai Vuong School of Mechanical Engineering, Hanoi University of Science and Technology, Hanoi City, Viet Nam;
Hai Phong University, Hai Phong, Viet Nam

Hung-Yu Wang Medical Physics & Informatics Lab., Department of Electronics Engineering, National Kaohsiung University of Science and Technology, Kaohsiung, Taiwan, ROC;
Biomedical Engineering, Kaohsiung Medical University, Kaohsiung, Taiwan, ROC

Jia-Ming Wu Department of Biomedicine Engineering, Department of Medical Physics, Chengde Medical University, Chengde, Hebei, China;
Department of Radiation Oncology, Yee-Zen Hospital, Tao Yuan City, Taiwan, ROC

G. E. Yalovega Faculty of Physics, Southern Federal University, Rostov-on-Don, Russia

Vladimir Yamshchikov Institute for Electrophysics and Electric Power RAS, Saint-Petersburg, Russia

Shyh-An Yeh Medical Physics & Informatics Lab., Department of Electronics Engineering, National Kaohsiung University of Science and Technology, Kaohsiung, Taiwan, ROC

Weldegebriel G. Yohannes Department of Chemistry, College of Natural and Computational Sciences, Addis Ababa University, Addis Ababa, Ethiopia

Anatoly S. Yudin I. I. Vorovich Institute of Mathematics, Mechanics and Computer Sciences, Southern Federal University, Rostov-on-Don, Russia

Yu. I. Yurasov Research Institute of Physics, Southern Federal University, Rostov-on-Don, Russia;
Southern Scientific Centre RAS, Rostov-on-Don, Russia

Igor Zabiyaka Research and Education Center “Materials”, Don State Technical University, Rostov-on-Don, Russia

Igor Yu. Zabiyaka Material Science Department, Don State Technical University, Rostov-on-Don, Russia

D. A. Zhilin Southern Federal University, Rostov-on-Don, Russia

S. V. Zubkov Research Institute of Physics, Southern Federal University, Rostov-on-Don, Russia

Part I
Processing Techniques of Advanced Materials

Chapter 1
Influence of Composition and Structure of Pt-Based Electrocatalysts on Their Durability in Different Conditions of Stress-Test

Elizaveta Moguchikh, Kirill Paperj, Angelina Pavlets, Anastasia Alekseenko, Maria Danilenko, and Aleksey Nikulin

Abstract Stability in the course of exploitation and catalytic activity in reactions, taking place on the electrodes, are the most important characteristics of electrocatalysts that determine their application in fuel cells. Relationship of the electrochemical behavior of Pt/C and PtCu/C catalysts with their morphology is studied in this chapter. In according with results of our study, Pt(Cu)/C materials with core-shell architecture of two-component nanoparticles can be a promising direction in electrocatalysis. Such materials can exhibit high specific characteristics, while being characterized by a reduced content of platinum and a low percentage of d-metal dissolution. The resulting Pt/C catalysts are characterized by surface area values from 11 to 80 $m^2/g(Pt)$, average crystallite size from 1.1 to 5.7 nm, mass fraction of platinum from 18 to 39% and relative stability during long-term stress testing of more than 70%, which is comparable to or exceeds this value for the commercial catalyst JM20.

1.1 Introduction

In recent years, research in the development of low temperature fuel cells (LT PEMFC) has become important due to the growing environmental problems in the world. LT PEMFC are devices that are promising alternative energy sources [1–3]. One of the most important parts of low-temperature fuel cells is a membrane coated with catalytic layers [1–5]. It is the component part of the device that makes it possible to increase the efficiency of current-forming reactions: electrooxidation of methanol and hydrogen, electroreduction of oxygen (ORR) [6, 7].

The nanoparticles (NPs) of platinum and its alloys deposited and evenly distributed over the surface of the carbon support are considered promising materials used as catalysts in the membrane-electrode block of fuel cells (FCs) [1–7]. Unfortunately, the high cost of platinum is one of the factors that impede the widespread use of devices based on low-temperature FCs [6–8]. The stability of the catalyst is its ability

E. Moguchikh · K. Paperj · A. Pavlets · A. Alekseenko (✉) · M. Danilenko · A. Nikulin
Chemistry Department, Southern Federal University, Rostov-on-Don, Russia
e-mail: an-an-alekseenko@yandex.ru

I. A. Parinov et al. (eds.), *Advanced Materials*, Springer Proceedings in Materials 6, https://doi.org/10.1007/978-3-030-45120-2_1

to maintain high functional characteristics during the operation of the LT PEMFC [1–8]. Thus, one of the urgent tasks is the development of Pt-containing catalysts with a low percentage of precious metal and, at the same time, with high specific characteristics, in particular high stability [8–11].

Methods of studying the structural and electrochemical characteristics of catalysts are of great importance in the field of research of alternative energy sources [1, 5–8]. The study of the relationship between the conditions of electrochemical measurements and the degradation mechanisms of platinum-containing materials plays a special role.

Stability is the ability of materials to maintain their functional characteristics during prolonged electrochemical testing [12–15]. As we know, in the process of a stress test, a deterioration of the initial characteristics of the material is observed, which is associated with its degradation. The degradation of platinum-containing catalysts in a fuel cell depends on several parameters related to the operating conditions of the membrane-electrode block and to the structure and composition of the electrocatalyst, for example the size of the NPs, their distribution over the surface of the substrate, and the type of support. Various studies of the degradation process have shown what changes can occur with the catalysts (Fig. 1.1).

Most studies present two major degradation processes associated with the oxidation of a carbon support (Corrosion of Carbon Support) and the degradation of platinum NPs (Dissolution of Pt NPs and Alloy d-Metal) [16].

During the degradation of the carbon support, the detachment of carbon parts with deposited metal particles occurs. This process leads to a loss of electronic contact and a subsequent decrease in the qualitative characteristics of the samples [17–19].

It is known that the larger the average size of NPs and the mass fraction of platinum in the catalyst, the higher is the stability of Pt/C electrocatalysts [17–20]. An electrocatalyst containing large NPs degrades to a lesser extent during the operation of a fuel cell. This occurs due to the almost complete absence of processes associated

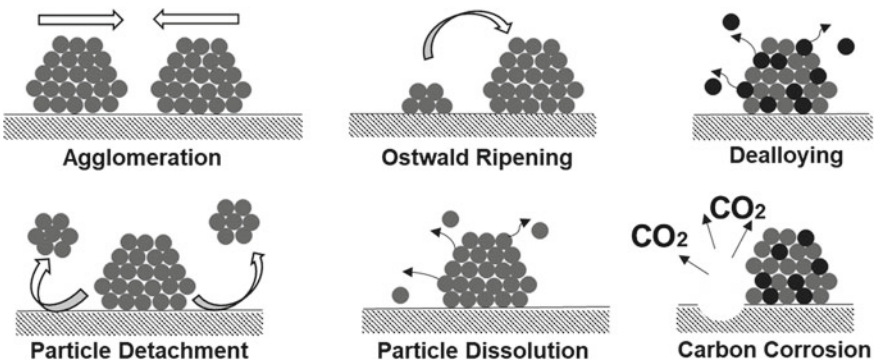

Fig. 1.1 Degradation processes Pt/C and PtM/C electrocatalysts during operation in the membrane-electrode assembly

with the movement of NPs on the surface of the support, the aggregation and dissolution of small platinum NPs due to their strong fixation on a carbon support and greater thermodynamic stability of large particles. However, such materials are also characterized by a small electrochemically active surface area [12, 16, 17, 20, 21].

Catalysts containing platinum NPs smaller than 2 nm are more susceptible to degradation due to the greater contribution of the oxidation of the carbon support. The increased rate of this oxidation can be associated with the catalytic activity of platinum NPs, which accelerate the process of carbon oxidation [18–21].

The transition to bimetallic NPs made it possible to reduce the degree of degradation of the obtained electrocatalysts [12, 22]. Apparently, the d-metal stabilizes the system due to the fact that a certain fraction of platinum NPs, which is located on the surface of the alloying component, does not have a direct contact with the carbon substrate. This reduces the catalytic effect of the noble metal on the oxidation of the carbon support [12, 23].

Testing in the membrane-electrode block is the best way to measure the stability of the materials, but they are rather laborious, expensive and energy intensive. Therefore, many studies are aimed at the rapid assessment in laboratory conditions, which is closest to real conditions [12, 22–24]. The most common method of studying the stability of electrocatalysts in laboratory conditions is the repetition of a cyclic potential sweep, accompanied by periodic measurement of ESA and specific activity of the catalyst [12].

For stress-tests carried out in laboratory conditions, an important role is played by the range of potentials, sweep speed, electrolyte composition, medium, and temperature [12, 16–18, 20]. Many authors argue that the contribution of each of the above degradation processes is unequal and depends on the range of stress test potentials [10, 11, 14].

There are two main areas of potentials for studying the degradation of platinum-containing electrocatalysts [17, 18, 20, 24]. In the range 0.4–1.0 V, degradation processes mainly occur associated with the conversion of metal NPs distributed over the surface of the support. At potentials above 1.1 V, processes leading to material degradation due to oxidation of the carbon support make a greater contribution [18, 22, 24, 25].

The purpose of this study is to identify the relationship between structural characteristics and corrosion-morphological stability during stress testing of platinum electrocatalysts for low-temperature fuel cells.

1.2 Experimental Part

As the materials under study, various methods of liquid-phase synthesis were used to obtain a number of Pt/C electrocatalysts that differ in the mass fraction of platinum and the crystallite size and a series of PtCu/C materials obtained by the liquid-phase synthesis method with the assumed structure of the shell-core NPs and an alloy

Table 1.1 Catalyst names and reducing agents used

Sample	Reducing agents
S-1, S-2	Hydrazine hydrate
S-3, S-4, S-10	Sodium borohydride
S-5	Formic acid
S-6, S-11	Ethylene glycol
S-7, S-8, S-9, S-12, S-13, S-14, S2-1, S2-2, S2-3, S2-4, S2-5	Formaldehyde

with different architecture of the NPs. The obtained samples were compared with each other, as well as with the behavior of the commercial Pt/C electrocatalyst JM (Johnson Matthey, 20% Pt).

1.2.1 Preparation of Pt/C Catalysts

The synthesis of platinum-carbon catalysts was carried out by chemical reduction of the Pt (IV) precursor ($H_2PtCl_6 \cdot 6H_2O$) in the liquid phase. Vulcan XC-72 brand carbon black was used as a support. The synthesis of each of the samples was repeated at least three times, which made it possible to evaluate the reproducibility of the structural and electrochemical characteristics of the obtained materials.

Platinum-carbon catalysts were obtained by chemical reduction in the liquid phase using various reducing agents according to Table 1.1. More synthesis methods are described previously in [26].

1.2.2 Preparation of PtCu/C Catalysts

Platinum-copper electrocatalysts were obtained by sequential reduction of metals in several stages, with a gradual decrease in the concentration of the copper precursor and an increase in the concentration of the platinum precursor to create a uniform shell. The molar ratio in the obtained samples was Pt:Cu = 1:1 and the loading of metals 30% (20% Pt). Electrocatalysts were obtained by liquid phase synthesis with carbon black Vulcan XC-72 used as a carbon support, and sodium borohydride as a reducing agent. The preparation of PtCu/C catalysts is described in more detail in the article [27].

1.2.3 Characterization of the Catalysts Structure

The mass loading of metals in the samples was determined by the mass of the residue, which consisted of Pt and copper (II) oxide, remaining unburned after heating to 800 °C. The ratio of copper and platinum in the samples was determined by X-ray fluorescence analysis on spectrometer with complete external reflection of X-ray radiation RFS-001 (Research Institute of Physics, Southern Federal University). Control over the metal component composition of the catalysts was carried out before and after the stress testing.

To determine the average crystallite size, the X-ray phase analysis (XRD) was used. The X-ray diffractograms of Pt/C materials were recorded in the angle range $2\theta = 15°–55°$ on an ARL X'TRA diffractometer (Thermo Fisher Scientific, Switzerland) using filtered CuKα radiation ($\lambda = 0.154056$ nm) at room temperature. The calculation of D_{av} was carried out for a characteristic reflection of 111 by the Scherrer formula [26].

The microstructure of the samples was studied by transmission electron microscopy (TEM). Photographs were taken with a JEM-2100 microscope (JEOL, Japan) at a voltage of 200 kV and a resolution of 0.2 nm.

1.2.4 Electrochemical Measurements

Electrochemical measurements were carried out in a standard three-electrode cell at a temperature of 25 °C. 0.1 M $HClO_4$ saturated with argon was used as the electrolyte. All potentials in the work are given relative to a reversible hydrogen electrode. The studied catalyst was deposited on the end face of a rotating disk electrode in the form of catalytic "inks", as described in [28].

Before measuring the electrochemically active surface area (ESA) of the catalyst, the electrolyte was saturated with argon for 40 min. 100 cycles are recorded in the potential range from −0.23 to 1.26 V relative to the silver chloride electrode. The sweep rate is 200 mV/s.

Calculation of ESA was carried out by the amount of electricity spent on the electrochemical adsorption and desorption of atomic hydrogen, taking into account the contribution of the charging currents of the double electric layer, as described in [28].

As methods for assessing the degree of degradation electrocatalysts, were selected the cyclic voltammetry methods in the potential range 0.6–1.0 V (RHE) with a sweep rate of 100 mV/s and 0.6–1.4 V (RHE) with a sweep rate of 100 mV/s. The cycling was carried out in a 0.1 M solution of $HClO_4$ saturated with argon at 25 °C; the number of cycles that were recorded—5000 and 500 respectively. After every 500 or 100 cycles, two CV were recorded at a potential sweep rate of 20 mV/s in the potential range from −0.23 to 1.26 V relative to the silver chloride electrode. According to the second CV, ESA was calculated as described previously.

The stability was assessed by the relative change in the ESA of platinum before (S^0_{ESA}) and after (S^j_{ESA}) stress test according to Formula (1.1).

$$\text{Stability} = \left(S^j_{ESA}/S^0_{ESA}\right) \times 100\%, \tag{1.1}$$

where j is the number of potential sweep cycles carried out before a specific S_{ESA} measurement, S^0_{ESA} is the initial area measured after standardization.

The degree of degradation was calculated using Formula (1.2):

$$\text{Degree of degradation} = \left(1 - S^j_{ESA}/S^0_{ESA}\right) \times 100\%. \tag{1.2}$$

1.3 Results and Discussion

1.3.1 The Effect of the Size of Pt NPs on the Degree of Degradation of Pt/C Electrocatalysts

In the course of the research work, 8 Pt/C catalyst were synthesized with various NP sizes from 1.1 to 5.7 nm and a close platinum mass fraction of 20% (Table 1.2). Figure 1.2 schematically depicts the arrangement of platinum NPs on the surface of a carbon support for catalysts characterized by a close metal mass fraction and different average NP sizes.

X-ray diffraction patterns of the studied catalysts have the form characteristic of the deposited Pt/C materials (Fig. 1.3).

The presence of nanosized crystallites of platinum causes a broadening of the characteristic platinum maxima, and with a decrease in the average crystallite size

Table 1.2 Structural and electrochemical characteristics of the synthesized Pt/C catalysts

Sample	ω(Pt), %	D_{av}, nm	ESA^0, $m^2/g(Pt)$	S_{geom}, $m^2/g(Pt)$	Degree of aggregation
S-1	19 ± 0.6	5.7	12 ± 1	48	0.75
S-2	21.8 ± 0.7	5.2	13 ± 1	54	0.76
S-3	20.2 ± 0.6	3.7	20 ± 2	75	0.73
S-4	20.7 ± 0.6	3.5	49 ± 5	79	0.38
S-5	18 ± 0.5	2.6	54 ± 5	106	0.49
S-6	23.5 ± 0.7	2.1	59 ± 6	135	0.56
JM20	20 ± 0.6	2.0	86 ± 9	140	0.39
S-7	19.5 ± 0.6	1.3	78 ± 8	214	0.63
S-8	19 ± 0.6	1.1	111 ± 11	248	0.55

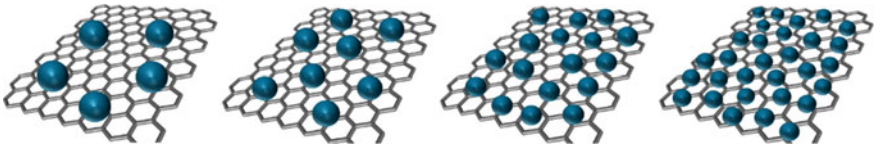

Fig. 1.2 Schematic representation of the location of NP platinum of various sizes on the surface of the carbon support of catalysts with a close mass fraction of metal

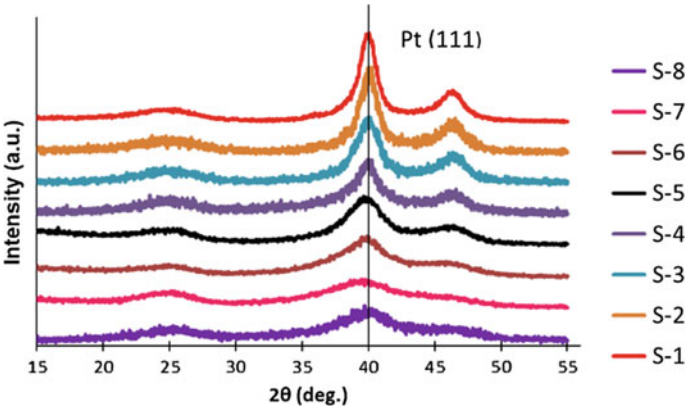

Fig. 1.3 XRD patterns of the Pt/C materials

(D_{av}), this broadening increases. The results of calculating the D_{av} according to the Scherrer equation are shown in Table 1.2.

The smallest platinum crystallites 1.1 and 1.3 nm are characterized by samples S-8 and S-7, respectively, obtained by the liquid-phase synthesis method using formaldehyde as a reducing agent. Samples S-1 and S-2 obtained using hydrazine as a reducing agent contain platinum crystallites of the largest size of all synthesized samples—more than 5 nm.

In order to assess the degree of aggregation of NPs (the fraction of platinum particles "stuck together" during the synthesis), we compared the electrochemical (experimentally determined) and geometric (calculated value) surface areas.

For each of the samples, the degree of aggregation was calculated using (1.3):

$$\text{Degree of aggregation} = 1 - \frac{\text{ESA}}{S_{geom}} \tag{1.3}$$

where ESA is the electrochemically active surface area determined according to the CV data; S_{geom} is the geometric area calculated as

$$S_{geom} = \frac{6 * 1000}{D_{NP} * \rho(\text{Pt})} \tag{1.4}$$

where ρ(Pt) is the platinum density equal to 21.4 g/cm^3; D_{NP} was calculated using the Scherrer equation using X-ray analysis data.

The higher the difference between the values of the electrochemical and geometric areas, the higher the parameter—the degree of aggregation, and the investigator, the higher the proportion of large NPs. So, for samples S-1, S-2, S-3, S-6 and S-7, the highest degree of aggregation of platinum particles was determined.

On the CV obtained during standardization of the electrodes, a change in the currents in the hydrogen region is observed for all Pt/C materials (Fig. 1.4). This may be due to the cleaning of the surface of the catalysts from organic compounds remaining after synthesis. Thus, in the process of standardization, a significant change in the parameters of the hydrogen, and often oxygen, regions of the CV occur, followed by stabilization of the electrode characteristics of the material (Fig. 1.4). The largest number of development cycles is observed for catalysts S-6, S-8 and commercial JM20.

The electrochemically active surface area was determined after the standardization stage by the method of cyclic voltammetry (Fig. 1.5). During prolonged stress testing, two CVs were recorded every 500 cycles to calculate the intermediate ESA values. Figure 1.5 shows the initial and final (after stress testing) CV Pt/C catalysts. Voltammograms of all investigated electrocatalysts have a characteristic form for nanosized platinum (Fig. 1.5). The currents in the hydrogen region are maximum for sample S-8 (Fig. 1.5). Accordingly, this material is also characterized by the highest active surface area among the obtained Pt/C catalysts (Table 1.2).

For samples S-1, S-2, and S-3, the currents in the hydrogen region are noticeably lower in comparison with other Pt/C catalysts presented.

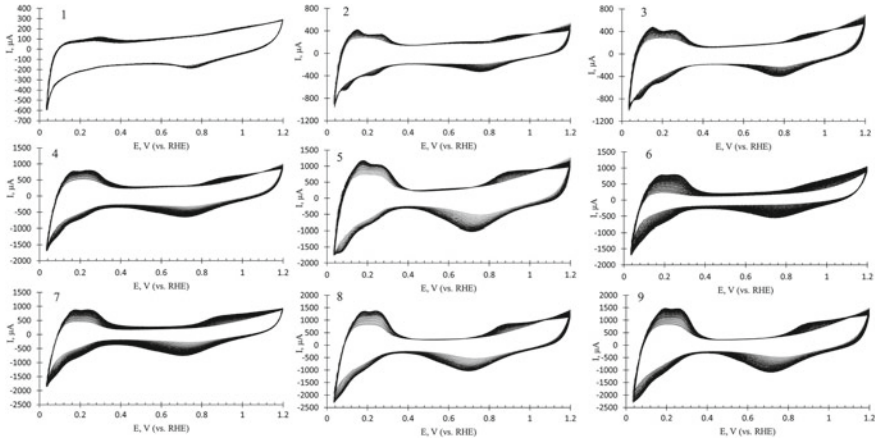

Fig. 1.4 Cyclic voltammograms of the metal-carbon catalysts in the process of standardizing cycling. Samples: 1—S-1, 2—S-2, 3—S-3, 4—S-4, 5—S-5, 6—S-6, 7—JM20, 8—S-7, 9—S-8100 cycles. The sweep rate of the potential is 200 mV/s. 0.1 M $HClO_4$ solution saturated by Ar at room temperature

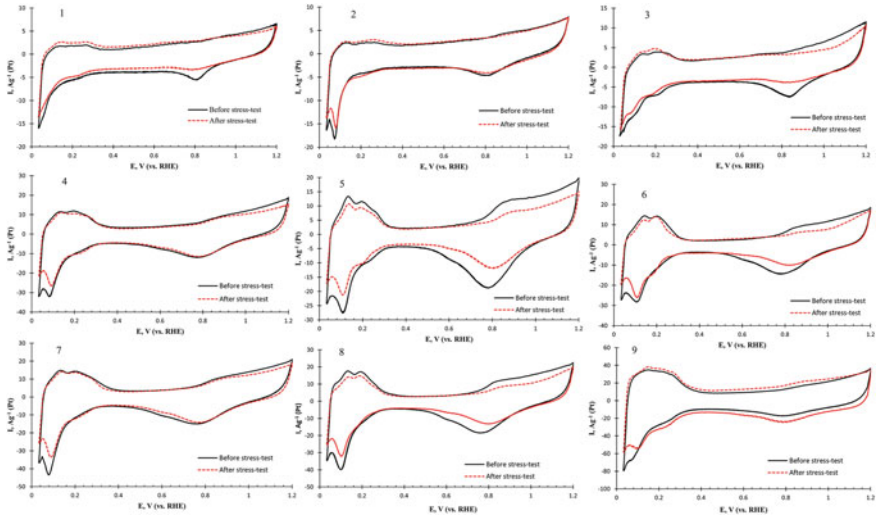

Fig. 1.5 Cyclic voltammograms of commercial Pt/C electrodes after surface standardization. Sample: 1—S-1, 2—S-2, 3—S-3, 4—S-4, 5—S-5, 6—S-6, 7—JM20, 8—S-7, 9—S-8. Electrolyte is 0.1 M $HClO_4$ saturated by Ar at room temperature. The sweep rate is 20 mV/s

The experiment showed that for the majority of the studied samples the ratio is satisfied: the smaller the average diameter of the platinum crystallites contained in the Pt/C catalyst, the higher the active surface area is characterized by the sample (Table 1.2). It is worth noting that sample S-7 falls out of this dependence, containing relatively small platinum crystallites of about 1.3 nm and, at the same time, characterized by a smaller surface area compared to the commercial analogue of JM20 (Table 1.2). Sample S-7 apparently contains larger platinum NPs consisting of small crystallites, as indicated by the high degree of aggregation.

It is important to note that when comparing the initial CV and CV after stress testing, a decrease in currents in the hydrogen region is observed for samples S-5, S-6, JM20, S-7, S-8, which leads to a more pronounced decrease in surface area (Fig. 1.5; Table 1.2).

The degree of degradation of Pt/C catalysts during repeated (5000 cycles) voltammetric cycling in the potential range 0.6–1.0 V was estimated by the change in the electrochemically active surface area (Fig. 1.6). It is believed that this potential range corresponds to the "soft mode" of stress testing, in which processes associated with platinum NPs (separation of particles from the surface, agglomeration, dissolution of platinum) make a significant contribution to the degradation of the electrocatalyst [17].

The highest stability is demonstrated by samples S-1, S-2, S-3 and S-4, more than 90%, characterized by the largest platinum crystallite size (Table 1.3; Fig. 1.6). Larger particles are better attached to the carbon support and, therefore, to a lesser

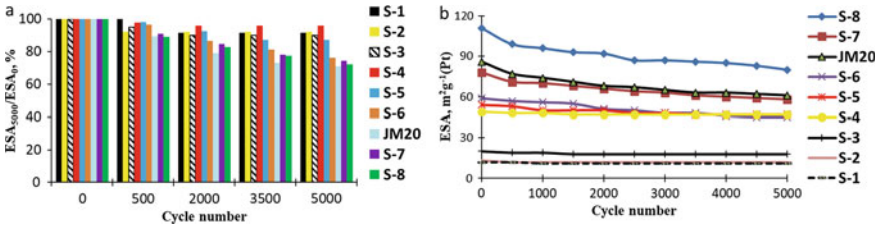

Fig. 1.6 Dependence of the relative degree of degradation (**a**) and ESA (**b**) on the number of cycles during cycling in the potential range 0.6–1.0 V

Table 1.3 Sample characteristics calculated after stress testing

Sample	ESA^{5000}, $m^2/g(Pt)$	Relative stability, %
S-1	11 ± 1	92
S-2	12 ± 1	92
S-3	18 ± 2	90
S-4	47 ± 5	96
S-5	47 ± 5	87
S-6	45 ± 5	76
JM20	61 ± 6	71
S-7	58 ± 6	74
S-8	80 ± 8	72

extent detach and aggregate. These samples were obtained using reducing agents of hydrazine and sodium borohydride.

Samples S-6, S-7, S-8 and the JM20 catalyst are characterized by the lowest stability during prolonged stress testing—about 70% and the lowest average crystallite size from 1.1 to 2.1 nm. The rapid degradation of these materials is associated with the small size of the NPs, which are irreversibly detached from the surface of the support, agglomerate during cycling, dissolve and reprecipitate to form larger particles.

It should be noted that sample S-4 shows high relative stability throughout the stress test, despite the relatively large crystallite size of 3.5 nm and a moderate surface area of 49 $m^2/g(Pt)$. On the one hand, this high stability can be explained by the equal distance of platinum NPs from each other on the surface of the support and, therefore, they tend to aggregate to a lesser extent, as well as crystallites of more than 3 nm are better attached to the carbon support. It is important to note that all samples are characterized by a monotonous decrease in ESA during stress testing (Fig. 1.6b). Despite the high degree of degradation, the highest residual surface area is characterized by sample S-8, the value of which exceeds the ESA of the commercial analogue—JM20.

Thus, we can conclude that with an increase in the particle size of platinum, the relative stability of Pt/C catalysts increases with prolonged cyclicity.

1.3.2 The Effect of the Spatial Distribution of Pt NPs on the Degree of Degradation of Pt/C Electrocatalysts

To study the effect of the spatial distribution of Pt NPs, 5 materials were obtained with different mass fractions of platinum, but with a close average crystallite size of about 2.0 nm (Table 1.4; Fig. 1.7). It was based on the idea that in these materials, with a close degree of aggregation, platinum NPs are located at different distances from each other. The larger the mass fraction, the smaller the distance between the NPs.

The obtained samples are characterized by a mass fraction of platinum from 23 to 39% and an average crystallite size of about 2.1 nm (Table 1.4). It should be noted that with an increase in the mass fraction of platinum in the samples, there is a slight increase in the average crystallite size, as well as a decrease in ESA (Table 1.4).

The calculated values of the distance between the NPs show that the larger the mass fraction of platinum in the sample, the smaller the distance between the particles due to their larger number (Table 1.4).

For all the studied Pt/C catalysts, an increase in the currents in the hydrogen region from cycle to cycle is observed. Figure 1.8 shows the intermediate and final CV stress tests for clarity. The most pronounced decrease in currents in the hydrogen region is characteristic of catalyst S2-1 and the commercial analogue of JM20, which is characterized by low relative stability of 71% (Fig. 1.8; Table 1.5).

The relative stability of the catalysts increases with an increase in the mass fraction of platinum in the samples (Table 1.5; Fig. 1.9a). The highest stability during prolonged stress testing is characterized by sample S2-5 88%, which also shows the

Table 1.4 Structural and electrochemical characteristics of Pt/C samples

Sample	ω(Pt) (%)	D_{av} (nm)	ESA^0, $m^2/g(Pt)$	S_{geom}, $m^2/g(Pt)$	Degree of aggregation	λ, nm
JM20	20 ± 0.6	2.0	86 ± 9	140	0.39	9.3
S2-1	23.5 ± 0.7	2.1	59 ± 6	135	0.56	8.7
S2-2	32 ± 1.0	2.1	73 ± 7	134	0.45	6.8
S2-3	33.6 ± 1.0	2.3	68 ± 7	122	0.44	7.5
S2-4	35 ± 1.1	2.3	59 ± 6	120	0.51	7.4
S2-5	39 ± 1.2	2.3	48 ± 5	124	0.61	6.4

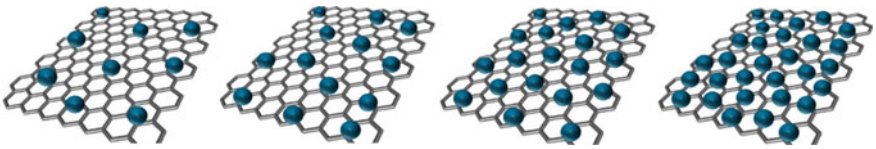

Fig. 1.7 Schematic representation of the spatial distribution of platinum NPs on the surface of a carbon support with a close average crystallite size

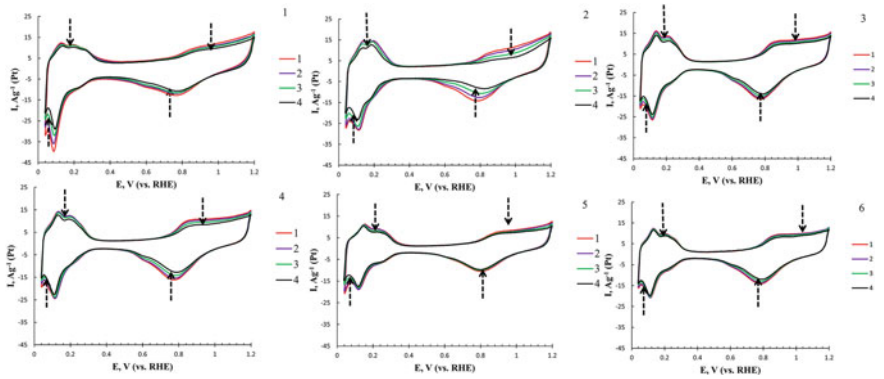

Fig. 1.8 Initial cyclic voltammograms, 500, 2000 and 5000 cycles (1, 2, 3 and 4 respectively). The sweep rate of the potential is 20 mV/s. 0.1 M $HClO_4$ solution saturated by Ar at room temperature. Samples: 1—JM20, 2—S2-1, 3—S2-2, 4—S2-3, 5—S2-4, 6—S2-5

Table 1.5 Characteristics of Pt/C samples calculated after stress testing

Sample	ESA^{5000}, $m^2/g(Pt)$	Relative stability, %
JM20	61 ± 6	71
S2-1	45 ± 5	76
S2-2	59 ± 6	81
S2-3	57 ± 6	84
S2-4	51 ± 5	86
S2-5	42 ± 4	88

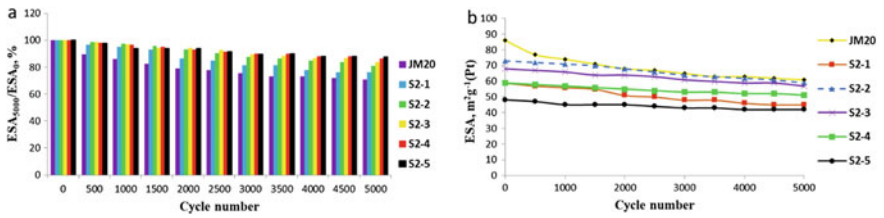

Fig. 1.9 Dependence of the relative degree of degradation (**a**) and ESA (**b**) on the number of cycles during cycling in the potential range 0.6–1.0 V

lowest surface area throughout the entire cycle (Table 1.5; Fig. 1.9). The calculated value of the degree of particle aggregation for this sample is the highest among all studied, and this fact indicates that platinum NPs S2-5 consist of several crystallites, which is confirmed by the low initial ESA.

For the remaining Pt/C catalysts, the values of the degree of aggregation are close, and, therefore, it is possible to compare the effect of the average distance between platinum particles on stability (Table 1.5). Relative stability increases in the series

JM20 > S2-1 > S2-2 > S2-3 > S2-4. As previously indicated, the irreversible processes of changes in the catalysts during stress testing are associated with the aggregation of Pt particles and the complete separation of NPs from the surface of the carbon support. When considering these samples, we can conclude that for catalysts with a small mass fraction of platinum, the most characteristic method of degradation may be the separation of platinum NPs, and, as a consequence, a decrease in ESA. The contribution of the aggregation of platinum NPs to the degradation of samples with a low loading of platinum (about 20%) is less evident. For samples with a higher metal content, the separation of NPs is apparently less characteristic, and aggregation processes are difficult, since the particles are equidistant from each other. All these factors lead to increased stability in prolonged stress testing.

Samples S2-2, S2-3 and commercial JM20 are characterized by the highest residual surface area (Fig. 1.9b).

All studied materials confirmed a straightforward relationship: with an increase in the mass fraction of platinum in the catalyst, relative stability increases (the degree of degradation decreases).

Additionally, the inverse proportional dependence of the stability of the catalysts on the distance between the particles is determined. The higher the mass fraction of platinum in the sample, and, correspondingly, the lower the λ value (at a close degree of aggregation and the average crystallite size of platinum), the higher the relative stability of the catalyst during prolonged stress testing in the "soft" range of potentials. It is possible that the detachment of NPs makes a greater contribution to the degradation of catalysts, since for Pt/C with a small mass fraction of platinum, the loss of a part leads to a significant decrease in surface area.

Sample S2-2 is distinguished from the general dependence, which is characterized by an average distance between particles and at this low stability.

1.3.3 The Effect of the Structure of Bimetallic Nanoparticles on the Stability of Catalysts with Stress Testing

To study the stability of the catalysts in the "hard" mode of stress testing, PtCu/C catalysts with the "solid solution" and "shell-core" structures were obtained.

The actual composition of the obtained samples turned out to be close to the calculated one: the mass fraction of metals in PtCu/C and Pt(Cu)/C samples is 28% and 29%, with a pure platinum content of 21% and 20%, respectively (Table 1.6). The results obtained by X-ray fluorescence method confirmed that the ratio of metals in the samples is close to the calculated 1:1.

Photographs of platinum-copper catalysts obtained by TEM (Fig. 1.10) show a large number of small-sized (2–4 nm) Ns. The Pt(Cu)/C sample is characterized by the presence of large NPs or aggregates of NPs, 10–15 nm in size. Taking into account the multistage procedure for producing the Pt(Cu)/C catalyst, as well as the presence of NPs of various sizes in this material, it can be assumed that part of the precursors

Table 1.6 Structural and electrochemical characteristics of the studied catalysts

Sample	The composition of the metal component		ω(Pt + Cu), %	ω(Pt), %	D_{av}, nm	ESA^0, $m^2/g(Pt)$
	Initial	After standart. CV				
Pt(Cu)/C	$Pt_{0.8}Cu$	$Pt_{1.5}Cu$	29	20	3.9	96 ± 10
PtCu/C	$Pt_{1.0}Cu$	$Pt_{2.1}Cu$	28	21	3.2	75 ± 8
HiSPEC	Pt	Pt	20	20	2.0	98 ± 10

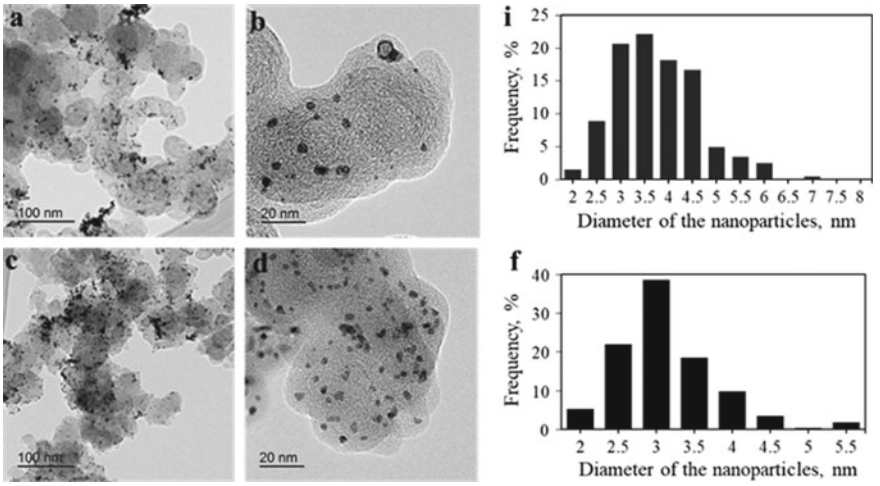

Fig. 1.10 Transmission electron microscopy photographs (**a**, **b**, **c**, **d**) and diagrams (**i**, **f**) of the nanoparticles size distribution for "core-shell" Pt(Cu)/C (**a**, **b**, **i**) and "Solid Solution" PtCu/C (**c**, **d**, **f**) samples

at each subsequent synthesis stage is spent not only on the growth of particles formed at the previous stage, but also on the formation of new platinum NPs. Note that for a certain number of large particles in the Pt(Cu)/C sample, the shell-core architecture is clearly distinguishable, however, for NPs with a size of 2–3 nm, the determination of the platinum shell by TEM data is impossible. For a commercial Pt/C sample, the average NP size is 2.0 nm according to TEM.

Based on the histograms of the size distribution of NPs (Fig. 1.10c, f), we can conclude that there is a wider size distribution and a larger average NP size for the Pt(Cu)/C sample in comparison with the PtCu/C material, which was obtained by the simultaneous reduction of precursors.

The development and cleaning of the surface of NPs, occurring on all the studied catalysts in the process of their electrochemical standardization, leads to the growth and subsequent stabilization of the current strength (Fig. 1.11).

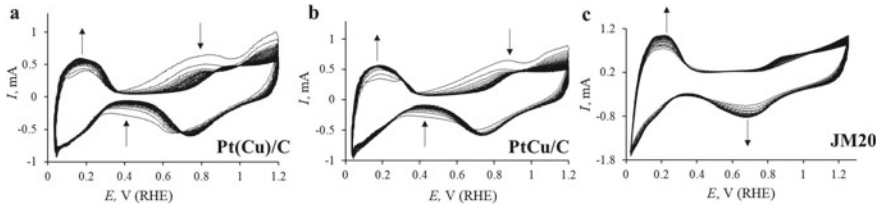

Fig. 1.11 Cyclic voltammograms of the metal-carbon catalysts in the process of standardizing cycling. The sweep rate of the potential is 200 mV/s. 0.1 M $HClO_4$ solution saturated by Ar at room temperature

The nature of the change in the type of CV is similar for both bimetallic catalysts, the establishment of stationary current values occurs rather quickly, after 10–20 cycles. The presence of shallow maximums of the anode current in the potential region of about 0.8 V in the first cycles of the potential sweep can be due to the selective dissolution of copper atoms from the Pt–Cu solid solution [29]. We should like to note that the type of standardizing CV for Pt/C and PtCu/C electrocatalysts are different. This is due to the presence of an alloying component in the bimetallic system.

Initially, the stability of PtCu/C catalysts was studied in the "soft" test mode: 5000 cycles in the potential range 0.6–1.0 V (Fig. 1.12). The structure of platinum-copper catalysts also affects the change in the composition of the metal component as a result of standardization and stress testing. The NPs in the Pt(Cu)/C catalyst obtained by successive multi-stage reduction of precursors seem to acquire a uniform protective platinum shell faster. Therefore, for the Pt(Cu)/C catalyst, the selective dissolution of copper during standardization and the subsequent stress test in the potential range 0.6–1.0 V is much less pronounced than for the PtCu/C sample (Table 1.7). At the same time, both bimetallic electrocatalysts show higher stability than the commercially available Pt/C sample (Fig. 1.12a). We believe that bimetallic NPs are more firmly attached to the surface of the carbon support and their tendency to peel and agglomerate is less than that of Pt NPs. Note that in the "soft" multiple cycling mode, even less resistant to Pt/C degradation material retains about 60% of its ESA (Table 1.7; Fig. 1.12b).

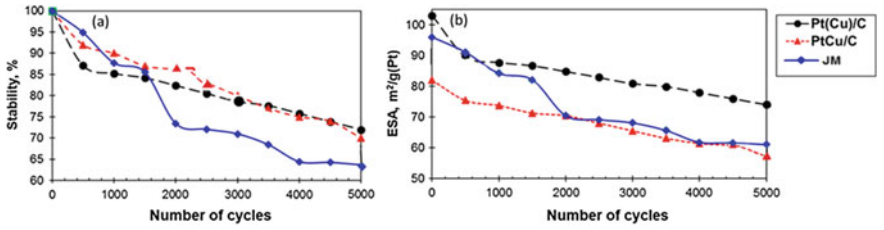

Fig. 1.12 Dependence of the relative stability (**a**) and ESA (**b**) on the number of cycles during cycling in the potential range 0.6–1.0 V

Table 1.7 Summary table of the results of stress testing of platinum-copper and Pt/C materials

Stress testing conditions	Sample	Stability, %	Composition after stress testing
After stress-test 0.6–1.0 B (5000 cycles)	Pt(Cu)/C	82	$PtCu_{0.6}$
	PtCu/C	70	$PtCu_{0.4}$
	HiSPEC	64	
After stress-test 0.6–1.4 B (500 cycles)	Pt(Cu)/C	79	$PtCu_{0.5}$
	PtCu/C	79	$PtCu_{0.3}$
	HiSPEC	15	

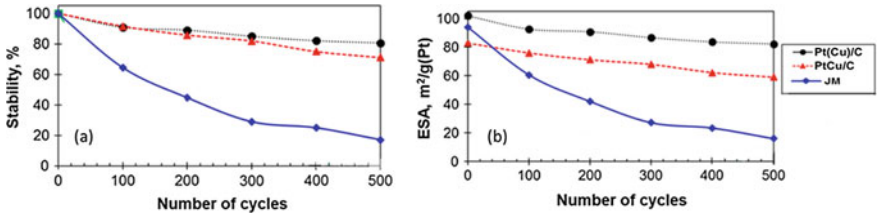

Fig. 1.13 Dependence of the relative stability (**a**) and ESA (**b**) on the number of cycles during cycling in the potential range 0.6–1.4 V, 500 cycles

As a result, the minimum decrease in the active surface of platinum according to the results of the stress test was demonstrated by the Pt(Cu)/C sample. Expanding the range of stress testing potentials to 0.6–1.4 V, as expected, led to an increase in the rate of catalyst degradation. Moreover, the differences in the behavior between Pt/C and platinum-copper samples intensified: after 500 cycles, the stability of the Pt(Cu)/C and Pt/C catalysts was 82 and 72%, while for JM it was 20% (Fig. 1.13a).

After the stress test, ESA and the relative stability of platinum-copper catalysts are 4–8 times higher than for Pt/C (Table 1.7; Fig. 1.13b). It has already been noted that at high potentials, platinum catalyzes the oxidation of a carbon support in the direct contact zone, which facilitates the separation of NPs. Apparently, the presence of copper atoms at the NP/support interface decreases the catalytic activity of the metal with respect to the carbon oxidation reaction.

A comparative study of platinum-carbon materials with different mass fractions of metal showed that in almost all cases there is a direct relationship between the loading of platinum in the electrocatalyst and the increase in its resistance to degradation during stress testing in the potential range 0.6–1.0 V.

1.4 Conclusions

A number of new Pt/C catalysts with a mass fraction of 18 to 39% and an average crystallite size from 1.1 to 5.7 nm were obtained by liquid-phase synthesis methods using various reducing agents.

It was determined that a decrease in the average crystallite size of platinum leads to an increase in the area of the electrochemically active surface of the electrocatalyst, but at the same time, its resistance to degradation during prolonged cycling in the "soft" range of potentials decreases.

It is shown that materials with the smallest diameters of platinum crystallites are characterized by reduced relative stability, but they have the largest residual areas after stress testing, which makes them promising for use in low-temperature fuel cells.

A comparative study of the electrochemical behavior of platinum-copper and commercial Pt/C catalysts with a 20% loading of platinum under different voltammetric stress testing modes showed that bimetallic systems exhibit higher stability, especially under severe cycling conditions, when the potential variation range is 0.6–1.4 V. The positive effect of the doping component on stability can be due to a more solid nanoparticles fixation on the surface of the support and a lower rate of carbon oxidation at the interface with nanoparticles compared to Pt/C. The thermodynamic stability of the metal nanoparticles themselves in platinum-copper catalysts can also be higher than in Pt/C, due to the larger average size of the NPs.

An important role in the behavior of the catalysts is played not only by the qualitative composition of NPs (alloying with copper), but also by their structural features. A Pt(Cu)/C sample obtained by multistage metal deposition is characterized by a lower degree of degradation in comparison with a catalyst based on Pt-Cu NPs with a solid solution structure. The reason for the established differences may be a higher concentration of platinum in the surface layers of Pt(Cu)/C NPs in the "as obtained" state, which leads to the rapid formation of a protective platinum shell during subsequent selective dissolution of copper.

Most of the obtained Pt/C and PtCu/C catalysts are characterized by comparable or superior electrochemical characteristics to the commercial analog of JM20.

Acknowledgements This research was supported by the Ministry of Education and Science of the Russian Federation (project No. 13.3005.2017/4.6).

References

1. R. O'Hayre, S.-W. Cha, W. Colella, F.B. Prinz, *Fuel Cell Fundamentals*, 2nd edn. (Wiley Inc., New York, 2009), p. 576
2. N.V. Korovin, Int. Sci. J. **10**, 8 (2004)
3. V.S. Bagotskiy, N.V. Osetrova, A.M. Skudin, Electrochemistry **39**, 1027 (2003)
4. G. Crawley, *Fuel Cell Today*, vol. 1 (2006)

5. D. Thompsett, *Handbook of Fuel Cells. Fundamentals, Technology and Applications* (2003), vol. 3, p. 6
6. A.B. Yaroslavtsev, Y.A. Dobrovolsky, N.S. Shaglaeva, L.A. Frolova, E.V. Gerasimova, E.A. Sanginov, Russ. Chem. Rev. **81**, 191 (2012)
7. S. Litster, G. McLean, Power Sources **130**, 61 (2004)
8. H. Lv, D. Li, D. Strmcnik, A.P. Paulikas, N.M. Markovic, V.R. Stamenkovic, Nano Energy **29**, 149 (2016)
9. O.T. Holton, J.W. Stevenson, Platin. Metals Rev. **57**, 259 (2013)
10. E.H. Yu, U. Krewer, K. Scott, Energies **3**, 1499 (2010)
11. J. Chen, D.S. Jiang, G.A. Cameron, B. Hards, R.J. Potter, Platin. Metals Rev. **31**, 173 (1987)
12. S.V. Belenov, AYu. Pakharev, NYu. Tabachkova, E.B. Mikheykina, L.L. Vysochina, T.A. Lastovina, Int. J. Hydrogen Energy **41**, 1609 (2016)
13. I.N. Leontyev, S.V. Belenov, V.E. Guterman, P. Haghi-Ashtiani, A.P. Shaganov, B. Dkhil, J. Phys. Chem. **115**, 5429 (2011)
14. H. Zhu, X. Li, F. Wang, Int. J. Hydrogen Energy **36**, 9151 (2011)
15. A.A. Alekseenko, V.E. Guterman, V.A. Volochaev, Springer Proc. Phys. **175**, 37 (2016)
16. N.V. Smirnova, A.B. Kuriganova, D.V. Leontyeva, I.N. Leontyev, A.S. Mikheykin, Kinet. Catal. **54**, 262 (2013)
17. C. Chunhua, G. Lin, L. Hui-Hui, Yu. Shu-Hong, Nano Lett. **12**, 5885 (2012)
18. U.A. Paulus, A. Wokaun, G.G. Scherer, T.J. Schmidt, V. Stamenkovic, N.M. Markovic, P.N. Ross, Electrochim. Acta **47**, 3787 (2002)
19. M. Oezaslan, F. Hasche, P. Strasser, J. Phys. Chem. Lett. **4**, 3273 (2013)
20. M. Ji, J. Liu, J. Zhang, H. Zhu, Nano Res. **8**, 271 (2015)
21. R. Awasthi, C.S. Sharma, Int. J. Electrochem. Sci. **9**, 5607 (2014)
22. D.A. Cantane, F.E.R. Oliveira, S.F. Santos, F.H.B. Lima, Appl. Catal. **136**, 351 (2013)
23. V.E. Guterman, A.A. Alekseenko, V.A. Volochaev, NYu. Tabachkova, Inorg. Mater. **52**, 23 (2016)
24. D. Wang, H.L. Xin, R. Hovden, H. Wang, Y. Yu, D.A. Muller, F.J. DiSalvo, H.D. Abruña, Nat. Mater. **12**, 81 (2013)
25. M.R. Tarasevich, V.A. Bogdanovskaya, V.N. Andreev, Catal. Ind. **6**, 159 (2014)
26. A.A. Alekseenko, V.E. Guterman, V.A. Volochaev, S.V. Belenov, Inorg. Mater. **51**, 1258 (2015)
27. A.A. Alekseenko, E.A. Moguchikh, O.I. Safronenko, V.E. Guterman, Int. J. Hydrogen Energy **43**, 22885 (2018)
28. A.A. Alekseenko, V.E. Guterman, S.V. Belenov, V.S. Menshikov, NYu. Tabachkova, O.I. Safronenko, E.A. Moguchikh, Int. J. Hydrogen Energy **43**, 3676 (2018)
29. L. Dubau, M. Lopez-Haro, J. Durst, F. Maillard, Catal. Today **262**, 146 (2016)

Chapter 2
Investigation of the Effect of Different Organic Additives on Morphology and Electrocatalytic Activity of Platinum Nanomaterials Towards Oxygen Reduction Reactions

Sergey V. Belenov, Weldegebriel G. Yohannes, Nikolay V. Lyanguzov, and Vadim A. Volochaev

Abstract In the present study, different carbon-supported platinum nanomaterials were prepared using electrodeposition method and the influences of some organic additives, such as potassium citrate, Nafion and polyvinylidene fluoride (PVDF) on the morphology, electrochemically active surface area (ESA) and electrocatalytic activity of platinum nanomaterials (Pt/Vulcan XC-72) were evaluated. The materials were electrodeposited on a rotating disk electrode (RDE) from the electrolyte hexachloroplatinic acid (H_2PtCl_6) and H_2SO_4 in the absence and presence of the organic additives. The materials obtained were characterized using powder X-ray diffraction, scanning electron microscopy, electrochemical methods. In addition, the electrocatalytic activity of the materials towards oxygen reduction reactions was evaluated by employing linear sweep voltammetry on RDE at 1000 rpm. The presence of the organic additives increased the overpotential at the growth stage of the particles, leading to a decrease in the particle size and hence an increase in the ESA of platinum nanoparticles from 19 to 43 $m^2/g(Pt)$ The electrocatalysts prepared using the different organic additives have the following increasing order of electrochemical activities towards the ORR in an aqueous solution of $HClO_4$: citrate < without the organic additives < Nafion < PVDF in the potential range of ca. 0.7–0.9 V. This electrochemical behavior can be attributed to the differences in the particle size, ESA, and the morphology of the synthesized carbon-supported platinum nanomaterials.

S. V. Belenov (✉) · V. A. Volochaev
Chemistry Faculty, Southern Federal University, Zorge St. 7, Rostov-on-Don, Russia 344090
e-mail: sbelenov@sfedu.ru

W. G. Yohannes
Department of Chemistry, College of Natural and Computational Sciences, Addis Ababa University, Addis Ababa, Ethiopia

N. V. Lyanguzov
Physical Faculty, Southern Federal University, Zorge St. 5, Rostov-on-Don, Russia 344090

Southern Research Center RAS, Rostov-on-Don, Russia 344006

I. A. Parinov et al. (eds.), *Advanced Materials*, Springer Proceedings in Materials 6, https://doi.org/10.1007/978-3-030-45120-2_2

2.1 Introduction

Controlling the morphology, microstructure, and electrochemical properties of platinum electrodeposits with a developed surface is a key factor to enhance catalytic activity of electrode materials. This can be possibly achieved by varying electrodeposition parameters and incorporating different organic additives into the electrolyte used [1, 2]. One of the main reasons for the degradation of Pt-based electrocatalysts is the loss of the electrochemically active surface area by agglomeration of catalyst particles. Metal nanoparticles, because of their small size and high surface energy, have an inherent tendency toward the formation of agglomerates (bigger particles) to minimize their high surface energy and hence to be stabilized. Organic additives (stabilizing agents), usually surface active substances or polymers, are often used to prevent the metal particles against agglomeration, to control the size and shape by adsorbing to the particle surfaces or by separating the metal nanoparticles from each other via electrostatic or steric stabilization [3–6]. Thus, employing organic additives can effectively influence the structure of the prepared Pt nanoparticles to attain improved electrocatalytic activity, to obtain smaller size, uniform dispersion and highly dispersed Pt nanoparticles over the supporting carbon materials by limitation of the growth of metal nanoparticles. In our previous study [7], the use of the organic compound ethylene glycol in the electrodeposition of platinum over the carbon support Vulcan XC-72 resulted in a significant decrease in the Pt nanoparticles size and an enhanced catalytic activity towards oxygen reduction reaction. To remove the organic additives from the obtained catalysts, it usually necessary thermal and/or oxidative post-treatment. Harsh conditions of post-treatment may lead to agglomeration of metal nanoparticles, whereas soft conditions may result in an incomplete removal of organic additives, causing subsequent reduction in the catalytic activity of the resulting material [8]. Nevertheless, a number of publications [9–11] have shown that certain types of post-treatment of Pt/C catalysts, such as washing with different alcohol, centrifugation, heat treatment in inert atmosphere etc. can lead to a complete removal of additives and highly effective catalysts towards oxygen reduction reaction that are comparable or can have even higher activity than that of commercial electrocatalysts.

Citric acid and its salts are often used as organic additives in the formation of platinum nanoparticles in the chemical reduction of platinum precursor [12–15]. Citrates are characterized by low cost, high efficiency as a stabilizing agent and the simplicity to remove residual of the additive from the prepared material. Chou et al. [12] using different aqueous solutions containing citric acid prepared enhanced catalytic activity of Pt/C and Pt–Ru/C electrocatalysts by a factor of about 1.5 and 2.8, respectively compared to those prepared without involving the additives. The authors attributed the increased electroactivities to the citric acid playing dual roles as both a stabilizing agent and particle size reducing agent in the aqueous solutions. In other studies, it was shown that some additives such as polyvinylpyrrolidone (PVP) affected not only the average size but also the shape of the platinum nanoparticles [4, 16, 17]. Tang et al. [16] reported that when the ratio of PVP/Pt varies, it allows

changing not only the average size of nanoparticles but also their shape. Ye et al. [4] studied the effect of PVP on the surface area and catalytic activity of Pt catalyst and demonstrated that PVP being adsorbed onto some of the surface of growing platinum crystals, complicates further deposition of platinum atoms on these surfaces, resulting in a significant change in the morphology of the obtained Pt deposits. This leads to an increase in the value of ESA and catalytic activity in the methanol oxidation reaction as compared to a Pt catalyst synthesized without the addition of PVP. Sharma et al. [17] synthesized platinum nanoparticles via electrodeposition method using CNT coated carbon fiber and reported an enrichment of the catalytic active Pt surfaces such as Pt (100) upon increasing PVP concentration.

The proton conductive polymer Nafion is commonly used as a binding material when the porous dispersed Pt/C catalyst layer is applied onto the surface of electrodes and also in the formation of catalytic active layer in the membrane electrode assemblies (MEAs) of fuel cells. Moreover, in some cases the polymer Nafion is used as a stabilizer in the wet chemical synthesis of platinum nanoparticles. Liu et al. [18] reported that using a small amount of Nafion resulted in higher activity towards ORR as compared to platinum black and commercial Pt/C material while the activity of these catalysts in MOR was found to be very low.

The analysis of literature data indicates that the introduction of organic additives into platinized electrolyte and variation of their concentration affects the microstructure and the catalytic activity of the platinum materials. However, there are limited studies on the effects of organic additives of different natures on platinum crystallite size, particle size, ESA, morphology and electrochemical behavior of the synthesized catalysts. Therefore, the objective of the present work was to prepare carbon-supported platinum nanomaterials by electrodeposition from the electrolyte hexachloroplatinic acid (H_2PtCl_6) and H_2SO_4 in the absence and presence of different organic additives such as potassium citrate, Nafion and PVDF and to investigate their influence on platinum crystallite size, particle size, morphology and electrocatalytic activity of the prepared platinum nanomaterials towards oxygen reduction reactions.

2.1.1 Research Purpose

It is investigated the effect of different organic additives during electrochemical deposition of Pt on carbon supported on morphology and electrocatalytic activity of obtained platinum nanomaterials towards oxygen reduction reactions.

2.2 Experimental

2.2.1 Preparation of Electrode

Carbon black Vulcan XC-72 (Cabot Corporation, with surface area of 270 $m^2\ g^{-1}$) was used as carbon support. The carbon support for the platinum nanoparticles turns out to be critically important to provide high surface area for their dispersion, stability and electrical conductivity. Hence, a homogeneous suspension was prepared by mixing Vulcan XC-72 carbon, isopropanol and Nafion by ultrasonication and magnetic stirring. Then, the resulting suspension was pipetted onto a previously dried polished and cleaned surface of glassy carbon disc electrode to form a thin porous carbon layer (ca. 4 μm). Further details for the method of preparation of the carbon layer and the electrodes is described in [7].

2.2.2 Electrodeposition of Platinum

Electrochemical experiments were carried out using a common three-electrode cell at room temperature, glassy carbon electrode is coated with a layer of Vulcan XC-72 carbon-Nafion as working electrode, a platinum wire as a counter electrode and a saturated KCl/AgCl electrode as reference electrode. However, all the potentials in this work are given relative to standard hydrogen electrode (SHE) unless otherwise noted. Electrodeposition of platinum was conducted using a rotating disc glassy carbon electrode at a speed of 1000 rpm, as described in [19].

Electrochemical measurements were performed with potentiostat-galvanostat and rotator (Pine Research Instrumentation, USA). Galvanostatic electrodeposition technique was conducted in 1 M H_2SO_4, 5 mM chloroplatinic acid (H_2PtCl_6) aqueous solution in the presence and absence of the organic additives such as potassium citrate, Nafion and PVDF.

2.2.3 Characterization of Pt/C

2.2.3.1 Characterization of Structure

The morphology of prepared Pt/C electrodes and average size of the electrodeposited Pt particles were investigated by scanning electron microscopy (Zeiss Supra 25, 20 keV). In order to analyze morphology of prepared Pt/C electrodes and Pt particles size and distribution of carbon-supported using image analysis software called ImageJ.

The X-ray powder diffraction data were obtained using ARL X'TRA diffractometer, CuK_α radiation ($\lambda = 1.54056$ Å). Measurements were carried out in the range of 2θ angles 35°–50° with scan rate—0.5°/s.

A zero-background holder and polymer tissues were used in order to mount the samples. The crystallite size for all the prepared Pt/C electrodes is calculated from the width of (111) diffraction peak using Scherer equation (2.1).

$$D = \frac{0.95x\lambda}{\beta_{2\theta}\cos\theta} \tag{2.1}$$

where D is the average crystallite size in (nm), λ is the wave length ($\lambda = 1.54056$ Å), $\beta_{2\theta}$ and θ are the full width at half maximum (FWHM) and a diffraction angle of (111) reflection in radians, respectively.

2.2.3.2 Electrochemical Measurements

After electrodeposition of Pt on carbon, the electrode was rinsed thoroughly with bi-distilled water and the obtained catalyst electrode was examined in a freshly prepared 100 mL of 0.1 M $HClO_4$ solution. $HClO_4$ was used as an electrolyte in all electrochemical measurements because it is considered as a non-adsorbing or a weakly adsorbing electrolyte unlike H_2SO_4 and H_3PO_4. Prior to each electrochemical experiment, pure argon was purged through the electrolyte for 30 min to remove oxygen dissolved in the solution. Then, the electrode was CV scanned with 100 cycles at a scan rate of 200 mV s^{-1} in the potential range between −0.04 and 1.2 V versus SHE. Then, cyclic voltammograms (2 cycles) with a scan rate of 20 mV s^{-1} were used to determine the ESA of the Pt catalysts. The ESA was estimated by measuring the charge associated with the hydrogen adsorption/desorption at the potential region about −0.03 to 0.3 V as detailed in [20]. Briefly, determination of the electrochemically active surface area was carried out by measuring the quantity of electricity consumed according to Formula (2.2).

$$ESA = \frac{Q}{m \times 210} \tag{2.2}$$

where, Q is the average charge for the hydrogen adsorption and desorption (μC) which is obtained after double-layer correction; m is the mass of platinum loading (μg) and the numerical value 210 (μC cm^{-2}) represents the charge required to oxidize a monolayer of hydrogen on Pt surface.

Linear sweep voltammograms (LSVs) on a rotating disk electrode (RDE) were measured to evaluate the electrocatalytic activity of the obtained Pt/C materials towards oxygen reduction reactions (ORR). In this case, after the ESA measurements, a 0.1 M $HClO_4$ electrolyte solution was saturated with oxygen at atmospheric pressure for about 1 h. Then, while continuing to purge oxygen gas, the potential of the working electrode was changed from 1.196 to 0.020 V with a sweep rate of

20 mV s^{-1}. The different disk electrode rotation rates were the following: 400, 600, 1000, 1400, 1800 and 2400 rpm. To compare the activity of the catalysts, measured currents were normalized by the mass of platinum (A/g of Pt) and/or by the ESA of the catalyst (mA/cm^2 of Pt) [21].

2.3 Results and Discussion

2.3.1 Platinum Electrodeposition on Carbon Supported

In order to obtain deposits of platinum with the highest value of ESA, cathodic current corresponding to platinum electrodeposition was optimized according to the results given in a previous study [7] and was found to be ca. 1.42 mA. The addition of the organic additives increases the deposition overpotential of platinum (Fig. 2.1) possibly due to their adsorption on the surface of the carbon support and on the growing platinum particles. However, there is no such a significant difference observed in the effect of the studied organic additives at the growth stage of the Pt particles above 2 s ($t > 2$ s) as shown in Fig. 2.1.

Figure 2.2 shows diffractogram patterns for the prepared catalysts in the presence and absence of the organic additives. The diffractogram patterns exhibit reflections that are characteristic for pure platinum phase for the prepared catalysts.

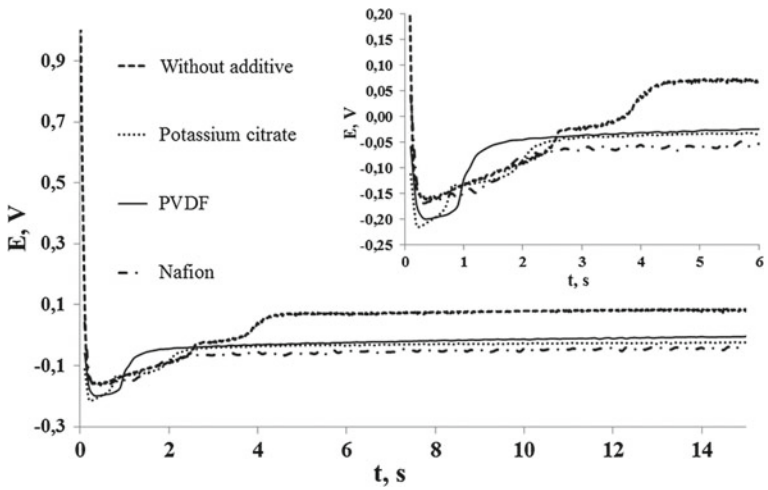

Fig. 2.1 Chronopotentiograms for the electrodeposition of platinum on the surface of the carbon support Vulcan XC-72, cathodic current = 1.42 mA, rotation rate—1000 rpm. The electrolyte is an aqueous solution of 5 mM H_2PtCl_6, 1MH_2SO_4 in the presence and absence of the various organic additives: 0.01 M potassium citrate, 0.01% polyvinylidene fluoride (PVDF), 0.01% Nafion

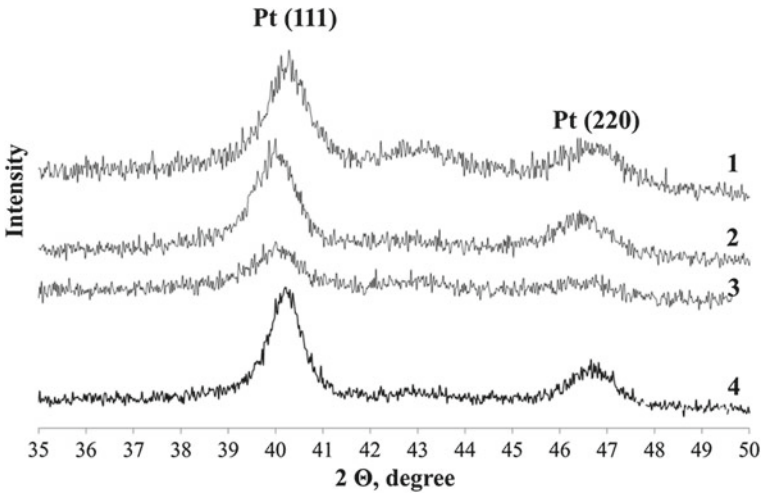

Fig. 2.2 Diffractograms for Pt/C materials. The electrolyte is an aqueous solution of 5 mM H_2PtCl_6, 1M H_2SO_4 in the presence of various additives: 1—0.01% Nafion, 2—0.01% PVDF, 3—0.01 M potassium citrate, 4—without additives

All the synthesized materials exhibit clear characteristic diffraction peaks to the corresponding Pt (111) and the Pt (200) crystal planes emerged at 2θ values about 40 and 46, respectively. However, the 'full width at half maximum reflection' (FWHM) for the platinum materials formed under various conditions are considerably different. The most pronounced broadened reflection is noticed in the case of the organic additive potassium citrate. In fact, this is consistent with the result from Scherrer's equation (see, Sect. 2.2). The incorporation of potassium citrate into the electrolyte resulted in the reduction of the average platinum crystallite size from 10 to 7 nm (Table 2.1).

The organic additives Nafion and PVDF also reduce the average size of platinum crystallites, but to a lesser extent relative to that of potassium citrate. The decrease in the crystallites size can be attributed to the adsorption of additives on the growing platinum particles which in turn leads to the inhibition of further growth of the particles. The result found using the organic additives is consistent with the findings of

Table 2.1 Characteristics of platinum electrodeposits obtained in aqueous electrolytes with different organic additives, deposition time—15 s, cathodic current—1.42 mA, $Q \approx 21$ μC, weight of electrodeposited platinum ≈ 10.78 μg

Additives	D (XRD) (nm)	ESA (m^2g^{-1} Pt)	D (SEM) (nm)
Without additives	10 ± 0.5	19 ± 1	150
Potassium citrate	7 ± 0.5	34 ± 2	85
Nafion	8 ± 0.5	35 ± 2	115
PVDF	9 ± 0.5	43 ± 2	135

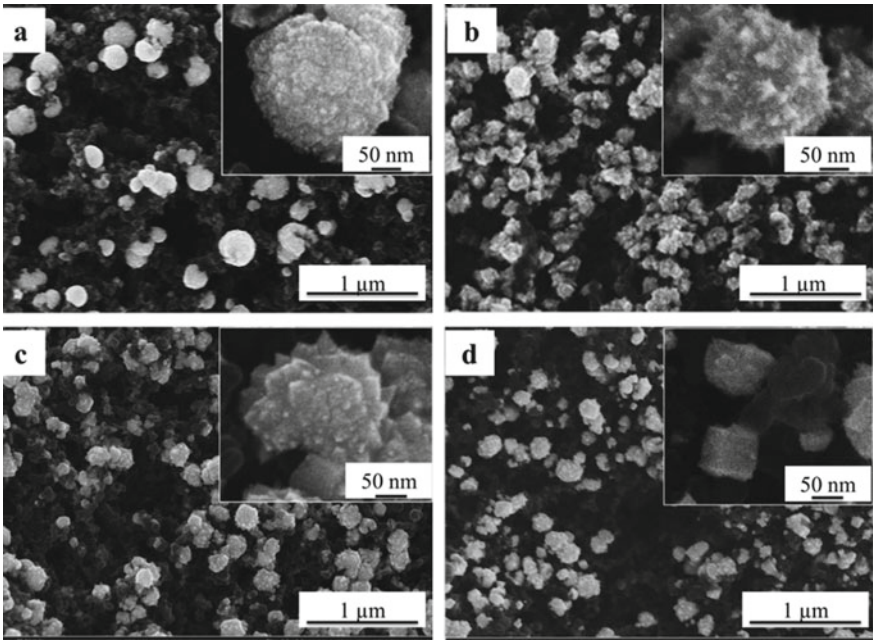

Fig. 2.3 SEM images at different magnifications for Pt particles obtained by electrodeposition on a carbon support in an aqueous electrolyte: **a** without any additives, **b** 0.01 M potassium citrate, **c** 0.01% of polyvinylidene fluoride (PVDF), **d** 0.01% Nafion

previous reports from [4, 5, 12, 17, 18]. The obtained platinum particles on Vulcan XC-72 (Fig. 2.3) are large aggregates with a wide range of size distribution (predominantly from 85 to 150 nm) consisting of fused crystallites with size ranging from 7 to 10 nm.

Based on the results of SEM analysis, the introduction of the organic additives into the electrolyte resulted in a reduction of the average size of the deposited platinum particles (Table 2.1; Fig. 2.3). Most notably, this effect is pronounced in the presence of potassium citrate. The average particle size of the deposits decreased approximately from 150 nm to 85 nm. The average particle size of platinum for the materials determined using the SEM corresponds well with the average size of the crystallites of platinum calculated from XRD. Thus, for the electrocatalyst prepared in the electrolyte containing the organic additive, according to the SEM (Fig. 2.3a) is characterized by spherical platinum deposits with the size dispersion of ca. 50–250 nm and with an average platinum crystallite size of about 10 nm (Table 2.1). When considering the SEM images at a higher magnification (the inset of Fig. 2.3a), it is noticeable that platinum deposits consist of small size of Pt nanoparticles with a high degree of roughness. Incorporation of the investigated organic additives not only reduces the size of the platinum particles formed during electrodeposition, but also has demonstrated a significant impact on the microstructure of the deposits.

Figure 2.3d exhibits the preferential formation of cubic shape of platinum nanoparticles [Pt (100)] in the presence of the organic additive PVDF, while the particles obtained using potassium citrate have characteristic sharp edges (Fig. 2.3b) and such changes in the microstructure of the deposits should in turn affect the electrochemically active surface area and electrocatalytic activity towards oxygen reduction reaction.

2.3.2 *Activity of Platinum Nanomaterials Towards Oxygen Reduction Reactions*

Therefore, evaluation of the ESA and activities of the catalysts towards ORR were carried out. When the organic additives are introduced into the platinized electrolyte, the ESA value increased 1.5–2 times compared to that synthesized in the electrolyte without any additives (Table 2.1).

It is noticeable that the cyclic voltammograms (Fig. 2.4) of the Pt/C materials obtained in the presence of the various organic additives have not significant differences and have the overall features of a typical cyclic voltammogram for Pt/C catalyst, showing that there is no considerable difference in the Pt/C loading among the formed materials. Moreover, the current values in the double layer region are considerably increased for the materials prepared in the presence of the organic additives

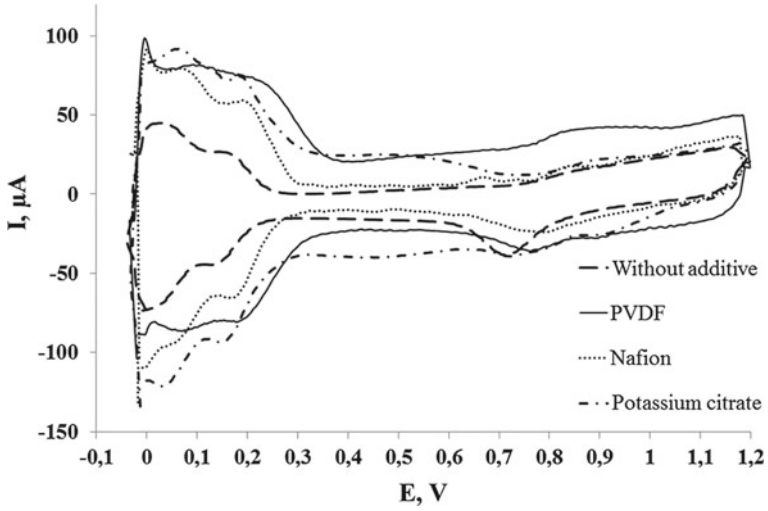

Fig. 2.4 Cyclic voltammograms for the obtained Pt/C electrodes by electrodeposition in the presence of various additives: 0.01 M potassium citrate, 0.01% PVDF, 0.01% Nafion. Electrolyte—0.1 M $HClO_4$ with saturated argon at atmospheric pressure, sweep rate—0.02 V/s

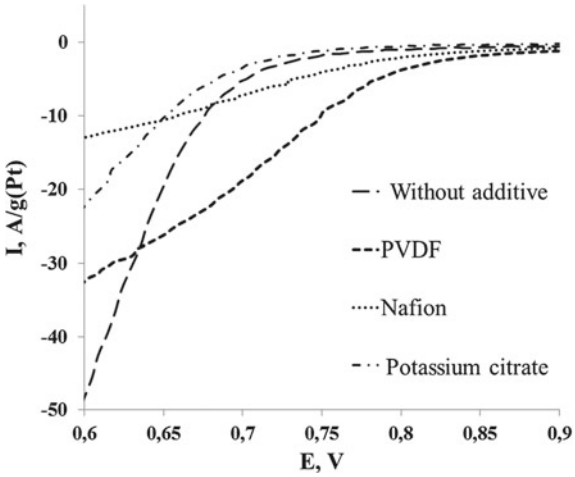

Fig. 2.5 LSV curves in the potential range from 0.6 to 0.9 V for Pt/C electrodes obtained by electrodeposition in the presence of various additives: 0.01 M potassium citrate, 0.01% PVDF, 0.01% Nafion. Electrolyte—0.1 M $HClO_4$ oxygen saturated at atmospheric pressure, sweep rate—0.02 V/s

with the exception of the catalyst obtained using Nafion. From the investigated additives, PVDF is found to be the most effective organic additive from the point of view of achieving high ESA [43 m^2/g (Pt)] (Table 2.1). It has to be noted that direct correlation between the average platinum particle size and the ESA of platinum is not observed. The smallest size of platinum particle is obtained in the case of using potassium citrate, while the ESA of this material [34 m^2/g (Pt)] is lower than that of the electrocatalyst obtained using PVDF [43 m^2/g (Pt)]. This is possibly due to the influence of the additives not only on the size of the particles but also on the surface roughness of the particles.

The obtained Pt/C catalysts by electrodeposition method are of great interest from the point of view of clarifying the relationship between the different levels of microstructural characteristics and catalytic activity of the carbon-supported platinum materials. The catalytic activity of the prepared platinum catalysts towards ORR varies significantly (Fig. 2.5). The organic additive PVDF notably increases the catalytic activity of Pt/C material as compared to a similar catalyst prepared without using the additives and this may be possibly associated with a higher ESA and with a greater proportion of active platinum crystal faces such as Pt (100), which have higher catalytic activity. Similar results were reported by Housmans et al. [22], indicating higher catalytic activity on the Pt(100) facets for methanol electrooxidation.

On the other hand, despite the addition of potassium citrate increases the value of the ESA, catalytic activity of the resulting Pt/C catalyst for the ORR is somewhat reduced and the catalyst prepared in the presence of Nafion shows a slight increase in the cathodic current in the potential range of 0.7–0.8 V (Fig. 2.5), compared to the material produced without the addition of the additives. However, at potentials $E <$ 0.7 V, the catalytic activity of Pt/C obtained in the presence of Nafion is significantly lower than the material obtained in the absence of the additives. Thus, the addition of additives into platinized electrolyte, depending on the nature of the organic additives, may positively or negatively affect the catalytic activity of the resulting

Pt/C catalyst. The highest catalyst activity is obtained in the presence of PVDF, apparently not only due to high ESA, but also attributed to the shape of the obtained carbon-supported platinum nanoparticles. PVDF has resulted greater proportion of the preferential catalytically active platinum nanocubes with Pt(100) facets, which is in a good agreement with the literature results from [2, 17, 20, 23, 24].

2.4 Conclusions

The study showed that the different organic additives used adsorbed on the platinum surface in different ways and hence affected the morphology, ESA and catalytic activity of Pt/C materials to different extents. The usage of the organic additives such as potassium citrate, Nafion and PVDF increases the overpotential of the electrodeposition process, resulting in a decrease in particle size and an increase in the ESA of the Pt catalysts. In particular, the addition of potassium citrate has resulted in the reduction of the average size of the platinum particles more than 1.5 times. On the other hand, electrochemical measurements indicated that PVDF has resulted more than 2-fold enlargement in the ESA and an enhanced electrocatalytic activity of the material towards ORR. The ESA of platinum was found to be much more dependent on the surface roughness of the metal particles than on their size. The activity of Pt/C catalysts in the ORR is determined not only by the corresponding ESA but also by the predominant type of active crystal surfaces constituting the Pt nanoparticles.

Acknowledgements This work was performed in the framework of the state task of the Russian Federation No 13.3005.2017/4.6.

References

1. Y.D. Gamburg, Z. Giovanni, *Theory and Practice of Metal Electrodeposition* (Springer, Science & Business Media, 2011)
2. R.M. Antoniassi, J.C.M. Silva, T. Lopes, N.A. Oliveira, E.V. Spinacé, Int. J. Hydrogen Energy **42**(48), 28786 (2017)
3. Y.W. Jun, J.H. Lee, J.S. Choi, J. Cheon, J. Phys. Chem. B. **109**, 14795 (2005)
4. F. Ye, W. Hu, T. Zhang, J. Yang, Y. Ding. Electrochim. Acta **383**, 386 (2012)
5. F. Ye, L. Chen, J. Li, J. Li, X. Wang. Electrochem. Commun. **10**, 476 (2008)
6. A. Quintanilla, V.C.L. Butselaar-Orthlieb, C. Kwakernaak, W.G. Sloof, M.T. Kreutzer, F. Kapteijn, J. Catal. **271**(1), 104 (2010)
7. W. Yohannes, S.V. Belenov, V.E. Guterman, L.M. Skibina, V.A. Volotchaev, N.V. Lyanguzov, J. Appl. Electrochem. **45**, 623 (2015)
8. P. Serp, J.L. Figueiredo, *Carbon Materials for Catalysis* (Wiley, Hoboken, 2009)
9. J.M. Sieben, M.M. Duarte, C.E. Mayer, J. Alloys Compd. **509**, 4002 (2011)
10. P.L. Kuo, W.F. Chen, H.Y. Huang, I.C. Chang, S.A. Dai, J. Phys. Chem. B. **110**, 3071 (2006)
11. C.L. Hui, X.G. Li, I.M. Hsing, Electrochim. Acta **51**, 711 (2005)
12. H.Y. Chou, C.K. Hsieh, M.C. Tsai, Y.H. Wei, T.K. Yeh, C.H. Tsai, Thin Solid Films **584**, 98 (2015)

13. G.A. Attard, J.Y. Ye, P. Jenkins, F.J. Vidal-Iglesias, E. Herrero, S.G. Sun, J. Electroanal. Chem. **688**, 249 (2013)
14. I. Ojea-Jiménez, V. Puntes, J. Am. Chem. Soc. **131**(37), 13320 (2009)
15. L. Pei, K. Mori, M. Adachi, Langmuir **20**(18), 7837 (2004)
16. Z. Tang, D. Geng, G. Lu, J. Colloid Interface Sci. **287**, 159 (2005)
17. R. Sharma, K.K. Kar, Electrochim. Acta **156**, 199 (2015)
18. Z. Liu, Z.Q. Tian, S.P. Jiang, Electrochim. Acta **52**, 1213 (2006)
19. A.J. Bard, L.R. Faulkner, J. Leddy, C.G. Zoski, *Electrochemical Methods: Fundamentals and Applications* (Wiley, New York, 1980)
20. V.E. Guterman, A.Y. Pakharev, N.Y. Tabachkova, Appl. Catal. A: Gen. **453**, 113 (2013)
21. V.E. Guterman, S.V. Belenov, A.A. Alekseenko, N.Y. Tabachkova, V.A. Volochaev, Russ. J. Electrochem. **53**(5), 531 (2017)
22. T.H. Housmans, A.H. Wonders, M.T. Koper, J. Phys. Chem. B. **110**(20), 10021 (2006)
23. C. Wang, H. Daimon, T. Onodera, T. Koda, S. Sun, Angew. Chem. Int. Ed. **47**(19), 3588 (2008)
24. I.N. Leontyev, S.V. Belenov, V.E. Guterman, P. Haghi-Ashtiani, A.P. Shaganov, B. Dkhil, J. Phys. Chem. C. **115**(13), 5429 (2011)

Chapter 3
X-ray Spectroscopy Study of the Atomic and Electronic Structure of Polyacrylonitrile-Based Nanocomposites at Different Stages of Formation

M. A. Kremennaya, V. A. Shmatko, T. A. Mikhailova, E. V. Pronina, K. D. Kosolapova, and G. E. Yalovega

Abstract Study the atomic and electronic structure of polyacrylonitrile (PAN) during IR-annealing and the formation of Co/PAN nanocomposite based on a combination of computer simulation methods and X-ray absorption spectroscopy was carried out. Using the Density Functional Theory method, structural models of pure PAN and Co/PAN nanocomposite were obtained and electronic density of states was calculated. X-ray absorption spectra for the obtained structural models were calculated and showed good agreement with the experiment. The densities of states demonstrated that polymer form changes from non-conducting to conducting during annealing process.

3.1 Introduction

Conductive polymers with poly conjugated systems are great interest due to their unique physicochemical properties, which allow their use in various fields of chemistry, physics and materials science [1]. Among these materials, polyacrylonitrile (PAN) occupies a special place. PAN is able to change the electronic structure during heat treatment, in particular during IR pyrolysis. PAN pyrolysis makes it possible to obtain a structures with various electrical properties controlled conductivity, as well as low cost and simple material manufacturing technology [2]. Adding of metal salts (Ni, Co, Cu, Ag, Fe) into the PAN also allows one to change the electrical conductivity of nanocomposites films [3]. Moreover, PAN exhibits excellent catalytic properties [4], and can be used as an adsorbent [5]. It can be used in tribology or microelectronics as thin films deposited on the surface [4]. The study of the atomic and electronic structures of such materials and their dependence on the synthesis

M. A. Kremennaya (✉) · V. A. Shmatko · T. A. Mikhailova · E. V. Pronina · K. D. Kosolapova · G. E. Yalovega
Faculty of Physics, Southern Federal University, Zorge str. 5, Rostov-on-Don, Russia 344090
e-mail: kremennayamariya@gmail.com

I. A. Parinov et al. (eds.), *Advanced Materials*, Springer Proceedings in Materials 6, https://doi.org/10.1007/978-3-030-45120-2_3

parameters is an important task, the solution of which opens up possibilities for creating nanocomposites with desired properties.

A study of the electronic structure of various materials is usually carried out using a combination of photoelectron spectroscopy and X-ray absorption spectroscopy. Photoelectron spectroscopy allows studying occupied electronic states, as well as the valence band. X-ray absorption spectroscopy allows the study of free electronic states. In addition, the use of the density functional theory for studying the atomic and electronic structure of various carbon materials is widespread [6–10]. As well as an approach that includes a combination of density functional theory to obtain model structures and calculation of X-ray absorption spectra to verify these models [11–13]. X-ray absorption spectra are sensitive to changes in the charge, to small changes in bond lengths (up to 0.01 Å) and angles, which allows an accurate simulation of the atomic and electronic structure of the studied objects.

In this chapter, we present the results of study the atomic and electronic structure of polyacrylonitrile during IR-annealing and the formation of Co/PAN nanocomposite based on a combination of computer simulation methods and X-ray absorption spectroscopy.

3.2 Experiment and Methods

Density functional theory (DFT) calculations were performed in ADF code [14]. The atomic and electronic structures were simulated for the initial structure of polyacrylonitrile, during IR pyrolysis and formation of Co/PAN nanocomposite. Geometry optimization was carried out using the BPE [15] exchange-correlation potential with TZP basic set.

Theoretical X-ray absorption spectra were calculated with the FDMNES code [16]. Near edge X-ray absorption fine structure (NEXAFS) spectra for C K-edge and Co $L_{2,3}$-edge were calculated by the finite difference method at the full potential. The radius of the calculated cluster was 5.5 Å. The obtained spectra were convoluted by Lorentzian to remove occupied states.

A detailed description of the Co/PAN nanocomposite preparation is given in [17]. Experimental NEXAFS spectra for Co $L_{2,3}$-edge were recorded at the Elettra Sincrotrone Trieste (Italy), Materials Science Beamline. Spectra were obtained in the partial KVV Auger electron yield detection mode.

3.3 Results and Discussion

A structure reorganization of PAN is observed at various temperatures during IR-annealing (Fig. 3.1) [18–21]. The initial structure is a polymer consisting of chains with conjugated triple bonds C≡N (Stage **1**). Stage **2**: cyclization (100–200 °C), the interaction of nitrile groups with the formation of a regular linear network.

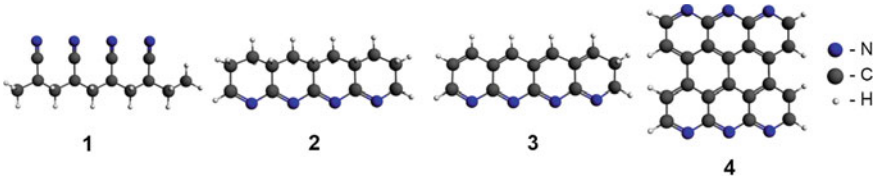

Fig. 3.1 Structural models of PAN: **1**—initial structure, **2**—stage of cyclization at 200–300 °C, **3**—stage of carbonization at 250–450 °C, **4**—stage of intermolecular carbonization at 450–1300 °C

Stage **3**: carbonization (250–450 °C), polymerization by nitrile groups and dehydrogenation of the hydrocarbon chain occur. Stage **4**: intermolecular carbonization (400 °C and higher), crosslinking of linear polymer chains with the formation of a spatially cross-linked polymer. Further heating (up to 1300 °C) leads to the formation of a graphite-like structure with a small content of nitrogen atoms.

Theoretical X-ray absorption spectra were calculated for four cases of the structure evolution before and after PAN IR-annealing. The theoretical NEXAFS spectrum for the initial structure of PAN (1) is shown in Fig. 3.2. The shape and energy position of the spectral features coincides with the experimental spectra given in [22–24]. Theoretical spectrum **1** has an intense peak A at an energy of 286.8 eV, which refers to C1s (C≡N) → $\pi^*_{C\equiv N}$ transitions, peak B at 288.5 eV refers to C1s (C-H) →

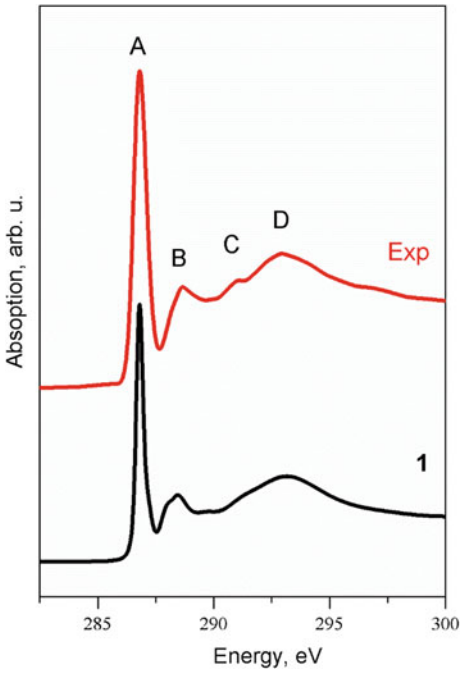

Fig. 3.2 Comparison of experimental and theoretical PAN C K-edge NEXAFS spectra; experimental spectra taken from [22]

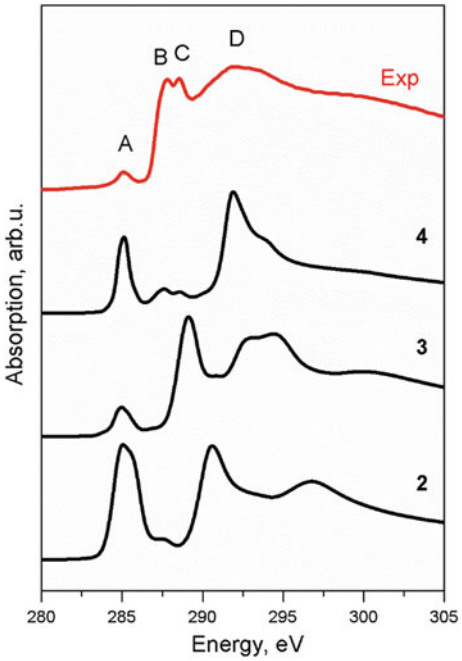

Fig. 3.3 Comparison of experimental C K-edge NEXAFS spectra for pure PAN film annealed at 260–440 °C [25] and theoretical NEXAFS spectra of PAN during IR-annealing (Models **2–4**)

$2\pi^*_{C-C}$ transitions and peak C at 293.3 eV corresponding to C1s (C-H) → $\sigma^*_{C=C}$ transitions [23].

The next block of comparisons is carried out with the experimental spectrum for pure PAN film annealed at 260–440 °C, obtained in [25] (Fig. 3.3). Peak A at 285.1 eV for presented spectrum can be characterized as C1s(C–H) → $\pi^*_{C=C}$ transitions, peak B at 287.8 eV as C1s(C–H) → σ^*_{C-H} transitions, peak C as 288.5 eV is C1s(C–H) → $2\pi^*_{C-C}$ transitions, peak D as 292.3 to C1s(C–H) → σ^*_{C-H} transitions [23].

The theoretical spectrum **2** corresponds to the structure of PAN at the stage of cyclization. There are three intense peaks at energies of 285.1, 290.6 and 296.8 eV, as well as a shoulder at 287.8 eV. The energy positions of peak A and shoulder B coincide with the experimental spectrum. In spectrum **3** for PAN at the carbonization stage, the energy position coincides for the spectral feature of A with the experimental spectrum. However, the peak D is doubled and shifted along the energy to the right, and double peaks B and C are also not observed. In the theoretical spectrum **4** for PAN at intermolecular carbonization stage, the energy position of the singularity A coincides with the experimental position and its intensity is higher, the peaks B and C are present. The spectral feature D is narrower than the experiment. It can be seen from the figure, the theoretical spectrum for the structure of a spatially cross-linked polymer (**4**) reproduces the main spectral features of the experimental spectrum. However, the intensities of the spectral features for all theoretical spectra are overestimated because in the calculation models, only one polymer layer is taken into account and there is no consideration for interaction with oxygen.

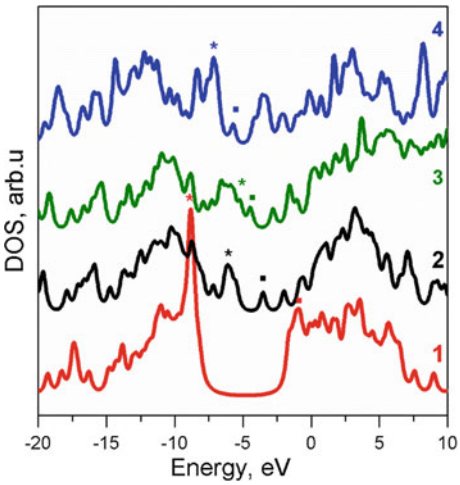

Fig. 3.4 Density of states in PAN at various stages of IR-annealing

The densities of states were calculated for the initial PAN structure and PAN during IR-annealing (Fig. 3.4). As can be seen, the band gap decreases and the state of the substance changes from non-conducting to conducting in the IR-annealing process [26]. The asterisk indicates the highest occupied states and point indicates the lowest unoccupied states.

In [25] was found that cobalt binds to nitrogen atoms in the pyridine rings and is in the oxidic form. Based on these data, the Co/PAN nanocomposites structure **5** was simulated (Fig. 3.5b) and X-ray absorption spectra for Co $L_{2,3}$-edge were calculated. Figure 3.5a shows a comparison with the experimental spectrum.

The theoretical spectrum shows good agreement with the experimental one. Diffuse spectral features of the experimental spectrum are associated with energy resolution. Peak A in the presented spectra corresponds to L_3, and peak B to L_2. Splitting at L_3 peak indicates that cobalt is in a 2+ state [27]. Thus, the applied research technique allows us to consider the electronic structure not only from the side of the polymer matrix, but also from the side of the inject metal into the structure.

3.4 Conclusion

The atomic and electronic structures for the initial structure of polyacrylonitrile, during IR pyrolysis and formation of Co/PAN nanocomposite were simulated using the density functional theory. Theoretical C K and Co $L_{2,3}$-edges absorption spectra were calculated for all obtained models. Theoretical NEXAFS spectra showed good agreement with experimental spectra. However, the intensities of spectral features for theoretical spectra are overestimated, what can be reduced by adding additional layers of polymer and oxygen molecules. The densities of states calculations for the initial PAN and PAN during IR-annealing structures showed that polymer form changes

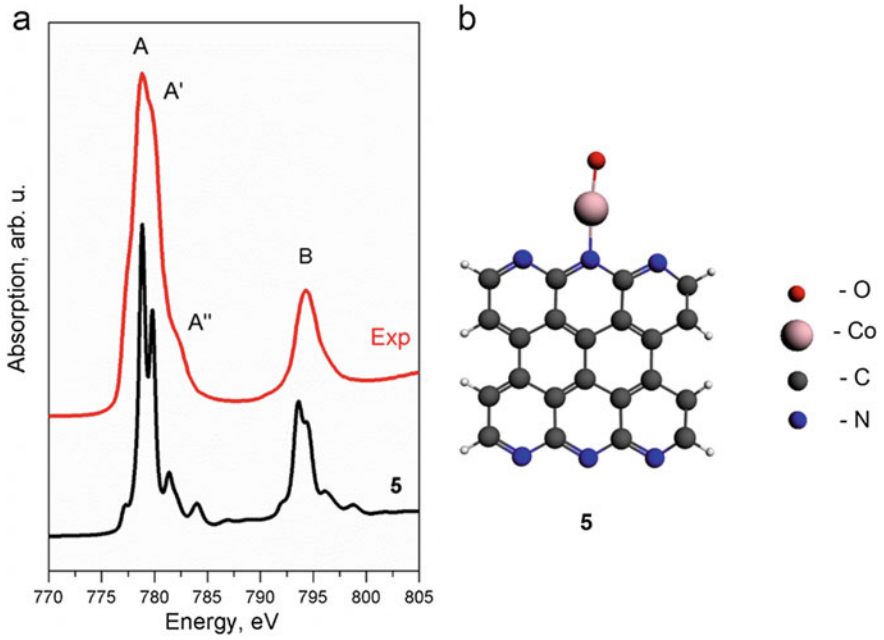

Fig. 3.5 Comparison of experimental and theoretical Co $L_{2,3}$-edge spectra for Co/PAN (**a**) and structural model **5** of Co/PAN nanocomposites (**b**)

from non-conducting to conducting during annealing process. The analysis showed that cobalt is in 2+ oxidation state. Thus, the applied technique, which includes computer simulation and X-ray absorption spectroscopy, allowed us to analyze the electronic structure both from the side of the polymer matrix and from the side of the metal added into the structure.

Acknowledgements This work was supported by the Southern Federal University (Project no. VN_GR_07_2017-30).

References

1. D.G. Muratova, E.V. Yakushko, L.V. Kozhitov, A.V. Popkova, M.A. Pushkarev. Mod. Electron. Mater. **2**, 70 (2016)
2. T.A. Bednaya, S.P. Konovalenko, Russ. Microelectron. **47**, 112 (2018)
3. E.A. Stefanescu, C. Daranga, C. Stefanescu, Materials **2**, 2095 (2009)
4. G. Tourillon, D. Guay, A. Fontaine. Faraday Discuss. Chem. Soc. **89**, 275 (1990)
5. Z. Jiang, Y. Liu, G. Zeng, W. Xu, B. Zheng, X. Tana, S. Wang. RSC Adv. **5**, 25389 (2015)
6. C. Ehlert, W.E.S. Unger, P. Saalfrank, C. Phys. Chem. Chem. Phys. **16**, 14083 (2014)
7. S.G. Minasian, J.M. Keith, E.R. Batista, K.S. Boland, S.A. Kozimor, R.L. Martin, D.K. Shuh, T. Tyliszczak, L.J. Vernon. J. Am. Chem. Soc. **135**, 14731 (2013)

8. D.R. Nascimento, A.E. DePrince, J. Phys. Chem. Lett. **8**, 2951 (2017)
9. P.A. Denis, F. Iribarne, J. Mol. Struc-Theochem. **907**, 93 (2009)
10. G. Bertoni, L. Calmels, Micron **37**, 486 (2006)
11. J.P. Rueff, Y. Joly, F. Bartolome, M. Krisch, J. L. Hodeau, L. Marques, M. Mezouar, A. Kaprolat, M. Lorenzen, F. Sette. J. Phys.: Condens. Matter. **14**, 11635 (2002)
12. M. Brzhezinskaya, V. Shmatko, G. Yalovega, A. Krestinin, I. Bushkin, E. Bogoslavskaya, J. Electr. Spectr. Rel. Phen. **196**, 99 (2014)
13. A. Nikitin, L.-Å. Näslund, Z. Zhang, A. Nilsson, Surf. Sci. **602**, 2575 (2008)
14. G. te Velde, E.J. Baerends. Phys. Rev. B. **44**, 7888 (1991)
15. J.P. Perdew, K. Burke, M. Ernzerhof. Phys. Rev. Lett. **77**, 3865 (1996)
16. O. Bunau, Y. Joly. J. Phys.: Condens. Matter. **21**, 345501 (2009)
17. G. Yalovega, T. Semenistaya. Solid State Phenom. **257**, 175 (2017)
18. R. Janus, P. Natkański, A. Wach et al. J. Therm. Anal. Calorim. **110**, 119 (2012)
19. C.R. Wu, W.R. Salaneck. Synth. Met. **16**, 147 (1986)
20. S.Y. Jin, M.H. Kima, Y.G. Jeong, Y.I. Yoon, W.H. Park. Mater. Des. **124**, 69 (2017)
21. Q. Luo, X. Yang, X. Zhao, D. Wang, R. Yin, X. Li. J. An. Appl. Catal. B-Environ. **204**, 304 (2017)
22. J. Wang, H.D.H. Stöver, A.P. Hitchcock, T. Tyliszczak. J. Synchrotron Rad. **14**, 181 (2007)
23. O. Dhez, H. Ade, S.G. Urquhart, J. Electron Spectrosc. Relat. Phenom. **128**, 85 (2003)
24. H. Ade, X. Zhang, S. Cameron, C. Costello, J. Kirz, S. Williams. Science. **258**, 972 (1992)
25. G. Yalovega, T. Semenistaya, V. Shmatko, M. Kremennaya, N. Tsud, Radiat. Phys. Chem. (2019). https://doi.org/10.1016/j.radphyschem.2019.04.006
26. S.K. Nataraj, K.S. Yang, T.M. Aminabhavi. Prog. Polym. Sci. **37**, 487 (2012)
27. F.M.F. de Groot, M. Abbate, J. van Elp, G.A. Sawatzky, Y.J. Ma, C.T. Chen, F. Sette, J. Phys.: Condens. Matter **5**, 2277 (1993)

Chapter 4
Morphology and Structure of Carbon Nanoparticles Generated from Graphite Nitrate Co-intercalation Compound. Effect of Sonication Regime

E. V. Raksha, A. A. Davydova, Yu. V. Berestneva, M. V. Savoskin, V. A. Glazunova, A. N. Vdovichenko, O. N. Oskolkova, P. V. Sukhov, V. V. Gnatovskaya, I. A. Verbenko, and Yu. I. Yurasov

Abstract Few-layer graphenes and nanoscrolls have been prepared by exfoliation of the triple graphite nitrate co-intercalation compound (GNCC) as well as pre-thermally expanded GNCC in liquid media. Graphite nitrate sequentially co-intercalated with ethyl formate and acetic acid and thermally expanded graphite (TEG) obtained from it were used as precursors of carbon nanoparticles. Ethanol, acetonitrile and a mixture of DMFA:H_2O (9:1 by volume) were used as solvents for liquid phase exfoliation of GNCC and TEG assisted with sonication. The microstructure and morphology of obtained few-layer graphenes and nanoscrolls were investigated by transmission electron microscopy (TEM). Planar sizes of the as-prepared few-layer graphenes reached several tens of μm and their thickness was within 1–10 atomic layers according to TEM data. Sonication regime effect on the resulting carbon nanoparticles morphology was studied. It was shown that sonication with a power of 70 W (42 kHz) provided obtaining of the few-layer graphene suspensions containing also single-layered graphene particles. The sonication with 315–630 W

E. V. Raksha (✉) · A. A. Davydova · M. V. Savoskin · A. N. Vdovichenko · O. N. Oskolkova · P. V. Sukhov · V. V. Gnatovskaya
Supramolecular Chemistry Department, L.M. Litvinenko Institute of Physical-Organic and Coal Chemistry, 70, R. Luxemburg Street, Donetsk 83114, Ukraine
e-mail: elenaraksha411@gmail.com

Yu. V. Berestneva
Biotechnology Laboratory, Federal State Budget Scientific Institution "Federal Scientific Centre of Agroecology, Complex Melioration and Protective Afforestation of the Russian Academy of Sciences", 97, Universitetsky Avenue, Volgograd, Russia 400062

V. A. Glazunova
Department of High-Pressure Physics and Advanced Technologies, Donetsk Institute for Physics and Engineering named after A.A. Galkin, 72, R. Luxemburg Street, Donetsk 83114, Ukraine

I. A. Verbenko · Yu. I. Yurasov
Research Institute of Physics, Southern Federal University, 194, Stachki Avenue, Rostov-on-Don 344090, Russia

Yu. I. Yurasov
Southern Scientific Centre RAS, 41, Chehova Sreet, Rostov-on-Don 344006, Russia

I. A. Parinov et al. (eds.), *Advanced Materials*, Springer Proceedings in Materials 6, https://doi.org/10.1007/978-3-030-45120-2_4

(22 kHz) leads to the formation of carbon nanoscrolls. It was found that ethanol is more preferable medium for carbon nanoparticles generation as compared to acetonitrile. Liquid phase exfoliation of GNCC and pre-thermally expanded GNCC allows obtaining dispersions of carbon nanoparticles with various morphology—single- and few-layer graphenes, nanoscrolls as well as small graphene particles.

4.1 Introduction

There are three promising routes for graphene production from natural graphite: reduction of graphene oxide, electrochemical exfoliation of graphite, and liquid-phase exfoliation of graphite, graphite co-intercalation compounds or thermally expanded graphite. Both anions and cations, including their solvated forms, can intercalate between graphene sheets via oxidation or reduction reactions, respectively, forming graphite intercalation compounds. A variety of applications for graphite intercalation compounds have been proposed or realized, including use as thermally expansion and liquid phase exfoliation precursors [1–7]. The synthesis, composition and properties of a broad range of binary and triple graphite nitrate co-intercalation compounds containing different organic co-intercalant species have been studied [4, 5]. They have pre-organized structure for graphene particles generation due to enlarged distance between the nearest graphene layers filled with intercalant species. Such structural reorganization of graphite matrix is responsible for graphite nitrate intercalation compounds application as precursors of carbon nanoparticles generation in mild conditions.

This chapter presents the results on the production of nanoscrolls and few-layer graphenes by sonication of graphite nitrate co-intercalated with ethyl formate and acetic acid (GNCC) prepared by natural graphite chemical treatment and pre-thermally expanded GNCC in different solvents. Sonication regime effect on the resulting carbon nanoparticles morphology was also studied.

4.2 Experimental

At the first step graphite nitrate co-intercalation compound was prepared as a starting material for the thermally expanded graphite production and generation of carbon nanoparticles dispersions. GNCC was synthesized in a thermostatic reactor at 20 °C. Nitric acid with a density of 1.502 g cm^{-3} (98%) was added to the sample of natural flake graphite GT-1 (Zavalie Graphite Works, Kirovograd region, Ukraine). The mixture was stirred for 10 min. Then co-intercalants (ethyl formate and acetic acid) were sequentially added in equal amounts to the reaction mixture and the system was stirred again for 10 min. The consumptions of nitric acid and each co-intercalant were 0.6 and 6 cm^3 per 1 g of graphite, respectively. Resulted GNCC was separated by filtration and dried at 20 °C until the sample mass became constant. Thermally

expanded graphite was obtained from GNCC by the thermal shock mode of heating (900 °C). Dispersions of carbon nanoparticles were obtained by liquid phase exfoliation of the GNCC as well as TEG at different sonication regimes (42 kHz and 70 W; 22 kHz and 315–630 W). Ethanol, acetonitrile and mixture of DMFA and H_2O (9:1 by volume) were used as media for liquid phase exfoliation of GNCC and TEG. Carbon nanoparticles dispersions were prepared by adding of GNCC (0.5 g dm^{-3}) or (0.3 g dm^{-3}) to examined solvents and sonication of mixtures for 1 h. Dispersions were sprayed on TEM grid and investigated using JEOL JEM-200 transmission electronic microscope. Absorption spectra were recorded on a UV-VIS spectrometer (Helios Gamma, Thermo Electron Corporation, USA). The dispersions of carbon nanoparticles in ethanol and acetonitrile were used as the samples, and the pure ethanol and acetonitrile were used as a reference.

4.3 Results and Discussion

The structure of acceptor-type graphite intercalation compounds is very specific. Their quasi-two-dimensional layers of intercalants are quite labile, being not connected to a rigid graphite matrix by covalent bonds. These negatively charged layers alternate with positively charged graphene layers. Organic co-intercalants additionally stabilize the graphite nitrate through the formation of hydrogen bonds network. Interplanar space filled with co-intercalants species increases up to 7.8 Å for such compounds [1]. This structural reorganization of graphite matrix may be considered as a pre-organization process for few-layer and single-layer graphene formation. Thus, GNCCs are prospective compounds for the liquid phase exfoliation and graphene-like particles generation. However, GNCCs possess ability of thermal expansion [1, 5]. Thermally expanded graphite, obtained from GNCCs can also be used as a precursor for liquid phase exfoliation.

Graphite nitrate sequentially co-intercalated with ethyl formate and acetic acid was used as source of carbon nanoparticles. Spontaneous bloating of particles for these compounds has been observed in its drying process at 20 °C. Thermally expanded graphite, obtained from this GNCC was also investigated as a precursor for carbon nanoparticles with different morphology.

Dispersions of carbon nanoparticles were obtained by GNCC exfoliation in ethanol and acetonitrile induced by ultrasound (22 kHz, 315 and 470 W). The duration of the sonication was 1 h. Then, the samples were centrifuged (7 min, 3000 rpm). The dispersions obtained were investigated by UV spectroscopy and transmission electron microscopy (TEM). It should be noted that treatment of intercalated graphite compounds with alcohols is used as a method of graphite matrix exfoliation without additional temperature influence [2, 8]. Since our investigations were carried out mainly on the co-intercalated compounds of the IV and II intercalation stages, it was difficult to expect a complete graphite lattice exfoliation into monolayer graphene particles which formation was demonstrated earlier [2].

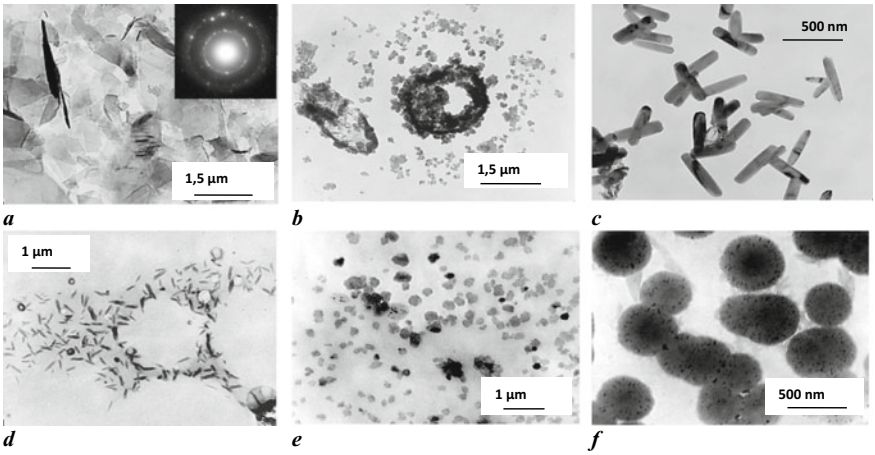

Fig. 4.1 TEM images of carbon nanoparticles obtained in ethyl alcohol (**a**–**d**) and acetonitrile (**e**, **f**) by sonication of the graphite nitrate co-intercalated with ethyl formate and acetic acid

An analysis of the dispersions obtained in ethyl alcohol and acetonitrile by the TEM method revealed that carbon nanoparticles of various morphologies can be generated by this technique. Most commonly, a mixture of particles is formed, which includes graphene-like particles of various sizes (both single-layer and few-layer), nanoscrolls, and small amorphous nanocarbon particles.

Figure 4.1 shows typical TEM micrographs of carbon nanoparticles obtained by GNCC exfoliation in ethanol induced by ultrasound (22 kHz, 470 W). The planar sizes of obtained individual few-layer graphene particles reach several micrometers (Fig. 4.1a). A large number of small particles with planar sizes up to 200 nm is also formed in the system (Fig. 4.1b). Nanoscrolls with a length of 50–400 nm were present in the dispersions (Fig. 4.1c, d) in significant amount.

The solvent effect on the graphite matrix exfoliation of the synthesized GNCC was also investigated. Acetonitrile was also used as a liquid medium for the GNCC exfoliation. TEM images of carbon nanoparticles obtained by GNCC sonication in this solvent are shown in Fig. 4.1e, f.

By passing from ethyl alcohol to acetonitrile, an increase in the degree of structural deformation is observed for particles formed as a result of GNCC sonication. At the same time, a small number of few-layer graphene particles were present in the samples. However, most commonly a large number of amorphous small particles with sizes up to 1 nm was formed as a result of GNCC sonication in acetonitrile. Apparently, such intercalants as ethyl formate and acetic acid, which, when interacting with nitric acid, can generate free radical particles, as well as acetonitrile involved in chain transfer reactions, contribute to a significant increase in the number of defects and fragmentation of graphene planes formed upon GNCC exfoliation. Aggregates of small clusters have different morphologies and are characterized by the absence of a crystalline structure.

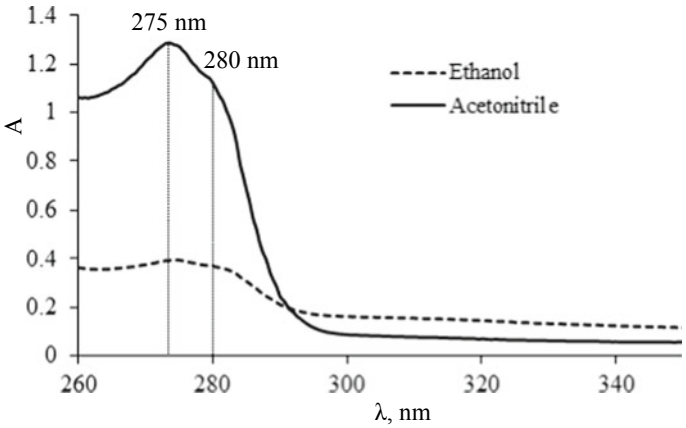

Fig. 4.2 Representative UV absorption spectra of the dispersions obtained by exfoliation of GNCC in ethanol and acetonitrile (sonication: 1 h, 22 kHz, 470 W)

UV absorption spectra obtained for carbon nanoparticles dispersions show an absorption peaks at 275 nm for both ethanol and acetonitrile media (Fig. 4.2). Additional peaks were observed at near 280 nm for both ethanol and acetonitrile dispersions. Such character of absorption spectra can be due to the presence of nanoparticles with different types of morphology (graphenes and nanoscrolls as well as small clusters with different morphologies and a large number of structural defects) in the studied dispersions. Further investigations to detail the features of considered dispersions absorption spectra are required.

Thus, carbon nanoparticles of various sizes and diverse morphologies can be obtained by exfoliation of triple GNCC in acetonitrile and ethanol. Acetonitrile contributes to the formation of a larger number of structural defects in graphene planes and to the generation of amorphous carbon particles with sizes less than 1 nm.

Carbon nanoparticles (few-layer graphenes and nanoscrolls) were also obtained by sonication of thermally expanded graphite in the mixture of DMFA:$H_2O = 9:1$ by volume. Graphite nitrate sequentially co-intercalated with ethyl formate and acetic acid was used as a source of thermally expanded graphite. It was demonstrated that sonication with a power of 70 W and higher frequency (42 kHz) produced suspensions of few-layer graphene particles containing also single-layer graphenes. The sonication with 315–630 W (22 kHz) leads to the formation of carbon nanoscrolls (Fig. 4.3) with a diameter of about 30–80 nm and a length from 140 to 200 nm along with few-layer graphenes. Thus, it was shown that variation of the sonication conditions leads to obtaining of carbon nanoparticles with different morphology.

Thus, in accordance with the TEM data, the formation of few-layer graphene particles and nanoscrolls as a result of the liquid phase exfoliation of TEG based on the graphite nitrate co-intercalation compound is established. It is shown that a change in the ultrasonic treatment regime leads to the production of carbon nanoparticles with different morphologies.

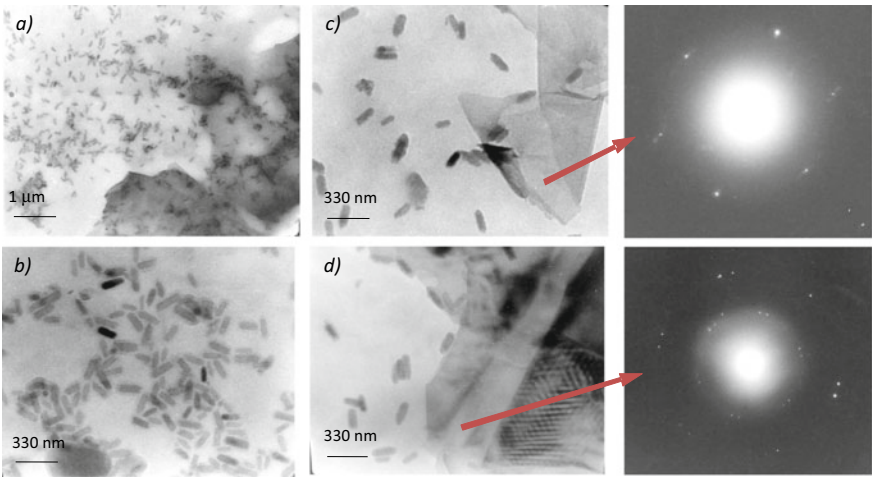

Fig. 4.3 Representative TEM images and electron diffraction pattern of carbon nanoparticles obtained by sonication of thermally expanded graphite in the mixture of DMFA:H_2O = 9:1 by volume. Sonication power: 315 W (**a**, **b**), 470 W (**c**), 630 W (**d**); 22 kHz

4.4 Conclusion

The presence of carbon nanoparticles (few-layer graphenes and nanoscrolls) in the exfoliation products of triple graphite nitrate co-intercalation compound in different media has been established by the transmission electron microscopy method. It was shown that varying the solvent nature makes it possible to obtain different types of carbon nanoparticles. Graphene-like particles with planar sizes up to several micrometers were formed from GNCC in ethyl alcohol. Acetonitrile contributes to a significant increase in the number of defects and fragmentation of graphene planes formed by GNCC exfoliation. TEG exfoliation in DMFA:H_2O mixture leads to the few-layer graphenes and nanoscrolls generation.

The presented results revealed graphite nitrate co-intercalation compounds as well as thermally expanded graphite to be a promising source of carbon nanoparticles. Exfoliation of GNCC or TEG in liquid media by sonication can be simple and effective route for obtaining carbon nanoparticles under mild conditions at large scales.

References

1. M.V. Savoskin, A.P. Yaroshenko, G.E. Whyman, R.D. Mysyk, J. Phys. Chem. Sol. **67**, 1127–1131 (2006)
2. M.V. Savoskin, V.N. Mochalin, A.P. Yaroshenko, N.I. Lazareva, T.E. Konstantinova, I.V. Barsukov, I.G. Prokofiev, Carbon **45**, 2797–2800 (2007)

3. M.V. Savoskin, A.N. Vdovichenko, E.V. Raksha, Yu.V. Berestneva, V.Yu. Vishnevskij, O.M. Padun, I.A. Verbenko, Yu.I. Yurasov, in *Proceedings of the 2016 International Conference on "Physics, Mechanics of New Materials and Their Applications"*, ed. by I.A. Parinov, S.-H. Chang, M.A. Jani(Nova Science Publishers, New York), pp. 115–120 (2017)
4. M.V. Savoskin, A.N. Vdovichenko, E.V. Raksha, Yu.V. Berestneva, V.Yu. Vishnevskij, A.P. Prudchenko, V.A. Glazunova, K.P. Andryushin, Yu.I. Yurasov, in *Proceedings of the 2017 International Conference on "Physics, Mechanics of New Materials and Their Applications"*, ed. by I.A. Parinov, S.-H. Chang, V.K. Gupta (Nova Science Publishers, New York), pp. 7–13 (2018)
5. A.A. Voitash, V.Yu. Vishnevsky, Yu.V. Berestneva, E.V. Raksha, A.V. Muratov, A.B. Eresko, V.A. Glazunova, V.V. Burhovetskiy, G.K. Volkova, M.V. Savoskin, in *Applied Aspects of Nano-Physics and Nano-Engineering*, ed. by K. Levine, A.G. Syrkov (Nova Science Publishers, New York), pp. 25–28 (2019)
6. G. Bepete, E. Anglaret, L. Ortolani, V. Morandi, K. Huang, A. Penicaud, K. Drummond, Nat. Chem. **9**, 347–352 (2017)
7. W. Sirisaksoontorn, A.A. Adenuga, V.T. Remcho, M.M. Lerner, J. Am. Chem. Soc. **133**, 12436–12438 (2011)
8. E.D. Grayfer, A.S. Nazarov, V.G. Makotchenko, S.J. Kim, V.E. Fedorov, J. Mater. Chem. **21**, 3410–3414 (2011)

Chapter 5
Formation of Surface Micro and Nanostructures When Exposed to Laser UV and VUV Radiation of Nanosecond Duration

Vladislav Khomich, Vladimir Yamshchikov, and Sergey Mikolutskiy

Abstract Micro- and nanostructures improved different surface properties, which is used in various fields of science and technology. It is of a great interest to develop the physical foundations of new effective methods for creation of such structures. The paper proposes a method of direct laser micro- and nanostructuring based on nanosecond lasers with radiation of UV and VUV range. The method allows surface laser treatment of materials with different physical properties: metallic alloys, ceramics, diamond-like films, semiconductors. Formation of surface micro and nanostructures on the surfaces of diamond-like film, germanium, aluminum oxide and zirconium bronze is demonstrated. A theoretical model of nanostructure formation on solid surface melted by nanosecond laser pulse is considered. Moreover, a simple model for formation of conical structures at laser ablation without melting is described.

5.1 Introduction

The formation of micro- and nanostructures on the material surface can improve its optical, tribological, adhesive, hydrophilic and other technical properties [1–5]. Also it enhance biocompatibility between living tissues and implants employed in dentistry and orthopedics. Due to that fact surface micro- and nanostructuring found its application in microelectronics, nanophotonics, selective nanocatalysis, spectroscopy, power optics, machine manufacturing, medicine, and so on. Therefore, it is of a great interest to develop new effective methods for obtaining surface structures with characteristic sizes less than 100 nm.

It is generally known that there are a lot of methods and techniques for producing nanomaterials and surface nanostructures. They are laser irradiation with use of projection-masks; interference of two or more laser beams; combination of laser beam with the tip of atomic force microscope; direct laser nanostructuring by pico- and femtosecond lasers [2, 6–8].

V. Khomich · V. Yamshchikov (✉) · S. Mikolutskiy
Institute for Electrophysics and Electric Power RAS, Saint-Petersburg, Russia
e-mail: yamshchikov@ras.ru

I. A. Parinov et al. (eds.), *Advanced Materials*, Springer Proceedings in Materials 6, https://doi.org/10.1007/978-3-030-45120-2_5

In this paper we consider results on direct laser micro- and nanostructuring by nanosecond lasers with ultraviolet (UV) and vacuum ultraviolet (VUV) radiation of different wavelengths (157, 193 and 355 nm). Moreover, the chapter describes a mechanism of nanostructure formation on the solid surface by nanosecond laser radiation.

5.1.1 Research Purpose

The formation of micro and nanostructures on solid surfaces exposed to laser UV and VUV radiation of nanosecond duration is investigated. A theoretical model of nanostructure formation on solid surface by nanosecond laser pulse melting the material is proposed.

5.1.2 Research Scope

At this study, we consider the following frameworks of the problem:

(i) experimental setup for direct laser micro- and nanostructuring with nanosecond lasers;
(ii) theoretical models of nanostructure formation on the solid surface under the action of nanosecond laser pulse;
(iii) analysis of surface topography after laser treatment by UV and VUV radiation.

5.2 Research Method

5.2.1 Experimental Setup for Direct Laser Micro- and Nanostructuring

In our experiments we use a simple method of so called "direct" laser nanostructuring [9, 10], which does not require the use of projection masks, the surface shielding with small micro- and nanoparticles, or the interference of two or more laser beams on the surface of material. This method is effective and affordable in implementation due to simple optical scheme. The method includes only one stage, which is laser irradiation of the surface with high intensity enough for melting or sublimation of the material. As sources of coherent light, we use nanosecond lasers generated UV and VUV radiation of different wavelengths (157, 193 and 355 nm). Nanosecond lasers are simpler and more reliable in operation at a relatively low cost. They have higher output energy and stability of radiation pulses than femtosecond lasers.

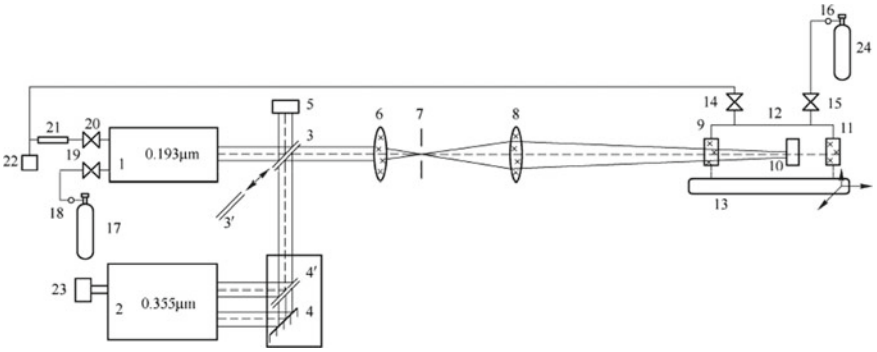

Fig. 5.1 Scheme of experimental setup for direct laser micro- and nanostructuring. 1—ArF-laser; 2—NdYAG laser; 3—translucent mirror; 4—turning mirror; 5—laser radiation energy meter; 6—condenser; 7—diaphragm; 8—projection lens; 9, 11—fluorite windows; 10—irradiated sample; 12—gas chamber; 13—scanning table; 14, 15, 19, 20—gas valves; 16, 18—pressure regulators; 17—balloon with premix; 21—halogen filter; 22—the vacuum pump; 23—pump; 24—balloon with a gas mixture

Figure 5.1 shows a scheme of an experimental setup [11] consisting of two laser sources: an excimer ArF laser 1 and a pulsed solid-state NdYaG laser 2 operating at the third harmonic. The radiation from the selected laser with a system of dichroic mirrors 3, 3′ and mirrors 4, 4′ is directed to the forming optical system consisting of the condenser 6, the diaphragm 7 and the projection lens 8, and then through the fluorite window 9 of the gas chamber 12 on the sample 10. The gas chamber allows sample irradiation in gas media, if it is necessary. The gas chamber is mounted on a three-coordinate positioner 13 controlled by a PC to move the irradiation spot along the surface (scanning) of the sample fixed inside.

The experimental setup allows laser treatment of material samples with laser pulses of 20 ns duration at wavelengths of 193 and 355 nm. The use of fluoride laser with wavelength of 157 nm allows surface modification of almost any material. The combination of a short pulse duration and a short wavelength radiation absorbed in the micrometer layer makes it possible to affect a thin (near several μm) surface layer, in which large temperature gradients are created, which contribute to the formation of new micro- and nanostructures.

In a case of fluoride laser [12] the whole optical path and material sample are inserted in a gas chamber, because of intensive absorption of radiation with a wavelength of 157 nm in the atmosphere. A scheme of this chamber is shown in Fig. 5.2. The chamber can be pumped up with a nitrogen or other working gas. It comprises a window for laser beam entrance 1, a transparent window 8 from polymethyl methacrylate to observe the sample to be irradiated, and also a control mechanism 7 for sample displacement and a sample adjustment with the help of a sample holder 5. Focusing lens 4 and splitting plate 2 were also placed inside the chamber. The laser was connected with the chamber by flexible tube 1. A chamber flange 9 could

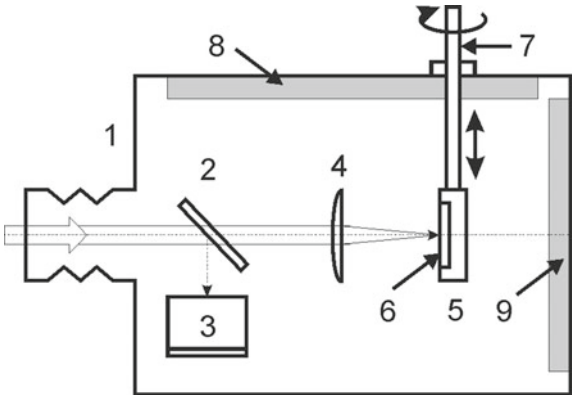

Fig. 5.2 Scheme of the gas chamber: 1—flexible tube for laser beam entrance; 2—fluorite plate; 3—energy meter; 4—focusing lens; 5—sample holder; 6—sample; 7—sample control mechanism; 8—transparent window; 9—removable flange

be easily removed allowing to change the sample 6 in the chamber and also to adjust a position of the mentioned optical elements 2, 4 and the laser energy meter 3.

The investigation and obtaining of surface topography characteristics of irradiated samples were carried out using the NewView 7300 optical profilometer, the Alpha 300 atomic force microscope (AFM) and the Phenom Pro X table scanning electron microscope. The pulse energy density was estimated as the ratio of the measured laser radiation energy to the characteristic cross-sectional area of the focused laser beam.

5.2.2 Theoretical Model of Nanostructure Formation on the Solid Surface Melted by Nanosecond Laser Pulse

There are many models of direct laser nanostructuring of a wide range of technological materials (metals, ceramics, diamond films, polymers) for a variety of surface modification processes [9, 12–14]:

(i) laser-induced evaporation in the absence of melting,
(ii) etching,
(iii) deposition,
(iv) the combined effect of melting and evaporation,
(v) laser pulse melting the surface of solids in the absence of intense evaporation,
(vi) stress relaxation in the material in the form of nanostructures.

In this chapter we consider the mechanism for nanostructure formation on the solid surface melted by nanosecond laser pulse. Two parts can be mentioned by the solution of this task. In the first part, the process of material melting under the action of laser pulse and the Stefan problem with the corresponding boundary conditions is being solved. In the second part, the process of a melted layer cooling at the expense of heat conductivity into the solid phase together with a theory explaining

the formation of crystalline seeds is being considered [9]. In the result, we obtain the expression for the characteristic size of nanostructures depending on the pulse duration and energy.

So let us consider a semi-infinite one-dimensional plane of material at initial temperature $T = T_{in}$ for $x \in [0, \infty]$. The material is heated with heat flux of pulsed laser radiation. The flux causes the material to melt down leaving an interval $[0, y(t)]$ occupied by material melt, where $y(t)$ is moving boundary of two phases (liquid and solid). Using heat equations for each phase with corresponding boundary conditions we have

$$\frac{\partial^2 T_1}{\partial x^2} = \frac{1}{a_1}\frac{\partial T_1}{\partial t}, \quad 0 < x < y(t), \tag{5.1}$$

$$\frac{\partial^2 T_2}{\partial x^2} = \frac{1}{a_2}\frac{\partial T_2}{\partial t}, \quad y(t) < x < \infty, \tag{5.2}$$

$$T_2(x, 0) = T_2(\infty, t) = T_{in}, \tag{5.3}$$

$$\frac{\partial Q(t)}{\partial t} = -\lambda \frac{\partial T_1}{\partial x}|_{x=0}, \tag{5.4}$$

$$T_1\big|_{x=y(t)} = T_2\big|_{x=y(t)} = T_k, \tag{5.5}$$

where a, λ, c are the thermal diffusivity, thermal conductivity, and specific heat capacity, respectively; ρ is the material density; $Q(t)$ is the energy absorbed per unit area during $t < \tau$, where τ is the pulse duration; T_k is the melting temperature. Liquid phase is denoted by number 1, solid phase is denoted by number 2.

Making certain simplifications [9] and solving this system of equations we get transcendental equation to define β:

$$2c\rho(T_k - T_{in})\sqrt{\frac{a}{\pi}} = \left\{\sqrt{2}H\rho\beta\left[\exp\left(\beta^2/2a\right) - 2\right] + Q(\tau)/\tau\right\} erfc\frac{\beta}{\sqrt{2a}} \tag{5.6}$$

This parameter β allows us to calculate melting depth of different materials irradiating with laser pulses of various duration and energy.

After laser pulse ends a phase transition process starts. Liquid phase transforms into solid one. The crystallization with nanostructure formation occurs if cooling rate of molten metal is high enough. To determine the cooling rate we need to solve the problem of molten layer cooling into solid phase [9].

Using variation principle in basic heat conduction law [15] and kinetic equation in nucleation theory [16] we obtain the size of nucleating center of solid phase in supercooled liquid:

$$r(t) = v_0 d \exp\left(-\frac{U}{kT_k}\right)\frac{kT_k^2}{U\varepsilon}\left\{\frac{h}{U+h} - \exp\left(-\frac{U\varepsilon t}{kT_k^2}\right) + \frac{U}{U+h}\exp\left[-\frac{\varepsilon t(U+h)}{kT_k^2}\right]\right\}$$
$$\approx R\left[1 - \exp\left(-\frac{U\varepsilon t}{kT_k^2}\right)\right], \tag{5.7}$$

$$R = \frac{v_0 d \exp(-U/kT_k) kT_k^2 h}{\varepsilon U(U+h)}. \tag{5.8}$$

Here v_0 is the Debye frequency of atom oscillation in supercooled liquid, d is the characteristic size per atom, U is the activation energy for atom transition, kT is the thermal energy, $\Delta\mu$ is the difference of atom chemical potentials in supercooled liquid at temperature T and phase change temperature of T_k ($\Delta\mu = h(T_k - T)/T_k$), where h is the heat of phase change per atom).

For example, at cooling rates $\varepsilon \approx 10^7$ °C/s average characteristic size is about 10 nm. By reducing the cooling rate to 10^6 °C/s and 10^5 °C/s distribution function shifts to larger sizes with a maximum at r ≈ 100 and ~500 nm, respectively.

5.2.3 *Nanostructure Formation Without Melting*

For some materials such as diamond-like film the surface melting at nanosecond laser pulses is practically absent. A possible mechanism of surface structure formation is a non-homogeneous laser vaporization giving rise to a formation of cones having sub-micron lateral sizes.

It is proposed that the growth of cones is initiated by material non-homogeneities represented by particles having a higher ablation threshold F'_a then threshold F_a of surrounding material. Particles can originally be available in the material or on its surface before irradiation, or can be created in a course of multipulse irradiation as a result of laser-induced chemical transformations. These submicron particles are situated in the peaks of cones. Laser fluence F for cones formation should be in a range $F_a < F < F'_a$, otherwise even these more resistant to ablation particles can be removed from the surface.

Surface relief in a shape of cones represents an example of self-organizing surface structures at laser ablation. After many pulses the slope i of the lateral surface of cones (Fig. 5.3) changes and is self-adjusted to the incident laser beam in such a way that incident laser fluence F becomes exactly equal to a ablation threshold $F_a(i)$ for lateral surface of the cone [12]:

$$F = F_a(i) = \frac{A(i=0)F_a(i=0)}{A(i)\cos i}. \tag{5.9}$$

Here A is the local surface absorption factor depending on the angle of beam incidence i on the lateral surface of the cone. As follows from evident geometrical

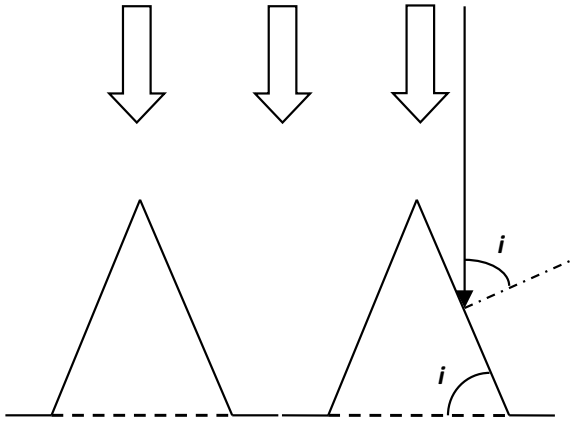

Fig. 5.3 Scheme of cone formation at laser irradiation; i is an angle of beam incidence on the lateral surface of the cone

consideration, i is simultaneously the angle at the cone base. The relation (5.9) means that laser ablation stops on cone surface with such angle at the cone base for the given laser fluence F, even at a continuation of irradiation with pulses with such laser fluence. Although the ablation continues to go on parts of the material surface with other slopes having another angle of radiation incidence, it can be a base plane of the material or surface of other cones with other slopes, for which the incidence angle i' of incoming radiation is smaller: $i' < i$.

The relation (5.9) is valid when two following conditions are fulfilled:

$$d \gg \lambda \; and \; d > 2\sqrt{\chi \cdot \tau}. \tag{5.10}$$

Here d is a lateral (along the surface) size of the cones, λ is a radiation wavelength, χ is the thermal diffusivity of the material, τ is a pulse duration. The first inequality is a condition of geometrical optics applicability, and the second inequality provides a difference in heating rates of lateral cone surface and of the base material plane around the cone. This difference provides the emergence and further growth of cone from the base plane. Thus, the minimal cone size can be evaluated from (5.10) as

$$d_{\min} > \max(\lambda, 2\sqrt{\chi \cdot \tau}). \tag{5.11}$$

Thus, if we know the thermal diffusivity of the material and laser radiation parameters, we could estimate the minimal lateral size of structures forming without melting.

5.3 Results and Discussion

5.3.1 Processing by a F2-Laser with Wavelength of 157 Nm

The radiation of fluoride laser with extremely short wavelength of 157 nm makes possible the treatment of superhard materials such as ceramics and diamond like films. In our experiments we study the formation of submicron structures on the surface of a diamond like film on a rough copper substrate. The samples were irradiated by fluoride laser with 100 laser pulses with an incident energy density of about 3 J/cm^2 at still laser spot. The analysis of irradiated sample surface is carried out by an atomic-force microscope (AFM).

AFM analysis shows that for diamond-like film the initial non-irradiated surface already contains nanograins with characteristic lateral sizes from 40 to 70 nm and a small enough aspect ratio about 0.1–0.15 (Fig. 5.4a). After irradiation with laser energy density of 3 J/cm^2 conical structures with lateral size from 200 to 600 nm were formed (Fig. 5.4b). The aspect ratio of these structures was about 1.

The formation of conical structures on diamond-like film surface can be explained by model of laser ablation without melting mentioned above. In our case for laser ablation of diamond-like film, which is accompanied with a material grafitisation, probable candidates for particles at the peaks of cones can be a material formations from a so-called “hard carbon”, which is intermediate phase between diamond and graphite. According to (5.11) and considering that the thermal diffusivity of material at high temperature stage is about 1 mm^2/s and the pulse duration is 20 ns, we obtain the minimal lateral size of surface structures is about 280 nm. Such simple estimation agrees well with cone sizes 200–600 nm observed in the experiment (Fig. 5.4).

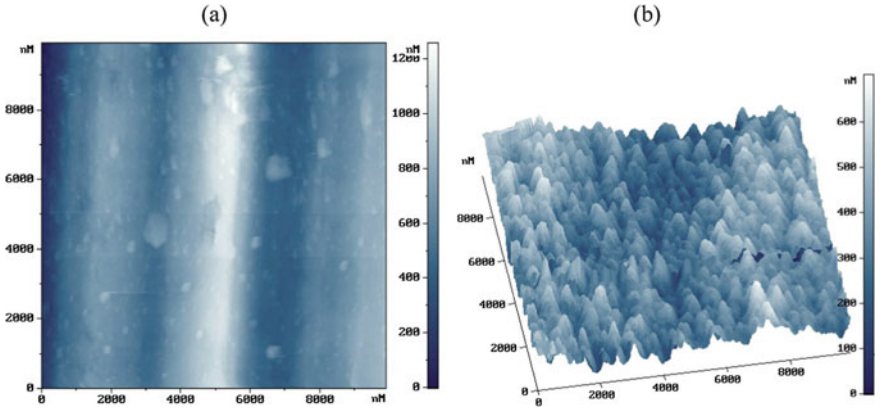

Fig. 5.4 AFM images of non-irradiated diamond-like film (**a**) and diamond-like film after irradiation by 100 pulses of fluoride laser with energy density of 3 J/cm^2 (**b**)

5.3.2 *Processing by ArF-Laser with Wavelength of 193 Nm*

Another source of coherent radiation, which is suitable for nanostructuring, is the excimer ArF-laser with a wavelength of 193 nm, since its radiation strongly absorbed by most materials [14, 17]. In this work the formation of nanoreliefs on germanium surface is carried out by one laser beam without any optional devices and masks. After the necessary preparatory procedures, germanium samples were irradiated by laser pulses with energy density from 2 to 4 J/cm^2 and pulse duration of 20 ns.

AFM-analysis shows the formation of various types of surface micro- and nanostructures in different parts of irradiation zone. In Fig. 5.5 one can see relief of non-irradiated germanium surface and nanostructures in peripheral low-intensity region of the irradiation spot. They have the form of bulbs with rounded peaks with characteristic dimensions along the surface of 40–120 nm and height of 40–70 nm. Considering the model for nanostructure formation on the solid surface melted by laser pulse (5.1–5.8) with material parameters for germanium and laser irradiation conditions for ArF-laser, we obtain the estimation for average diameter of nanostructures on germanium surface is about 20 nm after the action of 1 laser pulse.

Moreover, on the germanium surface AFM-analysis shows the formation of another various types of micro- and nanostructures in different parts of irradiation zone [17]. In the region of shallow melt one can see the relief in the form of hexa- and pentagonal cells with characteristic dimensions along the surface of 300–500 nm and the height of the edges between the cells of 20–25 nm. Near the center of the spot in the region of "deep" melt wavy relief arises with period of about 1500 nm and amplitude of about 700 nm. In the ablation zone of central part of the spot we can see wavelike relief with periods of 200–400 nm and amplitude of about 150 nm. Considering these experimental data, we propose five main types of surface reliefs formed by nanosecond laser pulses melting the solid surface [17].

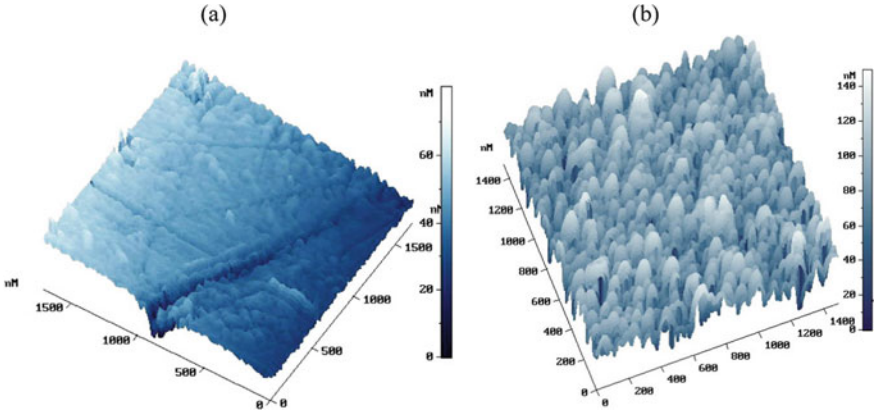

Fig. 5.5 AFM images of non-irradiated germanium surface (**a**) and germanium after irradiation by 20 pulses of ArF-laser with energy density of 2–4 J/cm^2 (**b**)

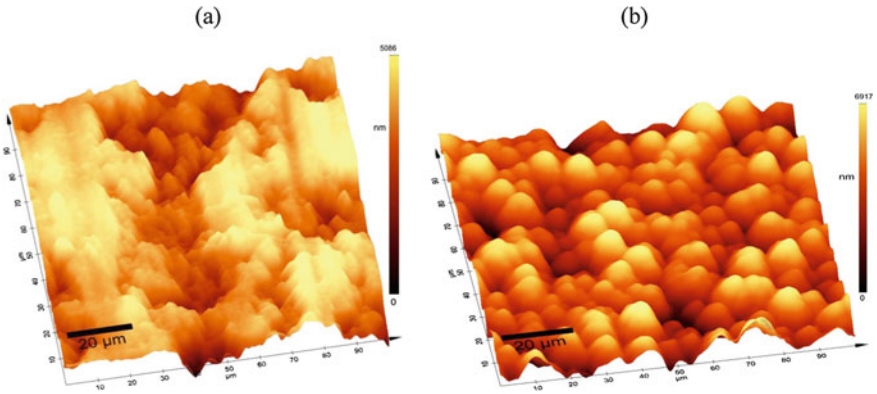

Fig. 5.6 AFM images of non-irradiated aluminum oxide surface (**a**) and aluminum oxide after irradiation by scanning beam of Nd:YaG-laser with scanning speed of 0.25 mm/s and energy density of 0.2 J/cm^2 (**b**)

5.3.3 Processing by a Nd:YaG-Laser with Wavelength of 355 Nm

Now we consider micro- and nanostructuring by solid-state Nd:YaG-laser working on third harmonic with wavelength of 355 nm. It is suitable for processing even ceramic materials such as aluminum oxide. Irradiation by scanning beam of solid-state laser at scanning speed of 0.25 mm/s, energy density of about 0.2 J/cm^2 and frequency of 100 Hz leads to formation of surface round structures with lateral size from 5 to 15 μm and height of about 1–2 μm (Fig. 5.6). This result can be used for changing tribological or adhesive material properties [4, 18].

Interesting results were obtained in a case of processing the zirconium bronze surface by scanning beam of Nd:YaG-laser. Figure 5.7 shows the structures in the form of submicron spherical drops with diameter of 500 nm located on the tops of conical legs with lateral size of 300–400 nm at a characteristic distance between structures along the surface of 1.5–2 μm [4]. This type of structures is also known as microjets. The formation of such structures was observed at laser pulse energy densities from 0.6 to 1.2 J/cm^2, and the number of spherical structures per unit area increases with increasing laser pulse energy density. It was also found that the number of such structures per unit area increases with a decrease in the scanning speed of the laser beam over the surface [4].

The growth of structures in the form of submicron spherical droplets on the legs can be explained by the combined action of melting and evaporation in a certain range of energy densities above the melting threshold. For example, modulation of the surface topography in the form of capillary waves with micron periods for metals and alloys [19, 20] leads to the corresponding modulation of temperature and evaporative pressure along the surface in the form of a certain two-dimensional quasi-periodic lattice. The melt during such inhomogeneous evaporation is squeezed

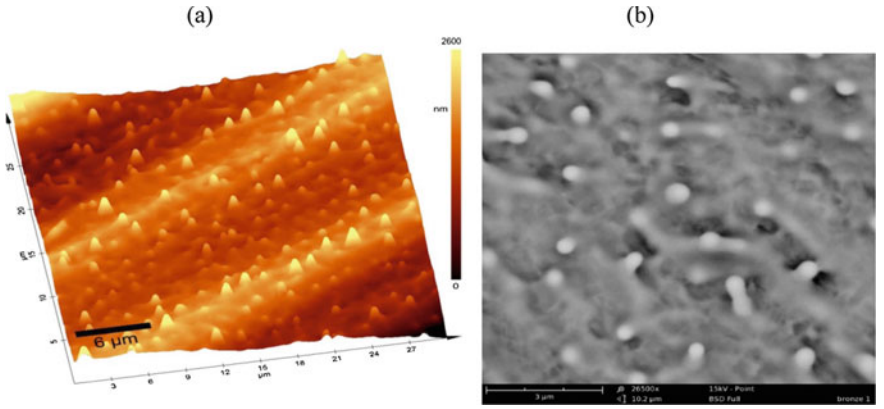

Fig. 5.7 Images of bronze surface irradiated by scanning beam of Nd:YaG-laser with energy density of 1.2 J/cm^2 by means of AFM (**a**) and SEM (**b**)

along the surface to the places of the minimum evaporation pressure, where the liquid jets of the melt are released mainly in the direction transverse to the surface. In this case, the surface tension forces lead to the development of spherical droplets at the ends of these jets at the final stage of their development, when the action of pulsed evaporation pressure ends and solidification of the melt begins.

Materials with surface processed in this way could be used in different fields of science and technology. For example, we use laser surface micro- and nanostructuring in diffusion welding, where heterogeneous materials such as metallic alloys connect to each other in special chamber at high temperature and pressure [4].

5.4 Conclusion

A method of direct laser micro- and nanostructuring by nanosecond lasers with UV and VUV radiation of different wavelengths (157, 193 and 355 nm) is proposed. A theoretical model of nanostructure formation on solid surface melted by nanosecond laser pulse is considered. Moreover, a simple model for formation of conical structures at laser ablation without melting is described. Both models give consistent results according to experimental data for corresponding processes of laser treatment. Using the radiation of nanosecond F2-laser, ArF-laser and Nd:YaG-laser micron, submicron and nanostructures were obtained on the surfaces of diamond-like film, germanium, aluminum oxide and zirconium bronze. These types of structures can be used in nanophotonics, spectroscopy, microelectronics, machine manufacturing, nuclear industry, aviation, space technology, and many other fields of science and technology.

Acknowledgements This research was performed into framework of State assignment of IEE RAS.

References

1. F. Luo, W. Ong, Y. Guan, F. Li, Sh Sun, G.C. Lim, M. Hong, Appl. Surf. Sci. **328**, 405 (2015)
2. T. Csizmadia, T. Smausz, C. Tapai, J. Kopniczky, X. Wang, M. Ehrhardt, P. Lorenz, K. Zimmer, L. Orosz, E. Varga, E. Oszko, B. Hopp, J. Laser Micro Nanoeng. **10**(2), 110 (2015)
3. V.Yu. Fominskii, S.N. Grigor'ev, R.I. Romanov, V.N. Nevolin. Techn. Phys. **57**(4), 516 (2012)
4. Yu.A. Vashukov, S.F. Demichev, V.D. Elenev, T.V. Malinskiy, S.I. Mikolutskiy, Yu.V. Khomich, V.A. Yamshchikov, Appl. Phys. **1**, 82 (2019). (in Russian)
5. P.F. Rios, H. Dodiuk, S. Kenig, S. McCarthy, A. Dotan, J. Adhes. Sci. Technol. **20**(6), 563 (2006)
6. K. Vestentoft, J.A. Olesen, B.H. Christensen, P. Balling, Appl. Phys. A **80**, 493 (2005)
7. Y. Nakata, T. Okada, M. Maeda, Proc. SPIE Int. Soc. Opt. Eng. **5662**, 749 (2004)
8. X. Wang, Y. Lu, J. Appl. Phys. **98**, 114304 (2005)
9. S.I. Mikolutskiy, V.Yu. Khomich, V.A. Shmakov, V.A. Yamshchikov, Nanotechnol. Russ. **6**(11–12), 733 (2011)
10. V.N. Tokarev, V.A. Shmakov, R.R. Khasaya, S.I. Mikolutskiy, S.V. Nebogatkin, V.Yu. Khomich, V.A. Yamshchikov, in *Proceedings of the 29th International Congress on Applications of Lasers and Electrooptics*, Anaheim, USA, p. 1257 (2010)
11. Yu.A. Zheleznov, T.V. Malinskiy, S.I. Mikolutskiy, Yu.V. Khomich, V.N. Tokarev, R.R. Khasaya, V.A. Yamshchikov, Appl. Phys. **3**, 83 (2014). (in Russian)
12. V.N. Tokarev, V.Yu. Khomich, V.A. Shmakov, V.A. Yamshchikov, Phys. Chem. Mater. Treat. **4**, 18 (2008). (in Russian)
13. V.Yu. Khomich, V.A. Shmakov, Phys. Uspekhi **58**, 455 (2015)
14. D.V. Ganin, S.I. Mikolutskiy, V.N. Tokarev, V.Yu. Khomich, V.A. Shmakov, V.A. Yamshchikov, Quantum Electron. **44**(4), 317 (2014)
15. J. Christian, in *The Theory of Transformations in Metals and Alloys*. Pergamon, Oxford, 1200 p. (1975)
16. M.A. Biot, *Variational Principles in Heat Transfer*. Oxford University Press, Oxford, 185 p. (1970)
17. S.I. Mikolutskiy, R.R. Khasaya, Yu.V. Khomich, V.A. Yamshchikov, J. Phys: Conf. Ser. **987**, 012007 (2018)
18. Yu.A. Zheleznov, T.V. Malinskiy, Yu.V. Khomich, V.A. Yamshchikov, Inorg. Mater.: Appl. Res. **9**(3), 460 (2018)
19. S.A. Ahmanov, V.I. Emel'yanov, N.I. Koroteev, V.N. Seminogov. Phys. Uspekhi **147**, 675 (1985)
20. V.N. Elkin, T.V. Malinskiy, S.I. Mikolutskiy, R.R. Khasaya, Yu.V. Khomich, V.A. Yamshchikov, Phys. Chem. Mater. Treat. **6**, 5 (2016). (in Russian)

Chapter 6
The Effect of Preliminary Laser Surface Treatment on the Mechanical Properties of a Solid-Phase Compound of an Iron-Nickel Alloy in Diffusion Welding

Yury Khomich and Vladimir Yamshchikov

Abstract Laser micro- and nanostructuring is used in various fields of science and technology, because it can improve different surface properties. The chapter considers a method of direct laser micro- and nanostructuring of metallic surfaces and an effect of such preliminary laser surface treatment on the mechanical properties of solid-phase joints made by diffusion welding. For laser treatment it is proposed to use scanning beam of Nd:YAG laser with a wavelength of 355 nm. Analysis of surface topography of samples treated by nanosecond laser was performed by optical profilometer. After the diffusion welding tensile tests were performed on conjunction samples cut out from welded workpieces. These tests showed that preliminary laser processing of the surface of samples made of nickel alloy leads to an improvement in the mechanical properties of the conjunction obtained by diffusion welding. It leads to an increase in the tensile strength up to 29% and tensile strain up to 20%. The pulse energy density at laser surface treatment significantly affects the properties of welded joint. Also the preliminary laser treatment of surfaces allows one to reduce the temperature of diffusion welding.

6.1 Introduction

Laser surface modification with the formation of micro and nanostructures is used in various fields of science and technology. Laser processing can improve electron-emission, radiative, tribological, hydrophobic and hydrophilic surface properties of materials [1–5]. Also the formation of periodic micron and submicron structures with specified geometry parameters by means of laser irradiation of the surface can lead to an improvement in the adhesion properties of materials and, thereby, an increase in the quality of the joint at a diffusion welding of homogeneous and dissimilar metals and alloys [6, 7]. The diffusion welding is a junction method, in which the parts

Y. Khomich · V. Yamshchikov (✉)
Institute for Electrophysics and Electric Power RAS, Saint Petersburg, Russia
e-mail: yamshchikov@ras.ru

I. A. Parinov et al. (eds.), *Advanced Materials*, Springer Proceedings in Materials 6, https://doi.org/10.1007/978-3-030-45120-2_6

come into contact under the conditions of a defined continuous pressure and heat up in the contact area or in the entire volume at a given temperature for a certain time [8]. In diffusion welding the connection is achieved due to mutual diffusion at the atomic level of the surfaces of the parts to be welded. The advantages of diffusion welding include the possibility of welding parts of different thickness and surfaces with a large area. This method is widely used in the nuclear industry, aviation and space technology.

In this paper we consider results on direct laser micro- and nanostructuring of the metallic surfaces and the effect of this preliminary laser surface treatment on the mechanical properties of solid-phase joints made by diffusion welding.

6.1.1 Research Purpose

The effect of preliminary laser surface treatment on the mechanical properties of a solid-phase compound of a nickel alloy in diffusion welding is investigated. A method of direct laser micro- and nanostructuring is proposed for sample surface treatment.

6.1.2 Research Scope

At this study, we consider the following frameworks of the problem:

(i) direct laser micro- and nanostructuring with nanosecond lasers;
(ii) theory of nanostructure formation on the solid surface under action of laser pulse;
(iii) analysis of surface topography of samples treated by nanosecond laser;
(iv) diffusion welding of irradiated samples and tensile tests for compounds obtained.

6.2 Research Method

6.2.1 Experimental Setup for Direct Laser Micro- and Nanostructuring

Various methods are used, among them applying of projection masks, interference of two or more laser beams, combination of laser radiation with the tip of a scanning probe microscope, and direct laser nanostructuring using picosecond and femtosecond lasers.

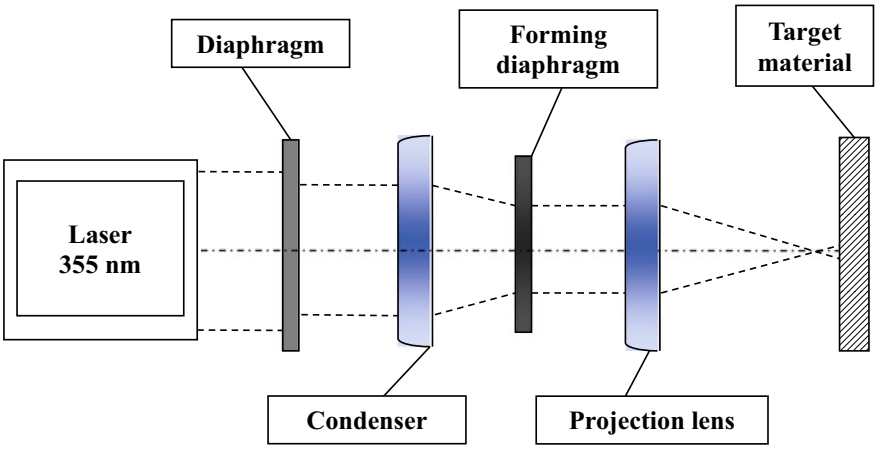

Fig. 6.1 Scheme of projection-optical system for method of direct laser micro and nanostructuring

In our experiments, we use the method of direct laser micro and nanostructuring with nanosecond lasers. This method is very affordable and effective in implementation, because it has a simple projection-optical system shown in Fig. 6.1. The method includes only one stage. It is a laser irradiation of the surface with intensity sufficient for melting or sublimation of the material. Scanning the surface by laser beam with high repetition rate of radiation pulses opens up the possibility of nanostructuring sufficiently large extended surface areas. As sources of coherent light we use nanosecond lasers generated UV and VUV radiation. At a relatively low cost, such lasers are simpler and more reliable in operation; they have higher output energy and stability of radiation pulses than femtosecond lasers.

Based on said above, an experimental setup for direct laser micro- and nanostructuring of the solid surface was created with use of ArF laser with a wavelength of 193 nm [9] and an Nd:YAG laser operating at the third harmonic with a wavelength of 355 nm [10]. When replacing the gas mixture and the optics, the ArF laser can work as an F2 laser and generate nanosecond radiation pulses with an extremely short wavelength of 157 nm. This allows one to perform surface modification of almost any material.

The combination of the short wavelength absorbed in the micrometer layer and the short pulse duration makes it possible to influence a small (several micrometers) surface layer, in which large temperature gradients are created, which contribute to the formation of new micro- and nanostructures. The shape and size of these structures also depend on the energy density, wavelength, number of pulses in the laser spot, as well as on the pulse repetition rate and the scanning speed of the laser beam over the surface [11]. As mentioned above laser processing can also influence the surface properties of a material. This can be used in laser technologies for surface preparation in diffusion welding.

In this chapter we performed experimental studies on diffusion welding with preliminary laser processing of the welded surfaces of workpieces made of nickel alloy (ChS57). For the experiments we used cylindrical samples with a diameter of 22 mm and a height of 18 mm. In order to prevent the formation of oxides on the surface of the workpieces during laser processing, the samples were placed in a sealed chamber from which air was evacuated and an inert gas (argon) was injected under a pressure of 1.5 atm. The surfaces to be welded were pretreated with radiation of Nd:YAG laser pulses with a wavelength of 355 nm. The pulse duration was 10 ns, the pulse repetition rate was 100 Hz and the cross-section radius of the laser spot in the workpiece plane was 220 μm. The laser beam was moved along the surface of the workpieces along a raster path (snake) at a speed of 1 mm/s and a pitch of 10 μm along the x-axis and 30 μm along the y-axis. The main variable laser processing parameters were pulse energy density and number of laser pulses per unit area.

6.2.2 *Nano- and Microstructure Formation Under the Action of Laser Pulse*

The duration of pulses of nanosecond laser radiation is much longer than the electron-phonon relaxation time, which is several or tens of picoseconds for various materials. Therefore, thermal processes occur already during laser exposure to the material. The depth of the surface layer modified by laser radiation is determined by a thermal diffusion length during the duration of the laser pulse τ.

$$L_T = 2\sqrt{\chi \cdot \tau}. \tag{6.1}$$

Here χ is the thermal diffusivity of the material. When irradiated with nanosecond pulses, L_T turns out to be much larger than for femtosecond pulses. For metals the depth of the modified layer reaches several microns. This can be crucial for a number of practical applications, for example in the case diffusion welding. From the theoretical point of view there are many models of direct laser nanostructuring of a wide range of technological materials (metals, ceramics, diamond films, polymers) for a variety of surface modification processes: laser-induced evaporation in the absence of melting; etching; deposition; the combined effect of melting and evaporation; laser pulse melting the surface of solids in the absence of intense evaporation; stress relaxation in the material in the form of nanostructures [11–14].

In a case of heat-resistant nickel alloy, which consists of many different elements, defining the mechanism of surface structure formation is a very complicated task. However, for simple evaluation of sizes of surface structures formed by laser radiation one can use formula for lateral size of long roughness periods [14]:

$$d_{\min} > \max(\lambda, L_T), \tag{6.2}$$

where λ is a radiation wavelength. We use a third harmonic of Nd:YAG laser with a wavelength of 355 nm. Considering that in our case the thermal diffusivity χ of nickel alloy is about 6 mm^2/s and the pulse duration is 10 ns, we obtain the thermal diffusion thickness L_T near to 500 nm. Thus, for our case minimal lateral size of surface structures is about 500 nm.

6.2.3 *Diffusion Welding*

Diffusion welding is widely used in many engineering industries. The implementation of welding in hot isostatic press extends the technological capabilities of this method. Improving the quality of the connection and expanding the allowable temperature range of welding remains to be a relevant task.

Diffusion welding is pressure welding in which parts contact at a set continuous pressure and are heated in the contact area or in the entire volume at a given temperature for a specified time. We performed diffusion welding in gasostat (Abra, Switzerland) under hot isostatic pressing (ISP) conditions. The scheme of diffusion welding in gasostat is presented on Fig. 6.2a. Figure 6.2b shows cyclograms of temperature and pressure changes during diffusion welding. Welding of workpieces was carried out at temperature 1000 °C and at temperature 1160 °C. In both cases working continuous pressure was about 160 MPa. The welding time was about 3 h.

We performed experimental investigation on diffusion welding with preliminary laser processing of the welded surfaces of workpieces made of nickel alloy (ChS57). Two modes with different energy density of laser radiation were used for sample

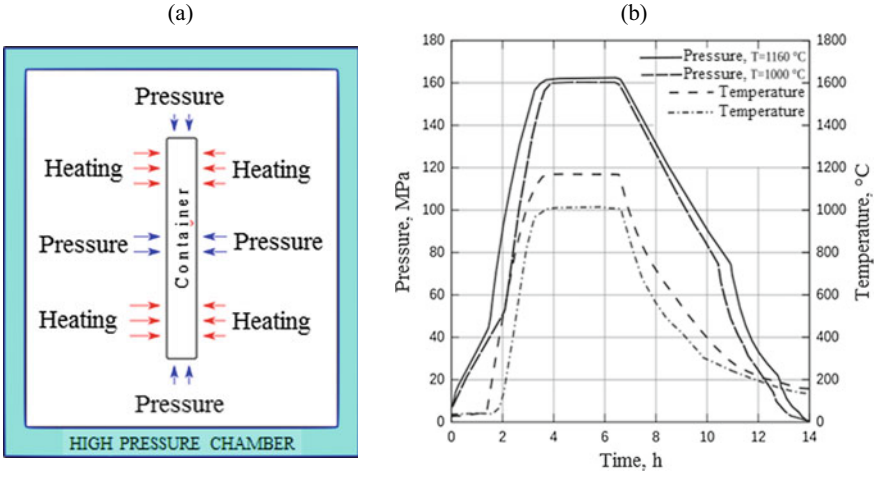

Fig. 6.2 Scheme of diffusion welding (**a**) and cyclograms of temperature and pressure changes during diffusion welding (**b**)

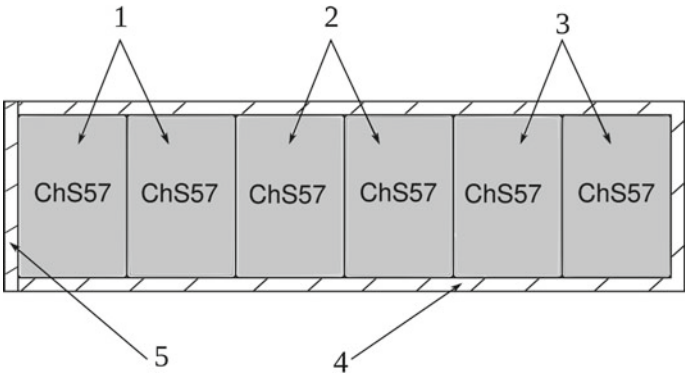

Fig. 6.3 Vacuum container with three groups of samples: (1) laser treatment with the energy density 2 J/cm^2 (mode 1); (2) laser treatment with the energy density 3 J/cm^2 (mode 2); (3) samples with non-irradiated surface; (4) thin walled container; (5) container cover

surface treatment: mode 1 with the energy density 2 J/cm^2, mode 2 with the energy density 3 J/cm^2. After laser treatment the samples were placed in a container as shown on Fig. 6.3. The container was sealed by an electron beam in a vacuum and then it was placed in a gasostat.

6.3 Results and Discussion

6.3.1 Processing by a Scanning Beam of Nd:YAG Laser

As mentioned above the sample surfaces were pretreated by scanning beam of Nd:YAG laser working on third harmonic with a wavelength of 355 nm. The pulse duration was 10 ns, the pulse repetition rate was 100 Hz and the cross section radius of the laser spot in the workpiece plane was about 200 μm. The laser beam was moved along the surface of the workpieces along a raster path (snake) at a speed of 1 mm/s.

The profiles of the irradiated surface were analyzed with an optical profilometer (Zygo NewView 7300). Figure 6.4a shows surface profile of nickel alloy marked as ChS57 without laser treatment, where only mechanical treatment traces are visible in the form of furrows with a width of 10–40 μm and a height of 5 μm. Surface profile after laser treatment with a pulse energy density of 1 J/cm^2 is shown in Fig. 6.4b and c presents an optical image of the same irradiated surface of ChS57. As can be seen, after laser irradiation the initial grooves begin to break into round hill-shaped islands with transverse dimensions from 5 to 10 μm and a height of approximately 500 nm.

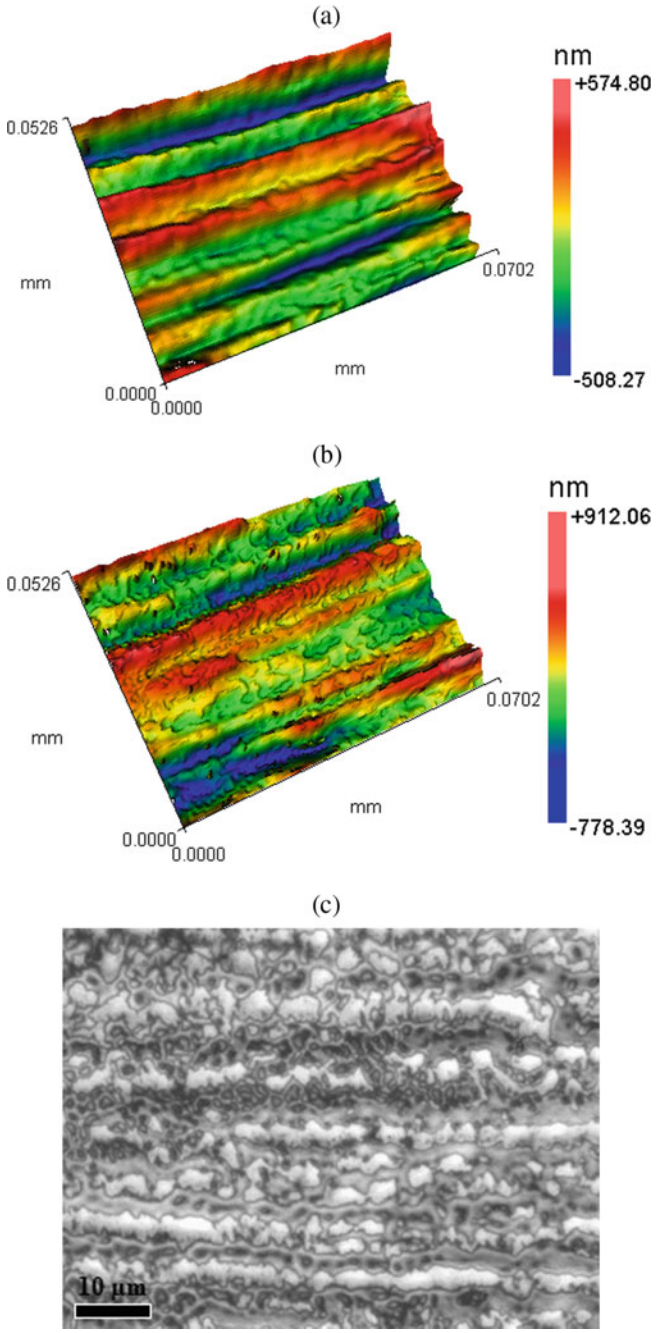

Fig. 6.4 Profilometry data for non-irradiated ChS57 surface (**a**) and surface after laser treatment with energy density of 1 J/cm^2 (**b**) with its optical image (**c**)

For further diffusion welding sample laser processing was performed in two modes with different energy density of laser radiation: mode 1 with the energy density 2 J/cm^2, mode 2 with the energy density 3 J/cm^2.

6.3.2 *Tensile Tests After Diffusion Welding of Samples Treated by Laser*

After laser treatment, the nickel alloy samples were placed in a container, which was sealed by an electron beam in a vacuum. Then the diffusion welding in gasostat was carried out at certain conditions mentioned above (Fig. 6.2). After the diffusion welding tensile tests were performed at room temperature on conjunction samples cut out from welded workpieces. In the result of tensile tests for nickel alloy conjunctions we obtained average tensile strength and tensile strain for different welding temperatures and modes of laser treatment.

Figure 6.5 shows tensile strength of welded joints of ChS57 samples without preliminary processing and after laser modification in modes 1 and 2. They are obtained at welding temperatures $T = 1160$ °C and $T = 1000$ °C. For temperature $T = 1160$ °C the tensile strength of the conjunctions with laser treatment reaches 630 MPa. There is an increase of the tensile in both modes by 12% compared to control non-irradiated samples. When the temperature of hot isostatic pressing is reduced to 1000 °C, the effect of laser treatment on the tensile strength in mode 1 becomes even more significant and reaches 29%. Thus, preliminary laser treatment with an energy density of 2 J/cm^2 provides an increase in the tensile strength at the welding temperature of 1000 °C and at a temperature of 1160 °C.

Similar results are observed for tensile strain also called an elongation at break (Fig. 6.6). At a temperature of 1160 °C the tensile strain of the laser treated conjunctions in both modes increased by 20% compared to the control non-irradiated

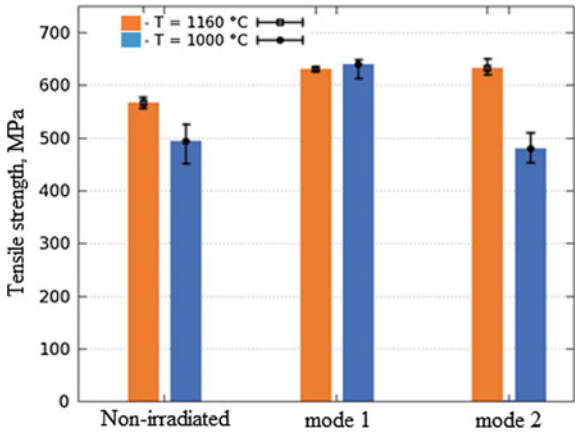

Fig. 6.5 Tensile strength of welded joints of ChS57 samples without preliminary processing and after laser modification; welding temperature $T = 1160$ °C (orange column) and $T = 1000$ °C (blue column)

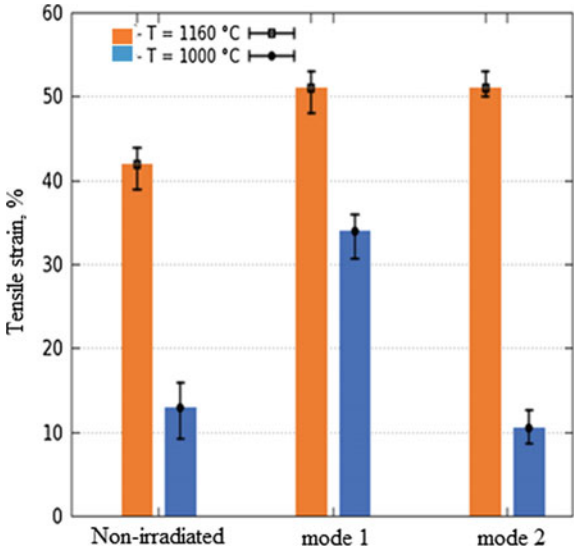

Fig. 6.6 Tensile strain (elongation at break) of welded joints of ChS57 samples without preliminary processing and after laser modification; welding temperature $T = 1160$ °C (orange column) and $T = 1000$ °C (blue column)

samples. However, at the temperature near 1000 °C these values differ significantly. For mode 1, the elongation increased by 2.6 times, and for mode 2 decreased by 20%. Thus, the pulse energy density during surface laser treatment of welded samples significantly affects the mechanical characteristics of the welded joint.

Let us consider some possible reasons for the improvement of mechanical properties in welded joints with preliminary laser treatment of the surface. It is known that the diffusion coefficient along the grain boundaries can be some orders of magnitude higher than the values in the grain volume [15]. Therefore, the creation of ultra-fine-grained material on the surface under the action of a laser can significantly increase the density of the mesh along the grain boundaries and provide a more active diffusion in the material.

The second reason for improving the mechanical properties of the welded joint may be a more uniform distribution of the degree of deformation in conjunctions with preliminary laser surface treatment. The creation of micro and nanostructures on the surfaces to be welded results in more efficient slamming of irregularities in the joint area [16].

In our results, the preliminary laser treatment of surfaces allows one to reduce the temperature of diffusion welding. At a reduced temperature, the phenomenon of low-temperature superplasticity can play a significant role in the character of the solid-phase conjunction. This phenomenon is observed in metals and alloys, which are characterized by a structure with an ultra-fine grain with a diameter of about 1 μm or less [17, 18]. Such average size of the grains can be formed during the preliminary laser treatment. Early by us it has been shown that the lower energy density of the laser pulses, the smaller characteristic size of the surface structures [13, 14]. This circumstance is consistent with the results of experiments in which a higher quality

conjunction was obtained in mode 1 with a lower energy density of irradiation pulses than in mode 2 at a welding temperature reduced to 1000 °C.

6.4 Conclusion

Preliminary laser processing of the surface of samples made of nickel alloy leads to an improvement in the mechanical properties of the conjunction obtained by diffusion welding. In particular, it leads to an increase in the tensile strength up to 29% and tensile strain up to 20%. The pulse energy density at laser surface treatment significantly affects the properties of welded joint. Also the preliminary laser treatment of surfaces allows one to reduce the temperature of diffusion welding. Thus, the present method of preliminary surface laser treatment for welded samples can be used in nuclear industry, aviation and space technology to improve bonding quality of dissimilar materials.

Acknowledgements This research was performed with the support of Presidium of the Russian Academy of Sciences, the Basic Research Program I.7. The authors thank Elkin V. N. and Malinsky T. V. for their assistance in conducting experiments and discussing the results of the work.

References

1. H.A. Quintana, E. Song, G.T. Wang, J.A. Martinez, Chem. Eng. Process Technol. **1**, 1008 (2013)
2. C.-T. Hsieh, J.-M. Chen, H.-H. Lin, H.-C. Shih, Appl. Phys. Lett. **83**, 3383 (2003)
3. V.Yu. Fominskii, S.N. Grigor'ev, R.I. Romanov, V.N. Nevolin. Tech. Phys. **57**(4), 516 (2012)
4. C.H. Crouch, J.E. Carey, J.M. Warrender, M.J. Aziz, E. Mazur, Appl. Phys. Lett. **84**(11), 1850 (2004)
5. M.C. Ferrara, L. Pilloni, S. Mazzarelli, L. Tapfer, J. Phys. D Appl. Phys. **43**, 095301 (2010)
6. V.N. Elkin, V.P. Gordo, V.V. Melukov, Bull. PNRPU Mech. Eng. Mater. Sci. **183**(7), 673 (2013) (in Russian)
7. Yu.A. Vashukov, S.F. Demichev, V.D. Elenev, T.V. Malinskiy, S.I. Mikolutskiy, Yu.V. Khomich, V.A. Yamshchikov, Appl. Phys. **1**, 82 (2019) (in Russian)
8. N.F. Kazakov, *Diffusion Welding of Materials* (Mashinostroenie, Moscow, 1976), 312 p (in Russian)
9. S.I. Mikolutskiy, R.R. Khasaya, Yu.V. Khomich, V.A. Yamshchikov, J. Phys: Conf. Ser. **987**, 012007 (2018)
10. S.I. Mikolutskiy, R.R. Khasaya, Yu.V. Khomich, in *Proceedings of the 14th Sino-Russia Symposium on Advanced Materials and Technologies*, November 2017 (Metallurgical Industry Press, Beijing, 2017), p. 319
11. V.Yu. Khomich, V.A. Shmakov, Physics Uspekhi **58**, 455 (2015)
12. D.V. Ganin, S.I. Mikolutskiy, V.N. Tokarev, V.Yu. Khomich, V.A. Shmakov, V.A. Yamshchikov, Quantum Electron. **44**(4), 317 (2014)
13. S.I. Mikolutskiy, V.Yu. Khomich, V.A. Shmakov, V.A. Yamshchikov, Nanotechnol. Russ. **6**(11–12), 733 (2011)

14. V.N. Tokarev, V.Yu. Khomich, V.A. Shmakov, V.A. Yamshchikov, Phys. Chem. Mater. Treat. **4**, 18 (2008) (in Russian)
15. M.Kh. Mukhametrakhimov, Lett. Mater. **3**, 276 (2013) (in Russian)
16. R.G. Khazgaliev, M.F. Imayev, R.R. Mulyukov, F.F. Safin. Lett. Mater. **5**(2), 133 (2015) (in Russian)
17. M.W. Mahoney, Superplastic properties of alloy 718, in *Superalloy 718—Metallurgy and Applications*, ed. by E.A. Loria (The Minerals, Metals & Materials Society, 1989), p. 391
18. R.Ya. Lutfullin, O.A. Kaibyshev, O.R. Valiakhmetov, M.Kh. Mukhametrakhimov, R.V. Safiullin, R.R. Mulyukov, Perspect. Mater. **4**, 21 (2003) (in Russian)

Chapter 7
The Nucleation and Development of Wear in Nanocomposite Coatings Under the Action of a Discrete Vapor-Droplet Flow

Valery N. Varavka, Oleg V. Kudryakov, Igor Yu. Zabiyaka, and Natalia I. Bronnikova

Abstract The analysis of the initial stage of wear initiation in crystalline materials with a heterogeneous structure under cyclic impact loading is conducted. Wear under these conditions begins with the formation of fatigue defects. Depending on the structure of the material and loading conditions, they are formed as cracks, pores or craters. A theoretical model is proposed for calculating the duration of their nucleation. The parameters of the model for its application in the conditions of droplet impingement erosion, in particular, under the influence of a discrete vapor-droplet flow, are considered and determined. The results of model calculations are presented in comparison with the experimental data of bench droplet tests for steel samples 20Cr13 with a sorbite structure and samples with a vacuum ion-plasma coating of the TiAlSi-system with a 3D-nanocomposite structure. It is shown that under conditions of contact cyclic loads, the wear resistance of materials and coatings is primarily determined by structural parameters. Based on the presented calculation results and experimental data, the use of the proposed model for the design of wear-resistant materials and coatings is recommended. Experimental data on the development of wear of the ion-plasma TiAlSi-coating upon droplet impingement action are also presented. Chipping of the coating occurs by the formation of fragmented porous cracks.

7.1 Introduction

From the applied point of view, the most problematic field of knowledge in studying of the fatigue wear of various industrial materials is the stage of nucleation of fracture sites, which can be cracks, pores, microcraters. Thus, when studying crack nucleation due to difficulties in instrumental fixing of cracks at the early stages of its development, it is necessary to resort to the method of analogies or use empirical coefficients in calculation models. This approach leads to uncontrolled computational errors.

V. N. Varavka · O. V. Kudryakov (✉) · I. Yu. Zabiyaka · N. I. Bronnikova
Material Science Department, Don State Technical University, Rostov-on-Don, Russia
e-mail: kudryakov@mail.ru

I. A. Parinov et al. (eds.), *Advanced Materials*, Springer Proceedings in Materials 6, https://doi.org/10.1007/978-3-030-45120-2_7

In this regard, the goal of the work was to develop a universal computational and analytical model that describes the stage of initiation of fatigue defects in order to increase the accuracy of estimates of the performance of materials under conditions of impact and fatigue loading. The universality of the model refers to its applicability to most industrial materials and coatings. As an applied use of such a model, the field of exploitation of materials and coatings in the conditions of droplet impingement erosion is determined, for example, when the blade turbine equipment is operating in an environment with vapor-droplet condensate. Based on these conditions, the analytical task of constructing a model is to establish expressions for calculating the number of impacts of droplets N_3 with a turbine blade, which are necessary for the formation of a fatigue defect of critical size in a material or coating.

7.2 Theoretical Foundations of the Calculate-Analytical Model

The final equation for calculating N_3 should include mechanical, kinetic and structural components, each of them characterizes a separate side of the complex process of droplet impingement erosion [1–6]. Moreover, the action of all components of the total number of impacts N_3 on the process of formation of a fatigue defect occurs at each collision simultaneously. Moreover, the interaction of the mechanical, kinetic and structural components of the impact-droplet effect on the material or coating has a commutative character. The universality of the developed model and the commutative nature of the contributions of all its components can be ensured provided that all components of the model are connected by a single theoretical basis. When the object of the study is crystalline materials or coatings, such a unified basis for the components of the model can be the theory of defects in the crystal structure, namely, the theory of dislocations. We consider this thesis as applied one to each component of the droplet-impacts process.

The mechanical component is associated with the density of mobile dislocations ρ_{m} arising from a single drop impact. In the process of multiple impacts, the number of mobile dislocations increases, they move in the metal matrix along the slip planes under the action of shear stresses σ_{s} until they form flat clusters ("pile-up" with a critical density ρ_{kr}) at the nearest insurmountable barriers. We take as $\rho_{\mathrm{kr}} = 10^{16}\ \mathrm{m}^{-2}$ the dislocation density, the excess of which leads to spontaneous breaking of interatomic bonds in the metal and the formation of a crack nucleus. Then the mechanical component of the number of impacts is expressed as $N_3 = f(\rho_{\mathrm{kr}}/\rho_{\mathrm{m}})$.

The kinetic component of the number of impacts N_3 takes into account the dependence of the dislocation energy on its velocity V_{d}. Dislocation glide upon impact occurs at a high speed. It is known from the theory of dislocations that as the speed of a dislocation increases, its energy increases in accordance with an expression similar to Einstein's expression for bodies moving with speeds close to the speed of light. For a dislocation velocity, the limit is the speed of sound in a crystal C_0. When V_{d}

$= C_0$, the dislocation energy becomes infinite. Therefore, under the conditions of droplet impacts, the kinetic component of the number of collisions is expressed as $N_3 = f(V_d/C_0)$.

The structural component of the number of impacts N_3 must take into account two circumstances. First, upon impact, the movement of dislocations is limited by the size of the structural element of the metal matrix, within which the free path of the dislocations is possible. For polycrystalline materials, grain size D is usually considered as such an element. On the other hand, secondly, within the grain there can be various obstacles to the movement of dislocations: particles of secondary phases, small-angle boundaries, the dislocations fixed by atmospheres, and stacking faults. Even if there are no such obstacles in the structure of the material, there is lattice resistance—Peierls stress. Therefore, the structural component of the number of impacts must take into account both of these points and will be a function of two variables $N_3 = f(D, \Delta G)$, where ΔG is Gibbs free energy to activate the process of overcoming a moving dislocation of obstacles within the structural element D. The mechanism of overcoming the obstacle depends on the nature of the obstacle and can be different, which determines the value of ΔG for each specific type of material structure.

The dislocation concept of the model, the analysis of its components, and the commutative principle of their interaction lead to the following theoretical expression for the value of N_3 calculation [7]:

$$N_3 = \frac{\rho_{kr}}{\rho_m} \cdot \sqrt{1 - \left(\frac{V_d}{C_0}\right)^2} \cdot \frac{D}{l_0} \cdot e^{-\frac{\Delta G}{kT}} \tag{7.1}$$

where l_0 is the path traveled by moving dislocations in one loading cycle (single impact/collision); k is the Boltzmann constant; T is the thermodynamic temperature.

7.3 Estimation of the Model Parameters

To use expression (7.1) as a calculation method for evaluating the wear resistance of materials and coatings under conditions of cyclic liquid-droplet impacts, it is necessary to express the quantities entering into it (such as ρ_m, V_d, l_0, ΔG) in terms of measured impact/collision parameters, such as droplet size R_0 and collision velocity V_0.

Thus the value of ρ_m at the established stage of plastic flow is exclusively a function of stress σ_s and temperature. The simplest dependence, consistent with theory and experiment [8, p. 25]:

$$\rho_m = \alpha \cdot \left(\frac{\sigma_s}{\mu \cdot b}\right)^2 \tag{7.2}$$

where μ is the shear modulus; b is the Burgers vector; α is the coefficient taken under normal conditions as $\alpha = \text{const} \approx 1$.

The shear stress in the slip plane, under the action of which the sliding of dislocations occurs, is considered as the stress σ_s in expression (7.2). Stress σ_s can be expressed in terms of impact parameters. In some of our works (see, for example, [4]), the stress in the surface layer of the target metal in the center of the collision zone during a single loading cycle (droplet impact) is expressed in relative units of $\rho_0 \cdot c_0 \cdot V_0$, called the hydraulic impact approximation, where ρ_0 is the density of the unperturbed liquid, c_0 is the speed of sound in a liquid under normal conditions (for water $\rho_0 = 1000$ kg/m^3, $c_0 = 1500$ m/s). Under the conditions that the average level of acting stresses during a complete cycle of a single loading (collision) is determined by the value of $\sigma_m = 0.33 \cdot \rho_0 \cdot c_0 \cdot V_0$, and the dislocation glides over the entire time of this cycle with a length $\tau = 2 \cdot R_0/V_0$, we can switch from the applied external stress σ_m to the shear stress in the slip plane σ_s. To do this, we use the Schmidt-Boas law for a polycrystal:

$$\sigma_m = M_p \times \sigma_s \tag{7.3}$$

where M_p is the Taylor factor, component: $M_p = 2.9$ for bcc-metals and $M_p = 3.06$ for fcc-metals [8, p. 30]. Then, in accordance with formula (7.2), the stress σ_s is expressed in terms of the impact parameters:

$$\sigma_s = \frac{0.33 \cdot \rho_0 \cdot c_0 \cdot V_0}{M_p} \tag{7.4}$$

Under impact loading, the strain rate can reach very large values (more than 10^2 s^{-1}). In this case, plastic deformation (hardening) is controlled by phonon and electronic braking of dislocations. The sliding velocity of dislocations for these conditions is determined by the braking coefficient B from the expression [8, p. 31]:

$$V_d = \sigma_s \times b/B \tag{7.5}$$

where the values of the braking coefficient B are in a rather narrow range $10^{-5} \ldots 10^{-4}$ Ns/m^2, for further calculations we accept $B = 10^{-4}$ Ns/m^2.

Taking into account expressions (7.4) and (7.5) and assuming the linearity of the motion law, the mean free path of dislocations per loading cycle (one droplet impact) is defined as $l_0 = V_d \cdot \tau$ and can be written as:

$$l_0 = \frac{0.66 \cdot R_0 \cdot \rho_0 \cdot c_0 \cdot b}{B \cdot M_p} \tag{7.6}$$

The determination of the energy of overcoming of structural obstacles by dislocations ΔG requires a more detailed analysis.

From classical works on the theory of dislocations (for example, [8–10]), it is known that the energy ΔG is a function of stress σ_s and depends on the shape and

distribution of obstacles, as well as on the field of internal stresses between obstacles. In general terms, the value of ΔG in (7.1) can be represented as:

$$\Delta G(\sigma_s) = \Delta F \cdot \left(1 - \frac{\sigma_s}{\sigma_\tau}\right) \tag{7.7}$$

where ΔF is the activation energy of the process of overcoming obstacles without applying external stress, value of ΔF actually determines the strength of the obstacles with respect to the movement of dislocations; σ_τ is the internal stress existing in the material and allowing the dislocation to pass through the obstacle at the minimum values of ΔG; the flow stress of the solid at $T = 0$ K is taken as σ_τ.

Values σ_τ and ΔF are the properties of the material and, in the general case are expressed through its basic physical characteristics μ and b:

$$\sigma_t = \alpha_1 \cdot \mu \cdot b/l; \quad \Delta F = \alpha_2 \cdot \mu \cdot b^3. \tag{7.8}$$

The value l in the expression (7.8) represents the distance between the obstacles. Coefficients α_1 and α_2 characterize obstacles in their resistance to the motion of dislocations. In metal-physical terminology, α_1 and α_2 classify obstacles by strength. Between the parameters l, α_1 and α_2 there is a rather strict correlation. So, strong or large particles of secondary phase precipitates are determined by the coefficient $\alpha_2 = 2$, and the linear average statistical distance between the precipitates is taken as l. Small particles cutting by dislocation, as well as the dislocation "forest", formed, for example, during strain hardening, considered medium-strength obstacles. Such obstacles have a coefficient $\alpha_2 = (0.2–1.0)$, and as l is taken the distance between the dislocations, i.e. $l = 1/\sqrt{\rho_d}$. Low-strength obstacles include atoms of an element dissolved in the lattice (for example, during quenching) or Peierls resistance of the lattice (at a relatively low dislocation density ρ_d). In this case $\alpha_2 < 0.2$, and the value l has a size commensurate with the Burgers vector b.

This data indicates that a deterministic inverse relationship is observed between the values σ_τ and ΔF: as the strength of the obstacles increases, the stress in the lattice σ_τ between the obstacles weakens, respectively, the energy of overcoming obstacles ΔF increases.

The physical meaning of coefficient α_1 is not completely clear. According to the results of our studies, including numerical experiments, we can say that for compact metal materials in which dislocation interactions are determined by the type of microstructure and the free path of dislocations is always greater than the distance between dislocations ($D > 1/\sqrt{\rho_m}$), coefficient α_1 in expression (7.8) can not be used, i.e. $\alpha_1 = 1$. Coefficient α_1, different from 1, is relevant for nanomaterials and nanostructured coatings. For this category of materials, coefficient α_1 in expression (7.8) acts as a regulator of the Burgers vector value. This fact may indirectly indicate that plastic deformation in nanomaterials is carried out with the participation of partial or grain boundary dislocations.

Thus, the presented calculation and analytical model is universal with respect to materials and coatings of various nature, for which the dislocation concept of the

considered processes is applicable. The obtained basic expression of model (7.1) is based on the principle of commutativity of components: the generation of mobile dislocations, their sliding speed and free path, the mechanism for overcoming structural obstacles. It determines the number of loading cycles N_3 necessary for the formation of a critical local dislocation density that initiates a fatigue defect formation. The morphology of the resulting defect (crack, pore, microcrater) depends on the properties of the material and was considered in some of our previous works [4–6]. The free path of dislocations is limited by the size of the structural element of the matrix. By default, this element is the grain size, for thin monolayers of coatings—their thickness. The model also includes such characteristics of the material as: the speed of sound in the crystal, its temperature, the activation energy of the process of overcoming obstacles by dislocations, the stress in the slip plane, the resistance of the lattice (Peierls stress), etc. The main feature of the model is that the calculations are based on either known reference material characteristics (μ, b, M_p), or measured process parameters (V_0, R_0). This makes the model practically feasible, in particular, in the conditions of droplet impingement erosion of materials and coatings.

7.4 Research Results and Discussion

As an applied use of the calculation model (7.1), its numerical solutions were obtained for those materials for which experimental data of bench tests under the conditions of droplet cyclic impacts had been carried out. This made it possible to compare and evaluate the calculated and experimental results. Comparative data was obtained for two congruent materials with the heterogeneous structure of same type:

(i) steel 20Cr13 after quenching and high tempering, the samples had a trivial sorbite structure, which is not shown in the illustrations;
(ii) vacuum ion-plasma coating of the TiAlSi-system with the structure of a 3D-nanocomposite on a steel substrate, its structure is shown in Fig. 7.1.

The materials under study are structurally congruent, since morphologically similar globular dispersed particles (obstacles for dislocations) are arranged in an orderly manner in their matrix determining the range of mobile dislocations. The fundamental difference between the presented materials is expressed in the different composition of the matrices and particles, as well as in the mean free path of the dislocations.

The ion-plasma technology of magnetron deposition provided for the layered formation of a TiAlSi coating due to the alternate evaporation of elements from two cathodes of various compositions. However, self-organization processes taking place in systems with Al and Si, the mechanisms of which are still not well understood [11, 12], led to the formation of a modulated structure with a spatially ordered arrangement of phase components in the form of a 3D-composite. A phase analysis of the coating structure was not performed. The scatter of nanoparticle diameters in the coating was 10–77 nm with an average size of 38 nm (assuming equiaxial morphology). The average distance between particles in the composite matrix was

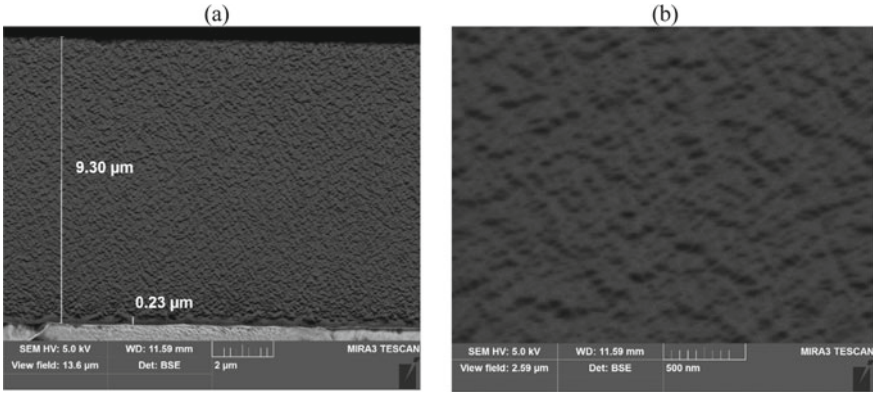

Fig. 7.1 The structure of the coating of the TiAlSi-system in cross-section at various magnifications, scanning electron microscopy: **a** coating of 9.3 μm thickness with a Ti sublayer (0.23 μm), **b** modulated structure of a 3D-nanocomposite in the coating of the TiAlSi-system

~50 nm. In calculations, this value was taken as the value of l for the coating. Moreover, the mechanism of interaction of dislocations with reinforcing particles was not regulated. It can be assumed that the interaction of dislocations with obstacles in the TiAlSi coating is carried out according to the principle of "cutting" or "cutting with bending". However, additional metal-physical studies are needed to refine the data on this issue. In the regard of such uncertainty, the value of coefficient α_1 in expression (7.8) for coating the TiAlSi-system was calculated as $\alpha_1 = l \cdot \sqrt{\rho_m}$. TiAlSi coating refers to systems with a mixed ion-metal bond in which dislocations have a fairly high degree of mobility [8]. This determines the appropriateness of applying the developed calculation and analytical model to similar systems and comparing the results of calculations with classical metal systems (such as steel 20Cr13 with a sorbite structure), for which the theory of dislocations is basic.

Comparative calculated and experimental data obtained using the calculation-analytical model and testing of samples on a droplet impact stand are shown in Table 7.1.

In Table 7.1, the value of m_0 was obtained during bench tests and represents the number of droplet impacts required to start the loss of mass of the sample, that is, to start wear. For the impact droplets loads under consideration, the value of m_0 characterizes the incubation period of droplet impingement erosion, which includes both the stage of the onset of the defect (cracks, pores, microcrater) and the stage of its development before the start process of mass loss by the sample:

$$m_0 = N_3 + N_p, \tag{7.9}$$

where N_3 is the number of impacts for the initiation of a crack, N_p is the number of impacts for the development of a crack to a critical size and the beginning of chipping of wear particles; it is not possible to differentiate the experimental value of m_0 on

Table 7.1 Summary data on the calculated and experimental characteristics of the samples

Material	Characteristics of material						
	ρ (kg/m^3)	E (GPa)	ν	μ (MPa)	b (10^{-10} m)	Lattice type	C_0 (m/s)
20Cr13 (sorbite)	7670	218	0.30	79	2.5	bcc	1956
3D-composite of TiAlSi-system	3840	148	0.24	60	3.9	fcc	2131

Material	Structure parameters				Impact parameters: V_0 = 250 m/s; R_0 = 0.55 mm		
	M_p	α_2	D (m^{-6})	l (m^{-6})	Calculations		Experiment
					N_3	α_0	m_0
20Cr13 (sorbite)	2.9	2.0	100	0.35–0.50	4655	0.280	16,630
3D-composite of TiAlSi-system	3.06	2.0	9.3	0.05	16,730	0.445	37,650

N_3 and N_p by metal-physical methods; $\alpha_0 = N_3/m_0$ is the coefficient characterizing the contribution of the nucleation stage to the total value m_0.

Without going into details of the calculation algorithm, we note that the model also allows one to obtain the dependences of the number of impacts N_3, necessary for the initiation of a fatigue defect in the coating, on the speed of impact (collision) V_0 for fixed values of the droplet size R_0. Such dependences for the studied materials (steel 20Cr13 and TiAlSi coating) are presented in Fig. 7.2.

A comparison of the graphs in Fig. 7.2 shows that, at any collision velocity V_0, the TiAlSi coating at the stage of initiation of a fatigue crack provides about a three times

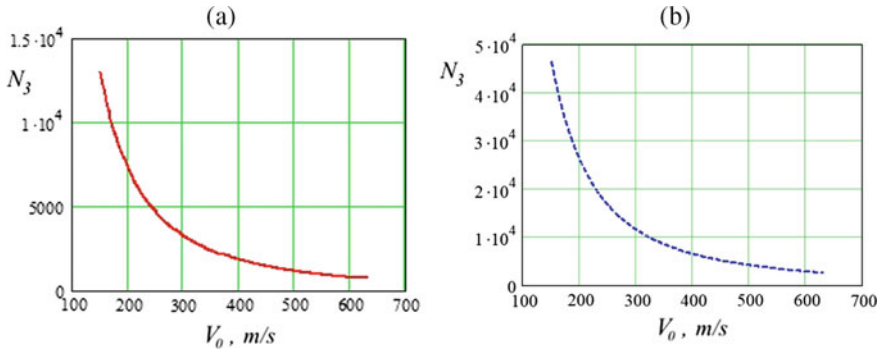

Fig. 7.2 The calculated dependences of the number of impacts N_3, necessary for the initiation of cracks, on the impact velocity V_0 at $R_0 = 0.55$ mm: **a** sorbite of steel 20Cr13, **b** 3D-nanocomposite coating of the TiAlSi-system

higher resistance to drop impact than steel 20Cr13. The experimental data of bench tests show the advantage of the coating by 2.26 times with respect to the parameter m_0 (see Table 7.1 and sources [13, 14]). The calculations concern only the nucleation stage, while the experimental parameter m_0 includes both the nucleation stage and the stage of development of fatigue defects. Hence, a preliminary conclusion can be made that the effectiveness of protecting the surface of metal products by applying a TiAlSi coating is determined, first of all, by an increase in the duration of the stage of initiation of fatigue defects. The preliminary conclusion is due to the fact that, because of the instrumental difficulties in studying this stage, one has to rely on the calculated data.

Usage of TiAlSi-system coatings to increase wear resistance during droplet impact cyclic loading has features not only at the stage of nucleation of defects, but also at the stage of their sustainable development. In the performed study the behavior of the nanocomposite coating, an unusual fact that needs explanation is noteworthy. At the stage of sustainable development of fatigue cracks, they possess a discrete character of development and are presented as a chain of narrow pores (Fig. 7.3a, c). Each such structural element (narrow pore) of a crack in a TiAlSi coating is 0.6–0.8 μm in length. With a dislocation density that ensures material breakage ($\rho_{kr} \approx 10^{16}$ m^{-2}), the distance between dislocations in a flat pile-up of a crack fragment will be about 10 nm, i.e., a cluster should consist of 60-80 dislocations. A simple calculation shows that the stresses in the head dislocation zone of such an accumulation will exceed the

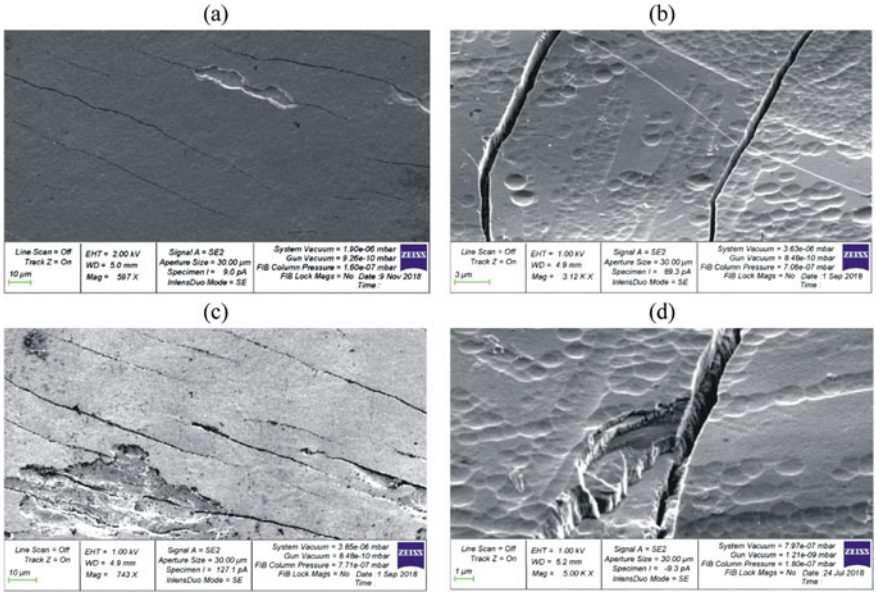

Fig. 7.3 Successive stages of TiAlSi-system coatings wear under contact cyclic loads, scanning electron microscopy: **a**, **b** beginning (**a**) and development (**b**) of the growth stage of fatigue cracks, **c**, **d** the beginning (**c**) and development (**d**) of the coating chipping stage

hardness of the coating (22–27 GPa, for functionally-graded or multilayer coatings the mathematical model [15, 16] can be applied). Therefore, chipping of the coating begins already at the stage of their discrete (with pores) development (Fig. 7.3a, c). After the pores merge and the crack faces are formed (Fig. 7.3b), the development of wear does not occur due to further chipping of the coating, but after the crack propagates into the base metal (Fig. 7.3d). Apparently, the main regulator of this process is the adhesion strength of the coating: with slow adhesion, the coating continues to chip, while with high adhesion, cracks deepen.

7.5 Conclusion

The results obtained show that there are structural parameters that determine the wear resistance under conditions of contact cyclic loads. Therefore, the limitation of the mobility of dislocations is the main structural principle for the significant increase the wear resistance. The implementation of this principle in coatings allows, among other things, one to increase the contribution of the nucleation stage N_3 of fatigue defects ($\alpha_0 = 0.445$ in Table 7.1) to the overall level of wear resistance m_0.

Structural parameters are the basis for the developed analytical model. The correspondence of the calculation results and experimental data, presented in the article, allows us to recommend the proposed model for the targeted design of wear-resistant materials and coatings.

The presented results are based on the concept of the dislocation nature of the considered processes, and they show a good correlation with experiment. It seems to us that they deserve attention, but also it requires a deeper critical analysis, taking into account the fact that, in the general opinion, dislocation interactions in nanostructured materials, which include the TiAlSi-system coating, are significantly limited or even impossible.

Acknowledgements This research was performed into framework of financing RFBR grant number 18-08-00546.

References

1. H. Itoh, N. Okabe, Trans. JSME (A) **59**, 2736 (1993)
2. R.H. Richman, ASM Handb. ASM Int. **11**, 1013 (2002)
3. M. Ahmad, M. Casey, N. Sürken, Wear **267**, 1605 (2009)
4. V.N. Varavka, O.V. Kudryakov, J. Frict. Wear **36**(1), 71 (2015)
5. V.N. Varavka, O.V. Kudryakov, J. Frict. Wear **36**(2), 153 (2015)
6. O.V. Kudryakov, V.N. Varavka, J. Surf. Invest. X-ray Synchrotron Neutron Tech. **9**(1), 203 (2015)
7. V.N. Varavka, O.V. Kudryakov, I.S. Morozkin, I.Yu. Zabiyaka, N.I. Bronnikova, J. Phys: Conf. Ser. **1281**, 012085 (2019)

8. H.J. Frost, M.F. Ashby, *Deformation-Mechanism Maps. The Plasticity and Creep of Metals and Ceramics* (Pergamon, Oxford, New York, Sydney, 1982), 166 p
9. B. de Meester, C. Yin, M. Doner, H. Conrad, in *Rate Processes in Plastic Deformation*, ed. by J.C.M. Li, A.K. Mukherjee (A.S.M., Metals Park, OH, 1975), 746 p
10. J.P. Hirth, J. Lothe, *Theory of Dislocations* (McGraw Hill, New York, London, 1968), 791 p
11. A. Cavaleiro, J.T. de Hosson (eds.), *Nanostructured Coatings* (Springer, New York, 2007), 752 p
12. V.N. Varavka, O.V. Kudryakov, I.Yu. Zabiyaka, N.I. Bronnikova, in *Physics, Mechanics of New Materials and Their Applications*, ed. by I.A. Parinov, S.-H. Chang, Y.-H. Kim (Nova Science Publishers, New York, 2019), pp. 1–12
13. V.N. Varavka, O.V. Kudryakov, A.V. Ryzhenkov, in *Piezoelectrics and Nanomaterials: Fundamentals, Developments and Applications*, ed. by I.A. Parinov (Nova Science Publishers, New York, 2015), 105 p
14. O.V. Kudryakov, V.N. Varavka, Inorg. Mater. **51**(15), 1508 (2015)
15. A.S. Vasiliev, E.V. Sadyrin, B.I. Mitrin, S.M. Aizikovich, A.L. Nikolaev, Russ. Eng. Res. **38**(9), 735 (2018)
16. S.S. Volkov, A.S. Vasiliev, E.V. Sadyrin, in *MATEC Web of Conferences*. EDP Sciences, vol. 226 (2018), p. 03018

Chapter 8
Mechanical Properties Derived by Spherical Indentation of TiN Coating Deposited by a Method Combining Magnetron Sputtering and Arc Evaporation

Evgeniy Sadyrin, Roman Karotkiyan, Nikolay Sushentsov, Sergey Stepanov, Igor Zabiyaka, Evgeniy Kislyakov, and Alexander Litvinenko

Abstract The chapter presents a comprehensive analysis of the nanoindentation derived mechanical characteristics (elastic modulus and indentation hardness) of the TiN coating deposited using the method combining magnetron sputtering and arc evaporation on a steel substrate. For the nanoindentation experiments, spherical indenter was used. The results of studies of microstructure, chemical composition, and also measurements of the coating thickness using a focused ion beam on a scanning electron microscope are presented.

8.1 Introduction

Deposition of TiN coating has become a widespread solution for improving lifetime and performance of cutting tools [1–3], prosthesis replacements and fixation devices [4, 5], steam turbine blades and power equipment [6, 7], medical instruments [8], drills [9], diffusion barriers [10], and other technological applications. As conventional testing methods (tensile-compression tests and dynamic methods measuring frequency of elastic vibrations of a rod made of a test material) cannot be applied to such small objects as thin films, for the estimation of the mechanical properties of TiN coatings nanoindentation experiments using Berkovich indenter are often conducted [11–13], whereas Vikers [14, 15], cube corner [16] and spherical [17] indenters are not as much widespread. Nevertheless, indentation testing with spherical indenters is a promising technique because of the non-singular nature of the stress fields produced by such indenters, which makes the analysis and testing less

E. Sadyrin (✉) · R. Karotkiyan · I. Zabiyaka · E. Kislyakov · A. Litvinenko
Research and Education Center "Materials", Don State Technical University, Rostov-on-Don, Russia
e-mail: ghostwoode@gmail.com

N. Sushentsov · S. Stepanov
Volga State University of Technology, Yoshkar-Ola, Russia

I. A. Parinov et al. (eds.), *Advanced Materials*, Springer Proceedings in Materials 6, https://doi.org/10.1007/978-3-030-45120-2_8

complex [18] and more suitable for the mathematical modelling of indentation of the thin films, functionally graded or multilayered coatings [19–26]. Moreover, the extent of damage and plasticity is minimized in the course of the experiment using the spherical indenter as compared to sharp and flat indenters [27–31].

8.1.1 Research Purpose

In the present research, the behavior of the mechanical properties of the TiN coating deposited on steel substrate using a method combining magnetron sputtering and arc evaporation was studied using the spherical indentation. The investigation was supplemented by the measurement of the coating thickness, chemical composition and microgeometrical parameters.

8.1.2 Research Scope

At this study, we consider the following frameworks of the problem:

(i) mechanical properties estimation for the TiN coating;
(ii) measurement of the coating thickness using scanning electron microscope (SEM) with the focused ion beam;
(iii) evaluation of the chemical composition of the coating using energy by dispersive X-ray spectroscopy on SEM;
(iv) determination of the microgeometrical characteristics of the surface using atomic-force microscopy (AFM).

8.2 Research Method

8.2.1 Sample Preparation

The coating was deposited using an automated vacuum complex combining the methods of magnetron sputtering and arc evaporation based on the NNV-6 unit. An electric bias potential of 1.5 A was applied to the coating. TiN coating was applied at a total gas mixture pressure of 0.3 Pa. Coating deposition time was 10 min. Arc evaporator current was 100 A. The coating was deposited on a steel 12Cr18N10T substrate (analogue to steel AISI 321).

8.2.2 Scanning Electron Microscopy

The research of the coating thickness was conducted using SEM Crossbeam 340 (Zeiss, Germany) equipped with the focused ion beam. For surface visualisation we used Everhart-Thornley secondary electron detector with an acceleration voltage of 2 kV, chemical analysis was made using an X-ray microanalyzer Oxford Instruments X-Max 80.

8.2.3 Atomic Force Microscopy

The topography of the coating was studied using AFM Nanoeducator (NT-MDT, Russia) equipped with a tungsten probe. The non-contact mode was applied. Probe positioning was performed using the optical microscope integrated to the AFM. The scanning field was $36 \times 36\ \mu m^2$.

8.2.4 Nanoindentation Test

For the study of the mechanical properties of the coating, the nanoindentation device Nanotest 600 Platform 3 (Micro Materials, UK) was used. The series of experiments was conducted in a closed chamber at a constant temperature of 27 ± 0.2 °C.

Values of the restored effective Young's modulus E_{eff} and indentation hardness H for the coating were obtained using the multi-point method, which uses the approach proposed by Oliver and Pharr [32]. During the indentation test, the displacement of spherical indenter h was recorded while the load P was applied. The maximum value of the displacement (attained at $P_{\max}$) was denoted as $h_{\max}$. Thus, the output of each experiment was a load-displacement curve. Thus, the unloading "branch" of this curve was approximated by the function:

$$P = a(h - h_{\text{r}})^m \tag{8.1}$$

where a and m were fitting parameters, h_{r} was the residual depth of the imprint, i.e. the amount of displacement of the indenter at which the material ceased to resist during unloading (i.e., the force equals zero). Using this approximation, the derivative of $P(h)$, called indentation stiffness S, was determined at $h_{\max}$:

$$S = \frac{\mathrm{d}P}{\mathrm{d}h}(h_{\max}) \tag{8.2}$$

Then the depth of the deflection out of contact h_s was calculated:

$$h_s = \epsilon \frac{P_{max}}{S} \tag{8.3}$$

where ϵ is geometrical constant, for the paraboloid of revolution [33]; $\epsilon = 0.75$.

After that the contact depth h_s was calculated:

$$h_c = h_{max} - h_s \tag{8.4}$$

On the following step the radius of the contact circle was established:

$$a = \sqrt{2Rh_c - h_c^2} \tag{8.5}$$

where R is the radius of the spherical indenter.

The reduced Young's modulus was determined according to the formula:

$$E_r = \frac{S\sqrt{\pi}}{2\beta\sqrt{A_c}} \tag{8.6}$$

where A_c was the projected contact area (the projection of the contact surface on a plane orthogonal to the axis of indentation), for the ideal sphere $A_c = \pi a^2$. Indentation hardness was then calculated using the following formula:

$$H = \frac{P_{max}}{A_c} \tag{8.7}$$

Effective Young's modulus of the coating was calculated as

$$E_{eff} = \frac{S\sqrt{\pi}}{2\sqrt{A_c}} \tag{8.8}$$

Finally, we calculated the restored effective Young's modulus:

$$E_{eff}^r = (1 - v^2)\left(\frac{1}{E_r} - \frac{1 - v_i^2}{E_i}\right)^{-1} \tag{8.9}$$

The dependence of the restored effective Young's modulus on the maximum penetration depth of a spherical indenter with a radius of curvature of 20 μm was established. The positions for the indentations were chosen using optical microscope integrated into the nanoindentation device. In each indentation series P_{max} was the same, 12 identical indentations were performed with 70 μm column and row offset. However, P_{max} increased from series to series, totally from 2.5 to 250 mN.

8.3 Results and Discussion

8.3.1 Coating Thickness and Chemical Composition

The thickness of the TiN coating was obtained by etching of the surface of the sample with a focused ion beam. The thickness was 1.49 μm, standard deviation was 0.02 μm (the average of six measurements in Fig. 8.1).

The energy-dispersive X-ray spectroscopy analysis revealed the chemical composition of the coating by measuring average data on the three specters on the three surface areas (Fig. 8.2). The summary on the data obtained is shown in Table 8.1, which demonstrates a high quality of deposition from the point of view of the chemical composition of the coating.

8.3.2 Microgeometrical Characteristics

The average surface roughness R_a was measured by the obtained AFM image (Fig. 8.3) using software (Gwyddion, Czech Metrology Institute, Czech Republic). Due to the irregularities observed on the visualized surface (cavern-shaped artifacts of deposition) we considered measurement of the roughness based on a single profile as not being completely indicative. Thus, average roughness R_a was measured in three directions (horizontal, vertical and diagonal).

For each of the directions we constructed five profiles. Following that the average value with the standard deviation was calculated. Maximum height of roughness was also calculated and denoted as R_t. Thus, average R_a by 15 profiles was 198.9 nm,

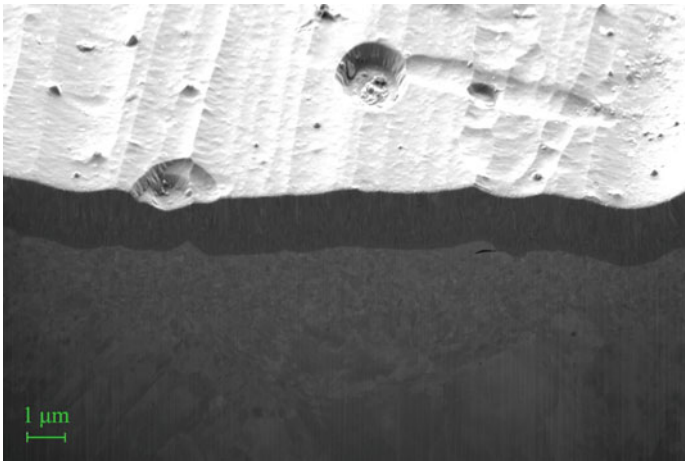

Fig. 8.1 Etched TiN coating with the focused ion beam

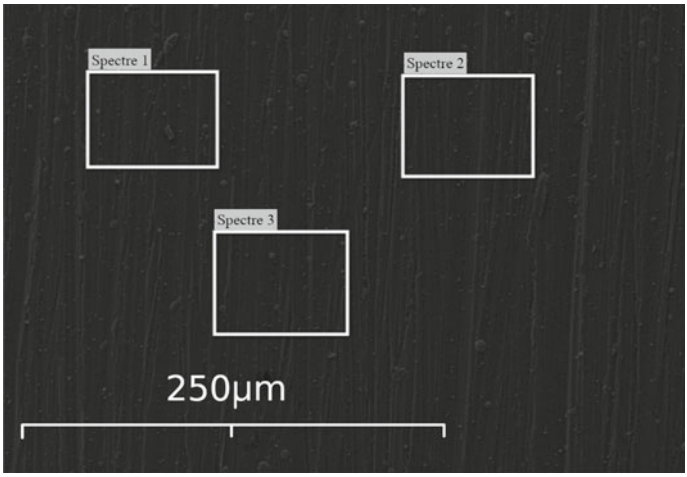

Fig. 8.2 Areas selected for the energy-dispersive X-ray spectroscopy

Table 8.1 Chemical composition of the TiN coating

Chemical element	Spectrum 1	Spectrum 2	Spectrum 3
N	47.07	42.73	46.22
O	–	5.42	–
Al	0.12	0.11	0.12
Si	0.10	0.10	0.09
Ti	50.04	49.11	51.08
Cr	0.65	0.54	0.53
Fe	1.78	1.62	1.60
Ni	0.24	0.22	0.26
Cu	–	0.14	0.10
Sum	100.00	100.00	100.00

standard deviation was 53.0 nm, R_t was 1.97 μm. Although the sample possessed a developed surface relief, its R_a value was significantly lower than those reported in literature for different types of steel substrate preparation, ranging from 0.03 to 7.0 μm in the investigation by Steinmann et al. [34]. At the same time, in our previous research [35] we obtained average roughness of 10.7 nm of TiN coating deposited on a mirror polished steel 40Cr (analogue to AISI 5135) using ion plasma deposition.

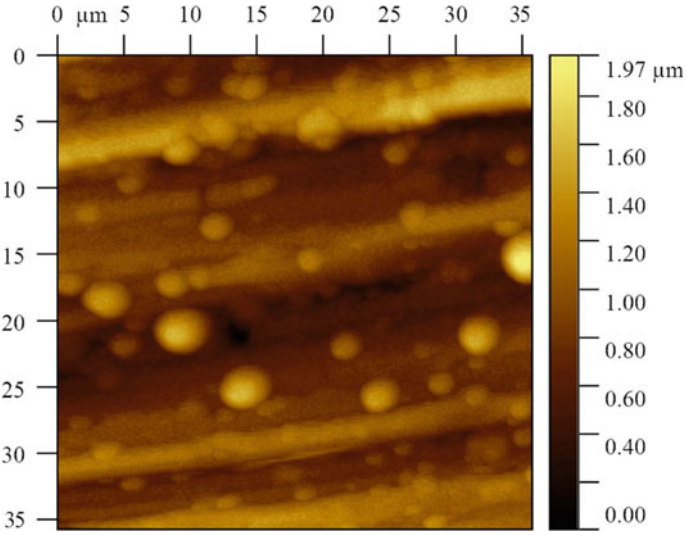

Fig. 8.3 AFM image of the TiN coating under research

8.3.3 Mechanical Properties

Figure 8.4 demonstrates some of the load-displacement curves obtained in the nanoindentation series. Table 8.2 summarizes the analysed values for the restored effective Young's modulus and indentation hardness for different P_{max}. The following constants were used during the analysis: $E_i = 1141$ GPa, $v_i = 0.07$ [32] $v = 0.3$ [36].

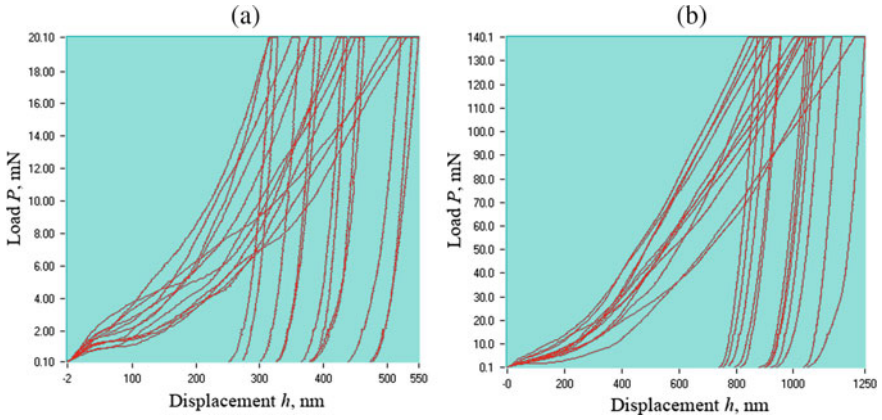

Fig. 8.4 Load-displacement curves obtained for the series with P_{max} of 20 mN (**a**), and 140 mN (**b**)

Table 8.2 Mechanical properties estimation for the TiN coating

P (mN)	E^r_{eff} (GPa)	±	H (GPa)	±	$h_{\max}$ (nm)
2.5	38.67	9.53	0.22	0.08	101.95
5	45.52	14.49	0.20	0.10	229.67
10	60.44	17.19	0.29	0.10	291.51
15	75.60	14.88	0.38	0.12	346.67
20	75.42	12.16	0.37	0.07	433.26
30	87.03	19.53	0.46	0.13	591.43
40	102.66	12.59	0.62	0.09	531.00
50	106.99	13.70	0.68	0.16	616.21
60	118.70	18.21	0.78	0.15	652.25
70	126.25	15.55	0.87	0.17	681.65
80	134.54	21.13	0.95	0.17	706.18
90	132.88	11.97	0.94	0.14	793.84
100	134.77	14.06	0.94	0.15	885.76
120	137.68	11.44	0.99	0.09	999.14
140	146.30	8.86	1.13	0.12	1030.51
160	144.19	11.88	1.18	0.11	1128.78
180	161.14	22.47	1.09	0.25	1453.30
200	155.68	13.77	1.20	0.19	1407.51
250	158.38	19.22	1.39	0.22	1523.17

The overall behavior of both restored effective Young's modulus and indentation hardness demonstrate increase in its values with increase of indentation load and depth (Fig. 8.5). On the interval of maximum depth $h_{\max}$ from 344 to 433, both mechanical properties demonstrate stable state and afterwards begin to increase rapidly, presumably because of huge amount of plastic deformation inside the coating and increasing of the influence of the substrate on the effective values. For both mechanical characteristics the next stable segment stretches from 706 to 999 nm on depth. After this segment, the growth of the properties is not pronounced, indicating dominance of the properties of the substrate over the those for the coating. The values obtained partially fit in the ranges obtained earlier for the TiN coating via bulge test in the research by Karimi et al. [37] (160–260 GPa) and are close to the indentation results in the same paper (160–280 GPa), where authors also remarked notable variation of mechanical properties with the increase of indentation depth. The values obtained are significantly lower than those for the reactively and non-reactively magnetron sputtered TiN coatings obtain in the paper of Mayrhofer et al. [38] using computer-controlled microhardness tester. Presumably accurate experimental examination of the mechanical properties of such complex systems as coating-substrate

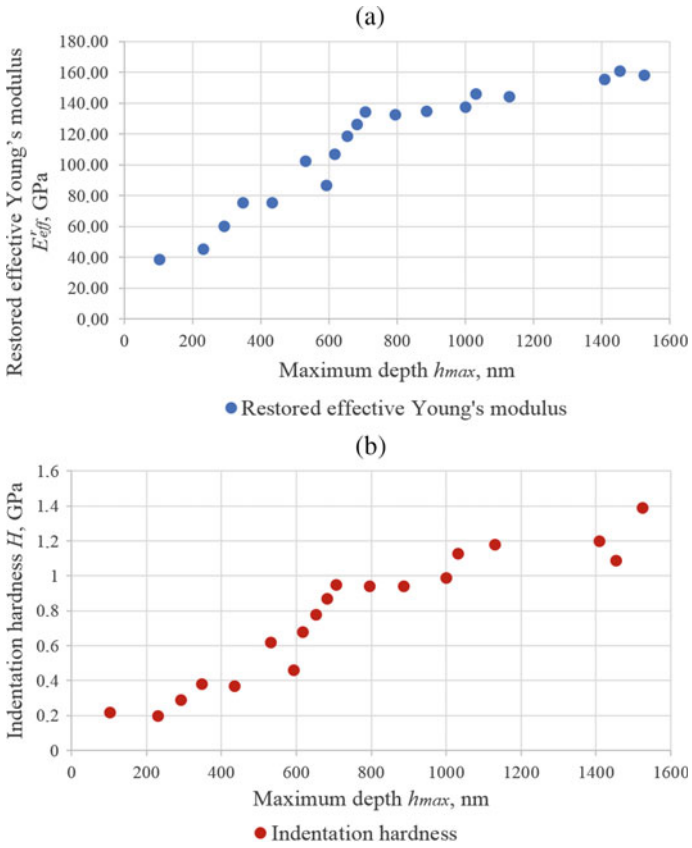

Fig. 8.5 Dependencies of the mechanical characteristics on the maximum indentation depth: **a** restored effective Young's modulus, **b** indentation hardness

(even for the case of a single layered coatings) should be supplemented by the mathematical modelling to obtain the elastic moduli of the coating to avoid influence of the substrate and surface roughness on the results.

8.4 Conclusion

The behavior of the mechanical characteristics on the indentation depth was experimentally obtained for the TiN coating deposited on 12Cr18N10T steel substrate by a method combining magnetron sputtering and arc evaporation. The values of the coating thickness and microgeometrical characteristics of the coating were derived using SEM and AFM, respectively, as well as chemical composition of the coating by means of energy-dispersive X-ray spectroscopy. Results demonstrated high

dependence of the mechanical properties on the indentation depth. For their further clarification the mathematical modelling of the indentation process of the spherical indenter into inhomogeneous by depth coating is required.

Acknowledgements This research was supported by RFBR grants Nos. 18-07-01397-a, 18-07-01177-a, and 18-57-00015 Bel_a. Experiments on nanoindentation, SEM and AFM were conducted in the Nanocenter of the Research and Education Center "Materials" (http://nano.donstu.ru/). E. V. Sadyrin was supported by the scholarship of the President of the Russian Federation No. SP-3672.2018.1.

References

1. H.E. Rebenne, D.G. Bhat, Surf. Coat. Technol. **63**(1–2), 1–13 (1994)
2. H.Y. Li, H.B. He, W.Q. Han, J. Yang, T. Gu, Y.M. Li, S.K. Lyu, Int. J. Precis. Eng. Manuf. **16**(4), 781–786 (2015)
3. P. Hedenqvist, M. Olsson, P. Wallén, Å. Kassman, S. Hogmark, S. Jacobson, Surf. Coat. Technol. **41**(2), 243–256 (1990)
4. Q. Wang, F. Zhou, C. Wang, M.F. Yuen, M. Wang, T. Qian, M. Matsumoto, J. Yan, Mater. Chem. Phys. **158**, 74–81 (2015)
5. A.P. Serro, C. Completo, R. Colaço, F. Dos Santos, C.L. Da Silva, J.M.C. Cabral, H. Araújo, E. Pires, B. Saramago, Surf. Coat. Technol. **203**(24), 3701–3707 (2009)
6. M.K. Lee, W.W. Kim, C.K. Rhee, W.J. Lee, Metall. Mater. Trans. A **30**(4), 961–968 (1999)
7. V.N. Varavka, O.V. Kudryakov, I.S. Morozkin, I.Y. Zabiyaka, N.I. Bronnikova, J. Phys.: Conf. Ser. **1281**(1), 012085 (2019)
8. P.V. Kola, S. Daniels, D.C. Cameron, M.S.J. Hashmi, J. Mater. Process. Technol. **56**(1–4), 422–430 (1996)
9. W.D. Sproul, R. Rothstein, Thin Solid Films **126**(3–4), 257–263 (1985)
10. S.Q. Wang, I. Raaijmakers, B.J. Burrow, S. Suthar, S. Redkar, K.B. Kim, J. Appl. Phys. **68**(10), 5176–5187 (1990)
11. H.C. Barshilia, K.S. Rajam, Bull. Mater. Sci. **27**(1), 35–41 (2004)
12. S.J. Bull, Thin Solid Films **688**, 137452 (2019)
13. L.W. Ma, J.M. Cairney, M.J. Hoffman, P.R. Munroe, Surf. Coat. Technol. **200**(11), 3518–3526 (2006)
14. A.R. Franco Jr., G. Pintaúde, A. Sinatora, C.E. Pinedo, A.P. Tschiptschin, Mater. Res. **7**(3), 483–491 (2004)
15. J. Richter, Surf. Coat. Technol. **162**(2–3), 119–130 (2003)
16. J.J. Roa, E. Jiménez-Piqué, R. Martínez, G. Ramírez, J.M. Tarragó, R. Rodríguez, L. Llanes, Thin Solid Films **571**, 308–315 (2014)
17. M. Kot, W. Rakowski, L. Major, J. Lackner, Mater. Des. **46**, 751–757 (2013)
18. K.L. Johnson, *Contact Mechanics* (Cambridge University Press, Cambridge, 1985)
19. E.V. Sadyrin, A.S. Vasiliev, S.S. Volkov, B.I. Mitrin, S.M. Aizikovich, WIT Trans. Eng. Sci. **122**, 209–221 (2019)
20. A.S. Vasiliev, Int. J. Eng. Sci. **142**, 230–241 (2019)
21. L.I. Krenev, E.V. Sadyrin, S.M. Aizikovich, T.I. Zubar, in *Advanced Materials—Techniques, Physics, Mechanics and Applications*. Springer Proceedings in Physics, vol. 193, ed. by I.A. Parinov, S.-H. Chang, M.A. Jani (Springer, Cham, Switzerland, 2017), pp. 397–405
22. I.I. Argatov, F.J. Sabina, Int. J. Eng. Sci. **50**(1), 132–143 (2012)
23. S.S. Volkov, A.S. Vasiliev, S.M. Aizikovich, N.M. Seleznev, A.V. Leontieva, PNRPU Mech. Bull. **4**, 20–34 (2016)

24. T. Chudoba, N. Schwarzer, F. Richter, Surf. Coat. Technol. **127**(1), 9–17 (2000)
25. L.I. Krenev, S.S. Volkov, E.V. Sadyrin, S.A. Chizhik, J. Eng. Phys. Thermophys. **91**(3), 594–600 (2018)
26. I.I. Kudish, S.S. Volkov, A.S. Vasiliev, S.M. Aizikovich, Math. Mech. Solids **23**(7), 1061–1080 (2018)
27. U. Ramamurty, S. Sridhar, A.E. Giannakopoulos, S. Suresh, Acta Mater. **47**(8), 2417–2430 (1999)
28. A.S. Vasiliev, S.S. Volkov, A.A. Belov, S.Y. Litvinchuk, S.M. Aizikovich, Int. J. Eng. Sci. **112**, 63–75 (2017)
29. A.S. Vasiliev, S.S. Volkov, S.M. Aizikovich, Mater. Phys. Mech. **35**(1), 175–180 (2018)
30. A.S. Vasiliev, E.V. Sadyrin, S.S. Volkov, E.A. Kislyakov, I. Sevostianov, in *AIP Conference Proceedings*, vol. 2188(1) (AIP Publishing, 2019), p. 040017
31. A.S. Vasiliev, E.V. Sadyrin, B.I. Mitrin, S.M. Aizikovich, A.L. Nikolaev, Russ. Eng. Res. **38**(9), 735–737 (2018)
32. W.C. Oliver, G.M. Pharr, J. Mater. Res. **7**(6), 1564–1583 (1992)
33. I.N. Sneddon, Int. J. Eng. Sci. **3**(1), 47–57 (1965)
34. P.A. Steinmann, Y. Tardy, H.E. Hintermann, Thin Solid Films **154**(1–2), 333–349 (1987)
35. E.V. Sadyrin, B.I. Mitrin, L.I. Krenev, S.M. Aizikovich, Vestnik Don State Tech. Univ. **15**(4), 37–45 (2015) (in Russian)
36. A.J. Perry, Thin Solid Films **193**, 463–471 (1990)
37. A. Karimi, O.R. Shojaei, T. Kruml, J.L. Marti, Thin Solid Films **308**, 334–339 (1997)
38. P.H. Mayrhofer, F. Kunc, J. Musil, C. Mitterer, Thin Solid Films **415**(1–2), 151–159 (2002)

Chapter 9
Studies on Predicting Spring-Back and Verifying the Effects of Temperature, Sheet Thickness and Punch Speed on Forming Force of V-Bending for SS400 Steel Plate

Gia-Hai Vuong, Thi-Hong-Minh Nguyen, and Duc-Toan Nguyen

Abstract The sheet metal forming process is a basic deformation method in the mechanical field. In particular, bending deformation processing is a universal processing method that is widely used to form sheet metal parts such as the aviation industry, shipbuilding, automotive and so on. During the sheet metal bending process, the spring-back and forming force are very important output parameters that need to be determined to ensure the accuracy and load capacity of machining equipment. To predict the spring-back of V-bending process for SS400 sheet material, various hardening models have been imported into FEM simulation software in order to predict and compare with corresponding experimental results of SS400 sheet material. To simulate spring-back of V-bending, the deformed results of V-shape from the forming simulation in Abaqus/Explicit should be imported into Abaqus/Standard, and then a static analysis will calculate the spring-back of V-bending. The results showed both hardening laws were in good agreement with experimental results due to the thick sheet of material. Moreover, the forming force magnitude of V-bending will vary according to machining conditions, geometric shapes of products, sheet materials, etc. Then, this study verifies the effect of technological and geometric parameters such as elevated temperature, punch speed and sheet thickness to bending force when forming a V-shape of SS400 sheet material and selects the optimum parameters using Taguchi design and ANOVA method.

G.-H. Vuong · T.-H.-M. Nguyen · D.-T. Nguyen (✉)
School of Mechanical Engineering, Hanoi University of Science and Technology, 1A-Dai Co Viet Street, Hai Ba Trung District, Hanoi City, Viet Nam
e-mail: toan.nguyenduc@hust.edu.vn

G.-H. Vuong
Hai Phong University, Hai Phong, Viet Nam

I. A. Parinov et al. (eds.), *Advanced Materials*, Springer Proceedings in Materials 6, https://doi.org/10.1007/978-3-030-45120-2_9

9.1 Introduction

Nowadays the steel sheet has been widely used in the processing of steel structures and shipbuilding. There are many different machining technologies applied in sheet processing such as cutting, welding, cyclone, bending and so on [1, 2]. Among of the products made from steel sheet, the parts machined by bending technology account for a large of proportion. The spring-back and the bending force of forming processes are often greatly influenced by technology parameters such as the thickness of the sheet, the velocity of bending punch, heating when bending, etc. Determining a suitable set of technology parameters is very necessary, it can help manufacturers save maximum production costs while still bringing high economic efficiency. To determine the influence of these technological parameters, many studies have now applied the Taguchi experimental method [1, 3] and have brought very good results. The Taguchi method experimental is based on empirical statistical analysis through minimizing the cost or experimental process while ensuring a reasonable set of design parameters. The advantage of this method is that many factors are considered at the same time, including confounding factors. The Taguchi method, when combined with other statistical tools, such as variance analysis (ANOVA), becomes a powerful tool for selecting suitable machining parameters. There are various studies have focused on spring-back and bending force calculation [4, 5], however, a universal solution has still not been found [6]. Plastic deformation of the steel sheets requires, at the design stage of manufacturing, taking into account specific properties of the sheet material, i.e., Young's modulus, yield stress, ratio of yield stress to ultimate tensile stress, and microstructure of the material [7].

In this study, in order to verify the effects of the hardening model on spring-back prediction, the kinematic and isotropic hardening models were used to simulate corresponding V-bending shapes by using ABAQUS/explicit software. the Taguchi method experimental was used to examine the influence of technological parameters such as elevated temperature, punch velocity and sheet thickness on the force when V-bending of SS400 steel plate. With the main purpose of reducing the bending force, this study uses three levels for each element through the orthogonal array of Taguchi L9 (3 $\bigwedge$ 3) [8, 9]. The Minitab software also used to analyze the ANOVA (Analysis of Variance), evaluate the effects of each parameter on the spring-back prediction and select the optimal parameters set the corresponding experiment.

9.2 Material and Hardening Model

9.2.1 Materials

The material used in this study is SS400 steel sheet, according to JISG 3101 [10] with a chemical composition as Table 9.1.

Table 9.1 Chemical composition of SS400 steel sheet

C	Si	Mn	P	S	Cr
0.19–0.21	0.05–0.17	0.4–0.6	0.04	0.05	≤0.3

The tensile test pieces are cut on a wire cutting CNC machine, the tensile specimens were cut from the sheet in parallel to the rolling direction in order to carry out uni-axial tensile tests. After that, the tensile specimens are honed smoothly with a armor paper. The shapes and dimensions of the specimens were prepared in accordance with TCVN 197-85 (197-2000) [11], as shown in Fig. 9.1.

The experiment tensile test pieces are carried out at different temperature conditions (room temperature, 300 and 600 °C) on the Hung Ta H-200kN compressor as shown in Fig. 9.2. The system heated tensile test is set as shown in Fig. 9.3.

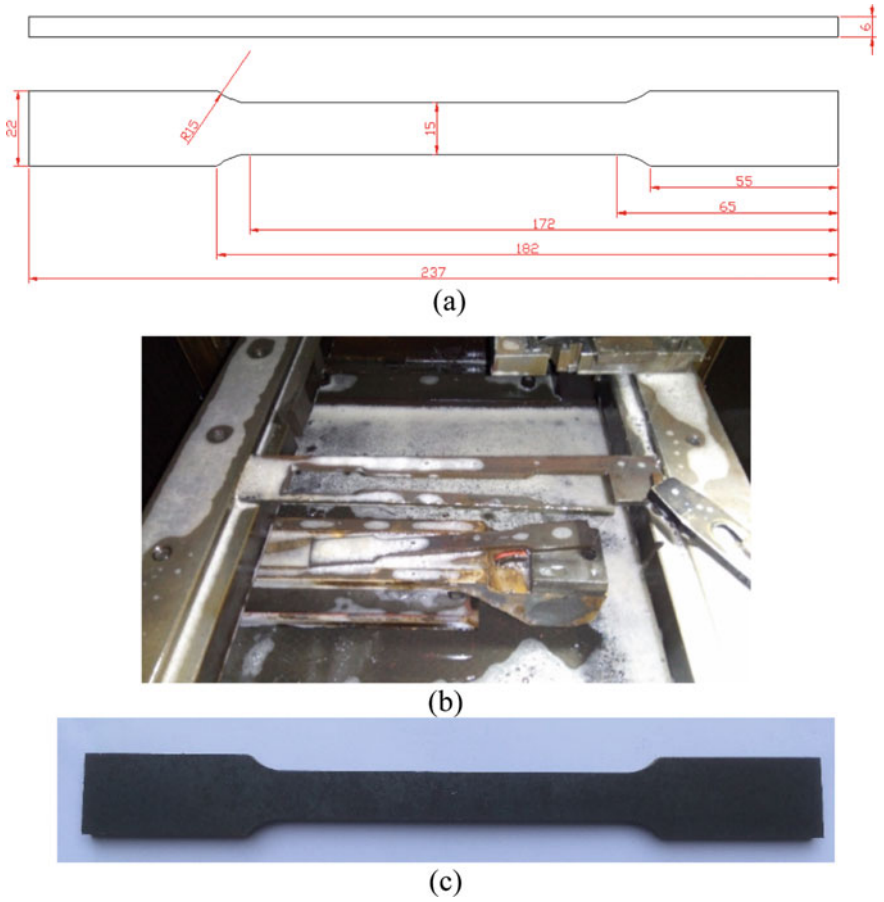

Fig. 9.1 Tensile test specimen: **a** dimensions, **b** wire cutting by CNC and **c** final shape

Fig. 9.2 Tensile and bending test machine

Fig. 9.3 Heat generation testing system

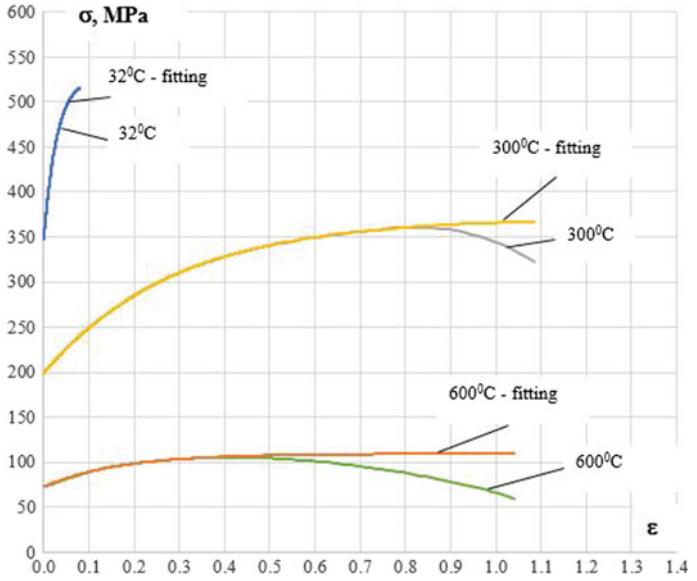

Fig. 9.4 Comparison of Voce's laws with experimental data at room and elevated temperatures

The experimental results of tensile tests at different temperature conditions are shown in Fig. 9.4.

9.2.2 Hardening Models

To identify the parameters of hardening model corresponding with the data after the tensile test by Voce's hardening law [12], the stress-strain curves as (9.1) were used. By using Excel 2013 software with SOLVER tool based on the method of summing the smallest deviations is easy to find the coefficients of the equation as shown in Table 9.2. The obtained coefficients will be declared in the input material model when performing numerical simulations by Abaqus software:

$$\bar{\sigma} = \sigma_Y + A(1 - \exp(-B\varepsilon_{eq}^{pl})) \tag{9.1}$$

Table 9.2 Hardening parameters at elevated temperatures determined by fitting curves following Voce's hardening law

Temperature (°C)	σ_Y	A	B
32	348.7	188.86	28.3293
300	199.3	171.56	3.452
600	72.43	36.89	6.0145

Table 9.3 Material attribute parameters for numerical simulation

Parameters	Levels
Temperature (°C)	32; 300; 600
Bending speed (mm/s)	1
Thickness sheet (mm)	6
Poisson's ratio	0.3
Young's modulus (MPa)	213,000 (32 °C) 184,410 (300 °C) 107,640 (600 °C)

where A and B are the plastic coefficients $\bar{\sigma}$, $\varepsilon_{\text{eq}}^{\text{pl}}$, and σ_{Y} are the equivalent stress, equivalent strain, and tension yield stress, respectively. Other material attribute parameters used to simulate the bending force prediction at different conditions are shown in Table 9.3.

To describe the hardening model, the Von-Mises yield surfaces that both translates (kinematic) and expanding (isotropic) are defined as [5]:

$$f(\sigma) = \frac{1}{2}\xi_j : \xi_j = \frac{1}{3}\bar{\sigma}_{\text{iso}}^2 \tag{9.2}$$

In the pure isotropic hardening case, there is only the size evolution of the yield locus then the back stress α in (9.3) is zero. When isotropic hardening law was used to simulate the uniaxial tension/compression tests then only parameters, σ_{Y}, A, and B in (9.1) are adopted as input data. The corresponding values of σ_{Y}, A, and B at room temperature can be used as 348 MPa, 188.86 MPa and 28.3293, respectively.

$$\alpha = \frac{C}{\gamma}(1 - e^{-\gamma\varepsilon_{\text{eq}}^{\text{pl}}}) \tag{9.3}$$

To introduce the Bauschinger effect, a kinematic hardening model was implemented to simulate tension/compression test and predict stress-strain curves evolution. To determine the kinematic hardening parameters C and γ in (9.3), back-stress α curve was first obtained by offsetting tensile stress-strain curve data about yield stress value (σ_{Y}) then fitting method based on the back-stress evolution law (9.3) was utilized to calculate calibration yields C and γ. Based on the back-stress evolution law at room temperature, (9.3) was utilized to calculate calibration yields C as 5350.272 MPa and γ as 17.7.

9.3 Experimental and Finite Element Method of V-Bending

9.3.1 Finite Element Model of V-Bending

To simulate spring-back and predict forming force when V-bending SS400 plate, the data collected from the test results and the calculation are using Abaqus/Explicit and then imported the deformed results into Abaqus/Standard, 3D Experience® 2016 HF2 (2016 HF2, Dassault Systèmes Simulia Corp., Providence, RI, USA, 2016). The V-bending models have depicted in Fig. 9.5 corresponding to the experimental setup of Fig. 9.2. Specifically, reduced-integration eight-node linear brick elements (C3D8R) are utilized for the blank. The die/tool and clamping parts are assigned as the rigid body. The size of the element for all parts corresponds to approximately 6 × 55 × 160 mm (Thickness × width × length). The boundary conditions in the model are as follows: a die part—ENCASTRE condition; a punch part: vertical movement; a sheet part: symmetrical boundary condition with respect to the center of the sheet. In order to determine to bend forming force through simulation and experiment, the bending part deformation of V-shaped part is done by moving the punch down vertically $\Delta Y = 18$ mm.

The corresponding experimental setup for the forming process of SS400 steel sheet bending is shown in Fig. 9.6.

Figure 9.7 presents the simulation results after spring-back occurrence for the case bending angle of 90° at room temperature. The error ($\Delta\alpha$) between simulation of isotropic and kinematic hardening law when compared with experimental result can be calculated as $\Delta\alpha = \alpha_{\text{Simulation}} - \alpha_{\text{Experimental}}$.

As shown in Fig. 9.7 with the thick sheet, the kinematic hardening model is in good agreement when comparing with an isotropic hardening model. Therefore, in this chapter, a kinematic hardening model was used to simulate the bending process of V-bending part at elevated temperature conditions.

Figure 9.8 depicts the experiment results after V-bending at elevated temperatures. The comparison of the bending force between experiments and corresponding finite

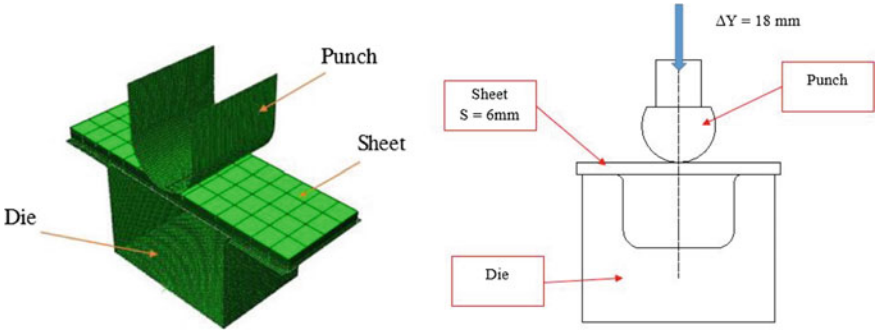

Fig. 9.5 V-bending models

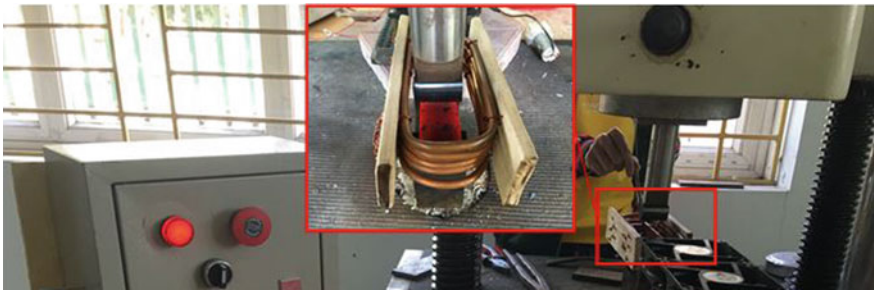

Fig. 9.6 Setup for V-bending experiment at elevated temperatures

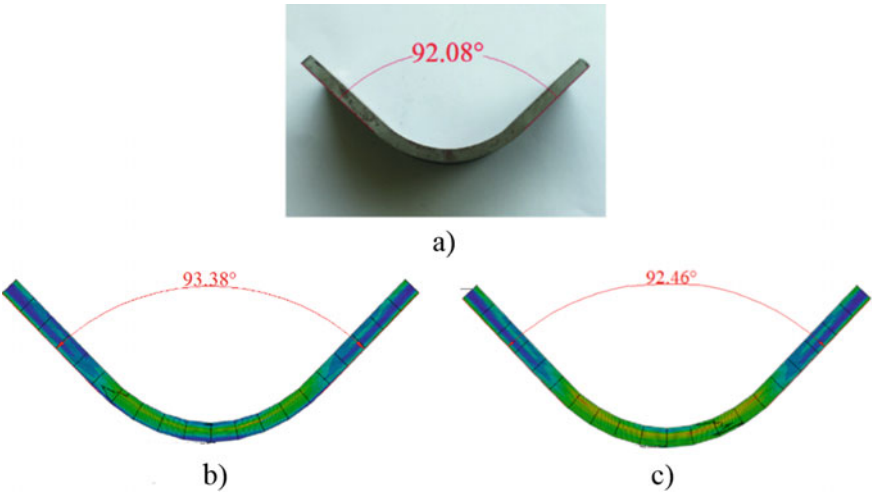

Fig. 9.7 V-bending test after spring-back (**a**) and simulation results spring-back based on isotropic (**b**) and kinematic (**c**) hardening models

element results are presented in Table 9.4. The error ($\Delta P\%$) between simulation and experimental results can be calculated as

$$\Delta P\% = \left| \frac{P_{\text{Simulation}} - P_{\text{Experimental}}}{P_{\text{Experimental}}} \right| \times 100\% \tag{9.4}$$

From Table 9.4, it is shown that the error value of bending force ΔP (%) between experiment and simulation has the highest value of 3.42%. Therefore it is possible to use numerical simulation methods to predict similar testing process.

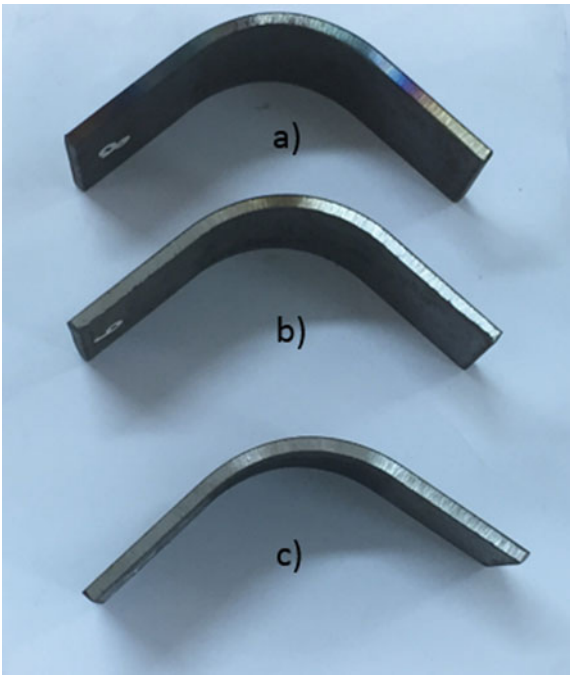

Fig. 9.8 The experimental result of V-bending tests at: 600 °C (**a**), 300 °C (**b**) and room temperature (**c**)

Table 9.4 Comparison of the bending force values between simulation and experiment

Temperature (°C)	P_{Sim} (N)	P_{Ex} (N)	ΔP (%)
32	28,022.1	29,014	3.42
300	27,827.2	28,322	1.74
600	20,423.7	19,333	2.89

9.3.2 Taguchi Orthogonal Array

The purpose of this study is to verify the effect of the input parameters on the desired output parameters. Therefore, the Taguchi method was chosen to allow the minimum of experiments needed to study the effect of parameters on an output characteristic and quickly adjust the input parameters to optimize the fastest output value.

In order to verify the effect of parameters on the forming force prediction P (N) by experiment, three parameters such as the thickness of the sheet (S), temperature (T) and bending speed (V) were selected according to Taguchi method. Table 9.5 lists the levels of parameter selection. During the experiment, there are 3 selected levels of each parameter. The L9 orthogonal array will be then used to design the experimental statistical method. At least 9 experiments are needed to test the effect of changing parameters on simulation results. The use of the Taguchi orthogonal algorithm will reduce the number of experimental designs from 27 to 9 experiments. The results of the simulated Taguchi experiments are shown in Table 9.6. The S/N

Table 9.5 Parameters and their level in experiment

Factor	Level		
	1	2	3
Temperature (°C) (T)	Room temperature (32)	300	600
Bending speed (mm/s) (V)	1	1.5	2
Thickness (mm) (S)	6	8	7

Table 9.6 The results according to Taguchi method

No.	T	V	S	P_{Ex} (N)	S/N_{Ex}
1	32	1	6	29,014	−89.252
2	32	1.5	8	66,000	−96.391
3	32	2	7	84,372	−98.524
4	300	1	8	61,619	−95.794
5	300	1.5	7	74,920	−97.492
6	300	2	6	37,970	−91.589
7	600	1	7	37,073	−91.381
8	600	1.5	8	19,333	−85.726
9	600	2	6	32,801	−90.318

noise ratio selected according to smaller is better conditions:

$$S/N = -10\log_{10}(MSD)^2 \tag{9.5}$$

where

$$MSD = \frac{(y_1^2 + y_2^2 + \cdots + y_n^2)}{n} \tag{9.6}$$

MSD is the mean squared deviation from the target value of the quality characteristic, and y_1, y_2, …, y_n, n are the results of experiments and the corresponding number of experiments.

The measurement results for 9 test samples according to Taguchi (Fig. 9.9) are given in Table 9.6. Effect of parameters of temperature (°C) (T), bending speed (mm/s) (V) and thickness (mm) (S) to forming force is calculated and analyzed for variance (ANOVA) as shown in Table 9.7.

The F-ratio test is a statistic tool to verify, which design parameters affect significantly the quality characteristic. It is defined as the ratio of the mean squared deviations to the mean squared error. The analysis of the F-ratio values reveals that the thickness of the sheet (S) is the most significant parameter. The thickness of the plate contributed with 53.17%, followed up by the temperature (T) contributed with 43.72% and the bending speed (V) is only 1.95% contribution on forming force.

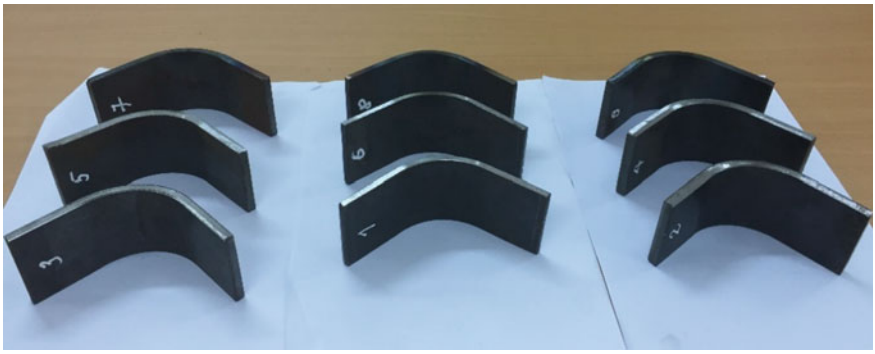

Fig. 9.9 Results of experiments when using the orthogonal array method Taguchi

Table 9.7 ANOM and ANOVA table of data affecting the forming force

Factor	Average by level			Sum of squares	Contribution (%)
	1	2	3		
T	−94.72	−94.96	−89.14*	65.034	43.72
V	−92.14*	−93.2	−93.48	2.908	1.95
S	−88.86*	−95.8	−94.17	79.089	53.17
Err.	–	–	–	1.672	1.16
Sum	–	–	–	148.731	100

* indicates Optimum level

As shown in Fig. 9.10, the optimal parameters for the best forming force are the temperature at level 3 of 600 °C, the thickness of the sheet (t) at level 1 of 6 mm and the bending speed at level 1 of 1 mm/s.

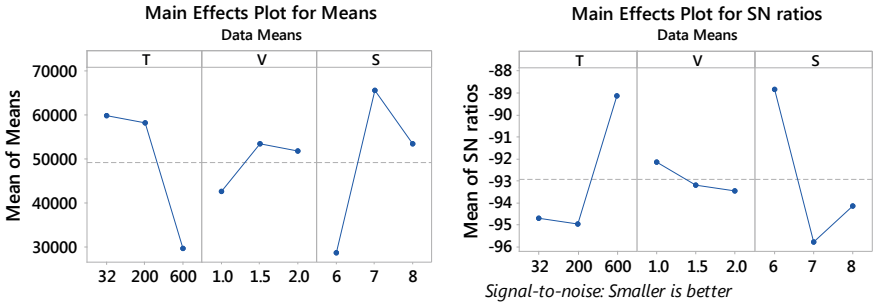

Fig. 9.10 Main effects plot for means

9.4 Conclusion

This study has been carried out to set up a system of experimental heated tensile testing of the SS400 steel sheet at elevated temperature conditions. A stress-strain curves at elevated temperatures has been shown that the higher the temperature, the lower the yield strength of the tensile test. The experimental and simulation results are in good agreement so that ABAQUS software could be used in spring-back prediction for V-bending SS400 steel sheet. Taguchi orthogonal array method with technological parameters such as temperature, bending speed, the thickness of workpiece has been conducted to evaluate the influence of input parameters on forming force when V-shaped bending. Experimental results and data analysis (ANOVA) have shown that processing conditions: temperature of 600 °C, bending speed of 1 mm/s and thickness of 6 mm will give the smallest bending force value.

Acknowledgements This research is funded by University Project at Hanoi University of Science and Technology under grant number "T2018-TĐ-204".

References

1. D.-T. Nguyen, Y.-S. Kim, Proc. IMechE Part B: J. Eng. Manuf. **224**(3), 435–445 (2009)
2. T.H. Pham, T.B. Mac, V.C. Tong, T.L. Banh, D.T. Nguyen, Adv. Mech. Eng. **8**, 1–11 (2016)
3. Y. Kim, Y. Kwon, J. Nam et al., Metal. Mater. Trans. A **31**(1), 93–98 (2000)
4. P.A. Eggertsen, K. Mattiasson, Int. J. Mech. Sci. **51**(7), 547–563 (2009)
5. M.L. Garcia-Romeu, J. Ciurana, I. Ferrer, J. Mater. Process. Technol. **191**(1–3), 174–177 (2007)
6. R.H. Wagoner, M. Li, Int. J. Plast. **23**(3), 345–360 (2007)
7. T. Trzepiecinski, H. Lemu, Metals **7**(9), 380 (2017)
8. G. Taguchi, *On-line Quality Control During Production* (Japan Standard Association, Tokyo, 1981)
9. B.T. Long, N.H. Phan, N. Cuong, N.D. Toan, Adv. Mech. Eng. **8**(7) (2016). https://doi.org/10.1177/1687814016657732
10. JIS G3101 SS400 Steel Plate Sheet for General Purpose Structural Steels, 86011881
11. M. M.-T. T. P. 1-2. TCVN 197:2002, 'TCVN 197'
12. E. Voce, J. Inst. Met. **74**, 537–562 (1948)

Chapter 10
Buckling Analysis of Folded Composite Plate Subjected to In-Plane Loading Condition

Bui Van Binh and Le Thuong Hien

Abstract This paper presents some numerical results of buckling analysis of a folded laminate composite plate using finite element method. The effects of fiber orientations, folding angle on buckling loads, and the corresponding mode shapes under in-plane loading condition were considered. Matlab programming using nine nodded rectangular isoparametric plate element with five degree of freedom per node based on Mindlin plate theory was built to solve the problems. A good agreement is found between the results of this technique and other published results available in the literature.

10.1 Introduction

Folded laminate composite plates are very useful in engineering. Applications for them have been found almost everywhere in various branches of engineering, such as roofs, sandwich plate cores, cooling towers, marine, aviation, and many other structures. Because of their high strength-to-weight ratio, easy to form, economical, and have much higher load carrying capacities than flat plates, which ensures their popularity and has attracted constant research interest since they were introduced.

Bending, free vibration and time displacement response of isotropic folded plates, composite folded plates have been studied in many works [1–13]. In that, folded plates analyzed only the structural members made of isotropic materials or modeled as an equivalent orthotropic plate or special cases of onefold; twofold folded laminate composite plates, or used otherwise method.

Buckling analysis is one of the most important studies for structures subjected to in-plane loads. These excellent information are buckling modes, buckling types, and critical buckling loads for the easy replacement with good load bearing capacity (which should be taken into the consideration at design process). In the previous

B. Van Binh (✉) · L. T. Hien
University of Power Electric, Hanoi, Viet Nam
e-mail: binhbv@epu.edu.vn

L. T. Hien
e-mail: hienlt@epu.edu.vn

I. A. Parinov et al. (eds.), *Advanced Materials*, Springer Proceedings in Materials 6, https://doi.org/10.1007/978-3-030-45120-2_10

works, Singh et al. [12] presented some results of buckling analysis of three dimensional braided composite plates under uniaxial loading using Inverse Hyperbolic Shear Deformation Theory. Liang et al. [13] presented nonlinear buckling analysis of variable stiffness composite plates based on the Koiter-Newton method. In the paper, a four-node quadrilateral element is developed based on the classical laminated plate theory, considering both the symmetrical and unsymmetrical laminates for variable stiffness composite plates.

Rasheed and Ahmadi [14] presented a lateral torsional buckling of anisotropic laminated thin-walled simply supported beams subjected to mid-span concentrated load.

Barbero et al. [15] presented some results of static and buckling analysis of laminated folded plates by using a mixed isostatic 24 (d.o.f) element.

By using finite strip analysis Ovesy et al. [16] presented buckling and free vibration of composite plates with cutout based on two different modeling approaches. In that, the formulations are based on Reddy type higher order plates theory in order to include the transverse shear stresses effect in case of moderately thick plates.

In this chapter, we used the nine-nodded isoparametric rectangular flat plate element to build home-made Matlab computer code based on the first-order shear deformation theory to buckling analyze composite folded plates. The effects of geometrical parameters on critical buckling loads and buckling mode shapes under in-plane loading condition were considered.

10.2 Theoretical Formulation

10.2.1 Displacement, Strain and Stress Fields

According to the Reissner-Mindlin plate theory, the displacements (u, v, w) are referred to those of the mid-plane (u_0, v_0, w_0) as

$$\begin{aligned} u(x, y, z, t) &= u_0(x, y, t) + z\theta_x(x, y, t) \\ v(x, y, z, t) &= v_0(x, y, t) + z\theta_y(x, y, t) \\ w(x, y, z, t) &= w_0(x, y, t) \end{aligned} \tag{10.1}$$

where t is the time; θ_x and θ_y are the bending slopes in the xz- and yz-plane (rotations about the y- and x-axes), respectively.

The z-axis is normal to the xy-plane that coincides with the mid-plane of the laminate positive downward and clockwise with x and y.

The generalized displacement vector at the mid-plane can thus be defined as

$$\{d\} = \left\{u_0, v_0, w_0, \theta_x, \theta_y\right\}^T \tag{10.2}$$

The strain-displacement relations can be taken as

$$\begin{Bmatrix} \varepsilon_{xx} \\ \varepsilon_{yy} \\ \varepsilon_{zz} \\ \gamma_{xy} \\ \gamma_{yz} \\ \gamma_{xz} \end{Bmatrix} = \begin{Bmatrix} \frac{\partial u_0}{\partial x} + z\frac{\partial \theta_x}{\partial x} \\ \frac{\partial v_0}{\partial y} + z\frac{\partial \theta_y}{\partial y} \\ 0 \\ \left(\frac{\partial u_0}{\partial y} + \frac{\partial v_0}{\partial x}\right) + z\left(\frac{\partial \theta_x}{\partial y} + \frac{\partial \theta_y}{\partial x}\right) \\ \frac{\partial w_0}{\partial y} + \theta_y \\ \frac{\partial w_0}{\partial x} + \theta_x \end{Bmatrix} \tag{10.3}$$

10.2.2 Finite Element Formulations

The Hamilton variation principle is used here to derive the laminate equations of motion. The mathematical statement of the Hamilton principle in the absence of damping can be written as [17]

$$\int_{t_1}^{t_2} \delta \left(\frac{1}{2} \int_V \rho \{\dot{u}\}^T \{\dot{u}\} \mathrm{d}V - \frac{1}{2} \int_V \{\varepsilon\}^T \{\sigma\} \mathrm{d}V - \int_V \{u\}^T \{f_b\} \mathrm{d}V \right) - \int_S \{u\}^T \{f_s\} \mathrm{d}S + \{u\}^T \{f_c\} \Bigg) \mathrm{d}t = 0 \tag{10.4}$$

In which:

$$T = \frac{1}{2} \int_V \rho \{\dot{u}\}^T \{\dot{u}\} \mathrm{d}V; \; U = \frac{1}{2} \int_V \{\varepsilon\}^T \{\sigma\} \mathrm{d}V; \tag{10.5}$$

$$W = \int_V \{u\}^T \{f_b\} \mathrm{d}V + \int_S \{u\}^T \{f_s\} \mathrm{d}S + \{u\}^T \{f_c\} \tag{10.6}$$

where U, T are the potential energy, kinetic energy; W is the work done by externally applied forces.

$u = [u, v, w]^T$ is the displacement of any generic point (x, y, z) in space.

In laminated plate theories, the membrane $\{N\}$, bending moment $\{M\}$ and shear stress $\{Q\}$ resultants can be obtained by integration of stresses over the laminate thickness. The stress resultants-strain relations can be expressed in the form:

$$\begin{Bmatrix} \{N\} \\ \{M\} \\ \{Q\} \end{Bmatrix} = \begin{bmatrix} [A_{ij}] & [B_{ij}] & [0] \\ [B_{ij}] & [D_{ij}] & [0] \\ [0] & [0] & [F_{ij}] \end{bmatrix} \begin{Bmatrix} \{\varepsilon^0\} \\ \{\kappa\} \\ \{\gamma^0\} \end{Bmatrix} \tag{10.7}$$

where

$$\left([A_{ij}],[B_{ij}],[D_{ij}]\right)=\sum_{k=1}^{n}\int_{h_{k-1}}^{h_k}\left([Q'_{ij}]_k\right)(1,z,z^2)\mathrm{d}z\quad i,j=1,2,6 \tag{10.8}$$

$$[F_{ij}]=\sum_{k=1}^{n}f\int_{h_{k-1}}^{h_k}\left([C'_{ij}]_k\right)\mathrm{d}z;\quad f=5/6;\ i,j=4,5 \tag{10.9}$$

n is the number of layers, h_{k-1}, h_k are the positions of the top and bottom faces of the kth layer. $[Q'_{ij}]_k$ and $[C'_{ij}]_k$ are the reduced stiffness matrices of the kth layer (see [18]).

In the present work, nine-nodded isoparametric quadrilateral element with five degrees of freedom per nodes is used. The displacement field of any point on the mid-plane given by:

$$\begin{aligned}&u_0=\sum_{i=1}^{9}N_i(\xi,\eta)\cdot u_i;\ v_0=\sum_{i=1}^{9}N_i(\xi,\eta)\cdot v_i;\ \mathrm{w}_0=\sum_{i=1}^{9}N_i(\xi,\eta)\cdot w_i;\\&\theta_x=\sum_{i=1}^{9}N_i(\xi,\eta)\cdot\theta_{xi};\ \theta_y=\sum_{i=1}^{9}N_i(\xi,\eta)\cdot\theta_{yi}\end{aligned} \tag{10.10}$$

where

$N_i(\xi,\eta)$ is the shape function associated with node i in terms of natural coordinates (ξ,η).

The free vibration analysis is used to determine natural frequencies by given equation:

$$\left\{[M]-\omega^2[K]\right\}=\{0\} \tag{10.11}$$

The eigenvalue type of buckling equation can be expressed as in the following steps by dropping force terms and conceded to

$$\{[K]+\lambda_{\mathrm{CR}}[K_G]\}\{\Delta d\}=\{0\} \tag{10.12}$$

where, $[K_G]$ is the geometric stiffness matrix; $\{\Delta d\}$ is the displacement increment vector and λ_{CR} is the critical mechanical load at which the structure buckles; $[M]$, $[K]$ are the global mass matrix, stiffness matrix, respectively.

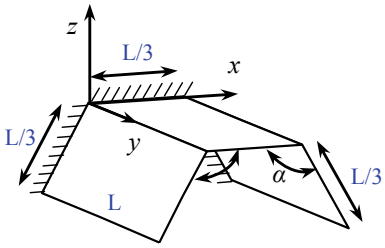

Fig. 10.1 Two folded composite plate

Table 10.1 Comparison of first five natural frequencies (Hz) of two folded composite plates for different folding angle, [90°/90°/90°], thickness t = 3 cm

Folding angle α	Source	f_1	f_2	f_3	f_4	f_5
90°	Present	63.3(0.47%)	69.7(0.14%)	150.5(1.44%)	156.7(0.47%)	204.0(1.04%)
	[9]	63.6	69.8	152.7	158.3	201.9
120°	Present	59.5(0.34%)	63.1(0.47%)	150.3(1.44%)	153.9(0.71%)	193.5(1.36%)
	[9]	59.3	63.4	152.5	155.0	190.9
150°	Present	42.3(0%)	60.7(0.16%)	133.8(1.75%)	144.9(0.48%)	149.9(1.25%)
	[9]	42.3	60.8	131.5	145.6	151.8

10.3 Numerical Results

10.3.1 Validation Example

In this section, the first five natural frequencies of a cantilever twofolded composite plate studied by Guha Niyogi [9] are recalculated (Fig. 10.1).

The layout of the plate is shown in Fig. 10.1 with the dimension $L = 1.5$ m, total thickness $t = 0.03$ m, physical and mechanical properties of material: $E_1 = 60.7$ GPa, $E_2 = 24.8$ GPa, $G_{12} = G_{13} = 12.0$ GPa, $\upsilon_{12} = 0.23$, $\rho = 1300$ kg/m^3.

Three cases are considered for different folding angle $\alpha = 90°, 120°, 150°$ with fiber orientation [90°/90°/90°].

Comparison first five natural frequencies (Hz) of our results have been compared with published results given by Guha Niyogi [9] and presented in Table 10.1.

It is shown that the five natural frequencies are in excellent agreement with the percentage difference of peak values less than 1.75% of each other.

10.3.2 Buckling Analysis of Folded Laminated Plate

Consider a twofolds folded composite plate is shown in Fig. 10.2, the material properties shown in Table 10.2, the dimension $L = 1.5$ m, total thickness $t = 0.005$ m, folding

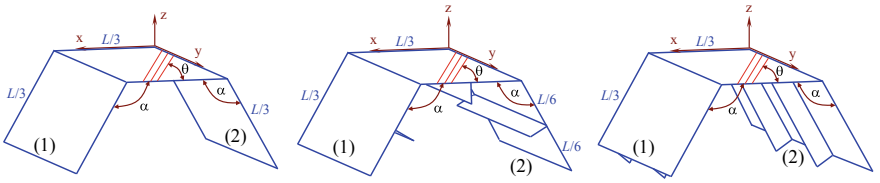

Fig. 10.2 Geometry of stiffened folded composite plate

Table 10.2 Boron-Epoxy material properties

E_1 (GPa)	E_2 (GPa)	G_{12} (GPa)	G_{13} (GPa)	υ_{12}	υ_{13}	ρ (kg/m^3)
206.9	20.7	5.2	5.2	0.3	0.3	1724

angle α ($\alpha = 90°$; $\alpha = 120°$; $\alpha = 150°$), Lamination schemes: symmetric in-axis configurations [0°/90°/0°/90°/0°]; and off-axis configurations [θ°/−θ°/θ°/−θ°/θ°] are constructed.

Three following cases for different stiffener orientations are studied:

Case 1. Unstiffened folded composite plate (Fig. 10.2a).
Case 2. Three y-stiffeners are attached below the folded plate running along the length of the plates (width of stiffening plate taken equal to 0.1 m and thickness remaining same as the original folded plate) (Fig. 10.2b).
Case 3. Two x-stiffeners are attached below the folded plate along transverse direction (Fig. 10.2c) (width of stiffening plate taken equal to 0.1 m and thickness remaining same as the original folded composite plate).

The boundary conditions:

- At edges $y = 0$: $u = v = w = \theta_x = \theta_y = \theta_z = 0$ (without the edges of stiffeners).
- At edges (1) and (2): $u = v = 0$ (without the edges of stiffeners).

Loading condition The plate subjected to a uniform knife-edge loading $q = 5$ N/m along its edge of $y = L$ towards the negative direction of the y-axis while the bottom edge is constrained to move.

In the sub-sections below, the eigenvalue buckling analysis calculates a scaling factor for the existing loads, if a unit load is applied, the scaling factor yields the buckling load.

The non-dimensional buckling load parameters is as follows: $\lambda^*_{CR} = \frac{\lambda_{CR} a^2}{E_2 t^3}$.

10.3.2.1 Effect of Stiffeners

To observe the effects of stiffener on critical load, the plates having laminate schemes [45°/−45°/45°/−45°/45°] and [0°/90°/0°/90°/0°] (cross-ply) are considered. The

results presented in Figs. 10.3 10.4, 10.5 and 10.6 have been compared for different cases.

We denote cases of the plate with and without stiffeners as follow:

(i) Case of the plate without stiffener is WOS (Case 1)
(ii) Case of the plate with *y*-stiffeners is WYS (Case 2)
(iii) Case of the plate with *x*-stiffeners is WXS (Case 3).

For flat plate: folding angle $\alpha = 180°$ and laminate schemes [45°/−45°/45°/−45°/45°] (Fig. 10.3).

For flat plate: folding angle $\alpha = 180°$ and laminate schemes [0°/90°/0°/90°/0°] (Fig. 10.4).

For folded plate: folding angle $\alpha = 120°$ and laminate schemes [45°/−45°/45°/−45°/45°] (Fig. 10.5).

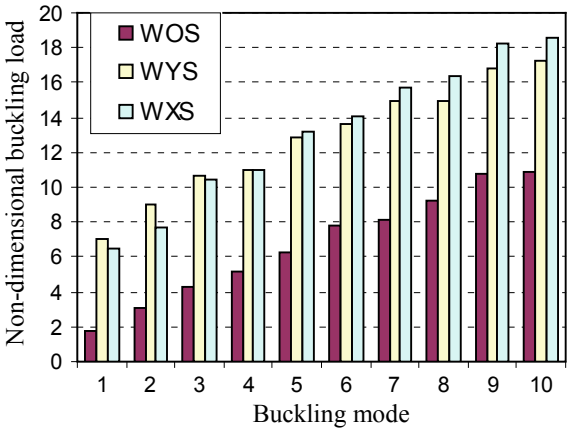

Fig. 10.3 Effects of stiffeners on buckling load of flat composite plate [45°/−45°/45°/−45°/45°]

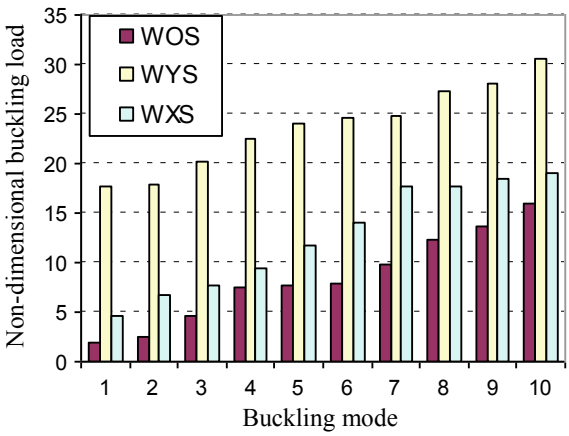

Fig. 10.4 Effects of stiffeners on buckling load of flat composite plate [90°/0°/90°/0°/90°]

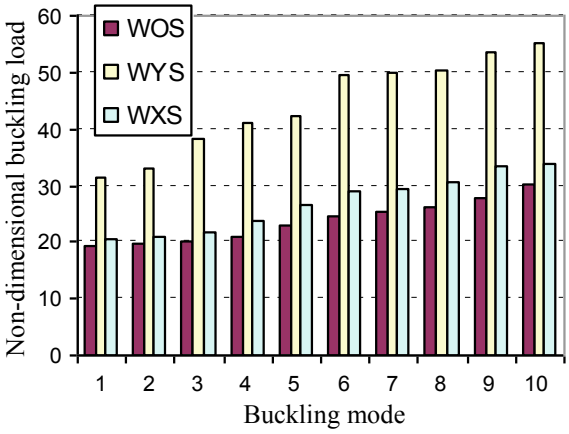

Fig. 10.5 Effects of stiffeners on buckling load of folded composite plate [45°/−45°/45°/−45°/45°]

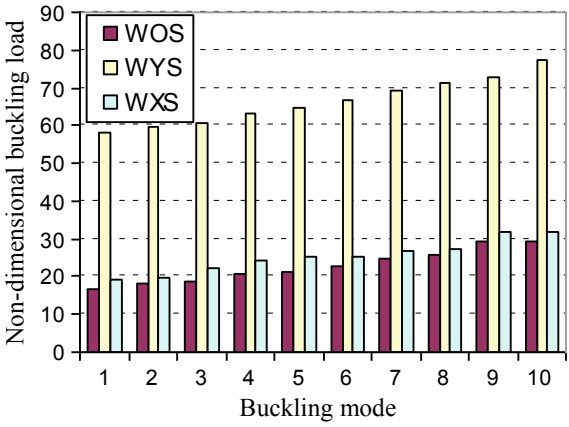

Fig. 10.6 Effects of stiffeners on buckling load of folded composite plate [90°/0°/90°/0°/90°]

For folded plate: folding angle $\alpha = 120°$ and laminate schemes [0°/90°/0°/90°/0°] (Fig. 10.6).

It is observed that case of WYS is the best process of reinforcement for buckling with the compressive loading and the case of WYS is the worst process of reinforcement. For both of laminate schemes: buckling load of the plate descended form case of WYS to case of WXS and case of WOS.

Figures 10.7 and 10.8 plotted buckling modes of flat plate Case 1 and folded plate Case 3, respectively.

10.3.2.2 Effect of Fibre Orientations

In this subsection, we calculated the buckling load of the plates for various ply orientations of $\theta = 15°$, 30°, 45°, 60°, 75° and [0°/90°/0°/90°/0°]. The lamination

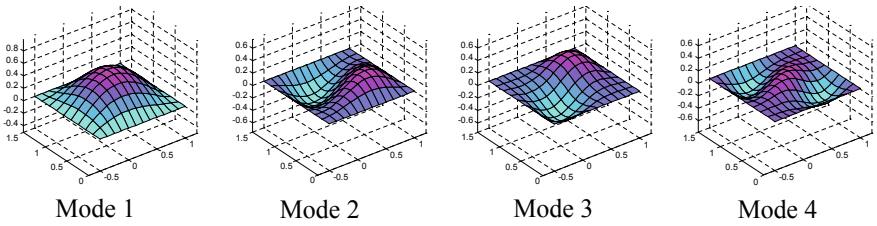

Fig. 10.7 Buckling mode of flat plate Case 1, folding angle $\alpha = 180°$, [45°/−45°/45°/−45°/45°]

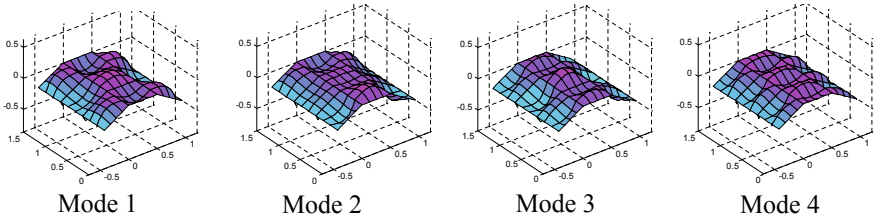

Fig. 10.8 Buckling mode of folded plate Case 3, folding angle $\alpha = 150°$, [90°/0°/90°/0°/90°]

schemes are [$\theta°/-\theta°/\theta°/-\theta°/\theta°$] and laminate scheme is [0°/90°/0°/90°/0°]. The buckling load, plotted in Fig. 10.3, shows the influence of ply orientation for different cases.

We denote:

$\theta = 15^0$ $\theta = 45^0$ $\theta = 75^0$

$\theta = 30^0$ $\theta = 60^0$ Cross-ply

For folded plate of Case 2: folding angle $\alpha = 90°$ and laminate schemes [0°/90°/0°/90°/0°] (cross-ply) (Fig. 10.9).

For folded plate of Case 2: folding angle $\alpha = 120°$ and laminate schemes [0°/90°/0°/90°/0°] (cross-ply) (Fig. 10.10).

For folded plate of Case 2: folding angle $\alpha = 150°$ and laminate schemes [0°/90°/0°/90°/0°] (cross-ply) (Fig. 10.11).

In this numerical analysis, buckling loads of three cases (Case 1; Case 2 and Case 3) were determined but only the effects of stiffeners for Case 2 were plotted in Figs. 10.9, 10.10 and 10.11. From the results, we obtained that buckling load of cross-ply plate were significantly higher than others fibre orientational schemes.

Four buckling mode of folding angle $\alpha = 150°$ of Case 2 (three y-stiffeners) were plotted in Fig. 10.12.

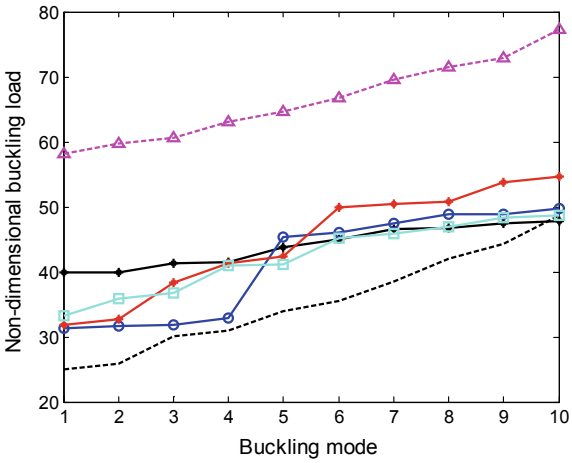

Fig. 10.9 Effects of stiffeners on buckling load for folding angle $\alpha = 90°$

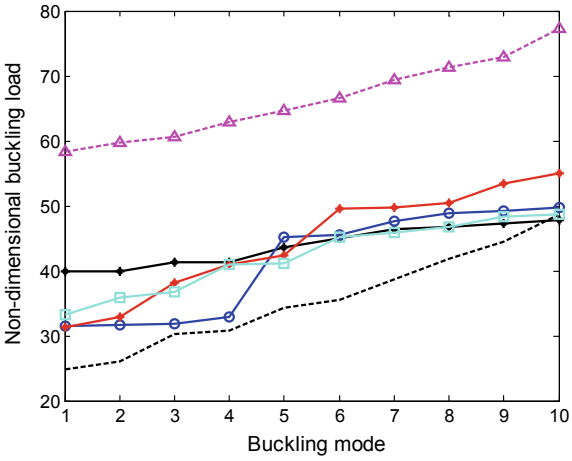

Fig. 10.10 Effects of stiffeners on buckling load for folding angle $\alpha = 120°$

10.3.2.3 Effect of Folding Angles

In this subsection, the effects of folding angles on buckling load have been investigated. The plates having lamination schemes of [45°/−45°/45°/−45°/45°] and [90°/0°/90°/0°/90°] are taken to these analyses. The present results have been compared in Fig. 10.13a, b for four cases (with flat plate $\alpha = 180°$).

In this numerical analysis, buckling loads of three cases (Case 1, Case 2 and Case 3) were also determined but only the effects of folding angles for Case 2 were plotted in Fig. 10.13a, b. From the calculated results, we found that the buckling load of flat plates are significantly lower than the others cases of folding angles.

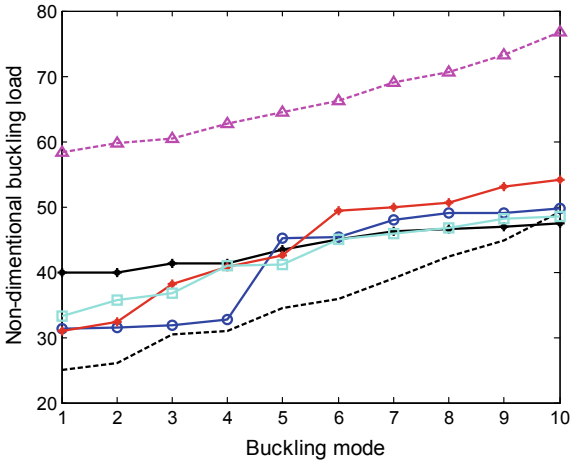

Fig. 10.11 Effects of stiffeners on buckling load for folding angle $\alpha = 150°$

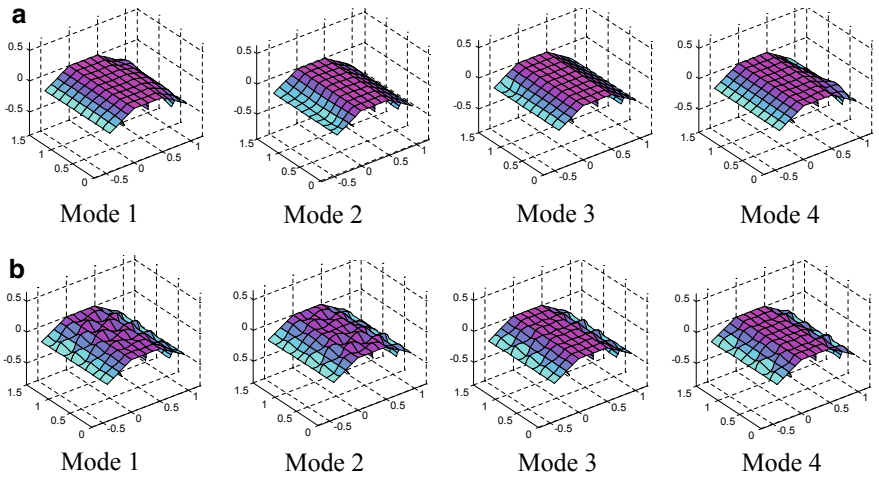

Fig. 10.12 **a** Buckling mode of case 2, folding angle $\alpha = 150°$, [45°/−45°/45°/−45°/45°]. **b** Buckling mode of Case 2, folding angle $\alpha = 150°$, [0°/90°/0°/90°/0°]

10.4 Numerical Results

A finite element analysis was conducted to predict the buckling load of un-stiffened and stiffened folded composite plate for three types of stiffeners. The transverse shear deformation, the rotary inertia of plate and stiffeners are considered in the present method to see that is the more advanced in presented model. The model is used to obtain the buckling responses for folded laminate plates with different folding

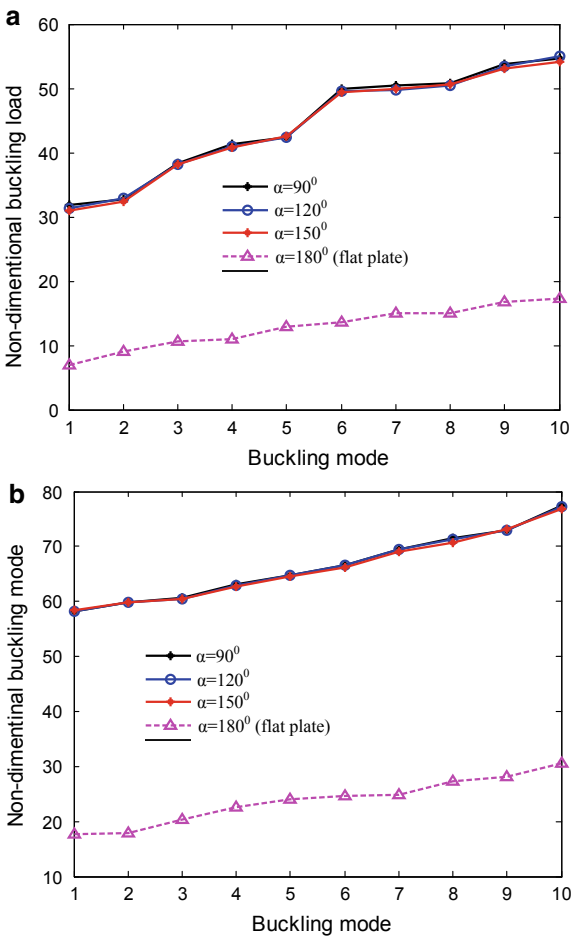

Fig. 10.13 **a** Effects of folding angles on buckling load for case 2, [45°/−45°/45°/−45°/45°]. **b** Effects of folding angles on buckling load for Case 2, [0°/90°/0°/90°/0°]

angles, stiffeners orientations under compressive loading condition. The results of this study will serve as a benchmark for future research for designing folded composite structures and sandwich structures made of composite materials, as it was extremely quick and reliable in producing design results.

References

1. J.E. Goldberg, H.L. Leve, Int. Assoc. Bridg. Struct. Eng. **17**, 58–86 (1957)
2. D. Yitzhaki, M. Reiss, J. Struct. Div. ASCE **88**, 107–142 (1962)
3. Y.K. Cheung, Proc. ASCE **94**, 1365–1378 (1968)
4. Y.K. Cheung, J. Struct. Div. ASCE **12**, 2963–2979 (1969)
5. S. Maleki, Comput. Struct. **40**, 527–538 (1991)
6. Y. Lavy, P. Bar-Yoseph, G. Rosenhouse, Comput. Struct. **42**, 433–446 (1992)

7. T. Irie, G. Yamada, Y. Kobayashi, J. Acoust. Soc. Am. **76**(6), 1743–1748 (1984)
8. B. Perry, P. Bar-Yoseph, G. Rosenhouse, Comput. Struct. **44**, 177–183 (1992)
9. S. Pal, A. Guha Niyogi, J. Reinf. Plast. Compos. **27**, 692–710 (2008)
10. S. Haldar, A.H. Sheikh, Finite Elem. Anal. Des. **42**, 208–226 (2005)
11. T.I. Thinh, B. Van Binh, T.M. Tu, Vietnam. J. Mech., VAST **34**(3) (2012)
12. D.B. Singh, B.N. Singh, Compos. Struct. **157**, 360–365 (2016)
13. K. Liang, Q. Sun, Y. Zhang, Compos. Struct. **206**, 681–692 (2018)
14. H. Ahmadi, H.A. Rasheed, Compos. Struct. **185**, 348–361 (2018)
15. E.J. Barbero, A. Madeo, G. Zagari, R. Zinno, G. Zucco, Compos. Struct. **116**, 223–234 (2014)
16. H.R. Ovesy, J. Fazilati, Compos. Struct. **94**, 1250–1258 (2012)
17. K.-J. Bathe, *Finite Element Procedures* (Prentice Hall, Upper Saddle River, NJ 1996)
18. T.I. Thinh, *Composite materials* (Viet Nam Education Publishing House, Hanoi 1994) (in Vietnamese)

Chapter 11
The Effect of Strain Rate on Chip Formation and Cutting Process During High-Speed Cutting of A6061 Aluminum Alloy

Pham Thi Hoa, Banh Tien Long, Nguyen Duc Toan, Doan Thi Huong, and Pham Duc Thanh

Abstract Nowadays, increasing productivity and quality of machining become major challenges of the metal cutting process. Due to the complexity of the chip formation process at high cutting speeds, the finite element method (FEM) has been widely used as an approximate solution. In the metal cutting, the chip formation is essentially concerned with the large strains and the high strain rates. In this chapter, two numerical models with and without strain rate effects are proposed. An appropriate model is then verified by comparing the simulated cutting forces under varying cutting parameters. The simulation model with strain rate is consistent with the experimental value, whereas the model without strain rate underestimates the cutting forces. The strain rate also modifies the cutting forces owing to the stresses that occurred at cutting regions and significantly affected by the strain rate.

11.1 Introduction

Nowadays, along with the development of machining industry, metal cutting is one of the key techniques. Research on chip formation problems during cutting helps to improve the surface quality of the workpiece and reduce machining time. Strain rate influences the chip formation and other factors during cutting. Therefore, research on strain rate of cutting has attracted significant attentions. Sun et al. [1] studied the strain rate in the primary shear zone. They showed that there is a distinct peak shift in the shear strain rate distribution during saw-tooth chip formation, while there is a stable peak position of the strain rate distribution during continuous chip formation.

P. T. Hoa (✉) · D. T. Huong
Hung Yen University of Technology and Education, Hung Yen, Viet Nam
e-mail: hoapt2108@gmail.com

B. T. Long · N. D. Toan
School of Mechanical Engineering, Hanoi University of Science and Technology, Hanoi, Viet Nam

P. D. Thanh
Hanoi University of Transport and Communications, Hanoi, Viet Nam

I. A. Parinov et al. (eds.), *Advanced Materials*, Springer Proceedings in Materials 6, https://doi.org/10.1007/978-3-030-45120-2_11

Moreover, the primary shear zone thickness during saw-tooth chip formation is more localized and smaller than that during continuous chip formation during cutting of AISI 1045 and AA6082-T6 alloys. Jaspers and Dautzenberg [2] studied the strain, strain rate, and temperature during chip generation. They proposed a method to determine the strain and strain rate from which to identify the chip stock. List et al. [3] determined the strain, strain rate in the high shear speed area. The authors compared the deformation and strain rate between experimental and simulation models, which showed a good correlation. Some studies highlighted the strain and the rate of strain occurring during shearing such as in [4, 5].

In this study, the effect of strain on the cutting process of aluminum alloy A6061 is simulated. Simulation results of stress and strain with strain rates and without strain rates effect are compared. From the simulated and measured shear forces, it is found that at high-speed, the strain rate significantly affects the performance of the cutting process.

11.2 Mechanical Properties of A6061 Aluminum Alloy

In this study, the workpiece material of A6061 aluminum alloy is used. This material is widely used in industry because of its excellent properties regarding wear resistance, weldability, and strength. Major chemical compositions and physical properties of A6061 aluminum alloy are shown in Tables 11.1 and 11.2, respectively. Figure 11.1 shows the tensile stress-strain curve of A6061 aluminum alloy.

Table 11.1 Chemical composition of A6061 aluminum alloy (%wt.)

Si	Fe	Cu	Mn	Mg	Cr	Zn	Ti	Al
0.4–0.8	0.7	0.15–0.4	0.15	0.8–1.2	0.04–0.4	0.25	0.15	Remainder

Table 11.2 Physical properties of A6061 aluminum alloy

Physical properties	Value	Physical properties	Value
Melt temperature (°C)	582–652	Elastic modulus (GPa)	68.9
Thermal conductivity coefficient (W/m K)	167	Resistance (Ω m)	3.99×10^{-6}
Specific heat capacity (J/g °C)	0.896	Fracture strength (MPa)	96.5
Density (kg/m^3)	2.7	Tensile strength (MPa)	276
Hardness (HB)	95	Poisson's ratio	0.33

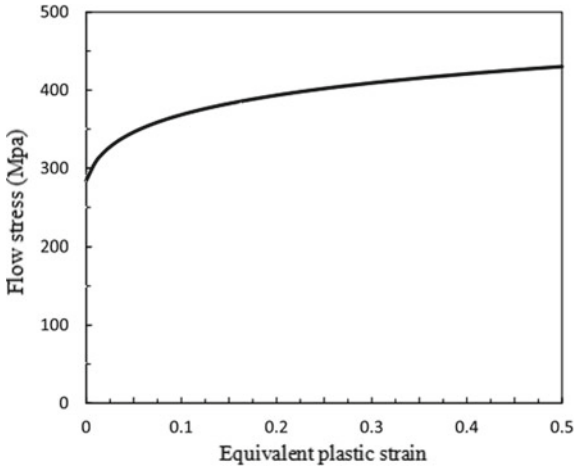

Fig. 11.1 Tensile stress-strain curve of A6061 aluminum alloy

11.3 Influence of Strain Rate on Stress in High-Speed Cutting

The strain rate can affect the chip formation and stress during cutting. During high-speed milling alloy aluminum, the yield stress decreases with the increase of strain rate. This is because the aluminum alloy is capable of average deformation speed. To accurately simulate the cutting process in high-speed milling of A6061 aluminum alloy, this study considers the effect of deformation speed and includes the properties of materials in the simulation model. When the strain rate is higher than 10^3 s^{-1}, the shear stress increases rapidly as shown in Fig. 11.2 [6–8]. Therefore, the stress will be increased quickly if the strain rate exceeds 10^3 s^{-1}.

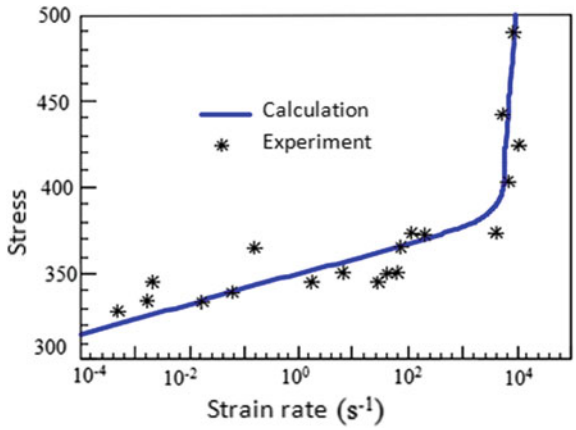

Fig. 11.2 Relationship between stress and strain rate for A6061 aluminum alloy [7, 8]

11.4 Simulation Model

This study employs the Bao–Wierzbicki (B-W) material fracture model, which indicates that the fracture occurs when the accumulated plastic strain reaches a critical value. The accumulated equivalent plastic strain or damage parameter based on the B-W model is given by [6]

$$D = \int_0^{\varepsilon_f} \frac{\sigma_H}{\overline{\sigma}} \mathrm{d}\overline{\varepsilon} = \left(\frac{\sigma_H}{\overline{\sigma}}\right)_{\mathrm{av}} \overline{\varepsilon}_f \tag{11.1}$$

where $\left(\frac{\sigma_H}{\overline{\sigma}}\right)_{av}$ is the average stress triaxiality.

The equivalent strain to fracture can be described by the curve-fit formulae given as follows [6]

$$\overline{\varepsilon}_f = 0.1225\left(\frac{\overline{\sigma}_H}{\overline{\sigma}} + \frac{1}{3}\right)^{-0.46} \text{ for } \frac{\overline{\sigma}_H}{\overline{\sigma}} = -\frac{1}{3} \div 0 \tag{11.2}$$

$$\overline{\varepsilon}_f = 0.19\left(\frac{\overline{\sigma}_H}{\overline{\sigma}}\right)^2 - 0.18\left(\frac{\sigma_H}{\overline{\sigma}}\right) + 0.21 \text{ for } \frac{\overline{\sigma}_H}{\overline{\sigma}} = 0 \div 0.4 \tag{11.3}$$

$$\overline{\varepsilon}_f = 0.15\left(\frac{\overline{\sigma}_H}{\overline{\sigma}}\right)^{-1} \text{ for } \frac{\overline{\sigma}_H}{\overline{\sigma}} = 0.4 \div 0.95 \tag{11.4}$$

The variation of the equivalent strain to fracture as a function of average stress triaxiality is shown in Fig. 11.3, which is determined by using (11.2)–(11.4) for A6061 aluminum alloy.

The commercial software Abaqus/Explicit 6.14.1 is employed for simulation of chip formation and determination of cutting force for A6061 aluminum alloy.

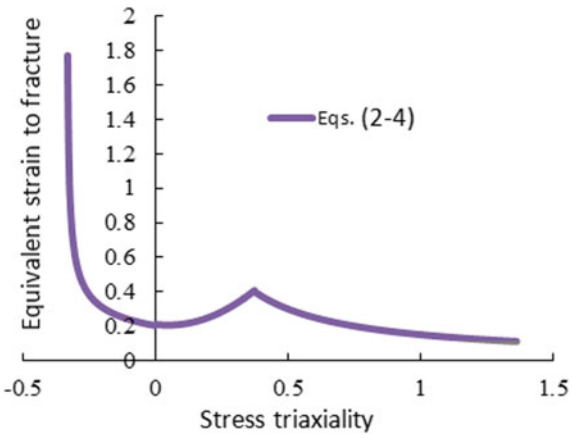

Fig. 11.3 Fracture curve of A6061 aluminum alloy based on the B-W model

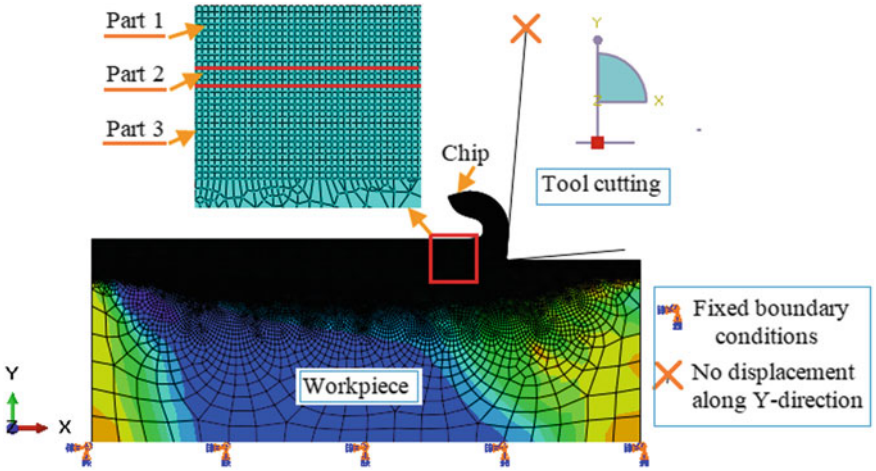

Fig. 11.4 Finite element model of cutting problem

Figure 11.4 shows a two-dimensional (2D) finite element (FE) model for the cutting problem. The model consists of four geometrical parts as shown in Fig. 11.4. The uncut chip portion is represented by part 1, which is coupled to the workpiece support (part 3) by the passage zone of tool tip (part 2). Part 3 plays the role of a sacrificial layer, which directly interacts with the cutting tool. This layer is modeled by a mesh of three elements with a total thickness larger than the cutting-edge radius. A major part of the chip is formulated from the elements in the uncut chip portion. Another part arises from the elements in the sacrificial layer if they are not completely damaged. The remaining elements in the damaged zone, which are completely damaged, will be removed.

11.5 Results and Discussion

11.5.1 Influence of Strain Rate on Stress and Strain During Chip Formation

The effect of strain rate on stress and strain generated is simulated. Simulation was performed under the cutting speed of 1000 m/min, and the cutting depth of 1.5 mm.

The stress-strain results for two cases: with and without strain rate, are shown in Fig. 11.5. The simulated stresses without and with strain rate are 565 and 838 MPa, respectively, as shown in Fig. 11.5. Hence, the stress with strain rate is about 33.9% higher than that without strain rate. The equivalent plastic strains (EPSs) with and without strain rate show the similar behavior as the stress. Specifically, EPSs determined in the absence of the influence of the strain rate is 1.87 MPa, compared to

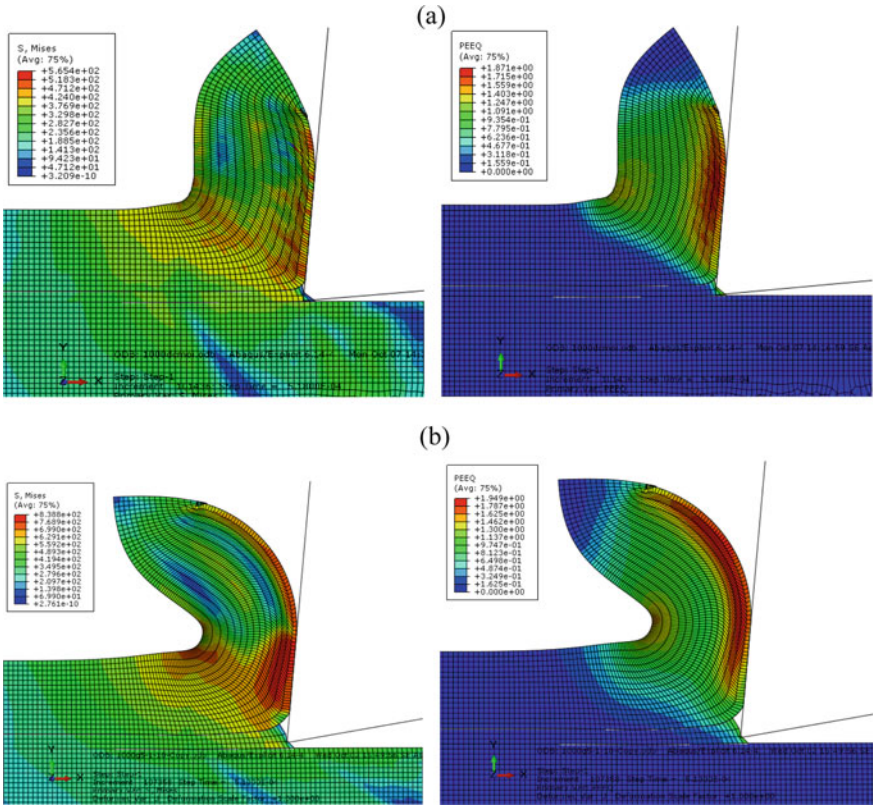

Fig. 11.5 Simulated stress and strain during milling of A6061 aluminum alloy ($V = 1256$ m/min, $t = 0.5$ mm): **a** without strain rate; **b** with strain rate

1.94 MPa for the case with the influence of the strain rate. Thus, EPSs with strain rate increases by 3.7% compared to the case without strain rate. On the other hand, the shape of the chip also varies with each case as shown in Fig. 11.5. In the case with strain rate (see Fig. 11.5a), the formed chip has a higher level of curved shape than that of the chip formed in Fig. 11.5b.

11.5.2 Effect of Strain Rate on Cutting Force

Figure 11.6 shows the progress of simulated cutting forces during milling at a cutting speed of 1256 m/min and a cutting depth of 1.5 mm. The cutting force by the model with strain rate is higher than that of the model without strain rate (see Fig. 11.6). To further assessing the effect of strain rate on the cutting force, experimental and simulated cutting forces at cutting speeds of 1000, 1256, 1512 m/min, and cutting

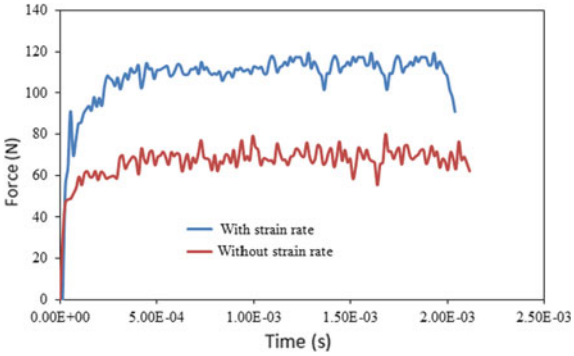

Fig. 11.6 Simulated cutting forces during milling of A6061 aluminum with and without strain rate effect ($V = 100$ m/min, $t = 1.5$ mm)

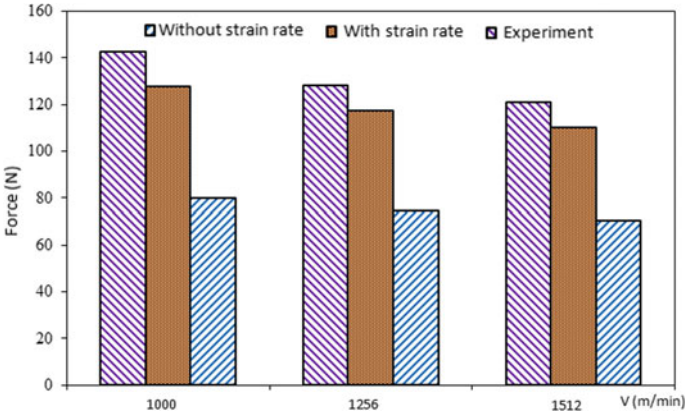

Fig. 11.7 Measured and simulated cutting force with and without strain rate effect

Table 11.3 Comparison of cutting forces with and without strain rate

	V (m/min)	1000	1256	1512
$F(N)$	Experiment (F_E)	142.83	128.42	121.26
	With strain rate (F_S)	127.89	117.74	110.25
	Without strain rate (F_{NS})	80.19	74.81	70.48
$\% \Delta F$	With strain rate (F_S)	10.39	8.31	9.07
	Without strain rate (F_{NS})	43.85	41.17	41.87

depth of 1.5 mm are compared as shown in Fig. 11.7. From Fig. 11.7, the deviations of simulated and measured cutting forces are summarized in Table 11.3. The results showed that at the cutting speed 1256 m/min, the maximum deviation of the measured (F_E) and the simulated forces with strain rate (F_S) is 10.39%; compared to a deviation

of about 43.85% without strain rate. The smallest error of cutting force with strain rate is 8.31% at the cutting speed of 1512 m/min; compared to about 41.17% without strain rate at the cutting speed of 1000 m/min.

11.6 Conclusion

When cutting is performed at high speed, the strain rate significantly influences the chip formation and cutting force in milling of A6061 aluminum alloy. Following conclusions are obtained from this study:

(i) the simulated stresses and EPSs during chip formation with strain rate are higher than those without strain rate;
(ii) the comparisons of measured and simulated the cutting force with and without strain rate show that it is of significance importance to take into account the strain rate in the finite element model, especially for high-speed cutting condition.

References

1. C.Z. Duan, M.J. Wang, J.Z. Pang, G.H. Li, J. Mater. Process. Technol. **178**, 274–277 (2006)
2. S.P.F.C. Jaspers, J.H. Dautzenberg, J. Mater. Process. Technol. **121**(1), 123–135 (2002)
3. G. List, G. Sutter, X.F. Bi, A. Molinari, A. Bouthiche, J. Mater. Process. Technol. **213**, 693–699 (2013)
4. B. Shi, J. Manuf. Sci. Eng. **132**(5) (2013)
5. A. Hor, F. Morel, J.-L. Lebrun, Int. J. Mech. Sci. **67**, 108–122 (2013)
6. Y. Bao, T. Wierzbicki, Int. J. Mech. Sci. **46**(1), 81–98 (2004)
7. D.R. Lesuer, G.J. Kay, M.M. LeBlanc, in *Third Biennial Tri-Laboratory Engineering Conference on Modeling and Simulation*, pp. 3–5 (2001)
8. A. Manes, L. Peroni, M. Scapin, M. Giglio, Procedia Eng. **10**, 3477–3482 (2011)

Chapter 12
Prediction of Temperature Distribution in PCBN Cutting Tools in Orthogonal Turning 9XC Hardened Alloy Steels

Dung Thi Quoc Nguyen

Abstract In this research, a numerical model of temperature distribution in PCBN cutting tools in orthogonal turning 9XC hardened alloy steel was developed. The heat sources generated at cutting zones were determined by theoretical calculations. The temperature distribution in the cutting tool, chip, and workpiece was found by using the heat transfer equations combined with finite element analysis. The isotherms obtained from the numerical model are high compatible with those obtained from experimental measurements. The results indicate that the numerical model has satisfied the requirements and can be applied to similar machining conditions.

12.1 Introduction

In metal cutting, cutting temperature plays an important role in determining machining efficiency. The cutting temperature influences the mechanical properties of the workpiece and cutting tool, thus affecting the cutting forces and the tool life, integrity, and quality of the machined surface.

There are several methods for determining cutting temperature such as thermoelectricity, thermocouple, infrared radiation, mapping the change in structure and hardness of materials depended on temperature, determining the color of hardened steels, coating the materials working as the temperature indicators on the examined surface, etc., but all methods have not yielded accurate results since it is not directly accessible to the heat-generating area. The development of coating technology allowed the use of thermistor sensors to measure the temperature at the tool-chip interface. However, all the tested coating layers were peeled off at the beginning of the cutting process and after that, the sensor was damaged by chips [1]. Thus far, no simple method with high accuracy has been identified to measure temperatures in the cutting zone, even during orthogonal cutting. This is especially difficult for the PCBN cutting tool since the material has very high hardness and it does not

D. T. Q. Nguyen (✉)
Faculty International Training, Thai Nguyen University of Technology, Thai Nguyen, Viet Nam
e-mail: quocdung@tnut.edu.vn

I. A. Parinov et al. (eds.), *Advanced Materials*, Springer Proceedings in Materials 6, https://doi.org/10.1007/978-3-030-45120-2_12

conduct electricity, so the use of the thermistor method and the machining the holes for placing thermocouple has encountered with difficulties. In fact, only a few studies have been accomplished to measure the temperature of the PCBN cutting tools using thermocouples or temperature indicators or measuring infrared radiation [2–4]. Therefore, the analytical models predicting the temperature in PCBN cutting tools received much interest from researchers [3, 5–7]. In this study, a numerical model for determing temperature distribution in the PCBN cutting tool when orthogonal turning 9XC hardened alloy steels has been developed based on the heat transfer model and finite element analysis.

12.2 Temperature Calculation

12.2.1 Thermal Model

The steady, two-dimensional heat transfer equation during orthogonal cutting can be written as [8]

$$\rho c\left(u_x\frac{\partial T}{\partial x}+u_y\frac{\partial T}{\partial y}\right)-k\left(\frac{\partial^2 T}{\partial x^2}+\frac{\partial^2 T}{\partial y^2}\right)+q(x,y)=0. \tag{1}$$

where ρ, c, k, T, q are the density, specific heat, thermal conductivity, temperature, and heat generation rate per unit volume, respectively; x, y are the coordinates, and u_x and u_y are the velocity components in the x and y directions.

This equation must be solved in the region illustrated in Fig. 12.1 [9], which represents the boundary conditions that the equation must satisfy. Solving (1) can be done numerically using the finite element method [10]. The solution yields the temperature distribution over the solution region.

12.2.2 Heat Generation Rate in the Primary Deformation Zone q_1

The rate of plastic deformation heat generated per unit area in the primary deformation zone q_1 is calculated from the shear stress τ_{AB} and sliding velocity V_s in the shear plane [11]. For simplicity, assume that the velocity is constant over the length of the shear plane [12]. The equation of q_1 can be written as

$$q_1=\tau_{AB}V_s=\frac{(F_c\cos\phi-F_t\sin\phi)\sin\phi\cos\alpha}{wt\cos(\phi-\alpha)}V, \tag{2}$$

where F_c and F_t are the tangential and axial components of the cutting force, respectively; w and t are the width and thickness of the chip corresponding to the depth of

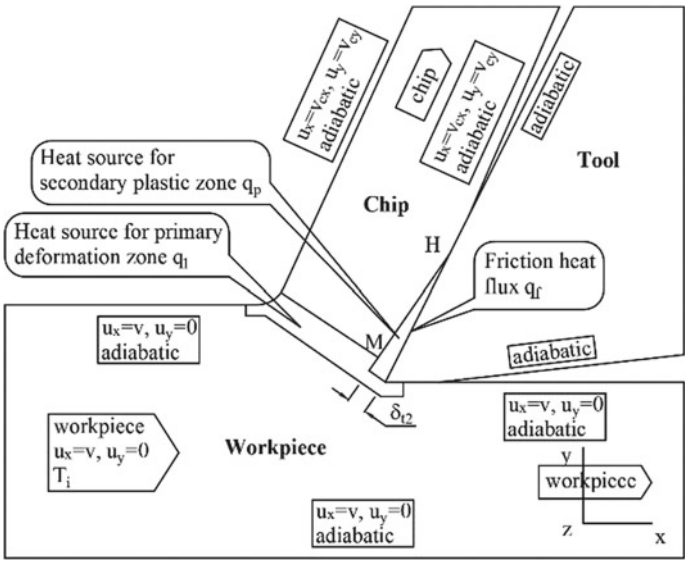

Fig. 12.1 Boundary conditions for the thermal model [9]

cut a and the feed rate d; ϕ and α are the shear and the rake angles, V is the cutting speed.

12.2.3 Heat Generation Rate in the Secondary Plastic Zone q_2

The heat generation rate on the secondary plastic region q_2 includes two components: $q_2 = q_f + q_p$ where q_f is the heat generated due to the friction between the chip and the rake face of the cutting tool and q_p is the heat generated due to the plastic deformation of the chip in the secondary zone.

12.2.3.1 Heat Generation Rate Due to Friction Between the Chip and the Rake Face q_f

The rate of frictional heat generated per unit area at the tool-chip interface q_f is calculated from the shear stress $\tau_{(x)}$ and sliding velocity $V_{(x)}$ of the chip. Both of them vary along the tool-chip interface as shown in Fig. 12.2 [12–14]. With τ_s is the average shear stress, l is the total contact length, l_1 is the length of the adhesive part, over which the shear stress is constant, V_c is the chip velocity. Assume that $l \approx 2l_1$ and the shear stress varies linearly on the length of contact l_1, the equation of q_f is given by [9]:

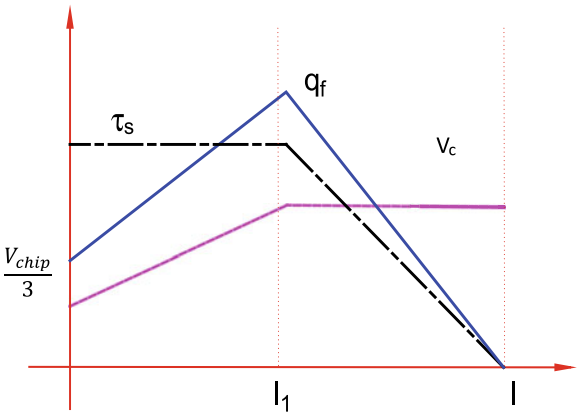

Fig. 12.2 Variation of velocity, stress and friction heat on tool-chip interface [9]

$$q_f = \begin{cases} \frac{\tau_s V_c}{3}\left(1 + \frac{4x}{l}\right) & 0 \le x \le l/2 \\ 2\tau_s V_c\left(1 - \frac{x}{l}\right) & l/2 \le x \le l \end{cases} \tag{3}$$

12.2.3.2 Heat Generation Rate in the Secondary Plastic Zone q_p

The rate of plastic heat generated per unit volume in the secondary zone is given by [15]

$$q_p = \tau_{\text{sec}}\dot{\gamma}_{\text{sec}} = \frac{(F_c \sin\alpha + F_t \cos\alpha)V \sin\phi}{lw\delta t_2 \cos(\phi - \alpha)}. \tag{4}$$

where τ_{sec} is the shear stress at the tool-chip interface, which is assumed to be constant along the interface, $\dot{\gamma}_{\text{sec}}$ is the strain rate in the secondary plastic area, which varies linearly from constant value along the tool-chip interface to zero along the boundary HM in Fig. 12.1; l and w are the contact length, and contact width of the tool-chip interface, respectively; δt_2 is the maximum thickness of the secondary plastic zone: $\delta t_2 = 0.05$ mm or 1/8 for the range of shear speeds considered (Fig. 12.1) [8, 15].

12.2.3.3 Equivalent Shear Stress in the Secondary Plastic Zone τ_s'

For simplicity, consider the heat generated by plastic deformation and friction in the secondary zone is equivalent to the heat generated due to the equivalent friction in the tool-chip interface. Denote $\tau'_{(x)}$ as the variable equivalent stress and τ_s' is constant equivalent stress, τ_s' can be found by the law of conservation of energy as

$$Q_2 = \int_0^{l/2} \frac{\tau_s' V_c}{3}\left(1 + \frac{4x}{l}\right) w dx + \int_{l/2}^{l} 2\tau_s' V_c\left(1 - \frac{x}{l}\right) w dx = F_F V_c. \tag{5}$$

$$\tau_s' = \frac{F_F}{wl\left(\frac{1}{3}+\frac{1}{4}\right)} = \frac{12F_F}{7wl}. \tag{6}$$

Substituting $\boldsymbol{\tau}_s'$ into (3) to find the rate of heat generated in secondary zone $q_2(x)$.

12.2.4 Heat-Generation Rate at the Tool Flank-Work Interface q_w

The flank wear land is considered flat and parallel to the finished surface. The stress distributions are assumed uniform along with the interface. The rate of heat generated over the flank wear land is constant and given by [13]:

$$q_3 = K_c \frac{VF_C}{tw} = 0.0671 VF_c \frac{1}{t_1 w}, \tag{7}$$

where K_c is the experimentally cutting force coefficient.

12.2.5 Experimental Parameters

It is necessary to carry out the experiments to estimate the input parameters for solving (1). The experiments were conducted on HOWA STRONG 860 (Japan) lathe at the machining conditions: cutting speed of $v = 119.3$ m/min; depth of cut $a = 3$ mm, and the feed rate $d = 0.06$ mm/rev. The PCBN triangular inserts were used with the geometric parameters as shown in Table 12.1. The cutting forces were measured by a three-component force dynamometer (Kistler 9257BA) after machining the length of 50 mm which is equivalent to 2.19 s of cutting.

The chip thickness t_c and the contact length of the tool-chip interface l are measured on the SEM image of the chip root and tool rake face. The values of dimensions, cutting forces, and velocities are summarized in Table 12.2. The material properties include heat conductivity k, density ρ and specific heat c, where the density ρ is considered unchanged, while the heat conductivity k and specific heat c are the temperature dependent. For the 9XC workpiece and PCBN cutting tool, the material properties are given as [3]: PCBN cutting tool material: $\rho = 3120$ (kg/m^3); k varies from $k_{(20\,^\circ\mathrm{C})} = 100$ (W/mK) to $k_{(900\,^\circ\mathrm{C})} = 130$ (W/mK); c varies from $c_{(20\,^\circ\mathrm{C})} = 1000$ (J/kg K) to $c_{(900^\circ\mathrm{C})} = 1966$ (J/kg K). Workpiece material of 9XC steel: The

Table 12.1 Geometry of PCBN insert

Tool	Rake angle α	Clearance angle γ	Side angle λ	Nose radius r (mm)
PCBN	−6°	6°	0°	0.8

Table 12.2 Experimental parameters to calculate the temperature

V (m/p)	d (mm/v)	a (mm)	t_c (mm)	l_c (mm)	r (t/t_c)	Φ (rad)	V_s (m/p)	V_c (m/p)	F_c (N)	F_t (N)	F_s (N)	F_F (N)
119.3	0.06	3	0.13	0.24	0.46	0.412	136.5	55.07	410.6	250.4	275.6	206.2

Table 12.3 The values of heat flux at the heat generating centers

τ_{AB} (N/mm^2)	A_s (mm^2)	q_1 (W/mm^2)	$\dot{\gamma}_{sec}$ 10^5(1/s)	τ_{sec} (N/mm^2)	τ'_s (N/mm^2)	q_{2max} (W/mm^2)	q_3 (W/mm^2)
919.32	0.45	1397	1.2	286	490	450	303

thermal properties can be considered as constant since they would not vary significantly within the range of testing temperature: $k = 47$ (W/mK); $\rho = 7800$ (kg/m^3); $c_{(20\,^\circ C)} = 486$ (J/kg K), ambient temperature $T_\infty = 20$ °C. The heat generation rates are calculated and summarized in Table 12.3.

12.2.6 Finite Element Model

A two-dimensional heat transfer simulation model was established as shown in Fig. 12.3. The set-up of the simulation model includes the tool insert, tool holder, the chip and workpiece. The process of meshing elements of the model is accomplished in ABAQUS software with appropriate control parameters so that the heat-generating areas are divided with fine-sized elements to achieve high accuracy. In total, the whole model is divided into 557,758 tetrahedral elements, each element has 4 nodes with a total of 2,231,032 nodes as shown in Fig. 12.3a.

With input parameters including the geometry of the survey area, the material properties of the tool and the workpiece, the specific heat flux and boundary conditions. The process of analyzing the temperature distribution in orthogonal turning 9XC hardened steel with PCBN cutting tool has been carried out and given the temperature distribution as shown in Fig. 12.3b.

The temperature distribution in PCBN cutting tools when orthogonal turning 9XC hardened alloy steel is also determined experimentally. Isotherms in the tool are obtained from the boundaries between melted and unmelted zones of the thin

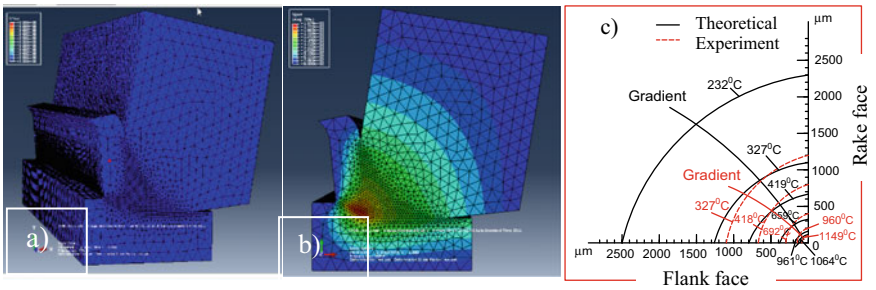

Fig. 12.3 Meshing simulation model (**a**), temperature distribution (**b**), and isotherms in cutting tools obtained from empirical measurement and numerical model (**c**)

layers of different materials with specific melting points coated on the surface of the cutting tool [16].

12.3 Results and Discussion

The results from the numerical and experimental models indicate that the heat generated during orthogonal turning 9XC hardened steel by PCBN cutting tool is very large. Although most cutting heat is carried away by the chip and only a small portion of the heat is transferred into the cutting tool, the temperature at the edge of the cutting tool is still very high. It can reach 1163 °C at the beginning of machining and 1537 °C after only 2.19 s when the tool is worn.

It can be seen that the reason for the very high temperature at the tool edge is the poor thermal conductivity of PCBN material while heat is continuously transferred to a fixed position on the tool. On the other hand, in the hard turning process, the machined materials have high hardness and durability. Thus, they require a large amount of destructive energy, which causes a large shear force which results in a high heat generation rate.

The isotherms obtained from the numerical are highly compatible with those obtained from experimental measurements. The differences at the melting boundaries of the coated materials are relatively small, namely: 0.2% at 419 °C (Zn), 5% at 659 °C (Al), 0.1% at 919 °C (Ag) and 7.8% at 1064 °C (Au) (Fig. 12.3c).

12.4 Conclusion

In this research, a numerical model investigating the temperature distribution in the PCBN cutting tool of the orthogonal turning 9XC hard ened alloy steel has been developed. The model is based on the calculations with certain assumptions.

Results from calculation and measurement show that the temperature at the cutting area during the orthogonal turning of 9XC hardened steel by PCBN tool is very high. High temperatures cause the change in mechanical properties of the binder of the PCBN material, leading to rapid wear and plastic deformation of the tool edge while accelerating chemical interaction and promoting wear mechanisms, result in faster damage to the cutting edge.

The isotherms achieved from the numerical model are highly compatible with those obtained from the experimental measurements since the differences are less than 7.8%. This demonstrates that the proposed numerical model has acceptable reliability and it can be applied to similar machining conditions.

References

1. S. Jaspers, *Metal Cutting Mechanics and Material Behaviour* (Technische Universiteit Eindhoven, Holland, 1999)
2. S. Lo Casto, E. Lo Valvo, F. Micari, J. Mech. Work. Technol. **20**, 35–46 (1989)
3. X.J. Ren, Q.X. Yang, R.D. James, L. Wang, J. Mater. Process. Technol. **147**, 38–44 (2004)
4. T. Ueda, M. Al Huda, K. Yamada, K. Nakayama, Ann. CIRP **4** (1999)
5. P.D. Dhikale, S.M. Shinde, A.P. Kulkarni, Int. Conf. Mater. Process. Characterzation **2**, 1907–1914 (2015)
6. H. Yana, J. Huab, R. Shivpuri, Sci. Technol. Adv. Mater. **6**, 540–547 (2005)
7. N.E. Karkalos, A.P. Markopoulos, J. Chem. Technol. Metall. **52**, 288–293 (2017)
8. A.O. Tay, M.G. Stevenson, G. de Vahl Davis, P.L.B. Oxley, Int. J. Mach. Tool Des. Res. **16**, 335–349 (1976)
9. Y. Dogu, E. Aslan, N. camuscu, J. Mater. Process. Technol. **171**, 1–9 (2006)
10. A.O. Tay, M.G. Stevenson, G. de Vahl Davis, Proc. Inst. Mech. Eng. Proc. **188**, 627–638 (1974)
11. M. Trent Edward, K. Paul Wright, *Metal Cutting*, Butterworth-Heinemann, New Delhi (2000)
12. M.C. Shaw, *Metals Cutting Principles* (Oxford University Press, New York, 1984)
13. X. Li, E.M. Kopalinsky, P.L.B. Oxley, Proc. Inst. Mech. Eng. **209**, 33–43 (1995)
14. N.N. Zorev, *International Research in Productions Engineering* (ASME, New York, 1963), pp. 48–57
15. P. Majumdar, R. Jayaramachandran, S. Ganesan, Appl. Therm. Eng. **25**, 2152–2168 (2005)
16. N.T.Q. Quoc Dung, P.Q. The, in *International Symposium on Technology for Sustainability*, Bangkok, Thailand, pp. 560–562 (2012)

Chapter 13
Study on the Optimal Sealing Technological Regime for Making Sport Wears from Waterproof Fabric

Tran Thuy Trang and Phan Thanh Thao

Abstract The article focuses on the separate and simultaneous influences of sealing technological effects: air temperature, sealing speed, roller pressure and nozzle pressure on resistance to water penetration, ultimate tensile strength, the adhesive strength of seam sealing after washed in processing sportwears made from waterproof fabrics. In this research, we used the analysis of variance method for two-elements case, planning method orthogonal experimental variety of factors, Microsoft Excel 2013 and Design Expert 11.0 software to process and analyse experiment results. The result which is to identify sealing technological elements has important effects on resistance to water penetration, ultimate tensile strength, the adhesive strength of seam sealing after washed. The result of this study is an useful guide in the actual production to improve the quality of links in order to save time and costs in the actual production in sportwear garment enterprises as well as Seam tape supplier in general and at TNG Investment and Trading Join Stock Company in particular.

13.1 Introduction

Nowadays, some products in fashion industry such as tents, single-layer or multi-layer jackets need to have waterproof function with certain levels of waterproofing. To achieve water-proof ability, in production, people not only use traditional sewing methods but also use one of two methods: welding sealing and sealing seam.

Actual productions at Song Cong 2 Garment Company of TNG Investment and Trading Joint Stock Company, sportswear products using the method of sealing seam are the dominant products. In order to evaluate product quality, the criteria of washing resistance, adhesive strength and water resistance are very important. Therefore, within the scope of the research, the authors focus on studying, conducting exploration and screening experiments, using mathematical tools to analyze the specific

T. T. Trang (✉) · P. T. Thao
Hanoi University of Science and Technology, Hanoi, Vietnam
e-mail: thuytrang091195@gmail.com

P. T. Thao
e-mail: thao.phanthan@hust.edu.vn

I. A. Parinov et al. (eds.), *Advanced Materials*, Springer Proceedings in Materials 6, https://doi.org/10.1007/978-3-030-45120-2_13

Table 13.1 Technical specification required

STT	Physical properties	Value
1	Layers	2
2	Width (inch)	58 inch
3	Face fabric	100% PET (PU: Laminated on face fabric)
4	Weight (g/m^2)	150
5	Weave type	Woven, Twill Fabric
6	Thickness (mm)	0.2 mm
7	Waterproofness (before washing)	≥12,000 mm H_2O
8	Waterproofness (after washing)	≥10,000 mm H_2O
9	Breaking strength (before washing)	≥1.1 dN/20 mm
10	Breaking strength (after washing)	≥0.9 dN/20 mm

levels of influence after washing. There are many technological factors that influence on the sealing seam quality, such as sealing temperature, sealing speed, wind pressure and compression strength of axis plots, etc. Experimental use of waterproof cloth with high quality processed products for sportswear at Song Cong 2 Garment Company of TNG Investment and Trading Joint Stock Company.

13.2 Experimental Research

13.2.1 Object of Researching

13.2.1.1 Fabric

Select the common waterproof fabrics used for sportswear produced at Song Cong 2 Garment Company of TNG Investment and Trading Joint Stock Company. Some specifications of ELM PES 2L TRANS T—experimental fabric are shown in Table 13.1.

13.2.1.2 Tape

Adhesive tape is a material which is used to paste over temporary seams of waterproofing materials (sealing seams or welding seams) with the aim of giving the

Table 13.2 Thermal and physical properties

Information	Tape ST604
Supplier	BEMIS
Tape type	ST604
Width	20 mm
Composition	100% PU
Gauge	89 μm
Softening point	105 °C

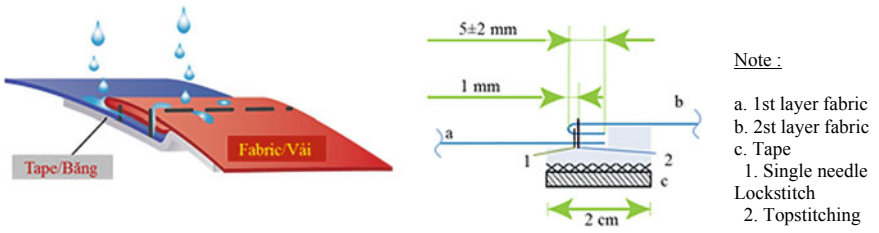

Fig. 13.1 Structure of seam sealing section

seams the necessary waterproofing and mechanical strength. Therefore, the structure, properties and number of layers of adhesive materials must be compatible with the structure, properties and number of layers of a waterproof fabric. In this research, select ST604 tape from BEMIS supplier. Technical information of the tape is shown in Table 13.2 [1].

13.2.1.3 Section: Figure 13.1

See Fig. 13.1.

13.2.1.4 Measuring Device

Experiments of the research was carried out at the technical department of Song Cong 2 Garment Company and the Company's Internal Lab, including the following equipment: lockstitch sewing machine, hot air tape sealing machine, washing machines, leaking test machine, and tensile testing machine. Washing test was performed according to DS034 standard, waterproof test—to DS270 standard, testing the adhesive strength of the sealing seam according to DS044 standard—standards of Decathlon Co., Ltd. (Strategic customer of Song Cong Garment Company 2) [2].

13.2.2 Research Methodology

We use ANOVA variance analysis method with one factor on Microsoft Excel 2013 software to process and analyze empirical data to evaluate the degree of individual impact of each paste technology to adhesion of sealing seam [3].

We use multivariate empirical planning method with the help of Design Expert 11.0 software, to design experiments, process and formulate empirical regression equations to study the simultaneous effects of the factors. Technology factors to the adhesion strength of the surface of all details glued on the research cloth [4].

13.2.2.1 Studying the Unique Effect of Each Factor to the Adhesive Strength of the Sealing Seam

The empirical data for these experiments is established by considering the influence of one factor, the values of this factor is changed, and the other factors remain at the value set by the technical department (the parameter is using in production) [3, 4].

Specifically, the recommended parameters from the technical department are [5]:

(i) air temperature 500 °C;
(ii) sealing speed 22 ft/min;
(iii) roller pressure 0.45 MPa;
(iv) nozzle pressure 0.06 MPa.

All of the factors are measurable and controllable variables. The change in the value of these factors is regular and based on the average value, the upper and lower values are wider than the value ranges commonly established in enterprises to ensure the total general and accurate experiments. Based on the actual production and recommended parameters of the Bemis supplier, we choose the range of variations of the paste technology factors in Table 13.3 [5–7].

Number of samples tested:

(v) the number of testing samples for each factor is 15 samples (each factor has 5 levels of change value; each level of sample is measured 3 times);
(vi) total number of testing: $15 \times 4 = 60$ (samples).

Table 13.3 Interval of 4 variables in the research

Elements	Air temperature (°C)	Sealing speed (ft/min)	Roller pressure (MPa)	Nozzle pressure (MPa)
Value	480	20	0.35	0.04
	490	21	0.40	0.05
	500	22	0.45	0.06
	510	23	0.50	0.07
	520	24	0.55	0.08

13.2.2.2 Studying the Effect of 4 Factors on the Adhesion Strength of the Sealing Seam

Number of samples tested: we use the orthogonal planning level 2 for 4 influencing factors. Then number of experiments is $N = 2^{k-p} + n_0 + 2k = 2^{4-1} + 4 + 2 \times 4 =$ 20 experiments. Each experimental plan is measured 3 times. Total number of tests: $20 \times 3 = 60$ (samples).

The change in the value of these technological parameters is regular and based on the average value. Based on the actual productions and recommended documents of the fabric and adhesive supplier, we choose the range of variability of factors in Table 13.4 [5–7].

13.3 Research Results

13.3.1 The Results of Each Factors Affect the Adhesion Strength of the Sealing Seam

See Table 13.5.

13.3.2 Effect of Air Temperature on Adhesive Strength of the Sealing Seam

Results of surveying the adhesive strength of seams on waterproofing fabrics in research of the individual effect of air temperature are presented in Table 13.5. Using Microsoft Excel 2013 software to conduct ANOVA variance analysis to assess the influence of the air temperature on the adhesive strength of the sealing seam. Results are presented in Table 13.6.

ANOVA analysis results in Table 13.6.

Table 13.4 Values and codes of 6 variables in the research

No.	Variable in research X_j	Value of real variable				
		−1.41	−1	0	1	1.41
1	Air temperature (°C)	450	470	500	530	550
2	Sealing speed (ft/min)	20	21	22	23	24
3	Roller pressure (MPa)	0.35	0.4	0.45	0.5	0.55
4	Nozzle pressure (MPa)	0.04	0.05	0.06	0.07	0.08

Table 13.5 Summary of test results measuring adhesive strength when changing each factor

Variable	Air temperature (°C)	Sealing speed (ft/min)	Roller pressure (MPa)	Nozzle pressure (MPa)	Waterproofness (before washing)	Appearance after washing	Water-proofness (after washing)	Adhesive strength (*N*)
Air temperature (°C)	480	22	0.45	0.06	Ok	Ok	Ok	17.61
	490	22	0.45	0.06	Ok	Ok	Ok	14.63
	500	22	0.45	0.06	Ok	Ok	Ok	13.58
	510	**22**	**0.45**	**0.06**	Ok	Ok	Ok	17.44
	520	22	0.45	0.06	Ok	Ok	Ok	15.47
Sealing speed (ft/min)	500	20	0.45	0.06	Ok	Ok	Ok	17.96
	500	21	0.45	0.06	Ok	Ok	Ok	17.18
	500	22	0.45	0.06	Ok	Ok	Ok	14.49
	500	23	0.45	0.06	Ok	Ok	Ok	12.45
	500	24	0.45	0.06	Ok	Ok	Ok	16.60
Roller pressure (Mpa)	500	22	0.35	0.06	Nok	Nok	Nok	16.34
	500	22	0.40	0.06	Ok	Nok	Nok	16.82
	500	22	0.45	0.06	Ok	Ok	Ok	17.27
	500	22	0.50	0.06	Ok	Ok	Ok	17.36
	500	22	0.55	0.06	Ok	Ok	Ok	17.66
Nozzle pressure (Mpa)	500	22	0.45	0.04	Ok	Nok	Nok	15.77
	500	22	0.45	0.05	Ok	Nok	Nok	18.23
	500	22	0.45	0.06	Ok	Ok	Ok	17.68
	500	22	0.45	0.07	Ok	Ok	Ok	17.34
	500	22	0.45	0.08	Ok	Ok	Ok	17.56

Table 13.6 ANOVA analysis results on the effect of air temperature factors to the adhesive strength of the seam sealing

Source of variation	SS	df	MS	*F*	*P*-value	*F* crit
Between groups	37.04967	4	9.262417	12.03401	0.000774	3.47805
Within groups	7.696867	10	0.769687	–	–	–
Total	44.74653	14	–	–	–	–

Table 13.7 ANOVA analysis results on speed factors to the adhesive strength of the sealing seam

Source of variation	SS	df	MS	*F*	*P*-value	*F* crit
Between groups	80.47929	4	20.11982	38.30272	1.05E−07	3.055568
Within groups	7.879267	15	0.525284	–	–	–
Total	88.35856	19	–	–	–	–

(i) $F = 12.03401 > F\text{th} = 3.47805$, i.e. air temperature affects the adhesive strength of the sealing seam with approximately 100% reliability;
(ii) the effect of the air temperature on the adhesive strength according to the rule of quartic equation: $y = -6E - 05x^4 + 0.1115x^3 - 81.454x^2 + 26434x - 3E + 06$; $R^2 = 1$.

13.3.2.1 Effect of Sealing Speed on Adhesive Strength of the Sealing Seam

Results of surveying the adhesive strength of seams on waterproofing fabrics in research of the individual effect of sealing speed are presented in Table 13.5.

Using Microsoft Excel 2013 software, we conducted ANOVA variance analysis to assess the influence of the sealing speed on the adhesive strength of the sealing seam. Results are presented in Table 13.6.

ANOVA analysis results in Table 13.7.

(i) $F = 38.30272 > F\text{th} = 3.055568$, i.e. sealing speed affects on the adhesive strength of the sealing seam with approximately 99% reliability;
(ii) the effect of sealing speed on the adhesive strength according to the rule of cubic equation:
$y = 0.675x^3 - 39.75x^2 + 776.95x - 5024.9$; $R^2 = 0.9936$.

13.3.2.2 Effect of Roller Pressure Force on Adhesive Strength of the Sealing Seam

Results of surveying the adhesive strength of seams on waterproofing fabrics in the study of the individual effect of roller pressure are presented in Table 13.5.

Table 13.8 ANOVA analysis results on the effect of roller pressure factors to the adhesive strength of the sealing seam

Source of variation	SS	df	MS	*F*	*P*-value	*F* crit
Between groups	4.229778	4	1.057444	2.081074	0.134146	3.055568
Within groups	7.621867	15	0.508124	–	–	–
Total	11.85164	19	–	–	–	–

We use Microsoft Excel 2013 software to conduct ANOVA variance analysis to evaluate the impact of roller pressure on the adhesive strength of the sealing seam. Results are presented in Table 13.8.

ANOVA analysis results in Table 13.8:

(i) $F = 2.081074 < F\text{th} = 3.055568$, i.e. the roller pressure has little effect on the adhesive strength of the sealing seam with approximately 98% reliability.
(ii) the influence of roller pressure on the adhesive strength of the sealing seam follows the quadratic equation: $y = -20.476x^2 + 24.769x + 10.193$; $R^2 = 0.985$.

13.3.2.3 Influence of Nozzle Pressure on Adhesive Strength of the Sealing Seam

Results of surveying the adhesive strength of seams on waterproofing fabrics in the study of the individual effect of nozzle pressure are presented in Table 13.5.

We use Microsoft Excel 2013 software to conduct ANOVA variance analysis to evaluate the impact of nozzle pressure on the adhesive strength of the sealing seam. Results are presented in Table 13.9.

ANOVA analysis results in Table 13.8 show:

(i) $F_A = 31.01385 > F\text{th} = 4.351244$, i.e. the nozzle pressure affects on the adhesive strength of the sealing seam with approximately 98% reliability;
(ii) the effects of the nozzle pressure on the adhesive strength according to the rules of cubic equation: $y = 170131x^3 - 30501x^2 + 1740.9x - 13.567$; $R^2 = 0.9847$.

Table 13.9 ANOVA analysis results on the effect of nozzle pressure factors to the adhesive strength of the sealing seam

Source of variation	SS	df	MS	*F*	*P*-value	*F* crit
Between groups	13.64165	4	3.410413	7.606191	0.001482	3.055568
Within groups	6.7256	15	0.448373	–	–	–
Total	20.36725	19	–	–	–	–

13.3.2.4 Simultaneous Effect of 4 Factors to the Adhesive Strength of the Sealing Seam

Design expert software is used in designing experiments, data processing and building experimental recurrent equation display the principal that 4 variables in researching influence on adhesive strength of the sealing seam. The adhesion strength equation is obtained after data processing (Table 13.10):

$$\begin{aligned} Y = {} & 17.05893 + 0.449013X_1 + 1.58392X_2 + 0.587240X_3 \\ & + 1.34350X_4 + 1.03725X_1X_2 + 0.72125\,X_1X_3 + 1.77517X_1X_4 \\ & + 0.32625X_2X_3 + 0.250263X_2X_4 - 0.15125X_3X_4 + 0.31357X_1^2 \\ & - 0.478929X_2^2 - 0.496429X_3^2 + 0.856071X_4^2 \end{aligned} \quad (13.1)$$

$R^2 = 0.9267$

X_1 is the air temperature; X_2 is the sealing speed; X_3 is the roller pressure and X_4 is the nozzle pressure.

Table 13.10 Summary of adhesive test results when changing 4 factors simultaneously

No.	x_1	x_2	x_3	x_4	Y			
					1st	2st	3st	Average
1	−1	−1	−1	−1	18.27	17.21	16.89	17.46
2	1	−1	−1	1	16.11	18.66	17.22	17.33
3	−1	1	−1	1	17.48	16.11	18.43	17.34
4	1	1	−1	−1	15.71	15.21	15.23	15.38
5	−1	−1	1	−1	17.12	17.12	16.34	16.86
6	1	1	1	−1	19.61	19.21	18.09	18.97
7	−1	1	1	1	16.89	17.43	18.01	17.44
8	1	−1	1	1	19.81	19.12	18.09	19.01
9	−1.41	0	0	0	17.60	16.34	15.89	16.61
10	1.41	0	0	0	18.62	17.12	17.89	17.88
11	0	−1.41	0	0	14.93	13.22	12.11	13.42
12	0	1.41	0	0	18.47	17.68	17.56	17.90
13	0	0	−1.41	0	15.13	14.21	15.11	14.82
14	0	0	1.41	0	17.25	15.72	16.32	16.43
15	0	0	0	−1.41	16.54	17.09	15.67	16.43
16	0	0	0	1.41	19.07	21.61	20.00	20.23
17	0	0	0	0	17.91	17.14	16.91	17.32
18	0	0	0	0	18.08	17.38	16.22	17.23
19	0	0	0	0	17.88	17.22	17.20	17.43
20	0	0	0	0	18.66	17.48	17.91	18.02

13.3.2.5 Comment

Considering the value of X_i ($i = 1 \div 4$) if we stand alone, then in the 4 coefficients (a_1, a_2, a_3, a_4) from (13.1), we see that the coefficient a_2 has the highest absolute value $|a_2| = 1.58392$, so the influence of X_2 or the sealing speed on adhesive strength is the greatest compared to the remaining variables X_1, X_3, X_4.

13.3.2.6 Analyze of the Effect of Each Factor on Adhesive Strength

Analyze the Effect of Air Temperature on Adhesive Strength

From (13.1) we have: $a_1X_1 = 0.449013X_1 \rightarrow a_1 = 0.449013 > 0 \rightarrow$ The variation of Y and X_1 is covariant. That is when $X_1\uparrow \rightarrow Y\uparrow$ and $X_1\downarrow \rightarrow Y\downarrow$. To increase adhesion strength (Y), it is necessary to increase (X_1), that is, increase the paste temperature. However, if the temperature is too high, it will lead to an unqualified fire.

Analyze the Effect of Sealing Speed on Adhesive Strength

From (13.1) we have: $a_2X_2 = 1.58392X_2 \rightarrow a_2 = 1.58392 > 0 \rightarrow$ The variation of Y and X_2 is covariant. That is when $X_2\uparrow \rightarrow Y\uparrow$ and $X_2\downarrow \rightarrow Y\downarrow$. To increase adhesion strength (Y), it is necessary to increase (X_2), that is, increase the speed of gluing. However, if the paste speed is too fast, the tape and fabric will not receive enough heat to bond.

Analysis of Effect of Roller Pressure on Adhesive Strength

From (13.1) we have: $a_3X_3 = 0.587240X_3 \rightarrow a_3 = 0.587240 > 0 \rightarrow$ The variation of Y and X_3 are covariant. That is when $X_3\uparrow \rightarrow Y\uparrow$ and $X_3\downarrow \rightarrow Y\downarrow$. To increase adhesion strength (Y), it is necessary to increase (X_3), that is, increase the roller compression force. However, if the compression pressure is too high, the glue in the tape will be exposed to the edge of the adhesive, affecting the aesthetics and quality of the seam.

Analysis of Effect of Nozzle Pressure on Adhesive Strength

From (13.1) we have: $a_4X_4 = 1.34350X_4 \rightarrow a_4 = 1.34350 > 0 \rightarrow$ The variation of Y and X_4 is covariant. That is when $X_4\uparrow \rightarrow Y\uparrow$ and $X_4\downarrow \rightarrow Y\downarrow$. To increase adhesion strength (Y), it is necessary to increase (X_4), that is, the wind pressure. However, if the increase in wind pressure is too high, it will cause unqualified fire.

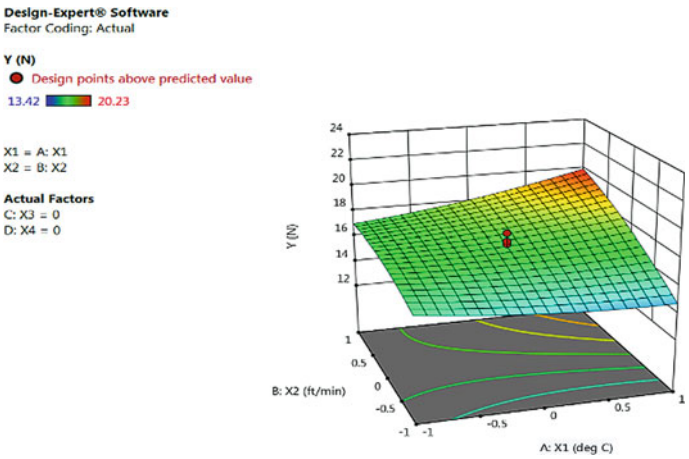

Fig. 13.2 3D graph showing the simultaneous effect of air temperature and sealing speed on adhesive strength

13.3.2.7 Analyze of the Interaction Effect of Technological Factors on Adhesive Strength

Interaction Effect Between Air Temperature and Sealing Speed on Adhesive Strength

From (13.1) we have: $a_{12}X_1X_2 = 1.03725X_1X_2 \rightarrow a_{12} = 1.03725 > 0 \rightarrow X_1X_2\uparrow \rightarrow Y\uparrow$ and $X_1X_2\downarrow \rightarrow Y\downarrow$. To increase adhesion strength (Y), X_1X_2 increases $\rightarrow X_1X_2 > 0$, then $X_1 > 0$ and $X_2 > 0$ or $X_1 < 0$ and $X_2 < 0$. Due to the fact that productions need to increase productivity, choose $X_1 > 0$ and $X_2 > 0$ and moreover, the quality is also focused, so it is necessary to select the sealing speed and air temperature to ensure high productivity and good adhesive quality (see Fig. 13.2).

Interaction Effect Between Air Temperature and Roller Pressure on Adhesive Strength

From (13.1) we have: $a_{13}X_1X_3 = 0.72125X_1X_3 \rightarrow a_{13} = 0.72125 > 0 \rightarrow X_1X_3\uparrow \rightarrow Y\uparrow$ and $X_1X_3\downarrow \rightarrow Y\downarrow$. In order to increase the adhesion strength (Y), the X_1X_3 decreases $\rightarrow X_1X_3 > 0$, then $X_1 > 0$ and $X_3 > 0$ or $X_1 < 0$ and $X_3 < 0$. This means that the variation of air temperature and roller pressure is uniform, It is necessary to adjust these parameters appropriately to achieve productivity and quality (see Fig. 13.3).

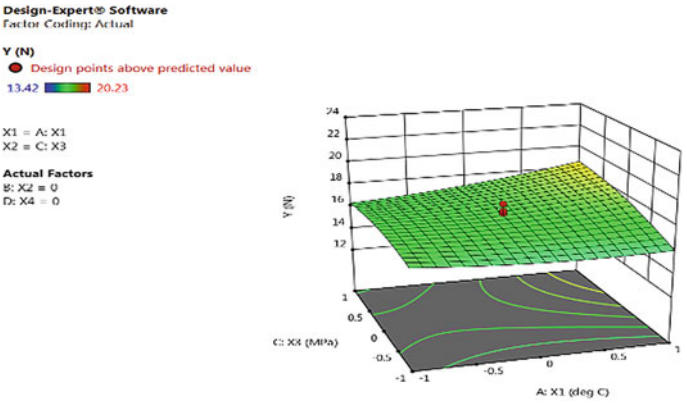

Fig. 13.3 3D graph showing the simultaneous effect of air temperature and roller pressure on adhesive strength

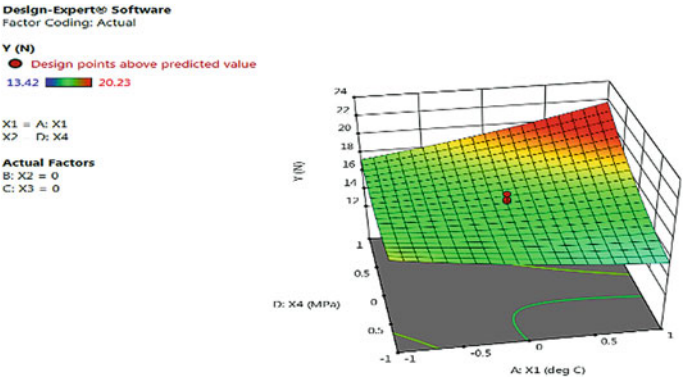

Fig. 13.4 3D graph showing the simultaneous effect of air temperature and the nozzle pressure on adhesive strength

Interaction Effect Between Air Temperature and Nozzle Pressure on Adhesive Strength

From (13.1) we have: $a_{14}X_1X_4 = 1.03725X_1X_4 \rightarrow a_{14} = 1.77517 > 0 \rightarrow X_1X_4\uparrow \rightarrow Y\uparrow$ and $X_1X_4\downarrow \rightarrow Y\downarrow$. To increase adhesion strength (Y), X_1X_2 increases $\rightarrow X_1X_4 > 0$, then $X_1 > 0$ and $X_4 > 0$ or $X_1 < 0$ and $X_4 < 0$. Due to the fact that production needs to increase productivity, choose $X_1 > 0$ and $X_4 > 0$ and moreover, the quality is also focused, so it is necessary to choose roller pressure and air temperature to ensure high productivity and good adhesive quality (see Fig. 13.4).

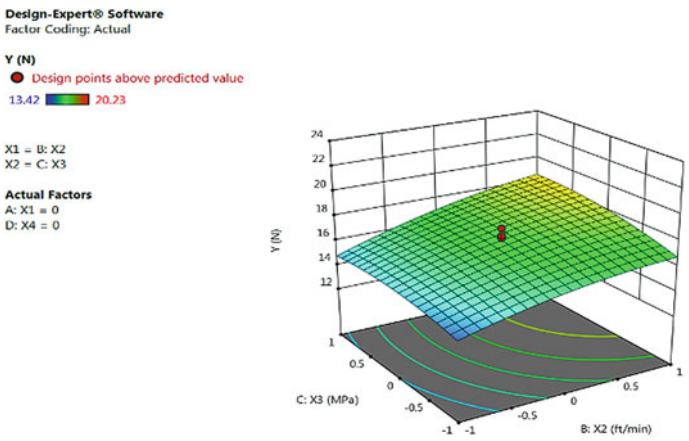

Fig. 13.5 3D graph showing the simultaneous effect of sealing speed and roller pressure on adhesive strength

Interaction Effect of Sealing Speed and Roller Pressure on Adhesive Strength

From (13.1) we have: $a_{23}X_2X_3 = 0.023625X_2X_3 \rightarrow a_{23} = 0.032625 > 0 \rightarrow X_2X_3\uparrow \rightarrow Y\uparrow$ and $X_2X_3\downarrow \rightarrow Y\downarrow$. To increase adhesion strength (Y), X_2X_3 increases $\rightarrow X_2X_3 > 0$, then $X_2 > 0$ and $X_3 > 0$ or $X_2 < 0$ and $X_3 < 0$. Due to the fact that production needs to increase productivity, choose $X_2 > 0$ and $X_3 > 0$ and moreover, the quality is also focused, so it is necessary to choose the sealing speed and roller pressure to ensure high productivity and good adhesive quality (see Fig. 13.5).

Effect of Interaction Between Sealing Speed and Nozzle Pressure on Adhesive Strength

From (13.1) we have: $a_{24}X_2X_4 = 0.250263X_2X_4 \rightarrow a_{24} = 0.250263 > 0 \rightarrow$ The variation of Y and X_2X_4 are covariant. That is when $X_2X_4\uparrow \rightarrow Y\uparrow$ and $X_2X_4\downarrow \rightarrow Y\downarrow$. To increase adhesion strength (Y), X_2X_4 increases $\rightarrow X_2X_4 > 0$, then $X_2 > 0$ and $X_4 > 0$ or $X_2 < 0$ and $X_4 < 0$. Due to the fact that production needs to increase productivity, choose $X_2 > 0$ and $X_4 > 0$ and moreover, the quality is also focused, so it is necessary to choose the paste speed and wind pressure to ensure high productivity and good adhesive quality (see Fig. 13.6).

Influence of Interaction Between Roller Pressure and Nozzle Pressure on Adhesive Strength

From (13.1) we have: $a_{34}X_3X_4 = -0.15125X_3X_4 \rightarrow a_{34} = -0.15125 < 0 \rightarrow$ The variation of Y and X_3X_4 is inversely. That is when $X_3X_4\uparrow \rightarrow Y\downarrow$ and $X_3X_4\downarrow \rightarrow$ Y$\uparrow$.

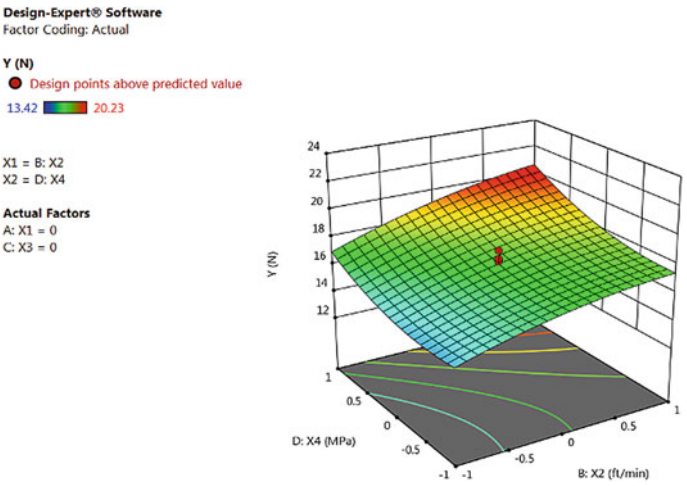

Fig. 13.6 3D graph showing the effect of sealing speed and nozzle pressure on adhesive strength

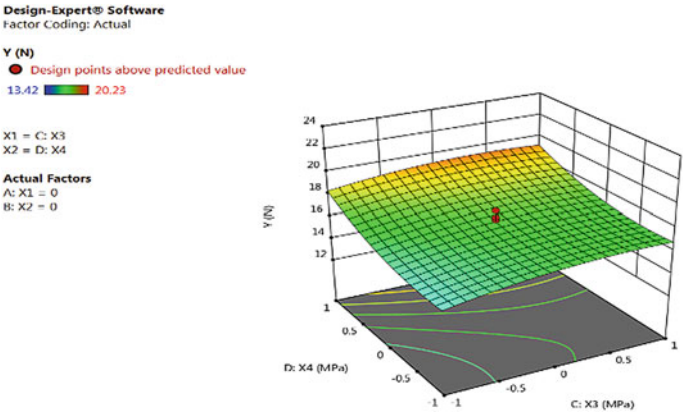

Fig. 13.7 3D graph showing the simultaneous effect of roller pressure and nozzle pressure on adhesive strength

To increase adhesion strength (Y), X_3X_4 decreases $\rightarrow$ $X_3X_4 < 0$, $X_3 > 0$ and $X_4 < 0$ or $X_3 < 0$ and $X_4 > 0$. This means the variability of roller compression and torch pressure are reversible variables. It is necessary to adjust these parameters reasonably to achieve productivity and quality (see Fig. 13.7).

13.3.2.8 Determining the Optimum Value of the Paste Technology Parameters Ensures the Adhesive Strength of the Surface of the Part Is the Largest

From the empirical regression equation expressing the law of the effect of 4 factors of gluing technology on the adhesive strength of the sealing seam in research, we conduct optimization of problems by Design Expert 11.0 software. Data processing results find an optimal solution:

(i) optimal value of variables (coded form): $X_1 = 0.912315$; $X_2 = 0.901385$; $X_3 = 0.764905$; $X_4 = 0.190739$;
(ii) the maximum value of the adhesive strength: $Y_{\max} = 21.1254$ (N).

From the calculation result for the coding variable, we can calculate the value of the real variable: $X_1 = 530$ (°C); $X_2 = 23$ (ft/min); $X_3 = 0.49$ (MPa); $X_4 = 0.06$ (MPa).

13.4 Conclusion

(1) We performed experimental exploration to evaluate the individual influence of some technological factors of taping machines such as: air temperature, sealing speed, roller pressure, and nozzle pressure to adhesive strength of the sealing seam on 2-layer waterproof fabrics, 100% PET base layers and coated with PU used for sewing sportswear at Song Cong 2 Garment Company branch of TNG Corporation. It has shown that there are three technology factors of a research tape machine: (i) the air temperature, (ii) the sealing speed, (iii) the nozzle pressure, which significantly affect on the adhesive strength; the roller pressure has influence but lesser extent.
(2) ANOVA analysis results show that the air temperature affects on the adhesion strength with a high confidence of approximately 100%:
$y = -6E - 05x^4 + 0.1115x^3 - 81.454x^2 + 26434x - 3E + 06$; $R^2 = 1$
(3) ANOVA analysis results show that the sealing speed affects on the adhesion strength with approximately 99% reliability:
$y = 0.675x^3 - 39.75x^2 + 776.95x - 5024.9$; $R^2 = 0.9936$
(4) ANOVA analysis results show that the roller pressure has little effect on the adhesion strength with approximately 98% reliability:
$y = -20.476x^2 + 24.769x + 10.193$; $R^2 = 0.985$
(5) ANOVA analysis results show that the nozzle pressure has little affects on the adhesion strength with approximately 98% reliability:
$y = 170131x^3 - 30501x^2 + 1740.9x - 13.567$; $R^2 = 0.9847$
(6) The adhesion strength equation is obtained after data processing:
$Y = 17.05893 + 0.449013X_1 + 1.58392X_2 + 0.587240X_3 + 1.34350X_4 + 1.03725X_1X_2 + 0.72125X_1X_3 + 1.77517X_1X_4 + 0.32625X_2X_3 + 0.250263X_2X_4 - 0{,}15125X_3X_4 + 0.31357X_1^2 - 0.478929X_2^2 - 0.496429X_3^2 + 0.856071X_4^2$

(7) Study on using 100% polyester woven fabric and PU coating, Bemis ST604 tape and the parameter as below:

- air temperature is 530°C; sealing speed is 23 ft/min; roller pressure is 0.49 MPa; nozzle pressure is 0.06 MPa;
- the highest value of the adhesive strength is 21.1254 N.

(8) The above results are useful guides in the actual production at Song Cong 2 Garment Company, helping technicians to adjust the optimal technology regime to ensure product quality stability, contributing to increasing the efficiency of high-class sports clothing products from waterproof fabrics productions.

References

1. *Seam Sealing Tape* (Bemis Associates Inc., Shirley, 2019)
2. *Decathlon Standard* (Decathlon, Ascq, 2019)
3. N. Van Lan, *Processing Statistical Data and Applied Examples in the Textile Industry.* (National University Press, Ho Chi Minh, 2003)
4. P.T. Thao, Building data-sheet of amendment to correct the optimal sealing technological regime for making high quality garment products from waterproof fabrics in the tropical seasonal climate of Vietnam, 2007–2008 (2008)
5. Parameter Document for 305122 Black (TNG Investment and Trading JSC, Thai Nguyen, 2019)
6. *ST604 Data Sheet* (Bemis Associates Inc., Shirley, 2019)
7. Test Report for ST604 305122 (Bemis Associates Inc., Shirley (2019)

Part II
Physics of Advanced Materials

Chapter 14
Equation for Density Matrix Systems of Identical Particles

Boris V. Bondarev

Abstract The equations for the statistical operator and the density matrix are considered here for a single particle and a system of identical particles when dissipative forces act on them. From the equation for the density matrix, a kinetic equation can be obtained when the density matrix is diagonal. These equations are the basis for the study of the simplest models of nanophysics.

14.1 Introduction

In quantum mechanics, the most general description of the system is the statistical operator $\hat{\varrho}$. The statistical operator must be normalized at any time

$$\mathrm{Tr}\,\hat{\varrho} = 1, \tag{1.1}$$

self-adjoint

$$\hat{\varrho}^* = \hat{\varrho} \tag{1.2}$$

and positively definite. A correct equation describing the evolution of a statistical operator must ensure that these properties are preserved over time.

For the first time the equation for the statistical operator:

$$\hat{\varrho} = \hat{\varrho}(t, q), \tag{1.3}$$

where q is the quantum coordinate of the system was obtained by Lindblad [1]. This equation has the form:

$$\mathrm{i}\,\hbar\dot{\hat{\varrho}} = [H\,\hat{\varrho}] + \mathrm{i}\hbar\hat{D}, \tag{1.4}$$

B. V. Bondarev (✉)
Moscow Aviation Institute, Moscow, Russia
e-mail: bondarev.b@mail.ru

I. A. Parinov et al. (eds.), *Advanced Materials*, Springer Proceedings in Materials 6, https://doi.org/10.1007/978-3-030-45120-2_14

where $\hat{H}$ is the Hamiltonian of the system,

$$\hat{D} = \sum_{jk} C_{jk}\{[\hat{a}_j\hat{\varrho}, \hat{a}_k^+] + [\hat{a}_j, \hat{\varrho}\hat{a}_k^+]\}, \tag{1.5}$$

C_{jk} are some numbers, and $\hat{a}_j$ is an arbitrary operator. The operator $\hat{D}$ is called the dissipative operator. This statement can be written as

$$\hat{D} = \sum_{jk} C_{jk}\{2\hat{a}_j\hat{\varrho}\hat{a}_k^+ - \hat{a}_k^+\hat{a}_j\hat{\varrho} - \hat{\varrho}\hat{a}_k^+\hat{a}_j\}. \tag{1.6}$$

14.2 Equation for the Density Matrix of One Particle

The density matrix is related to the operator $\hat{\varrho}\ (t, q)$ formula

$$\varrho_{nn'}(t) = \int \varphi_n^*(t, q)\hat{\varrho}(t, q)\varphi_{n'}(t, q)\mathrm{d}q. \tag{2.1}$$

This formula specifies the density matrix $\varrho_{nn'}(t)$ in the n-representation. Wave function $\varphi_n(t,q)$ can be found from the Schrödinger equation:

$$\mathrm{i}\,\hbar\dot{\varphi}_n = \hat{H}\varphi_n. \tag{2.2}$$

The equation for the density matrix was derived from the Liouville–Von Neumann equation in [2, 3]. This equation is analogous to the Lindblad equation and has the form:

$$\begin{aligned}\mathrm{i}\,\hbar\dot{\varrho}_{nn'} &= \sum_m (H_{nm}\varrho_{mn'} - \varrho_{nm}H_{mn'}) \\ &+ \mathrm{i}\,\hbar\{\sum_{mm'}\gamma_{nm,m'n'}\varrho_{mm'} - 1/2\sum_m(\gamma_{nm}\varrho_{mn'} + \varrho_{nm}\gamma_{mn'})\},\end{aligned} \tag{2.3}$$

where H_{nm} are the matrix elements of the Hamiltonian $\hat{H}$ system, $\gamma_{nm,m'n'}$ is some matrix,

$$\gamma_{nn'} = \sum_m \gamma_{mn'nm}. \tag{2.4}$$

Equation (2.3) can be written as

$$\mathrm{i}\hbar\dot{\varrho}_{nn'} = \sum_m (H_{nm}\varrho_{mn'} - \varrho_{nm}H_{mn'}) + \mathrm{i}\hbar D_{nn'}, \tag{2.5}$$

where $D_{nn'}$ is a dissipative matrix, which will now be equal to

$$D_{nn'} = \sum_{mm'} \gamma_{nm,m'n'} \varrho_{mm'} - 1/2 \sum_{m} (\gamma_{nm} \varrho_{mn'} + \varrho_{nm} \gamma_{mn'}). \tag{2.6}$$

Compare this formula with the formula (1.6), we establish that

$$\gamma_{nm,m'n'} = 2 \sum_{jk} C_{jk} a_{nm,j} a^{+}_{m'n',k}, \tag{2.7}$$

where $a_{nm,j}$ are matrix elements of the operator $\hat{a}_j$.

The diagonal element $\varrho_{nn'}$ is the probability w_n that the system is in the state n. This value satisfies the normalization condition:

$$\sum_{n} \varrho_{nn} = 1. \tag{2.8}$$

This formula is similar to the formula (1.1).

In addition, the density matrix ϱ_{nm} satisfies the following condition:

$$\varrho^{*}_{nm} = \varrho_{mn}. \tag{2.9}$$

The same condition is subject to Hamiltonian:

$$H^{*}_{nm} = H_{mn}. \tag{2.10}$$

Consider the system where the density matrix ϱ_{nm} at an arbitrary time t is in the diagonal state:

$$\varrho_{nm} = w_n \delta_{nm}, \tag{2.11}$$

where δ_{nm} is the Kronecker symbol. Then from (3.3) we obtain

$$\dot{w}_n = \sum_{m} (p_{nm} w_m - p_{mn} w_n), \tag{2.12}$$

where

$$p_{nm} = \gamma_{nm,mn} = 2\pi/\hbar \sum_{NM} \left| \upsilon_{nN,mM} \right|^2 W_M \delta(\varepsilon_n - \varepsilon_m + E_N - E_M), \tag{2.13}$$

there is a probability of transition of the system in a unit of time from the state m to the state n,

$$W_N = v \exp(-\beta E_N)$$

there is a possibility that the environment is in an equilibrium state with quantum numbers N, and E_N is its energy in this state, ν is the normalization factor, $\beta = 1/(k_B T)$ is the inverse temperature; $\upsilon_{nN,mM}$ are the matrix elements of the system interaction with its environment. Formula (2.13) is the *Golden rule of Fermi*.

14.3 The Hierarchy for the Statistical Operators

Consider a system consisting of N identical particles. The statistical operator $\hat{\varrho}$ describing the state of such a system can be written as

$$\hat{\varrho} = \hat{\varrho}(t, q_1, q_2, \ldots, q_N) \equiv \hat{\varrho}(1, 2, \ldots, N. \tag{3.1}$$

Here, the numbers in parentheses indicate the indices of the variables that are affected by this operator. The statistical operator, as well as any other operator describing the state of the system of identical particles, must be symmetric:

$$\hat{\varrho}(\ldots, i, \ldots, j, \ldots) = \hat{\varrho}(\ldots, j, \ldots, i, \ldots). \tag{3.2}$$

We take the following normalization condition for the statistical operator:

$$\mathrm{Tr}_{1\ldots N}\hat{\varrho}(1, 2, \ldots, N) = N!. \tag{3.3}$$

The Hamilton operator for the system of identical particles can be represented as a sum

$$\hat{H}(1, 2, \ldots, N) = \sum_{i=1}^{N} \hat{H}(i) + 1/2 \sum_{i=1, j=1, j\neq i}^{N} \hat{H}(i, j) \tag{3.4}$$

where $\hat{H}(i)$ is a single-particle Hamiltonian, i.e. the energy operator of one particle without taking into account its interaction with other particles; $\hat{H}(i, j)$ is the interaction operator of two particles. A single-particle Hamiltonian may contain dissipative terms. The two-particle Hamiltonian must be symmetric:

$$\hat{H}(i, j) = \hat{H}(j, i). \tag{3.5}$$

Under this condition, the Hamiltonian (3.4) will also be symmetric.

Let us temporarily omit the summation operation in the expression (1.5) and write it as follows:

$$\hat{D} = \left[\hat{a}\hat{\varrho}, \hat{a}^{+}\right] + \left[\hat{a}, \hat{\varrho}\hat{a}^{+}\right]. \tag{3.6}$$

Suppose that the dissipative processes occurring in the system are due to the stochastic interaction of particles with the heat reservoir. Each particle interacts with it independently of other particles. In this case, the multi-particle operator a in the expression (3.6) can be represented as a sum:

$$\hat{a} = \hat{a}(1, \ldots, N) = \sum_{i=1}^{N} \hat{a}(i), \tag{3.7}$$

where operator $\hat{a}(i)$ characterizes the effect of the heat reservoir on one of the particles. Substituting this sum into the expression (3.6) gives

$$\hat{D} = \sum_{i=1}^{N} \sum_{j=1}^{N} \left\{ \left[\hat{a}(i)\hat{\varrho}, \hat{a}^{+}(j) \right] + \left[\hat{a}(i), \hat{\varrho}\hat{a}^{+}(j) \right] \right\}. \tag{3.8}$$

Of practical interest is the equation for the single-particle statistical operator $\hat{\varrho}(1)$, which is determined by the ratio:

$$\hat{\varrho}(1) = 1/(N-1)! \mathrm{Tr}_{2\ldots N} \hat{\varrho}(1, 2, \ldots, N). \tag{3.9}$$

From this definition, condition (3.3) implies the normalization condition for the

$$\mathrm{Tr}_1 \hat{\varrho}(1) = N. \tag{3.10}$$

We define a two-particle statistical operator $\hat{\varrho}(1, 2)$ as

$$\hat{\varrho}(1, 2) = 1/(N-2)! \mathrm{Tr}_{3\ldots N} \hat{\varrho}(1, 2, \ldots, N). \tag{3.11}$$

This operator satisfies the normalization condition:

$$\mathrm{Tr}_{12} \hat{\varrho}(1, 2) = N(N-1).$$

14.4 The Equation for the Statistical Operators

We assume that (1.4) is true for the operator (3.1). To obtain the equation for the derivative of the one-particle operator $\hat{\varrho}(1)$, we apply to both parts of (1.4) the convolution operation $\mathrm{Tr}_{2\ldots N}$. Since

$$\mathrm{Tr}_i [\hat{H}(i) \hat{\varrho}(1, 2, \ldots, N)] \equiv 0,$$

using the definition (3.9), we obtain:

$$\mathrm{Tr}_{2\ldots N}\sum_{i=1}^{N}[\hat{H}(i)\hat{\varrho}(1,2,\ldots,N)] = (N-1)![\hat{H}(1)\hat{\varrho}(1)].$$

By virtue of identity:

$$\mathrm{Tr}_{ij}[\hat{H}(i,j)\hat{\varrho}(1,2,\ldots,N)] \equiv 0,$$

taking into account the property (3.5) and the definition (3.11), we will have

$$\begin{aligned}
&\mathrm{Tr}_{2\ldots N}1/2\sum_{i=1,j=1,j\neq i}^{N}[\hat{H}(i,j)\hat{\varrho}(1,2,\ldots,N)]\\
&= 1/2\mathrm{Tr}_{2\ldots N}\left\{\sum_{i=1,j=2,j\neq i}^{N}[\hat{H}(1,j)\hat{\varrho}(1,2,\ldots,N)]\right.\\
&\quad\left.+\sum_{i=2,j=2,j\neq i}^{N}[\hat{H}(1,j)\hat{\varrho}(1,2,\ldots,N)]\right\}\\
&= 1/2(N-1)!\mathrm{Tr}_2[\hat{H}(1,2)\hat{\varrho}(1,2)].
\end{aligned}$$

Likewise

$$\begin{aligned}
\mathrm{Tr}_{2\ldots N}\hat{D} &= \mathrm{Tr}_{2\ldots N}\{[\hat{a}(1)\hat{\varrho},\hat{a}^{+}(1)]+[\hat{a}(1),\hat{\varrho}\hat{a}^{+}(1)]\\
&\quad+\sum_{i=2}^{N}([\hat{a}(i)\hat{\varrho},\hat{a}^{+}(1)]+[\hat{a}(i),\hat{\varrho}\hat{a}^{+}(1)]\\
&\quad+[\hat{a}(1)\hat{\varrho},\hat{a}^{+}(i)]+[\hat{a}(1),\hat{\varrho}\hat{a}^{+}(i)])\\
&\quad+\sum_{i=2}^{N}\sum_{j=2}^{N}([\hat{a}(i)\hat{\varrho},\hat{a}^{+}(j)]+[\hat{a}(i),\hat{\varrho}\hat{a}^{+}(j)])\}\\
&= (N-1)!\{[\hat{a}(1)\hat{\varrho}(1),\hat{a}^{+}(1)]+[\hat{a}(1),\hat{\varrho}(1)\hat{a}^{+}(1)]\\
&\quad+[\mathrm{Tr}_2\hat{a}(2)\hat{\varrho}(1,2),\hat{a}^{+}(1)]+[\hat{a}(1),\mathrm{Tr}_2\hat{\varrho}(1,2)\hat{a}^{+}(2)]\},
\end{aligned}$$

since

$$\mathrm{Tr}_i\left[\hat{a}(i),\hat{\varrho}\hat{a}^{+}(j)\right]\equiv 0,\quad \mathrm{Tr}_j\left[\hat{a}(i)\hat{\varrho},\hat{a}^{+}(j)\right]\equiv 0.$$

Having collected together the expressions, we come to the equation:

$$\begin{aligned}
i\hbar\dot{\hat{\varrho}}(1) &= [\hat{H}(1)\hat{\varrho}(1)]+1/2\mathrm{Tr}_2[\hat{H}(1,2)\hat{\varrho}(1,2)]\\
&\quad+i\hbar\{[\hat{a}(1)\hat{\varrho}(1),\hat{a}^{+}(1)]+[\hat{a}(1),\hat{\varrho}(1)\hat{a}^{+}(1)]\\
&\quad+[\mathrm{Tr}_2\hat{a}(2)\hat{\varrho}(1,2),\hat{a}^{+}(1)]+[\hat{a}(1),\mathrm{Tr}_2\hat{\varrho}(1,2)\hat{a}^{+}(2)]\}. \qquad (4.1)
\end{aligned}$$

14.5 The Equation for the Density Matrix

We denote the matrix elements of operators $\hat{\varrho}(1)$, $\hat{\varrho}(1,2)$, $\hat{H}(1)$, $\hat{H}(1,2)$ and $\hat{a}(1)$ in a certain n-representation as

$$\begin{aligned}
&\varrho_{n_1 n_1'} = \varrho_{11'}, \quad \varrho_{n_1 n_2, n_1' n_2'} = \varrho_{12,1'2'},\\
&H_{n_1 n_1'} = H_{11'}, \quad H_{n_1 n_2, n_1' n_2'} = H_{12,1'2'},\\
&a_{n_1 n_1'} = a_{11'},
\end{aligned}$$

and write (4.1) in matrix form:

$$\begin{aligned}
\mathrm{i}\hbar\dot{\varrho}_{11'} = &\sum_{n_2}[H_{12}\varrho_{21'}] + 1/2\sum_{n_2 n_3 n_4}[H_{12,34}\varrho_{43,21'}]\\
&+ \mathrm{i}\hbar\{\sum_{n_2 n_3}([a_{12}\varrho_{23}, a^{+}_{31'}] + [a_{12}, \varrho_{23}a^{+}_{31'}])\\
&+ \sum_{n_2 n_3 n_4}([a_{34}\varrho_{43,12}, a^{+}_{21'}] + [a_{12}, \varrho_{21',34}a^{+}_{43}])\}. \qquad (5.1)
\end{aligned}$$

The two-particle density matrix $\varrho_{12,1'2'}$, describing the state of the boson system must be symmetric. Whereas the two-particle density matrix of the fermion system must be antisymmetric. Approximately this matrix can be expressed through a single-particle density matrix as follows:

$$\varrho_{12,1'2'} = \varrho_{11'}\varrho_{22'} \pm \varrho_{12'}\varrho_{21'}, \qquad (5.2)$$

where the plus sign corresponds to bosons and the minus sign corresponds to fermions. Swap the first two variables and the second two in this formula and get

$$\varrho_{21,2'1'} = \varrho_{22'}\varrho_{11'} \pm \varrho_{21'}\varrho_{12'}. \qquad (5.3)$$

It is seen that these two-particle density matrices are symmetric:

$$\varrho_{12,1'2'} = \varrho_{21,2'1'}. \qquad (5.4)$$

Substitute the expression (5.2) in (5.1). We come to the equation for a single-particle density matrix:

$$\begin{aligned}
\mathrm{i}\hbar\dot{\varrho}_{11'} = &\sum_{n_2}[H_{12}\varrho_{21'}]\\
&+ 1/2\sum_{n_2 n_3 n_4}[H_{12,34}(\varrho_{42}\varrho_{31'} \pm \varrho_{41'}\varrho_{32})]
\end{aligned}$$

$$+ \mathrm{i}\hbar\{\sum_{n_2 n_3}([a_{12}\,\varrho_{23}, a^{+}_{31'}] + [a_{12}, \varrho_{23} a^{+}_{31'}])$$
$$+ \sum_{n_2 n_3 n_4}([a_{34}(\varrho_{41}\,\varrho_{32} \pm \varrho_{42}\,\varrho_{31}), a^{+}_{21'}]$$
$$+ [a_{12}, (\varrho_{23}\,\varrho_{1'4} \pm \varrho_{24}\,\varrho_{1'3}) a^{+}_{43}])\}. \tag{5.5}$$

Two-part matrix $H_{12,1'2'}$ the fermions are anti-symmetric, i.e. it satisfies the relations:

$$H_{12,1'2'} = -H_{21,1'2'} = -H_{12,2'1'} = H_{21,2'1'}. \tag{5.6}$$

For bosons, this matrix is symmetric:

$$H_{12,1'2'} = H_{21,1'2'} = H_{12,2'1'} = H_{21,2'1'}. \tag{5.7}$$

We transform the summand with a two-particle Hamiltonian:

$$\sum_{n_2 n_3 n_4}([H_{12,34}(\varrho_{42}\,\varrho_{31'} \pm \varrho_{41'}\,\varrho_{32})]$$
$$= \sum_{n_2 n_3 n_4}([H_{12,34}, \varrho_{42}\varrho_{31'}] \pm [H_{12,34}, \varrho_{41'}\varrho_{32}]).$$

Swap the indexes n_3 and n_4 in the second part of this equation. We will have

$$\sum_{n_2 n_3 n_4}([H_{12,34}(\varrho_{42}\,\varrho_{31'} \pm \varrho_{41'}\varrho_{32})]$$
$$= \sum_{n_2 n_3 n_4}([H_{12,34}, \varrho_{42}\,\varrho_{31'}] \pm [H_{12,43}, \varrho_{31'}\varrho_{42}])$$
$$= \sum_{n_2 n_3 n_4}[(H_{12,34} \pm H_{12,43}), \varrho_{42}\,\varrho_{31'}]$$
$$= 2\sum_{n_2 n_3 n_4}[H_{12,34}, \varrho_{42}\,\varrho_{31'}].$$

This equality is true by virtue of the formulas (5.6) and (5.7).
Enter the symbol:

$$\gamma_{12,31'} = 2a_{12}\,a^{+}_{31'}, \tag{5.8}$$

Write (5.5) with this notation [4, 5]:

$$\mathrm{i}\hbar\dot{\varrho}_{11'} = \sum_{n_2}[H_{12}\,\varrho_{21'}] + \sum_{n_2 n_3 n_4}[H_{12,34}, \varrho_{42}\,\varrho_{31'}]$$

$$
\begin{aligned}
&+ \mathrm{i}\,\hbar/2 \sum_{n_2 n_3} (2\gamma_{12,31'}\varrho_{23} - \gamma_{23,12}\varrho_{31'} - \gamma_{31',23}\varrho_{12}) \\
&+ \sum_{n_2 n_3 n_4} \{(\varrho_{14}\,\varrho_{23} \pm \varrho_{24}\varrho_{13})\gamma_{34,21'} \\
&- \gamma_{34,12}(\varrho_{24}\,\varrho_{1'3} \pm \varrho_{1'4}\varrho_{23}) + \gamma_{12,43}(\varrho_{32}\,\varrho_{41'} \pm \varrho_{42}\varrho_{31'}) \\
&- (\varrho_{31}\,\varrho_{42} \pm \varrho_{41}\,\varrho_{32})\gamma_{21',43}\}. \qquad (5.9)
\end{aligned}
$$

This is the desired equation for the density matrix.

14.6 Kinetic Equation

Substitute the diagonal matrix (2.11) in (5.9):

$$\varrho_{12} = w_1\,\delta_{12}. \qquad (6.1)$$

We will have after we put $n_2 = n_1$, the following equation:

$$
\begin{aligned}
\partial w_1/\partial t = &\sum_{n_2} (\gamma_{12,21} w_2 - \gamma_{21,12} w_1) \\
&+ 1/2 \sum_{n_2} w_1\, w_2 \{\gamma_{21,21} \pm \gamma_{12,21} - (\gamma_{12,12} \pm \gamma_{21,12}) \\
&+ \gamma_{12,12} \pm \gamma_{12,21} - (\gamma_{21,21} \pm \gamma_{21,12})\}.
\end{aligned}
$$

Reducing the terms containing elements of the matrix $\gamma_{12,12}$ and $\gamma_{21,21}$, we obtain the kinetic equation:

$$\partial w_1/\partial t = \sum_{n_2} \{\gamma_{12,21} w_2 (1 \pm w_1) - \gamma_{21,12} w_1 (1 \pm w_2)\}. \qquad (6.2)$$

Substitution of formula (2.13) in

$$p_{12} = \gamma_{12,21}, \qquad (6.3)$$

results that (6.2) can be written as

$$\partial w_1/\partial t = \sum_{n_2} \{p_{12} w_2 (1 \pm w_1) - p_{21}\, w_1 (1 \pm w_2)\}. \qquad (6.4)$$

where p_{12} is the probability of transition of a particle per unit time from the state n_2 to the state n_1.

14.7 The Energy of the System of Identical Particles Unitary Matrix

We write a known expression for the average energy of the particle system:

$$E = \sum_{n_1 n_2} H_{12} \varrho_{21} + 1/2 \sum_{\{n\}} H_{12,34}\, \varrho_{34,12}, \tag{7.1}$$

where $\{n\} = n_1, n_2, n_3, n_4$.

Let a κ-representation of the density matrix will be diagonal, i.e., has the form:

$$\tilde{\varrho}_{\kappa\kappa'} = w_\kappa\, \delta_{\kappa\kappa'}, \tag{7.2}$$

$$\tilde{\varrho}_{\kappa_1\kappa_2,\kappa_1'\kappa_2'} \equiv \tilde{\varrho}_{12,1'2'} = w_{12}^{(11)}(\delta_{11'}\, \delta_{22'} \pm \delta_{12'}\, \delta_{21'}). \tag{7.3}$$

where probabilities w_κ and $w_{12}^{(11)}$ satisfy the conditions:

$$\sum_\kappa w_\kappa = N, \quad \sum_{\kappa_1\kappa_2 \neq \kappa_1} w_{12}^{(11)} = N(N-1). \tag{7.4}$$

The probability $w_{12}^{(11)}$ determines that both of the condition of κ_1 and $\kappa_2 \neq \kappa_1$ occupied by particles.

The transition from the n-representation to the κ-representation is carried out using the unitary matrix $U_{n\kappa}$, which is determined by the relation:

$$\sum_n U_{n\kappa}\, U_{n\kappa'}^* = \delta_{\kappa\kappa'}. \tag{7.5}$$

If the unitary matrix is known, then the density matrix in the κ-representation is found by the formula:

$$\tilde{\varrho}_{\kappa\kappa'} = \sum_{nn'} U_{n\kappa}\, \varrho_{nn'}\, U_{n'\kappa'}^*. \tag{7.6}$$

Since the expression (7.1) in any representation has the same form, substituting the expression (7.2) and (7.3) in this formula will give

$$E = \sum_\kappa \varepsilon_\kappa w_\kappa + 1/2 \sum_{\kappa_1\kappa_2 \neq \kappa_1} \varepsilon_{12} w_{12}^{(11)}, \tag{7.7}$$

where

$$\varepsilon_\kappa = \sum_{nn'} U_{n\kappa}^* H_{nn'} U_{n'\kappa} \tag{7.8}$$

is the energy of a particle in a state κ,

$$\varepsilon_{12} = 2 \sum_{\{n\}} U^*_{1\kappa_1} U^*_{2\kappa_2} H_{12,34} U_{3\kappa_1} U_{4\kappa_2} \tag{7.9}$$

is the interaction energy of two particles, one of which is in the state κ_1, and the other is in the state κ_2.

14.8 Variational Principle

In thermodynamics, the variational principle was developed, which along with the quantum (5.7) leads to the same results. Only now we are talking about systems of particles in the state of thermodynamic equilibrium. That is why now in a few words we will talk on the variation principle.

The thermodynamic potential Ω of the particle system is related to the average internal energy E, entropy S, absolute temperature T, chemical potential μ and the average number of particles N:

$$\Omega = E - S\,T - \mu N. \tag{8.1}$$

The function $y = y(x)$ describing the equilibrium state of the system can be found by the Lagrange method. To do this, the thermodynamic potential should be expressed through this function $\Omega = \Omega(y)$, differentiated by this function and to equate the derivative with zero:

$$\partial\Omega/\partial y = 0. \tag{8.2}$$

As a result, we obtain the equations for the equilibrium function.

With energy, almost everything is clear from the previous section, but it is not clear why we started talking about the unitary matrix. The fact is that entropy can be written only for the density matrix in the diagonal form (7.2). For example, the entropy of the fermion system in the first approximation, when the binary probability

$$w^{(11)}_{12} = w_1\, w_2 \tag{8.3}$$

for $\kappa_1 \neq \kappa_2$, equal to

$$S = -k_{\mathrm{B}} \sum_{\kappa} \{(1 - w_\kappa) \ln(1 - w_\kappa) + w_\kappa \ln w_\kappa\}. \tag{8.4}$$

In the first approximation, the energy of the fermions is

$$E = \sum_{\kappa} \varepsilon_{\kappa} w_{\kappa} + 1/2 \sum_{\kappa_1 \kappa_{2 \neq \kappa_1}} \varepsilon_{12} w_1 w_2 \tag{8.5}$$

provided that $\varepsilon_{11} = 0$.

Now that we know the thermodynamic potential as a function of w_{κ}, we will find the derivative of it. As a result, we get [6]:

$$w_{\kappa} = 1/\left\{1 + \mathrm{e}^{\beta(\overline{\varepsilon_{\kappa}} - \mu)}\right\}, \tag{8.6}$$

where

$$\overline{\varepsilon_{\kappa}} = \varepsilon_{\kappa} + \sum_{\kappa'} \varepsilon_{\kappa\kappa'} w_{\kappa'} \tag{8.7}$$

is the average energy of one fermion in the state κ.

14.9 Correlation Function

The variational principle allows us to find not only the probability w_{κ}, but also the binary probability $w_{12}^{(11)}$. To do this, we introduce the so-called correlation function $\xi_{\kappa\kappa'}$ using the ratio

$$w_{\kappa\kappa'}^{(11)} = w_{\kappa} w_{\kappa'} (1 - \delta_{\kappa\kappa'}) + \xi_{\kappa\kappa'}. \tag{9.1}$$

14.10 The Probability of Transition of a Particle

The probability of transition p_{12} particles from the state of κ_2 to the state κ_1, according to the Fermi rule (2.13) must depend on the difference $\overline{\varepsilon_1} - \overline{\varepsilon_2}$ medium energy particles in these states. As it is known, the thermodynamic equilibrium of a particle system obeys the Boltzmann rule. Thus, the probability of transition of a particle in equilibrium can always be represented as

$$p_{12} = p_{12}^{(\mathrm{o})} \mathrm{e}^{-\beta(\overline{\varepsilon_1} - \overline{\varepsilon_2})/2}, \tag{10.1}$$

where

$$p_{12}^{(\mathrm{o})} = p_{21}^{(\mathrm{o})},$$

$\overline{\varepsilon_i}$ is the average energy of particles in a state of κ_i.

Let the system of particles come to a state of thermodynamic equilibrium. Since the probability w_κ is now time-independent, the right side of (6.4) is zero. Thus, the principle of detailed equilibrium in this case is expressed by the equality:

$$p_{12}\, w_2(1 \pm w_1) = p_{21}\, w_1(1 \pm w_2) \tag{10.2}$$

Substituting the expression (10.1) into this equation, after simple transformations, we obtain

$$(1 \pm w_1)/w_1\, \mathrm{e}^{-\beta\overline{\varepsilon_1}} = (1 \pm w_2)/w_2\, \mathrm{e}^{-\beta\overline{\varepsilon_2}}, \tag{10.3}$$

where the left part depends on κ_1, and the right on κ_2. This is possible only if both parts of the equality are equal to the same constant value. We denote this value as $\mathrm{e}^{-\beta\mu}$, where μ is the chemical potential. Come to the equation:

$$(1 \pm w)/w = \mathrm{e}^{\beta(\bar{\varepsilon}-\mu)}, \tag{10.4}$$

in which the average energy of the particle $\bar{\varepsilon}$ according to the formula (8.7) is a functional depending on the distribution function w. Only knowing the dependence of the energy $\bar{\varepsilon}$ on the probability w, it is possible to find the distribution of particles by states.

For equilibrium systems of non-interacting particles, (10.4) leads to Fermi–Dirac or Bose–Einstein functions:

$$w = 1/\left[1 \pm \mathrm{e}^{\beta(\varepsilon-\mu)}\right], \tag{10.5}$$

where the energy ε is the eigenvalue of a single-particle Hamiltonian.

14.11 Conclusion

Equation (5.9) given here gives an opportunity to use it to describe the motion of identical particles in various problems of nanophysics. It should be noted that the presence of a dissipative term in this equation leads this equation to a kinetic equation for the probability.

References

1. G. Lindblad, Commun. Math. Phys. **48**, 119–130 (1976)
2. B.V. Bondarev, Theor. Math. Phys. **100**, 33–43 (1994)
3. B.V. Bondarev. *The Method of Density Matrices in the Quantum Theory of Cooperative Phenomena*, 2nd edn. (Sputnik+, Moscow, 2013), p. 621 (in Russian)
4. B.V. Bondarev, Phys. A **176**, 366–386 (1991)

5. B.V. Bondarev, Vestn. MAI **8**, 61–64 (2001)
6. B.V. Bondarev *The Method of Density Matrices in the Quantum Theory of Superconductivity*, 2nd edn. (Sputnik+, Moscow, 2016), p. 112 (in Russian)

Chapter 15
Crystal Structure and Dielectric Properties of Layered Perovskite-Like Solid Solutions $Bi_{3-x}Lu_xTiNbO_9$ ($x = 0$, 0.05, 0.1) with High Curie Temperature

S. V. Zubkov and S. I. Shevtsova

Abstract The structural and electrophysical characteristics of a number of solid solutions of layered perovskite-like oxides $Bi_{3-x}Lu_xTiNbO_9$ ($x = 0$, 0.05, 0.1) have been studied. According to the data of powder X-ray diffraction, all the compounds are single-phase with the structures of two-layer Aurivillius phases) ($m = 2$) with the orthorhombic crystal lattice (space group A21am). The temperature dependence of the relative permittivity $\varepsilon/\varepsilon_0(T)$ compounds have been measured and showed that the Curie temperature of the perovskite-like oxides $Bi_{3-x}Lu_xTiNbO_9$ increases with the doping parameter x up to $T_C = 964$ °C.

15.1 Introduction

The Aurivillius phases (APs) [1–4] are a large family of bismuth-containing layered perovskite-like compounds, the chemical compositions of which are described by the general formula $A_{m-1}Bi_2B_mO_{3m+3}$. The crystal structure of APs is alternating $[Bi_2O_2]^{2+}$ layers, between which there are m perovskite-like $[A_{m-1}B_mO_{3m+1}]^{2-}$ layers, where positions A are occupied by ions with large radii [Bi^{3+}, Ca^{2+}, Sr^{2+}, Ba^{2+}, Y^{3+}, Pb^{2+}, Na^{+}, K^{+}, Th^{4+}, Ln^{3+}, and Lu^{3+} (lanthanides)] and the positions B inside oxygen octahedra are occupied with ions of small radii (Ti^{4+}, Nb^{5+}, Ta^{5+}, W^{6+}, Mo^{6+}, Fe^{3+}, Mn^{4+}, Cr^{3+}, and Ga^{3+}). Layered perovskite-like compounds of bismuth oxides of the APs family are promising lead-free materials for applying in piezoelectric devices, in particular, at high temperatures and high frequencies. They demonstrate low temperature coefficients of dielectric and piezoelectric losses, and low aging temperatures, in addition to high Curie temperatures ($T_C \leq 965$ °C) [5, 6]. In recent years, more attention has been placed on the design and studies of new

S. V. Zubkov (✉)
Research Institute of Physics, Southern Federal University, 194, Stachki Ave, Rostov-on-Don, Russia 344090
e-mail: svzubkov61@mail.ru

S. I. Shevtsova
Institute of Earth Science, Southern Federal University, 40, Zorge Str., Rostov-on-Don, Russia 344090

I. A. Parinov et al. (eds.), *Advanced Materials*, Springer Proceedings in Materials 6, https://doi.org/10.1007/978-3-030-45120-2_15

APs [7–11]. The APs such as $SrBi_2Nb_2O_9$ (SBN), $SrBi_4Ti_4O_{15}$ (SBTi), $SrBi_2Ta_2O_9$ (SBTa), $La_{0.75}Bi_{3.25}Ti_3O_{12}$ (BLT) and so on were accepted as excellent materials for the energy independent ferroelectric memory with small access time (FeRAM) [12–16]. Bi_3TiNbO_9 (BTNO) with $m = 2$ that consists of $(Bi_2O_2)^{2+}$ layers between which there are $(BiTiNbO_7)^{2-}$ layers [17] is a promising material for fabricating high temperature piezoelectric sensors because of their very high Curie temperature T_C (914–921 °C) [5, 17], despite the fact that the piezoelectric modulus of BTNO ceramic is fairly low ($d_{33} < 7$ pC/N) [18]. Numerous examples [19–31] showed that replacements of atoms in *A*- and also in B-positions of an APs crystal lattice led to the change in the structure, the dielectric properties and significantly influenced the polarization processes in these compounds.

In this work, we have synthesized a number of new solid solutions of layered perovskite-like oxides $Bi_{3-x}Lu_xTiNbO_9$ ($x = 0$, 0.05, 0.1) in which proportions between amounts of Bi^{3+} and Lu^{3+} ions entering in A-position was varied. We have studied their crystal lattices, the dielectric and electrophysical characteristics. The ionic radius of Lu^{3+} is significantly smaller than the ionic radius of Bi^{3+} ion, which must lead to significant distortions of the crystal structure of the obtained substitutional solid solutions and influence their dielectric characteristic and the value of Curie temperature, T_C.

15.2 Experimental

The polycrystalline solid solutions of layered perovskite-like oxides $Bi_{3-x}Lu_xTiNbO_9$ ($x = 0$, 0.05, 0.1) have been synthesized by two stage solid phase reaction, consisting of a synthesis stage and a sintering stage. The powders of oxides Bi_2O_3, TiO_2, Nb_2O_5 and oxide Lu_2O_3 with 99% purity became the starting materials for the synthesis, and were taken in the calculated stoichiometric ratio. After the initial compounds were weighted and preliminarily ground, the synthesis was carried out at a temperature of 860 °C for 6 h. Then, the repeated grinding was performed, and the powder was pressed into 1–1.5 mm thick pellets of a 10 mm in diameter, and the final burning was carried out at a temperature of 1100 °C for 4 h.

Structural analysis of the sintered materials was carried out using X-ray DRON-3 M diffractometer a BSV21-Cu X-ray tube. The Cu$K_{\alpha 1,\alpha 2}$ radiation was selected from the total spectrum using a Ni filter.

The X-ray diffraction patterns were measured in the range of 2θ angles from 10° to 65° with a pitch of 0.04° and exposure for 4 s. The spectrum profile was analyzed and the line position were determined and their indexing (hkl) according to the chosen unit cell model were performed using the PCW-2.4 program [32].

To perform the electric measurements, Ag–Pd electrodes were deposited on the plane surface of the ceramic samples. The measurements were carried out using an E7-20 LCR immittance meter in the frequency range 100 kHz–1 MHz in the temperature range from room temperature to 980 °C.

15.3 Results and Discussion

The crystal structure of APs $Bi_{3-x}Lu_xTiNbO_9$ ($x = 0, 0.05, 0.1$) was determined by X-ray powder diffraction. The diffraction patterns of all the compounds correspond to the AP phase with $m = 2$. Figure 15.1 shows the XRD patterns of the Lu_x samples. It was found that all prepared APs crystallized in the orthorhombic system with unit cell space group A21am (36) (Joint Committee for Powder Diffraction Standard (JCPDS) No. 38-1257) and no other impurity diffraction peaks are observed, which indicates that the Lu ions are successfully entered into the crystal structure of BLuTN.

The highest intensity diffraction peaks are referred to the (115) orientation, according to the (112 $m + 1$) peak of the AP compounds. The highest intensity of the main diffraction peak (115) indicates that all the samples are randomly oriented and polycrystalline. As seen at the inset of Fig. 15.1, the diffraction peak (115) shifts toward higher angle with the increasing x, implying the decrease in the cell volume.

Table 15.1 gives the unit cell parameters and volumes, calculated tolerance factors, t, the maximum values of the relative permittivity $\varepsilon/\varepsilon_0$ at a frequency of 100 kHz

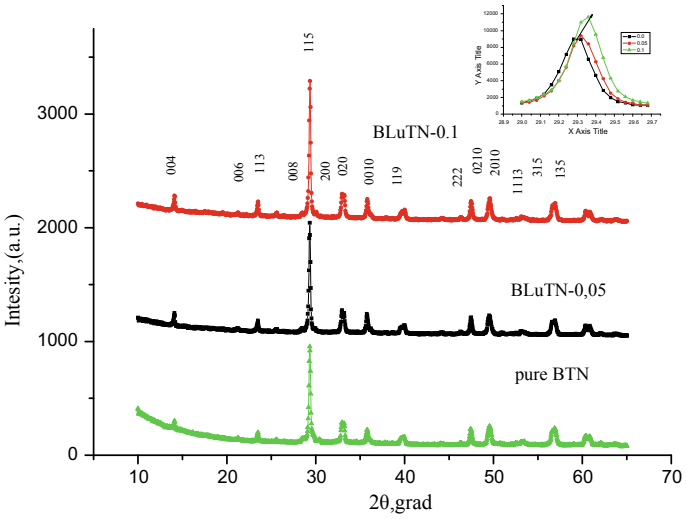

Fig. 15.1 X-ray diffraction patterns of powders: (1) Bi_3TiNbO_9, (2) $Bi_{2.95}Lu_{0.05}TiNbO_9$, (3) Bi2.9 Lu0.1TiNbO9

Table 15.1 Unit cell parameters a, b, c and volume V, tolerance-factor, t, relative permittivity $\varepsilon/\varepsilon_0$ at a frequency of 100 kHz, Curie temperature, T_C, and activation energy

Compound	a, Å	b, Å	c, Å	V, Å^3	t	$\varepsilon/\varepsilon_0$	T_C, °C
Bi_3TiNbO_9	5.3941	5.4339	25.099	735.67	0.972	1500	921
$Bi_{2.95}Lu_{0.05}TiNbO_9$	5.3933	5.43033	25.068	734.176	0.9709	1450	958
$Bi_{2.9}Lu_{0.1}TiNbO_9$	5.3923	5.4292	25.0625	733.726	0.97016	800	964

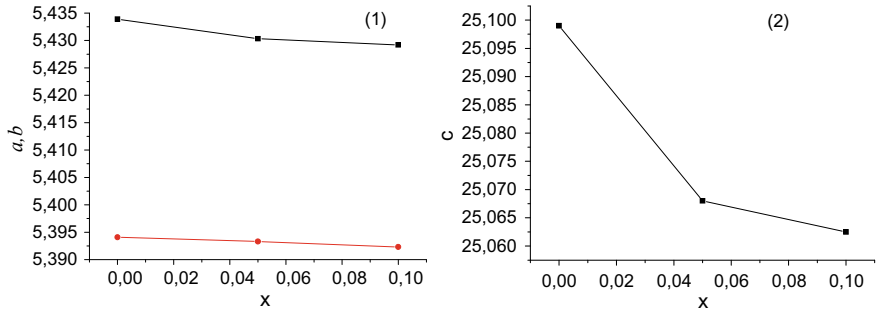

Fig. 15.2 Dependence of the unit cell parameters a, b, c on x in solid solutions $Bi_{3-x}Lu_xTiNbO9$ ($x = 0, 0.05, 0.1$): (1) parameters *a, b (Å)* and (2) parameter *c (Å)*

and the Curie temperatures T_C. As is seen from Table 15.1, the unit cell volume in the noted series of solid solutions decreases by more than 2.5% as x increases to 0.1 (Fig. 15.2). This is related to the difference in the values of ionic radii in positions A of the perovskite-like layers, where Bi^{3+} ions are replaced with Lu^{3+} ions with smaller radius (Bi = 1.38 Å, Lu^{3+} = 1.1 Å [33]). It can be noted that a decrease in the unit cell volume with an increase in x is due to significant decrease in parameter c along the crystallographic direction [001], whereas, in this case, parameters a and b increase.

The changes of the unit cell parameters of the $Bi_{3-x}Lu_xTiNbO_9$ ($x = 0, 0.05, 0.1$) solid solutions with the AP structure take place according to the Vegard law (Fig. 15.2). The obtained values of the rhombic $\Delta b = (b - a)/a$ and tetragonal $\Delta c = (c' - a_t)/a_t$ deformations (where $a_t = (a + b)/a$ is the average tetragonal period and $c' = 3c/(8 + 6m)$ is the average thickness of the single perovskite layer) (Table 15.2) [4]. As is seen from Table 15.2, the rhombic distortion of the pseudo-perovskite cell of APs substantially decreases as parameter x is varied from 0 to 0.1 as compared to that in undoped Bi_3TiNbO_9. All the APs series demonstrates an increase in the tolerance factor, t, due to a decrease in the amount of Bi^{3+} ions with the largest ionic radius, while the average tetragonal period a_t and the average thickness of a single perovskite layer decrease systematically.

Table 15.2 Unit cell volume, V, parameter of the tetragonal period, a_t, octahedron height along c-axis, c', deviation of the unit cell of cubic shape, $\delta c'$, rhombic distortion, Δb, relative change in the unit cell volume, $(V - V_x)/V_x$, bismuth–oxygen layer, c_0

Compound	V, Å^3	a_t, Å	c', Å	$\delta c'$, %	δb, %	$(V - V_x)/V_x$, %	c_0,
Bi_3TiNbO_9	735.67	3.8288	3.765	−1.67	0.732	0.0	3.765
$Bi_{2.95}Lu_{0.05}TiNbO_9$	734.176	3.7602	3.7602	−1.73	0.7	0.2	3.7602
Bi2.9Lu0.1TiNbO$_9$	733.72	3.7593	3.776	−1.75	0.661	0.25	3.77593

The tetragonal distortion of APs significantly changes in the range of $x = 0-0.1$; the octahedra are in a compressed state along c-axis in pseudo-perovskite layers. The relative permittivity $\varepsilon/\varepsilon_0$ and the dielectric loss tangent tanδ were measured in $Bi_{3-x}Lu_xTiNbO_9$ ($x = 0, 0.05, 0.1$) at frequencies 100–1000 kHz (Fig. 15.3a–d). All the temperature dependences of the permittivity have sharp maxima, the positions of which are associated with the Curie temperatures, T_C of these compounds.

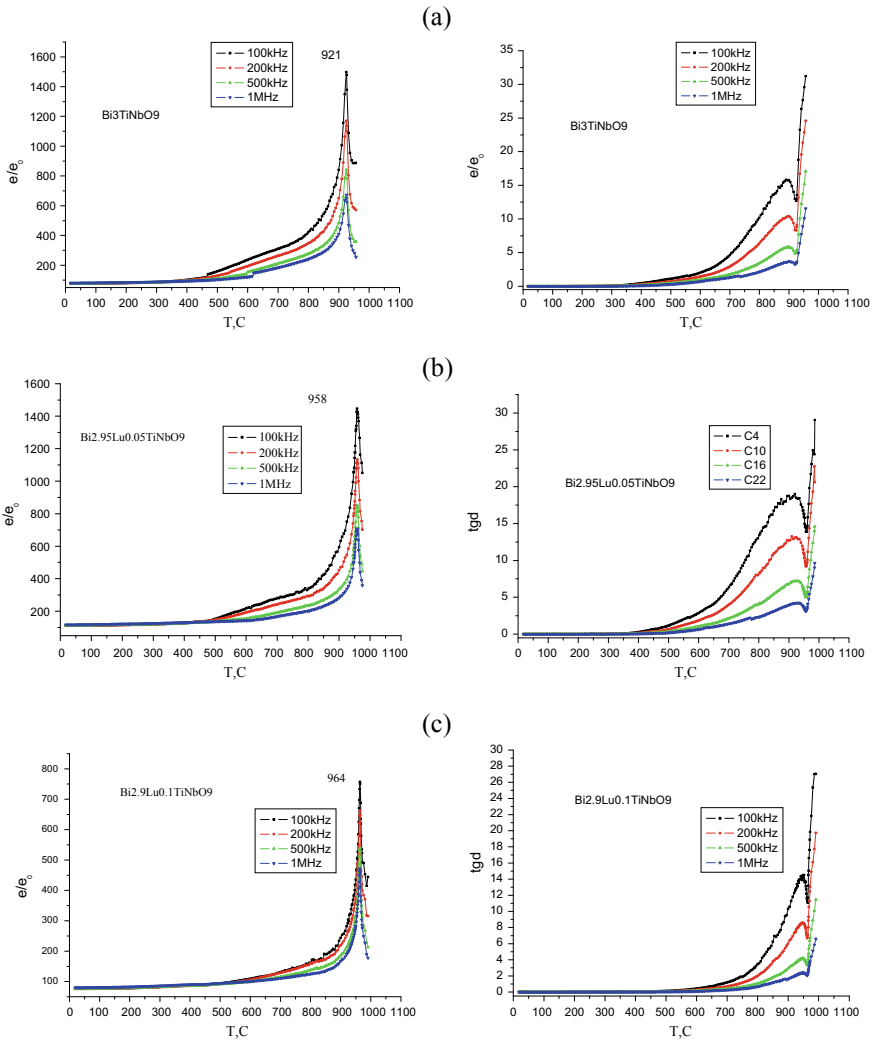

Fig. 15.3 Temperature dependence of the relative permittivity $\varepsilon/\varepsilon_0$ and the loss tanδ for APs $Bi_{3-x}Lu_xTiNbO_9$ ($x = 0, 0.05, 0.1$) at 0.1–1.0 MHz: **a** Bi_3TiNbO_9, **b** $Bi_{2.95}Lu_{0.05}TiNbO_9$, **c** $Bi_{2.9}Lu_{0.1}TiNbO_9$

Correspondingly, the dielectric loss curves have clear minima at the Curie temperature T_C. The positions of the dielectric loss maxima are independent of frequency for all APs, which indicate the absence of relaxor properties in these compounds. The maximum Curie temperature $T_C \approx 964$ °C was obtained for the $Bi_{2.9}Lu_{0.1}TiNbO_9$ composition. The Curie temperature T_C of the studied APs decreases with an increase in the unit cell parameters a and b and its volume V and decreases with parameter c. This dependence is directly related to the correlation between the tolerance-factor, t and the value of Curie temperature, T_C, characteristic of APs [19, 21].

Tolerance factor, t was introduced by Goldschmidt [34] as a parameter that determines the ionic packing in cubic cells: $t = (R_A + R_O)/\sqrt{2}(R_B + R_O)$, where R_A and R_B are cation radii in positions A and B, respectively, and R_O is the oxygen ion radius. Later this rule was also used for determination of the stability of the perovskite-like $[A_{m-1}B_mO_{3m+1}]^{2-}$ layers.

In this work, we calculated tolerance-factor, t, using the values of the ionic radii by Shannon (O^{2+} (coordination number (CN) = 6) $R_O = 1.40$ Å; R^{3+}_{Bi} (CN = 12) = 1.38 Å; R^{3+}_{Lu} (CN = 12) = 1.1 Å, Nb^{5+} (CN = 6) $R_{Nb} = 0.64$ Å; Ti^{4+} (CN = 6) = 0.605 Å). The ionic radii for the coordination with R^{3+}_{Bi} (CN = 12) and R^{3+}_{Lu} (CN = 12) are not given in [33], and these values were determined from the dependences of their ionic radii on the coordination numbers extrapolated to the region of high values. As is seen from Table 15.1, the members of the series $Bi_{3-x}Lu_xTiNbO_9$ (x = 0, 0.05, 0.1) demonstrated dependence of Curie temperature, T_C, on the calculated values t of the tolerance-factors, which enables us to predict its value for other values of x.

The temperature dependences of the loss tangent tanδ (Fig. 15.3) show the sharp increase in the dielectric losses at high temperatures (>650 °C) for Bi_3TiNbO_9 and at lower temperatures (>350 °C) for the $Bi_{3-x}Lu_xTiNbO_9$ (x = 0, 0.05, 0.1) series. This was due to a high amount of charge carriers, whose concentration sharply increases at high temperatures due to the formation of oxygen vacancies. However, the consideration of the values of tanδ for various APs at a certain temperature, e.g., Curie temperature, T_C, showed that they differ by several times, indicating substantially different degrees of imperfection of the APs crystal structure.

The obtained values of the activation energies of the charge, E_a, in $Bi_{3-x}Lu_xTiNbO_9$ (x = 0, 0.05, 0.1) are given in Table 15.3 for low- and high-temperature regions. The typical dependence of lnσ on 1000/T, where σ is the specific conductivity that was used for determination of E_a is shown in Fig. 15.4 for APs $Bi_{2.9}Lu_{0.1}TiNbO_9$. From Fig. 15.4, it is well seen that there are free temperature

Table 15.3 Activation energy (E_a) obtained from the Arrhenius plot

Compound	ΔT (E_a = 0.05 eV), °C	ΔT (E_a= 0.3 eV), °C	ΔT (E_a = 0.7 eV), °C	ΔT (E_a = 1.1–1.2 eV), °C
Bi_3TiNbO_9	20–170	170–300	300–640	640–921
$Bi_{2.95}Lu_{0.05}TiNbO_9$	20–280	280–320	320–630	630–958
$Bi_{2.9}Lu_{0.1}TiNbO_9$	20–300	300–360	360–730	730–964

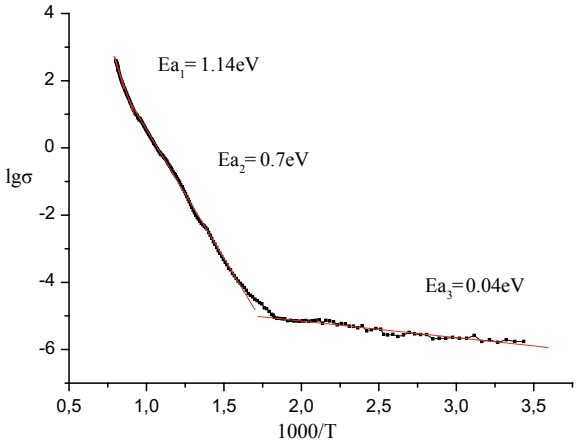

Fig. 15.4 Dependence of ln σ_0 on 1000/T for $Bi_{2.95}Lu_{0.05}TiNbO_9$ sample

regions, in which E_a has substantially different values. The activation energy, E_a, is calculated using the Arrhenius relationship:

$$\rho = \rho_0 \exp(E_a/k_B T) \ln(\sigma) = -(W/k_B T) + \ln(\sigma_0),$$

where E_a is the activation energy of the charge carriers, k_B is the Boltzmann constant, and T is the absolute temperature. From this above equation, it can be seen that the relationship between ln ρ and $1/T$ is a linear relationship.

The behavior of activation energy for all compounds can be separated into three temperature regions. The values of activation energy for $Bi_{2.95}Lu_{0.05}TiNbO_9$ ceramics in different temperature regions are 0.04, 0.7 and 1.14 eV as shown in Fig. 15.4. The E_a value of the $Bi_{2.95}Lu_{0.05}TiNbO_9$ ceramic in region I at 1 MHz is 0.04 eV. This value is very similar to the first-ionization energy of oxygen vacancies ($VO \rightarrow VO + e' \bullet$, ~ 0.1 eV). The values are close to 0.7 eV, consistent with half of the second-ionization energy of oxygen vacancies. By increasing donor additives, the temperature interval with the activation energy E_a for pure Bi_3TiNbO_9 varies from 20–170 to 20–280 K for $Bi_{2.95}Lu_{0.05}TiNbO_9$ and $Bi_{2.9}Lu_{0.1}TiNbO_9$ [35, 36].

This is due to the fact that, at high temperatures, intrinsic defects, the formation of which requires high activation energy, are main charge carriers. At low temperatures, the activation energy is mainly determined by impurity defects and has significantly lower values. It should be noted that the value of activation energy for Bi_3TiNbO_9 at high temperatures increases with increasing parameter a. For $x = 0.1$, it actually increases by 2 times compared with a pure compound and becomes higher two times than for all members of the $Bi_{3-x}Lu_xTiNbO_9$ ($x = 0, 0.05, 0.1$), whereas their values are comparable at low temperatures.

As it was shown in [35–39], the dielectric properties of APs can be substantially dependent on microstructure characteristics of the samples such as the density, the grain sizes, and the porosity of the ceramics.

Figure 15.5 shows the electron-microscopy images of the fracture surfaces of the

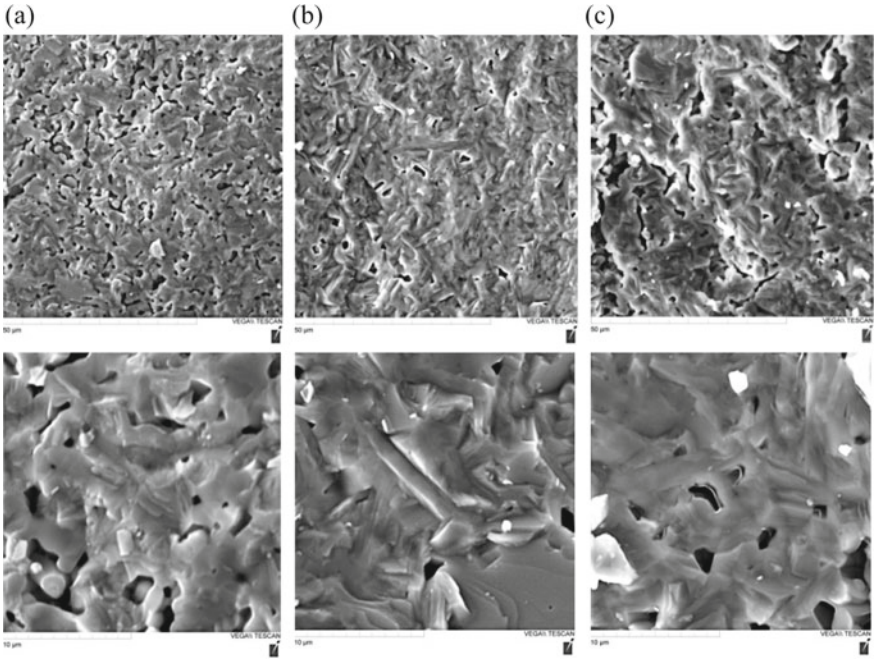

Fig. 15.5 SEM images of the fracture surfaces of **a** $Bi_{3-x}Lu_xTiNbO_9$ ($x = 0$), **b** $Bi_{3-x}Lu_xTiNbO_9$ ($x = 0.05$) and **c** $Bi_{3-x}Lu_xTiNbO_9$ ($x = 0.1$) ceramics

$Bi_{3-x}Lu_xTiNbO_9$ ($x = 0.0, 0.05, 0.1$) ceramics. We can see in all the images that the ceramic samples consist of plane grains are characteristic for the APs samples. These plane grains form during their high-anisotropic growth when the growth rate in the direction perpendicular to *c*-axis is significantly higher than that along *c*-axis [24]. The grain thickness in the $Bi_{3-x}Lu_xTiNbO_9$ ($x = 0.0, 0.05,0.1$) samples is equal to 0.2–0.4 μm, which is an order of magnitude less than their diameter of 20–30 μm. It can be noted as well that the grain sizes increase as the Lu content in the samples increases. The increase in the grain size is associated with formation of intermediate low-melting phases favoring the grain growth at the grain boundaries during their crystallization.

The image of a thin cross-section of ceramic (Fig. 15.6) shows the presence of two phases (not in a structural sense). The main phase (light in Fig. 15.6) is close to the estimated stoichiometry ~ $Bi_{2.87}Lu_{0.04}Ti\ Nb_{0.95}O_{7.7}$ (the error of the method is 5–10%, rel. Bi = ±0.3, Lu = ±0.02, Ti = ±0.1, Nb = ±0.2, O = ±0.5). The formula is based on the normalization that the number of Ti atoms is equal to unity.

The secondary phase (gray in Fig. 15.6) can be represented by the formula $Bi_{15}Lu_2Ti_{15}Nb_5O_{63}$. Perhaps this is an amorphous phase (see Fig. 15.5). This compound includes not only large pores, but also the surface of microcrystals, which can also be seen from their fuzzy forms in the electron-microscopy images (Fig. 15.5). Since the secondary phase is a dielectric, it can significantly affect the ferroelectric

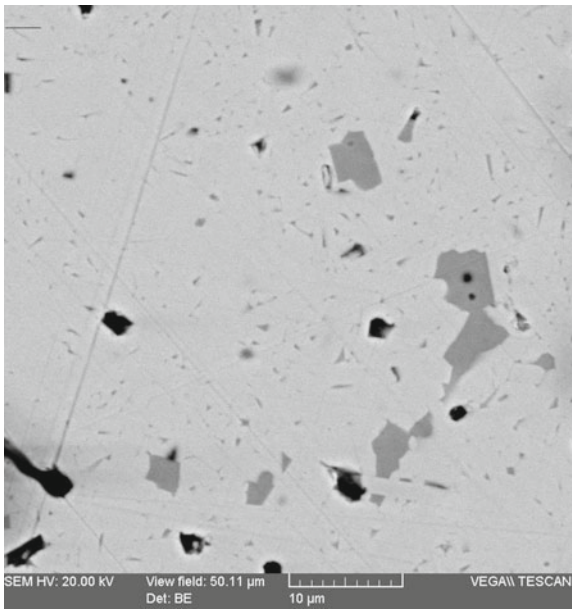

Fig. 15.6 Image of thin cross-section of ceramics

parameters of ceramics. In the remaining samples, an estimated analysis of the composition on ceramic chips was performed. They also found two phases. The main phase with Lu_x. The secondary phase has approximately the same composition as the sample presented here.

15.4 Conclusion

A new series of layered perovskite-like oxides $Bi_{3-x}Lu_xTiNbO_9$ ($x = 0$, 0.05, 0.1) has been synthesized. The X-ray diffraction studies show that all the compounds are single-phase and have the APs structure with orthorhombic unit cells (space group A21am). The microstructural study of the synthesized compounds revealed the presence of two phases, one of which is amorphous. The amorphous phase is not only between the crystals, but also covers them and exerts an effect on the growth of the crystals and the dielectric properties. The permittivity was measured to a temperature of 980 °C. The Curie temperature T_C increases from 921 °C ($x = 0$) to 964 °C (for $x = 0.1$). The value $T_C = 964$ °C for $Bi_{2.9}Lu_{0.1}TiNbO_9$ is one of the highest values observed for the perovskite-like bismuth-titanium AP oxides known to date.

Acknowledgements This work was financially supported by the Ministry of Science and Higher Education of the Russian Federation (State assignment in the field of scientific activity, Southern Federal University, 2020).

References

1. B. Aurivillius, Arkiv. Kemi. **1**, 463 (1949)
2. B. Aurivillius, Arkiv. Kemi. **1**, 499 (1949)
3. B. Aurivillius, Arkiv. Kemi. **2**, 512 (1950)
4. V.A. Isupov, J. Inorg. Chem. **39**, 731 (1994)
5. S.V. Zubkov, V.G. Vlasenko, J. Phys. Solid State **59**(12), 2325 (2017)
6. S.V. Zubkov, V.G. Vlasenko, V.A. Shuvaeva, S.I. Shevtsova, J. Phys. Solid State **58**(1), 42 (2016)
7. I.A. Zarubin, V.G. Vlasenko, A.T. Shuvaev, Inorg. Mater. **45**, 555 (2009)
8. V.G. Vlasenko, A.T. Shuvaev, I.A. Zarubin, V.V. Vlasenko, Phys. Solid State **52**, 744 (2010)
9. Z.G. Gai, M.L. Zhao, W.B. Su, C.L. Wang, J. Liu, J.L. Zhang, J. Electroceram **31**, 143 (2013)
10. M.A. Bekhtin, A.A. Bush, K.E. Kamentsev, A.G. Segalla, Inorg. Mater. **52**, 557 (2016)
11. Z. Zhang, H. Yan, X. Dong, Y. Wang, Mater. Res. Bull. **38**, 241 (2003)
12. A. Ando, M. Kimura, Y. Sakabe, Jpn. J. Appl. Phys. **42**, 520 (2003)
13. R.Z. Hou, X.M. Chen, J. Mater. Res. **20**, 2354 (2005)
14. R.Z. Hou, X.M. Chen, Solid State Commun. **130**, 469 (2004)
15. Y. Noguchi, I. Miwa, Y. Goshima, M. Miyayama, Jpn. J. Appl. Phys. **39**, 1259 (2000)
16. Y. Yao, C. Song, P. Bao, D. Su, D.X. Lu, J. Appl. Phys. **95**, 3126 (2004)
17. R.W. Wolfe, R.E. Newnham, D.K. Smith, Ferroelectrics **3**, 11971 (2004)
18. A. Moure, L. Pardo, C. Alemany, J. Eur. Ceram. **21**, 1399 (2001)
19. V.G. Vlasenko, S.V. Zubkov, V.A. Shuvaeva, Phys. Solid State **57**, 900 (2015)
20. Z.Y. Zhou, X.L. Dong, H. Chen, H.X. Yan, J. Am. Ceram. Soc. **89**, 1756 (2006)
21. S.V. Zubkov, V.G. Vlasenko, V.A. Shuvaeva, S.I. Shevtsova, Phys. Solid State **58**, 42 (2016)
22. Z.X. Cheng, X.L. Wang, Appl. Phys. Lett. **90**, 222902 (2007)
23. R. Aoyagi, H. Takeda, S. Okamura, T. Shiosaki, Mater. Res. Bull. **38**, 25 (2003)
24. H.X. Yan, C.G. Li, J.G. Zhou, Jpn. J. Appl. Phys. **40**, 6501 (2001)
25. Z.X. Cheng, X.L. Wang, Appl. Phys. Lett. **89**, 032901 (2006)
26. Z.G. Gai, J.F. Wang, Appl. Phys. Lett. **90**, 052911 (2007)
27. S.J. Zhang, Solid State Commun. **140**, 154 (2006)
28. Z.X. Cheng, X.L. Wang, J. Phys. D **43**, 242001 (2010)
29. M. Matsushita, R. Aoyagi, H. Takeda, Jpn. J. Appl. Phys. **43**, 7164 (2004)
30. R. Aoyagi, S. Inai, Y. Hiruma, T. Takenaka, Jpn. J. Appl. Phys. **44**, 7055 (2005)
31. Z.X. Cheng, X.L. Wang, J. Appl. Phys. **107**, 084105 (2010)
32. W. Kraus, G. Nolze, *Powder Cell for Windows, Version2.*3 (Federal Institute for Materials Research and Testing, Berlin (1999)
33. R.D. Shannon, Acta crystallographica Section A. crystal physics. Diffr. Theor. Gen. Crystallogr. **32**, 75 (1976)
34. V.M. Goldschmidt, *Geochemisca Veterlun* (NorskeVidenkap, Oslo, 1927)
35. A. Moure, L. Pardo, J. Appl. Phys. **97**, 084103 (2005)
36. H. Zhang, H. Yan, M.J. Reece, J. Appl. Phys. **108**, 014109 (2010)
37. V.G. Vlasenko, S.V. Zubkov, V.A. Shuvaeva, K.G. Abdulvakhidov, S.I. Shevtsova, Phys. Solid State **56**(8), 1554 (2014)
38. B. Jiménez, L. Pardo, A. Castro, P. Millán, R. Jiménez, M. Elaatmani, M. Oualla, Ferroelectrics **241**, 279 (2000)
39. D. Kajewski, Z. Ujma, K. Szot, M. Paweczyk, Ceram. Int. **35**, 2351 (2009)

Chapter 16
Fabrication and Investigation of InSb Thin Films for IR SAW Photodetectors

M. E. Kutepov, T. A. Minasyan, D. A. Zhilin, V. E. Kaydashev, G. Y. Karapetyan, K. G. Abdulvakhidov, S. I. Shevtsova, and E. M. Kaidashev

Abstract The two-stage pulsed laser deposition growth of thin InSb films on (111) Si and on $LiNbO_3$ YX-128° substrates was studied using a thin InSb buffer layer deposited at a low temperature. This approach improves carrier mobility in InSb base layer, which largely determines the sensitivity of IR photodetectors at room temperature. The response speed in the near-IR range at $\lambda = 985$ nm was 1.92 ms, and the decay time was 1.67 ms, under xenon lamp radiation with mechanical modulation. The photosensitivity of the InSb/(111) Si film was about 1 A/W at 293 K. The response time of the sample was~6.8 μs, the time of complete recovery was ~34.5 μs, under laser diode radiation with a wavelength of 840 nm, power 1 mW.

16.1 Introduction

Among the $A^{III}B^{V}$ semiconductors, InSb has the smallest band gap (~0.17 eV) at room temperature and an extremely high electron mobility. Due to these characteristics, InSb is widely used in infrared (IR) optoelectronics, microwave and THz range devices, and magnetic field sensors.

Another promising application of thin films, as well as various InSb nanostructures, may be IR surface acoustic wave (SAW) photodetectors. It is well known that in such devices ZnO films and nanorods are widely used for detecting UV radiation. The use InSb thin films and nanostructures as a sensitive element in SAW photodetectors will expand the range of applications of these devices by adding the IR region.

InSb is a narrow-gap semiconductor with a low effective mass and has the highest electron mobility among III–V semiconductors. Due to these electronic characteristics, InSb is a good candidate for use in infrared detectors, various high-speed devices, and magnetic sensors [1–3].

M. E. Kutepov · T. A. Minasyan · D. A. Zhilin · V. E. Kaydashev · G. Y. Karapetyan · K. G. Abdulvakhidov · S. I. Shevtsova · E. M. Kaidashev (✉)
Southern Federal University, 200/1 Stachki Ave, Rostov-on-Don, Russia 344090
e-mail: kaidashev@mail.ru

V. E. Kaydashev
Moscow Institute of Physics and Technology, 9, Institutskiy, per, Dolgoprudny, Russia 141701

I. A. Parinov et al. (eds.), *Advanced Materials*, Springer Proceedings in Materials 6, https://doi.org/10.1007/978-3-030-45120-2_16

InSb heteroepitaxy on Si substrates is very difficult to achieve due to the large mismatch of the lattice parameters between (approximately 19.3%) these materials. Two main methods are used to solve this problem. The first method uses various buffer layers, such as GaAs and/or Ge [4–6]. In the second method, at the initial stage of growth, surface reconstruction is formed on Si substrates by In and Sb atoms [7, 8]. Some groups [9, 10] managed to grow InSb films on substrates that are very different in structural characteristics (GaAs and Si) using a two-stage growth method. It was shown that this method is more efficient and suitable for most tasks [11, 12]. The method consists of the growth of a low-temperature InSb layer (180–240 °C) and the subsequent growth of a high-temperature InSb layer (350–440 °C) using molecular beam epitaxy.

It is well known that films with a better crystalline structure and smaller defects have better electrical characteristics (mobility and carrier concentration, conductivity, etc.). Since the first InSb layer is grown at a relatively low temperature, it is of low quality. Further, the temperature rises (about 350 °C) to spray the second layer with a better crystalline structure. However, the authors of [1] report that the growth temperature of the second InSb layer is limited due to the degradation of the first InSb layer at higher temperatures. The authors of [1] managed to grow an InSb film with high crystal quality and good electrical properties, using a gradual increase in the growth temperature of the second InSb layer during deposition.

16.2 Experimental

16.2.1 Synthesis

InSb films were synthesized on YX-128° $LiNbO_3$ piezoelectric substrates and on (111) Si substrates by pulsed laser deposition (PLD). As a target, we used a single-crystal InSb target of stoichiometric composition. The radiation from an excimer KrF laser (248 nm, 15 ns) was focused on a rotating InSb target (2×5 mm^2, energy density 2 J/cm^2). The YX-128° $LiNbO_3$ substrate (1×2) cm^2 in size was located at a distance of 5 cm from the target at a temperature of (250–500) °C. The chamber was previously pumped out to a pressure of $(2–5) \times 10^{-5}$ mBar. To improve the structural, electrophysical, and optical properties of thin InSb films on (111) Si substrates, we used a two-stage synthesis method. First, an InSb buffer layer was deposited at a temperature of 250 °C with a thickness $h_1 = 5–30$ nm. Then we deposited the main InSb layer with a thickness $h_2 = 150–200$ nm.

16.2.2 Study of InSb Thin Films Structure

X-ray diffraction studies of thin InSb films on $LiNbO_3$ and (111) Si substrates were carried out on a D2 Phaser Bruker X-ray diffractometer with a position-sensitive detector LYNXEYE with Cu Kα radiation (30 kV, 10 mA, scan step 0.01°). A study of the structure of films on $LiNbO_3$ substrates obtained at synthesis temperatures of 400–475 °C showed that with an increase in the synthesis temperature from 400 to 450 °C, the structure of the films improves, the intensity of the (111) InSb reflection (25.4°) increases, and the (222) reflex appears InSb (52.17°) (Fig. 16.1).

This InSb/Si (111) film (Fig. 16.2) was synthesized as follows: a thin InSb buffer layer with a thickness of $h_1 = 20$ nm was sprayed at a low temperature $T_1 = 250$ °C and a reduced laser pulse repetition rate of 1 Hz, and the main layer with a thickness of $h_2 = 150$ nm was sprayed at a temperature of $T_2 = 500$ °C and a pulse repetition rate of 10 Hz. The reduced laser pulse repetition rate and the growth temperature of the buffer layer improve its crystalline structure and reduce mechanical stresses. The subsequent growth of the InSb main layer, proceeding on its own sublayer, leads to the formation of a cubic structure with the film predominantly oriented in the (111) direction, with (111) InSb ‖ (111) Si (Fig. 16.2) (Fig. 16.3).

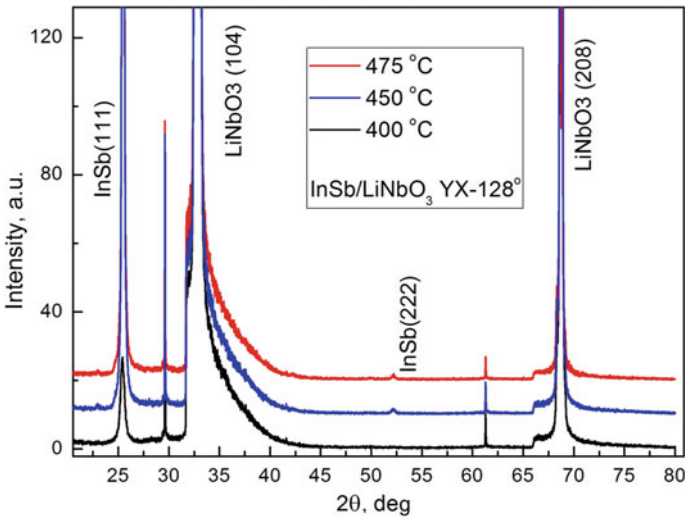

Fig. 16.1 X-ray diffraction patterns of InSb films on $LiNbO_3$ substrates

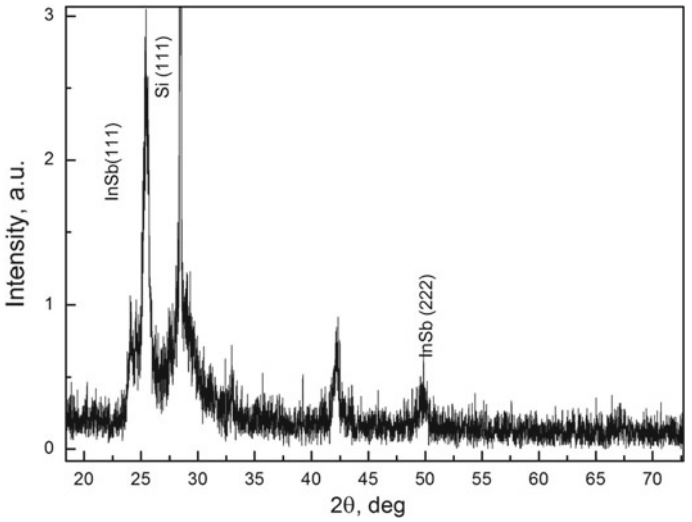

Fig. 16.2 X-ray diffraction pattern of the InSb film on the Si (111) substrate. $h_1 = 20$ nm, $h_2 = 150$, $T_1 = 250$ °C, $T_2 = 500$ °C

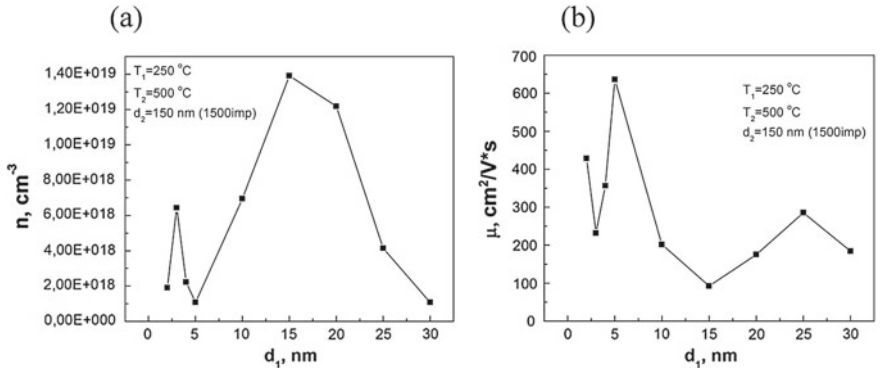

Fig. 16.3 Dependences of the concentration (**a**) and mobility (**b**) of charge carriers on the thickness of the first InSb layer

16.2.3 Investigation of the Electrical Properties of Thin InSb Films on $LiNbO_3$ and (111) Si Substrates

The concentration and mobility of charge carriers were investigated by van der Pauw method. To study the Hall effect, ohmic contacts made of gold were deposited on the samples by pulsed laser deposition. The current flowing through the sample is measured using a Keithley 2000 multimeter. The magnetic field in the sample is created using two permanent magnets, the value of the magnetic field induction in

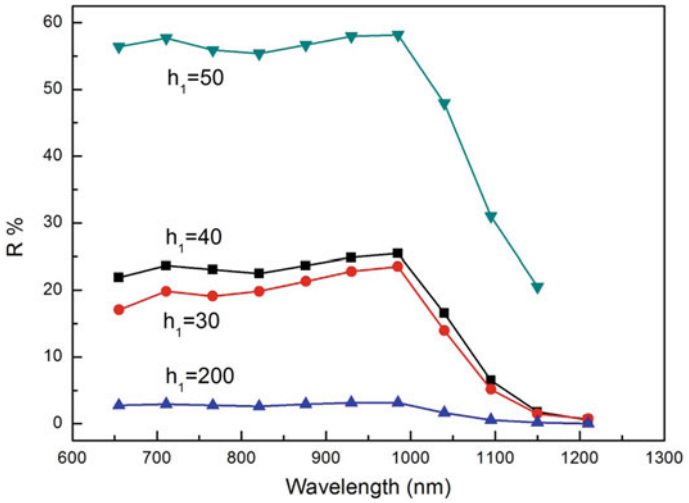

Fig. 16.4 Plot of the photosensitivity of InSb/Si (111) films versus wavelength in the range 650–1150 nm; h_1—thickness of buffer layer

the gap between them is 0.3 T. The sample is located between the permanent magnets so that the magnetic field is perpendicular to the plane of the sample. The Hall U voltage between the Hall contacts was measured using another Keithley 3 multimeter.

The plots of the concentration and mobility of InSb film carriers on the thickness of the buffer layer (Fig. 16.4) show that the maximum mobility and minimum carrier concentration are observed at a buffer layer thickness of 5 nm.

16.2.4 Optical Properties of Thin InSb Films

The photosensitivity, the photoresponse times, and the photocurrent decay times of thin InSb/(111) Si films in the near IR range were studied using a monochromator. The change in the resistance of the InSb films was measured using a Keithley 2000. The $\Delta R/R \times 100\%$ dependence on the wavelength for the InSb film ($\mu = 425\ \text{cm}^2/\text{V s}$, $n = 2.4 \times 10^{18}\ \text{cm}^{-3}$, $\rho = 6 \times 10^{-3}\ \Omega\ \text{cm}$) in the range 650–1150 nm is shown in Fig. 16.4. The maximum photosensitivity was observed at a wavelength of $\lambda =$ 985 nm (Fig. 16.5).

The photo-response speed and decay time of a sample with $h_1 = 5$ nm at a wavelength of $\lambda = 985$ nm (IR radiation power 1 mW) were measured using a Tektronix TDS 2024B digital storage oscilloscope (Fig. 16.6). IR radiation was modulated with a rotating shutter. The response speed in the near-IR range at $\lambda = 985$ nm was 1.92 ms, and the decay time was 1.67 ms. The maximum photosensitivity of the InSb/(111) Si film 1 A/W.

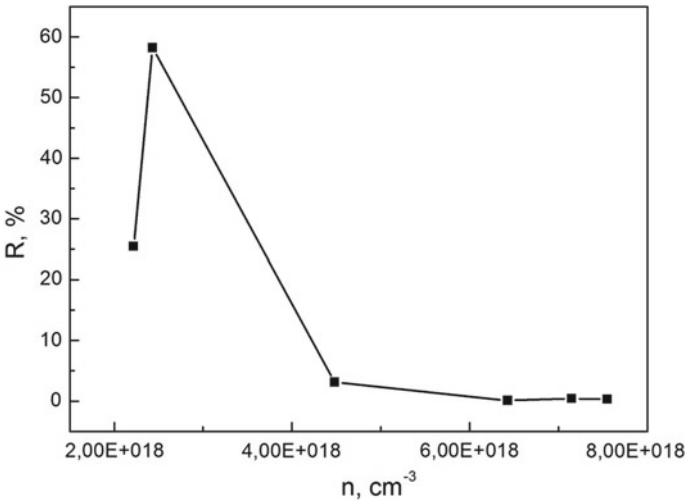

Fig. 16.5 Plot of the photosensitivity of InSb/Si (111) films on the carrier concentration at a wavelength of $\lambda = 985$ nm. With increasing carrier concentration, photosensitivity decreases. The concentration and mobility of charge carriers at the maximum are $n = 2.43226 \times 10^{18}$ cm^{-3} and $\mu = 425.2504522$ cm^2/V s, respectively

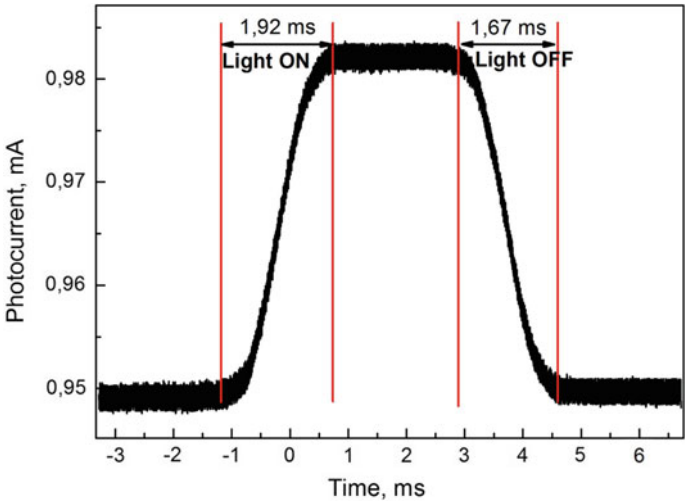

Fig. 16.6 Oscillogram of the photo-response (at room temperature) of an InSb film ($\mu = 425$ cm^2/V s, $n = 2.4 \times 10^{18}$ cm^{-3}, $\rho = 6 \times 10^{-3}$ Ω cm) at a wavelength of $\lambda = 985$ nm (IR radiation power 1 mW)

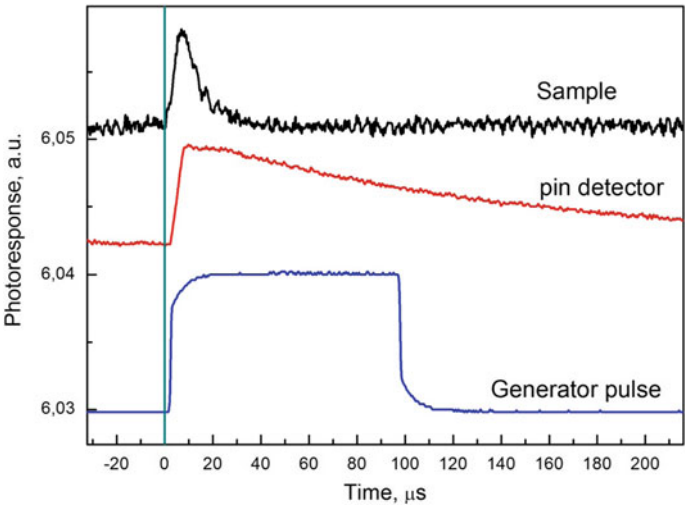

Fig. 16.7 Photo-response (at room temperature) of sample InSb (111) Si ($\mu = 425$ cm^2/V s, $n = 2.4 \times 10^{18}$ cm^{-3}, $\rho = 6 \times 10^{-3}$ Ω cm) to the KEM-34 quantum module pulse. The response time of the sample was ~6.8 μs, the time of complete recovery was ~34.5 μs. A response of a pin photodetector DET 10A/M to the KEM-34 quantum module pulse is inserted for comparison

The speed of the sample in Fig. 16.6 is determined by the speed of the modulator. For a more accurate estimation of speed, the sample was irradiated with an IR laser diode (KEM-34 quantum diode module) used to modulate the signals of optical communication lines. Modulation of laser diode radiation with a wavelength of 840 nm, power 1 mW, was carried out by a rectangular pulse generator. The rise time of the response of the sample was ~6.8 μs, the time of complete recovery was ~34.5 μs under laser diode pulse radiation (Fig. 16.7).

16.3 Conclusion

A technique has been developed for pulsed laser deposition of InSb thin films on YX-128° $LiNbO_3$ piezoelectric substrates and on (111) Si substrates. The structural, electrical, and optical properties of InSb films were studied. The two-stage growth of thin InSb films on (111) Si substrates was studied using a thin InSb buffer layer deposited at a low temperature, which makes it possible to increase the electronic mobility of the InSb base layer, which largely determines the sensitivity of IR photodetectors at room temperature. The maximum sensitivity was observed for a sample with a thickness of the first layer of 5 nm. The photosensitivity of the InSb/(111) Si film was about 1 A/W at 293 K. The response time of the sample was ~6.8 μs, the time of complete recovery was ~34.5 μs, under laser diode radiation with a wavelength of 840 nm, power 1 mW.

Acknowledgements This research work is supported by Russian Education and Science Ministry, the project No. 16.5405.2017/8.9.

References

1. S. Khamseh, Y. Yasui, K. Nakayama, K. Nakatani, M. Mori, K. Maezawa, Jpn. J. Appl. Phys. **50**, 04DH13 (2011)
2. X. Zhu, W. Sun, X. Cao, X. Zhang, L. Zhang, F. Tao, Proc. SPIE **8419**, 841915 (2013)
3. T. Zhang, S.K. Clowers, M. Debnath, A. Bennett, C. Roberts, J.J. Haris, R.A. Stradling, L.F. Cohen. Appl. Phys. Lett. **84**, 4463 (2004)
4. J.I. Chyi, D. Biswas, S.V. Lyer, N.S. Kumar, H. Morkoc, R. Bean, K. Zanio, H.Y. Lee, H. Chen, Appl. Phys. Lett. **54**, 1016 (1989)
5. M. Mori, D.M. Li, M. Yamazaki, T. Tambo, H. Ueba, Appl. Surf. Sci. **104–105**, 563 (1996)
6. M. Mori, Y. Tsubosaki, T. Tambo, H. Ueba, C. Tatsuyama, Appl. Surf. Sci. **117–118**, 512 (1997)
7. D.M. Li, M. Atoji, T. Okamoto, T. Tambo, C. Tatsuyama, Surf. Sci. **417**, 210 (1998)
8. D.V. Gruznev, B.V. Rao, T. Tambo, C. Tatsuyama, Appl. Surf. Sci. **190**, 134 (2002)
9. K. Kanisawa, H. Yamaguchi, Y. Huirayama, Appl. Phys. Lett. **76**, 589 (2000)
10. M. Mori, M. Saito, Y. Yamashita, K. Nagashima, M. Hashimoto, C. Tatsuyama, T. Tambo, J. Cryst. Growth **301–302**, 207 (2007)
11. M. Mori, M. Saito, K. Nagashima, K. Ueda, Y. Yamashita, C. Tatsuyama, T. Tambo, K. Maezawa, Phys. Status Solidi C **5**, 2772 (2008)
12. M. Mori, M. Saito, K. Nagashima, K. Ueda, T. Yoshida, K. Maezawa, J. Cryst. Growth **311**, 1692 (2009)

Chapter 17
The Investigation of Optical and Dielectric Properties of Ferroelectric BSN Ceramics Doped with Rare-Earth Elements

L. V. Grigoryev, A. A. Semenov, and P. Yu Belyavskiy

Abstract The chapter presents the results of studies of X-ray diffraction analysis, the temperature dependence of the permittivity, the frequency dependence of $\varepsilon(T)$ and the absorption coefficient of electromagnetic radiation in the frequency band 0.1–1.0 THz for samples of $Sr_{0,61}Ba_{0,39}Nb_2O_6$ ceramics doped with rare-earth ions Ce, La, Nd, Yb.

17.1 Introduction

Ferroelectric barium-strontium niobate (BSN) ceramics is a solid solution of the composition $Sr_xBa_{1-x}Nb_2O_6$ with different variations of the parameter x, lying in the range from 0.25 to 0.75. BSN has the structure of tetragonal tungsten bronze and are uniaxial polar compounds. BSN are typical representatives of relaxor ferroelectrics, which causes interest to them due to the set of their unique electro-optical, pyroelectric, and piezoelectric properties [1–3]. In BSN ceramics, we can control the degree of smearing of the phase transition, its temperature position of transition between the ferroelectric to the paraelectric state, and the optical and electrophysical properties by varying the composition of the ceramic or introducing dopants [4]. From an analysis of the literature data on the electrophysical and electro-optical properties of $Sr_xBa_{1-x}Nb_2O_6$ ceramics, it follows that doping of ceramics with rare-earth ions leads to an increase in pyroelectric properties, piezoelectric properties, electro-optical and photorefractive characteristics of the material, which makes it possible to successfully use the barium-strontium niobate ferroceramics at MW and THz spectral range, radio photonics devices, dynamic holography devices, optical memory, laser beam control devices and nonlinear optical photonics devices [5–7].

L. V. Grigoryev (✉)
ITMO University, St. Petersburg, Russia
e-mail: grigoryev@oi.ifmo.ru; lvgrigoryev@itmo.ru

L. V. Grigoryev · A. A. Semenov · P. Y. Belyavskiy
ETU "LETI", St. Petersburg, Russia

I. A. Parinov et al. (eds.), *Advanced Materials*, Springer Proceedings in Materials 6, https://doi.org/10.1007/978-3-030-45120-2_17

This chapter presents the results of a study of the optical, photoelectric, and dielectric properties of BSN ferroelectric ceramics ($x = 0.61$) doped with Ce, La, Yb, and Nd ions.

17.2 Sample Preparation

The synthesis of samples of BSN ferroelectric ceramics and doped with rare-earth metal ions ceramics BSN: Ln, where Ln is a rare-earth element from a number of lanthanides, was carried out according to the classical ceramic technology of solid-phase synthesis from Nb_2O_5, $BaCO_3$, $SrCO_3$ precursors. Alloying impurities in the form of oxides or nitrates of rare-earth metals: La_2O_3, Nd_2O_3, Yb_2O_3, $Ce(NO_3)_3$ were loaded into the initial charge. The concentration of dopants was set in the range 1.2–1.3%.

In order to remove moisture from the feedstock for synthesis, the oxide powders were heated to 150 °C and dried at this temperature for 3 h. Homogenization and grinding of the feedstock for the charge was carried out in a ball mill with agate balls in anhydrous alcohol for 8 h. Next, the charge was dried, polyvinyl alcohol was added to the dried feedstock, and then tablets with a diameter of 15.0 mm and a thickness of 2.5 mm were formed under the pressure of 200 MPa. Pressed tablets were placed in a muffle furnace on a platinum base and sprinkled with powder of the same composition in order to prevent the volatilization of the components during the synthesis. Solid phase synthesis of ferroelectric ceramics was carried out in a muffle furnace in a normal atmosphere. The exposure time of the samples at the synthesis temperature was 2 h. Next, the samples cooled with the furnace. Then, the ceramic samples were ground, and Pt electrodes were deposited on their surface.

17.3 Structural Properties

The structural properties of BSN ceramic samples were studied by soft X-ray diffractometry using an DRON-3M automated X-ray diffractometer. Obtaining diffraction X-ray diffraction patterns from ceramic samples without the presence of artifacts on them directly depends on both the choice of the X-ray source and the magnitude of the accelerating voltage applied to the anode of the X-ray tube. The reason for the sharp decrease in the signal-to-noise ratio in the X-ray diffraction pattern, as a rule, is the response of the X-ray photodetector to spurious fluorescence radiation present in the measuring channel of the diffractometer. In this regard, to obtain the correct diffraction pattern, we used an X-ray tube with an anode made of copper. To obtain stable characteristic radiation, the voltage at the anode of the tube should be in the range from 25.0 to 28.0 kV and was chosen equal to 26.0 kV. Given the magnitude of the accelerating voltage applied to the anode of the X-ray tube, Cu-Kα radiation was used. In order to monochromatize X-rays—to isolate the Cu-Kα line from the

output spectrum of a tube, a selectively absorbing β-filter was placed in front of the ceramic sample. The Bragg angles 2θ were measured in the range from 20° to 50° with a step of $\Delta 2\theta = 0.05°$. The pulse accumulation time at the measurement point was 15 s; the measurements were carried out at room temperature.

As it is known, almost all the physical properties of ceramic samples of ferroelectrics are determined by the degree of defectiveness of their structure. The difference between ceramic and single-crystal ferroelectrics is that the ceramic structure consists of a "mosaic" randomly distributed in the sample volume, from regions in which three-dimensional periodicity in the arrangement of ferroelectric atoms is maintained. In the "mosaic" version of the structure of ferroelectric ceramics of strontium niobate-barium, the size of the coherent scattering (CSR) regions of X-ray radiation can be taken as a measure of the structural defectiveness. In essence, these will be micro-sized areas (mosaic elements). Therefore, based on the estimation of CSR sizes using the Selyakov–Scherrer formula [8], it is possible to estimate the sizes of "mosaic" structural trace elements of a ferroelectric present in the volume of BSN ferroelectric ceramics [9].

The barium-strontium niobates in the concentration variation range $x = 0.25$–0.75 are single-phase and belong to the structure of unfilled tetragonal tungsten bronze, in which 5/6 cationic positions in the three-dimensional structure are filled. The main structural element of this ferroelectric is a three-dimensional framework of niobium oxide Nb_2O_6, which is formed by joining the vertices of the NbO_6 octahedra and forming three types of structural channels along the polar axis: triangular, pentagonal and quadrangular [10]. The general structural formula for the BSN ferroelectric can be represented as the expression $A_2B_4C_4Nb_{10}O_{30}$. In the barium-strontium niobates structure, positions A located inside the quadrangular channels are partially filled with Sr. Positions B inside the pentagonal channels are filled with statistically distributed atoms Ba and Sr. C positions located inside the narrowest channels of a triangular section are not filled with atoms. The presence of the filling of B channels by barium and strontium atoms, obeying a statistical distribution, allows variation in the percentage composition of barium and strontium atoms to affect the relaxing characteristics of a ferroelectric. In addition, the introduction of dopants, the ionic radius of which is commensurate with the ionic radius of barium or strontium atoms, also allows us to widely vary the relaxation characteristics of a ferroelectric, but without changing the percentage composition of barium and strontium atoms. In addition, the introduction of doping atoms into the BSN composition with an ionic radius close to the ionic radii of barium and strontium can lead to the presence of bulk fluctuations in the composition of the ferroelectric.

The X-ray diffraction pattern of the synthesized ceramic sample without the introduction of doping impurities is shown in Fig. 17.1. Only a set of reflections corresponding to the BSN material are observed in the X-ray diffraction pattern. The average size of the coherent scattering regions in the studied ceramics amounted to 280 Å in the (001) direction. An analysis of X-ray diffraction data confirmed that the studied samples of barium-strontium niobates ceramic had a structural type of tetragonal tungsten bronze. The unit cell parameters of ceramics had values of $a =$ 12.466 Å and $c = 3.954$ Å, which is in good agreement with published data [11].

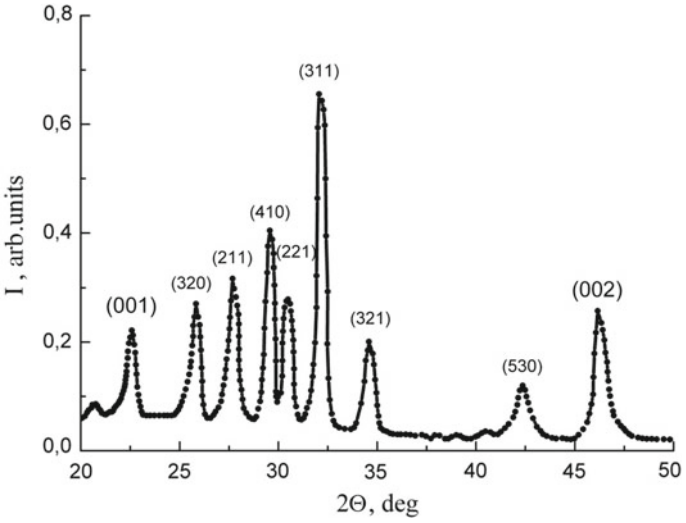

Fig. 17.1 X-ray diffraction pattern of $Sr_{0.61}Ba_{0.39}Nb_2O_6$

17.4 Dielectric Properties

The temperature dependences of the permittivity ε were studied in the temperature range from 288 to 400 K at frequencies of 10 kHz, 100 kHz, 1 MHz. The measurements were carried out on the basis of a stand consisting of HIOKI 3535, HIOKI 3533 RLC meters, a specially designed sample holder with a heater and shielded RF inputs, placed in a fore-vacuum cryostat, a programmable precision PID temperature regulator, a thermocouple temperature meter, and a PC controller with special software. All devices were integrated into the command-measuring network of the test bench, which made it possible to measure temperature, heat the sample according to a linear law, and study dielectric characteristics in real time. The heating rate of the sample was 0.2 K/s. The temperature dependence of the permittivity of BSN ceramic samples with a Sr/Ba percentage of 61% ($Sr_{0.61}Ba_{0.39}Nb_2O_6$) is shown in Fig. 17.2. The measurements were performed at a frequency of 100 kHz, the amplitude was 0.5 V.

It can be seen from the figure that the temperature dependence $\varepsilon(T)$ for non-doped barium-strontium niobates ceramics had the form of a monotonic asymmetric with respect to the position of the curve maximum with regions of monotonous growth and sharp decline. The phase transition temperature for undoped ceramics corresponds to 83 °C. The type of temperature dependence of the permittivity, as well as the position of the maximum (phase transition temperature), coincides with published data [12]. Figure 17.3 shows the temperature dependence of the permittivity, measured for ceramic samples of barium-strontium niobates doped with cerium, neodymium, lanthanum, and ytterbium ions. The frequency and amplitude of the sinusoidal signal were the same as measured by $\varepsilon(T)$ for a sample of non-doped BSN ceramics.

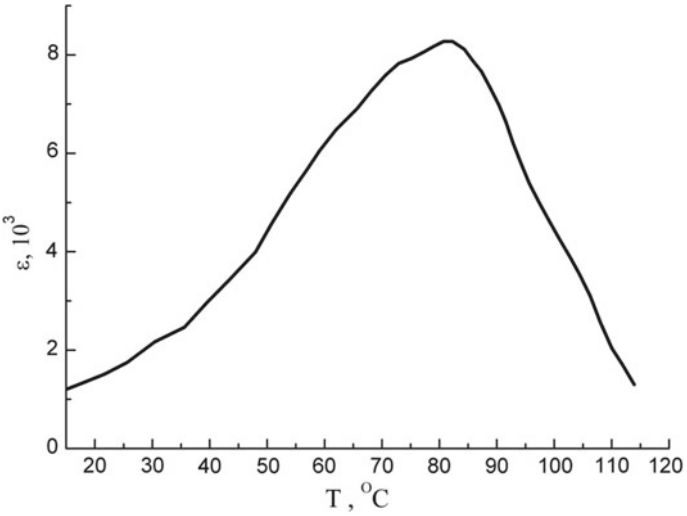

Fig. 17.2 Temperature dependence of the permittivity of BSN-61 ceramics

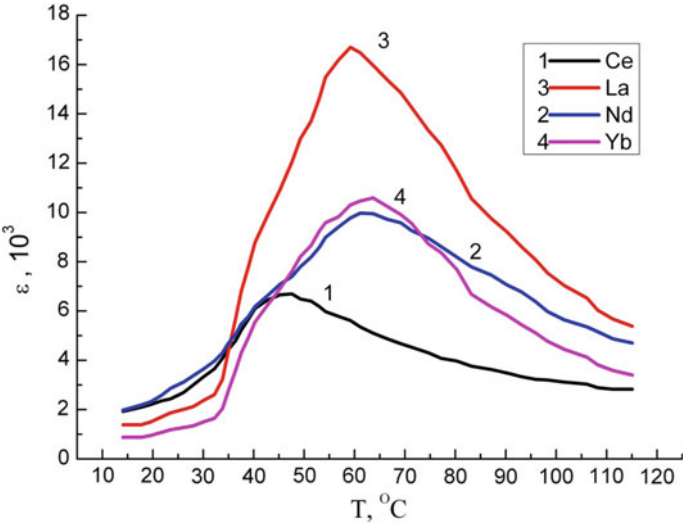

Fig. 17.3 Temperature dependence of the permittivity of BSN: REM ceramic samples: 1-BSN:Ce; 2-BSN:Nd; 3-BSN:La; 4-BSN:Yb

The temperature dependences of the permittivity of the doped samples changed in comparison with Fig. 17.2. For the cerium-doped sample, there is a sharp increase in the dependence $\varepsilon(T)$ and its gentle decline. The position of the maximum shifted significantly to lower temperatures and amounted to 47.6 °C. For the neodymium- and ytterbium-doped samples, the positions of the maxima $\varepsilon(T)$ are close in position:

for BSN: Nd $T_{max} = 61.1$ °C, and for BSN: Nb $T_{max} = 63.7$ °C. However, the form of the temperature dependences $\varepsilon(T)$ for these samples is radically different: the $\varepsilon(T)$ dependence for the BSN: Nd sample has regions of gentle growth and gentle decline, the graph is close to symmetric with respect to the maximum point. For the BSN: Yb sample, the plot of $\varepsilon(T)$ also contains a region of growth and a region of gentle decline, however, the region of growth consists of two regions: a quasilinear region of growth of $\varepsilon(T)$ from 15 to 35 °C and a region of sharp increase in permittivity ε in the range temperatures from 35 °C to the phase transition point. The temperature dependence of the permittivity for a lanthanum-doped sample looks in a separate way. The temperature dependence of the permittivity $\varepsilon(T)$ consists of a growth region consisting of a quasilinear region in the temperature range from 15 to 33 °C, a region of a sharp increase in permittivity in the temperature range from 35 °C to the phase transition point. After the phase transition point, the dependence $\varepsilon(T)$ decreases almost at the same rate as it grows. The temperature position of the maxima of the $\varepsilon(T)$ dependence in the doped samples practically coincides; the phase transition temperatures differ by 2.6°. In addition, the permittivity values for these samples have close values. The lanthanum-doped sample has the highest permittivity; the ε value in the vicinity of the phase transition point is 1.7 times larger than the samples containing neodymium or ytterbium ions and 2.83 times larger than the ε value corresponding to the phase transition point for the sample containing cerium or sample BSN non-doped ceramics.

Thus, when the Sr/Ba ratio in the studied ceramics is 61% (BSN-61 ceramics), the alloying of barium-strontium niobates ceramics with rare-earth metal ions, in a percentage ratio of 1.2–1.3%, made it possible to significantly change the phase transition temperature compared to the initial ceramics. The values of the temperature of the phase transition from the type of alloying ions of rare-earth metals are given in Table 17.1.

The results of studies of the temperature dependences of the permittivity $\varepsilon(T)$ for lanthanum-doped ceramics are shown in Fig. 17.4. The measurements were performed at frequencies of 10 kHz, 100 kHz, and 1 MHz.

From literature data, it is known that in non-doped BSN ceramics, the frequency dependence of the position of the maximum of the permittivity on temperature is characteristic of ferroelectric relaxators [13]. For samples of barium-strontium niobates ceramics doped with rare-earth metal ions, with an increase in the frequency of the measuring signal from 10 kHz to 1 MHz, a shift in the position of the maxima

Table 17.1 Effect of doping with rare-earth metal ions on the phase transition temperature in BSN-61 ceramics

Ceramic sample	The concentration of rare earth ions, %	Phase transition temperature, T, °C
BSN-61	0	85
BSN-61: Nd_2O_3	1.3	61.1
BSN-61: La_2O_3	1.2	59.2
BSN-61: Yb_2O_3	1.3	63.7
BSN-61: CeO_2	1.3	47.6

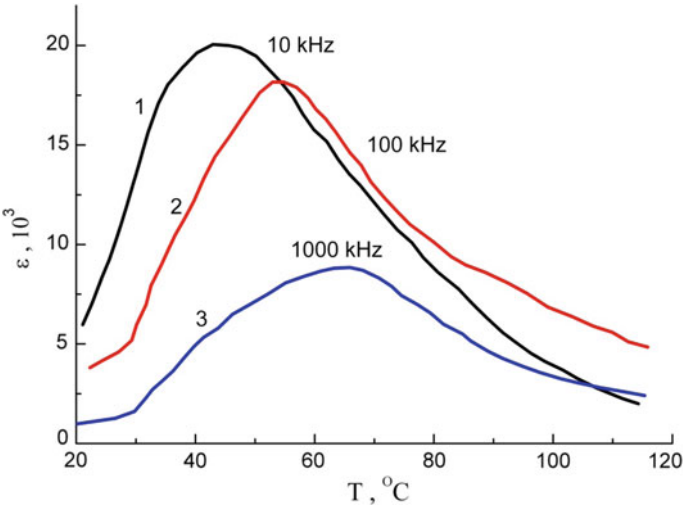

Fig. 17.4 Change in the $\varepsilon(T)$ dependence of BSN:La ceramics for different measurement frequencies: 1—the measurement frequency is 10 kHz; 2—measurement frequency is 100 kHz; 3— measurement frequency is 1000 kHz

of the permittivity curves to a region of higher temperatures is observed, and at the same time, the permittivity decreases. Thus, the behavior of the $\varepsilon(T)$ dependence for ceramic samples doped with rare-earth metal ions completely coincides with that described in the literature for relaxor ferroelectrics.

17.5 Optical Properties at THz

The spectral dependence of the absorption coefficient in the terahertz spectrum $\alpha(\nu)$ for barium-strontium niobates ceramic was studied using a radio-frequency photon generation of THz radiation with a time resolution [9]. The spectral band of the installation was in the range 0.1–1.0 THz. The terahertz radio photon spectrometer is based on the classical scheme: a pulsed IR femtosecond laser was used to pump a direct-gap semiconductor (InAs), which was placed inside a cryostat through which a magnetic field was transmitted from a powerful solenoid. The irradiation of the surface of a direct-gap semiconductor by the incident radiation of a femtosecond IR laser coupled with a magnetic field applied to the semiconductor determined the emission characteristics of the generated electron-hole pair in the semiconductor. Then, terahertz radiation passed through the BSN ceramic sample under study and focused on a nonlinear electro-optical crystal. The polarization of the crystal medium changed in proportion to the absorbed energy of the incident terahertz radiation, which affects the polarization state of the probe beam. The probe beam was subsequently divided

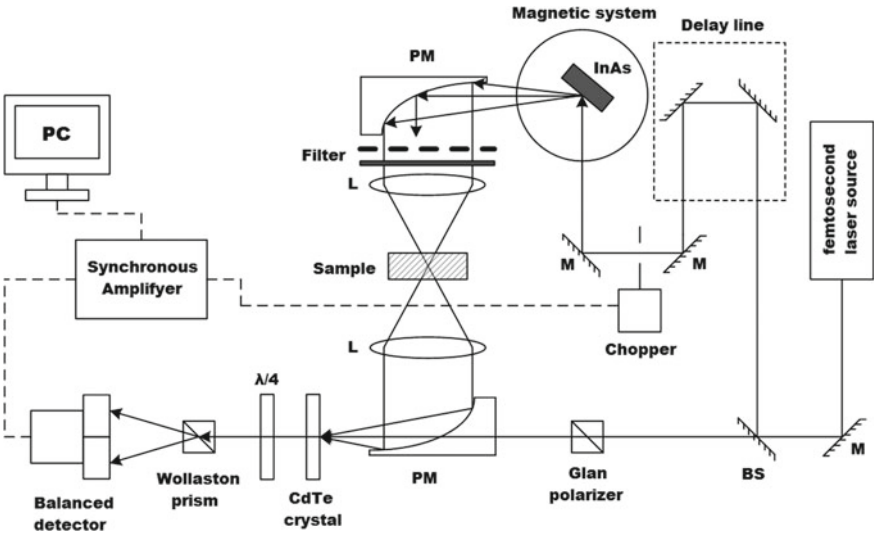

Fig. 17.5 Scheme of a terahertz radio photon spectrometer with time resolution

by a Wollaston prism into two beams with orthogonal polarizations and the difference in their intensities was recorded using a balanced detector. The waveform was obtained by changing the phase between the pump beam and the reference beam by the operation of the optical delay line. To obtain the desired dependence $\alpha(\nu)$, the recorded signal was subjected to Fourier transform to obtain the frequency domain of the transmission spectrum of the sample (Fig. 17.5).

The spectral dependences of the absorption coefficient $\alpha(\nu)$ of BSN ceramic samples in the terahertz range are shown in Fig. 17.6. The spectral dependence $\alpha(\nu)$ for non-doped BSN ceramics in the spectral range of 0.1–1.0 THz is a flat monotonic curve with a region of slight increase in the absorption coefficient in the band of 0.45–0.65 THz. The absorption coefficient for non-doped BSN ceramics does not exceed 15%. A completely different type of dependence $\alpha(\nu)$ takes place for ceramic samples doped with rare-earth metal ions. The spectral dependence $\alpha(\nu)$ for the lanthanum-doped sample has the form of a monotonically decreasing curve with a plateau region in the spectral band of 0.35–0.9 THz. For neodymium-doped ceramics, the dependence $\alpha(\nu)$ has the form of a complex curve consisting of several regions: a monotonically decreasing curve in the band of 0.1–0.5 THz, a plateau region in the band of 0.5–0.6 THz, and a broad peak of insignificant intensity in the band of 0.67–0.75 THz passing into the region of monotonic decay in the band of 0.75–1.0 THz. The spectral dependence of $\alpha(\nu)$ for cerium-doped ceramics has the form different from the curves of $\alpha(\nu)$ for the previously considered samples. In the 0.1–0.33 THz band, the curve monotonically decreases from 40 to 35% and further, in the 0.33–1.0 THz band, there is a broad peak with a maximum of about 0.6 THz.

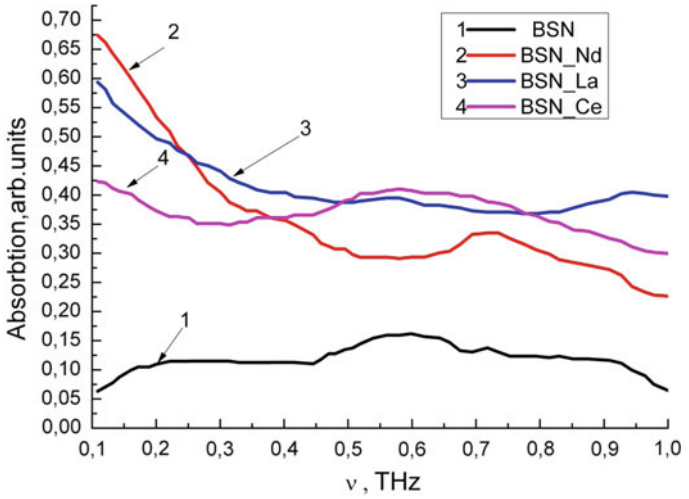

Fig. 17.6 Spectral dependence of the absorption coefficient of BSN ceramic samples at the terahertz range: 1-BSN-61; 2-BSN:Nd; 3-BSN:La; 4-BSN:Ce

17.6 Conclusions

Doping of BSN ceramics with rare-earth metal ions leads to a significant decrease in the phase transition temperature relative to the temperature position of the phase transition for non-doped ceramics $Sr_xBa_{1-x}Nb_2O_6$, $x = 0.61$. The influence of rare-earth metal ions doping on the behavior of the temperature dependence in BSN ceramics is more significant than a change in the Sr/Ba ratio in the composition of the ceramic. According to published data, a change in the Sr/Ba ratio from 61 to 75% changes the phase transition temperature from 85 to 48 °C. At the same time, when the Sr/Ba ratio is equal to 61% in barium-strontium niobate ceramics, the introduction of rare-earth metal ions in its composition in a percentage ratio of about 1.5% allows one to reduce the phase transition temperature from 85 °C for pure BSN-61 to 61.1 °C when doping ceramics Nd-ions. In the case of introducing Yb-ions into the ceramic composition, the phase transition temperature was 63.7 °C. In the case when lanthanum ions were introduced into the composition of the initial ferroelectric ceramics, the phase transition temperature was 59.2 °C. The greatest shift in the temperature of the phase transition to lower temperatures was found when doping ferroelectric ceramics with cerium ions, in this case the phase transition temperature was 47.6 °C.

For all samples of barium-strontium niobate ceramics, both doped with rare-earth metal ions and non-doped (BSN-61), the behavior of the dependence of $\varepsilon(T)$ on the frequency of the measuring signal was studied. For this, the dependences $\varepsilon(T)$ at three frequencies of the sinusoidal measuring signal were studied for all samples: 10 kHz, 100 kHz, and 1 MHz. The amplitude of the measuring signal supplied to the sample was maintained in all cases equal to 0.5 V. In the experiment, all samples

showed a shift in the position of the maxima of the permittivity curves $\varepsilon(T)$ to higher temperatures with increasing frequency, and at the same time, the permittivity decreased. Thus, the behavior of the $\varepsilon(T)$ dependence for ceramic samples doped with rare-earth metal ions completely coincides with that described in the literature for relaxor ferroelectrics.

The study of the spectral dependence of the absorption coefficient $\alpha(\nu)$ in all types of the studied samples showed that the introduction of rare-earth metal ions into the $Sr_{0.61}Ba_{0.39}Nb_2O_6$ ceramic composition leads to a significant change in the dependence $\alpha(\nu)$. The spectral dependence of the absorption coefficient of non-doped BSN ceramics has the form of a flat curve with a region of slight excess. The absorption coefficient for this material lies in the terahertz range of the spectrum in the range of 10–15%. This allows the use of such ceramics as part of THz radiation sensors, only if a layer absorbing submillimeter radiation is deposited on the ceramic surface. The introduction of rare-earth metal ions into the $Sr_{0.61}Ba_{0.39}Nb_2O_6$ ceramic composition can significantly increase the absorption coefficient of radiation in the terahertz region of the spectrum and form materials having regions of increased absorption or materials having $\alpha(\nu)$ in individual terahertz spectral bands. The introduction of cerium ions makes it possible to synthesize ferroelectric ceramics suitable for creating pyroelectric sensors in the THz range with increased sensitivity in the band of 0.4–0.9 THz. Alloying BSN ceramics with neodymium ions allows one to synthesize a ferroelectric medium for a pyrodetector, which has a uniform sensitivity in the band of 0.5–0.65 THz and an increased sensitivity in the band of 0.7–0.75 THz. The introduction of lanthanum ions into the composition of $Sr_{0.61}Ba_{0.39}Nb_2O_6$ ceramics makes it possible to synthesize ferroelectric material suitable for creating pyroelectric sensors in the THz range with uniform sensitivity in the spectral band of 0.35–0.95 THz.

References

1. G.N. Tolmachev, A.P. Kovtun, I.N. Zakharchenko, I.M. Aliev, A.V. Pavlenko, L.A. Reznichenko, I.A. Verbenko. Phys. Solid State **57**, 2050 (2015)
2. P.R. Wilmont, R. Herger, B.D. Patterson, R. Windiks, Phys. Rev. B **7**, 144114 (2005)
3. K.A. Vorotilov, V.M. Mukhortov, A.S. Sigov, *Integrated Ferroelectric Devices.* (M. Energoatomizdat, 2011), 175p (in Russian)
4. T.R. Volk, V.A. Salobutin, L.I. Ivleva, N.M. Polozkov, R. Pankrat. M. Veleke, Phys. Solid State **42**, 2066 (2000)
5. D.V. Isakov, M.S. Belsley, T.R. Volk, L.I. Ivleva, Appl. Phys. Lett. **92**, 032904 (2008)
6. U. Doerfler, R. Piechatzek, T. Woike, M.K. Imlay, V. Wirth et al. *Appl. Phys.* B **68**(5), 843 (1999)
7. D. Kasprowicz, T. Runka, A. Speghini, D. Falcomer, J. García Solé, M. Bettinelli, J. Lumin. **128**, 985–987 (2008)
8. A.A. Rusakov, *X-ray Analysis of Metals* (Atomizdat, Moscow, 1977), 480p (in Russian)
9. V.I. Iveronova, G.P. Revkevich. *Theory of X-ray Scattering*. (Moscow State University Press, Moscow, 1972), 246p (in Russian)
10. P.B. Jameison, J. Chem. Phys. **48**(11), 5048–5057 (1968)
11. T. Tsurumi, Y. Hoshino, J. Am. Ceram. Soc. **72**, 278 (1989)

12. J. Oliver, R.R. Neurgaonkar, L. Corss, J. Appl. Phys. **64**(1), 37 (1988)
13. W.H. Huang, D. Viehland, R.R. Neurgaonkar, J. Appl. Phys. **76**(1), 490 (1994)

Chapter 18
Universal Technique to Determine the Intensity of the Optical Fields, Generated by Laser Interference Meter of Displacements

I. P. Miroshnichenko, I. A. Parinov, and V. P. Sizov

Abstract Universal technique is proposed in the work. The relationships for determining the intensity of the optical fields generated by the laser interference displacement meter based on a two-way laser interferometer with combined branches and implementing the method of highlighting the surface of the test object are described in detail. The proposed relations allow one to carry out computational and theoretical modeling and study of functional characteristics in the interests of creating new promising optical instruments for measuring the displacements of the surfaces of objects under control.

18.1 Introduction, Problem Statement, Initial Relations and Assumptions

Currently, one of the most relevant and promising areas for improving stationary and mobile diagnostic systems is the development of high-precision non-contact measurement tools for measuring the movement of surfaces of control objects to diagnose the state of structural materials and products, for example, when using acoustic active methods of non-destructive testing.

There are known high-precision non-contact means for measuring the movement of surfaces of control objects [1–3], based on a two-way laser interferometer with combined branches [4, 5], and implementing the method of highlighting the surface of the control object [6]. They are developed using modern laser technologies and new methods of optical interferometry, scientifically justified [6–8], tested and used in solving various problems [9, 10].

Successful application and further development of these devices is possible when creating a scientific and methodological apparatus that allows for computational and

I. P. Miroshnichenko (✉)
Don State Technical University, Rostov-on-Don, Russia
e-mail: ipmir@rambler.ru

I. A. Parinov · V. P. Sizov
Southern Federal University, Rostov-on-Don, Russia

I. A. Parinov et al. (eds.), *Advanced Materials*, Springer Proceedings in Materials 6, https://doi.org/10.1007/978-3-030-45120-2_18

theoretical modeling and research of functional characteristics in the interests of creating new promising optical means for measuring the movement of surfaces of control objects that implement the method of highlighting the surface of the control object. It is the purpose of developing the results described in this chapter.

The pointed laser interference displacement meter (see Fig. 18.1) can be represented as optically coupled and sequentially placed coherent electromagnetic radiation source 1, optical system 2, beam splitter 3, reflector 4, and photodetector 5.

In this case, the beam splitter with a known amplitude transmission is located in the plane S. The Cartesian coordinate system $\{x, y, z\}$ is associated with this plane. The reflector is located in a plane S_3 that is under an angle α to the beam splitter and at a distance h from it. The beam splitter receives coherent radiation from a luminous point O' that is initially determined by coordinates $x_0, y_0, z_0 = 0$. For example, a sinusoidal diffraction grating can be used as a beam splitter. The photodetectors used to analyze the interference pattern are located in the Fresnel or Fraunhofer zone.

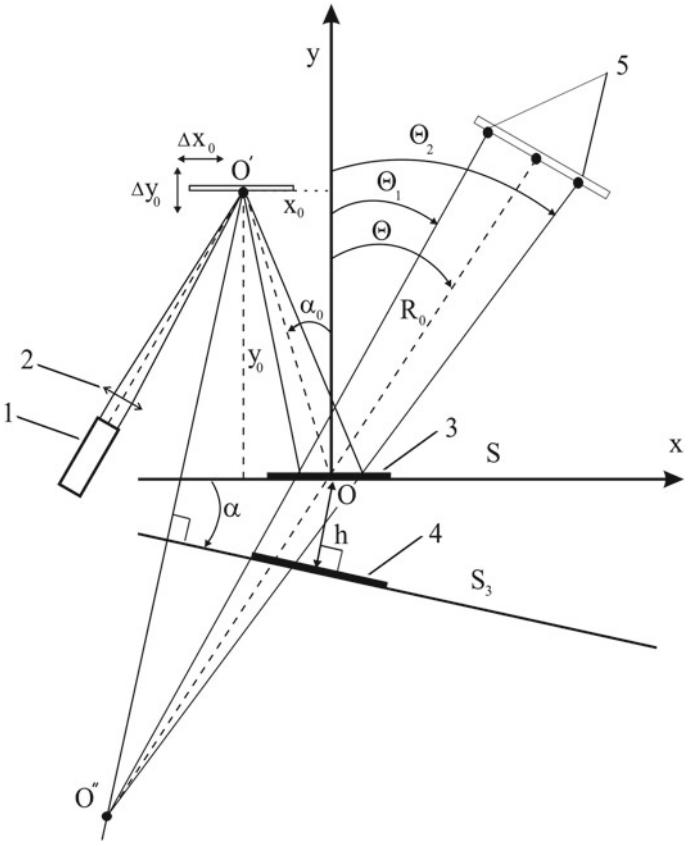

Fig. 18.1 Scheme of the displacement meter

This device allows one to determine the movement of the surface of the control object in two cases by creating an interference pattern in the area where the photodetector devices are located. In the first case, when there is a "luminous point" on the surface of the control object, which occurs when the focused laser radiation is reflected and is indicated on the scheme O'. In the second case, a reflector is connected to the surface of the control object. In the first case, the parameters of the interference pattern must determine the change of coordinates Δx_0, Δy_0, in the second, if x_0, y_0 are unchanged, it is necessary to find the values α and h.

Thus, to determine the movement of the surface of object, it is necessary to find an electromagnetic field, scattered by the device in the Fresnel zone, where there is an interference pattern and its dependence on the position of a luminous point x_0, y_0 or from the parameters characterizing the location of the reflecting surface α and h.

The mathematical formulation of the problem is as follows. The electromagnetic field E, H according to the uniqueness of the solution of the boundary value problem must satisfy:

(i) Maxwell Equations:

$$rotH = i\omega\tilde{\varepsilon}_0 E; \quad rotE = -i\omega\tilde{\mu}_0 H, \tag{18.1}$$

where $\tilde{\mu}_0$ and $\tilde{\varepsilon}_0$ are the magnetic and dielectric permittivity of vacuum.

(ii) Radiation condition:

$$\lim_{R\to\infty}\left(\frac{\partial E}{\partial R} + ikE\right) = 0. \tag{18.2}$$

(iii) Boundary conditions on the surface of the interferometer.

It is assumed that the thickness of the beam splitter and its absorption coefficient are zero.

It is necessary to solve the electrodynamic problem of determining the intensity of the optical field in the area where the photodetector devices are located, depending on the movement of the "luminous point" and the parameters of the measuring device.

18.2 Relations for Determining the Strength and Intensity of the Electromagnetic Field at Observation Points

To determine the distribution of the field intensity in the area of the location of photodetectors, we use Green's theorem in tensor form, which connects vector fields in different areas of space [11]:

$$F_{s'}(P') = \int\limits_V Q_s G^s_{s'} \mathrm{d}v + \frac{1}{4\pi} \int\limits_S [G^s_{s'} \nabla_r F^r - F^s \nabla^p G_{ps'}) + \varepsilon_{\mathrm{rsm}} n^r G^s_{s'} \varepsilon^{ikm} \nabla_i F_k - \varepsilon_{\mathrm{rsm}} n^r F^s \varepsilon^{ikm} \nabla_i G_{ks'})] \mathrm{d}S. \tag{18.3}$$

We impose mixed Dirichlet–Neumann boundary conditions on the Green's tensor function [12], and also take into account that the electromagnetic field has a transverse character and satisfies the Maxwell equations. Then, the components of the vector E in the observation area can be expressed as tangent components of the electric field strength vector E_τ on the surface where the sources are located:

$$E_{S'} = \frac{1}{4\pi} \int\limits_s (E^2 (\nabla_1 G^{Д}_{2s'} - \nabla_2 G^N_{1s'}) + E^3 (\nabla_1 G^{Д}_{3s'} - \nabla_3 G^N_{1s'})) ds \cdot \tag{18.4}$$

Here, the dashed indices are referred to the observation points that we will define in the spherical coordinate system $\{r', \Theta', \psi'\}$, and the 1, 2, 3 indices are referred to the source points that lie on the surface of the beam splitter ($y = 0$). The coordinate with the index "1" coincides (with the opposite sign) with the unit normal $\bar{n}$ to S, external to the area V under consideration.

If a spot close to a circle is formed on the beam splitter from the source, it is convenient to enter a cylindrical coordinate system, where "1" $\to y$, "2" $\to \rho$, "3" $\to \varphi$; $E_{s'}$ is the covariant vector, E^i is the contravariant vector, ∇_i is the covariant derivative, $G^{ДN}{}_{is'}$ is the Green's tensor function that satisfies a non-uniform equation:

$$\nabla^p \nabla_p G_{is'} + k^2 G_{is'} = -4\pi g_{is'} \delta(r - r'), \tag{18.5}$$

where $g_{is'}$ is the operator of coordinate transformation:

$$g_{is'} = \frac{\partial \xi_\nu}{\partial x^i} \frac{\partial \xi'_\nu}{\partial x^{s'}}. \tag{18.6}$$

In this case, it is performed a summing on ν, and the coordinates ξ_ν are Cartesian.

The Green's tensor function must satisfy the following boundary conditions:

$$\nabla^1 \overset{N}{G}_{1\tilde{S}} = \frac{\partial}{\partial y} \overset{N}{G}_{y\tilde{S}} = 0; \quad \overset{D}{G}_{2\tilde{S}} = \overset{D}{G}_{3\tilde{S}} = 0 \in S. \tag{18.7}$$

For a round spot on the surface of the beam-splitter, it is convenient to describe the sources in a cylindrical coordinate system $\{\rho(2), \varphi(3), y(1)\}$:

$$x = \rho \cdot \sin\varphi; \quad y = y; \; z = \rho \cdot \cos\varphi.$$

$$\text{Lamé coefficients}: \; h_{\rho'} = 1, \quad h_{\varphi'} = \rho, \quad h_{y'} = 1. \tag{18.8}$$

Observation points are usually defined in a spherical coordinate system $\{r', \Theta', \Psi'\}$:

$$x' = r' \sin\Theta' \sin\Psi'; \; y' = r' \cos\Theta'; \; z' = r' \sin\Theta' \cos\Psi'. \tag{18.9}$$

$$\text{Lamé coefficients}: \; h_{r'} = 1; \; h_{\Theta'} = r'; h_{\varphi'} = r' \cdot \sin\Theta'.$$

With this in mind, the coordinate conversion operator calculated by (18.6) has the following form:

$$g_{\rho r'} = \sin\varphi \sin\Theta' \sin\psi' + \cos\varphi \sin\Theta' \cos\psi' = \sin\Theta' \cos(\varphi - \psi');$$

$$g_{\rho\Theta'} = \sin\varphi r \cos\Theta' \sin\psi' + \cos\varphi \cos\Theta' \cos\psi' r' = r \cos\Theta' \cos\left(\varphi - \psi'\right);$$

$$g_{\rho\psi'} = \sin\varphi r' \sin\Theta' \cos\psi' - \cos\varphi r' \sin\Theta' \sin\psi' = r' \sin\Theta' \sin\left(\varphi - \psi'\right);$$

$$g_{\varphi r'} = \rho \cos\varphi \sin\Theta' \sin\psi' - \rho \sin\varphi \sin\Theta' \cos\psi' = \rho \sin\Theta' \sin\left(\psi' - \varphi\right);$$

$$g_{\varphi\Theta'} = \rho \cos\varphi r' \cos\Theta' \sin\psi' - \rho \sin\varphi r' \cos\Theta' \cos\psi' = \rho r' \cos\Theta' \sin\left(\psi' - \varphi\right);$$

$$g_{\varphi\psi'} = \rho \cos\varphi r' \sin\Theta' \cos\psi' + \rho \sin\varphi r' \sin\Theta' \sin\psi' = \rho r' \sin\Theta' \cos\left(\varphi - \psi'\right);$$

$$g_{yr'} = \cos\Theta';$$

$$g_{y\Theta'} = -r' \sin\Theta';$$

$$g_{y\psi'} = 0. \tag{18.10}$$

By using (18.4), we write the expressions for the Θth component of the electric field strength:

$$E_{\Theta'} = \frac{1}{4\pi} \int\limits_s (E^{\rho}(\nabla_y G^D_{\rho\Theta'} - \nabla_{\rho} G^N_{y\Theta'}) + E^{\varphi}(\nabla_y G^D_{\varphi\Theta'} - \nabla_{\varphi} G^N_{y\Theta'}))ds. \tag{18.11}$$

Here:

$$G^D_{\rho\Theta'} = G^D g_{\rho\Theta'}; \quad G^N_{y\Theta'} = G^N g_{y\Theta'}; \quad G^D_{\varphi\Theta'} = G^D g_{\varphi\Theta'}, \tag{18.12}$$

where

$$G^N = \frac{e^{ikr}}{r} + \frac{e^{ikr^*}}{r^*}; \quad G^D = \frac{e^{ikr}}{r} - \frac{e^{ikr^*}}{r^*}, \tag{18.13}$$

r^* is the distance between the observation point and the point that is a mirror image of the source point; it is defined by the following expression:

$$\begin{aligned}(r^*)^2 &= (x - x')^2 + (y + y')^2 + (z - z')^2 \\ &= (\rho \cdot \sin\varphi - r' \cdot \sin\Theta' \cdot \sin\Psi')^2 + (y + r' \cdot \cos\Theta')^2 \\ &\quad + (\rho \cdot \cos\varphi - r' \cdot \sin\Theta' \cdot \cos\Psi')^2;\end{aligned} \tag{18.14}$$

r is the distance between the observation point and the source point;

$$\begin{aligned}r^2 &= (x - x')^2 + (y - y')^2 + (z + z')^2 \\ &= (\rho \cdot \sin\varphi - r' \cdot \sin\Theta' \cdot \sin\Psi')^2 + (y - r' \cdot \cos\Theta')^2 \\ &\quad + (\rho \cdot \cos\varphi + r' \cdot \sin\Theta' \cdot \cos\Psi')^2.\end{aligned} \tag{18.15}$$

By using (18.10), we write the covariant derivatives, included in (18.11):

$$\begin{aligned}\nabla_y G^D_{\rho\Theta'} &= \nabla_y G^D_{(\rho\Theta')}[r' \cos\Theta' \cos(\varphi - \psi')] \\ &= \frac{\partial G^D}{\partial y} \cdot r' \cdot \cos\Theta' \cdot \cos(\varphi - \psi') \\ &= \frac{\partial r}{\partial y} \cdot \frac{\partial G^D}{\partial r} \cdot r' \cdot \cos\Theta' \cdot \cos(\varphi - \psi'),\end{aligned} \tag{18.16}$$

where

$$\begin{aligned}\frac{\partial r}{\partial y} &= \frac{y - y'}{r} = \frac{y - r'\cos\Theta'}{r}; \\ \frac{\partial r}{\partial \rho} &= \frac{1}{r}((\rho \sin\varphi - r' \sin\Theta' \sin\psi')\sin\psi' + (\rho\cos\varphi - r\sin\Theta'\cos\psi')\cos\varphi) \\ &= \frac{1}{r}(\rho - r'\sin\Theta'\cos(\varphi - \psi'); \\ \frac{\partial r}{\partial \varphi} &= \frac{1}{r}((\rho \sin\varphi - r' \sin\Theta' \sin\psi')\rho\cos\psi' - (\rho\cos\varphi - r\sin\Theta'\cos\psi')\rho\sin\varphi) \\ &= \frac{\rho}{r} r' \sin\Theta'\cos(\varphi - \psi'); \\ \frac{\partial r^*}{\partial y} &= \frac{y + y'}{r} = \frac{y + r'\cos\Theta'}{r}.\end{aligned} \tag{18.17}$$

Substituting (18.17) and taking into account that $\frac{\partial}{\partial r} \cdot \frac{e^{ikr}}{r} = -\frac{e^{ikr}}{r^2}(1 - ikr)$, we obtain:

$$\nabla_\rho G^N_{y\Theta} = \left\{ -\frac{e^{ikr}}{r^2}\frac{1}{r}[\rho - r'\sin\Theta'\cos(\varphi-\psi')](1-ikr) \right.$$
$$\left. -\frac{e^{ikr*}}{(r^*)^2}\frac{1}{r^*}[\rho - r'\sin\Theta'\cos(\varphi-\psi')](1-ikr^*) \right\} \cdot r' \cdot \sin\Theta';$$
$$\nabla_y G^N_{\rho\Theta'} = \left[-\frac{e^{ikr}}{r^2}(1-ikr)\frac{y - r'\cdot\cos\Theta'}{r} + \frac{e^{ikr^*}}{(r^*)^2}(1-ikr^*)\cdot\frac{y + r'\cdot\cos\Theta'}{r^*} \right]$$
$$\times \rho \cdot r' \cdot \cos\Theta' \cdot \sin(\psi' - \varphi);$$
$$\nabla_\varphi G^N_{y\Theta'} = -2\frac{e^{ikr}}{r^2}\cdot(1-ikr)\frac{1}{r}\cdot\rho\cdot r'\cdot\sin\Theta'\sin(\varphi-\psi')\cdot r'\cdot\sin\Theta';$$
$$\nabla_y G^D_{\rho\Theta} = \left[-\frac{e^{ikr}}{r^2}\cdot(1-ikr)\cdot\frac{1}{r}\cdot(y - r'\cos\Theta') + \frac{e^{ikr^*}}{(r^*)^2}\cdot(1-ikr^*) \right.$$
$$\left. \cdot\frac{1}{r^*}(y + r'\cos\Theta') \right] \times r'\cdot\cos\Theta'\cdot\cos(\varphi-\psi'). \tag{18.18}$$

The expression for the Θ'th component of the electric field strength is defined as:

$$\nabla_\rho G^N_{y\Theta'} = \nabla_\rho G^N_{(y\Theta')}\cdot(-r'\cdot\sin\Theta') = -\frac{\partial G^N}{\partial\rho}\cdot r'\cdot\sin\Theta'$$
$$= -\frac{\partial r}{\partial\rho}\cdot\frac{\partial G^N}{\partial r}\cdot r'\cdot\sin\Theta';$$
$$\nabla_y G^D_{\varphi\cdot\Theta'} = \nabla_y G^D_{(\varphi\cdot\Theta')}\rho\cdot r'\cdot\cos\Theta'\cdot\sin(\psi'-\varphi)$$
$$= \frac{\partial G^D}{\partial y}\cdot\rho\cdot r'\cdot\cos\Theta'\cdot\sin(\psi'-\varphi)$$
$$= \frac{\partial r}{\partial y}\frac{\partial G^D}{\partial r}\cdot\rho\cdot r'\cdot\cos\Theta'\cdot\sin(\psi'-\varphi); \tag{18.19}$$

$$\nabla_\varphi G^N_{y\cdot\Theta'} = \nabla_\varphi\cdot G^N_{(y\cdot\Theta')}\cdot(-r'\cdot\sin\Theta') = -\frac{\partial G^N}{\partial\varphi}\cdot r'\cdot\sin\Theta'$$
$$= -\frac{\partial r}{\partial\varphi}\cdot\frac{\partial G^N}{\partial\varphi}\cdot r'\cdot\sin\Theta'. \tag{18.20}$$

Substituting (18.20) into (18.11) at $y = 0$ and using the Lamé coefficients for cylindrical (18.8) and spherical (18.9) coordinate systems, we consider the physical components of the vector E. The expression for determining the Θth component of the electric field strength vector has the form:

$$E_{(\Theta')} = \frac{1}{4\pi}\int_s 2\frac{e^{ikr}}{r^2}(1-ikr)\left(E_{(\rho)}\left(\frac{r'}{r}\cos^2\Theta'\cos(\varphi-\psi')\right.\right.$$
$$\left.\left. -\frac{\rho}{r}\sin\Theta' + \frac{r'}{r}\sin^2\Theta'\cos(\varphi-\psi')\right)\right.$$

$$+E_{(\varphi)}\left[\frac{r'}{r}\cdot\cos^2\Theta'\cdot\sin(\psi'-\varphi)-\frac{r'}{r}\cdot\sin^2\Theta'\cdot\sin(\varphi-\psi')\right]\Bigg\}ds; \tag{18.21}$$

$$E_{(\Theta')}=\frac{1}{2\pi}\int\limits_s\frac{e^{ikr}}{r^2}\cdot(1-ikr)\cdot\left\{E_{(\rho)}\left[\frac{r'}{r}\cos(\varphi-\psi')-\frac{\rho}{r}\sin\Theta'\right]\right.$$
$$\left.+E_{(\varphi)}\cdot\frac{r'}{r}\cdot\sin(\psi'-\varphi)\right\}\mathrm{d}s. \tag{18.22}$$

Similarly, we can write for the Ψ'th component of the vector E at the observation point:

$$E_{\psi'}=\frac{1}{4\pi}\int\limits_s[E^{\rho}(\nabla_y G^D_{\rho\cdot\psi'}-\nabla_\rho G^N_{y\cdot\psi'})+E^{\varphi}(\nabla_y G^D_{\varphi\cdot\psi'}-\nabla_\varphi G^N_{y\cdot\psi'})]ds, \tag{18.23}$$

where

$$\begin{aligned}
\nabla_y G^D_{\rho\cdot\psi'}&=\nabla_y G^D_{(\rho\psi')}g_{\rho\psi'}=\nabla_y G^D_{(\rho\psi')}\cdot r'\cdot\sin\Theta'\cdot\sin(\varphi-\psi')\\
&=2\cdot\frac{e^{ikr}}{r^2}\cdot(1-ikr)\cdot\frac{r'}{r}\cdot\cos\Theta'\cdot r'\cdot\sin(\varphi-\psi')\cdot\sin\Theta';\\
\nabla_\rho G^N_{y\psi'}&=-2\cdot\frac{e^{ikr}}{r^2}\cdot(1-ikr)\cdot\frac{1}{r}[\rho-r'\sin\Theta'\cos(\varphi-\psi')]\cdot 0=0;\\
\nabla_y G^D_{\varphi\psi'}&=2\cdot\frac{e^{ikr}}{r^2}\cdot(1-ikr)\cdot\frac{r'}{r}\cdot\cos\Theta'\cdot\rho\cdot r'\cdot\sin\Theta'\cdot\cos(\varphi-\psi');\\
\nabla_\varphi G^N_{y\psi'}&=0.
\end{aligned} \tag{18.24}$$

The expression for determining the Ψ'th component of the electric field strength vector will have the following form:

$$E_{(\psi')}=\frac{1}{2\pi}\int\limits_s\frac{e^{ikr}}{r^2}\cdot(1-ikr)\cdot\left\{E_{(\rho)}\cdot\frac{r'}{r}\cos\Theta'\sin(\varphi-\psi')\right.$$
$$\left.+E_{(\varphi)}\cdot\frac{r'}{r}\cdot\cos\Theta'\cdot\cos(\varphi-\psi')\right\}ds; \tag{18.25}$$

$$E_{(\psi')}=\frac{1}{2\pi}\int\limits_s\frac{e^{ikr}}{r^2}\cdot(1-ikr)\cdot\frac{r'}{r}\cdot\cos\Theta'\cdot[E_{(\rho)}\cdot\sin(\varphi-\psi')+E_{(\varphi)}\cos(\varphi-\psi')]ds. \tag{18.26}$$

Thus, to determine the field in the observation area, we need to know the field on the surface of the beam-splitter. For the case of placing the photodetector in the far zone, we can put $r=r'=R_0$ in the amplitude multiplier. Taking into account only the terms with the first degree $(1/R_0)$ in the amplitude and leaving the difference of the stroke in the phase multiplier r and r', we get:

$$E_{(\Theta')} = -\frac{ik}{R_0} \cdot \frac{e^{ikR_0}}{2\pi} \int_0^{\rho_0} \int_0^{2\pi} \left[E_{(\rho)} \cdot \cos(\varphi - \psi') \right.$$
$$\left. - E_{(\varphi)} \cdot \sin(\varphi - \psi') \right) e^{-ik \cdot \rho \cdot \sin\Theta' \cdot \cos(\varphi - \psi')} \rho d\rho d\varphi; \tag{18.27}$$

$$E_{(\Psi')} = -\frac{ik}{R_0} \cdot \frac{e^{ikR_0}}{2\pi} \int_0^{\rho_0} \int_0^{2\pi} \cos\Theta' \cdot e^{-ik \cdot \rho \cdot \sin\Theta' \cdot \cos(\varphi - \psi')} \cdot \left[E_{(\rho)} \sin(\varphi - \psi') \right.$$
$$\left. + E_{(\varphi)} \cdot \cos(\varphi - \psi') \right] \rho d\rho d\varphi. \tag{18.28}$$

The intensity distribution in the observation area can be determined using the formula:

$$I = E_{\Theta'} \cdot \overline{E_{\Theta'}} + E_{\Psi'} \cdot \overline{E_{\Psi'}}, \tag{18.29}$$

where $\overline{E_{\Theta'}}$, $\overline{E_{\Psi'}}$ are the complex conjugate values to $E_{\Theta'}$, $E_{\Psi'}$.

By using the relations (18.22) and (18.26), we can calculate the distribution of the intensity of the optical field at any point of space $y > 0$. By using the Formula (18.27) and (18.28), we can find the field at points remote from the surface of the beam-splitter at a distance corresponding to the far zone. To do this, it is necessary to find the components of the electric field vector tangent to the beam-splitter surface. The field can be represented as a field falling on the surface of the beam-splitter and a mirror-reflected field. A falling field is a field from a source that can be represented as a round hole. The reflected field can be determined using the image method [13], taking into account the beam splitter's transmittance.

18.3 Relations for Determining the Field Falling on the Beam-Splitter Surface

Let us find the calculated relations for determining the field falling from the source to the beam splitter surface using a spherical coordinate system. The source of the field is represented as the radiation of the source passing through a circular aperture with a radius a that is in the plane $\tilde{y} = 0$ (Fig. 18.2). Consider two cases of polarization of a plane wave falling on a circular diaphragm in perpendicular and in parallel:

(i) at polarization along $\tilde{z}$ − axis, we get $\overline{E} = \overline{k} \cdot E_z$; (18.30)

(ii) at polarization along $\tilde{x}$ − axis, we get $\overline{E} = \overline{i} \cdot E_x$. (18.31)

To solve the problem, we introduce two coordinate systems (cylindrical and spherical) with the beginning at the center of the diaphragm (Fig. 18.2). The polar

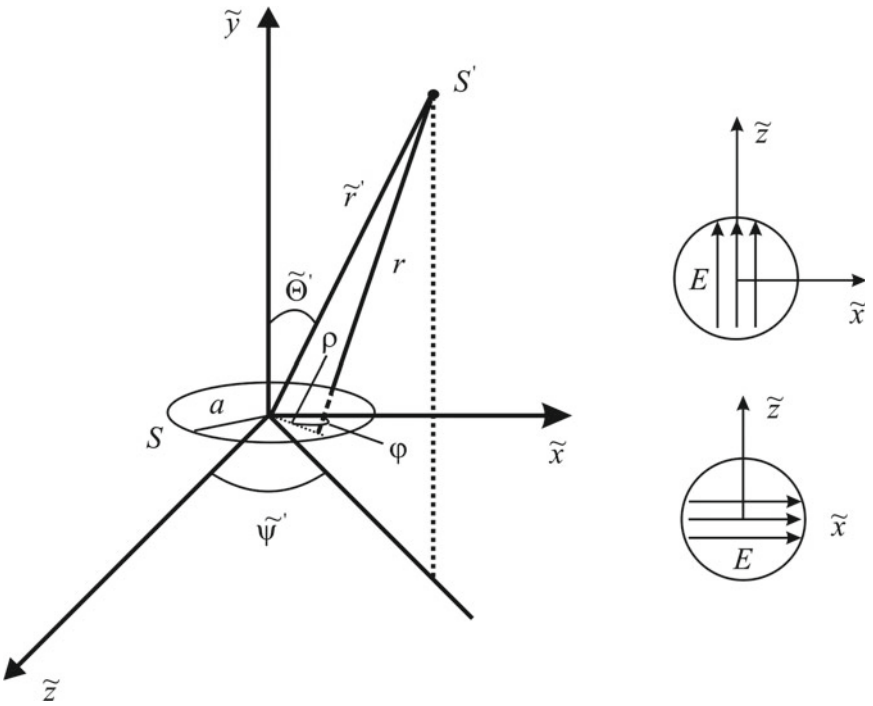

Fig. 18.2 Calculation scheme

coordinate system $\{\tilde{\rho}, \tilde{\varphi}\}$ is related to the Cartesian coordinate system $\{\tilde{x}, \tilde{z}\}$ as follows:

$$\tilde{x} = \tilde{\rho} \sin \tilde{\varphi}; \quad \tilde{z} = \tilde{\rho} \cos \tilde{\varphi}. \tag{18.32}$$

We write the tangent components $E_{\tilde{\rho}}$ and $E_{\tilde{\varphi}}$ in the plane $y = 0$ for perpendicular polarization, through (18.30), or parallel polarization, through (18.31), using a formula coupling the components of vectors in different orthogonal coordinate systems:

$$E_{\bar{k}} h_{\bar{k}} = \frac{\partial x^m}{\partial \bar{x}^k} E_m h_m, \tag{18.33}$$

where $E_{\bar{k}}$ and E_m are the physical components of the vector E in different coordinate systems, respectively, h_i are the corresponding Lamé metric coefficients. In this case, the index k is referred to a cylindrical coordinate system, and the index m is referred to a Cartesian coordinate system.

Lamé coefficients in a cylindrical coordinate system have the form:

$$h_\rho = 1; \quad h_\varphi = \rho; \quad h_y = 1. \tag{18.34}$$

I. For perpendicular polarization:

$$E_\rho h_\rho = \frac{\partial \tilde{z}}{\partial \tilde{\rho}} E_z h_z \rightarrow E_\rho = E_z \cos\tilde{\varphi};$$
$$E_\varphi h_\varphi = \frac{\partial \tilde{z}}{\partial \tilde{\varphi}} E_z h_z \rightarrow E_\varphi = -E_z \sin\tilde{\varphi}. \tag{18.35}$$

Cylindrical components E_ρ, E_φ in the opening of the diaphragm, are the sources of the field that falls on the beam-splitter.

To determine the field falling on diaphragm we can use the relations (18.22) and (18.26), which couple E_τ on some surface (in this case, the diaphragm aperture) and field at observation points (in this case, the points on the surface of the beam splitter). To do this, substitute (18.35) in the expressions (18.22) and (18.26), assuming that $E_z = \text{const} = 1$, and we get:

$$E_{\Theta'} = \frac{1}{2\pi} \int_S \frac{e^{ikr}}{r^2} \cdot (1 - ikr) \cdot \left(\frac{r'}{r} \cdot \cos\psi' - \frac{\rho}{r} \cdot \cos\varphi \cdot \sin\Theta' \right) \mathrm{d}s; \tag{18.36}$$

$$E_{\psi'} = \frac{1}{2\pi} \int_S \frac{e^{ikr}}{r^2} \cdot (1 - ikr) \cdot \frac{r'}{r} \cdot \cos\Theta' \cdot \sin\Psi' \mathrm{d}s, \tag{18.37}$$

where r is the distance between the diaphragm aperture points and the observation points, r' is the distance between the center of the spherical coordinate system and the observation points. The beginning of this spherical coordinate system is located at the center of the diaphragm aperture and differs from the spherical coordinate system introduced earlier in (18.9). Assuming in the amplitude multiplier $r = r'$ and $kr \gg 1$, we have:

$$E_{\tilde{\Theta}'} = -\frac{ik}{r'} \cdot \frac{1}{2\pi} \int_S e^{ikr} \cdot \left(\cos\tilde{\psi}' - \frac{\rho}{r} \cdot \cos\tilde{\phi} \cdot \sin\tilde{\Theta}' \right) ds$$
$$= -\frac{ik}{r'} \cdot \cos\tilde{\psi}' \cdot \frac{1}{2\pi} \int_S e^{ikr} ds + \frac{ik}{(r')^2} \cdot \cos\tilde{\Theta}' \cdot \frac{1}{2\pi} \Bigg) \int_S e^{ikr} \cdot \rho \cdot \sin\tilde{\phi} \cdot ds; \tag{18.38}$$

$$E_{\tilde{\psi}'} = \frac{ik}{r'} \cdot \cos\Theta' \cdot \sin\psi' \cdot \frac{1}{2\pi} \int_S e^{ikr} \mathrm{d}s. \tag{18.39}$$

or, neglecting the second term in (18.38), we get expressions for spherical components of the electric field strength:

$$E_{\tilde{\Theta}'} = -\frac{ik}{r'} \cdot \cos\tilde{\psi}' \cdot \frac{1}{2\pi} \int\limits_S e^{ikr} ds; \tag{18.40}$$

$$E_{\tilde{\psi}'} = \frac{ik}{r'} \cdot \cos\tilde{\Theta}' \cdot \sin\tilde{\psi}' \cdot \frac{1}{2\pi} \int\limits_S e^{ikr} ds. \tag{18.41}$$

II. Similarly, for the parallel polarization, instead (18.35), we have:

$$E_\rho = E_x \cdot \sin\varphi; \quad E_\varphi = E_x \cdot \cos\varphi. \tag{18.42}$$

and instead (18.40) and (18.41), we have:

$$E_{\tilde{\Theta}'} = -\frac{ik}{r'} \cdot \sin\psi' \cdot \frac{1}{2\pi} \int\limits_S e^{ikr} \mathrm{d}s; \tag{18.43}$$

$$E_{\tilde{\Psi}'} = \frac{ik}{r'} \cdot \cos\Theta' \cdot \cos\psi' \cdot \frac{1}{2\pi} \int\limits_S e^{ikr} ds. \tag{18.44}$$

Consider the integral in these expressions:

$$I = \int\limits_S e^{ikr} \mathrm{d}s, \tag{18.45}$$

where

$$\begin{aligned} r &= \sqrt{(\rho\sin\varphi - r'\sin\Theta'\sin\psi')^2 + (r'\cos\Theta')^2 + (\rho\cos\varphi - r'\sin\Theta'\cos\psi')^2}; \\ &\quad \rho^2\sin^2\varphi - 2\rho r'\sin\varphi\sin\Theta'\sin\psi' + r'^2\sin^2\Theta'\sin^2\psi' + r'^2\cos^2\Theta' \\ &\quad + \rho^2\cos^2\varphi - 2\rho r'\cos\varphi\sin\Theta'\cos\psi' + r'^2\sin^2\Theta'\cos^2\psi' \\ &= \rho^2 - 2\rho r'\sin\Theta'\cos(\varphi - \psi') + r'^2\sin^2\Theta' + r'^2\cos^2\Theta' \\ &= r^2 = \rho^2 - 2\rho r'\sin\Theta'\cos(\varphi - \psi') + r^2. \end{aligned} \tag{18.46}$$

Then

$$I = \int\limits_0^a \int\limits_0^{2\pi} e^{ik\sqrt{\rho^2 - 2\rho\cdot r'\cdot\sin\Theta'\cdot\cos(\varphi-\psi') + (r')^2}} \rho d\rho d\varphi; \tag{18.47}$$

$$r \approx r'\sqrt{1 - \frac{2\rho}{r'}\sin\Theta'\cos(\varphi - \psi')}.$$

For the Fresnel zone, we have:

$$r = r'\left[1 - \frac{\rho}{r'}\sin\Theta'\cos(\varphi - \psi')\right]; \tag{18.48}$$

$$I = e^{ikr'}\int_0^a\int_0^{2\pi} e^{-ik\cdot\rho\cdot\sin\Theta'\cdot\cos(\varphi-\psi')}\rho d\rho d\varphi.$$

Due to [14]:

$$\int_0^{2\pi} e^{-ik\rho\sin\Theta'\cos(\varphi-\psi')}d\varphi = 2\pi J_0(k\rho\sin\Theta'), \tag{18.49}$$

then we have:

$$I = e^{ikr'}\int_0^a \rho 2\pi J_0(k\rho\sin\Theta')d\rho = e^{ikr'}2\pi\frac{a}{k\sin\Theta'}J_1(ka\sin\Theta'), \tag{18.50}$$

where J_1 is the Bessel function of 1st order.

Substituting (18.50) into (18.40) and (18.41), we get for perpendicular polarization:

I.

$$E_{\Theta'} = -i\frac{e^{ikr'}}{r'}\frac{a\cos\psi'}{\sin\Theta'}J_1(ka\sin\Theta') = -A\cos\psi'; \tag{18.51}$$

$$E_{\psi'} = i\frac{e^{ikr'}}{r'}\frac{a\cos\Theta'\sin\psi'}{\sin\Theta'}J_1(ka\sin\Theta') = A\cos\Theta'\cos\psi'. \tag{18.52}$$

Similar for parallel polarization, we get:

II.

$$E_{\Theta'} = -i\frac{e^{ikr'}}{r'}\frac{a\sin\psi'}{\sin\Theta'}J_1(ka\sin\Theta') = -A\sin\psi'; \tag{18.53}$$

$$E_{\psi'} = i\frac{e^{ikr'}}{r'}\frac{a\cos\Theta'\cos\psi'}{\sin\Theta'}J_1(ka\sin\Theta') = -A\cos\Theta'\cos\psi', \tag{18.54}$$

where

$$A = i\frac{e^{ikr'}}{r'}\frac{aJ_1(ka\sin\Theta')}{\sin\Theta'}. \tag{18.55}$$

Relationships (18.51)–(18.55) determine the field that passed through the diaphragm, and they can be used to calculate the field falling on the surface of the beam-splitter at different polarizations.

18.4 Relations for Determining the Total Field on Beam-Splitter Surface

To determine the distribution of light intensity in the observation area, it is necessary to calculate the field on the surface of the beam-splitter, which consists of the falling field found in Sect. 18.3 and the field of the imaginary source. To solve this problem, it is convenient to introduce three local Cartesian coordinate systems $\{x, y, z\}$ and the spherical coordinate systems $\{r, \Theta, \psi\}$ coupled with them, having origins at points O, O', O''. Coordinates without strokes are referred to the coordinate systems with origins on the beam-splitter surface at a point O; coordinates with one stroke correspond to the coordinate systems at a point O' located at the center of aperture; and two strokes are referred to a coordinate system with an origin at the center of the mirror source O'' (Fig. 18.3).

It is necessary to determine the tangent components of the falling field on the surface $y = 0$ in a cylindrical coordinate system with the origin at a point O. Therefore, knowing $E_{\tilde{\Theta}'}$, $E_{\tilde{\Psi}'}$, $E_{\tilde{r}'} \approx 0$ let us go to E_ρ and E_φ.

The relationship between the entered coordinate systems is defined as follows. The coordinate system $\{x', y', z'\}$ is obtained by rotating around the z-axis by an angle α_0 in the positive direction and then parallel translation on $(-x_0)$ and y_0, respectively (see Fig. 18.3). The coordinate system $\{x'', y'', z''\}$ is mirrored with respect to $\{x', y', z'\}$, where the y-axis direction is changed to opposite. This system is derived from $\{x, y, z\}$ by turning on an angle $[-(\alpha_0 + 2\alpha)]$ and parallel shear along the x-axis on $\left(-x_0''\right)$ and along the y-axis on $\left(-y_0''\right)$.

The relationships between these coordinate systems and the main coordinate system are as follows:

$$\begin{aligned} x' &= (x + x_0)\cos\alpha_0 + (y - y_0)\sin\alpha_0; \\ y' &= -(x + x_0)\sin\alpha_0 + (y - y_0)\cos\alpha_0; \\ z' &= z. \end{aligned} \tag{18.56}$$

$$\begin{aligned} x'' &= \left(x + x_0''\right)\cos(\alpha_0 + 2\alpha) - \left(y + y_0''\right)\sin(\alpha_0 + 2\alpha); \\ y'' &= \left(x + x_0''\right)\sin(\alpha_0 + 2\alpha) + \left(y + y_0''\right)\cos(\alpha_0 + 2\alpha); \\ z'' &= z, \end{aligned} \tag{18.57}$$

where

$$x_0'' = x_0\cos 2\alpha + 2h\sin\alpha + y_0\sin 2\alpha;$$

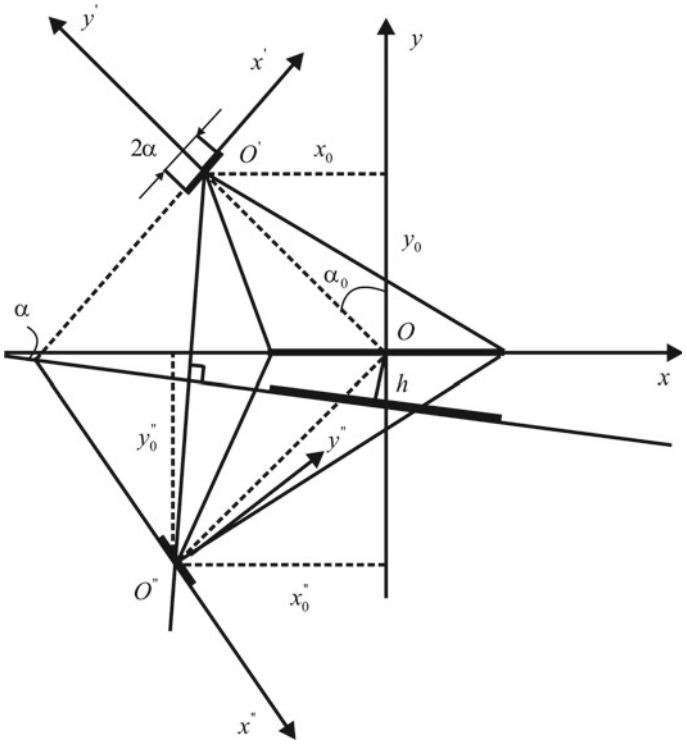

Fig. 18.3 Calculation scheme

$$y_0'' = -x_0 \sin 2\alpha + 2h \cos \alpha + y_0 \sin 2\alpha. \tag{18.58}$$

In these expressions, the values of the parameters x_0, y_0, α_0 and α, h, respectively, determine the position in space of the luminous point and the reflecting surface; they are clear from Fig. 18.3. The Cartesian coordinates with origin at a point O' are expressed in spherical coordinates with origin at the point O':

$$\begin{aligned} x' &= r' \cdot \sin \Theta' \cdot \sin \Psi'; \\ y' &= r' \cdot \cos \Theta'; \\ z' &= r' \cdot \sin \Theta' \cdot \cos \Psi'. \end{aligned} \tag{18.59}$$

Cartesian coordinate system can be expressed in terms of a basic cylindrical coordinate system $\{y, \rho, \varphi\}$ that is coupled with a point O:

$$x = \rho \sin \varphi; \quad y = y; \quad z = \rho \cos \varphi. \tag{18.60}$$

From the Formula (18.56), we express the relationship of the main Cartesian coordinate system with the entered Cartesian coordinate system with the origin at

the point O':

$$\begin{aligned} x &= -x_0 + x' \cdot \cos\alpha_0 - y' \cdot \sin\alpha_0; \\ y &= y_0 + x' \cdot \sin\alpha_0 - y' \cdot \cos\alpha_0; \\ z &= z'. \end{aligned} \tag{18.61}$$

Substitute (18.59) into (18.61) and get the relations that connect the main Cartesian coordinate system and the spherical coordinate system with the origin at the point O:

$$\begin{aligned} x &= -x_0 + r' \sin\Theta' \sin\Psi' \cos\alpha_0 - r' \cos\Theta'; \\ y &= y_0 + r' \sin\Theta' \sin\Psi' \sin\alpha_0 + r' \cos\Theta' \cos\alpha_0; \\ z &= r' \sin\Theta' \cos\Psi'. \end{aligned} \tag{18.62}$$

Substitute (18.62) into (18.60) and get relations, defining cylindrical coordinates centered at the point O, through Cartesian coordinates centered at the point O':

$$\begin{aligned} \rho \sin\varphi &= -x_0 + x' \cos\alpha_0 - y' \sin\alpha_0; \\ \rho \cos\varphi &= z'; \\ y &= y_0 + x' \sin\alpha_0 + y' \cos\alpha_0. \end{aligned} \tag{18.63}$$

Let us express cylindrical coordinates centered at a point O through spherical coordinates centered at a point O':

$$\begin{aligned} & y = y_0 + r' \sin\Theta' \sin\Psi' \sin\alpha_0 + r' \cos\Theta' \cos\alpha_0; \\ & tg\varphi = \frac{x}{z} = \frac{-x_0 + r' \sin\Theta' \sin\Psi' \cos\alpha_0 - r' \cos\Theta' \sin\alpha_0}{r' \sin\Theta' \cos\Psi'}; \\ & \rho = \sqrt{r'^2 \sin\Theta'^2 \cos^2\Psi' + (-x_0 + r' \sin\Theta' \sin\Psi' \cos\alpha_0 - r' \cos\Theta' \sin\alpha_0)^2}. \end{aligned} \tag{18.64}$$

Let us express spherical coordinates centered at a point O' through cylindrical coordinates at a point O:

$$\begin{aligned} r' &= \sqrt{\rho^2 + 2\rho x_0 \sin\varphi + x_0^2 + (y - y_0)^2}; \\ tg\Psi' &= \frac{(\rho \sin\varphi + x_0)\cos\alpha_0 + (y - y_0)\sin\alpha_0}{\rho \cos\varphi}; \\ \cos\Theta' &= \frac{-(\rho \cdot \sin\varphi + x_0)\sin\alpha_0 + (y - y_0)\cos\alpha_0}{\sqrt{\rho^2 + 2\rho \cdot x_0 \sin\varphi + x_0^2 + (y - y_0)^2}}. \end{aligned} \tag{18.65}$$

The electromagnetic radiation of the laser passed through a circular diaphragm and polarized along the x'-axis in a spherical coordinate system with the origin at

a point O' was obtained above (18.53) and (18.54). Next, we need to get a falling field expressed in a cylindrical coordinate system with the origin at a point O. This requires the transverse components of the vector E:

$$E_\rho = \frac{\partial\Theta'}{\partial\rho}\frac{h_{\Theta'}}{h_\rho}E_{\Theta'} + \frac{\partial\Psi'}{\partial\rho}\frac{h_{\Psi'}}{h_\rho}E_{\Psi'}; \quad E_\varphi = \frac{\partial\Theta'}{\partial\varphi}\frac{h_{\Theta'}}{h_\varphi}E_{\Theta'} + \frac{\partial\Psi'}{\partial\varphi}\frac{h_{\Psi'}}{h_\varphi}E_{\Psi'}, \quad (18.66)$$

where

$$\begin{aligned} &h_\Theta = r; \quad h_\rho = 1; \quad h_\varphi = \rho; \quad h_\varphi = \rho; \\ &h_\Psi = r\cdot\sin\cdot\Theta; \quad h_y = 1. \end{aligned} \quad (18.67)$$

Define the necessary components of expression (18.66):

$$\begin{aligned} &\frac{\partial\Theta'}{\partial\rho}\frac{h_\Theta}{h\varphi} = r'\frac{\partial\Theta'}{\partial\rho}; \qquad \frac{\partial\Theta'}{\partial\varphi}\frac{h_\Theta}{h\varphi} = \frac{r'}{\rho}\frac{\partial\Theta'}{\partial\varphi}; \\ &\frac{\partial\Psi'}{\partial\rho}\frac{h_\Psi}{h\rho} = r'\sin\Theta'\frac{\partial\psi'}{\partial\rho} \quad \frac{\partial\Psi'}{\partial\varphi}\frac{h_\Psi}{h_\varphi} = \frac{r'\sin\Theta'}{\rho}\frac{\partial\Psi'}{\partial\varphi} \end{aligned} \quad (18.68)$$

From (18.65) we have:

$$\begin{aligned} r' &= \sqrt{\rho^2 + 2\cdot\rho\cdot x_0\cdot\sin\varphi + x_0^2 + (y-y_0)^2}; \\ \Theta' &= \arccos\frac{y}{r} = \arccos\frac{-(\rho\sin\varphi + x_0)\sin\alpha_0 + (y-y_0)\cos\alpha_0}{\sqrt{\rho^2 + 2\rho x_0\sin\varphi + (y-y_0)^2}}. \end{aligned} \quad (18.69)$$

Derivatives in (18.66) have the forms:

$$\begin{aligned} \frac{\partial\psi'}{\partial\rho} &= \frac{1}{1+\left[\frac{(\rho\sin\varphi+x_0)\cos\alpha_0+(y-y_0)\sin\alpha_0}{\rho\cos\varphi}\right)\Big]^2} \\ &= \frac{-x_0\cos\varphi\cos\alpha_0 + (y-y_0)\sin\alpha_0\cos\varphi}{\rho^2\cos^2\varphi + [(\rho\sin\varphi + x_0)\cos\alpha_0 + (y-y_0)\sin\alpha_0]^2}; \\ \frac{\partial\Psi'}{\partial\rho}\frac{h_\Psi}{h_\rho} &= \frac{\sqrt{r'^2 - y'^2}\cdot[-x_0\cdot\cos\varphi\cdot\cos\alpha_0 - (y-y_0)\cdot\sin\alpha_0\cdot\cos\varphi]}{\rho^2\cos^2\varphi + [(\rho\cdot\sin\varphi + x_0)\cos\alpha_0 + (y-y_0)\sin\alpha_0]^2}; \\ \frac{\partial\Psi'}{\partial\varphi} &= \frac{1}{1+\left[\frac{(\rho\sin\varphi+x_0)\cos\alpha_0+(y-y_0)\sin\alpha_0}{\rho\cos\varphi}\right]^2} \\ &= \frac{\rho\cdot\cos\varphi\cdot\rho\cdot\cos\varphi\cdot\rho\cos\alpha_0 + \rho\cdot\sin\varphi[(\rho\cdot\sin\varphi + x_0)\cos\alpha_0 + (y-y_0)\sin\alpha_0]}{\rho^2\cos^2\varphi} \\ &= \frac{\rho^2\cdot\cos\alpha_0 + \rho\cdot x_0\sin\varphi\cdot\cos\alpha_0 + \rho(y-y_0)\sin\varphi\cdot\sin\alpha_0\Big]}{\rho^2\cdot\cos^2\varphi + [(\rho\cdot\sin\varphi + x_0)\cos\alpha_0 + (y-y_0)\sin\alpha_0]^2}; \\ \frac{\partial\Psi'}{\partial\varphi}\frac{h_\Psi}{h_\varphi} &= \frac{\sqrt{r'^2 - y'^2}[\rho\cdot\cos\alpha_0 + x_0\sin\varphi\cdot\cos\alpha_0 + (y-y_0)\sin\varphi\cdot\sin\alpha_0]}{\rho^2\cdot\cos^2\varphi + [(\rho\cdot\sin\varphi + x_0)\cos\alpha_0 + (y-y_0)\sin\alpha_0]^2}; \end{aligned} \quad (18.70)$$

$$(18.71)$$

$$\frac{\partial\Theta'}{\partial\rho}\frac{h_\Theta}{h_\rho} = \frac{r'}{\sqrt{r'^2 - y'^2}}\left\{\sin\varphi\cdot\sin\alpha_0 + \frac{[-(\rho\sin\varphi + x_0)\sin\alpha_0 + (y - y_0)\cos\alpha_0](\rho + \sin\varphi)}{(r')^2}\right\}; \tag{18.72}$$

$$\frac{\partial\Theta'}{\partial\varphi}\frac{h_\Theta}{h_\varphi} = \frac{1}{\sqrt{r'^2 - y'^2}}\left\{\cos\varphi\cdot\sin\alpha_0\cdot r' + \frac{[-(\rho\sin\varphi + x_0)\sin\alpha_0 + (y - y_0)\cos\alpha_0]x_0\cos\varphi}{r'}\right\}. \tag{18.73}$$

Thus, the following field falling from the diaphragm, expressed in the components of the cylindrical coordinate system, takes place on the surface $y = 0$:

$$E^{\text{пад.}}_{\rho} = \frac{\bar{r}'}{\sqrt{(\bar{r}')^2 - (\bar{y}')^2}}\left[\sin\varphi\cdot\sin\alpha_0 + \frac{\bar{y}'(\rho + x_0\sin\varphi)}{(\bar{r}')^2}\right]E_{\Theta'} + \frac{\sqrt{(\bar{r}')^2 - (\bar{y}')^2}\cdot\left[-x_0\cos\varphi\cdot\cos\alpha_0 - y_0\cos\varphi\cdot\sin\alpha_0\right]}{\rho^2\cos^2\varphi + (\bar{x}')^2}E_{\Psi'}; \tag{18.74}$$

$$E^{\text{под.}}_{\varphi} = \frac{\bar{r}'}{\sqrt{(\bar{r}')^2 - (\bar{y}')^2}}\left[\cos\varphi\cdot\sin\alpha_0 + \frac{\bar{y}'\cdot x_0\sin\varphi}{(\bar{r}')^2}\right]E_{\Theta'} + \frac{\sqrt{(\bar{r}')^2 - (\bar{y}')^2}\cdot\left[\rho\cdot\cos\alpha_0 + x_0\cdot\sin\varphi\cdot\cos\alpha_0 - y_0\sin\varphi\cdot\sin\alpha_0\right]}{\rho^2\cos^2\varphi + (\bar{x}')^2}E_{\Psi'}, \tag{18.75}$$

where

$$\begin{aligned}\bar{r}' &= \sqrt{\rho^2 + 2\cdot\rho\cdot x_0\sin\varphi + x_0^2 + y_0^2};\\ \bar{x}' &= (\rho\cdot\sin\varphi + x_0)\cos\alpha_0 - y_0\sin\alpha_0;\\ \bar{y}' &= -(\rho\cdot\sin\varphi + x_0)\sin\alpha_0 - y_0\cos\alpha_0.\end{aligned} \tag{18.76}$$

Expressions for the field of imaginary source are obtained similarly to the falling field from the aperture, only in formulae (18.74)–(18.76), it is necessary to replace one stroke with two, and instead x_0, y_0, α_0 substitute them on x_0'', y_0'', $-(\alpha_0 + 2\alpha)$, respectively:

$$E^3_{\rho} = \frac{\bar{r}'}{\sqrt{(\bar{r}')^2 - (\bar{y}')^2}}\left[\sin\varphi\cdot\sin(-\alpha_0 + 2\alpha) + \frac{\bar{y}'(\rho + x_0''\sin\varphi)}{(\bar{r}')^2}\right]E_{\Theta'} + \frac{\sqrt{(\bar{r}')^2 - (\bar{y}')^2}\cdot\left[-x_0''\cos\varphi\cdot\cos(-\alpha_0 + 2\alpha) - y_0''\cos\varphi\cdot\sin(-\alpha_0 + 2\alpha)\right]}{\rho^2\cos^2\varphi + (\bar{x}')^2}E_{\Psi'}; \tag{18.77}$$

$$E^3_{\varphi} = \frac{\bar{r}'}{\sqrt{(\bar{r}')^2 - (\bar{y}')^2}}\left[\cos\varphi\cdot\sin(-\alpha_0 + 2\alpha) + \frac{\bar{y}'\cdot x_0''\sin\varphi}{(\bar{r}')^2}\right]E_{\Theta'}$$

$$+\frac{\sqrt{(\bar{r}')^2-(\bar{y}')^2}\cdot\left[\rho\cdot\cos(-\alpha_0+2\alpha)+x_0''\cdot\sin\varphi\cdot\cos(-\alpha_0+2\alpha)-y_0''\sin\varphi\cdot\sin(-\alpha_0+2\alpha)\right]}{\rho^2\cos^2\varphi+(\bar{x}')^2}E_{\Psi'},\tag{18.78}$$

where

$$\begin{aligned}x_0'' &= x_0\cos 2\alpha + 2h\sin\alpha + y_0\sin 2\alpha;\\ y_0'' &= -x_0\sin 2\alpha + 2h\cos\alpha + y_0\sin 2\alpha.\end{aligned}\tag{18.79}$$

The total field on the surface of the beam-splitter can be written as the sum of the field falling from the source that is passed through the diaphragm, and the field from the imaginary source that is diffracted on the beam-splitter:

$$E_\rho = E_\rho^{\text{пад.}} + T(\rho,\varphi)E_\rho^{\text{з}};\quad E_\varphi = E_\varphi^{\text{пад.}} + T(\rho,\varphi)E_\varphi^{\text{з}},\tag{18.80}$$

where $T(\rho, \varphi)$ is the amplitude transmission of the beam-splitter.

Thus, the relationships to determine the field distribution on the surface of beam-splitter of laser interferometer are obtained. The field distribution is presented in the form of the tangential components of the electric field strength vector E_ρ and E_φ, expressed in cylindrical coordinates, taking into account the diffraction at a circular aperture and transmittance of the beam-splitter.

18.5 Relations for Determining the Field and Intensity in the Location Area of Photodetectors in the Case of Using Sinusoidal Diffraction Grating as Beam-Splitter

Thus, we can say that in Sect. 18.3 the calculated relations were found for determining the field falling from the source on the beam-splitter surface using a spherical coordinate system. In Sect. 18.4, we obtained the relations for determining the field on the surface of the beam-splitter of a laser interferometer, which are represented as tangent components of the electric field strength vector E_ρ and E_φ, expressed in cylindrical coordinates, taking into account the diffraction on the round hole and the transmission coefficient of the beam-splitter.

Now consider the case when a sine wave grating with a period τ and transmittance $T(x, z)$ is used as a beam-splitter. If the beam-splitter is fully illuminated, then the surface of the interferogram is rectangular and in this case, it is convenient to use a Cartesian coordinate system. In this regard, it is necessary to make a transition from formulae (18.27) and (18.28) with components E_Θ and E_Ψ, expressed in cylindrical coordinates to formulae with the same components expressed in Cartesian coordinates.

With this aim, we define E_ρ and E_φ through E_x and E_z:

$$E_\rho = E_z \cdot \cos\varphi + E_x \cdot \sin\varphi;$$
$$E_\varphi = -E_z \cdot \sin\varphi + E_x \cdot \cos\varphi. \tag{18.81}$$

So, expressions (18.27) and (18.28) take the forms:

$$E_{(\Theta')} = \frac{1}{2\pi}\int\limits_s \frac{e^{ikr}}{r^2}\cdot(1-ikr)\cdot\left[E_z\left(\frac{r'}{r}\cos\psi' - \frac{z}{r}\sin\Theta'\right)\right.$$
$$\left. + E_x\cdot\left(\frac{r'}{r}\cdot\sin\psi' - \frac{x}{r}\cdot\sin\Theta\right)\right]ds;$$
$$E_{(\psi')} = \frac{1}{2\pi}\int\limits_s \frac{e^{ikr}}{r^2}\cdot(1-ikr)\cdot\frac{r'}{r}\cdot\cos\Theta'\cdot(E_x\cdot\cos\psi' - E_z\sin\psi')ds. \tag{18.82}$$

If the interference pattern is observed in the far zone, and the source is located near the y-axis in the Fresnel zone, then the formulae for calculating the transverse components of the vector E have the forms:

$$E_{\Theta\perp} = A_0\cdot\cos\psi\cdot U(\Theta,\psi);\ E_{\Psi\perp} = -A_0\cdot\cos\Theta\cdot\sin\psi\cdot U(\Theta,\psi); \tag{18.83}$$

$$E_{\Theta||} = A_0\cdot\sin\psi\cdot\cos\alpha_0\cdot U(\Theta,\psi);$$
$$E_{\Psi||} = -A_0\cdot\cos\psi\cdot\cos\Theta\cdot\cos\alpha_0\cdot U(\Theta,\psi). \tag{18.84}$$

Here

$$U(\theta,\psi) = U_0\int\limits_S U(x,z)e^{ik\frac{x^2+z^2}{2R_0}}e^{-ik\sin\theta(x\sin\psi+z\cos\psi)}ds, \tag{18.85}$$

where $U(x,z)$ is the complex amplitude of the wave field; θ, ψ, R_0 are the spherical coordinates of observation points; x, z are the coordinates of source points that locate on the surface of the beam splitter (Fig. 18.1). Expression (18.85) includes a function $U(x,z)$ describing the optical field in the plane of the beam-splitter. To determine it, we use the image method [13], when the total field on the surface of the beam splitter is represented by a superposition of waves from a luminous point x_0, y_0 and an imaginary mirror point formed by the reflector, and it is necessary to take into account the amplitude transmission of the beam splitter. In accordance with the image method expressions for the complex amplitude of the light field on the surface of the beam splitter can be written as follows:

$$U(x,z) = A_0e^{ikr'} - T(x,z)e^{ikr''}, \tag{18.86}$$

where for the Fresnel zone:

$$r' = r_0 + \frac{(x+x_0)^2 - x_0^2 + z^2}{2r_0};\ r'' = r_0'' + \frac{\left(x+x_0''\right)^2 - x_0''^2 + z^2}{2r_0''};$$
$$r_0 = \sqrt{x_0^2 + y_0^2}, \tag{18.87}$$

where A_0 is a constant, $T(x, z)$ is the amplitude transmission of the beam-splitter. Substituting (18.86) and (18.87) in (18.85), as well as specifying $T(x, z)$, we get the ratio for calculating the field at the observed points. The intensity to which the photodetector reacts is equal to the square of the expression module (18.85). Consider the case where the field does not depend on z, and a sinusoidal lattice is used as the beam-splitter. Diffraction by a sinusoidal grating, as is known, leads to the formation of maxima of the first order ($m = \pm 1$). In this regard, it is advisable to place photodetectors in the regions corresponding to these maxima and consider the interference pattern in these directions, which is formed by the falling wave and the waves diffracted on the lattice.

To do this, we write the optical field in space $y > 0$ in accordance with (18.85) as follows (the amplitude multiplier is omitted here):

$$U_1 = \int_{-d}^{d} \left(e^{ikr'} + e^{\pm ik\frac{\lambda}{\tau}x} e^{ikr''}\right) e^{ik\frac{x^2}{2R_0}} e^{-ikx\sin\theta} \mathrm{d}x, \tag{18.88}$$

where τ is the period of the lattice, and the sign in the exponent of the second term is taken in accordance with the considered main maximum.

Substituting the values from (18.87) into this expression, we get the ratio for calculating the complex amplitude of the wave field in the form:

$$U_1 = e^{ikr_0} J_1 + e^{ikr_0''} J_2, \tag{18.89}$$

where

$$J_1 = \int_{-d}^{d} e^{i\left[k\left(\frac{1}{2r_0}+\frac{1}{2R_0}\right)x^2 + k\left(\frac{x_0}{r_0} - \sin\theta\right)x\right]} \mathrm{d}x; \tag{18.90}$$

$$J_2 = \int_{-d}^{d} e^{i\left[k\left(\frac{1}{2r_0''}+\frac{1}{2R_0}\right)x^2 + k\left(\frac{x_0''}{r_0''} - \sin\theta \pm \frac{\lambda}{\tau}\right)x\right]} \mathrm{d}x. \tag{18.91}$$

By using table values [26], integrals (18.90) and (18.91) can be reduced to Fresnel integrals of the form:

$$J = \int_{-d}^{d} e^{i\left(ax^2+bx\right)} dx = \frac{1}{\sqrt{a}} e^{i\nu} \int_{-\xi_1}^{\xi_2} \left(\cos\xi^2 + i\sin\xi^2\right) d\xi, \tag{18.92}$$

where

$$\nu = \frac{b^2}{4a};\ \xi_1 = -d\sqrt{a} + \sqrt{\nu};\ \xi_2 = d\sqrt{a} + \sqrt{\nu}, \tag{18.93}$$

a is the coefficient before $\left(ix^2\right)$ in the exponent of expressions (18.90) and (18.91), respectively, and b is the coefficient before (ix) in these exponents.

The light intensity according to (18.89) is calculated using the following formula:

$$I(\theta) = (e^{ikr_0}J_1(\theta) + e^{ikr_0''}J_2(\theta))(e^{ikr_0}J_1(\theta) + e^{ikr_0''}J_2(\theta))^*, \tag{18.94}$$

where (*) denotes a complex-conjugate quantity.

If the size of the beam-splitter is so large that diffraction at the edges can be neglected and the limits in (18.88) can be replaced by infinite ones, then the integrals (18.90) and (18.91) can be calculated using the following formulae [14]:

$$J_1 = e^{i\frac{\pi}{4}}\sqrt{\frac{2\pi R_0}{k}}\sqrt{\frac{r_0}{r_0 + R_0}}e^{ik\frac{r_0 R_0}{2(r_0+R_0)}\left(\frac{x_0}{r_0} - \sin\theta\right)^2}; \tag{18.95}$$

$$J_2 = e^{i\frac{\pi}{4}}\sqrt{\frac{2\pi R_0}{k}}\sqrt{\frac{r_0''}{r_0'' + R_0}}e^{ik\frac{r_0'' R_0}{2(r_0+R_0)}\left(\frac{x_0''}{r_0''} - \sin\theta \pm \frac{\lambda}{\tau}\right)^2}. \tag{18.96}$$

In accordance with these expressions and for simplicity, taking into account the amplitude multipliers of interfering waves (18.95) and (18.96), $r_0 = r_0'' = R_0$, the intensity at the observed points can be written as follows:

$$I = A_0(1 - \cos\gamma), \tag{18.97}$$

where

$$\gamma = \frac{k}{2}\left[-r_0 + \frac{r_0 R_0}{r_0 + R_0}\left(\frac{x_0}{r_0} - \sin\theta\right)^2 + r_0'' - \frac{r_0'' R_0}{r_0'' + R_0}\left(\frac{x_0''}{r_0''} - \sin\theta \pm \frac{\lambda}{\tau}\right)^2\right]. \tag{18.98}$$

If the beam-splitter is large, we can determine the spatial frequency of the phase change. The dependence of the spatial frequency at different points θ on the measured parameters is determined by the following relation:

$$\omega = \frac{\partial\gamma}{\partial\theta} = k\left[-\frac{r_0 R_0}{r_0 + R_0}\left(\frac{x_0}{r_0} - \sin\theta\right)\cos\theta + \frac{r_0'' R_0}{r_0'' + R_0}\left(\frac{x_0''}{r_0''} - \sin\theta \pm \frac{\lambda}{\tau}\right)\cos\theta\right]. \tag{18.99}$$

These formulae determine the dependence of the measured parameters of the interference pattern in the directions θ_1 and θ_2, where the photodetectors are located,

on the coordinates of the highlighted point x_0, y_0 on the surface, as well as on the location of the reflector α, h. So, if we put $\theta = \theta_1$ in (18.94), we get an expression of intensity in the right part, the value of which depends on the measured parameters:

$$I_1(x_0, y_0, \alpha, h) = (e^{ikr_0} J_1(\theta_1) + e^{ikr_0''} J_2(\theta_1))(e^{ikr_0} J_1(\theta_1) + e^{ikr_0''} J_2(\theta_1))^*. \tag{18.100}$$

Similarly, for the intensity measured by the second photodetector, which is located in the direction θ_2, we have:

$$I_2(x_0, y_0, \alpha, h) = (e^{ikr_0} J_1(\theta_2) + e^{ikr_0''} J_2(\theta_2))(e^{ikr_0} J_1(\theta_2) + e^{ikr_0''} J_2(\theta_2))^*. \tag{18.101}$$

If the control object surface is highlighted at constant parameters α, h of the interferometer, then the expressions (18.100) and (18.101) are a system of equations with respect to x_0, y_0. In the second case, when the reflector is a control object surface and the luminous point is stationary, a system of equations for determining the values of α, h is obtained. Similar considerations can be made in the case of large beam-splitter sizes. Thus, by measuring, for example, the spatial frequency of interference bands ω in the directions θ_1 and θ_2, it is possible to obtain a system of transcendental equations for determining x_0, y_0 or α, h, which can be solved in any known way.

18.6 Conclusion

It was developed universal technique, and also are derived and described in details the formulae for determining the intensity of the optical fields created by the laser interference meter of displacements based on two-way laser interferometer with combined branches, and implementing a method onto the surface of the test object. The proposed relationships allow for computational and theoretical modeling and research of functional characteristics in the interests of creating new promising optical means for measuring the displacement of control object surfaces.

Acknowledgements The work was supported by the grant of Russian Foundation for Basic Research, No. 19-08-00365, Ministry of Education and Science of the Russian Federation: projects Nos. 3.5378.2017/VU (organization of the implementation of researches), 9.9770.2017/BCh (the basic part of the state task).

References

1. V.E. Alekhin, I.P. Miroshnichenko, A.G. Serkin, V.P. Sizov, *Optical device for measuring surface movements of control objects*. Russian Patent No. 2343402, 10.01.2009 (in Russian)

2. I.P. Miroshnichenko, I.A. Parinov, E.V. Rozhkov, *Optical interference device for measuring surface movements of control objects*. Russian Patent No. 2512697, 10.04.2014 (in Russian)
3. I.P. Miroshnichenko, I.A. Parinov, IOP Conf. Ser.: Mater. Sci. Eng. **572**, 012065 (2019)
4. A.N. Matveev, *Optics* (Higher School, Moscow, 1985), p. 351 (in Russian)
5. A.S. Batrakov, M.M. Butusov, G.P. Grechka, *Laser Measuring Systems* (Radio and Communications, Moscow, 1981), p. 456 (in Russian)
6. V.E. Alekhin, I.P. Miroshnichenko, V.P. Sizov, Russ. J. Nondestr. Test. **43**(2), 113 (2007)
7. V.E. Alekhin, I.P. Miroshnichenko, V.A. Nesterov, V.P. Sizov, Russ. J. Nondestr. Test. **43**(9), 592 (2007)
8. V.E. Alekhin, I.P. Miroshnichenko, A.G. Serkin, Meas. Tech. **51**(10), 26 (2008)
9. I.P. Miroshnichenko, I.A. Parinov, E.V. Rozhkov, A.G. Serkin, Metallurgist **50**(7–8), 408 (2006)
10. I.P. Miroshnichenko, A.G. Serkin, Metallurgist **54**(3–4), 189 (2010)
11. F.M. Morse, G. Feshbach, Methods of theoretical physics. Mosc. Inostr. Lit., **2,** 896 (1960)
12. N.V. Kovalenko, *Antenna Gratings* (Rostov State University Press, Rostov-on-Don, 1971), pp. 17–33 (in Russian)
13. F.M. Morse, G. Feshbach, Methods of theoretical physics. Mosc. Inostr. Lit. **1**, 930 (1958)
14. E. Janke, F. Emde, F. Lesh, *Special Functions* (Science, Moscow, 1977), p. 342

Chapter 19
Strength of Interatomic Bonds at High-Angle Grain Boundaries in Iron

Yuri F. Migal

Abstract The numerical model of the high-angle boundary is used for quantum-chemical calculations of the binding energy of atoms of impurity and alloying elements at the grain boundaries in iron. Elements of the fourth period, from potassium to krypton, are considered as impurity. It is shown that the bond strength between grains is primarily determined by the type of atoms located at the boundaries. To a lesser extent, the bond strength depends on the details of the arrangement of atoms.

19.1 Introduction

The properties of metals, including the strength properties of their surface, largely depend on grain boundaries (GBs) in metals [1–3]. In various metals, including steels, along with atoms of the base metal at grain boundaries there are atoms of impurities and alloying elements. Some of these elements can strengthen the bond between the grains, and others, on the contrary, weaken this bond depending on the relative arrangement of atoms at the boundaries, as well as on the magnitude of the chemical bond between these atoms and the surface of the grains. The degree of dependence of the GBs strength in metals on the presence of various elements at the boundaries is one of the actual issues in the theory of metals.

The segregation phenomenon in iron and its influence on the strength properties of iron have been studied in a significant number of works devoted to the GBs. For example, in [4–6] detailed studies using specific models were conducted for segregating elements, including C, P, S, Zn, Cu. The peculiarity of these works is that they study particular situations when certain impurity atoms are considered in a certain configuration of iron atoms. Along with this, works of a more general content are known [7–9], where atoms of different elements are studied in typical configurations of atoms of the base metal. The main task of these works is to compare these elements according to the degree of strengthening of the metal.

Y. F. Migal (✉)
Southern Scientific Center of Russian Academy of Sciences, 41, Chekhov prosp, Rostov-on-Don, Russian Federation 344006
e-mail: ymigal@mail.ru

I. A. Parinov et al. (eds.), *Advanced Materials*, Springer Proceedings in Materials 6, https://doi.org/10.1007/978-3-030-45120-2_19

In our opinion, it is interesting to consider and compare the strengthening and softening properties of a large group of elements containing entire periods of these elements. Such a statement of the problem is possible within the framework of some generalized model of segregation in metal (for example, in iron). With its help, it would be possible to classify the strengthening properties of various elements in relation, for example, to iron, regardless of the atomic configuration characteristics of these elements in iron. This approach would be most useful when creating steels with specified properties.

Another, more accurate approach to the study of the strengthening properties of elements should be obviously based on the analysis of all possible configurations of atoms of these elements in the metal and the subsequent summation of the data obtained. Since any metal contains at the same time a huge variety of atomic impurities with a variety of properties, the exact approach is an almost impossible task.

In favor of a less accurate generalized model, experimental facts indicate that many elements, regardless of what different equilibrium positions they have in the structure of iron, generally harden iron. It follows from this unambiguity that the strengthening effect of an element depends more on the pair interaction of atoms of this element with iron atoms than on the details of the relative arrangement of atoms. Such a statement is difficult to prove, but in many known cases it turns out to be true.

Based on the experience of our previous studies, we can assume that to obtain generalized results about the influence of various impurity elements on the strength of iron, it is possible to use simplified models in which the different types of configurations characteristic of this element are averaged in some way.

In [10, 11] we calculated the binding energy of polyatomic complexes simulating grain boundaries in iron. We investigated the influence of the chemical composition of grain boundaries, including atoms of impurity and alloying elements, on the bond strength between grains. In these case methods based on the DFT approximation were applied. With their help, quantum-chemical calculations of the binding energy of complexes including elements from the first six periods of the periodic table were carried out. The results of the calculations are in qualitative agreement with the well-known theoretical and experimental data on the influence of these elements.

In these calculations, we used two different models of GBs, the cluster model and the slab model, which contain a large number of simplifications. These models did not take into account the variety of specific conditions available on different types of GBs (more details will be discussed below). In this chapter, we propose a new slab model that simulates a common defect in metals, namely the high-angle grain boundary.

The main purpose of this article is to show that the dependences in the distribution of chemical elements by the degree of hardening of iron obtained in different ways are close to each other, despite the significant differences in both the variants of the mutual arrangement of atoms in iron and the models used.

19.2 High-Angle Grain Boundary Model

First, we describe a simplified ("flat") slab model, which was used earlier in our calculations [10, 11]. This model consists of several atomic layers. The central inner layer contains atoms of impurity elements, and the outer layers consist of iron atoms. If the system is subjected to thermal or mechanical action, it can decay into two parts. In this case, the impurity atoms, as shown by calculations, are located on the surface of one of these parts (Fig. 19.1).

The energy E_d required to disintegrate the system into two parts was determined by the formula

$$E_d = |E_0 - E_1 - E_2|, \tag{1}$$

where E_0 is the binding energy of the whole system, E_1 and E_2 are the binding energies of the decayed parts.

By using this model, it was found, in particular, that in the presence of carbon or boron atoms on the GB, the energy required for the disintegration of the system is greater than in the presence of sulfur or phosphorus atoms. These and other obtained results are in agreement with the experimental data and theoretical results of other authors (see, for example, [12–15]).

In this chapter, an attempt is made to obtain similar results using a model that more accurately simulates the interactions of atoms at the grain boundaries. From all variety of known types of GB, it is necessary to choose some type of boundary allowing introduction on this boundary of atoms of impurity elements. Such boundaries include, in particular, the high-angle boundary, which can be represented as a set of points of contact of two sets of atomic planes with two different orientations in space. The angle between these planes must exceed 20° [16]. Atoms of impurity or alloying elements may be located in the voids arising from such a contact.

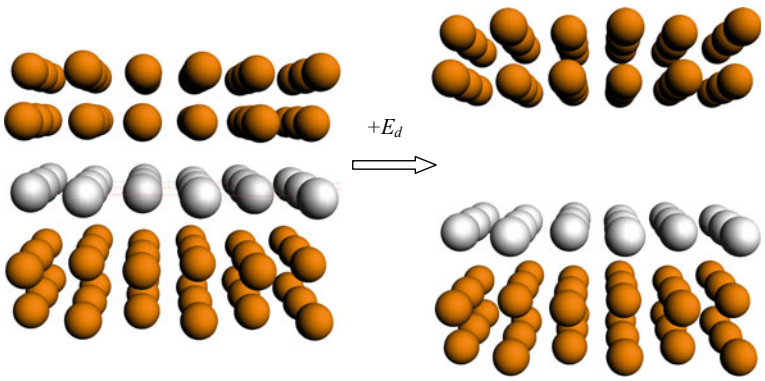

Fig. 19.1 Flat model of the grain boundary in iron with the surface (100) and the decay of this boundary into two parts [10]; atoms of alloying or impurity elements are in the middle layer

Thus, the system of parallel atomic planes, used in the case of the flat model, in this more realistic model is replaced by two systems of planes that touch each other inside some layer. In fact, this layer is the grain boundary.

Next, we consider a variant in which two systems of contacting atomic layers with Miller indices (100) are located to each other under an angle equal to 43°. This angle is chosen so that the position of atoms in space can be represented as a set of elementary cells in the crystal. This configuration of atoms allows the use of classical methods for calculating crystal structures.

Elements of the fourth period of the periodic table were considered as impurity and alloying elements in this work. If the size of the atoms or ions of these elements is smaller or comparable to the size of the iron atom, then such atoms are freely placed in the voids available on the GB. If such placement is energetically disadvantageous, the whole complex is unstable and will be disintegrated.

The left part of Fig. 19.2 presents the scheme of arrangement of atoms of iron and one more of representatives of the fourth group—titanium in new model on start of calculations. The arrangement of atoms in this case has been chosen so that only the outer surfaces of the system and the high-angle boundaries are defects of this periodic atomic structure.

The structure shown in the figure is a fragment of a system that periodically repeats in a plane parallel to two mutually perpendicular x- and y-axes. Here three elementary cells conjugated along the x-axis are shown. Geometric parameters of one elementary cell are: $a_x = 6.425$ a.u., $a_y = 2.87$ a.u. Total number of atoms in such a cell is 22. Among them there are 20 atoms of Fe and 2 atoms of Ti.

The vertical layer in the middle of the picture, which consists of alternating Fe and Ti atoms, depicts the common boundary of the two grains in given projection.

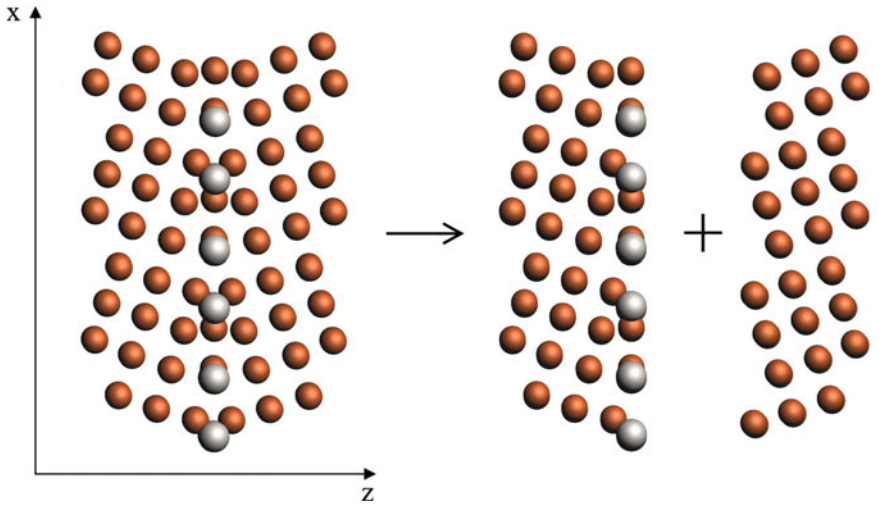

Fig. 19.2 Decay of high-angle GB containing impurity titanium atoms; Ti atoms are represented by light grey balls; the atomic system is presented in an unrelaxed form

The right side of the picture shows the system after the decay that occurred at the grain boundary.

The initial atomic configuration shown in Fig. 19.2, corresponds to the periodic arrangement of atoms specified at the start of calculations. In the result of atomic interactions taken into account in the model, relaxation occurs in the system, and the arrangement of atoms becomes less symmetrical.

The configuration of atoms after relaxation is presented in Fig. 19.3. The main results of relaxation are: (i) violation of the order in the atomic configuration characteristic of an ideal solid (this violation is a consequence of the existence of the grain boundary); (ii) compression of the atomic system along the z-axis caused by the action of transverse internal forces in the system. The latter phenomenon is an artifact of the model. It is explained by the fact that the model does not take into account the interaction of the investigated system with neighboring atoms located in the metal outside this system.

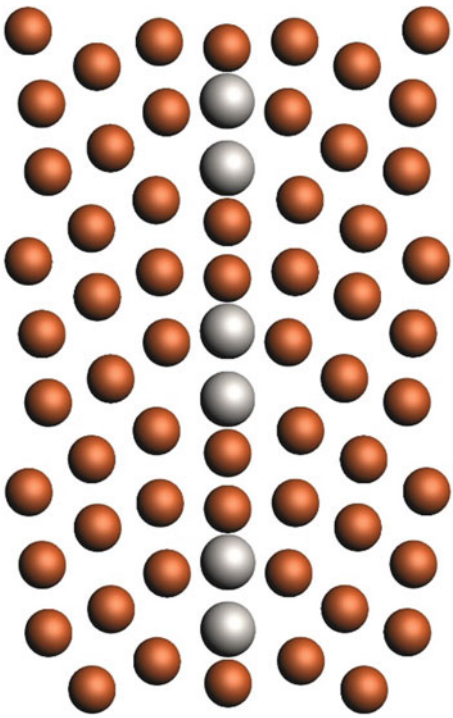

Fig. 19.3 GB model containing titanium atoms (relaxed state)

19.3 Results of Calculations and Discussion

This model was used to calculate the same values that were calculated earlier in [10, 11]. These values include the binding energy E_0 of the initial cell, the energies of its parts E_1 and E_2, as well as the energy E_d required for decay of the cell into parts. The energy E_1 corresponds to the part of the cell that contains the impurity atoms. The value of E_d was calculated by using formula (1). Calculations of the values E_0, E_1 and E_2 were carried out using the ADF-BAND software package [17], based on the DFT approximation.

The results of the calculations are presented in Table 19.1.

From the obtained data it follows that the values of E_0, E_1 and E_d for iron containing elements of the fourth period as impurities, initially increase and then decrease with the growth of the atomic number of the element. In the case of krypton, the decay energy of the cell is zero, i.e., in the presence of this element, the cell spontaneously decays. It should be noted that the results obtained are actually a consequence of the Periodic Law.

Table 19.1 Total energy E_0 of initial cell, energies E_1, E_2 of decayed parts and energy E_d, required for decay of cell

Element's number	Impurity element	E_0, eV	E_1, eV	E_2, eV	E_d, eV
19	K	−188.9	−105.1	−82.5	1.3
20	Ca	−193.6	−108.7	−82.5	2.4
21	Sc	−201.2	−115.5	−82.5	3.2
22	Ti	−207.8	−119.7	−82.5	5.6
23	V	−210.9	−122.3	−82.5	6.1
24	Cr	−211.8	−122.8	−82.5	6.5
25	Mn	−212.0	−123.2	−82.5	6.3
26	Fe	−211.2	−122.4	−82.5	6.3
27	Co	−209.8	−121.4	−82.5	5.9
28	Ni	−203.6	−115.3	−82.5	5.8
29	Cu	−199.4	−111.9	−82.5	5.0
30	Zn	−195.2	−108.3	−82.5	4.4
31	Ga	−199.8	−112.8	−82.5	4.5
32	Ge	−202.9	−116.1	−82.5	4.3
33	As	−203.6	−117.3	−82.5	3.8
34	Se	−200.5	−115.8	−82.5	2.2
35	Br	−194.4	−110.4	−82.5	1.5
36	Kr	**?**	−101.8	−82.5	0

Note the "**?**" sign in the column with E_0 means that the corresponding value for this element is undefined. A cell with such an element disintegrates spontaneously

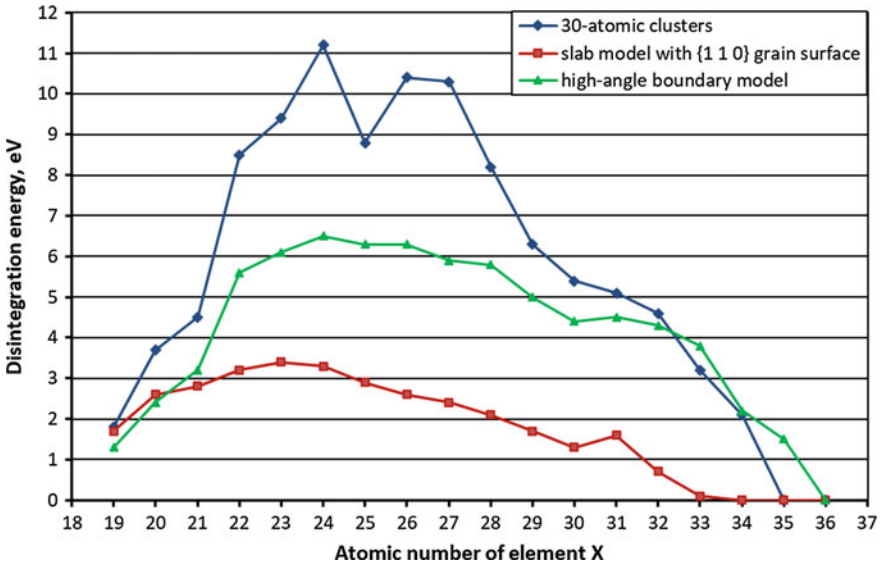

Fig. 19.4 Dependence of the decay energy of an atomic system on the atomic number of an impurity element located at the grain boundary

These numerical data are consistent with data from our previous work obtained by using the flat model. From the fact that the energy required for the decay of the cell is maximum for the atoms of titanium, vanadium, chromium, manganese, cobalt and nickel, and it is greater or comparable to the decay energy in the case of pure iron, it follows that these elements strengthen iron. This conclusion is consistent with known experimental and theoretical data (see, for example, [14, 15]).

In Fig. 19.4, the data from Table 19.1 relating to E_d are shown graphically. Here, for comparison, the data corresponding to the results of calculations performed earlier [10, 11] with the help of simpler cluster and slab models are presented. This representation allows us to clearly see that in this case there is a relationship of the decay energy on the atomic number of elements, similar to the dependencies obtained in previous calculations.

19.4 Conclusions

The binding energies of different atomic structures which were calculated by using the high-angle boundary model are qualitatively consistent with the results obtained earlier by using the flat model. It follows that the bond strength at grain boundaries in iron is mainly determined by the effects that are equally reproduced in these models - that is, the pair interactions between the atoms of the base metal (in this case, iron) and the atoms of alloying and impurity elements on the grain surface. The

dependence of the bond strength on details of the mutual arrangement of atoms is manifested to a lesser extent.

These facts make it possible to rank the elements located at grain boundaries by the magnitude of the chemical bonds between these elements and iron. The whole set of elements can be divided into three groups: (i) strengthening; (ii) softening and (iii) not significantly affecting the strength of boundaries. The elements of the fourth period which can be attributed to the strengthening elements are titanium, vanadium, chromium, manganese, cobalt and nickel. The softening elements include potassium, calcium, arsenic, scandium, selenium, bromine. These results are consistent with known experimental information about these elements.

Acknowledgements This work was performed within the framework of the state assignment of the South Scientific Center of RAS, number of state registration is AAAA-A16-116012610052-3.

References

1. P. Lejcek, *Grain Boundary Segregation in Metals*. Springer Series in Materials Science, vol. 136 (Springer, Berlin, 2010)
2. B.S. Bokstein, A.O. Rodin, B.B. Straumal eds. in Selected, peer reviewed papers from the international conference on grain boundary diffusion, stresses and segregation, DSS 2010, Moscow, Russia, 1–4 June 2010, pp 308 (2011)
3. M. Herbig, D. Raabe, Y.J. Li, P. Choi, S. Zaefferer, S. Goto, Phys. Rev. Lett. **112**, 126103 (2014)
4. W. Peng, H. Peng, G. Wu, J. Zhang, Comp. Mater. Sci. **171**, 109204 (2020)
5. M. Yuasa, M. Mabuchi, Phys. Rev. B **82**, 0941081 (2010)
6. J.L. Wang, R. Janisch, G.K.H. Madsen, R. Drautz, Acta Mater. **115**, 259 (2016)
7. M. Yamaguchi, M. Shiga, H. Kaburaki, Mater. Trans. **47**, 2682 (2006)
8. K.D. Bauer, M. Todorova, K. Hingerl, J. Neugebbauer, Acta Mater. **90**, 69 (2015)
9. M. Yamaguchi, Y. Nishiyama, H. Kaburaki, Phys. Rev. B **76**, 0354181 (2007)
10. YuF Migal, V.I. Kolesnikov, I.V. Kolesnikov, Comp. Mater. Science **111**, 503 (2016)
11. V.I. Kolesnikov, Y.F. Migal, I.V. Kolesnikov, E.S. Novikov, Dokl. Phys. Chem. **464**(1), 194 (2015)
12. M.P. Seah, Acta Metall. **28**, 955 (1980)
13. E.P. DeCarmo, J.T. Black, R.A. Kohser, *Materials and Processes in Manufacturing*, 10th edn. (Wiley, Hoboken, NJ, 2007)
14. P.-J. Cunat, *The Euro Inox Handbook of Stainless Steel* (Brussels, 2002)
15. H.J. Grabke, in *Impurities in Engineering Materials. Impact, Reliability, and Control*, ed. by C.L. Briant Marcel Dekker, New York, 1999), p. 143
16. G. Gottstein, *Physical Foundations of Materials Science* (Springer, Berlin, 2014)
17. G. te Velde, F.M. Bickelhaupt, E.J. Baerends, F.C. Guerra, S.J.A. van Gisbergen, J.G. Snijders, T. Ziegler, J. Comp. Chem. **22**, 931 (2001)

Chapter 20
Digital Microscopy Image Enhancement Technique for Microstructure Image Analysis of Bottom Ash Particle Polymer Composites

F. A. Hermawati, I. M. Kastiawan, and Muhyin

Abstract Polymer composites are composite materials with matrices of polymers with reinforcements using fibers or particles or both together. This study uses polypropylene polymer composite material with reinforcement of bottom ash particles. In the manufacture of polypropylene-shaped sheet (lamina) polymer composite materials with bottom ash particles, the process of assessing the composite characteristics of the polypropylene matrix such as the level of distribution of bottom ash particles as fillers in the polypropylene matrix through microscopic images is necessary. Analysis of the level of distribution of reinforcement particle is used to avoid the formation of filler particle agglomerates during the dispersion of various types of fillers in polymer resins. Bottom ash particles themselves have an irregular shape that requires particular analysis to distinguish a single particle and an agglomerate particle. Before the analysis step, the most crucial step at the beginning is to carry out the process of improving the quality of the input image, which aims to improve image contrast and eliminate unwanted noise. This chapter proposes an image enhancement method to enhance the quality of the microstructure image of a polymer composite that is analyzed using a digital microscope. The proposed method combines the multiresolution approach and the anisotropic diffusion method. From the experiment, this image enhancement method gives the best performance when it is compared with other techniques in the state of the arts.

20.1 Introduction

In the manufacture of polypropylene-shaped sheet (lamina) polymer composite materials with bottom ash particles, the process of assessing the composite characteristics of the PP matrix such as the level of distribution of bottom ash particles as fillers in the PP matrix through microscopic images is an essential act. We need an analysis

F. A. Hermawati (✉)
Department of Informatics, Universitas 17 Agustus 1945, Surabaya, Indonesia
e-mail: fajarastuti@untag-sby.ac.id

I. M. Kastiawan · Muhyin
Department of Mechanical Engineering, Universitas 17 Agustus 1945, Surabaya, Indonesia

I. A. Parinov et al. (eds.), *Advanced Materials*, Springer Proceedings in Materials 6, https://doi.org/10.1007/978-3-030-45120-2_20

of the level of distribution of reinforcement particles to avoid the formation of filler particle agglomerates during the dispersion of various types of fillers in polymer resins [1, 2]. Bottom ash particles have an irregular shape that requires particular analysis to distinguish a particle or an agglomerate of particles. Before the analysis step, the most crucial step at the beginning is to carry out the image enhancement process to improve the quality of the input image, which aims to improve image contrast and to eliminate noise.

In several studies of image analysis for composite materials, a microscopic image quality improvement technique is needed to reduce noise or unwanted artifacts in the image but still retain the characteristics and details of the image. As state of the art, we present several studies related to image enhancement techniques for analyzing microstructural images using Scanning Electron Microscope (SEM), Transmission Electron Microscope (TEM), or digital microscopes. Gaussian filter is a filter that is widely used to reduce noise both in the signal as performed by Hermawati et al. [3] or on the image. Campbell et al. [4] used Gaussian filters to reduce noise while maintaining differences in intensity between adjacent grains. According to Campbell, finding effective Gaussian filtering can also cause distortion. The chosen size of the filter will be able to reduce noise and distortion. They proposed a 3×3 filter size for optical image s of titanium Microstructures of the Ti_6Al_4V alloy taken using a digital microscope. Kundu et al. [5] also applied a 5×5 Gaussian filter with standard deviation $\sigma = 1.2$ to eliminate noise in the SEM image of a polymer composite using the natural blend system of natural rubber matrix (NR)—polybutadiene rubber (PBR)—reclaim rubber (RR) with silica as a reinforcement.

Meanwhile, Hiremath et al. [6] proposed the selective median switching filter in [7] to eliminate noise in the image of ductile cast iron microstructure. Martin-Herrero [8] implemented the image processing techniques in the reconstruction task of the 3D microstructure image of the C/C fiber composites from an X-ray contrast phase micro tomography. In the preprocessing stage, they applied the anisotropic diffusion method in [9] that can eliminate high-frequency noise while maintaining the edge. Duval et al. [10] suggested a bilateral filtering method to reduce noise in the homogeneous areas by slightly modifying the area of interest. They implemented this filter in the SEM image of the catalyst section that illustrates black cracks, partially filled pores that have a round dark grey shape with white spots and inclusion of zeolites which is scattered or aggregated white dots in neutral substrates (aluminum).

This study proposed an image enhancement technique for improving the microscopic image quality of polymer composites with reinforcement of bottom ash. This method will eliminate noise that can be the granules or white lines due to the forming process of the sheet material, for example, due to the operation of rolling or pressing. The proposed method combines the frequency-based technique with some spatial filtering based methods. This hybrid method, as presented by Hermawati et al. [11], can reduce noise in the image while maintaining the edge. We also propose a dark region enhancement stage to increase the contrast of the black area, which is the bottom ash particles area. The application of the proposed image enhancement method aims to improve the accuracy of the analysis of filler dispersions in the polymer matrix in measuring the strength of the tested material.

This chapter is composed of four sections. The second section presents how to obtain the Microstructure image from polymer composite material for the research and explain the proposed method to enhance the image. The results of the conducted experiment are presented in the third section. In this section, we also compare our proposed method with other techniques in state of the art. The fourth section presents conclusions and steps that need to be done in the next study.

20.2 Material and Method

20.2.1 Material Preparation

The materials used to make polymer composites with sisal fibers as reinforcement are thermoplastic polymers (polypropylene), bottom ash with specific mesh, and sisal fibers of a certain length. Concentrations based on weight will be prepared according to the variables determined before polymer melting. Polypropylene polymers with a specific weight are poured into a heating container with a temperature of 170 °C. This temperature corresponds to the melting temperature of polypropylene. After 100% melting, which takes almost 2 h for the weight of 300 g of polypropylene, bottom ash powder of coal is weighed and has a specific mesh particle size. Then, sisal fibers of a certain length were inserted into them in an amount that was also determined. After all fillers and boosters have been poured, stirring is carried out for 30 min at a certain speed. After the stirring time, the polymer composite material mixture is ready to be printed into a rectangular mold, 10 mm thick, 20 mm wide and 200 mm long with a pressure of 20 kg/mm^2 during 5 min. The polymer composite material after cooling is ready to be removed from the mold. For testing of filler distribution, the content is flattened or printed in the sheet form with a certain thickness and then captured by using a digital optical microscope Dino-lite with 200 times magnification. Figure 20.1 is the example of a microscopic image with bottom ash particles percentage of 2 and 5%. The image size obtained is 1280 $\times$ 1024 pixels.

20.2.2 Proposed Method

The proposed method is the development of the technique proposed by Hermawati et al. [11], which is used to eliminate speckle noise in ultrasound images, namely hybrid speckle noise reduction method, as described in Fig. 20.2. This method combines multiresolution wavelet approach with bilateral filtering and anisotropic diffusion technique. We add a method to increase the black pixels of the image that indicate the bottom ash particles and will be further analyzed. The proposed method consists of five main steps.

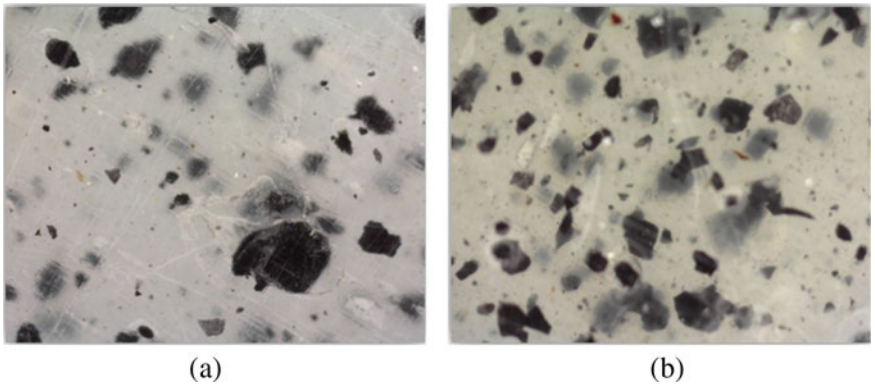

Fig. 20.1 Examples of microscopy image of polymer composite with bottom-ash particle percentage of **a** 2% and **b** 5%

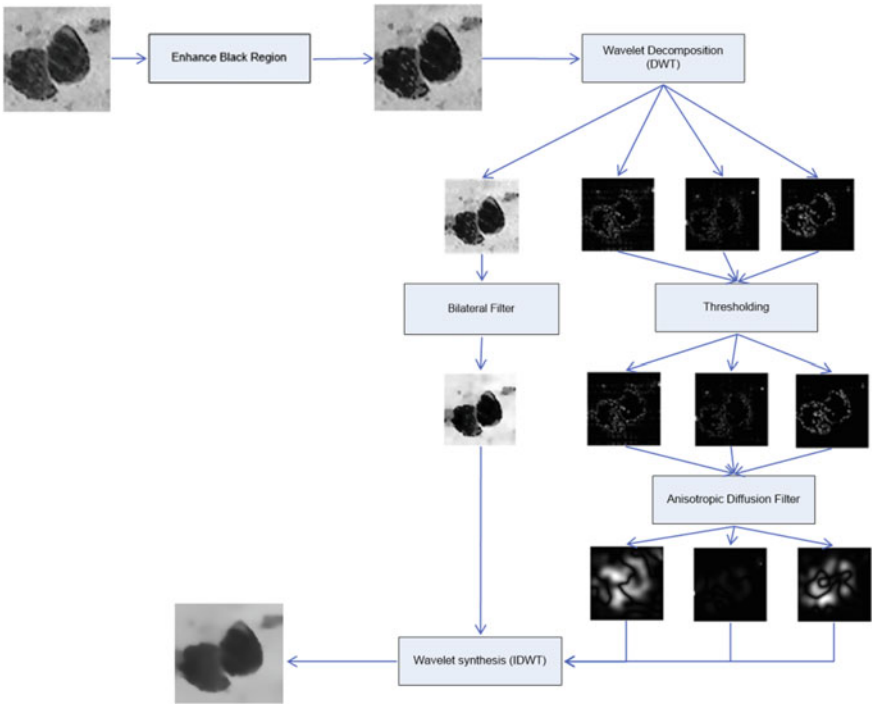

Fig. 20.2 Block diagram of proposed method

Firstly, the process of enhancing dark regions is done by using local statistics enhancement using a 3 × 3 neighboring window. Suppose $f(x, y)$ is an image, the enhanced image $g(x, y)$ is expressed as

$$g(x, y) = 0.5\ f(x, y); \quad \text{if}\, \mu(x, y) < 0.5\ \mu_G \tag{20.1}$$

where $\mu(x, y)$ is a local mean in 3 × 3 neighbourhood area with coordinates (x, y) at its centre and μ_G is an average of image intensities.

After that, the enhanced image g is decomposed using three-level discrete wavelet transform into one approximation image, A_3, and nine detail images, i.e. D_3^1, D_3^2, D_3^3 at the third level; D_2^1, D_2^2, D_2^3 at the second level and D_1^1, D_1^2, D_1^3 at the first level as described in Fig. 20.3. The detail images are processed sequentially using thresholding and anisotropic diffusion, whereas the approximation image is processed using bilateral filters starting from the third level. Furthermore, the four subbands at level 3 that have been processed are synthesised using the inverse discrete wavelet transform (IDWT) to get the approximation image at level 2. The same process is carried out until the first decomposition level. We implement the best parameters in [11].

Suppose A is an approximation image with i as centre coordinate of 5 × 5 neighbourhood window, w, and $j \in w$ is a pixel coordinate in window w that $i \neq j$. The bilateral function A, denoted as, $\hat{A}$ is expressed as the following expression [11]:

$$\hat{A}(i) = \frac{1}{C} \sum_{j \in w} \left(\frac{1}{\sigma_d \sqrt{2\pi}} \mathrm{e}^{-\left(\frac{(j-i)^2}{2\sigma_d^2}\right)} \right) \left(\frac{1}{\sigma_r \sqrt{2\pi}} \mathrm{e}^{-\left(\frac{(A(j)-A(i)^2}{2\sigma_r^2}\right)} \right) A(j) \tag{20.2}$$

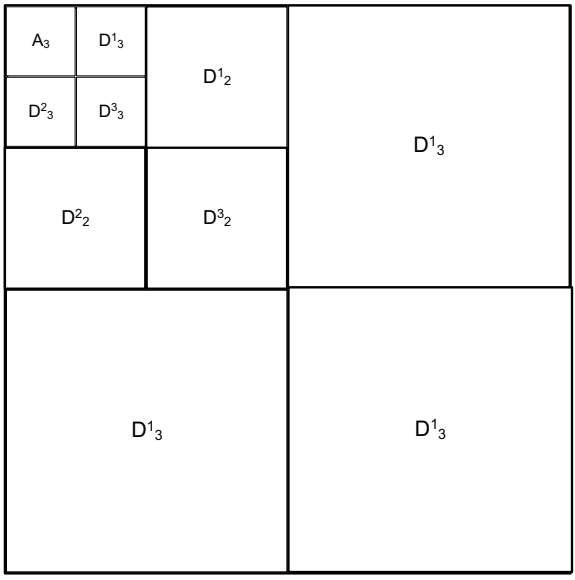

Fig. 20.3 Three-level wavelet decomposition

where (i) and $A(i)$ are the intensities at coordinate i; σ_d and σ_r are the standard deviations of Gaussian filter that control smoothing strength in the image domains, and C is a normalization constant. In this research, we use controlling parameter $\sigma_d = 3$ and $\sigma_r = 7\sigma_n$, where σ_n is the standard deviation of noise that equal to the threshold value of T in (3).

The following function obtains the threshold value, T that is implemented in the thresholding step for the detail images, D^1, D^2, D^3 [11]:

$$T = \frac{\left\| \text{median} \left(D_i^3 \right) \right\|}{0.6745} \tag{20.3}$$

where D_i^3 are image coefficients in diagonal image D^3.

20.3 Results and Discussion

Optical microscopic images used in the experiment can be seen in Fig. 20.1, with percentages of bottom ash reinforcement equals to 2%. Composite lamina sheets used have not been done by finishing or polishing, so that there are parts of pressure marks due to the rolling process during the process of making lamina, which is indicated by bright coloured lines. This is also a challenge in the process of improving the quality of microscopic images. To evaluate the results of enhanced microscopic image quality of polymer composites, we compared them with other methods used in state of the art research, i.e. Gaussian filter size 3×3, Gaussian filter size 5×5 with standard deviation 1.2, anisotropic diffusion, bilateral filter and selective median filter. Visually, the enhancement result for each method can be seen in Fig. 20.4. In Fig. 20.4, the bottom ash particles in the image that is processed by the proposed method are more clear and sharp than in the other images.

Since in this problem there is no reference image or ground truth of the processed image, then to evaluate the noise reduction level we use ENL (Equivalent Number of Looks) which is formulated as the ratio between (mean/standard deviation)^2 from the homogeneous image area [13–15]. Where the higher the value of ENL, the better the rate of removal of the number. However, to see the quality of the noise reduction method in maintaining edges, we measured ENL for the entire image. A low ENL value, which means that the variation of the intensities is high, will indicate that the level of edge presence is high. So the smaller the ENL value, the better the method of maintaining edges. The performance comparison of the image enhancement methods is presented in Table 20.1. In Table 20.1, it can be seen that the proposed hybrid method gives the lowest ENL value. The ENL value is comparable to the view in Fig. 20.4a in which appears a significant difference in intensity between the object and the background. The anisotropic diffusion method has a lower ENL value and is followed by the bilateral filtering technique. The Gaussian filter method for a 3×3 filter and a 5×5 filter and also the selective median filter have almost identical ENL value.

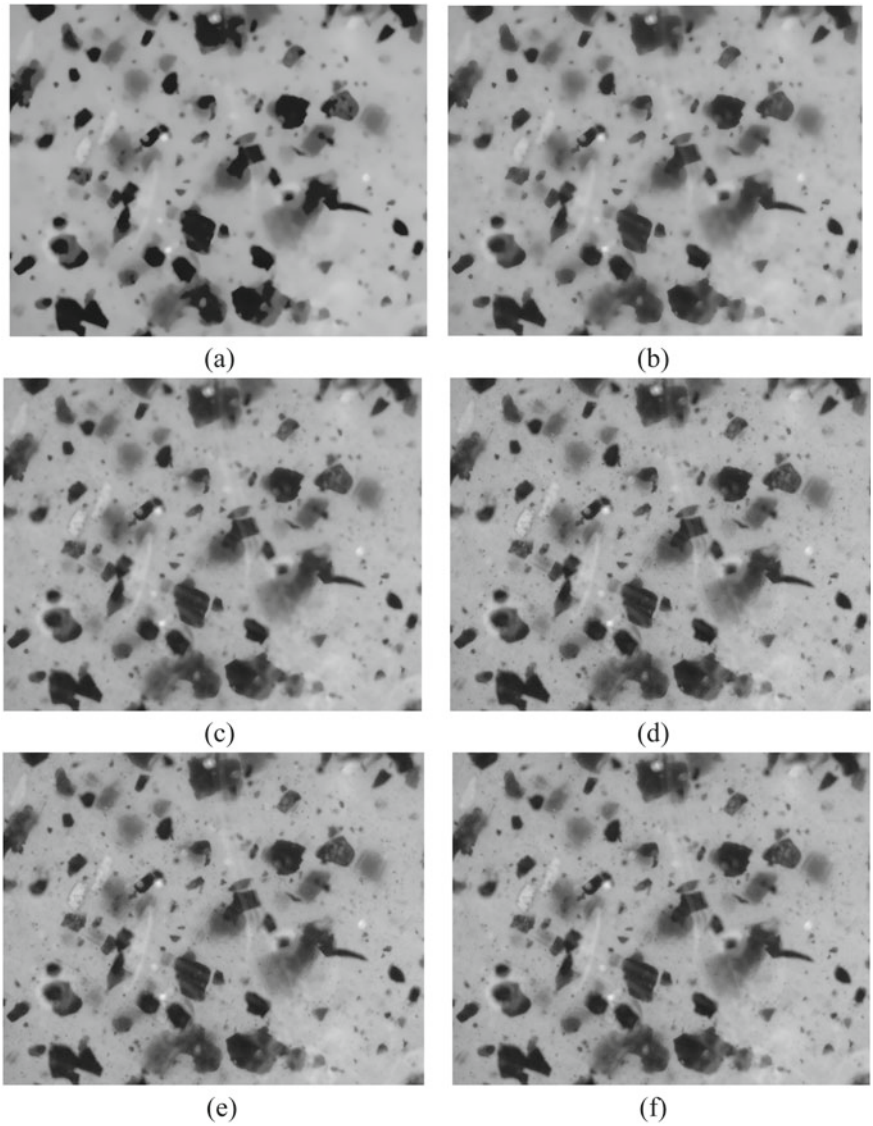

Fig. 20.4 Comparation of enhancement result using: **a** proposed method; **b** anisotropic diffusion; **c** bilateral filter; **d** selective median filter; **e** Gaussian filter 3×3; **f** Gaussian filter 5×5 with $\sigma = 1.2$

Table 20.1 Performance comparison of image enhancement method

Method	ENL
Hybrid enhancement method (proposed method)	152.769
Anisotropic diffusion (Perona Malik) [8]	159.5305
Bilateral filter [12]	160.0842
Selective median filter [6]	161.4238
Gaussian filter 3 × 3 [4]	161.1195
Gaussian filter 5 × 5 with $\sigma = 1.2$ [5]	161.1191

Figure 20.5 presents the histogram of the image enhancement results. From the histogram of the proposed method in Fig. 20.5a, we can separate precisely between the object (bottom ash particles) and the background (matrix). So the image segmentation result for getting the bottom ash particles has become more accurate when compared to other image enhancement methods such as shown in Fig. 20.6. We implemented the thresholding method with a threshold equal to 0.2 to obtain the binary images in Fig. 20.6.

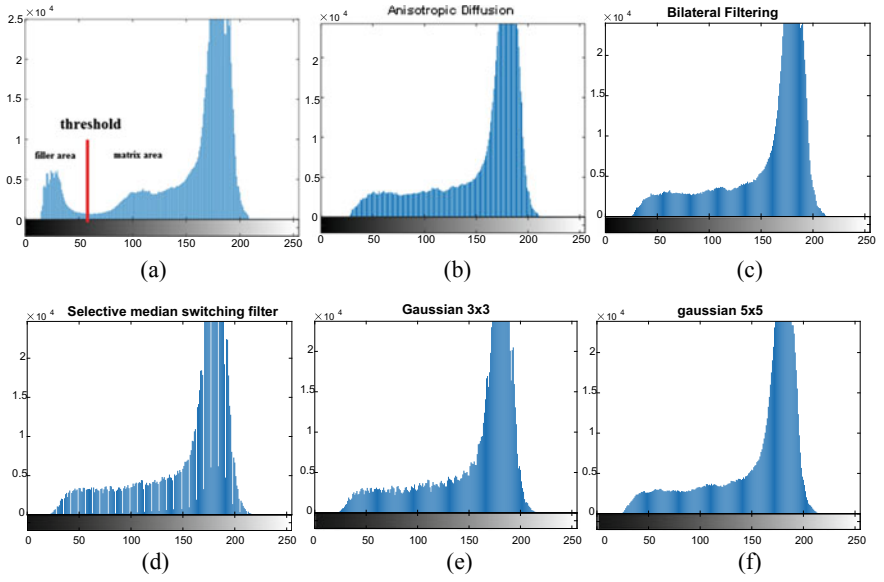

Fig. 20.5 Histograms of the enhanced image using: **a** proposed method; **b** anisotropic diffusion; **c** bilateral filter; **d** selective median filter; **e** Gaussian filter 3 × 3; **f** Gaussian filter 5 × 5 with $\sigma = 1.2$

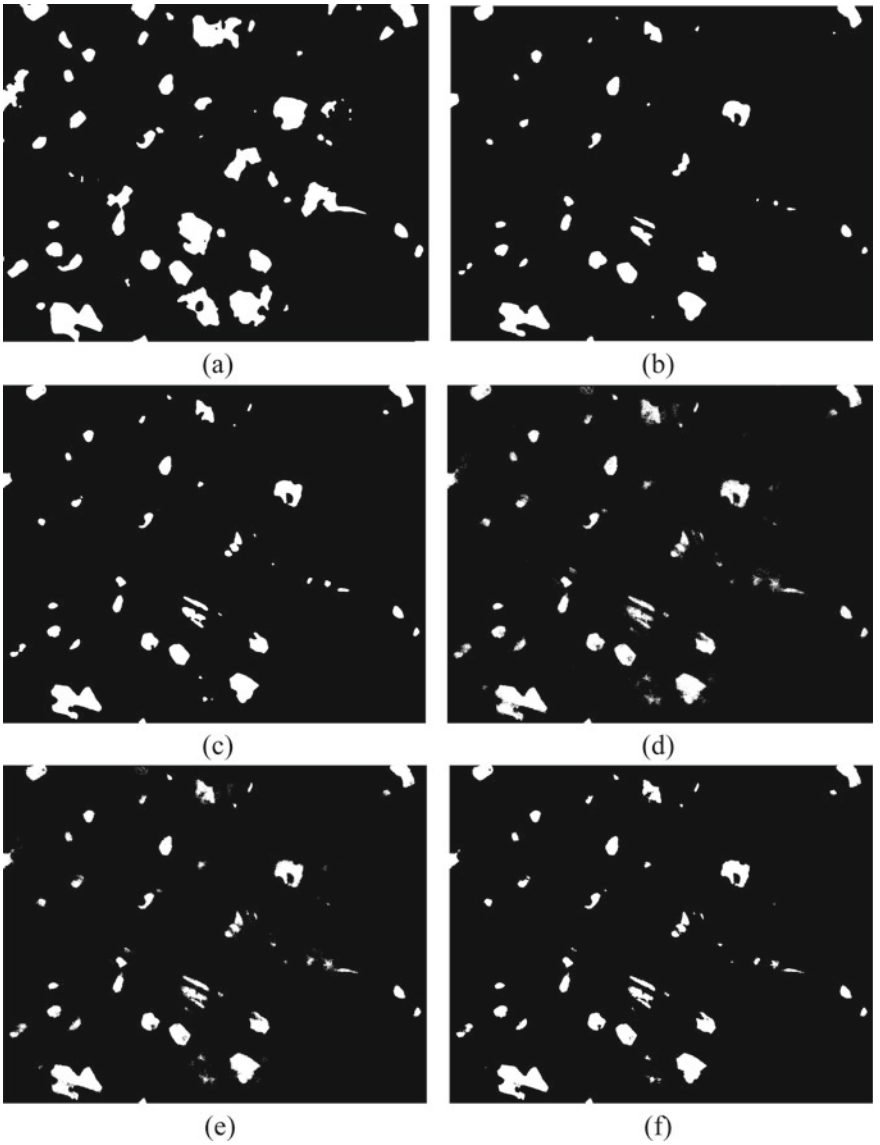

Fig. 20.6 Segmentation results of the enhanced image using: **a** proposed method; **b** anisotropic diffusion; **c** bilateral filter; **d** selective median filter; **e** Gaussian filter 3×3; **f** Gaussian filter 5×5 with $\sigma = 1.2$

20.4 Conclusion

Hybrid speckle-noise reduction method, which was preceded by the technique of repairing dark areas in microscopic images of polymer composites with bottom ash reinforcement was able to eliminate noise and scratches while maintaining image details. By applying this proposed noise reduction technique, the results of image segmentation by thresholding become more precise compared to other methods in state of the art. Furthermore, to analyze the dispersion level of bottom ash particles in polymer composites, segmentation and filler particle analysis need to be done.

Acknowledgements This research was funded from a leading applied research universities from The Ministry of Research, Technology & Higher Education of the Republic of Indonesia based on Grant No. 229/SP2H/LT/DRPM/2019 dated March 11, 2019 and contract number: 374/06/ST/LPPM/Lit/III/2019.

References

1. T. Glaskova, M. Zarrelli, A. Borisova, K. Timchenko, A. Aniskevich, M. Giordano, Compos. Sci. Technol. **71**, 1543 (2011)
2. T. Glaskova, M. Zarrelli, A. Aniskevich, M. Giordano, L. Trinkler, B. Berzina, Compos. Sci. Technol. **72**, 477 (2012)
3. F.A. Hermawati, Sugiono, Evonda, in *Advanced Materials Techniques, Physics, Mechanics and Applications*, ed by I.A. Parinov, S.-H. Chang, M.A. Jani, Springer International Publishing, Berlin, pp. 535–543 (2017)
4. A. Campbell, P. Murray, E. Yakushina, S. Marshall, W. Ion, Mater. Des. **141**, 395 (2018)
5. S. Kundu, P. Jana, D. De, M. Roy, in *Proceedings of 2015 IEEE International Conference on Electrical, Computer and Communication Technologies, ICECCT 2015* (2015)
6. P.S. Hiremath, A. Sadashivappa, P. Pattan, Int. J. Comput. Appl. **107**, 975 (2014)
7. P.S. Hiremath, A. Sadashivappa, Int. J. Image Process. **7**, 101 (2013)
8. J. Martin-herrero, C. Germain, *Carbon*, Elsevier, vol. 45, pp. 1242 (2007)
9. P. Perona, J. Malik, IEEE Trans. Pattern Anal. Mach. Intell. **12**, 629 (1990)
10. L. Duval, M. Moreaud, C. Couprie, D. Jeulin, H. Talbot, J. Angulo, in *2014 IEEE International Conference on Image Processing, ICIP 2014*, pp. 4862 (2014)
11. F.A. Hermawati, H. Tjandrasa, N. Suciati, Int. J. Electr. Comput. Eng. (IJECE) **8**, 1747 (2018)
12. L. Duval, M. Moreaud, C. Couprie, D. Jeulin, H. Talbot, J. Angulo, in *2014 IEEE International Conference on Image Processing, ICIP 2014*, pp. 4862–4866 (2014)
13. X. Fu, Y. Wang, L. Chen, J. Tian, Biomed. Signal Process. Control **18**, 30 (2015)
14. Y.M.M. Babu, M.V. Subramanyam, M.N.G. Prasad, Int. J. Electr. Comput. Eng. **5**, 984 (2015)
15. F. A. Hermawati, S. Sugiono, R. Octaviany, in *Seminar Nasional Otomasi Industri Dan Teknologi Informasi 2015 (SNOITI 2015)* (2015) (in Indonesian)

Chapter 21
Analysis of Effect of Oil Viscosity and Temperature on Dynamic Pressure Distribution in Internal Gear Motor and Pump

Pham Trong Hoa

Abstract The chapter analyzes the effect of oil temperature and dynamic viscosity on hydrodynamic pressure distribution of the oil lubrication film in the internal gear motor and pump. The Reynolds equation with appropriate boundary condition is solved to obtain 2D hydrodynamic pressure distribution by using the finite difference method (FDM). Numerical calculations point out that the oil temperature and viscosity have great effect on hydrodynamic pressure distribution as well as the maximum value of pressure.

21.1 Introduction

Internal gear motor and pump (IGMaP) is very popular in the field of hydraulic power applications [1]. Oil lubrication film is very important for rotating machines. Its role is to separate the relative rotating surfaces during operation or even at the rest [2]. In study [3], Pham pointed out that the hydrodynamic pressure in the oil film is much dependent on the rotating speed. The hydrodynamic pressure mountain will produce the capacity for the oil lubrication film to against with the radial load acting on the ring gear. The outer ring gear and inner housing surfaces is, therefore, protected during operation. It also means that if the oil film is failure, then the outer ring gear and inner housing will be in solid contact. It makes the IGMaP damages much sooner. Consequently, the lifespan of IGMaP is strongly reduced. This is unwanted phenomenon. Thus, calculation of hydrodynamic pressure distribution and estimation of the effect of working conditions are the fundamental issue to improve the performance of IGMaP [4]. Studying about the hydrodynamic pressure in the oil lubrication film have been performed by researchers such as [5, 6]. Lots of works have been studied regarding to IGMaP [7–9], however, the effect of oil temperature and viscosity on hydrodynamic pressure distribution has been not released so far. In

P. T. Hoa (✉)
University of Transport and Communications (UTC), No. 3 Cau Giay, Lang Thuong, Dong Da, Hanoi, Vietnam
e-mail: hoagtvt100@gmail.com

I. A. Parinov et al. (eds.), *Advanced Materials*, Springer Proceedings in Materials 6, https://doi.org/10.1007/978-3-030-45120-2_21

this study, by using the Finite Difference Method to solve the Reynolds equation, the effect of oil temperature and viscosity on the hydrodynamic pressure distribution are analyzed.

21.2 Formation of the Equation

An internal gear motor and pump has three main elements which are described in Fig. 21.1, e.g., a ring gear which is consider as rotor, a fixed-pinion gear which connected to shaft, and the housing (stator). The diameter of inner housing is slightly larger than that of the outer ring gear. The space between the outer ring gear and the inner housing is fully filled by working oil. This is called the thin lubrication film.

During operation, the oil film thickness is various for different position over circumferential direction as in Fig. 21.2. The oil film profile is calculated as follows,

$$h_{(\theta,e)} = c(1 + \varepsilon \cos\theta) \tag{21.1}$$

where ε is the eccentricity ratio; i.e., the ratio of eccentricity to radial clearance (e/c); θ is the angle from the central line (ZZ_0) to the measured point (H) along with the circumferential direction; c is the radial clearance.

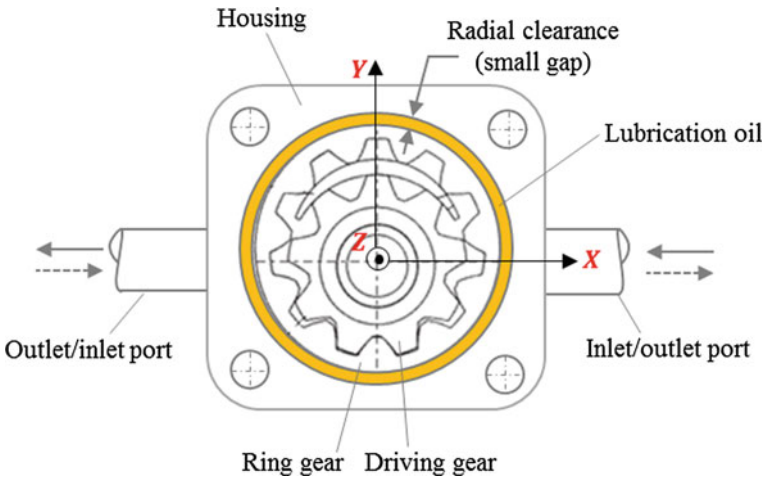

Fig. 21.1 Internal gear motor and pump

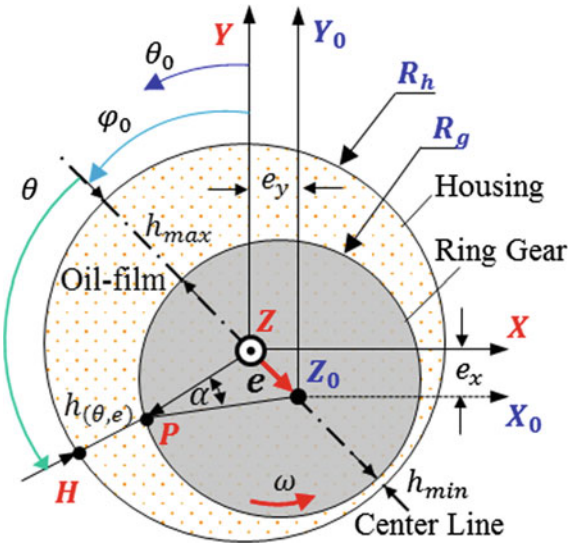

Fig. 21.2 Geometry of the ring gear

21.2.1 Hydrodynamic Pressure Distribution

The well-known Reynolds equation is used to calculate the pressure distribution. The Reynold's equation for incompressible liquid is described as follows [1]:

$$\frac{\partial}{\partial\theta}\left(\mathrm{h}^3\frac{\partial p}{\partial\theta}\right)+\frac{\partial}{\partial z}\left(\mathrm{h}^3\frac{\partial p}{\partial z}\right)=6\mathrm{U}\mu\frac{\partial h}{\partial\theta} \tag{21.2}$$

where h is the film thickness [m]; r is the ring gear radius [m]; L is the length of ring gear [m]; D is the diameter of the ring gear [m]; μ is the dynamic viscosity [Pa · s]; p is the pressure [Pa]; θ, z are hydrodynamic film co-ordinates [m].

Dynamic viscosity of the lubricant oil as a function of temperature can be computed according to Vogel-Cameron [10] as follows,

$$\mu_T = A \cdot e^{\frac{B}{T+C}} \tag{21.3}$$

where $C = 95$ °C is the constant coefficient; A and B is the fluid specific constant, for HLP 46, $A = 0.054$ mPa · s, $B = 921$ °C, T is the oil temperature.

The Reynolds equation has been solved by using the finite difference method (FDM) with appropriate boundary condition to obtain 2D hydrodynamic pressure distribution. Details of finite difference solution has been presented in study [1]. The computational calculation is present in Fig. 21.3. An in-house calculation tool has been coded in Matlab environment to optimize the calculation time. All the operating parameters and geometric parameters are considered as the input parameters for calculation. The mobility method is used firstly to predict the ring the eccentricity

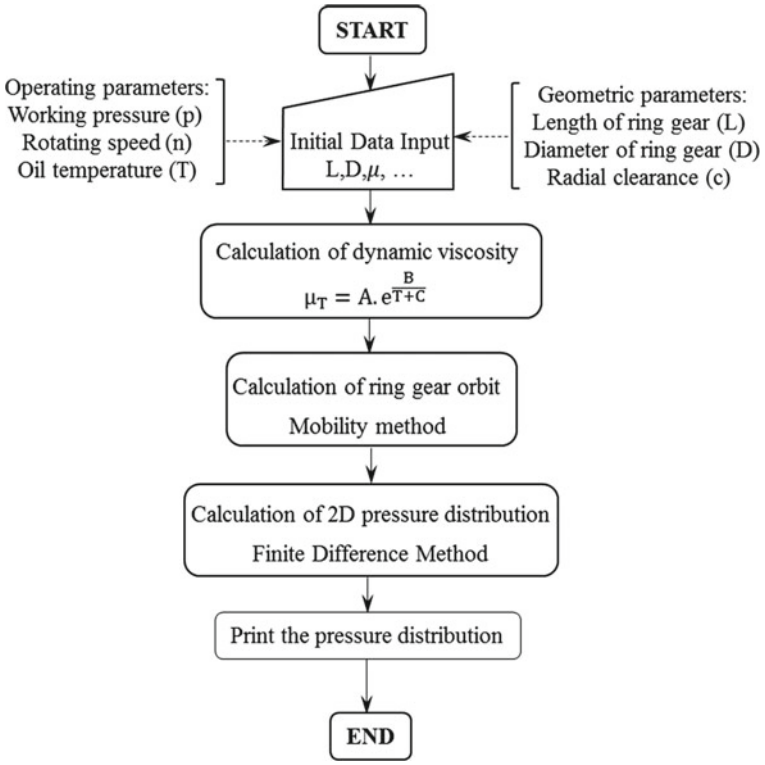

Fig. 21.3 Computational flow chart

of ring gear center. These parameters are considered as the input parameters to solve the Reynolds equation to obtain 2D hydrodynamic pressure distribution.

21.3 Simulation Results and Discussion

The input parameters for calculation are present in Table 21.1.

Table 21.1 Initial data input

Parameter	Symbol	Value	Unit
Length of ring gear	L	0.34	m
Diameter of ring gear	D	0.115	m
Radial clearance	c	60×10^{-6}	m
Rotating speed	n	1500	rpm
Working pressure	Δp	100	bar

21.3.1 Effect of Oil Temperature

2D dynamic pressure mountain in the oil lubrication film for various values of oil temperature is depicted in Fig. 21.4.

The dynamic pressure distributes evenly over the axial direction. For circumferential direction, the dynamic pressure area ranges from 110° to 290°. From Fig. 21.4, one can observe that for low values of oil temperature, the dynamic pressure mountain is higher than that of high values of oil temperature. For example, as oil temperature at value of 0 °C the maximum dynamic pressure is 27.20 bar. The maximum dynamic pressure downs to 10.82 bar when the oil temperature increases up to 90 °C.

The eccentricity is also changed according to the change of oil temperature as shown in Fig. 21.5. The eccentricity increases with the increase of the oil temperature, e.g., the eccentricity increases from 0.6 to 0.91 as the temperature increases from 0 to 90 °C. This is an unwanted phenomenon. Because it reduces the minimum film thickness. Consequently, the solid contact between the outer ring gear and inner housing is easy occurred. The changing of maximum dynamic pressure for various values of oil temperature is presented in Fig. 21.6. Contrary to the changing of

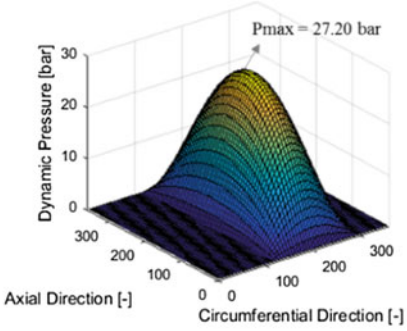

(a) Oil temperature at 0 °C

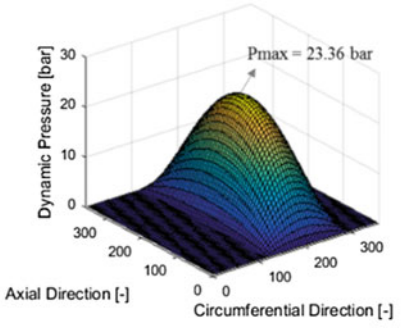

(b) Oil temperature at 30 °C

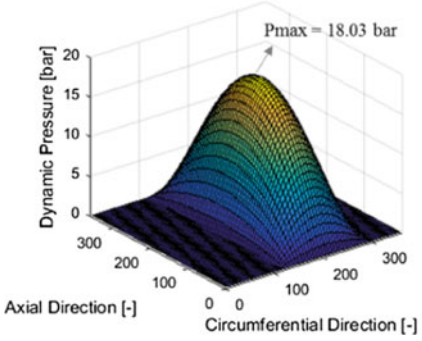

(c) Oil temperature at 60 °C

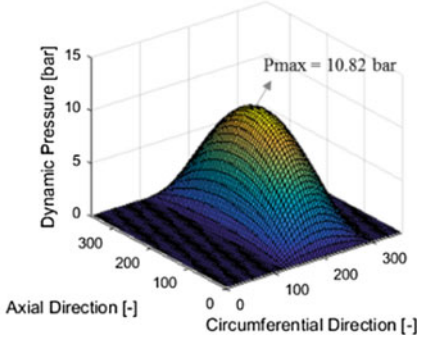

(d) Oil temperature at 90 °C

Fig. 21.4 Effect of oil temperature on 2D hydrodynamic pressure distribution

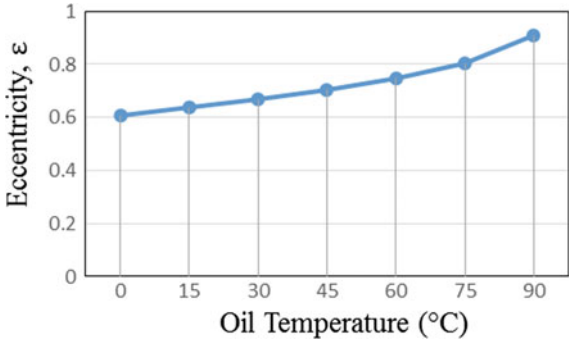

Fig. 21.5 Eccentricity over oil temperature

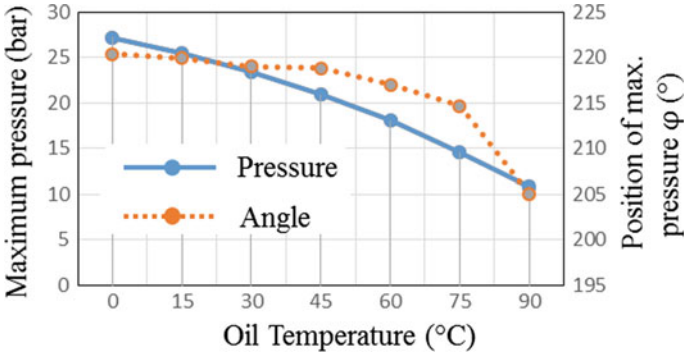

Fig. 21.6 Value and position of maximum pressure

eccentricity, the maximum pressure decreases with the increase of oil temperature. The decrease of maximum pressure leads to the decrease of the oil film capacity. In other words, it reduces the working ability of the internal gear motor and pump. Moreover, the position of maximum pressure also decreases with the increase of oil temperature, e.g., the position angle of maximum pressure decreases from 220° to 206° when the temperature increases from 0 to 90 °C. From these results one can conclude that the internal gear motor and pump should not operate at high values of oil temperature.

21.3.2 Effect of Oil Viscosity

Effect of oil type or oil viscosity on 2D dynamic pressure distribution is described in Fig. 21.7. It is obviously to see that for high values of dynamic viscosity, the dynamic pressure mountain is lower than that of high values of dynamic viscosity, e.g., the

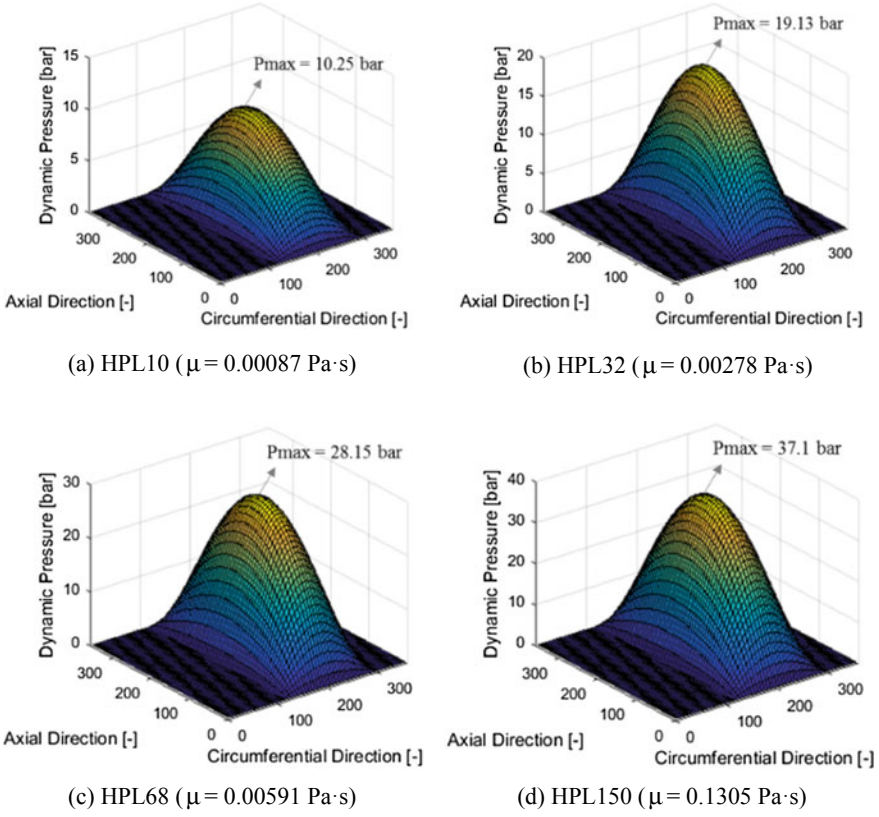

(a) HPL10 ($\mu = 0.00087$ Pa·s)

(b) HPL32 ($\mu = 0.00278$ Pa·s)

(c) HPL68 ($\mu = 0.00591$ Pa·s)

(d) HPL150 ($\mu = 0.1305$ Pa·s)

Fig. 21.7 Effect of oil dynamic viscosity on 2D hydrodynamic pressure distribution

maximum dynamic pressure increases about 3.7 times, from 10.25 to 37.1 bar as the oil viscosity increases from 0.00087 Pa·s for HLP10 to 0.1305 Pa·s for HP150.

The eccentricity of ring gear dependent on the dynamic viscosity is presented in Fig. 21.8. The eccentricity decreases with the increase of oil viscosity. For example, the eccentricity decreases from 0.95 to 0.42 when the dynamic viscosity increases from 0.0087 Pa·s for HLP 10 to 0.1305 Pa·s for HLP150. Contrary to the decrease of eccentricity, the value and position angle of maximum dynamic pressure increase with the increase of oil viscosity as depicted in Fig. 21.9. This will increase the oil film capacity. Consequently, the working ability of internal gear motor and pump is better when IGMaP operated at high value of dynamic viscosity.

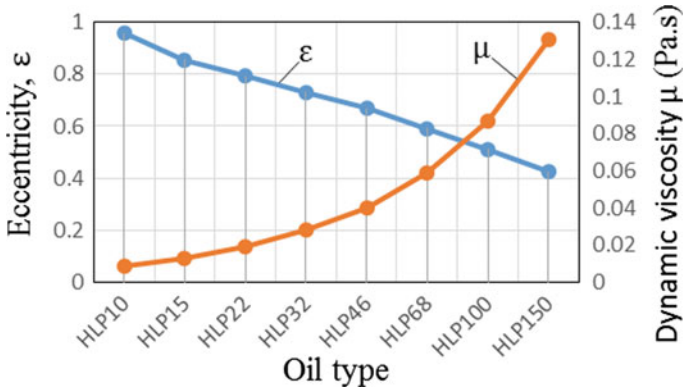

Fig. 21.8 Eccentricity *versus* oil viscosity

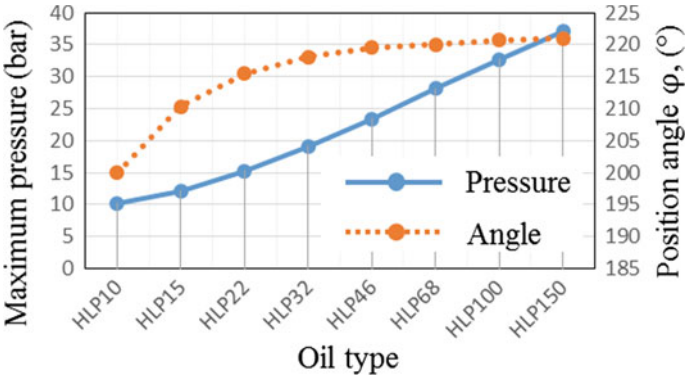

Fig. 21.9 Value and position of maximum pressure

21.4 Conclusion

Temperature and dynamic viscosity are two important parameters of hydraulic oil, which have great effect on dynamic pressure distribution, however it is not easy to assess. Based on the results presented in this study, some following conclusions can be drawn.

(1) The hydrodynamic pressure is proportional with the oil dynamic viscosity. The capacity of oil film increases with the increase of viscosity. If the dynamic viscosity of working oil is too low, the hydrodynamic pressure produces insufficient capacity for the oil film. It can lead to the solid contact. Therefore, it must be chosen the suitable oil type for each specific working condition.

(2) The hydrodynamic pressure is inversely proportional with the oil temperature. The solid contact between the outer ring gear and inner housing can be occurred, if IGMaP operates under high values of oil temperature. Therefore, if

IGMaP operates at high temperature, it must be checked the allowable condition otherwise the IGMaP will be damaged much sooner.

Acknowledgements This research is funded by Vietnam National Foundation for Science and Technology Development (NAFOSTED) under grant number 107.03-2019.17.

References

1. Trong Hoa Pham, *Analysis of the Ring Gear Orbit, Misalignment, and Stability Phenomenon for Internal Gear Motors and Pumps* (Shaker Verlag, Germany, 2018)
2. B.J. Hamrock, S.R. Schmid, B.O. Jacobson, *Fundamentals of Fluid Film Lubrication*, 2nd edn. (McGraw-Hill, New York, 2004)
3. T.H. Pham, L. Müller, J. Weber, J. Mech. Sci. Technol. **32**(7) (2018)
4. Trong Hoa Pham, J. Mech. Sci. Technol. **33**(2), 602–612 (2019)
5. M.A. Ahmad, S. Kasolang, R. Dwyer-Joyce, Appl. Mech. Mater. **315**, 977–981 (2013)
6. M. A. Omer, T.V.V.L.N. Rao, A.M.A. Rani, T. Nagarajan, F.M. Hashim, *Pressure Distribution in Hydrodynamic Journal Bearing*. MATEC Web of Conference. **13**, 05006 (2014). https://doi.org/10.1051/matecconf/20141305006
7. N.Y.Y. Inaguma, JTEKT Eng. J., **No. 1011E**, 64–73 (2014)
8. W. Song, Y. Chen, H. Zhou, Adv. Mech. Eng. **8**(10), 1–15 (2016)
9. D. Khalid, R. B. Weli, In: *1st International Conference* on Recent *Innovations* in *Engineering* and *Technology, SU-ICEIT 2016*, 162–168 (2016)
10. J. Ivantysys, M. Ivantysys, *Hydrostatische Pumpen und Motoren: Kontruktion und Berechnung* (Vogel Buchverlag, 1993) (in Germany)

Chapter 22
Experimental Investigation of Effect of Process Parameters on Surface Roughness in Electrochemical Machining

Loc P. Ngo, Tai P. Nguyen, and Thanh T. Tran

Abstract With the rapid development of removal technology of materials, manufacturing methods of advanced materials with highly flexible shape has been improved. Electro-chemical machining (ECM) is one of the most advanced manufacturing methods for not only manufacturing the high hardness metal with flexible profiles, but also provides a better solution to surface roughness of finished products and rate of material removal in the comparison with other advanced manufacturing methodologies such as electric discharge machining (EDM). However, there are many parameters involving to the ECM process such as velocity of the electrode, pressure of water, voltage, frequency and pulse of the current. Therefore, a set of optimization parameters for machining process of a material type is necessary to provide the best solution in industrial applications. This research focuses on investigating an optimal set of process parameters of the ECM machine by using the surface response methodology (SRM). A database of process parameters is generated by machining and minimizing the surface roughness of the SS AISI 316 stainless steel via suing the copper electrode. Then, an objective function (or regression function) is generated by applying the SRM to the selected database. Finally, genetic algorithm is used to achieve the optimal process parameters. Experiments are implemented with achieved processing parameters to analyze and validate the proposed method.

22.1 Introduction

The electro-chemical machining (ECM) is an anodic electrochemical dissolution process, in which the tools are used as a cathode and the workpiece play a role as an anode [1]. The surface roughness (SR) of the ECM processing plays an important role for the quality of a product after being manufactured [2, 3]. Thus, a method which is used for determining an optimal set of processing parameters to improve the SR of finished products in the ECM is necessary for recommending end-users

L. P. Ngo · T. P. Nguyen · T. T. Tran (✉)
Department of Global Production Engineering and Management, Vietnamese-German University, 2 Le Lai, Thu Dau Mot City, Binh Duong, Vietnam
e-mail: thanh.tt@vgu.edu.vn

I. A. Parinov et al. (eds.), *Advanced Materials*, Springer Proceedings in Materials 6, https://doi.org/10.1007/978-3-030-45120-2_22

in product fabrication. A new approach to improving the possibility of processing microstructure is presented in work [4]. In the paper, the researchers propose the possibility to manufacture different operation activities with the highly flexible for the control system in the term of feed rate, electrolyze flow across the surface of the tool and the workpiece [4]. The most important thing for the ECM processing is pulse power supply for the whole system. However, there are still many other aspects that must be done as the future research. Two of the most important things requires in this research is about the controller for the inter-electrolyze gap and the controller for control the anodic dissolutions. The work [2] has highlighted the current trend of the ECM and the future for this method. Based on this research, the micro-ECM (EMM) can be used as an effective post-processing method for treating the surface of the component after being manufacturing. The paper also points out many aspects in which that are not explored about electrochemical processing. As a conclusion, the paper suggests with the high precision development of medical and automotive industries, the development of micro-ECM will increase sharply in the next few years. A set of experiments are implemented in [5] in which the effect of pulsating current is validated for improving the quality of the components and its advantages in the comparison with the traditional power supply method. By using the technique to simplify the model for checking the condition of one to some parameters allows authors to achieve the result of a high rate for mass transport and minimizing the electrolyte heating during the process. The research also pointed out the average dissolution rate in PECM as controlled in the limitation by electrolyte heating. The final part of the research shows the produced gas bubbles in the anode and cathode. By applying pulsating current, the method could eliminate the generating of heat due to electrolyte process and control the accuracy and surface roughness of the final products. An approach is proposed in the research [6], in which a theoretical and experimental research is conducted for a relationship between the surface condition of the anode (or workpiece) and the prepared profiled of the cathode (tool). The tool is designed especially in microstructure in which the relationship could be determined. The manufacturing condition is controlled in the limitation of copying the profile of cathode to the anode. At the end of his research, the author has suggested the method for improving the micro-structure ability of ECM processes. The ultra-short pulse current in [7] was proposed for examining the change of electrode during the electrochemical machining processes based on the simulation methodology. In this research, a method called marker is used for building the 3D application which can simulate the condition of the surface of the electrode. The output of this research is a numerical approach for simulating the desired object using the 3D method. By using the mentioned tool combined with the BEM approach, the model was developed following Faradays law. This method can open a new technique for non-touch monitoring the surface of the electrode. Finally, this model has performed fully potential with medium to the very high complex shape of the electrode. An optimal combination of process parameters for an electrochemical machining process is proposed by using the particle swarm optimization algorithm [8]. Also, many works have been carried out for comparing the advantages of ECM and EDM in the production conditions [9, 10]. The results pointed out that ECM provides a more effective solution

for manufacturing these materials in high volume condition. In this meaning, the application of the ECM in this materials processing is the high-impact improvement for reducing processing time and the cost for manufacturing the tool electrode in the comparison with EDM process [12]. In [8, 9, 11], single objective or multi-objective optimization models are proposed for optimizing a set of process parameters of the electro-chemical machining process. The selection of optimum values of important process parameters such as the tool feed rate, electrolyte flow velocity, and applied voltage is proposed for the electrochemical machining processes [8]. However, this study ignores the important effect of pressure of water and frequency which play a very important role on the surface rough of finished products. The effect and parametric optimization of process parameters in [11] that are electrolyte concentration, feed rate and applied voltage is proposed for the electrochemical machining of EN-31 steel. This work also ignores the important effect of pressure of the fluid and frequency in machining process of the ECM.

In this chapter, the research focuses on the study about effectiveness of the processing parameters, which are current, voltage, the pressure of the fluid, cutting speed and pulse, of the ECM to the surface roughness of the finished product. Experiments are setup to collect the data of the effect from these parameters by using the design of the experiment. With achieved results, Minitab software is used to calculate the result from practical experiments. A Taguchi orthogonal array is built to narrow down the factors that can affect the variance of the SR. Then, WEKA software is used to a statistical model (or regression function) which illustrates the relationship between processing parameters to the SR of finished products. Finally, the mathematical model is validated by practical experiment with the optimal parameters determined by using the genetic algorithm (GA). A set of optimal parameters is used to repeat the experimental results that then are validated via measuring the SR of the achieved finished product by using the RTEC Universal 3D Profilometer. The achieved results are then compared to the ones in which another set of parameters are used for the ECM to show advancement of the proposed method.

22.2 Experimental Study

In this section, an experimental setup is introduced firstly with facilities that needed for experiments. In the next section, a section of work piece and tool materials are discussed. Then, a necessary procedure of the method of design of experiments are provided. Finally, experiments and data collections are made in the end of the section.

22.2.1 Experimental Preparation and Setup

For carrying out experimental studies, a list of equipment is used for the not only process the workpiece but also for preparing the workpiece and measuring the SR of

the workpiece after manufacturing. Additionally, the main purpose of this research is to find out the optimized parameter for industries applications, therefore, a set of modern machines have been used to examine the surface roughness of the final product. Facilities are used for experimental study including the ECM machine, AMADA Surface Grinder 126, Mitutoyo Portable Surface Roughness Measurement Surftest SJ-210, and RTEC Universal 3D Profilometer.

PEM Technology-PEM 600. Figure 22.1 shows an ECM machine which uses the pulse power monitoring. The machine consists of four main blocks as illustrated in Fig. 22.1. There are many control factors for this machine such as Velocity/feed rate (V_{min}), Electrolyze flow control (P), Voltage (U), Frequency (f), The pulse control unit (ms), Pressure of fluid (KPa) and Initial gap (mm).

AMADA Surface Grinder 126. This machine is used to eliminate the effect of the initial surface roughness of the workpiece to the surface quality of post-production. This machine is used to grind the workpiece for approximately achieving the SR of Ra = 0.1 μm. The advantage of this machine is that it applies the NC controller for controlling the wear of grinding disc.

Mitutoyo Portable Surface Roughness Measurement Surftest SJ-210. This instrument, shown in Fig. 22.2, is used for measuring the surface roughness of the tool before and after processing material as well as for measuring the finished surface. The initial assumption for this calibration is with normal value of 2.97 μm, tolerance is 0.02 μm. The whole measurement system is adjusted and measured until the value of Ra equal to 2.970 μm. After that, 50 experiments are recorded continuously. This process is used to set up a desired position for the whole system. The measurement system is shown in Fig. 22.3.

RTEC Universal 3D Profilometer. This instrument is used to measure the finish surface of the product for validation phrase.

Fig. 22.1 Electrochemical machining

Fig. 22.2 Mitutoyo SJ-210 (4 mN type)

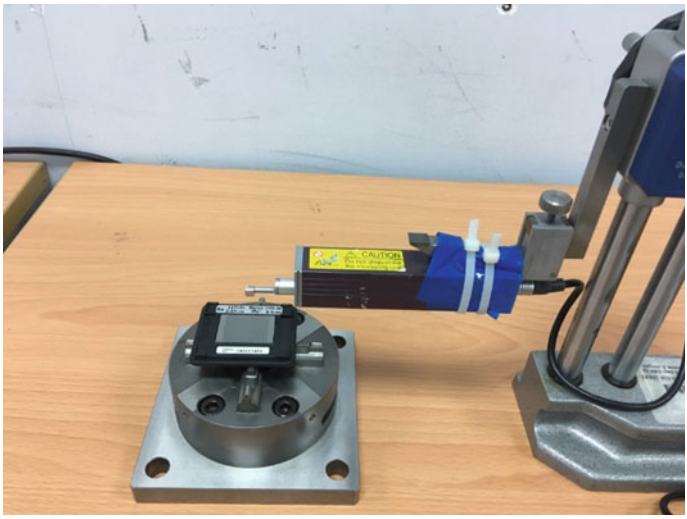

Fig. 22.3 Measurement system of Mitutoyo instrument

22.2.2 Selection of Work Piece and Tool Materials

Workpiece. To simulate the practical condition in industry, SS AISI 316 Stainless Steel which is already extruded to cylinder form with the diameter equal to 150 mm is chosen. AISI 316 Stainless Steel is the alloy of steel (around 62%) with Cr (maximum 18%), Ni (Maximum 14%), Mo (3%), Mn (%), C (0.8%) ("ASM materials Data Sheet"). With the hardness around HR = 79, higher corrosion compares with AISI 302 and AISI 304 and high melting point (around 1370 °C), AISI 316 stainless steel is widely used in food and pharmacy process equipment such as surgical implants and or the handle tools requires high chemical resistance process. The workpiece

Fig. 22.4 Surface of the workpiece after manufacturing

is then milled to achieve the initially flat surface. In the next step, the workpiece is processed throughout the drilling and the grinding machine to achieving the surface roughness Ra = 0.1 μm as shown in the Fig. 22.3.

The homogeneous SR ensures that the effect of initial surface quality of the workpiece does not affect to the final surface roughness of the finished product. The condition of the workpiece after manufacturing is shown in Fig. 22.3. The surface condition of the workpiece is different from the setting parameters. However, there is some zone in which the surface roughness of the workpiece after processing are quite high. Moreover, the surface roughness condition of the workpiece is nearly not changed during the testing condition, but the surface is oxidized after manufacturing the parameter set that caused high surface roughness.

Tool. PEM600 has the capability to use many types of conductive material for the ECM process. However, for the cost saving in industry, the cooper is used to manufacture the tool. Since, this paper focuses only on optimizing the surface roughness of the final product, this design ensures the uniformity effect of the substance flow in the whole area. For each experiment, the tool is manually ground by 2000 grit sandpaper which makes the SR of the tool achieve the value of Ra that is less than 0.1 μm. Figure 22.5 shows a sample surface of high roughness surface (left) and the surface of electrode after manufacturing (right). The surface roughness of the tool is measured in four positions and takes the average value of these four measures. They are the same method for measuring the finished surface of the workpiece, as shown in Fig. 22.4.

Fig. 22.5 Sample surface of high roughness surface (left) and the surface of electrode after manufacturing (right)

22.2.3 Design of Experiments

For the purpose of examining the influence of the machining parameters including feed rate, pressure, voltage frequency, and pulse on the SR on tested specimens, a full factorial design approach with range of each parameter is considered in Table 22.1 for the experiments

These parameters of feed rate, pressure, voltage, frequency and pulse, shown in Table 22.1, are selected by basing on the recommended parameters from manufacturers of the PEM600 machine. These parameters are also conducted via our experiences as we are operating the machine. The range of each parameter is chosen specifically as in Table 22.1. These ranges are divided into five levels for assessing the effect of each range into the response of surface roughness for the initial experiments. In other words, a single replicate of 5 factors with 5 levels would be used for experimental setup.

The selection for an experimental matrix of five control parameters can be based on a full factorial design in which the correlation between these control factors can be

Table 22.1 Electrochemical machining process parameters

Process parameters	Level 1	Level 2	Level 3	Level 4	Level 5
Feed rate (mm/min)	0.02	0.115	0.21	0.305	0.4
Pressure (kPas)	300	350	400	450	500
Voltage (V)	6	7.5	9	10.5	12
Frequency (Hz)	40	52.5	65	77.5	90
Pulse (ms)	0.5	1.625	2.75	3.875	5

examined and predicted. However, due to the wide range of each parameter (which are chosen from the suggested control parameters of machine manufacturer), the number of the experiment (n) is the combination of five parameters and which are divided into five level. It means that there are 5^5 (= 3125) experiments that must be implemented to obtain database for analysis. For optimizing the cost and time for collecting data, the approach of Taguchis's method is applied for five control parameters (Velocity/feed rate (Vmin), flow control (P), Voltage (U), Frequency (f), The pulse control unit (ms)). Based on the suggestions from Minitab software for fives control factors with five levels, the Taguchis L25 orthogonal arrays is chosen as shown in Table 22.2. Corresponding values for the Taguchis L25 orthogonal arrays are shown in Table 22.3. This array consists of 25 experiments which insignificantly

Table 22.2 Taguchis L25 orthogonal arrays

Number of experiments	Feed rate (mm/min)	Pressure (kPas)	Voltage (V)	Frequency (Hz)	Pulse (ms)
1	1	1	1	1	1
2	1	2	2	2	2
3	1	3	3	3	3
4	1	4	4	4	4
5	1	5	5	5	5
6	2	1	2	3	4
7	2	2	3	4	5
8	2	3	4	5	1
9	2	4	5	1	2
10	2	5	1	2	3
11	3	1	3	5	2
12	3	2	4	1	3
13	3	3	5	2	4
14	3	4	1	3	5
15	3	5	2	4	1
16	4	1	4	2	5
17	4	2	5	3	1
18	4	3	1	4	2
19	4	4	2	5	3
20	4	5	3	1	4
21	5	1	5	4	3
22	5	2	1	5	4
23	5	3	2	1	5
24	5	4	3	2	1
25	5	5	4	3	2

Table 22.3 Taguchis L25 orthogonal arrays: experimental values

Number of experiments	Feed rate (mm/min)	Pressure (kPas)	Voltage (V)	Frequency (Hz)	Pulse (ms)
1	0.02	300	6	40	0.5
2	0.02	350	7.5	52.5	1.625
3	0.02	400	9	65	2.75
4	0.02	450	10.5	77.5	3.875
5	0.02	500	12	90	5
6	0.115	300	7.5	65	3.875
7	0.115	350	9	77.5	5
8	0.115	400	10.5	90	0.5
9	0.115	450	12	40	1.625
10	0.115	500	6	52.5	2.75
11	0.21	300	9	90	1.625
12	0.21	350	10.5	40	2.75
13	0.21	400	12	52.5	3.875
14	0.21	450	6	65	5
15	0.21	500	7.5	77.5	0.5
16	0.305	300	10.5	52.5	5
17	0.305	350	12	65	0.5
18	0.305	400	6	77.5	1.625
19	0.305	450	7.5	90	2.75
20	0.305	500	9	40	3.875
21	0.4	300	12	77.5	2.75
22	0.4	350	6	90	3.875
23	0.4	400	7.5	40	5
24	0.4	450	9	52.5	0.5
25	0.4	500	10.5	65	1.625

afford for carrying out the practical experiments, but it still can be used to be analyzed based on Minitab software for plotting the effect of the single effect of each factor to the surface roughness of finished products. For further study and analysis, a set of control parameters are re-peat two times to avoid rare variations in setup of experiments. Also, two experiments with the same parameters are used for estimating the robustness of experiments.

22.2.4 Experiments and Data Collection

Based on the initial data and experimental setup as discussed in Sect. 22.2, Table 22.1 and the depth of cut for all experiments is set at a value of 0.1 (mm) in combination with above parameters. Due to the change in the initial position after grinding the surface of the workpiece and the tool, the processing time is not recorded. By applying these setting parameters, the achieved results of experiments are shown in Table 22.4 that shows the data after cutting the first and second sets of parameters. Due to a high noise in experimental process, Dixon's Q test (or Q-Test) is applied for eliminating the strange value from the collected data of the achieved data in which the surface

Table 22.4 Experimental results of surface response (SR, μm)

Number of experiments	Feed rate (mm/min)	Pressure (kPas)	Voltage (V)	Frequency (Hz)	Pulse (ms)	Surface rough (μm)
1	0.02	300	6	40	0.5	0.3
2	0.02	350	7.5	52.5	1.625	0.35
3	0.02	400	9	65	2.75	0.45
4	0.02	450	10.5	77.5	3.875	0.82
5	0.02	500	12	90	5	0.43
6	0.115	300	7.5	65	3.875	0.14
7	0.115	350	9	77.5	5	0.23
8	0.115	400	10.5	90	0.5	0.98
9	0.115	450	12	40	1.625	0.2
10	0.115	500	6	52.5	2.75	0.53
11	0.21	300	9	90	1.625	0.74
12	0.21	350	10.5	40	2.75	0.55
13	0.21	400	12	52.5	3.875	0.86
14	0.21	450	6	65	5	0.24
15	0.21	500	7.5	77.5	0.5	0.59
16	0.305	300	10.5	52.5	5	0.22
17	0.305	350	12	65	0.5	0.38
18	0.305	400	6	77.5	1.625	0.53
19	0.305	450	7.5	90	2.75	0.36
20	0.305	500	9	40	3.875	0.19
21	0.4	300	12	77.5	2.75	0.24
22	0.4	350	6	90	3.875	0.22
23	0.4	400	7.5	40	5	0.33
24	0.4	450	9	52.5	0.5	1.66
25	0.4	500	10.5	65	1.625	1.67

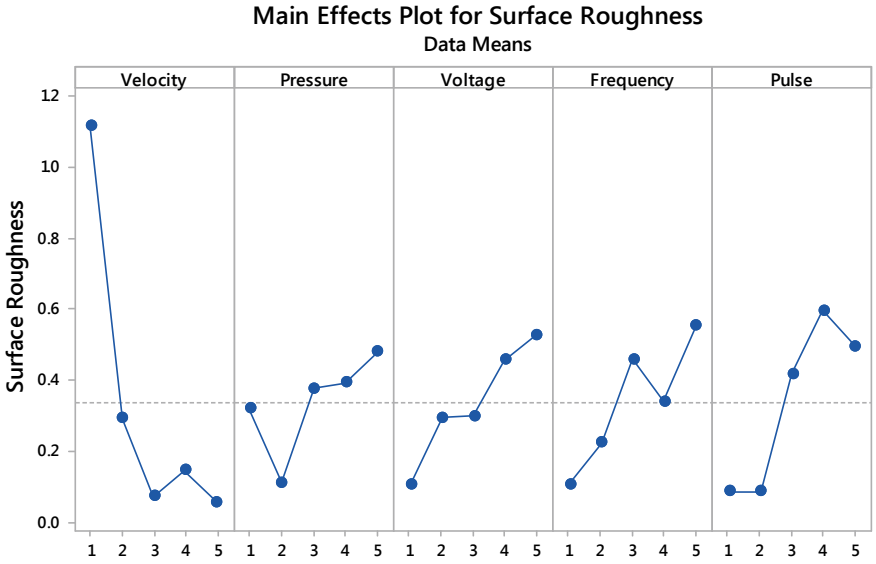

Fig. 22.6 Response value for each level of each control factors

roughness is the average number of the processed data. By using Minitab software for analyzing the results from the first 25 experiments (As L25 orthogonal arrays), the effect of each control parameter for the response value (surface roughness) is shown in Fig. 22.6. Indicating that Fig. 22.6 just illustrates the response for every single factor, the interaction between each factor cannot be shown by this analysis. Based on the analysis results from Minitab, each factor has the range in which the response for surface get the better value (smaller SR). This suggest that a higher accuracy will be improved with a higher amount of data. Thus, a new set of the control parameter might provide a further accuracy. In this research, results in Table 22.4 will be used for generating a statistical model (or regression function) and then an optimization process using the genetic algorithm is applied for an optimal set of process parameters. A further work will be explained in detail in the next section.

22.3 Optimal Selection of Process Parameters in ECM Process

22.3.1 Weka Software for Regression Model

We illustrate the relation between the control factors and the response of surface roughness of processed surface by ECM. A statistical model is built in which the output of this model is the value of surface roughness and the input is the value of

control parameters. In general, and for simplifier, a statistical model is a mathematical model in which the reality is described by an equation made by one or many input parameters and the output is the questionable factor. This model can be used for predicting the output value based on the input parameters. There are two kinds of the variable in a statistical model, the first one is dependent variables which is the value that needs to be explained or predicted. In this study, the dependent variables are the response of surface roughness. The second variables are the independent variable(s) which are used to explain or predict the dependent variables. In this study, independent variables are feed rate, flow pressure, voltage, frequency, and pulse. There are many approaches to build a statistical model. However, in this paper, the software called WEKA (Waikato Environment for Knowledge Analysis) is used. This software is widely used for the study of machine learning in many purposes such as classify and cluster. Based on the requirement for building the statistical model that illustrates that relationship between given parameters and the value of surface roughness, the classify function of WEKA is used. In simplify term, the classify term is usually used in machine learning science and it is referred to build an identification for of population based on the observed sample in that population. There are many kinds of filters (with difference algorithm) used for classification in WEKA. However, for simplify, this paper focuses only on two kinds of filter: Linear Regression and Least Square Regression. After choosing the filter that is used in WEKA for building the statistical model or objective function, the collected data is input into WEKA by excel CSV type. Cross-validation is chosen with the test option of building this model.

As the above results in Table 22.4, there is several statistical models that can been achieved by different methods via WEKA software. All these models can be used to machine setup and find the optimal sets of parameters for the response of surface roughness. However, the linear statistical model which is built by using the achieved data is not convenient for further optimization process. In stead of a linear statistical model, a nonlinear statistical model which is built by using the extension of achieved data in Table 22.4 is generated by using the WEKA software, the achieved results of a nonlinear statistical model (or regression function) are shown in (22.1) as

$$\begin{aligned} \mathrm{SR} = {} & -0.131\ \mathrm{V} - 0.0099\ \mathrm{U} + 0.0323\ \mathrm{MS} + 1.3213\ \mathrm{V}^2 + 0.30\ U^2 + 0.0084\ \mathrm{MS}^2 \\ & + 0.0014\ \mathrm{VU} - 0.2707\ \mathrm{VMS} + 0.3048 \end{aligned} \tag{22.1}$$

where V is velocity/feed rate, U is voltage, MS is the pulse control unit (ms). From the achieved results with WEKA software, the correlation coefficient is 0.3597, the root mean squared error is 0.5189 for the total number of instances of 45. As a prediction, the results also confirm that the weights of pressure of fluid and frequency, 0.0006 and 0.00035 respectively, play an insignificant role in reducing the SR in comparison with other factors. So, the terms of pressure of fluid and frequency are ignored in (22.1) for further optimization procedure. From (22.1) and Fig. 22.6, one can realize that the feed rate of machining processing plays an important role in reducing the

SR of finished products and the applied voltage can also be considered to support to reduce the surface roughness of finished products.

22.3.2 Optimal Selection of Process Parameters

In this statistical model, the single objective target has been solving for finding the optimized solution for the response of the surface roughness with objective function in (22.1). As mentioned above, based on the result with a high correlation coefficient of the statistical model built from the mixed results from two sets of original data with the processed data from Minitab is used for optimizing. The problem statement is stated as finding optimal processing parameters such that the objective function (22.1) is minimized subject to constraints and boundary conditions as shown in design matrix in Table 22.1. By using the genetic algorithm (GA), the optimal values of machining parameters are archived as feed rate of 0.4 mm/min, voltage of 12 V, and pulse of 0.5 ms. These values corresponding to the surface roughness of 0.17 μm are setup with new experiments for samples with goals for comparison and validation of the proposed method in the next section.

22.3.3 Analysis and Validation of Experimental Results

In the chapter, the achieved model a nonlinear statistical model will be validated and compared by practical ECM process for assessing the quality of the surface. In this approach, the optimal values of machining parameters are used to machine three sets of new samples with the optimal parameters for validation and comparison. After analyzing three manufactured samples, the results show that the averages of the SR of finished products corresponding to three times of experiments are 0.159 μm, 0.182 μm, and 0.212 μm, respectively. These numbers indicate the reliability of experiments with the same set of parameters. These values are also smaller than the calculated value in term of a formula [12] which is 0.21 μm. Figure 22.7 shows a small area of surface of manufactured sample with optimal parameters that is equivalent to the average of 0.159 μm. To show the variations of the SR of the achieved sample, the three lines (upper, middle, bottom) in Fig. 22.7 are investigated for validation.

Figure 22.8 shows the distributions of the arithmetical mean height (Ra) of the manufactured sample with the optimized parameters. The upper, middle, and bottom lines in Fig. 22.8 show variations of the Ra corresponding to the upper, middle, and bottom lines in Fig. 22.7. The results in Fig. 22.8 indicate that the averages of Ra are 0.132 in the upper line, 0.123 μm in the middle line, and 0.144 μm in the bottom line. Thus, these results show that the experimental surface roughness of the finished product is closer to the theoretical value that is 0.17. Also, based on the captured image in Figs. 22.7 and 22.8 about the surface of the sample after manufacturing by ECM, the surface of the products is in the familiar condition as the surface or the tool

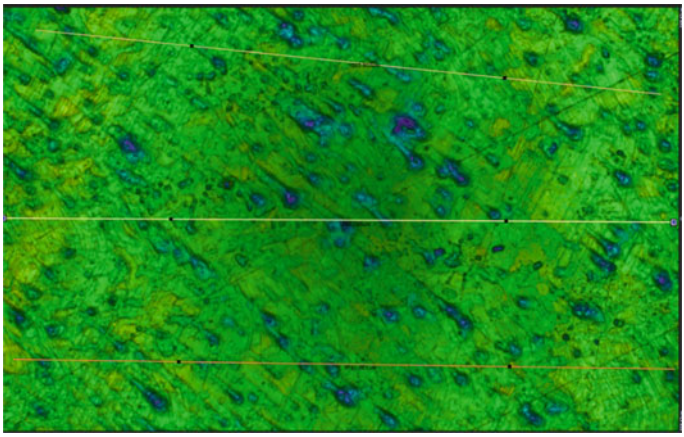

Fig. 22.7 Surface condition of the sample with optimized parameters

(for the optimized condition only). These results indicate that the achieved regression function is validated and useful for ECM users for manufacturing applications.

22.4 Conclusion

This paper investigates effects of the processing parameters, which are current, voltage, the pressure of the fluid, cutting speed and pulse, of ECM processing on the surface roughness of the finished products. In this approach, experiments are prepared, implemented, and collecting the data of the effect from these parameters by using the surface response methodology. With achieved results, the Minitab software is used to calculate and analyze the results of practical experiments in order to show considerable effects of each factor. Then, the WEKA software is used to generate a statistical model (or regression function) which illustrates the relationship between processing parameters to the SR of finished products. With the achieved model, a set of optimization parameters is achieved by using the genetic algorithm. Finally, the mathematical model is validated again by practical experiments with the optimal parameters for comparison. Further, as suggested in the discussion section, the five control parameters of the surface roughness could be a collapse by skipping the relationship of fluid pressure and the frequency. For the extension of future study, the value of fluid pressure and frequency must be chosen from the provided range. Also, a new approaching with the different filters should be used to illustrate the truly non-linear regression model in the future work.

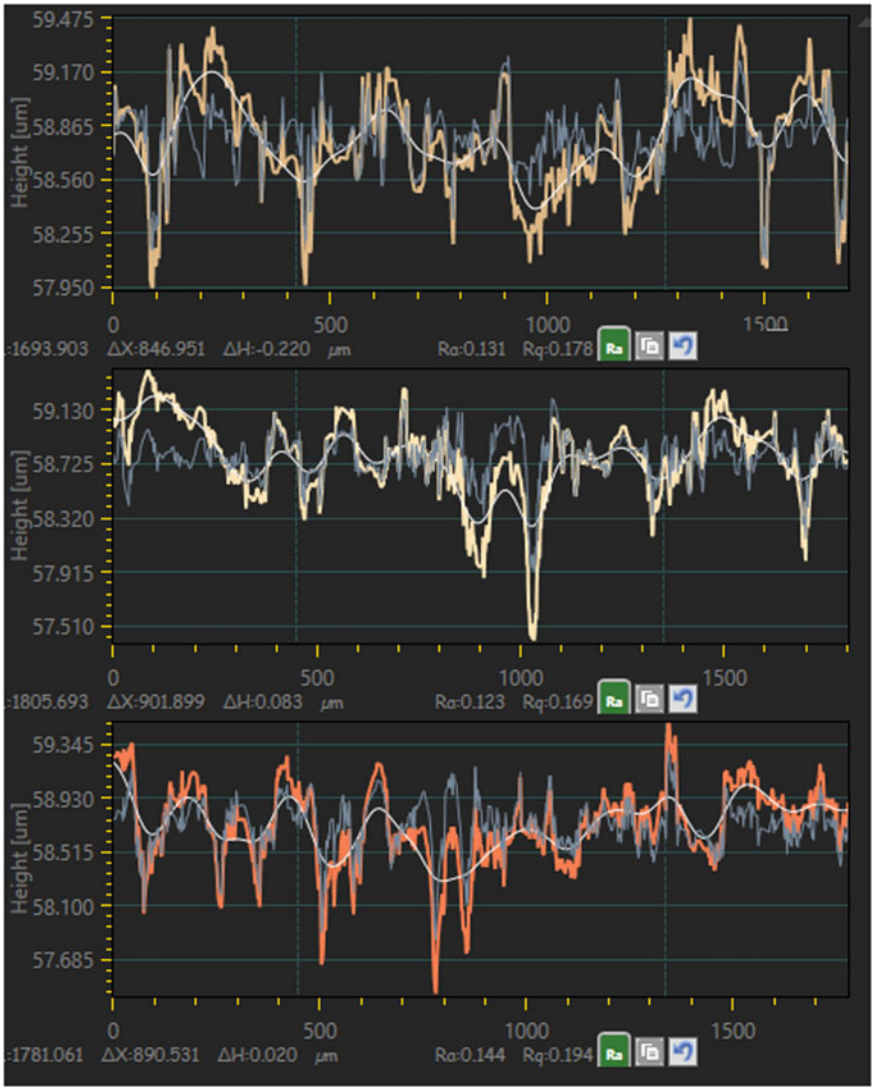

Fig. 22.8 Plot of the surface roughness of the sample with optimized parameters

Acknowledgements This work was supported by to the Ministry of Education and Training for the funded project of code KC-519 (Decision 5652 on 28/12/2018).

References

1. R.H. Todd, D.K. Allen, L. Alting, *Manufacturing Processes Reference Guide* (Industrial Press, New York, 1994)
2. B. Bhattacharyya, J. Munda, M. Malapati, Int. J. Mach. Tools Manuf **44**(15), 1577–1589 (2004)
3. K. Rajurkar, M.M. Sundaram, A.P. Malshe, Procedia CIRP **6**, 13–26 (2013)
4. B. Bhattacharyya, S. Mitra, A.K. Boro, Robot. Comput.-Integr. Manuf. **18**(3–4), 283–289 (2002)
5. M. Datta, D. Landolt, Electrochem. Acta **26**(7), 899–907 (1981)
6. J. Kozak, K. Rajurkar, Y. Makkar, J. Mater. Process. Technol. **149**(1–3), 426–431 (2004)
7. M. Purcar, L. Bortels, B. van den Bossche, J. Deconinck, J. Mater. Process. Technol. **149**(1–3), 472–478 (2004)
8. R.V. Rao, P.J. Pawar, R. Shankar, Proc IMechE J. Engg. Manuf. **222**, 949–958 (2008)
9. P. Asokan, R. Ravi Kumar, R. Jeyapaul, M. Santhi, Int. J. Adv. Manuf. Tech. **39**, 55–63 (2008)
10. C.-K. Yang, C.-P. Cheng, C.-C. Mai, A. Cheng Wang, J.-C. Hung, B.-H. Yan, Int. J. Mach. Tools Manuf. **50**(12), 1088–1096 (2010). https://doi.org/10.1016/j.ijmachtools.2010.08.006
11. D. Chakradhar, A.V. Gopal, Int. J. Mode. Optim. **1**, 113–117 (2011)
12. L.P.T. Huynh, H.A. Nguyen, H.Q. Nguyen, L.K.H. Phan, T.T. Tran. J. Korean Soc. Precis. Eng. **36**(8), 705–712 (2019)
13. K.-H. Choi, T.T. Tran, B.-S. Yang, D.-S. Kim, An new approach for intelligent control system design using the modified genetic algorithm, Int. J. Intelligent Systems Technologies and Applications, **9**(3/4), 300–315 (2010)

Chapter 23
Optimization of Surface Roughness and Vibration During Thermal—Assisted Milling SKD11 Steel Using Taguchi Method

Thi-Bich Mac, Banh Tien Long, and Duc-Toan Nguyen

Abstract This chapter used the Taguchi experimental design method in order to study the surface roughness and vibration during thermal-assisted milling of SKD11 steel. The effect of cutting parameters such as cutting speed, feed rate, cutting depth and support elevated temperatures on the output data were evaluated. Multi-objective optimization for minimum both surface roughness and vibration was also estimated to improve the cutting process. The optimal set of control parameters to achieve the minimum of surface roughness and vibration amplitude could be obtained as V_c = 280 m/min, f = 230 mm/min, t = 0.5 mm, T = 400 °C.

23.1 Introduction

The introduction and widespread use of high-strength, heat-resistant and hard-to-cut materials have increased the difficulty for manufacturing processes. A proposed solution to overcome these problems is to work with the thermal—assisted machining (TAM), also called hot machining processing.

The manufacturing industry has been developed with various thermal—assisted machining (TAM) such as electric, arc heating, high-frequency electromagnetic induction, laser beam, electron beam, plasma and so on. However, these technologies are suitable for some special machining methods, not for all. It is important to select the appropriate heating method otherwise the heat generation may damage the workpiece and then not to achieve the desired results [1]. Amin and Abdelgadir [2] have shown that electromagnetic induction heating can reduce vibrations by up to 98% and increase tool life many times when processing steel. Other works on induction

T.-B. Mac
Department of Mechanical Engineering, Hung Yen University of Technology and Education, Dan Tien, Khoai Chau, Hung Yen, Vietnam

B. T. Long · D.-T. Nguyen (✉)
School of Mechanical Engineering, Hanoi University of Science and Technology, No. 1A, Dai Co Viet, Hai Ba Trung, Hanoi, Vietnam
e-mail: toan.nguyenduc@hust.edu.vn

I. A. Parinov et al. (eds.), *Advanced Materials*, Springer Proceedings in Materials 6, https://doi.org/10.1007/978-3-030-45120-2_23

heat machining have been reported advantages of hot machining by investigators [3–6], and plasma-assisted machining [7, 8] and laser-assisted machining [9–11].

There are many studies on the influence of input parameters such as cutting speed, tool speed, cutting depth to output parameters including cutting force, cutting vibration, surface roughness, etc. at room and elevated temperatures [12–14]. Surface roughness and cutting vibration are some of the important output data to assess the quality of products and production costs. Kumar et al. [15] studied the effect of spindle rotation speed and tool speed on surface roughness when turning Carbon steel on CNC lathes. Five types of steel SAE8620, EN8, EN19, EN24 and EN47 are used for research, respectively. The results show that the spindle rotation and tool speed has a direct effect on surface roughness. Surface roughness increases as feed rate increases and spindle speed decreases.

The study of cutting process optimization was studied by various works [12, 16–20]. Chang et al. [17] analyzed surface roughness when processing Al_2O_3 embryos in the laser-heated process. The test results were analyzed by the Taguchi method and the optimal technology parameter set was established. Cutting speed has the strongest influence on surface roughness with 42.68% of the influence. Other parameters include the depth of cut, step forward and the frequency of pulses with less influence in order of 20.73%, 22.58%, and 14.01%, respectively. The optimal control parameter set is defined as t = 0.2 mm, V = 1500 rpm, f = 0.03 mm/r, and pulse frequency of 40 kHz.

In this chapter, the effect of cutting parameters on the surface roughness and vibration amplitude of the cutting process when processing SKD11 steel materials in the electromagnetic heating environment was studied. Processing experiments at room temperature and heating conditions are performed continuously. Subsequently, the optimum cutting and temperature parameters were obtained to achieve the multi-objective surface roughness and vibration amplitude based on the Taguchi method. The relationship between surface roughness and vibration amplitude depends on the cutting parameters at elevated temperatures that were built on the nonlinear tool—regression of Minitab software [17]. The results of the study were finally compared with experimental data for highly compatible results.

23.2 Experimental Work

23.2.1 Material

The Japanese standard SKD11 [JIS-G4404] is alloy steel commonly used in mold machining [21]. SKD11 steel has high-strength, impact resistance, and good deformation resistance. Moreover, it has the ability to keep the hardness at high temperatures for a long time. Therefore, SKD11 steel is often used in the production of extrusion molds, plastic injection molds, pressure molds, details that require special use properties and so on. Tables 23.1 and 23.2 are the chemical composition and

Table 23.1 Chemical composition of SKD11 steel,% mass [21]

C	Cr	Mo	Si	Mn	Ni	V
1.4–1.6	11–13	0.7–1.2	≤0.6	≤0.6	–	0.15–0.3

Table 23.2 Physical properties of SKD11 steel [22]

Physical properties	Value	Physical properties	Value
Specific weight (kg/m^3)	8400	Thermal expansion coefficient (10^{-6}/k)	11
Poisson's coefficient	0.3	Specific heat (J/kg °C)	461
Melting temperature (°C)	1733	Thermal conductivity (W/m K)	20.5

physical properties of SKD11 steel, respectively.

23.2.2 Experimental Design

The experiment was carried out on Taiwan's MC500 milling machine. Spindle rotation speed 100–30,000 rpm, spindle power of 15 kW, the movement speed of the machine table when processing 30,000 mm/min, the maximum running speed: 48,000 mm/min, travel stroke X × Y × Z version = 500 × 400 × 300 mm. Do not use coolant during processing. Figure 23.1 shows a schematic diagram of SKD11 steel milling with thermostatic support. The heating element consists of induction power source, frequency generating device and induction coil. Test pieces of dimensions 70 mm × 31 mm × 80 mm are placed on a jig. The amplitude of the cutting process vibration is assessed by the accelerometer mounted on the jig.

Study on using roughness meter SV—C3200 from Mitutoyo with Formtracepak software is shown in Fig. 23.2. The X- and Z-axis unit controllers are equipped with a linear encoder (ABS type on Z-axis) with high accuracy. Measuring the speed of the device: 0.02–5 mm/s. Method of measurement: the probe moves perpendicular

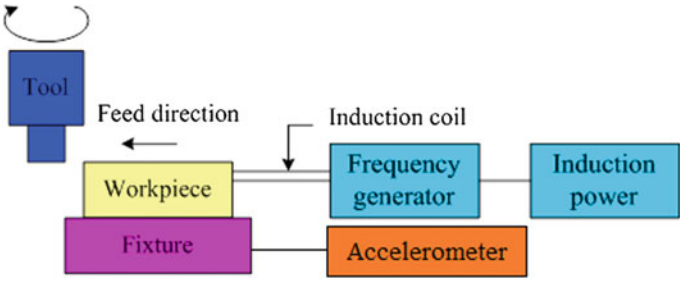

Fig. 23.1 Experimental diagram

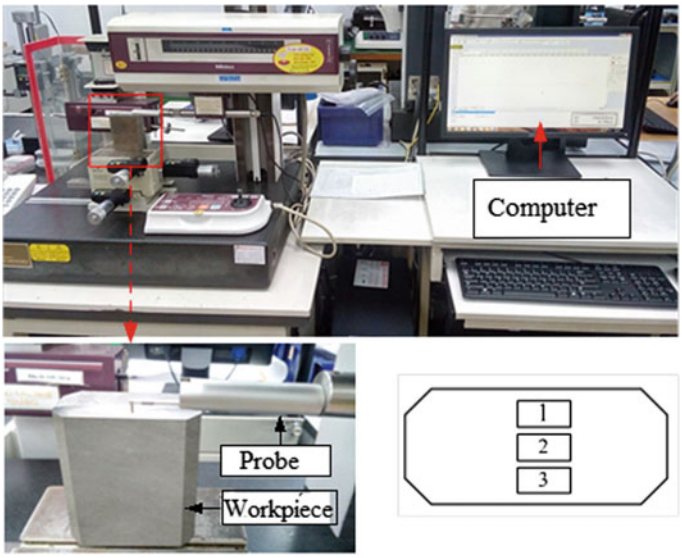

Fig. 23.2 Roughness meter and measuring positions

to the machining trace; measure at three positions 1, 2 and 3 as shown in Fig. 23.2 then calculate the average result.

The vibration measurement device is shown in Fig. 23.3. The LAN—XI data acquisition module has 4 inputs and 2 51.2 kHz frequency outputs from Bruel & Kjaer Denmark. PULSE FFT 7770 analysis module, 1–3 channels, PULSE FFT of Bruel & Kjaer Denmark. Triaxial DeltaTron 3-way accelerometer with TEDS 4525-B-001, titanium shell material.

23.3 Control Parameters and Levels

With the goal of experimental design and optimization of control parameters in a simple, effective, economical and experimental manner, the Taguchi experimental design method has been selected. This method allows each parameter to be independently evaluated and randomized by the orthogonal array (OA). With the ability to narrow the scope of specific studies or identify production problems with existing data by appreciating the characteristic value for the average performance close to the target value. The Taguchi method has become a popular option to improve product quality [23].

This study investigates the effect of cutting mode parameters such as cutting speed (V_c), cutting speed (f), cutting depth (t) and temperature (T) on surface roughness and vibration amplitude during the machining process. The measurement of the interaction between parameters through the S/N ratio. The S/N ratio is built for three

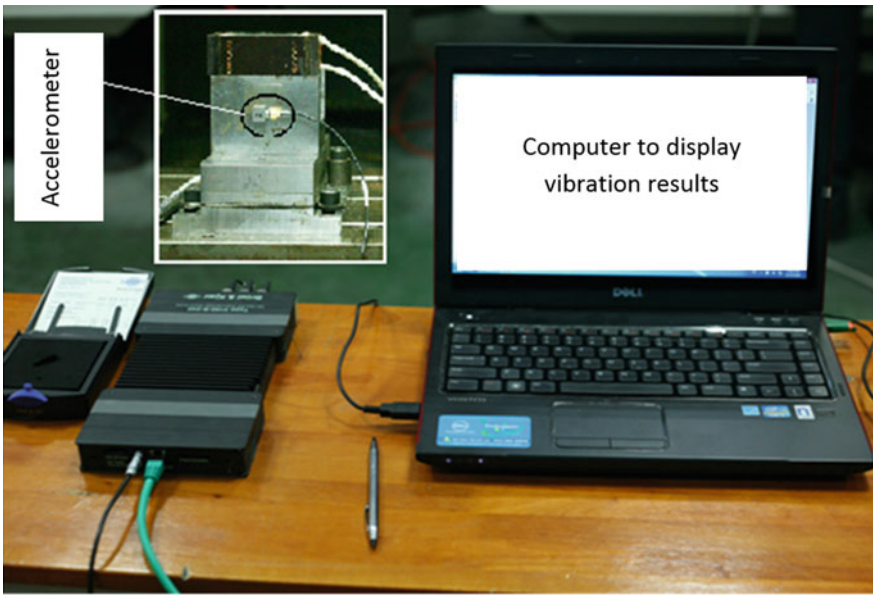

Fig. 23.3 Vibration measurement device for cutting process

goals following: bigger is better, smaller is better and normal is better. In this study, smaller is the better target is chosen. A better S/N ratio with a lower goal is expressed as (23.1).

$$\frac{S}{N} = -10\log_{10}\left[\frac{1}{n}\left(\sum_{i=1}^{n} y_i^2\right)\right] \tag{23.1}$$

where $\sum_{i=1}^{n} y_i^2$ is the sum of squares for all results of each experiment, n is the number of measurements for each experiment.

Table 23.3 is a level set of cutting parameters and temperature for work-piece with cutting speed ($V_c = 190$–280 m/min), feed rate ($f = 230$–380 mm/min), cutting depth ($t = 0.5$–1.5 mm) and temperature ($T = 200$–400 °C), respectively. The experiment

Table 23.3 Control parameters and levels

No	Control parameter	Unit	Level 1	Level 2	Level 3
1	V_c (A)	m/ph	190	235	280
2	f (B)	mm/ph	230	305	380
3	t (C)	mm	0.5	1.0	1.5
4	T (D)	°C	200	300	400

Table 23.4 Experimental matrix and output data

TN	V_c (m/min)	f (mm/min)	t (mm)	T (°C)	Ra (μm)	A_{XY} (dB)
1	190	230	0.5	200	0.128	141.601
2	190	305	1	300	0.137	147.405
3	190	380	1.5	400	0.159	148.931
4	235	230	1	400	0.091	141.919
5	235	305	1.5	200	0.176	151.139
6	235	380	0.5	300	0.126	139.388
7	280	230	1.5	300	0.109	148.343
8	280	305	0.5	400	0.090	137.004
9	280	380	1	200	0.162	147.632

is designed according to the method of orthogonal array Taguchi L9 with results of surface roughness (Ra) and vibration amplitude (A_{XY}), respectively, as Table 23.4.

23.4 Results and Discussion

23.4.1 Surface Roughness

Table 23.5 presents the ANOVA results for surface roughness (Ra) during the SKD11 cutting with the thermal—assisted machining (TAM). The results indicated that the elevated temperature had the greatest influence on the surface roughness with the percentage of 37.6%. The feed rate had a second influence level of 31.6%. Cutting speed and cutting depth have less influence of 24.1% and 21.8%, respectively. Figure 23.4 shows the effect of the S/N ratio of each control parameter on the surface roughness during processing. The optimal set of parameters could be obtained as A3B1C1D3 corresponding to $V = 280$ m/min, $f = 230$ mm/min, $t = 0.5$ mm and $T = 400$ °C, respectively.

Table 23.5 ANOVA results for surface roughness (Ra)

Parameter	Mean of multiple S/N ratio			Sum of squares	Contribution
	1	2	3		
A	17.03	17.96	18.68[a]	0.000683	0.241
B	19.31[a]	17.77	16.6	0.002387	0.316
C	18.93[a]	17.95	16.79	0.001647	0.218
D	16.26	18.17	19.24[a]	0.002839	0.376

[a]Optimal value

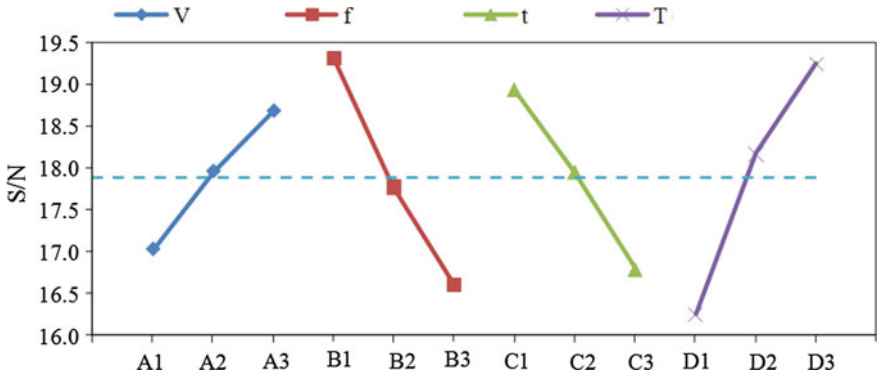

Fig. 23.4 S/N ratio of control parameters to surface roughness (Ra)

Table 23.6 ANOVA results for vibration amplitude ($A_{XY\text{-}T}$) during machining

Parameter	Mean of multiple S/N ratio			Sum of squares	Contribution
	1	2	3		
A	−43.28	−43.17[a]	−43.18	6.112	0.032
B	−43.16[a]	−43.23	−43.24	3.383	0.018
C	−42.88[a]	−43.26	−43.49	157.371	0.814
D	−43.33	−43.23	−43.08[a]	26.350	0.136

[a]Optimum level

23.4.2 Vibration

Table 23.6 presents the ANOVA results for the vibration amplitude of cutting process by TAM for SKD11 steel. The results show that during processing, the cutting depth has the greatest impact on the vibration amplitude of 81.4%, followed by the temperature supporting the cutting process of 13.6%, the effect of cutting speed and feed rate on the vibration amplitude is negligible. Figure 23.5 shows the influence of S/N ratio of control parameters on the vibration amplitude during processing. The optimal set of control parameters could be obtained as A2B1C1D3 corresponds to $V = 235$ m/min, $f = 230$ mm/min, $t = 0.5$ mm, $T = 400$ °C.

23.4.3 Multi-response Optimization

The above analysis presents the single optimization of output evaluation criteria such as surface roughness or cutting vibration. To find out the optimal set of parameters simultaneously for both surface roughness and cutting vibration, the study utilized Gray relational analysis (GRA). This method is effective in the study of objects with

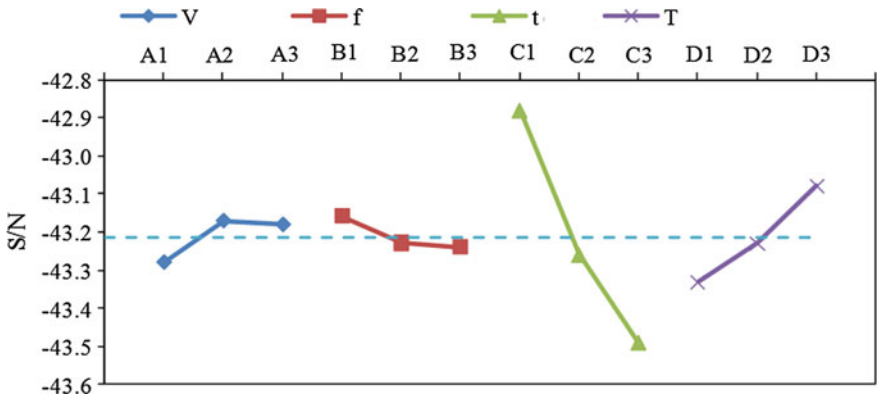

Fig. 23.5 S/N ratio of control parameters to the vibration amplitude $A_{\text{XY-T}}$

limited information. This technology effectively determines the complex relationship between the characteristics and qualities. Therefore, it becomes a powerful tool in the design of multi-objective optimization. The output target of both surface roughness and vibration amplitude is "lower-the-better". The normalized form of the original sequence as follows:

$$S_{kj} = \frac{\max X_{kj} - X_{kj}}{\max X_{kj} - \min X_{kj}} \tag{23.2}$$

where $j = 1 \ldots 9$; m is the number of experiments of Taguchi orthogonal array; $k = 1 \ldots n$, n is the number of process responses; max X_{kj} and min X_{kj} are corresponding the largest and smallest value of X_{kj} for the kth response; S_{kj} is the value after grey relational generation.

To determine the relationship between the best and actual experimental results, a gray relationship factor GZ_{kj} is calculated using the following formula:

$$\text{GZ}_{kj} = \frac{S_{k\min} - \xi S_{k\max}}{S_{kj} + \xi S_{k\max} k\max} \tag{23.3}$$

where ξ is the distinguishing coefficient, $0 < \xi < 1$. In this study, due to moderate discriminatory effects and good result stability, we select $\xi = 0.5$. GZ_{kj} is the coefficient of the gray relation of kth response in the jth experiment.

The grade of grey relation (G_j) is a coefficient that describes the weighted total of the gray relation, representing an overall evaluation of empirical data for multi-objective optimization. G_j is calculated using the formula:

$$\text{G}_j = \frac{1}{n} \sum_{k=1}^{n} \text{GZ}_{kj} \tag{23.4}$$

The normalized values of Ra and A_{XY}, the process reactions and the levels of gray relationships are given in Table 23.7. The higher the gray relationship level, the combination of quality characteristics are close to the desired level. Thereby, better process parameters correspond to better process responses. The results in Table 23.7 and Fig. 23.6 show that experiment No. 8 has the highest gray relationship. Therefore, this test is the first priority, followed by test numbers No. 4 and No. 6. Therefore, A3B2C1D2 is the optimal set of control parameters to achieve the minimum target Ra and A_{XY}.

Table 23.8 evaluates the percentage of influence of the control parameters on the gray relational grade. The results show that factor C (cutting speed) has the highest contribution to overall performance with 39.84%. The factor D (elevated temperature) has the second-highest contribution with 35.63%. Eventually, the factor A (cutting speed) and B (feed rate) with 14.04% and 10.49%, respectively. Figure 23.7 presents the effects of process parameters on the gray relational grade. The optimal set of

Table 23.7 Grey relational analysis results

Exp. No.	S (for Ra)	S (for A_{XY})	GZ (for Ra)	GZ (for A_{XY})	G	Order
1	0.525	0.336	0.488	0.598	0.543	4
2	0.627	0.745	0.444	0.401	0.423	6
3	0.849	0.850	0.371	0.370	0.371	8
4	0.016	0.359	0.968	0.582	0.775	2
5	1.000	0.999	0.333	0.333	0.333	9
6	0.502	0.175	0.499	0.740	0.620	3
7	0.286	0.809	0.636	0.382	0.509	5
8	0.000	0.000	1.000	1.001	1.000	1
9	0.876	0.760	0.363	0.396	0.380	7

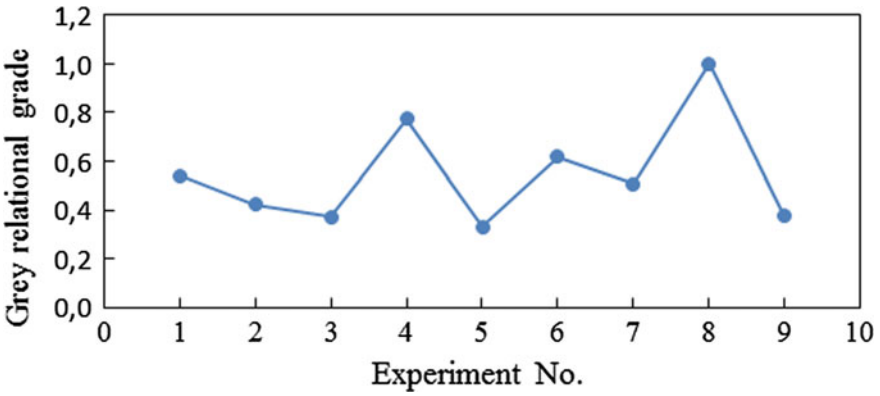

Fig. 23.6 The grey relational grade at various experiments

Table 23.8 Grey relational analysis results

Symbol	Factor	Grey relational grade			Max–min	Rank	Sum of squares	Mean square	Contributiton
		1	2	3					
A	V_c	0.445	0.576	0.630	0.184	3	0.0180	0.0090	14.04
B	f	0.609	0.585	0.457	0.152	4	0.0134	0.0067	10.49
C	t	0.721	0.526	0.404	0.317	1	0.0511	0.0255	39.84
D	T	0.419	0.517	0.715	0.297	2	0.0457	0.0228	35.63

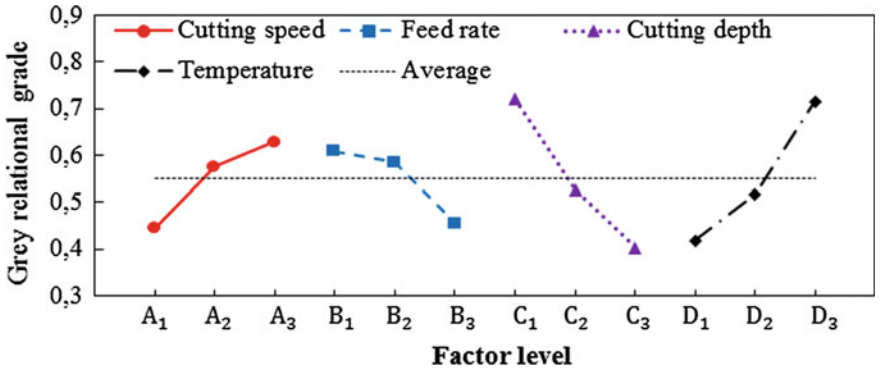

Fig. 23.7 Effects of each process parameter on the Grey relational grade

control parameters for surface roughness and vibration amplitude is A3B1C1D3, corresponding to $V_c = 280$ m/min, $f = 230$ mm/min, $t = 0.5$ mm, $T = 400$ °C.

23.5 Conclusions

The Taguchi method is used to experimentally design SKD11 steel milling in thermal—assisted machining (TAM) by electromagnetic induction. The influence of cutting parameters and elevated temperature on output parameters including surface roughness and cutting vibration amplitude were analyzed. The optimal design is implemented to determine the control parameters with multi-objective of both surface roughness and vibration amplitude could be obtained as cutting speed of 280 m/min, the feed rate of 230 mm/min, cutting depth of 0.5 mm and elevated temperature of 400 °C, respectively.

Acknowledgements This research is funded by Vietnam National Foundation for Science and Technology Development (NAFOSTED) under grant number 107.02-2019.300.

References

1. G. Gurav, P. R. B, S. Patil, Int. J. Eng. **4**(2), 55–61 (2016)
2. A.K.M.N. Amin, M. Abdelgadir, J. Manuf. Sci. Eng. Trans. ASME **125**(4), 674–680 (2003)
3. K.M.A. Lajis, A.K.M.N. Amin, A.N.M. Am, J. Eng. Appl. Sci. **2**, 421–427 (2009)
4. M. Baili, V. Wagner, G. Dessein, J. Sallaberry, D. Lallement, Appl. Mech. Mater. **62**, 67–76 (2011)
5. A. Amin, N.V. Talantov, Mech. Eng. Res. Bull. **9**, 52–62 (1986)
6. M. Thi-Bich, D. Van-Chien, B. Tien-Long, N. Duc-Toan, Metals (Basel) **8**(12) (2018)
7. G. Madhavulu, B. Ahmed, J. Mater. Process. Tech. **44**(3–4), 199–206 (1994)

8. Z.Y. Wang, K.P. Rajurkar, J. Fan, S. Lei, Y.C. Shin, G. Petrescu, Int. J. Mach. Tools Manuf **43**(13), 1391–1396 (2003)
9. P. Dumitrescu, P. Koshy, J. Stenekes, M.A. Elbestawi, Int. J. Mach. Tools Manuf **46**(15), 2009–2016 (2006)
10. B. Shi, H. Attia, R. Vargas, S. Tavakoli, Mach. Sci. Technol. **12**(4), 498–513 (2008)
11. M.J. Bermingham, P. Schaffarzyk, S. Palanisamy, M.S. Dargusch, Int. J. Adv. Manuf. Technol. **74**(9–12), 1487–1494 (2014)
12. R. Makwana, H. Prajapati, Int. Conf. Multidiscip. Res. Pract. **I**(Viii), 488–489 (2014)
13. L. Özler, A. Inan, C. Özel, Int. J. Mach. Tools Manuf **41**(2), 163–172 (2001)
14. T.L. Ginta, A.K.M.N. Amin, Int. J. Mach. Mach. Mater. **14**(2), 194–212 (2013)
15. N. S. Kumar, A. Shetty, A. Shetty, K. Ananth, H. Shetty, Procedia Eng. **38**(Icmoc), 691–697 (2012)
16. A.K.M.N. Amin, M.H.B.M. Saad, M.D. Arif, Adv. Mater. Res. **538–541**, 799–803 (2012)
17. C.W. Chang, C.P. Kuo, Int. J. Mach. Tools Manuf **47**(1), 141–147 (2007)
18. T.-B. Mac, V.-C. Dinh, T.-L. Banh, D.-T. Nguyen, Metals. **8**, 992 (2018)
19. P. Thi-Hoa, M. Thi-Bich, T. Van-Canh, B. Tien-Long, N. Duc-Toan, Int. J. Adv. Manuf. Technol. (2017). https://doi.org/10.1007/s00170-017-1063-x
20. T.-H. Pham, T.-B. Mac, V.-C. Tong, T.-L. Banh, D.-T. Nguyen, Adv. Mech. Eng. **8**(10), 168781401667329 (2016). https://doi.org/10.1177/1687814016673297
21. C. Wang, Y. Xie, L. Zheng, Z. Qin, D. Tang, Y. Song, Int. J. Mach. Tools Manuf **79**, 31–48 (2014)
22. C. Wang, F. Ding, D. Tang, L. Zheng, S. Li, Y. Xie, Int. J. Mach. Tools Manuf **108**, 13–26 (2016)
23. S. Du, M. Chen, L. Xie, Z. Zhu, X. Wang, Adv. Mech. Eng. **8**(10), 1–12 (2016)

Chapter 24
Assessment of the Surface Roughness of Metal Mechanical Parts by Microsoft Kinect V2

Bui Van-Bien, Banh Tien Long, and Nguyen Duc-Toan

Abstract In mechanical manufacturing, the surface roughness of a machined part is a significant parameter to evaluate the products' quality, and as a result, it must be thoroughly measured. Many researches have been studied over the past few to reduce the inherent drawbacks, such as contact, off-line inspection, speed of limited measurement, in the conventional measurement system using contact method. In this paper, the feasibility of the contactless inspection of part surface roughness using Microsoft Kinect v2 have been demonstrated. The part roughness parameters have been estimated by using of PCA plane fitting on point cloud data. In addition, the results received with the Microsoft Kinect v2 system are finally compared to those received with a stylus contact surface roughness measurement system to verify the proposed approach within this paper.

24.1 Introduction

Surface roughness, irregular geometry characteristic, consists of peaks and valleys on the produced part surfaces. In the result of the extremely effect to many functional attributes of mechanical part as well the cost of production, surface roughness is an important factor of part quality in industry. The assessment of surface roughness can be achieved in several aspects. Fundamentally, the surface roughness measurement methods can be categorized into two groups: direct measurement methods and non-contact methods [1]. The most common method uses the stylus probe instrument to move across the surface to determine vibrations generated by the surface roughness. In agreement with the given precision, the size of stylus head can be chosen. A main disadvantage of this method is the possibility to damage the surface being measured by the stylus tip. Another drawback besides is that the resolution of this instrument depends principally on the diameter of the probe tip. Non-contact methods have

B. Van-Bien (✉)
Department of Mechanical Engineering, Haiphong University, Haiphong, Vietnam
e-mail: bienbv80@dhhp.edu.vn

B. T. Long · N. Duc-Toan
School of Mechanical Engineering, Hanoi University of Technology and Science, Hanoi, Vietnam

I. A. Parinov et al. (eds.), *Advanced Materials*, Springer Proceedings in Materials 6, https://doi.org/10.1007/978-3-030-45120-2_24

been developed to overcome these limitations. In this paper, a new approach using point cloud data from Microsoft Kinect v2 for inspecting surface roughness has been proposed.

Over the last few decades, the procedure of digitizing the shape of physical objects, often abbreviated as the 3D-reconstruction, tends to be increasingly used everywhere from the entertainment to the industry [2, 3]. This has been nowadays widely made possible thanks to numerous technologies, namely laser scanners, stereovision, structured-light or the time of flight (ToF) for example. New applications still are found and existing applications to expand. On the issue of large objects, terrestrial laser scanners (TLS) are typically chosen because this technology allows collecting a large amount of accurate data very quickly. While trying to reduce costs and working on smaller pieces, on the contrary, digital cameras are regularly selected. Within this framework, concerning some features such as price or computation time, RGB-D cameras supply new possibilities for the modeling of complex structures, for instance in door mapping [2]. One of them, the Microsoft Kinect v1 launched in 2010, used the structured light technology to acquire the depth data, have met a great success in developer and scientific communities. The second version of Microsoft Kinect was released in 2014, which much improved the depth measurement accuracy. The latest Microsoft Kinect uses a ToF technology for acquiring the depth data. Compared with Kinect v1, the obtained point clouds from Kinect v2 have better quality and resolution as well as without limiting the interference from outside sources. The aim of this study was to identify the method for processing the point cloud data using of PCA plane fitting to estimate surface roughness according to a prepared experiment plan of measurements on Microsoft Kinect v2.

The rest of the paper is structured as follows. First, some researches related existing works about surface roughness assessment using machine vision are introduced in Sect. 24.2. How to calculate the surface roughness from point cloud data by a method known as Principal Component Analysis (PCA) is presented in detail in the Sect. 24.3. The experimental tests and discussions are depicted in Sect. 24.4. Finally, the conclusion and the potential improvement of this paper are discussed in the last section.

24.2 Related Works

Machine vision inspection is by far the most widely applied technology for quality control process. Using the computer vision techniques to investigate the surface roughness of a workpiece under various turning operations was introduced in [1]. The usefulness of this method was the non-contact measurements and ease of automation. In their works, to obtain the surface roughness of the workpiece by processing the surface image, a polynomial network with self-organized adaptive learning ability was selected. There was evidence that the polynomial network appropriately connected the input variables (cutting speed, feed rate, depth of cut, and the feature of surface image) with the output variable, surface roughness of the workpiece.

Hatemleh et al. [4] also informed that the surface roughness was one of the most important parameters describing the surface integrity of a component since a significant proportion of component failure starts at the surface due to either discontinuity or deterioration of the surface quality. Based on the differences between laser-peened, and unpeened samples, the significantly higher surface roughness on specimens processed with shot peening was realized in this study. Moreover, the roughness of the weld nugget was proved steadily higher than the corresponding base material undergoing the laser-peened or shot peening process, seemingly from the lower hardness found in the nugget.

To evaluate texture features from images of turned surfaces, the applicability of a geometrical model based Voronoi tessellation was investigated in [5]. With the purpose of assessment their symmetry, the centroidal cross-moments of the polygons were determined. Based on the number of symmetric polygons in the Voronoi diagram, the degree of homogeneity of the machined surface image was specified. As a result, the number of symmetrical polygons with low centroidal cross-moment should be greater for a surface that was machined under optimal cutting conditions.

Whereas, Kocer et al. [6] performed an experiment and demonstrated that the surface roughness measurements acquired by 3D image processing method was like the values received by a profilometer on machined samples. It was concluded that there had been limited research on estimating the surface roughness of castings by 3D scanning and the current methods such as stylus profilometry, optical microscopy and qualitative methods of visual inspection did not deliver repeatable results and was inefficient due to the time and cost involved.

For systems with Microsoft Kinect v2, the feasibility of applying a low-cost RGB-D camera with an appreciate accuracy to measure pavement roughness was checked [7]. Their works focused on collecting RGB, infrared, and depth data from different surface types with the different roughness levels at 10-m sections. Based on pixel-wise averaging over the acquired frames at each imaging position, a single depth frame was computed. The noise in each depth frame was reduced, the RGB images and the depth images were matched, and the RGB and depth images were also registered to create a 3D surface on the pavement surface. Although there are lots of researches for machine vision inspection as well as the capacity of Microsoft Kinect v2, non-method evaluates surface roughness using the Microsoft Kinect v2 until now.

24.3 Methodology

24.3.1 Measuring of Surface Roughness

As reported by International Standards Organization (ISO), average surface roughness (Ra) is defined as the average deviation of the surface profile from the mean line. The equation for average surface roughness can be written as follows

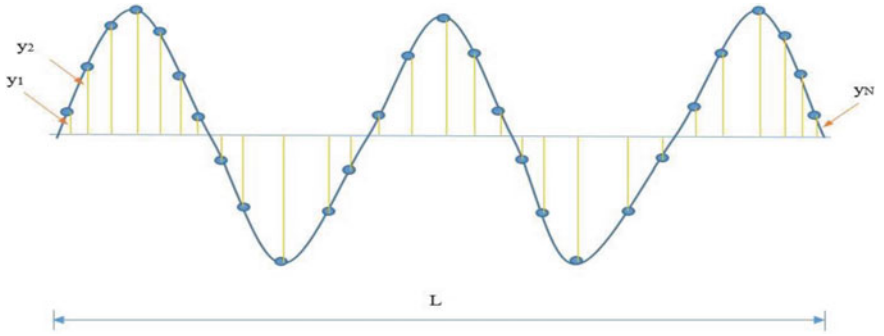

Fig. 24.1 Surface profile example

Fig. 24.2 Methodology: surface roughness determination

$$R_a = \frac{1}{L}\int_0^L |y(x)|\mathrm{d}x, \tag{24.1}$$

where L is the sample length of the profile, y is the coordinate of profile curve (see Fig. 24.1).

As can be seen from (24.1), the average surface roughness of mechanical parts can be determined by calculating the average of normal distances of the points in point cloud data from a nominal surface. A nominal surface can be defined as a surface that has not surface irregularities and is geometrically perfect. The framework of the methodology used while determining Ra using the Microsoft Kinect v2 is depicted in Fig. 24.2.

24.3.2 Data Acquisition Using Microsoft Kinect V2

The part surface whose surface roughness is to be measured first needs to be scanned using Microsoft Kinect v2. This device has two cameras, namely, an infrared camera and an RGB camera. Moreover, it also includes infrared light sources, each of which produces a modulated wave with a various amplitude. Each Microsoft Kinect v2 device has its own depth intrinsic parameters which are sensor and lens dependent. In the factory, the calibration process was implemented, and the intrinsic parameters of each Kinect v2 are stored in its internal memory. These parameters can be achieved with the help of the Kin2 toolbox developed for Matlab [8]. The depth intrinsic

Table 24.1 Depth intrinsic parameters

Parameters	Symbol	Values (pixels)
Focal length	F_x	362.8785
	F_y	362.8785
Principal point	Cx	253.8325
	Cy	204.4191
Radial distortion	K_1(2nd)	204.4191
	K_2(4th)	– 0.26981
	K_3(6th)	0.0888

parameters of the infrared camera in the Microsoft Kinect v2 device using in this paper are introduced in Table 24.1.

Based on the depth intrinsic parameters, the acquired depth map and the perspective projection relationship, the point cloud data of the mechanical part is obtained. Each pixel $p(u, v)$ in depth map corresponds to a point $P(X, Y, Z)$ in point cloud data. Then, X and Y of the point P are computed as follow

$$X = \frac{u - C_x}{F_x} \cdot Z, \tag{24.2}$$

$$Y = \frac{u - C_y}{F_y} \cdot Z, \tag{24.3}$$

where Z is the intensity value of the pixel $p(u, v)$ in the depth map.

In the next section, a brief overview of principal component analysis used to estimate the nominal surface is introduced.

24.3.3 PCA Plane Fitting

Generally, PCA is a statistical procedure to determine the number of uncorrelated variables in a large, high-dimensional dataset. These uncorrelated variables are called principal components which are axes that explain where variance is coming from. Nonetheless, it is assumed here that this is known; namely, that the surface of the mechanical parts being measured explains most of the variation. Hence, in this paper, the purpose of PCA is simply to try to find a representation of the nominal surface that can be used for further calculations.

Computationally, given a point cloud matrix **P**, the principal components are the eigenvectors of the cov(**P**), that is, the covariance matrix of **P**. The most common way to find the eigenvectors is through a process known as the Singular Value Decomposition (SVD). If a point cloud **P** is first conditioned by centering each column, the SVD will give the principal components and the amount of variance attributed to each component [9]. After obtaining the principal components, the principal component

scores are calculated. Specifically, these are the new coordinates of the dataset in the space spanned by the principal components.

In the developed MATLAB code, each coordinate, X, Y, and Z, is imported from the point cloud data into a data cell of size N by 3, where N is the number of points in point cloud data. The PCA plane fitting program is then used to this data cell to fit a plane to the point cloud on the data matrix. In the end, this returns a 3 by 3 data cell containing the principal components; the first, second and third columns represent the ordering of the principal components, respectively. The first two columns, which are the first two principal components, span the 2D space, that is, "X–Y plane". The third principal component is orthogonal to the first two and defines the normal vector of the plane. Combined, this generates a new 3D coordinate system. To obtain the points in this new coordinate system, the centered N by 3 data cell is multiplied with the 3 by 3 matrix containing the principal components. At the close, an N by 3 data cell is obtained that consists of the location of each point in the new coordinate system spanned by the principal components. At this time, the residuals are simply the new Z-coordinates since they are instantly referenced from X_0, Y_0, Z_0. Put it another way, by projecting the normal vector onto the X–Y plane, the peaks and valleys of the corresponding point cloud can be evaluated. Naturally, the PCA plane fitting program automatically measures the distances and outputs the average surface roughness value.

24.4 Results and Discussion

24.4.1 Experimental Setup

Using a Microsoft Kinect for Windows v2.0 sensor, a PC with system CPU Intel (R) Core i7-4790 3.6 GHz; RAM 12 GB; Video card Geforce NVIDIA GVN730D5-2GI, the hardware of this test is configured and shown in Fig. 24.3.

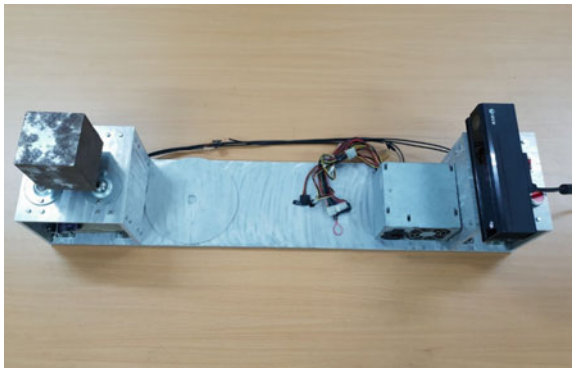

Fig. 24.3 Experimental setup

To capture and process data, the needed software are Window 10 operating system, MATLAB 2016a with image processing toolbox, Kinect for Windows hardware support package for MATLAB, Microsoft Kinect SDK V2.0_1409 and Microsoft Visual Studio 2015, Kin2 toolbox for MATLAB. The experimental process is proposed into the flowchart and depicted in Fig. 24.4.

For this experiment, two test parts are designed and manufactured out of A6061 and CT3. These parts are produced in an MANFORD MCB 850 machine with the same machining conditions, illustrated in Fig. 24.5.

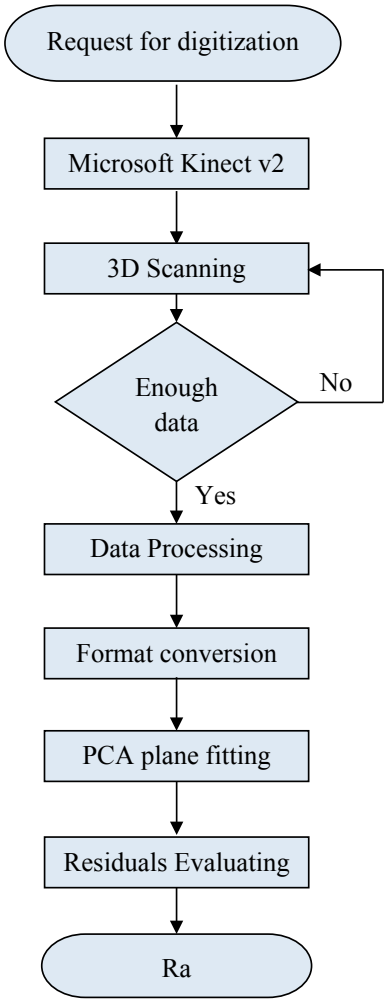

Fig. 24.4 Experimental process

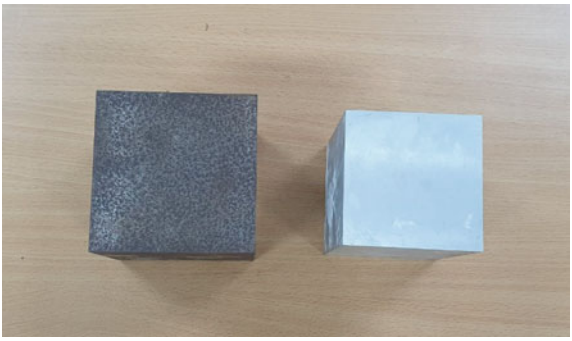

Fig. 24.5 Test parts

24.4.2 Assessment of Surface Roughness

Initially, the Microsoft Kinect v2 is used for acquiring the point cloud of the test parts. Before performing the measurement step, a calibration procedure is done on horizonal table surface. The dense point clouds obtained after scanning the test parts are shown in Figs. 24.6a and 24.7a. In order to trim the unnecessary points, an open source 3D point cloud processing software, MeshLab, is used and the point cloud is edited and processed. The resulting point clouds are then represented in Figs. 24.6b and 24.7b.

To compare the results obtained using the Microsoft Kinect v2 with a conventional instrument, the surface roughness is also measured using the portable surface roughness tester SJ-210 by Mitutoyo, Japan. The results are shown in Table 24.2.

The results obtained using the Microsoft Kinect v2 yielded a surface roughness value of 89.6 μm with a deviation of 8.131 μm which was closer to the value obtained by SL-210. It is also evident from the Table 24.2 that the surface roughness value of

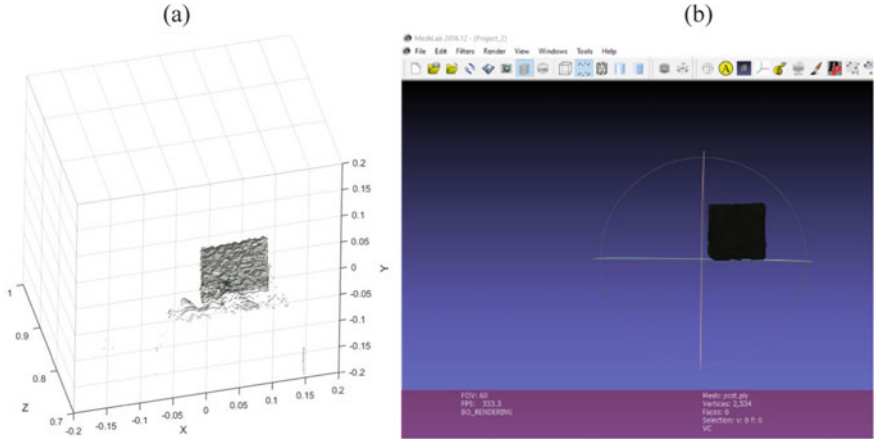

Fig. 24.6 Point cloud of steel cube surface: **a** before trimming, **b** after trimming

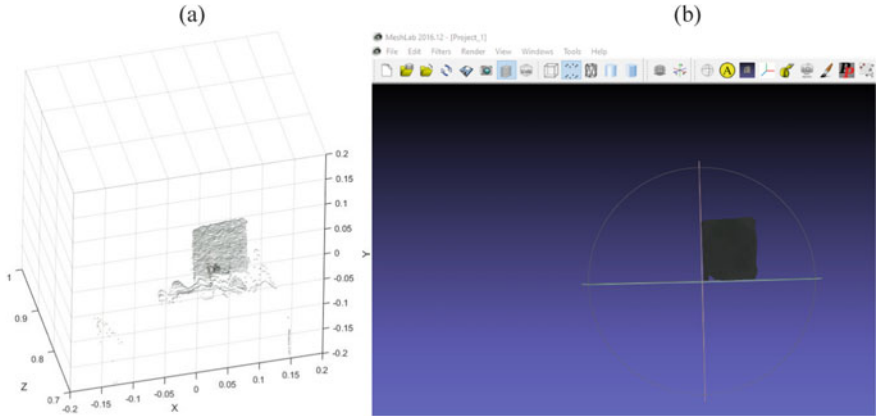

Fig. 24.7 Point cloud of aluminum cube surface: **a** before trimming, **b** after trimming

Table 24.2 Comparison of contact/now-contact surface roughness measurement values

Surface roughness values (with SJ-210)		Surface roughness values (with Kinect v2)	
Test part	μm	Test part	μm
Steel	81.469	Steel	89.6
Aluminum	80.325	Aluminum	91.5

aluminum measured by the Microsoft Kinect v2 is more than 14% of by SJ-210. This phenomenon comes from the highly reflective surface of aluminum then the point cloud includes lot of noises. Therefore, the proposed PCA method can be used as an alternative way for estimation surface roughness of independent metallic surfaces scanned by Microsoft Kinect v2.

24.5 Conclusion

In this paper, a new system for surface roughness assessment is proposed. The Microsoft Kinect v2 is used for the point cloud acquisition. In order to estimate the nominal surface of the point cloud data, the PCA plane fitting is built and programmed to calculate the surface roughness value. After experiments, it was observed that there was similarity between the values calculated from the processed method and the measurement made by a stylus profilometer. For future improvement of the developed system, software will be developed to increase the accuracy of this system.

References

1. B.Y. Lee, Y.S. Tarng, Int. J. Mach. Tools Manuf **41**(9), 1251 (2001)
2. K. Khoshelham, S.O. Elberink, Sensors **12**(2), 1437 (2012)
3. K. Kowsari, M.H. Alassaf, Int. J. Adv. Comput. Sci. Appl. **7**(1), 584 (2016)
4. O. Hatamleh, J. Smith, D. Cohen, R. Bradley, Appl. Surf. Sci. **255**(16), 7414 (2009)
5. A. Datta, S. Dutta, S.K. Pal, R. Sen, J. Mater. Process. Technol. **213**(12), 2339 (2013)
6. E. Koçer, E. Horozoğlu, I. Asiltürk, in *Seventh International Conference on Machine Vision (ICMV 2014)*, vol. 9445 (2015), pp. 944525
7. A. Mahmoudzadeh, A. Golroo, M.R. Jahanshahi, S.F. Yeganeh, Sensors (Switzerland) **19**(7) (2019)
8. J.R. Terven, D.M. Córdova-Esparza, Sci. Comput. Prog. **130**, 97 (2016)
9. M.E. Wall, A. Rechtsteiner, L.M. Rocha, in *A Practical Approach to Microarray Data Analysis*, ed. by D.P. Berrar, W. Dubitzky, M. Granzow. vol. 91 (Kluwer Academic Publishers: Boston) (2003)

Chapter 25
New Materials for Road Construction

N. I. Buravchuk, O. V. Guryanova, M. A. Jani, and E. P. Putri

Abstract The burned rocks of some mine dumps of the Rostov region are evaluated. The physicomechanical properties of the rocks as raw materials for the construction of the subgrade of the access railway track, the structural layers of pavement are investigated. The properties of fractioned gravel and crushing screenings from burned mine rocks are given. The features of hardening of the massif of a roadbed of burnt rocks of mine dumps are shown. The technology of the subgrade and pavement layers is described. The possibility of using materials from burned mine rocks in the construction of subgrade, the ground of roads and structural layers of pavement has been substantiated. The variants of pavement designs using materials from burnt rocks of mine dumps are considered. Practical work was done on the erection of the subgrade railway track and local technological roads, industrial sites and sidewalks. The successful operation of sections of the railway access road, technological roads and sidewalks confirms the feasibility of using burnt rocks of mine dumps in road construction. The use of mine dump rocks allows us to solve some environmental problems: reduce the number of quarries in the extraction of natural raw materials, preserve the natural landscape of the earth's surface, free land from dumps, and reduce pollution of water and air basins.

25.1 Introduction

Every year, the reserves of natural raw materials are depleted. Complicated conditions for its production, the cost of natural mineral raw materials increase. In the coal-industrial regions of any country, huge reserves of mine rocks are concentrated in

N. I. Buravchuk (✉) · O. V. Guryanova
I. I. Vorovich Mathematics, Mechanics and Computer Sciences Institute, Southern Federal University, Rostov-on-Don, Russia
e-mail: burav@math.rsu.ru

O. V. Guryanova
e-mail: oguryanova@sfedu.ru

M. A. Jani · E. P. Putri
University of 17 Agustus 1945, Surabaya, Indonesia

I. A. Parinov et al. (eds.), *Advanced Materials*, Springer Proceedings in Materials 6, https://doi.org/10.1007/978-3-030-45120-2_25

dumps. These are simultaneously extracted rocks during the development of coal deposits, extracted to the surface and stored in dumps. Such waste is a new type of raw material being technogenic. The accumulation of these wastes in terms of the quantity and quality of the contained raw materials suitable for producing useful products should be attributed to technogenic deposits [1]. In the context of increasing needs for natural mineral raw materials, the problem of the integrated use of all extracted raw materials and environmental protection is becoming of paramount importance and more acute every year. The prospects of using technogenic raw materials are obvious. The concept of integrated development of natural mineral resources involves the mandatory processing of waste into useful products as the final stage in the extraction of minerals. The task of improving the environmental situation in industrialized regions and expanding the range of new materials make this stage an indispensable necessity.

With significant bulks of mine dump rocks, their disposal level is low. Mine rocks are very diverse and unstable. This is one of the reasons hindering their use. However, with appropriate processing and preparation, the quality of this waste can be brought to the requirements of regulatory documents. The development of such technogenic deposits will expand the mineral resource base of many industries, solve some problems to improve the state of the environment in each coal-mining region.

Potential consumers of large volumes of coal industry waste can be road construction. Road construction is the most material-intensive area for the use of natural mineral raw materials. In this industry, there is an acute question of both improving the quality of structural layers of pavement and replacing natural materials, especially imported from other regions, with local, cheaper raw materials, in particular, with burnt rocks from mine dumps and ash and slag waste of thermal power plants. The development of effective road-building materials based on burned rocks and ash and slag waste, capable of working under conditions of increasing loads and climatic influences, and technologies for the manufacture of structural layers of pavement of increased bearing capacity are relevant. The use of fly ash and ash-slag mixture in road construction is known [2–4]. The use of burned mine dumps is not common.

25.1.1 Purpose of Research

The purpose of this work is to establish the possibility of using burnt mine rocks in the construction of the subgrade and structural layers of pavement.

25.1.2 Field of Study

We study the following issues:

1. composition and properties of burnt mine rocks;

2. ways to increase the uniformity and stability of the properties of burnt mine rocks;
3. physical and mechanical properties of burnt mine rocks as materials for the construction of the subgrade and structural layers of pavement;
4. features of the formation of the structure and properties of the materials of pavement based on burnt mine rocks.

25.2 Research Method

The object of research was burnt mine rocks accumulated in dumps in the Rostov region (Russia). Preliminary preparation of research objects was crushing and fractionating. Analytical and laboratory studies have been carried out in order to obtain information on the chemical and material composition of raw materials, physical and mechanical properties of burnt mine rocks. Technological tests were carried out on the use of burnt rocks of mine dumps in road construction. A complex of physico-chemical and technological studies allows us to determine the effectiveness and feasibility of using products from technogenic raw materials to ensure the reliability of the foundations and structural layers of pavement. Practical work on the construction of the subgrade and experimental sections of access technological roads using burnt rocks of mine dumps has been completed.

25.3 Results and Discussion

25.3.1 Characteristics of Burnt Rocks

In coal mining, the associated rocks with an admixture of coal are emitted to the surface and stored in dumps. Subsequent conversions of stockpiled rocks in the dump largely depend on their initial composition. Rocks in dumps are subjected to prolonged thermal exposure in an oxidizing environment. Self-firing of rocks in ovals occurs relatively evenly and lasts several years. The product of prolonged self-firing of mine rocks is burned rocks. According to the state of aggregation, the studied rocks belong to solid formations, namely grid materials (blocky, dispersed and finely dispersed). The grain composition largely depends on the characteristics of the source rocks. The rock in the dump is presented from dust and ash fines, fine gravel to blocks weighing several kilograms. On average, fragments from 6 to 100 mm in size prevail. Pieces larger than 600 mm are available. Chunks of unburned coal and layers of lightly burnt rock are found. A visual inspection of the rocks revealed the presence of sulfur, cementing rock fragments. Self-firing of fine-grained sandstones and sandstone shales gives the most durable burnt rocks, consisting of large pieces. The dump contains rocks of low strength and rocks having a compressive strength

of 110–120 MPa. The fine fraction is obtained from finely and coarse layered clay and carbonaceous shales, carbonate and glandular minerals having lower mechanical strength. Burned rocks with water absorption in the range of 5–10% are moderately burnt, and with water absorption less than 5% well burned. The color of the breed varies from dark pink to reddish-brown and purple.

The presence of clastic material in burned rocks, bonded with pelitic and siliceous natural cement to a state of conglomerate, ensures their high water-resistance and mechanical strength, reinforced by rock pressure and heat treatment. Under natural conditions, compaction and formation of rock-like rock occurred, the physical and mechanical properties of which depend on the degree of metamorphism and other characteristics. In the dump along with dense, well-burnt material, unburnt weak rocks, as well as coarse slag sintered with pieces of rock, can also locate. The quality of burnt rock in the dump can be determined by external inspection by the density of the structure, color, and the nature of the surface of the fracture of its pieces. A fractured and roughened or oily to the touch surface in a fracture indicates a poor qualitative material with a low bulk density and high water-absorption. Well-fired burned rocks of homogeneous composition, with a dense structure and a smooth stone-like surface in a fracture from dumps of anthracite coals are characterized by increased mechanical strength, resistance to abrasion, thermal and atmospheric influences. The specific effective activity of the radionuclides of the studied burned rocks does not exceed 370 Bq/kg. By this indicator, burned rocks belong to first class of materials, the use of which is unlimited.

By chemical composition (see Table 25.1), burned rocks are siliceous-aluminous, i.e. characterized by a relatively high content of silicon and aluminum oxides. The content of acid oxides is more than 70%. By the sum of the oxides of silicon, aluminum and iron, the burned rocks are acidic raw materials. According to the classification of Sivertsev [5], rocks can be characterized as siliceous-alumina. Minor losses during calcination indicate the completeness of firing rocks.

The largest clay-glandular module (0.4–0.57), in accordance with the classification of Knigina [6, 7], burned rocks belong to group I: mudstones are active and highly active. Burned rocks have a high chemical resistance: in relation to mineral acids—95 to 99% to alkalis—65.5 to 77.8%.

The chemical and mineral compositions of burned rocks are interconnected. Coal waste differs in mineralogical composition. The mineral component of mine rocks stored in heaps is represented by sedimentary rocks. These are clays, loams, mudstones, siltstones, sandstones, limestones, siliceous schists, carbonaceous rocks. Thermal effects on rocks during prolonged self-firing cause significant changes in their mineral mass and physical condition. At the same time, the structure, texture and properties of the source rocks change significantly. The different mineralogical composition of the rocks and the conditions of the natural process of burning out the carbonaceous component lead to the formation of products of varying degrees of calcination. According to the lithological composition, the rock masses of the studied dumps of former mines are clay. The composition of the clay component is hydromica with an admixture of kaolinite and chlorite. Clays in coal seams are

Table 25.1 Chemical composition of burnt mine rocks, %

Mine	SiO_2	Al_2O_3	Fe_2O_3	CaO	MgO	SO_3	TiO_2	$\sum(K_2O, Na_2O)$	Loss on ignition
Named Komsomol'skoy Pravdy	55.24	21.78	6.25	1.61	1.82	2.17	1.15	4.70	5.26
Named Petrovskogo	55.82	22.84	6.42	1.13	1.44	1.73	1.11	3.85	4.92
Named Vorovskogo	54.77	22.18	7.21	1.16	1.47	2.37	1.18	3.98	5.32
Mayskaya	56.58	21.32	5.75	1.27	2.54	2.78	1.00	4.07	4.32
No. 26	54.33	21.98	6.67	1.33	1.86	2.73	1.12	4.08	5.22
Sevryugovka	57.35	19.95	5.47	1.43	0.65	3.09	1.21	4.59	6.16
Sinegorskaya	54.90	18.68	7.50	1.89	2.23	4.34	1.09	5.25	4.50

so compacted under the influence of rock pressure that they have lost their ductility. Clay material is already dehydrated and greatly modified during self-firing. In terms of their basic physical and chemical properties, burned rocks are close to clays calcined at 800–1000 °C.

Changes that occur with rocks during thermal exposure were recorded during X-ray and differential thermal analysis of siltstones and mudstones [8]. In the initial sample of siltstone (Fig. 25.1a), the lines of diffraction reflection d/n = 0.238; 0.357 and 0.714 are characteristic of kaolinite, and peak intensities d/n = 0.331; 0.498 nm—for hydromica. Strong lines of montmorillonite 1.105 nm and quartz (d/n = 0.333; 0.425 nm) are noted.

The diffraction pattern of a sample of aleurolite calcined at 550 °C (Fig. 25.1b) is characterized by hydromica (d/n = 0.329 and 0.495 nm), quartz with a reflection of 0.334 nm. The lines of kaolinite disappear, which indicates its dehydration. For mudstones (Fig. 25.2), the presence of kaolinite can be judged along the lines of 0.238; 0.357; 0.714 nm, hydromica—according to the peak intensity of 0.331; 0.495 and 1.078 nm. The presence of quartz is confirmed by reflexes of 0.425; 0.333 nm; siderite—0.281 nm. On the diffraction pattern, taken from a sample of calcined quartz, mica-chlorite is observed.

When conducting petrographic studies using a MIN-8 polarizing microscope, it was found that burned rocks are composed of clay minerals, mainly represented by kaolinite and hydromica, terrigenous material in the form of quartz, feldspars, ferruginous minerals and carbonate inclusions.

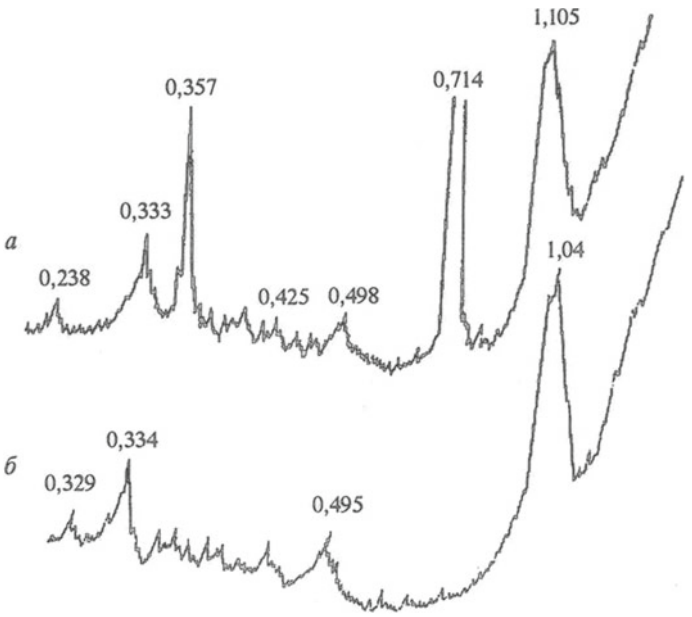

Fig. 25.1 Diffraction pattern of siltstone: **a** initial siltstone; **b** siltstone calcined at 550 °C

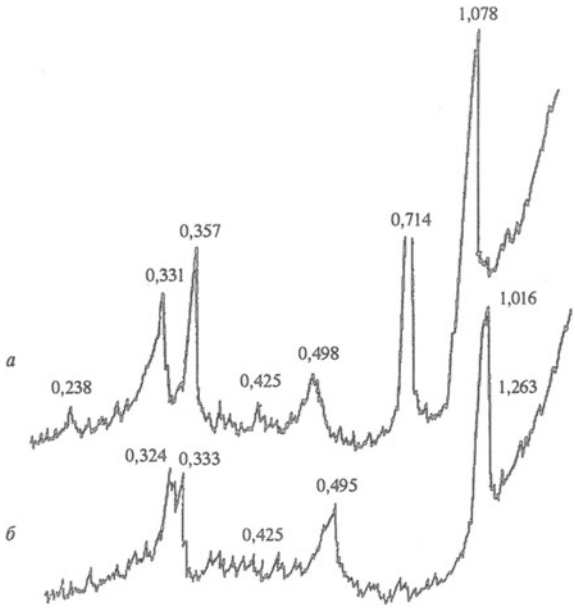

Fig. 25.2 Mudstone diffractogram: **a** initial mudstone; **b** argillite, calcined at 550 °C

The mineral composition of burned rocks contains quartz, clay minerals, carbonates in the form of calcite, magnesite, dolomite, gypsum and alkali metal sulfates, iron is in the form of pyrite, marcasite, hematite. There are feldspars, modifications of crystalline silica—tridymite, cristobalite. The vitreous phase is represented by glass mainly melilite composition. Unburned fuel particles present as impurities are metamorphosed to different degrees, are different from the initial state and are in the form of coke and semi-coke and graphitized carbonaceous matter.

An X-ray study of burned rocks revealed the following basic crystalline minerals: quartz and its modifications: iron in the form of magnetite and hematite; clay substance in the form of corundum, mullite. Secondary minerals are kaolinite, feldspars, sulfur, etc. Endograms associated with the removal of hygroscopic and bound water, exothermic effects due to oxidation of ferrous minerals, polymorphic transformations of quartz, burnout of carbonaceous substances, and decomposition of carbonates are observed on thermograms. Peaks in the thermograms appear as a result of processes occurring in that part of the rock that underwent insufficient firing in the dump or burned at a lower temperature. A well-calcined rock is thermally inert, and thermal effects are hardly detected on the differential thermal analysis curves of such rocks.

25.3.2 Burnt Mine Rocks for Subgrade Construction

The burnt rocks of mine dumps belong to the class of coarse-grained soils, which are uncemented deposits of fragments, between which there are no structural bonds

(gravel, pebble, wood, gravel, sand) thermally changed in the dump under conditions of prolonged self-firing at a temperature of about 1000 °C. The assessment of the studied rock masses allows us to consider them as potential raw materials for the construction of embankments, dams, subgrade. Mine rocks, unlike conventional soils, traditionally used for the construction of subgrade, have specific properties, and they should be attributed to special soils. The physical and mechanical properties of burnt mine rocks as soil for a subgrade were tested. Work was completed on the construction of a subgrade railway access track with a length of 27 km. For this, the rocks of the dumps of the mines of Sevryugovka and Sinegorskaya were used. The composition and condition of the mine rock provides the ability to replace the soil for the construction of the subgrade. The structural design of the subgrade of the access railway is shown in Fig. 25.3.

For laying rocks in the subgrade, their maximum fineness should not exceed 70 mm. Pieces of rock over 70 mm were crushed. Multiple transshipment of rocks with a bulldozer during shipment from the dump contributes to the averaging of rocks. The technology for the construction of subgrade from mine rocks is similar to the layered construction of the embankment from the traditional soil used. Dump mine rocks are well compacted. At the beginning of compaction in loose placer, individual grains of rock and crushed stone are easily distributed and mutually move. At the same time, large fractions of crushed stone play the role of a kind of spatial framework. Small particles fill the voids of the frame. These materials are well compacted, and dense packing of grains in the layer of the array is achieved. During this period, compaction can be carried out without moisture. When the initial sedimentation of the layer is achieved, further compaction requires overcoming the friction between the particles. To increase the compaction of the rock mass, watering is carried out. Water in this case facilitates compaction, as well as moisturizes fines and dust from well-burnt rock resulting from breaking of the edges of rubble during rolling. Maximum compaction is achieved with optimum moisture in the rock mass. Estimated water consumption 12–20 l/m^2. Compaction was completed when the deformation stopped

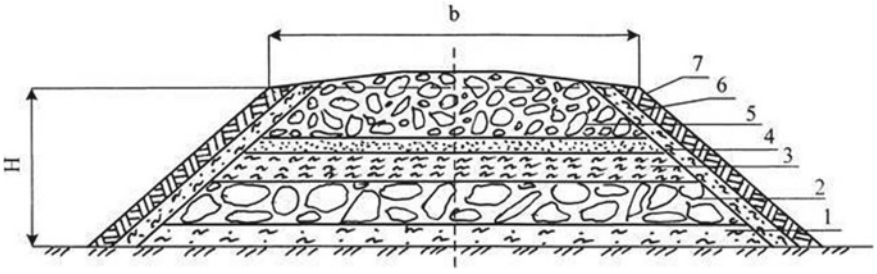

Fig. 25.3 Construction of the subgrade: 1—underlying layer of loam; 2—fractionated burned mine rock; 3—insulating layer of clay; 4—sand; 5—crushed stone from natural stone; 6—insulating layer of clay; 7—fertile soil; *b*—width of the main site; *H*—embankment height

after the passage of a heavy roller, and the density of the rock layer reached 1.85–1.90 g/cm^3. Similarly, from the burnt rocks of mine dumps, the foundation of roads is built.

The ash content of the rock mass is high (90–99%). However, dumps contain impurities of non-burnt rocks. Therefore, there is an option for laying waste rock with a protective and insulating screen made of clay soil or loam. When planning slopes, a layer of fertile soil was applied and sowing of perennial grasses was carried out on the slopes.

25.3.3 Physico-Mechanical Properties of Burnt Crushed Stone *from Mine Dumps*

According to the physico-mechanical properties, burnt mine rocks can be attributed to type III rocks, including rocks of heterogeneous strength, containing weak differences. Therefore, to obtain material from burned rocks of the required strength and durability, it is necessary to process mine rocks with enrichment in strength. The strength enrichment principle is based on the separation of materials of small fractions, the bulk of which are weak differences. Therefore, if, after crushing, the fine fraction is sieved from the products, then the remaining oversize product will be more uniform and strength. When crushing from burnt rocks, fractionated gravel, sand and crushing screenings can be obtained. Grain screenings according to the grain composition correspond to a sand-gravel mixture. Crushed stone and crushed sand from burned rocks [9] are not inferior in properties and quality to similar products from natural raw materials. In the result of the research, it was found that the crushed stone obtained by the two-stage crushing scheme of burned rocks of various terricones has the following main characteristics:

- grade of crushed stone by strength during the crushing test—800; 1000; 1200;
- mark for abrasion—I1; I2;
- frost resistance, the number of cycles of alternate freezing and thawing, not less than—25;
- bulk density, kg/m^3—1020 to 1240;
- voids, %—45 to 55;
- water absorption, %—0.5 to 5.0;
- porosity, %—3.0 to 12.0;
- true density, g/cm^3—2.5 to 2.7.

Particles of crushed stone from burnt rocks are characterized by a porous structure with a developed surface. This circumstance leads to a lower bulk density of such crushed stone in comparison with traditional. In this indicator, crushed stone from burnt rocks are similar to artificial porous aggregates. Unlike the latter, burned crushed stones have greater strength, determined by compression in the cylinder and lower values for water absorption. Due to the rigid structure of the crystal lattice,

micropores in the particles of crushed stone cannot pass into open pores, and water molecules do not penetrate into the space of micropores; therefore, water absorption of crushed stone from burnt rocks is low. There are no clay and silty particles in the crushed stone from burnt rocks, there is no clay in the lumps, and the content of grains of weak rocks does not exceed the permissible limits. The particle shape is angular, non-rounded, the surface is rough. The content in the crushed stone of lamellar and needle-like grains is up to 25%. Crushed stone withstands the tests for structural stability against all types of decay. Crushed stone does not contain impurities and components that are classified as harmful. However, metamorphosed unburned fuel particles may be present. In composition, they are different from the original fuel and consist of coking products. They are resistant to oxidation and durable when exposed to moisture and temperature extremes.

Sand from burnt rocks has a particle size modulus from 2.3 to 3.5, bulk density is 1250–1420 kg/m^3, voids are 35–50%, frost resistance of crushed stone fraction is 15 cycles of alternate freezing and thawing. Crusher screenings are a mixture of sand fraction and crushed stone fraction 5–10 mm. The content of crushed stone fractions varies in the range from 10 to 30%. Grade on strength of crushed stone fraction—800.

25.3.4 Materials from Burnt Rocks of Mine Dumps in Structural Layers of Pavements

Materials from mine rocks of a certain fractional composition are well compacted and are capable to form a monolith of increased bearing capacity over time. This feature of the rocks can be used in the construction of the subgrade, road foundations and structural layers of pavement.

Road construction materials should provide increased durability of pavement structures. Particular requirements apply to the materials used for the construction of roadbed. The material of the base layer must be able to self-strengthen over time in order to provide resistance to the increasing load, since continuously increasing loads act on the bases during operation. Such a structural layer can be created using materials from burnt mine rocks. The specificity of the formation of burned rocks leads to some features of their properties. One of them is the presence of hydraulic activity [10–12]. Due to the presence of active components capable of exhibiting astringent properties, materials of burnt rocks can be, over time, at some moisture, cemented and harden the structure of the material of the structural layer. The dense packing of grains in the material of the carrier layer creates a monolith of increased bearing capacity and stability. This design will be resistant to the effects of loads and alternating change of positive and negative temperatures. Another feature of burned rocks is associated with the macro- and microporous particle structure to be characteristic of heat-insulating materials. From this it follows that the base layer of burnt

rocks will also have heat-insulating properties. These materials can be used to create additional frost protection and thermal insulation layers.

For the construction of the underlying layer, crushed stone was used after the first crushing with a grain size from 20 to 150 mm. For the lower and middle layers of the bases, crushed stone fractions from over 40 to 80 mm and from over 80 to 150 mm are used; for the upper layers of bases and coatings—from over 20 to 40 mm and from over 40 to 80 mm. Crushed stone from burnt rocks is well compacted. Therefore, it is most efficient to lay it by the method of optimal mixtures. This crushed stone layer should be carried out with fractions of small crushed stone with successively decreasing sizes: 5–10, 10–20 and 20–40 mm. For laying crushed stone from burnt rocks, we can use a mixture of fractions: 5(3) – 20, 0–20 and 0–10 mm.

Fractionated crushed stone and crushed sand can be used in the structural layers of pavement. Figs. 25.4 and 25.5 show the variants of pavement, in the structural layers of which fractionated crushed stone from burnt rocks are used. The experimental sections of technological, access roads, industrial sites and sidewalks were made at the mines Almaznaya, Zamchalovskaya, Vostochnaya (Rostov Region, Russia).

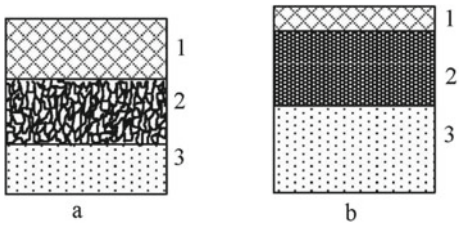

Fig. 25.4 Pavement design of the access roads of enterprises: **a** 1—fine-grained asphalt concrete, crushed stone fraction up to 15 mm, $h = 26$ cm; 2—crushed stone fraction 5–10 mm, $h = 26$ cm; 3—sand, $h = 15$ cm; **b** 1—fine-grained asphalt concrete, crushed stone fraction up to 15 mm, $h = 5$ cm; 2—black crushed stone fraction of 5–10 mm; $h = 20$ cm; 3—sand, $h = 35$ cm

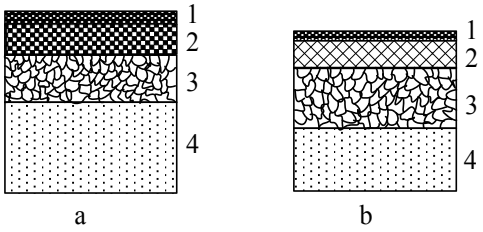

Fig. 25.5 Design of the road pavement roads improved light-weight type: **a** 1—surface treatment, crushed stone fraction 5–10 or 10–15 (20) mm; 2—crushed stone fraction 5–40 mm, treated bitumen, $h = 8$ cm; 3—crushed stone fraction 40–80 (150) mm, $h = 20$ cm; 4—sand, $h = 26$ cm; **b** 1—surface treatment, fraction crushed stone 5–10 or 10–15 (20) mm; 2—crushed stone fraction 5–40 mm, treated bitumen on the road, $h = 8$ cm; 3—crushed stone fraction 40–80 (150) mm, $h = 16$ cm; 4—sand, $h = 16$ cm

If the crushed stone mixture of the optimal grain composition is used for the construction of pavement layers, then the material is immediately distributed with a layer of the required thickness, leveled with a grader or bulldozer and compacted. The number of passes of the rollers is established empirically. The compacted layer can reach a thickness of 20 cm (in a loose body), but this requires at least 15–18 passes of the heavy roller in one place. With significant porosity of areas of the compacted layer, fines of 5–10 mm in size are scattered on them and additionally compacted with 1–2 passes of a heavy roller.

Figure 25.6 shows the transverse profile of pavement using materials from burned rocks. The thickness of the base is 20 cm, which is made of fractioned crushed stone: the bottom layer is from the St. 20–80 mm, the upper—their fractions of St. 5–20 mm with bitumen impregnation. A two-layer asphalt concrete coating is applied to the base: the upper layer is fine-grained and the lower layer is coarse-grained asphalt concrete. The strength and particle size distribution of crushed stone from the base of the road with asphalt concrete pavement did not change during the operation of the road. Fraction of crushed stone of St. 20–80 mm has a brand of strength 800, the fraction from 5 to 20 mm of Mark 1000.

Studies on the interaction of burned grains with bitumen show good adhesion. There is practically no exposure of crushed stone, the bitumen film is completely preserved on the surface of the crushed stone. Asphalt mixes for the upper layers of pavement use crushing screenings and crushed stone with grain sizes up to 40 mm. Thus, pavement for roads of category IV and V can be made using materials from burnt rocks of mine dumps. The positive experience in operating experimental sections of roads and sidewalks confirms the feasibility of using non-conventional technogenic raw materials in road construction. High-quality crushed stone from burnt rocks can be used in all structural layers of pavement.

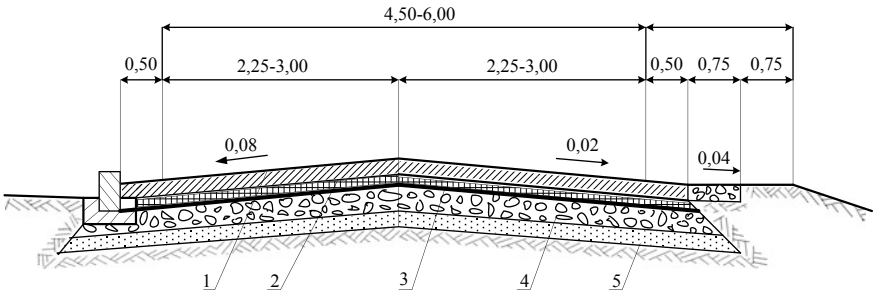

Fig. 25.6 Constructive transverse profile of auto-drive-ways with a carriage-way width of 4.5–6.0 m; pavement design: 1—medium-grained asphalt concrete, $h = 4$ cm; 2—coarse-grained asphalt concrete, $h = 5$ cm; 3—burnt rock crushed stone impregnated with bitumen, $h = 6.5$ cm; 4—base of burnt rock crushed stone, $h = 20$ cm; 5—sandy underlying layer, $h = 10$ cm

25.4 Discussion

Long-term service of any structure can be provided that the material of the structure meets the conditions of its operation. To ensure reliable resistance of the structure to increasing loads throughout the entire service life, it is necessary that the energy of structural bonds in the material of the structure is constantly increased. This is possible provided that the design has a self-densification system. Materials from mine rocks of a certain fractional composition have the ability over time to cement and reinforce the structure of the embankment massif, to form a monolith of increased bearing capacity and stability. Materials from burnt and burnt mine rocks can create a monolithic self-compacting system without introducing a binder. This ability of the rocks is due to their chemical and mineral composition, structural features, and activity. Burned rocks is the products of spontaneous firing, due to the nature of their formation and thermodynamic state; they have an increased supply of internal energy and corresponding reactivity and can significantly affect the strengthening of the massif. The main active components of burned rocks are metakaolinite, amorphous silica, aluminum oxides, and iron. The presence of these components is due to the specifics of their origin, and is associated with the presence of a number of structural defects that occur during physicochemical processes that occur during high-temperature firing of coal-bearing mine rocks. An important role is played by the nature of the surface of mineral particles, the presence of active surface centers, characterized by an increased energy potential. It is known that the surface of all solid materials contains Lewis acidic and basic branstedite active centers [13–16], which determine its activity. Obviously, for burnt rocks of mine dumps, when evaluating their activity, it is necessary to take into account both the presence of active components that appeared due to their formation and the Lewis and Brønsted type centers (synergistic effect). The presence of these factors has a structuring effect in the formation of an array of subgrade embankments. This new state of matter is the cause of the ability of burned rocks to cement. It is promising to use the potential of burnt mine crushed stone primarily for the construction of road pavement of III-IV road categories in the construction, reconstruction and repair of regional and local roads, and a large network of rural roads. The volumes of such work are large. When using such raw materials, in addition to saving natural mineral raw materials, the cost of transportation costs for delivering raw materials to the place of consumption is reduced, some environmental problems are solved to reduce the negative impact of the waste dump on the environment near its location.

A general condition for the use of mine rocks in road construction is the compliance of the strength of the structural layers of pavement constructed from them with the mechanical and physico-mechanical effects that can be expected in this layer. To make a decision on the use of mineral materials from burned rocks, it is necessary to conduct a comprehensive assessment of this technogenic raw material. The methodology for a comprehensive assessment of mine rocks includes three stages:

1. an engineering-geological survey of the rocks of mine dumps to obtain the necessary information about the nature of the occurrence of materials, the distribution

of moisture, density along the depth of the dump, the degree of homogeneity, the method of producing rocks;
2. an engineering-geological assessment of the indicators of physical and mechanical properties of rocks and materials from them, as determined in the laboratory, and establishment of the possibility and conditions for their use as materials for road construction;
3. taking into account the obtained laboratory data, it is carried out a study of the feasibility to use certain materials from rocks in specific road structures. In the case of a positive decision, special recommendations are developed on the design of the subgrade and road pavement from rocks of a specific mine dump and the features of the technology for their construction.

Due to the lower cost of materials from burnt rocks of mine dumps (on 25–30% lower than the cost of natural aggregates), the total cost of road construction works decreases.

Acknowledgements This research was carried out within the framework of financing of the Ministry of Education and Science of the Russian Federation for the project No. BCH0110-11/2017-20. Research was financially supported by Southern Federal University, 2020 (Ministry of Science and Higher Education of the Russian Federation) on the project VnGr /2020-04-IM.

References

1. K.I. Trubetskoy, Z.A. Terpogosov, V.G. Shitarev, Mountain J. **3**, 44–48 (1994). (In Russian)
2. The use of fly ash, ash and slag mixtures and slag from thermal power plants in road construction, in *Proceedings of the Union State*, vol. **82** (Moscow, 1975), 184p. (In Russian)
3. E.I. Putilin, B.C. Tsvetkov, *The Use of Fly Ash and Ash and Slag Mixtures in the Construction of Roads. Overview of Domestic and Foreign Experience in the Application of Waste from the Combustion of Solid Fuels at Thermal Power Plants* (Moscow, 2003), 123p. (In Russian)
4. N.F. Kosenko, V.V. Makarov, *Ecology and Industry of Russia* vol. 4 (2008), p. 44. (In Russian)
5. G.N. Sivertsev, Processes During Hardening of Fuel Slag and Burnt Rocks. Chemical Processes of hardening of Concrete (Moscow, Gosstroyizdat, 1961), pp. 108–122. (In Russian)
6. G.I. Knigina, *Construction Materials from Burnt Rocks* (Moscow, Stroyizdat, 1966), 206p. (In Russian)
7. G.I. Knigina, V.F. Zavadsky, *Microcalorimetry of Mineral Raw Materials in the Production of Building Materials* (Moscow, Stroyizdat, 1987), 144 p. (In Russian)
8. SZh Saybulatov, A.P. Kapustin, L.F. Kalmykova, V.T. Stanevich, News of universities. Constru. Archit. **3**, 60–64 (1991). (In Russian)
9. N.I. Buravchuk, O.V. Guryanova, News of higher educational institutions. North-Caucasus Region. Tech. Sci. **1**, 111 (2015). (In Russian)
10. L.I. Kataeva, Build. Mater. **7**, 23 (1996). (In Russian)
11. N.I. Buravchuk, V.M. Budnitsky, V.F. Brazhnikov, News of universities. North-Caucasus Region. Tech. Sci. **4**, 70 (1998). (in Russian)
12. N.I. Buravchuk, O.V. Guryanova, M.A. Jani, E.P. Putri, Advanced Materials—Proceedings of the International Conference on "Physics and Mechanics of New Materials and Their Applications", PHENMA 2017, in *Springer Proceedings in Physics*, ed. by A. Ivan, Parinov, Shun-Hsyung Chang, V.K. Gupta, vol. **207** (Springer Cham, Heidelberg, New York, Dordrecht, London, 2018), pp. 605–619

13. M.M. Sychev, E.N. Kazanskaya, A.A. Petukhov, University news. Chem. Technol. **10**, 85–88 (1987). (In Russian)
14. K. Tanab, *Solid Acids and Bases* (Moscow, Mir. 1973), 183p. (In Russian)
15. A.P. Nechiporenko, *Acid-Base Surface Properties Of Solids* (Guidelines. Leningrad, LTI, Lensoviet, 1989). 22p. (In Russian)
16. V.V. Yadykina, News of universities. Building **9**, 75 (2003). (In Russian)

Part III
Mechanics of Advanced Materials

Chapter 26
Finite Element Modelling of Active Composite Materials in ACELAN-COMPOS Package

Andrey Nasedkin

Abstract The paper deals with computer modelling in finite element software ACELAN-COMPOS of multiscale two-phase magnetoelectric (piezomagnetoelectric) bulk composites that consist of piezomagnetic and/or piezoelectric fractions of irregular structures. The proposed technique is based on the models of micro- and nanoscale materials with interface or surface effects, the effective moduli method, the modelling of representative volumes, and the use of finite element technologies for solving the problems in the representative volumes.

26.1 Introduction

In this paper, as active materials we will understand the materials in which sufficiently noticeable deformations can be caused by external nonmechanical influences. Such materials are piezoelectric, magnetoelectric, pyroelectric and other materials with coupling between mechanical fields and fields of a different nature: electric, magnetic or thermal. These materials are widely used in modern engineering as active elements of transducers, sensors, actuators and other devices. Recently, new materials with improved characteristics are being intensively developed to improve the efficiency of these devices. Especially important are the problems of developing active composite materials consisting of materials of different phases. Methods of mathematical and computer modelling help us to predict the effective properties of composite materials depending on the characteristics of the initial phases, their percentage ratio and the peculiarities of the internal structure.

The problems of determining effective properties, also called homogenization problems, can be solved on the basis of various approaches known in the mechanics of composite materials. For active materials whose behaviour is described by a sufficiently complicated system of differential equations, it is convenient to use the method of effective moduli. For example, for piezoelectric composites according to

A. Nasedkin (✉)
Institute of Mathematics, Mechanics and Computer Science, Southern Federal University, 8a, Milchakova Street, Rostov-on-Don, Russia 344090
e-mail: nasedkin@math.sfedu.ru

I. A. Parinov et al. (eds.), *Advanced Materials*, Springer Proceedings in Materials 6, https://doi.org/10.1007/978-3-030-45120-2_26

this method, it is necessary to solve a set of boundary-value problems of piezoelectricity (electroelasticity) with special boundary conditions providing for homogeneous materials the exact solutions with constant field gradients (strains, stresses, electric field and electrical induction). In a non-uniform representative volume, these gradients, naturally, will not be constant, but their averaged integral characteristics will permit to determine the effective moduli of the composite material [1, 2].

For nanostructured composites, in which inclusions or pores have nanodimensions, the nanoscale effect can be taken into account in the framework of the theory of surface stresses [3–8] and its generalizations to the problems with coupling fields [9–15]. In the theory of surface stresses for the interfaces of materials with different phases, the special equations are written that relate stress jumps in volumes with fields for surface stresses. Finally, in recent years, the technologies have been proposed for creating the new materials composed of piezoelectric matrix and of inclusions from other materials or pores, on which interface boundaries the particles of third type materials are deposited [16, 17].

To solve the homogenization problems for all active composites described in this paper, the specialized software was developed, which is based on the finite element solution of boundary problems in representative volumes and takes into account the main features of the internal structure of composites.

Namely, the program systems written in the APDL ANSYS language were created, which allow in the automated mode to solve in the ANSYS package the homogenization problems for active composites of various types and determining their effective moduli. To generate the structures of representative volumes in addition to the simple random ANSYS algorithm, external programs that implement various algorithms were created [1, 2, 18]: 3–x algorithm implemented by S.V. Bobrov, supporting the connectivity of finite elements of the first phase, up to 90% of inclusions of the second phase; 3–0 algorithm with a regular structure of connectivity of the first phase in three axial directions and with a closed structure of the elements of the second phase; cluster algorithms implemented by V. V. Remizov (Witten–Sander method, cluster of the second phase method; method of “growth out of the plane”; method of initial concentration, etc.).

However, in the ANSYS package there were no basic means for solving the problems of magnetoelectricity and there were no piezoelectric and magnetoelectric shell finite elements. In this regard, at the Department of Mathematical Modelling of Southern Federal University, a specialized finite element package ACELAN-COMPOS was developed. The ACELAN-COMPOS package is focused on solving the homogenization problems with coupled mechanical and electromagnetic fields. In this package, implemented new algorithms 3–3 connectivity [19, 20], supporting the connectivity of the two phases; algorithm 3–0 connectivity, creating the granular structures [21, 22]; and algorithm 1–3 connectivity, creating the structures with rod elements in a matrix [20, 22]. For all these models of representative volumes, the algorithms have been developed for the automated search for finite elements located at the interphase boundaries and placing shell elements on them that simulate the presence of surface effects for nanoscale inclusions or pores. For transversely isotropic materials, an algorithm was additionally implemented for the plate surface

elements, parallel to the coordinate axes, with the material properties that inherit the anisotropy structure of the neighbouring volume elements.

The models of magnetoelectricity and the models of representative volume elements of the ACELAN-COMPOS package are briefly presented in this paper. Other means of ACELAN-COMPOS and a more detailed presentation of models, algorithms and results are presented in [19–25].

26.2 Setting of Homogenization Problems

The technology of homogenization problem solving implemented in ACELAN-COMPOS is applicable for a fairly wide class of composite materials of various stochastic structures with coupling physical and mechanical fields. It is only important that linear stationary equations of divergent type should be considered. For example, let Ω be the representative volume of a piezomagnetoelectric (magnetoelectric) composite body consisting of two materials. We assume that this volume is filled with materials of two types (phases): $\Omega = \Omega^{(1)} \cup \Omega^{(2)}$. These phases can have various coupled fields. Thus, the phase $\Omega^{(1)}$ can have piezoelectric properties, while the phase $\Omega^{(2)}$ can be piezomagnetic. Another case is the active materials with inclusions or pores. Then, the first phase of the main fills up the volume or set of volumes $\Omega^{(1)}$, and the second phase (inclusions or pores) fills the volume or set of volumes $\Omega^{(2)}$. Here, for a porous material, the phase $\Omega^{(1)}$ should be connected.

For modelling of nanoscale effects in the framework of the Gurtin–Murdoch theory and its generalizations, surface fields are set on the interfaces of the two phases $\Gamma^s = \partial\Omega^{(1)} \cap \partial\Omega^{(2)}$. The external boundary of the representative volume $\Gamma = \partial\Omega$ will be used to specify the boundary conditions in the homogenization problems.

In accordance with the effective moduli method, we will consider in the volume Ω the following boundary value problem of the static theory of magnetoelectroelasticity with respect to the displacement functions $\mathbf{u}(\mathbf{x})$, the electric potential $\varphi(\mathbf{x})$ and the magnetic potential $\phi(\mathbf{x})$:

$$\mathbf{L}^{\mathrm{T}}(\nabla)\cdot\mathbf{T}=0,\quad \nabla\cdot\mathbf{D}=0,\quad \nabla\cdot\mathbf{B}=0,\quad \mathbf{x}\in\Omega, \tag{26.1}$$

$$\begin{aligned}&\mathbf{T}=\mathbf{c}\cdot\mathbf{S}-\mathbf{e}^{\mathrm{T}}\cdot\mathbf{E}-\mathbf{h}^{\mathrm{T}}\cdot\mathbf{H},\\ &\mathbf{D}=\mathbf{e}\cdot\mathbf{S}+\boldsymbol{\kappa}\cdot\mathbf{E}+\boldsymbol{\alpha}\cdot\mathbf{H},\ \mathbf{B}=\mathbf{h}\cdot\mathbf{S}+\boldsymbol{\alpha}^{\mathrm{T}}\cdot\mathbf{E}+\boldsymbol{\mu}\cdot\mathbf{H},\end{aligned} \tag{26.2}$$

$$\mathbf{S}=\mathbf{L}(\nabla)\cdot\mathbf{u},\quad \mathbf{E}=-\nabla\varphi,\quad \mathbf{H}=-\nabla\phi, \tag{26.3}$$

$$\mathbf{L}^{\mathrm{T}}(\nabla)=\begin{bmatrix}\partial_1 & 0 & 0 & 0 & \partial_3 & \partial_2\\ 0 & \partial_2 & 0 & \partial_3 & 0 & \partial_1\\ 0 & 0 & \partial_3 & \partial_2 & \partial_1 & 0\end{bmatrix},\quad \nabla=\begin{Bmatrix}\partial_1\\ \partial_2\\ \partial_3\end{Bmatrix}, \tag{26.4}$$

$$\mathbf{L}^{\mathrm{T}}(\mathbf{n})\cdot[\mathbf{T}]=\mathbf{L}^{\mathrm{T}}(\nabla^s)\cdot\mathbf{T}^s,\ \mathbf{n}\cdot[\mathbf{D}]=\nabla^s\cdot\mathbf{D}^s,\ \mathbf{n}\cdot[\mathbf{B}]=\nabla^s\cdot\mathbf{B}^s,\ \mathbf{x}\in\Gamma^s, \tag{26.5}$$

$$\mathbf{T}^s=\mathbf{c}^s\cdot\mathbf{S}-\mathbf{e}^{s\mathrm{T}}\cdot\mathbf{E}^s-\mathbf{h}^{s\mathrm{T}}\cdot\mathbf{H}^s, \tag{26.6}$$

$$\mathbf{D}^s=\mathbf{e}^s\cdot\mathbf{S}^s+\boldsymbol{\kappa}^s\cdot\mathbf{E}^s+\boldsymbol{\alpha}^s\cdot\mathbf{H}^s,\quad \mathbf{B}^s=\mathbf{h}^s\cdot\mathbf{S}^s+\boldsymbol{\alpha}^{s\mathrm{T}}\cdot\mathbf{E}^s+\boldsymbol{\mu}^s\cdot\mathbf{H}^s, \tag{26.7}$$

$$\mathbf{S}^s=\mathbf{L}(\nabla^s)\cdot(\mathbf{I}-\mathbf{n}\otimes\mathbf{n})\cdot\mathbf{u},\ \mathbf{E}^s=-\nabla^s\varphi,\ \mathbf{H}^s=-\nabla^s\phi,\ \nabla^s=\nabla-\mathbf{n}(\partial/\partial n), \tag{26.8}$$

$$\mathbf{u}=\mathbf{L}^{\mathrm{T}}(\mathbf{x})\cdot\mathbf{S}_0,\quad \varphi=-\mathbf{x}\cdot\mathbf{E}_0,\quad \phi=-\mathbf{x}\cdot\mathbf{H}_0,\quad \mathbf{x}\in\Gamma. \tag{26.9}$$

Here $\mathbf{T}=\{\sigma_{11},\sigma_{22},\sigma_{33},\sigma_{23},\sigma_{13},\sigma_{12}\}$, $\mathbf{S}=\{\varepsilon_{11},\varepsilon_{22},\varepsilon_{33},2\varepsilon_{23},2\varepsilon_{13},2\varepsilon_{12}\}$ are the arrays of the stress components σ_{ij} and the strain components ε_{ij}; $\mathbf{D}$ and $\mathbf{E}$ are the vectors of the electrical induction or the electric displacement and of the intensity electric field; $\mathbf{B}$ and $\mathbf{H}$ are the vectors of magnetic induction and of the intensity magnetic field, respectively; $\mathbf{c}=\mathbf{c}^{E,H}$ is the 6×6 matrix of stiffness moduli; $\mathbf{e}=\mathbf{e}^H$ is the 3×6 matrix of piezomoduli; $\mathbf{h}=\mathbf{h}^E$ is the 3×6 matrix of magnetostriction moduli or piezomagnetic moduli; $\boldsymbol{\kappa}=\boldsymbol{\kappa}^{S,H}=\boldsymbol{\varepsilon}^{S,H}$ is the 3×3 matrix of dielectric permittivity moduli (dielectric constants); $\boldsymbol{\alpha}=\boldsymbol{\alpha}^S$ is the 3×3 matrix of magnetoelectric coupling coefficients; $\boldsymbol{\mu}=\boldsymbol{\mu}^{S,E}$ is the 3×3 matrix of magnetic permeability moduli; $\mathbf{S}_0$, $\mathbf{E}_0$ and $\mathbf{H}_0$ are constant six-dimensional array, and three-dimensional vectors, respectively; the superscripts of the moduli indicate for which constant fields they were calculated; $(\ldots)^{\mathrm{T}}$ is the transpose operation.

Interface relations (26.5)–(26.8) on the interphase surface Γ^s are used only for modelling of composites at the nano-level. In (26.5)–(26.8), the surface fields and moduli are marked with superscript s; $[(\ldots)]=(\ldots)^{(1)}-(\ldots)^{(2)}$ is the jump of the corresponding quantity across the interphase boundary; $\mathbf{n}$ is the unit normal vector to Γ^s, external to the domain $\Omega^{(1)}$.

If the interface boundary conditions (26.5)–(26.8) are missing, then the problem (26.1)–(26.4), (26.9) is the homogenization problem for piezomagnetoelectric composite with usual phase sizes (inclusions or pores).

In the case of a composite of arbitrary anisotropy class to determine the full set of its effective moduli $c^{\mathrm{eff}}_{\beta\zeta}$, $e^{\mathrm{eff}}_{i\zeta}$, $h^{\mathrm{eff}}_{i\zeta}$, $\kappa^{\mathrm{eff}}_{ij}$, $\alpha^{\mathrm{eff}}_{ij}$, μ^{eff}_{ij}, it is required to solve the twelve problems (26.1)–(26.9), differing in boundary conditions (26.9), in which only one of the components $S_{0\Gamma}$, E_{0k}, H_{0k} should be set not equal to zero ($\gamma=1,2,\ldots,6$; $k=1,2,3$):

- problems I–VI ($\zeta=1,2,\ldots,6$)

$$S_{0\gamma}=S_0\delta_{\varsigma\gamma},\mathbf{E}_0=0,\mathbf{H}_0=0\Rightarrow c^{\mathrm{eff}}_{\beta\zeta}=\langle T_\beta\rangle/S_0,e^{\mathrm{eff}}_{i\zeta}=\langle D_i\rangle/S_0,h^{\mathrm{eff}}_{i\zeta}=\langle B_i\rangle/S_0, \tag{26.10}$$

- problems VII–IX ($j = 1, 2, 3$)

$$\mathbf{S}_0 = 0, E_{0j} = E_0\delta_{jk}, \mathbf{H}_0 = 0 \Rightarrow e^{\text{eff}}_{j\beta} = -\langle T_\beta \rangle / E_0, \kappa^{\text{eff}}_{ij} = \langle D_i \rangle / E_0, \alpha^{\text{eff}}_{ji} = \langle B_i \rangle / E_0, \tag{26.11}$$

- problems VII–IX ($j = 1, 2, 3$)

$$\mathbf{S}_0 = 0, \mathbf{E}_0 = 0, H_{0j} = H_0\delta_{jk} \Rightarrow h^{\text{eff}}_{j\beta} = -\langle T_\beta \rangle / H_0, \alpha^{\text{eff}}_{ij} = \langle D_i \rangle / H_0, \mu^{\text{eff}}_{ij} = \langle B_i \rangle / H_0, \tag{26.12}$$

where $\delta_{i\,j}$ is the Kronecker symbol; $\beta = 1, 2, \ldots, 6$; $i = 1, 2, 3$;

$$\langle (\bullet) \rangle = \frac{1}{|\Omega|} \left(\int\limits_{\Omega} (\bullet) d\Omega + \int\limits_{\Gamma^s} (\bullet)^s d\Gamma \right). \tag{26.13}$$

As we can see from (26.9)–(26.13), taking into account the interface conditions leads to the necessary of calculation of the averaged field characteristics not only by the volume Ω, but also by the interface boundary Γ^s. Since the interface boundaries complicate the internal structure of the representative volume, it is possible to solve boundary-value homogenization problems only numerically, for example, by the finite element method described below.

26.3 Finite Element Approximations

In order to solve the problems of magnetoelectroelasticity I–XII for an inhomogeneous composite material in a representative volume Ω, one can proceed to their weak statements and use the classical technique of finite element approximations. Let Ω_h be the region occupied by a finite element mesh, $\Omega_h \subseteq \Omega$, $\Omega_h = \Omega_h^{(1)} \cup \Omega_h^{(2)}$, $\Omega_h^{(j)} \subseteq \Omega^{(j)}$, $\Omega_h^{(j)} = \cup_k \Omega_{ek}^{(j)}$, where $\Omega_{ek}^{(j)}$ is a separate finite element with the number k and with the material properties of the phase $j = 1, 2$. Let also Γ_h^s be a grid of the surface finite elements, conforming with the volume mesh Ω_h, $\Gamma_h^s = \partial\,\Omega_h^{(1)} \cap \partial\,\Omega_h^{(2)}$, $\Gamma_h^s = \cup_m \Gamma_{em}^s$, where Γ_{em}^s is a separate surface finite element with number m, which is a common face of the corresponding volume elements $\Omega_{ek}^{(j)}$ on the phase interface ($\Gamma_h^s \approx \Gamma^s$).

We will use Lagrangian or serendipity finite elements with degrees of freedom of nodal displacements, electrical potentials and magnetic potentials. It is important that, due to the structure of the surface fields (26.5)–(26.8), we can use membrane elements with degrees of freedom of nodal displacements, electrical potentials and magnetic potentials (without degrees of freedom of the rotation angles). Then approximate solutions of $\mathbf{u}_h \approx \mathbf{u}$, $\varphi_h \approx \varphi$, $\phi_h \approx \phi$ on the finite element mesh Ω_h can be searched in the form

$$\mathbf{u}_h = \mathbf{N}_u^{\mathrm{T}} \cdot \mathbf{U}, \quad \varphi_h = \mathbf{N}_\varphi^{\mathrm{T}} \cdot \mathbf{\Phi}, \quad \phi_h = \mathbf{N}_\phi^{\mathrm{T}} \cdot \mathbf{\Psi}, \tag{26.14}$$

where $\mathbf{N}_u^{\mathrm{T}}$ is the matrix of basis or form functions for displacements; $\mathbf{N}_\varphi^{\mathrm{T}}$, $\mathbf{N}_\phi^{\mathrm{T}}$ are the row vector of basis functions for electric and magnetic potentials; $\mathbf{U}$, $\mathbf{\Phi}$, $\mathbf{\Psi}$ are the vectors of nodal displacements, electric potentials and magnetic potentials, respectively.

In accordance with the classical finite element technique, we approximate the continual weak formulation of the problems I–XII in the finite dimensional spaces associated with the basis functions from (26.14). Substituting (26.14) and similar representations of the projection functions $\delta\mathbf{u}_h$, $\delta\varphi_h$, $\delta\phi_h$ into weak statements of magnetoelectroelastic problem, we obtain the following finite element system

$$\mathbf{K} \cdot \mathbf{a} = \mathbf{F}, \tag{26.15}$$

$$\mathbf{K} = \begin{bmatrix} \mathbf{K}_{uu} & \mathbf{K}_{ub} \\ \mathbf{K}_{ub}^{\mathrm{T}} & -\mathbf{K}_{bb} \end{bmatrix}, \quad \mathbf{a} = \begin{Bmatrix} \mathbf{U} \\ \mathbf{b} \end{Bmatrix}, \quad \mathbf{F} = \begin{Bmatrix} \mathbf{F}_u \\ -\mathbf{F}_b \end{Bmatrix}, \tag{26.16}$$

$$\mathbf{K}_{bb} = \begin{bmatrix} \mathbf{K}_{\varphi\varphi} & \mathbf{K}_{\varphi\phi} \\ \mathbf{K}_{\varphi\phi}^{\mathrm{T}} & -\mathbf{K}_{\phi\phi} \end{bmatrix}, \ \mathbf{K}_{ub}^{\mathrm{T}} = \begin{Bmatrix} \mathbf{K}_{u\varphi}^{\mathrm{T}} \\ \mathbf{K}_{u\phi}^{\mathrm{T}} \end{Bmatrix}, \ \mathbf{a} = \begin{Bmatrix} \mathbf{U} \\ \mathbf{b} \end{Bmatrix}, \ \mathbf{F}_b = \begin{Bmatrix} \mathbf{F}_\varphi \\ \mathbf{F}_\phi \end{Bmatrix}. \tag{26.17}$$

Vectors $\mathbf{F}_u, \mathbf{F}_\varphi, \mathbf{F}_\phi$ in (26.16), (26.17) appear when taking into account the essential boundary conditions (26.9), and they are differ for various boundary conditions from (26.10)–(26.12).

In (26.15)–(26.17) the matrices contain both usual for the problems of the magnetoelectroelasticity the matrices, calculated on the volumes of finite element mesh, and the additional matrices, calculated on the interface boundaries. For example, the stiffness matrix $\mathbf{K}_{uu}$ has the following structure:

$$\mathbf{K}_{uu} = \mathbf{K}_{\Omega uu} + \mathbf{K}_{\Gamma uu}, \ \mathbf{K}_{\Omega uu}^{ek} = \int\limits_{\Omega_h} \mathbf{B}_u^{\mathrm{T}} \cdot \mathbf{c}^E \cdot \mathbf{B}_u d\Omega, \ \mathbf{K}_{\Gamma uu} = \int\limits_{\Gamma_h^s} \mathbf{B}_u^{s\mathrm{T}} \cdot \mathbf{c}^s \cdot \mathbf{B}_u^s d\Gamma, \tag{26.18}$$

$$\mathbf{B}_u = \mathbf{L}(\nabla) \cdot \mathbf{N}_u^{\mathrm{T}}, \quad \mathbf{B}_u^s = \mathbf{L}(\nabla^s) \cdot (\mathbf{I} - \mathbf{n} \otimes \mathbf{n}) \cdot \mathbf{N}_u^{\mathrm{T}}. \tag{26.19}$$

Taking into account (26.16)–(26.19), we can conlude that the matrix $\mathbf{K}$ of the system of linear algebraic (26.15) is symmetric. In addition, by virtue the properties of positive definiteness of the volume and surface energies, the matrix $\mathbf{K}_{uu}$ and $\mathbf{K}_{bb}$ will be at least non-negative definite. Therefore, the symmetric matrix $\mathbf{K}$ in (26.15) will have the properties of a quasi-defined matrix, typical for the problems with a saddle point.

In this connection, in ACELAN-COMPOS package we use an effective algorithms for symmetric positive definite and quasi-definite matrices for solving the system of linear algebraic (26.15) [26–28]. All basic procedures that we need in finite element manipulations, such as the degree of freedom rotations, mechanical, electric and

magnetic boundary condition settings, etc., we can also provide in a symmetric form.

26.4 Models of Representative Volumes and Some Results

In ACELAN-COMPOS package the representative volume element (RVE) is simulated in the form of a cubic array of finite elements, where the elements also have cubic shapes. In accordance with the accepted structure of second phase, we assign the properties of the skeleton material of the first phase to some part of the finite elements, and assign the properties of the second phase to the remaining part of the elements.

In ACELAN-COMPOS there are the opportunities to create different types of representative volumes. Examples of representative volumes, created by different algorithms of the ACELAN-COMPOS package, are shown in Figs. 26.1, 26.2, 26.3 and 26.4. In all cases, the percentage of occurrence of the second phase was approximately the same (about 15%), and the order of RVE is the same and equal $16 \times 16 \times 16$. Everywhere in Figs. 26.1a, 26.2a, 26.3a and 26.4a the whole RVE is shown, in Figs. 26.1b, 26.2b, 26.3b and 26.4b the elements of the first phase are shown, in Figs. 26.1c, 26.2c, 26.3c, and 26.4c the elements of the second phase are shown, and in Figs. 26.1d, 26.2d, 26.3d and 26.4d the surface elements are shown.

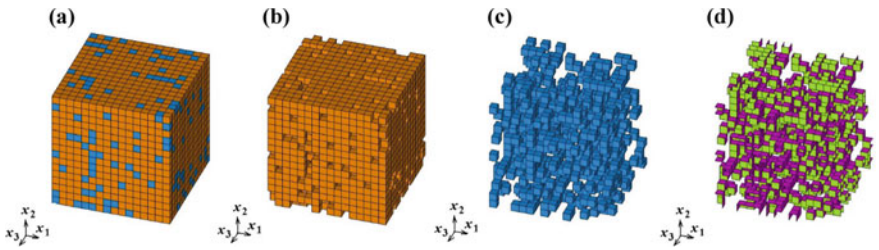

Fig. 26.1 Example of RVE of with a random arrangement of the elements of the second phase

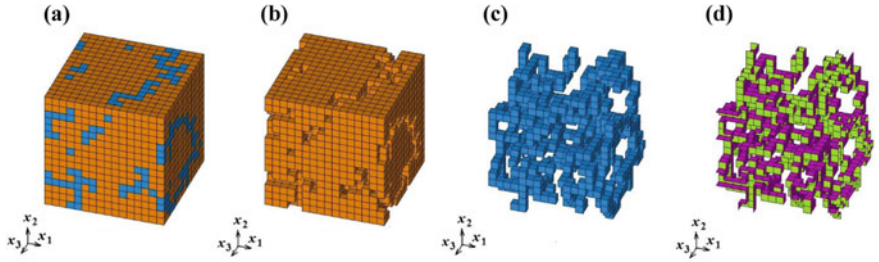

Fig. 26.2 Example of RVE with 3–3 connectivity (direct algorithm)

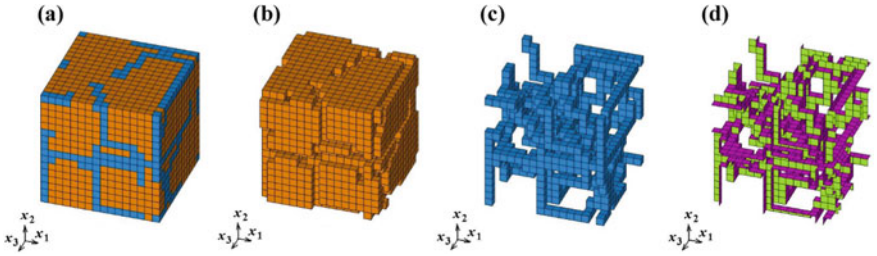

Fig. 26.3 Example of RVE with 3–3 connectivity (inverse algorithm)

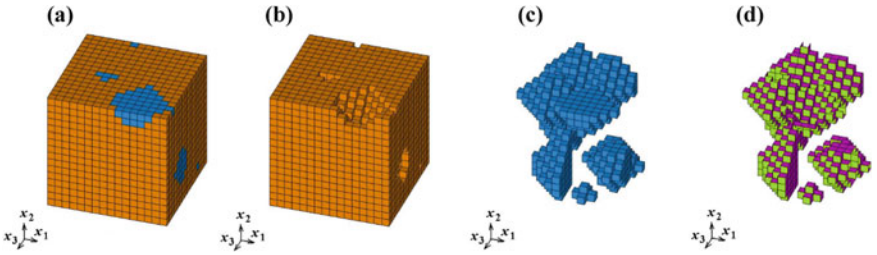

Fig. 26.4 Example of RVE with 3–0 connectivity

In the first case, the finite elements of second phase are selected by a random number generator (Fig. 26.1). It is obvious that the model created by using a simple random number generator is easy to build. However, such model does not support the connectivity of the elements for the first phase and does not reflect the connectivity structure of the elements for the second phase.

Two other algorithms in ACELAN-COMPOS create the structures of the two-component materials with the connectivity for both phases (3–3 connectivity) [19, 20, 22]. In the case of porous composites, the 3–3 connectivity algorithms generate materials with open porosity. In these algorithms, the representative volumes consist of domains with $8 \times 8 \times 8$ finite elements. Number 8 for the domain size was chosen for the convenience of implementing numerical procedures to verify the phase connectivity and generate different data structures. In a direct version of the 3–3 algorithm, the process of the domain generation is implemented in such way that the connectivity of the elements of the first phase is maintained through the domain vertices, and the connectivity of the structure of the second phase is maintained through the elements located approximately in the midpoints of the domain edges. In the inverted version of this algorithm, the first phase and the second phase are interchanged.

Each domain is created by a partially random way, and the representative volumes of $8n \times 8n \times 8n$ order are formed as a result of generating the sequence of n domains along each of three coordinate axes. Thus, generally speaking, each resulting domain differs from the other. Nevertheless, it maintains the connectivity of both phases and

the connectivity of the total volume structure, being formed either by a direct 3–3 algorithm or by an inverse 3–3 algorithm.

A detailed description of these algorithms is given in [19, 20]. Some examples of the representative volumes with the porosity $p \approx 15$ % for $n = 2$ (eight domains) are shown in Fig. 26.2 for direct algorithm and in Fig. 26.3 for inverse algorithm, respectively. As can be seen from Fig. 26.2, the direct algorithm distributes a significant amount of the framework elements (elements of the first phase) near the domain edges. On the contrary, the inverse algorithm gathers the most part of the framework elements (elements of the first phase) in the central part of the domain. For a larger number of domains ($n = 3$, $n = 4$, etc.), these effects are leveled, since some parts of the domain boundaries become located inside of the representative volume.

For simulate the element of second phase as granules, consisting of one or more structural elements not connected with other granules, in ACELAN-COMPOS package the 3–0 algorithm exists [20–22]. In the case of porous composites, the 3–0 connectivity algorithms generate materials with closed porosity. In this algorithm, the representative volumes also consist of domains with $8 \times 8 \times 8$ elements. The input user data are the granule size and the maximum quantum of inclusions. Random choice of the supporting elements for the granules ensures in the result the partially stochastic distribution of the elements of second phase in the RVE. The granule grows in the domain according to an algorithm that allows the granule to be shaped as possible close to the ball, while avoiding highly elongated elements.

As in 3–3 algorithms, each domain in 3–0 algorithm is created by a partially random way, and the representative volumes of $8n \times 8n \times 8n$ order are formed in the result of generating the sequence of domains along three coordinate axes. Thus, here each resulting domain differs from the other. Nevertheless, it maintains the connectivity of the elements of the main first phase. A detailed description of the 3–0 algorithm is contained in [20, 21]. One example of the RVE for $n = 2$ (eight domains), constructed by the 3–0 algorithm, is shown in Fig. 26.4.

In 1–3 (3–1) algorithm of the ACELAN-COMPOS package, the RVE contains rods placed in the skeleton of the main material. This is a simple algorithm based on placing two-dimensional pattern on the bottom of the volume and extruding it through the body [20, 24].

For nanostructured composites, for all variants of representative volumes, it is possible to automatically find the interphase boundaries Γ^s and place on them the shell (membrane) finite elements that simulate the surface effects (Figs. 26.1d, 26.2d, 26.3d and 26.4d). For the shell elements it is necessary to insure the anisotropy type, which corresponds to the anisotropy of the volume finite element. This correspondence was implemented only for transversely isotropic phases and for elements parallel to the Ox_1x_2 plane (painted in light green in Figs. 26.1d, 26.2d, 26.3d and 26.4d or x_3 axis (painted in crimson in Figs. 26.1d, 26.2d, 26.3d and 26.4d.

For representative volumes shown in Figs. 26.1, 26.2, 26.3 and 26.4, we will present here as an example the calculation results of solving the homogenization problem for a porous piezoceramic material without taking into account the surface effects (Table 26.1) and taking into account only uncoupled surface stresses according to the methodology presented in [29, 30] (Table 26.2). For RVE of this composite

Table 26.1 Effective moduli of porous piezoceramics PZT-5 without surface stresses

Relative moduli	SR, $p = 14.99$	3–3 (direct), $p = 14.84$	3–3 (inverse), $p = 15.21$	3–0, $p = 15.04$
$r(c_{11})$	0.76	0.71	0.69	0.66
$r(c_{12})$	0.72	0.65	0.62	0.61
$r(c_{13})$	0.71	0.64	0.61	0.58
$r(c_{33})$	0.75	0.69	0.68	0.64
$r(c_{44})$	0.81	0.79	0.78	0.77
$r(e_{31})$	0.73	0.66	0.64	0.56
$r(e_{33})$	0.84	0.83	0.83	0.81
$r(e_{15})$	0.80	0.77	0.77	0.74
$r(\kappa_{11})$	0.85	0.85	0.84	0.84
$r(\kappa_{33})$	0.84	0.83	0.83	0.83
$r(d_{31})$	0.95	0.92	0.92	0.88
$r(d_{33})$	0.99	0.98	0.99	0.98
$r(d_{15})$	0.98	0.98	0.98	0.96
$\lvert\Gamma^s\rvert/\lvert\Gamma\rvert$	1.91	1.32	1.13	0.68

Table 26.2 Effective moduli of porous piezoceramics PZT-5 with surface stresses

Relative moduli	SR, $p = 14.99$	3–3 (direct), $p = 14.84$	3–3 (inverse), $p = 15.21$	3–0, $p = 15.04$
$r(c_{11})$	1.09	0.98	0.93	0.77
$r(c_{12})$	0.93	0.85	0.80	0.70
$r(c_{13})$	0.92	0.84	0.79	0.66
$r(c_{33})$	1.09	0.98	0.92	0.75
$r(c_{44})$	1.08	1.00	0.98	0.88
$r(e_{31})$	0.84	0.78	0.74	0.63
$r(e_{33})$	0.84	0.83	0.83	0.81
$r(e_{15})$	0.83	0.80	0.79	0.76
$r(\kappa_{11})$	0.84	0.83	0.83	0.83
$r(\kappa_{33})$	0.83	0.82	0.82	0.82
$r(d_{31})$	0.59	0.63	0.66	0.75
$r(d_{33})$	0.60	0.66	0.69	0.83
$r(d_{15})$	0.76	0.80	0.81	0.87
$\lvert\Gamma^s\rvert/\lvert\Gamma\rvert$	1.91	1.32	1.13	0.68

the domain $\Omega^{(1)}$ occupied by the dense piezoceramics and the domain $\Omega^{(2)}$ occupied by the pores: $c_{\alpha\beta} = c_{\alpha\beta}^{E(i)}$, $e_{j\beta} = e_{j\beta}^{(i)}$, $\kappa_{jj} = \varepsilon_{jj}^{S(i)}$ for $\mathbf{x} \in \Omega^{(i)}$, $i = 1, 2$.

In Tables 26.1 and 26.2 we give the relative values of the effective material moduli $r(c_{\alpha\beta}) = c_{\alpha\beta}^{\text{eff}}/c_{\alpha\beta}$, $r(e_{j\beta}) = e_{j\beta}^{\text{eff}}/e_{j\beta}$, $r(\kappa_{jj}) = \kappa_{jj}^{\text{eff}}/\kappa_{jj}$ and $r(d_{j\beta}) = d_{j\beta}^{\text{eff}}/d_{j\beta}$ for porous piezoceramics PZT-5. Here $c_{\alpha\beta} = c_{\alpha\beta}^{E(1)}$, $e_{j\beta} = e_{j\beta}^{(1)}$, $\kappa_{jj} = \varepsilon_{jj}^{S(1)}$ and $d_{j\beta} = d_{j\beta}^{(1)}$ are the corresponding values for the dense piezoceramics, $\mathbf{d} = \mathbf{e} \cdot \mathbf{c}^{-1}$.

For dense piezoceramics PZT-5 we take the following mechanical, dielectric and piezoelectric constants: $c_{11}^{E(1)} = 12.1 \cdot 10^{10}$; $c_{12}^{E(1)} = 7.54 \cdot 10^{10}$; $c_{13}^{E(1)} = 7.52 \cdot 10^{10}$; $c_{33}^{E(1)} = 11.1 \cdot 10^{10}$; $c_{44}^{E(1)} = 2.21 \cdot 10^{10}$ (N/m^2); $e_{33}^{(1)} = 15.8$; $e_{31}^{(1)} = -5.4$; $e_{15}^{(1)} = 12.3$ (C/m^2); $\varepsilon_{11}^{S(1)} = 916\varepsilon_0$; $\varepsilon_{33}^{S(1)} = 830\varepsilon_0$; $\varepsilon_0 = 8.85 \cdot 10^{-12}$ (F/m). For the pores, we set negligibly small elastic moduli $c_{\alpha\beta}^{E(2)} = \eta c_{\alpha\beta}^{E(1)}$, $\eta = 1 \cdot 10^{-10}$, piezomoduli $e_{j\beta}^{(2)} = \eta$ (x1 C/m^2) and $\varepsilon_{jj}^{S(2)} = \varepsilon_0$. For the case of nanoporous piezoceramics with uncoupled surface stresses we accept the size of cube finite element $a = 1 \cdot 10^{-10}$ (m), $c_{\alpha\beta}^{s} = a\, c_{\alpha\beta}^{E(1)}$, $e_{j\beta}^{s} = 0$, $\kappa_{jj}^{s} = 0$.

It can be noted that even with the same porosity for the simple random (SR) algorithm, the area of interface boundaries $|\Gamma^s|$ is larger than for the 3–3 connectivity direct algorithms, the area of interface boundaries for the 3–3 direct algorithms is larger than for the 3–3 inverse algorithms, and the area of interface boundaries for the 3–3 inverse algorithms is larger than for the 3–0 algorithms. So, as we can conclude from Tables 26.1 and 26.2, for the representative volumes with SR distribution of inclusions and with 3–3 or 3–0 connectivity for various interphase areas we obtain different values of the effective moduli, moreover the SR model is slightly stiffer and more electromechanical active than the 3–3 models, and the 3–3 connectivity models are stiffer and more electromechanical active than the 3–1 model.

Accounting for surface stresses here is equivalent to the placement of elastic membrane elements on the interface boundaries. Therefore, when taking into account surface stresses, the size of the interface area has a very significant effect on the effective stiffness moduli (Table 26.2). Thus, we can conclude that the internal structures of nanoporous composites can have a significant effect on the effective stiffness moduli values. Meanwhile, from a comparison of Tables 26.1 and 26.2, we can infer that the uncoupled surface stresses have much less effect on the effective piezomoduli $e_{j\beta}^{\text{eff}}$ and almost do not influence on the dielectric permittivities κ_{jj}^{eff}.

Note that using the described approaches in [1, 2, 19, 21, 22, 29] the of homogenization problems were solved for different structures of representative volumes. Anisotropic elastic and piezoelectric composites were investigated, both on ordinary scale levels and on nanoscale. It was found that the types of connectivity and the internal structure of a composite can have a significant influence on effective moduli (see also Tables 26.1 and 26.2), and taking into account surface or interface effects can even lead to a change in the decreasing properties of moduli on their growth and even lead to superiority of effective moduli compared to moduli of initial phases (Table 26.2).

An analysis of the advantages and disadvantages of various algorithms for the formation of representative volumes is given in [20]. Additionally, it can be noted that

the piezoceramic finite elements of all types of representative volume structures can be automatically equipped with their elemental coordinate systems rotated relative to the initial Cartesian coordinate system in accordance with the direction of the non-uniform polarization fields [1, 2, 23, 31], and for 3—0 connectivity models the algorithms for the account of electrode surfaces for metallized interfaces have been developed [30, 31].

Acknowledgements The author is grateful for the support of the Ministry of Science and Higher Education of the Russian Federation, project No. 9.1001.2017/4.6.

References

1. A.V. Nasedkin, M.S. Shevtsova, in *Ferroelectrics and Superconductors: Properties and Applications*, ed. by I.A. Parinov (Nova Science Publication, NY, 2011), p. 231
2. A.V. Nasedkin, M.S. Shevtsova, in *Physics and Mechanics of New Materials and Their Applications*, ed. by I.A. Parinov, S.-H. Chang, (Nova Science Publication, NY, 2013), p. 185
3. V.A. Eremeyev, Acta Mech. **227**, 29 (2016)
4. M.E. Gurtin, A.I. Murdoch, Arch. Ration. Mech. Anal. **57**, 291 (1975)
5. M.E. Gurtin, A.I. Murdoch, Int. J. Solid. Struct. **14**, 431 (1978)
6. J.C. Hamilton, W.G. Wolfer, Surf. Sci. **603**, 1284 (2009)
7. J. Wang, Z. Huang, H. Duan, S. Yu, X. Feng, G. Wang, W. Zhang, T. Wang, Acta Mech. Solida Sin. **24**(1), 52 (2011)
8. K.F. Wang, B.L. Wang, T. Kitamura, Acta. Mech. Sin. **32**(1), 83 (2016)
9. T. Chen, Acta Mech. **196**, 205 (2008)
10. S.-T. Gu, Q.-C. He, J. Mech. Phys. Solids **59**, 1413 (2011)
11. S.-T. Gu, J.-T. Liu, Q.-C. He, Comput. Mat. Sci. **94**, 182 (2014)
12. S.-T. Gu, L. Qin, Int. J. Eng. Sci. **78**, 89 (2014)
13. G.Y. Huang, S.W. Yu, Phys. Status Solidi B **243**(4), R22 (2006)
14. X.H. Pan, S.W. Yu, X.Q. Feng, Sci. China Phys. Mech. Astron. **54**(4), 564 (2011)
15. Z. Yan, L. Jiang, Nanomaterials **7**, 27 (2017)
16. A.N. Rybyanets, A.A. Naumenko, J. Modern Physics. **4**(8), 1041 (2013)
17. A.N. Rybyanets, I.A. Shvetsov, M.A. Lugovaya, E.I. Petrova, N.A. Shvetsova, J. Nano Electron. Phys. **10**, 02005 (2018)
18. A.V. Nasedkin, A.A. Nasedkina, V.V. Remizov, Comput. Continuum Mech. **7**(1), 100 (2014)
19. A.B. Kudimova, D.K. Nadolin, A.V. Nasedkin, A.A. Nasedkina, P.A. Oganesyan, A.N. Soloviev, Mater. Phys. Mech. **37**, 16 (2018)
20. N.V. Kurbatova, D.K. Nadolin, A.V. Nasedkin, P.A. Oganesyan, A.S. Skaliukh, A.N. Soloviev, in *Analysis and Modelling of Advanced Structures and Smart Systems, Ser. Advanced Structured Materials*, ed. by H. Altenbach, E. Carrera, G. Kulikov, vol. 81 (Springer, 2018), p. 69
21. A.B. Kudimova, D.K. Nadolin, A.V. Nasedkin, P.A. Oganesyan, A.N. Soloviev, Mater. Phys. Mech. **37**, 25 (2018)
22. N.V. Kurbatova, D.K. Nadolin, A.V. Nasedkin, A.A. Nasedkina, P.A. Oganesyan, A.S. Skaliukh, A.N. Soloviev, in *Wave Dynamics and Composite Mechanics for Microstructured Materials and Metamaterials, Series Advanced Structured Materials*, ed. by M.A. Sumbatyan. vol. 59 (Springer, 2017), p. 133
23. T.E. Gerasimenko, N.V. Kurbatova, D.K. Nadolin, A.V. Nasedkin, A.A. Nasedkina, P.A. Oganesyan, A.S. Skaliukh, A.N. Soloviev, in *Wave Dynamics and Composite Mechanics for Microstructured Materials and Metamaterials, Ser. Advanced Structured Materials*, ed. by M.A. Sumbatyan. vol. 59 (Springer, 2017), p. 113

24. A.B. Kudimova, I.V. Mikhayluts, D.K. Nadolin, A.V. Nasedkin, A.A. Nasedkina, P.A. Oganesyan, A.N. Soloviev, Procedia Struct. Integrity **6**, 301 (2017)
25. A.V. Nasedkin, in *VIII ECCOMAS Thematic Conference on Smart Structures and Materials, VI International Conference on Smart Materials and Nanotechnology in Engineering* (CIMNE)—*SMART 2017, 5–8 June 2017, Madrid, Spain*, ed. by A. Guemes, A. Benjeddou, J. Rodellar, J. Leng, (2017), p. 1137
26. M. Benzi, G.H. Golub, J. Liesen, Acta Numer. **14**, 1 (2005)
27. M. Benzi, A.J. Wathen, in *Model Order Reduction: Theory, Research Aspects and Applications. Mathematics in Industry*, ed. by W.H.A. Schilders, H.A. van der Vorst, J. Rommes, vol. 13 (2008), p. 195
28. R.J. Vanderbei, SIAM J. Optim. **5**, 100 (1995)
29. G. Iovane, A.V. Nasedkin, in *Dynamical Processes in Generalized Continua and Structures, Ser. Advanced Structured Materials*, ed. by H. Altenbach, A. Belyaev, V. Eremeyev, A. Krivtsov, A. Porubov, vol. 103 (Springer, 2019), p. 293
30. A. Nasedkin, A. Nasedkina, A. Rybyanets, Ferroelectrics **508**, 100 (2017)
31. A.V. Nasedkin, A.A. Nasedkina, A.N. Rybyanets, Mater. Phys. Mech. **40**, 12 (2018)

Chapter 27
Finite Element Investigation of Effective Moduli of Transversely Isotropic Thermoelastic Materials with Nanoscale Porosity

Andrey Nasedkin, Anna Nasedkina, and Amirtham Rajagopal

Abstract Using the methods of effective moduli and finite elements, the effective properties of nanoporous thermoelastic transversely isotropic materials were studied for simple random and for closed structures of porosity. Nanoscale effects were modelled in the framework of the Gurtin-Murdoch model of interface stresses and of the high conductivity model. The modelling and solution of homogenization problems was performed in the ANSYS package, while structures of representative volumes with closed porosity were created in the ACELAN-COMPOS package. The effect of porosity, types of representative volumes and pore sizes on the values of the effective modules of nanoporous titanium is analysed.

27.1 Introduction

In recent years, there has been increased an interest for the theoretical problems of nanomechanics. Numerous investigations have revealed a size effect, which consists in changing the effective material moduli for nanoscale bodies in comparison with the corresponding values for macrodimension bodies. Various theories have been proposed to explain the scale factor. One such theory is the widely used model of surface elasticity. There are several reviews devoted to research on the theories of surface elasticity, their generalizations and applications [1–4]. In turn, among these theories, the most famous is the Gurtin-Murdoch model [5–7]. It can be shown that the use of this model is reduced to the fact that the external boundaries of the nanoscale body are covered with elastic membranes, in which the internal tensions are caused

A. Nasedkin (✉) · A. Nasedkina
Institute of Mathematics, Mechanics and Computer Science, Southern Federal University, 8a, Milchakova Street, Rostov-on-Don, Russia 344090
e-mail: nasedkin@math.sfedu.ru

A. Nasedkina
e-mail: anasedkina@sfedu.ru

A. Rajagopal
Department of Civil Engineering, Indian Institute of Technology, Hyderabad 502205, India
e-mail: rajagopal@iith.ac.in

I. A. Parinov et al. (eds.), *Advanced Materials*, Springer Proceedings in Materials 6, https://doi.org/10.1007/978-3-030-45120-2_27

by surface stresses. Elastic membranes can be placed on the interphase boundaries inside the body with inclusions or pores, which also allows modeling imperfect interfaces with stress jumps and interface surface effects for nanoinclusions or for nanopores [8–11].

For thermal problems the high conductivity model with surface thermal fluxes on the external boundaries or in the interphase surfaces is similar to the Gurtin-Murdoch model for elastic problems. The effective thermal conductivity coefficients for composite materials with imperfect boundaries and with micro- or nanoscale effects were determined in [12–19].

The Gurtin-Murdoch theory can be extended to thermoelastic problems for nanosized bodies and nanostructured composites. Thus, in [20–23] using this model the effective moduli of thermoelastic composites with spherical nanopores or nanoinclusions and the effective moduli of nanofibers have been studied. The finite element method was applied for thermoelastic materials with surface stresses or with interphase boundary conditions in [24–30].

In this chapter, we study the effective material properties of thermoelastic nanoporous materials of hexagonal syngony class or transversely isotropic materials with random and close structures of porosity. We considered porous material as extreme case of a two-phase bulk composite, when the stiffness moduli of inclusions have negligibly small. The nano-dimensionality of the pore boundaries was taken into account using the highly conducting model and the Gurtin-Murdoch model of surface stresses. This work is a continuation of the author's researches [27–30]. Here, the scale factor is associated with pore sizes and the influence of the structure of porosity on the effective moduli is analysed.

Finite element packages ANSYS and ACELAN-COMPOS were used to simulate representative volumes and to calculate the effective material properties. This approach is based on the theory of effective moduli of composite mechanics, modelling of representative volumes and the finite element method. In accordance with the effective moduli method we solve in the constructed volume the static thermoelastic and thermal problems with linear essential boundary conditions. Homogenization problems are solved numerically by the finite element method.

We used the regular cubic representative volumes with hexahedral thermoelastic finite elements and random and granular distributions of pores. To take into account the nanosized internal structure, the contact boundaries between material and pores were covered by the surface membrane thermoelastic elements. We also specified transversely isotropic material properties for the membrane elements, in accordance with the location of the element coordinate systems and the anisotropy type of the volume elements in these coordinate systems. Next, we calculate the averaged stresses and thermal fluxes, which determine the effective thermoelastic moduli.

As an example, the models of nanoporous material have been examined with different values of surface moduli, porosity and number of pores. The calculation results allowed us to analyze the dependence of the effective moduli on porosity and surface elements.

27.2 Homogenization Problems

Let Ω is a representative volume of thermoelastic material with nanodimensional porosity; $\Omega = \Omega^{(1)} \cup \Omega^{(2)}$; $\Omega^{(1)}$ is the region occupied by the materials of the first phase (main material or matrix); $\Omega^{(2)}$ is the aggregate of the regions occupied by the materials of the second phase (pores); $\Gamma = \partial\Omega$ is the external boundary of the representative volume Ω; Γ^i is the set of frontier surfaces of regions with different phases ($\Gamma^i = \partial\Omega^{(1)} \cap \partial\Omega^{(2)}$); $\mathbf{n} = \{n_1, n_2, n_3\}$ is the external unit normal vector to the boundary, outward with respect to $\Omega^{(1)}$; $\mathbf{x} = \{x_1, x_2, x_3\}$ is the vector of Cartesian coordinates. We assume that the parts $\Omega^{(1)}$ and $\Omega^{(2)}$ are filled with two different transversely isotropic thermoelastic materials. Then in the framework of linear static theory of thermoelasticity for $\mathbf{x} \in \Omega$ we assume the following system of equations:

$$\boldsymbol{\Lambda}^{\mathrm{T}}(\nabla) \cdot \mathbf{T} = 0, \quad \mathbf{T} = \mathbf{c} \cdot \mathbf{S} - \mathbf{b}\theta, \quad \mathbf{S} = \boldsymbol{\Lambda}(\nabla) \cdot \mathbf{u}, \tag{27.1}$$

$$\nabla^{\mathrm{T}} \cdot \mathbf{q} = 0, \quad \mathbf{q} = -\mathbf{k} \cdot \mathbf{G}, \quad \mathbf{G} = \nabla\theta, \tag{27.2}$$

$$\boldsymbol{\Lambda}^{\mathrm{T}}(\nabla) = \begin{bmatrix} \partial_1 & 0 & 0 & 0 & \partial_3 & \partial_2 \\ 0 & \partial_2 & 0 & \partial_3 & 0 & \partial_1 \\ 0 & 0 & \partial_3 & \partial_2 & \partial_1 & 0 \end{bmatrix}, \quad \nabla = \begin{Bmatrix} \partial_1 \\ \partial_2 \\ \partial_3 \end{Bmatrix}, \quad \mathbf{u} = \begin{Bmatrix} u_1 \\ u_2 \\ u_3 \end{Bmatrix},$$

$$\mathbf{k} = \begin{bmatrix} k_{11} & 0 & 0 \\ 0 & k_{11} & 0 \\ 0 & 0 & k_{33} \end{bmatrix}, \tag{27.3}$$

$$\mathbf{c} = \begin{bmatrix} c_{11} & c_{12} & c_{13} & 0 & 0 & 0 \\ c_{12} & c_{11} & c_{13} & 0 & 0 & 0 \\ c_{13} & c_{13} & c_{33} & 0 & 0 & 0 \\ 0 & 0 & 0 & c_{44} & 0 & 0 \\ 0 & 0 & 0 & 0 & c_{44} & 0 \\ 0 & 0 & 0 & 0 & 0 & c_{66} \end{bmatrix}, \quad \mathbf{T} = \begin{Bmatrix} \sigma_{11} \\ \sigma_{22} \\ \sigma_{33} \\ \sigma_{23} \\ \sigma_{13} \\ \sigma_{12} \end{Bmatrix}, \quad \mathbf{S} = \begin{Bmatrix} \varepsilon_{11} \\ \varepsilon_{22} \\ \varepsilon_{33} \\ 2\varepsilon_{23} \\ 2\varepsilon_{13} \\ 2\varepsilon_{12} \end{Bmatrix}, \quad \mathbf{b} = \begin{Bmatrix} \beta_{11} \\ \beta_{11} \\ \beta_{33} \\ 0 \\ 0 \\ 0 \end{Bmatrix}, \tag{27.4}$$

where σ_{ij}, ε_{ij} are the components of the stress tensor and the strain tensor, respectively; u_i are the components of the displacement vector $\mathbf{u}$; θ is the temperature increment from natural state; $\mathbf{q}$ is the heat flux vector; $\mathbf{G}$ is the temperature gradient vector; $\mathbf{c}$ is the 6×6 matrix of elastic stiffness moduli c_{ij}; $\mathbf{b}$ is the six-dimensional array of the thermal stress coefficients β_{ij}; $\mathbf{k}$ is the 3×3 matrix of thermal conductivities k_{ij}; $\mathbf{c} = \mathbf{c}^{(m)}$, $\mathbf{b} = \mathbf{b}^{(m)}$, $\mathbf{k} = \mathbf{k}^{(m)}$ for $\mathbf{x} \in \Omega^{(m)}$, $m = 1, 2$, and $\mathbf{c}$, $\mathbf{b}$, $\mathbf{k}$ have the structures characteristic transversely isotropic materials, $c_{66} = (c_{11} - c_{12})/2$; $(\ldots)^{\mathrm{T}}$ is the transpose operation; $(\ldots) \cdot (\ldots)$ is the scalar product operation.

According to Gurtin-Murdoch model of surface stresses, we suppose that on the nanosized boundaries Γ^s the following interphase condition is held:

$$\boldsymbol{\Lambda}^{\mathrm{T}}(\mathbf{n}) \cdot [\mathbf{T}] = \boldsymbol{\Lambda}^{\mathrm{T}}(\nabla^s) \cdot \mathbf{T}^s, \quad \mathbf{x} \in \Gamma^s, \tag{27.5}$$

where $[\mathbf{T}] = \mathbf{T}^{(1)} - \mathbf{T}^{(2)}$ is the stress jump over the interface between two phases; $\nabla^s = \nabla - \mathbf{n}(\partial/\partial n)$ is the surface nabla-operator; $\mathbf{T}^s = \{\sigma^s_{11}, \sigma^s_{22}, \sigma^s_{33}, \sigma^s_{23}, \sigma^s_{13}, \sigma^s_{12}\}$ is the array of the interface stresses σ^s_{ij}.

We assume that the surface stresses σ^s_{ij} are related to the surface strains ε^s_{ij} and the temperature θ by the formulas

$$\mathbf{T}^s = \mathbf{c}^s \cdot \mathbf{S}^s - \mathbf{b}^s\theta, \ \mathbf{S}^s = \mathbf{\Lambda}(\nabla^s) \cdot \mathbf{u}^s, \ \mathbf{u}^s = \mathbf{A} \cdot \mathbf{u}, \ \mathbf{A} = \mathbf{I} - \mathbf{n} \otimes \mathbf{n}, \tag{27.6}$$

where $\mathbf{c}^s$ is the 6×6 matrix of surface elastic stiffness moduli c^s_{ij}; $\mathbf{b}^s$ is the six-dimensional array of the thermal stress coefficients β^s_{ij} for the interface; $\mathbf{S}^s = \{\varepsilon^s_{11}, \varepsilon^s_{22}, \varepsilon^s_{33}, 2\varepsilon^s_{23}, 2\varepsilon^s_{13}, 2\varepsilon^s_{12}\}$ is the array of the interface strains ε^s_{ij}.

Analogically, we accept the equation of highly thermal conducting interface on the nanosized boundaries Γ^s

$$\mathbf{n}^{\mathrm{T}} \cdot [\mathbf{q}] = \nabla^{s\,\mathrm{T}} \cdot \mathbf{q}^s, \quad \mathbf{q}^s = -\mathbf{k}^s \cdot \mathbf{G}^s, \quad \mathbf{G}^s = \nabla^s\theta, \quad \mathbf{x} \in \Gamma^s, \tag{27.7}$$

where $\mathbf{q}^s$ is the surface heat flux vector; $\mathbf{G}^s$ is the surface temperature gradient vector; $\mathbf{k}^s$ is the 3×3 matrix of surface thermal conductivity.

Note that the structure of the matrices $\mathbf{c}^s$, $\mathbf{k}^s$ and the structure of the array $\mathbf{b}^s$, as well as the values of their coefficients depend on the shape and orientation of the interface boundary Γ^s. Since there is so little data for surface moduli, and they are quite contradictory, we will assume on the plane interface faces parallel to the coordinate axes the following structure of surface moduli.

We assume that for a composite with two transversally isotropic phases, the following surface moduli are available

$$\tilde{\mathbf{c}}^s = \begin{bmatrix} \tilde{c}^s_{11} & \tilde{c}^s_{12} & \tilde{c}^s_{13} & 0 & 0 & 0 \\ \tilde{c}^s_{12} & \tilde{c}^s_{11} & \tilde{c}^s_{13} & 0 & 0 & 0 \\ \tilde{c}^s_{13} & \tilde{c}^s_{13} & \tilde{c}^s_{33} & 0 & 0 & 0 \\ 0 & 0 & 0 & \tilde{c}^s_{44} & 0 & 0 \\ 0 & 0 & 0 & 0 & \tilde{c}^s_{44} & 0 \\ 0 & 0 & 0 & 0 & 0 & \tilde{c}^s_{66} \end{bmatrix}, \ \tilde{\mathbf{b}}^s = \begin{Bmatrix} \tilde{\beta}^s_{11} \\ \tilde{\beta}^s_{11} \\ \tilde{\beta}^s_{33} \\ 0 \\ 0 \\ 0 \end{Bmatrix}, \ \tilde{\mathbf{k}}^s = \begin{bmatrix} \tilde{k}^s_{11} & 0 & 0 \\ 0 & \tilde{k}^s_{11} & 0 \\ 0 & 0 & \tilde{k}^s_{33} \end{bmatrix}, \tag{27.8}$$

where $\tilde{c}^s_{66} = (\tilde{c}^s_{11} - \tilde{c}^s_{12})/2$.

Then, on flat interface faces, parallel to the plane Ox_1x_2, we have in (27.5)–(27.7) $\mathbf{n} = \{0, 0, 1\}$, $\nabla^s = \{\partial/\partial x_1, \partial/\partial x_2, 0\}$, $\mathbf{u}^s = \{u_1, u_2, 0\}$, $\mathbf{T}^s = \{\sigma^s_{11}, \sigma^s_{22}, 0, 0, 0, \sigma^s_{12}\}$, $\mathbf{S}^s = \{\varepsilon^s_{11}, \varepsilon^s_{22}, 0, 0, 0, 2\varepsilon^s_{12}\}$, $\mathbf{q}^s = \{q^s_1, q^s_2, 0\}$, $\mathbf{G}^s = \{G^s_1, G^s_2, 0\}$, $\mathbf{c}^s = \mathbf{c}^{s(12)}$, $\mathbf{b}^s = \mathbf{b}^{s(12)}$, $\mathbf{k}^s = \mathbf{k}^{s(12)}$, where

$$\mathbf{c}^{s(12)} = \begin{bmatrix} \tilde{c}^s_{11} & \tilde{c}^s_{12} & 0 & 0 & 0 & 0 \\ \tilde{c}^s_{12} & \tilde{c}^s_{11} & 0 & 0 & 0 & 0 \\ 0 & 0 & \tilde{c}^s_{33} & 0 & 0 & 0 \\ 0 & 0 & 0 & \tilde{c}^s_{44} & 0 & 0 \\ 0 & 0 & 0 & 0 & \tilde{c}^s_{44} & 0 \\ 0 & 0 & 0 & 0 & 0 & \tilde{c}^s_{66} \end{bmatrix}, \ \mathbf{b}^{s(12)} = \begin{Bmatrix} \tilde{\beta}^s_{11} \\ \tilde{\beta}^s_{11} \\ 0 \\ 0 \\ 0 \\ 0 \end{Bmatrix}, \mathbf{k}^{s(12)} = \tilde{\mathbf{k}}^s. \tag{27.9}$$

Meanwhile, on flat interface faces, parallel to the plane Ox_1x_3, in (27.5)–(27.7) we have $\mathbf{n} = \{0, 1, 0\}$, $\nabla^s = \{\partial/\partial x_1, 0, \partial/\partial x_3\}$, $\mathbf{u}^s = \{u_1, 0, u_3\}$, $\mathbf{T}^s = \{\sigma^s_{11}, 0, \sigma^s_{33}, \sigma^s_{13}, 0, 0\}$, $\mathbf{S}^s = \{\varepsilon^s_{11}, 0, \varepsilon^s_{33}, 2\varepsilon^s_{13}, 0, 0\}$, $\mathbf{q}^s = \{q^s_1, 0, q^s_3\}$, $\mathbf{G}^s = \{G^s_1, 0, G^s_3\}$, $\mathbf{c}^s = \mathbf{c}^{s(13)}$, $\mathbf{b}^s = \mathbf{b}^{s(13)}$, $\mathbf{k}^s = \mathbf{k}^{s(13)}$, where

$$\mathbf{c}^{s(13)} = \begin{bmatrix} \tilde{c}^s_{11} & 0 & \tilde{c}^s_{13} & 0 & 0 & 0 \\ 0 & \tilde{c}^s_{11} & 0 & 0 & 0 & 0 \\ \tilde{c}^s_{13} & 0 & \tilde{c}^s_{33} & 0 & 0 & 0 \\ 0 & 0 & 0 & \tilde{c}^s_{44} & 0 & 0 \\ 0 & 0 & 0 & 0 & \tilde{c}^s_{44} & 0 \\ 0 & 0 & 0 & 0 & 0 & \tilde{c}^s_{66} \end{bmatrix}, \ \mathbf{b}^{s(13)} = \begin{Bmatrix} \tilde{\beta}^s_{11} \\ 0 \\ \tilde{\beta}^s_{33} \\ 0 \\ 0 \\ 0 \end{Bmatrix}, \mathbf{k}^{s(13)} = \tilde{\mathbf{k}}^s. \tag{27.10}$$

Finally, on flat interface faces, parallel to the plane Ox_2x_3, in (27.5)–(27.7) we have $\mathbf{n} = \{1, 0, 0\}$, $\nabla^s = \{0, \partial/\partial x_2, \partial/\partial x_3\}$, $\mathbf{u}^s = \{0, u_2, u_3\}$, $\mathbf{T}^s = \{0, \sigma^s_{22}, \sigma^s_{33}, 0, \sigma^s_{23}, 0\}$, $\mathbf{S}^s = \{0, \varepsilon^s_{22}, \varepsilon^s_{33}, 0, 2\varepsilon^s_{23}, 0\}$, $\mathbf{q}^s = \{0, q^s_2, q^s_3\}$, $\mathbf{G}^s = \{0, G^s_2, G^s_3\}$, $\mathbf{c}^s = \mathbf{c}^{s(23)}$, $\mathbf{b}^s = \mathbf{b}^{s(23)}$, $\mathbf{k}^s = \mathbf{k}^{s(23)}$, where

$$\mathbf{c}^{s(23)} = \begin{bmatrix} \tilde{c}^s_{11} & 0 & 0 & 0 & 0 & 0 \\ 0 & \tilde{c}^s_{11} & \tilde{c}^s_{13} & 0 & 0 & 0 \\ 0 & \tilde{c}^s_{13} & \tilde{c}^s_{33} & 0 & 0 & 0 \\ 0 & 0 & 0 & \tilde{c}^s_{44} & 0 & 0 \\ 0 & 0 & 0 & 0 & \tilde{c}^s_{44} & 0 \\ 0 & 0 & 0 & 0 & 0 & \tilde{c}^s_{66} \end{bmatrix}, \ \mathbf{b}^{s(23)} = \begin{Bmatrix} 0 \\ \tilde{\beta}^s_{11} \\ \tilde{\beta}^s_{33} \\ 0 \\ 0 \\ 0 \end{Bmatrix}, \ \mathbf{k}^{s(23)} = \tilde{\mathbf{k}}^s. \tag{27.11}$$

As we can see, a two-phase composite consisting of two thermoelastic transversely isotropic phases with interface boundaries is characterized by 27 material moduli, for example, $c^{(m)}_{11}$, $c^{(m)}_{12}$, $c^{(m)}_{13}$, $c^{(m)}_{33}$, $c^{(m)}_{44}$, $\beta^{(m)}_{11}$, $\beta^{(m)}_{33}$, $k^{(m)}_{11}$, $k^{(m)}_{33}$, $m = 1, 2$, $\tilde{c}^s_{11}$, $\tilde{c}^s_{12}$, $\tilde{c}^s_{13}$, $\tilde{c}^s_{33}$, $\tilde{c}^s_{44}$, $\tilde{\beta}^s_{11}$, $\tilde{\beta}^s_{33}$, $\tilde{k}^s_{11}$, and $\tilde{k}^s_{33}$. If the representative volume does not have a pronounced anisotropy in the distribution of its components, then an homogeneous "equivalent" material will also be transversely isotropic and will be described by nine independent moduli, for example, c^{eff}_{11}, c^{eff}_{12}, c^{eff}_{13}, c^{eff}_{33}, c^{eff}_{44}, β^{eff}_{11}, β^{eff}_{33}, k^{eff}_{11} and k^{eff}_{33}.

Note, that the (27.2), (27.7) are satisfied identically, if $\theta = \theta_0 = \text{const}$ for $\mathbf{x} \in \Omega$, because for constant thermal field $\mathbf{G} = 0$, $\mathbf{G}^s = 0$, $\mathbf{q} = 0$, $\mathbf{q}^s = 0$. Then, the thermal problem (27.2), (27.7) is not used for solving the mechanical problem with thermal stresses (27.1), (27.5), (27.6), if the temperature field is constant. Therefore, as we

will see, the effective moduli $c_{11}^{\text{eff}}, c_{12}^{\text{eff}}, c_{13}^{\text{eff}}, c_{33}^{\text{eff}}, c_{44}^{\text{eff}}, \beta_{11}^{\text{eff}}, \beta_{33}^{\text{eff}}$ and the effective moduli $k_{11}^{\text{eff}}, k_{33}^{\text{eff}}$ can be found from separate problems.

For determination the effective moduli $c_{\alpha\beta}^{\text{eff}}$ and β_{jj}^{eff}, it is enough to solve the problems (27.1), (27.5), (27.6) in the representative volume Ω with the following boundary condition

$$\mathbf{u} = \mathbf{L}^{\mathrm{T}}(\mathbf{x}) \cdot \mathbf{S}_0, \quad \theta = \theta_0, \quad \mathbf{x} \in \Gamma, \tag{27.12}$$

where $\mathbf{S}_0$ is constant six-dimensional array and $\theta_0 = \text{const}$.

In the case of transversely isotropic composite to determine the effective thermo-mechanical moduli $c_{11}^{\text{eff}}, c_{12}^{\text{eff}}, c_{13}^{\text{eff}}, c_{33}^{\text{eff}}, c_{44}^{\text{eff}}, \beta_{11}^{\text{eff}}, \beta_{33}^{\text{eff}}$, it is required to solve the four problems (27.1), (27.5), (27.6), (27.12), differing in boundary conditions (27.12), in which only one of the components $S_{0\gamma}, \theta_0$ should be set not equal to zero ($\gamma = 1, 2, \ldots, 6$):

(i) problem I

$$S_{0\gamma} = S_0\delta_{1\gamma}, \theta_0 = 0 \Rightarrow c_{11}^{\text{eff}} = \langle\sigma_{11}\rangle/S_0, c_{12}^{\text{eff}} = \langle\sigma_{22}\rangle/S_0, c_{13}^{\text{eff}} = \langle\sigma_{33}\rangle/S_0, \tag{27.13}$$

(ii) problem II

$$S_{0\gamma} = S_0\delta_{3\gamma}, \theta_0 = 0 \Rightarrow c_{13}^{\text{eff}} = \langle\sigma_{11}\rangle/S_0 \approx \langle\sigma_{22}\rangle/S_0, c_{33}^{\text{eff}} = \langle\sigma_{33}\rangle/S_0, \tag{27.14}$$

(iii) problem III

$$S_{0\gamma} = S_0\delta_{4\gamma}, \theta_0 = 0 \Rightarrow c_{44}^{\text{eff}} = \langle\sigma_{23}\rangle/(2S_0), \tag{27.15}$$

(iv) problem IV

$$\mathbf{S}_0 = 0, \theta_0 \neq 0 \Rightarrow \beta_{11}^{\text{eff}} = \langle\sigma_{11}\rangle/\theta_0 \approx \langle\sigma_{22}\rangle/\theta_0, \beta_{33}^{\text{eff}} = \langle\sigma_{33}\rangle/\theta_0, \tag{27.16}$$

where $\delta_{i\,j}$ is the Kronecker symbol;

$$\langle(\ldots)\rangle = \frac{1}{|\Omega|}\left(\int\limits_{\Omega}(\ldots)d\Omega + \int\limits_{\Gamma^s}(\ldots)^s d\Gamma\right). \tag{27.17}$$

Next, in order to determine the effective coefficients $k_{11}^{\text{eff}}, k_{33}^{\text{eff}}$ it is sufficient to consider thermal conductivity (27.2) and interface relation (27.7) of highly thermal conducting. For setting the corresponding homogenisation problem, we adopt the boundary conditions in the following form ($\mathbf{G}_0 = \text{const}$)

$$\theta = \mathbf{x} \cdot \mathbf{G}_0, \mathbf{x} \in \Gamma. \tag{27.18}$$

Here for the case of transversely isotropic composite to determine the effective coefficients of thermal conductivities $k_{11}^{\text{eff}}, k_{33}^{\text{eff}}$ we can solve the two problems (27.2), (27.7), (27.18) with different boundary conditions (27.18) ($l = 1, 2, 3$):

(v) problem V

$$G_{0l} = G_0\delta_{1l} \Rightarrow k_{11}^{\text{eff}} = -\langle q_1 \rangle / G_0, \tag{27.19}$$

(vi) problem VI

$$G_{0l} = G_0\delta_{3l} \Rightarrow k_{33}^{\text{eff}} = -\langle q_3 \rangle / G_0. \tag{27.20}$$

In conclusion of this section we can mark that taking into account the surface effects for nanostructured composites leads to the appearance of boundary conditions (27.5)–(27.7) on the interface Γ^s and to the necessity of calculating by (27.17) the averaged stresses in (27.13)–(27.16) and heat fluxes in (27.19), (27.20) not only by the volume Ω, but also by the interface Γ^s.

27.3 Finite Element Approaches and Models of Representative Volumes

In order to solve the homogenization problems, we use the finite element approaches described in [27, 28]. These approaches include the simulation of the structure of a representative volume element (RVE) in the form of an array of finite elements and the finite element solution of elastic boundary problem with thermal stresses (27.1), (27.5), (27.6), (27.12) or thermal boundary problems (27.2), (27.7), (27.18).

We create a representative volume in the form of a cubic array of finite elements, where the elements also have cubic shapes. In accordance with the accepted porosity structure, we assign the properties of the skeleton material to some part of the finite elements, and assign the properties of the pores to the remaining part of the elements.

We compare two types of representative volumes. In the first case, the finite elements with properties of pores are selected by a random number generator. It is obvious that the model created by using a simple random number generator is easy to build. However, such model does not support the connectivity of the elements for the first phase and does not reflect the connectivity structure of the elements for the second phase (closed or open pores).

We also use the 3–0 algorithm from ACELAN–COMPOS package for simulation of pores as granules, consisting of one or more structural elements not connected with other granules [31–33]. In this algorithm, the representative volumes consist of domains with $8 \times 8 \times 8$ elements. Number 8 for the domain division was chosen for the convenience of implementing numerical procedures to generate data structures and verify the phase connectivity. The input user data are the size of RVE, the granule size and the maximum percentage of pores or inclusions in the representative volume.

Each domain is created by a partially random way, and the representative volumes of $8n \times 8n \times 8n$ order are formed in the result of generating the sequence of n domains along three coordinate axes. Thus, each resulting domain differs from the other. Nevertheless, it maintains the connectivity of the main phase in each domain and the connectivity of the total volume structure. A detailed description of the 3–0 connectivity algorithm from ACELAN–COMPOS package is contained in [32, 33].

At the next step, the generated structures were transferred to ANSYS finite element package, where all further operations were carried out. Then, the problems (27.1), (27.5), (27.6), (27.12) or (27.2), (27.7), (27.18) were solved for the representative volume using finite element technology and ANSYS package. In the end, in the ANSYS postprocessor the average stresses and thermal fluxes were automatically calculated by (27.17) according to (27.13)–(27.16), or (27.19), (27.20), and thus the full sets of the effective material moduli of thermoelastic composite were obtained.

It is important to note, that we generate the representative volume in a dimensionless form, with the edge of a separate finite element taken equal to dimensionless 1. Thus, the dimensionless spatial parameter will be equal to the minimum pore size l_0.

In order to model the surface effects in ANSYS for the elastic shell finite elements, we will specify only membrane stress options and a fictitious thickness h_m. We take the stiffness moduli $c_{m\alpha\beta}$ proportional to the stiffness moduli of the main material: $c_{m\alpha\beta} = k^s c^{(1)}_{\alpha\beta}$, where k^s is the dimensionless factor. For surface stiffness moduli $\tilde{c}^s_{\alpha\beta}$ from (27.8) we assume that $\tilde{c}^s_{\alpha\beta} = l_c c^{(1)}_{\alpha\beta}$, $l_c = 10^{-10}$ (m), and hence, $c_{m\alpha\beta} = k^s c^{(1)}_{\alpha\beta} = (k^s/l_c)\tilde{c}^s_{\alpha\beta}$. The dimensional analysis shows that $l_0 = l_c/k^s$, and therefore the coefficient k^s is inversely proportional to the minimum pore size l_0. Further, the dimensionless thickness of the shell elements was fixed $h_m = 1$, and in the computational experiments we varied the coefficient k^s and the porosity p. Similarly, we modeled the surface thermomechanical properties $\tilde{\beta}^s_{jj}$ and the surface thermal conductivity moduli $\tilde{k}^s_{jj}$ in the suitable shell elements.

For solving the thermoelastic problems (27.1), (27.5), (27.6), (27.12) with (27.13)–(27.16) we used a coupled twenty-node finite element SOLID226 with the displacements and the temperature as degrees of freedom in each node and with capability of thermoelastic analysis with thermal stresses.

For automatic coating of the inner boundaries of the pores in a cubic representative volume, the following algorithm has been used. First, the finite elements with the pore material properties are selected. Then the external boundaries of the obtained array of elements are covered by target contact elements TARGE170 using the command TSHAP, QUA8. Hence, the edges of all finite elements with the pore properties lying on the external surfaces of the set of these elements get covered by eight node contact elements (TARGE170 of the shape QUA8). Then the contact elements, located on the external border of the whole representative volume, are deleted and the remaining finite elements are changed to the eight node shell elements SHELL281 with the membrane stress only option.

Further, it was necessary to provide an anisotropy type for the shell elements SHELL281 which would be conformable with the anisotropy of the volume finite

elements SOLID226 and the structures of surface moduli (27.9)–(27.11). For a hexagonal system of anisotropy, supplementary procedure was implemented for the shell elements SHELL281 located perpendicular to the isotropy plane Ox_1x_2 by interchanging the stiffness moduli in rows and columns corresponding to the axes x_3 and x_2. As a result, all contact boundaries where thermoelastic structural elements are in contact with pores have been coated by the membrane finite elements which simulate the effect of surface stresses.

Some examples of the representative volume element for $n = 2$ (eight domains) are shown in Figs. 27.1 and 27.2, respectively. In these figures, percentage of pores $p = 15\%$ is the same.

Figure 27.1 shows an example of the representative volume generated by the simple random algorithm and Fig. 27.2 shows an example of the representative volume generated by the 3–0 algorithm from ACELAN–COMPOS package. In Figs. 27.1 and 27.2 on the left all, elements are shown, in the center only volume elements of the second phase are shown, and on the right only shell elements are shown. The

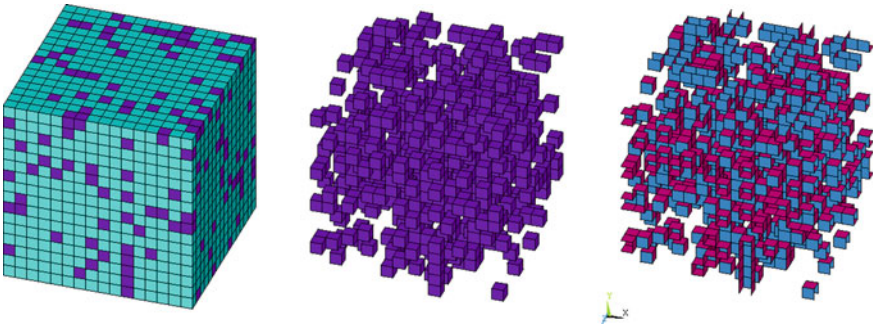

Fig. 27.1 Example of RVE obtained by sample random algorithm, porosity 15%, 3002 surface elements

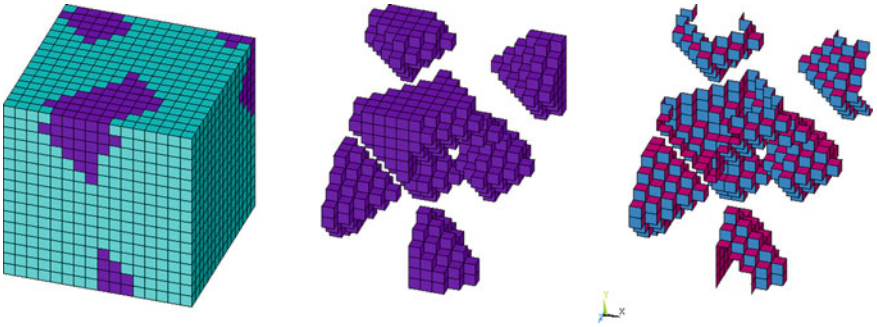

Fig. 27.2 Example of RVE obtained by ACELAN-COMPOS 3–0 algorithm, porosity 15%, 981 surface elements

shell elements located perpendicular to the plane $Ox_1x_2 = Oxy$ are shown in crimson color, and the shell elements located parallel to the plane Ox_1x_2 are shown in blue. The varicolored shell elements were endowed here with different anisotropic material properties, conformable to the structures of the surface stiffness moduli $\mathbf{c}^s$ from (27.9) to (27.11).

Here it can be noted that even with the same porosity for the simple random algorithm, the area of interface boundaries, usually, is substantially larger than for the 3–0 connectivity algorithm.

For solving the thermal problems (27.2), (27.7), (27.18) with (27.19), (27.20), we used a twenty-node thermal element SOLID90 as volume finite element and a eight-node thermal element SHELL132 as surface finite element.

27.4 Numerical Results

To provide an example, let us consider a nanoporous titanium. As it is known, the ordinary titanium is an anisotropic material of hexagonal symmetry. For numerical simulation we assume the following values of the material macro moduli of titanium with zero porosity: $c_{11} = 16.24 \times 10^{10}$ (N/m^2), $c_{12} = 9.2 \times 10^{10}$ (N/m^2), $c_{13} = 6.9 \times 10^{10}$ (N/m^2), $c_{33} = 18.7 \times 10^{10}$ (N/m^2), $c_{44} = 4.67 \times 10^{10}$ (N/m^2), $\alpha_{11} = \alpha_{33} = 8.4 \times 10^{-6}$ (K^{-1}), $\beta_{11} = \alpha_{11}(c_{11} + c_{12} + c_{13})$, $\beta_{33} = \alpha_{11}(2c_{13} + c_{33})$, $k_{11} = k_{33} = 15.5$ [W/(m K)], where superscript (27.1) is absent ($c_{\alpha\beta} = c^{(1)}_{\alpha\beta}$, etc.) The material constants for the pores [marked by superscript (27.2)] were taken equal to the following values: $c^{(2)}_{\alpha\beta} = \eta c^{(1)}_{\alpha\beta}$, $\eta = 1 \cdot 10^{-10}$, $\alpha^{(2)}_{jj} = \alpha^{(1)}_{jj}$, $k^{(2)}_{11} = k^{(2)}_{33} = 0.025$ [W/(m K)].

In the numerical experiments, we varied the values of multipliers k^s from $k^s = 10^{-6} \approx 0$ to 1. Figures 27.3 and 27.4 show the dependencies of the relative effective Young's moduli $r(E_1) = E^{\text{eff}}_1/E^{(1)}_1$ and $r(E_3) = E^{\text{eff}}_3/E^{(1)}_3$, with respect to the porosity p for the representative volumes constructed using the sample random algorithm and the 3–0 connectivity algorithm with two values of k^s.

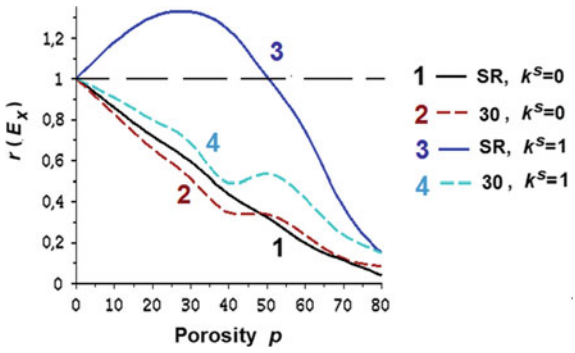

Fig. 27.3 Dependencies of the relative effective modulus $r(E_1)$ versus porosity for different coefficient k^s and for two models of RVE

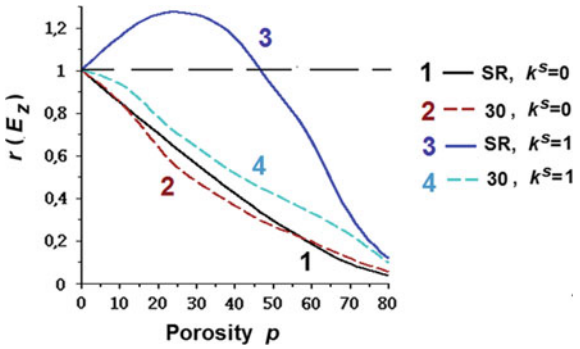

Fig. 27.4 Dependencies of the relative effective modulus $r(E_3)$ versus porosity for different coefficient k^s and for two models of RVE

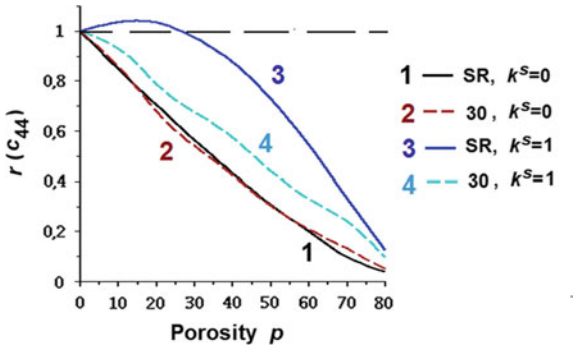

Fig. 27.5 Dependencies of the relative effective modulus $r(c_{44})$ versus porosity for different coefficient k^s and for two models of RVE

Here, $E_1 = 1/s_{11}$, $E_3 = 1/s_{33}$, $s_{11} = (c_{11}c_{33} - (c_{13})^2)/\Delta_c$, $s_{33} = (c_{11} + c_{12})/D_c$, $\Delta_c = (c_{11} - c_{12})/D_c$, $D_c = (c_{11} + c_{12})c_{33} - 2(c_{13})^2$.

Similarly, Fig. 27.5 shows the dependencies of the relative effective shear modulus $r(c_{44}) = c_{44}^{\text{eff}}/c_{44}^{(1)}$ with respect to the porosity p for the representative volumes constructed using the sample random algorithm and the 3–0 connectivity algorithm with two values of k^s.

As it can be seen from Figs. 27.3, 27.4 and 27.5, for small values of the coefficient k^s the surface stresses do not affect the Young's and shear moduli. However, for all values of porosity the surface stresses increase the effective stiffness moduli. Moreover, there are cases, where the nanoporous material have greater stiffness moduli than the same dense material. This situation takes place for the RVE obtained by the sample random algorithm with $k^s = 1$ for the Young's moduli E_1^{eff} and E_3^{eff} if $p < 50\%$, and for shear modulus c_{44} if $p < 25\%$ (see the curves 3 in Figs. 27.3, 27.4 and 27.5, where we have the inequalities $r(E_j) > 1$ or $r(c_{44}) > 1$).

Figures 27.3, 27.4 and 27.5 illustrate that the values of the effective Young's moduli and the values of the effective shear modulus are the largest for the simple random algorithm in the presence of surface stress. This effect is explained by the fact that for the composites obtained by the 3–0 connectivity algorithms the number of interface elements is much smaller than for similar composites with an arbitrary

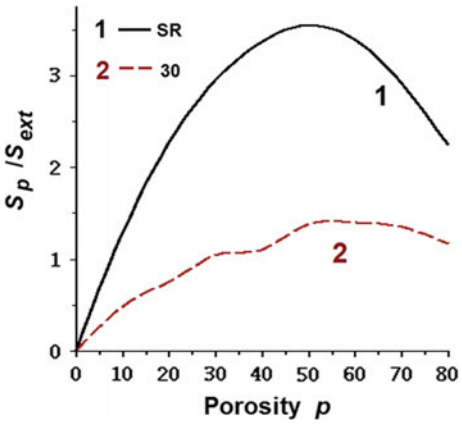

Fig. 27.6 Dependencies of the relative pore surface versus porosity for two models of RVE

pore distribution (see Fig. 27.6). Thus, we can be conclude that the internal structures of nanoporous composites can have a significant effect on the values of effective stiffness moduli.

We also emphasize that the porosity and the surface effects have the opposite influence on the effective stiffness: a simple increase of porosity leads to a decrease in effective stiffness moduli, but an increase of the surface stiffness moduli or a decrease of the pore size leads to a increase of the effective stiffness. The porosity growth up to certain limits enlarge the areas with surface stresses (see Fig. 27.6). Therefore, as the porosity of the nanostuctured material grows, the stiffness moduli can both decrease and increase. For example, for large values of the factor k^s the increase of porosity for small p leads to a growth of the effective Young's moduli and shear modulus, and with further increase of porosity the effective Young's moduli and shear modulus begin to decrease.

Thus, as in [1, 34–37], from the analysis of the computational experiments, we observed the following trends. If we compare two similar porous materials, one of which has an usual dimension of pores and the other has nanosized pores, then for the nanosized porous materials at the expense of the surface stresses the effective stiffness will be greater than for the porous materials of usual dimension of pores. Furthermore, for the porous solid of the macroscopic size of pores the effective stiffness moduli decrease with the porosity growth. Meanwhile, the effective stiffness moduli of nanoporous materials with the same porosity may either decrease or increase depending on the surface moduli values, porosity structure, type of connectivity, dimensions and number of pores. We can observe similar effects for the effective thermal conductivity coefficients.

Acknowledgements The work was done in the framework of the Ministry of Science and Higher Education of Russia project No. 9.1001.2017/4.6 in part of the analysis of algorithms for creating granular composite structures and in the framework of the RFBR project 16-58-48009 IND_omi and DST in part of analyzing the effective properties of nanostructured porous thermoelastic composites.

References

1. V.A. Eremeyev, Acta Mech. **227**, 29 (2016)
2. J.C. Hamilton, W.G. Wolfer, Surf. Sci. **603**, 1284 (2009)
3. J. Wang, Z. Huang, H. Duan, S. Yu, X. Feng, G. Wang, W. Zhang, T. Wang, Acta Mech. Solida Sin. **24**(1), 52 (2011)
4. K.F. Wang, B.L. Wang, T. Kitamura, Acta. Mech. Sin. **32**(1), 83 (2016)
5. M.E. Gurtin, A.I. Murdoch, Arch. Ration. Mech. Anal. **57**, 291 (1975)
6. M.E. Gurtin, A.I. Murdoch, Int. J. Solids Struct. **14**(6), 431 (1978)
7. A.I. Murdoch, Q. J. Mech. Appl. Math. **29**, 245 (1976)
8. G. Chatzigeorgiou, A. Javili, P. Steinmann, Math. Mech. Solids. **20**, 130 (2015)
9. H.L. Duan, J. Wang, Z.P. Huang, B.L. Karihaloo, J. Mech. Phys. Solids **53**, 1574 (2005)
10. A. Javili, P. Steinmann, J. Mosler, Comput. Methods Appl. Mech. Engrg. **317**, 274 (2017)
11. H. Le Quang, Q.-C. He, Mech. Mater. **40**, 865 (2008)
12. H. Le Quang, T.-L. Phan, G. Bonnet, Int. J. Therm. Sci. **50**, 1428 (2011)
13. H. Le Quang, D.C. Pham, G. Bonnet, Q.-C. He, Int. J. Heat Mass. Transf. **58**, 175 (2013)
14. S. Graham, D.L. McDowell, J. Heat Transfer **125**(3), 389 (2003)
15. V.I. Kushch, I. Sevostianov, V.S. Chernobai, Int. J. Eng. Sci. **83**, 146 (2014)
16. H. Le Quang, Int. J. Heat Mass. Transf. **95**, 162 (2016)
17. J.T. Liu, S.T. Gu, E. Monteiro, Q.-C. He, Comput. Mech. **53**, 825 (2014)
18. L. Wu, Int. J. Eng. Sci. **48**, 783 (2010)
19. J. Xiao, Y. Xu, F. Zhang, Compos. Struct. **189**, 553 (2018)
20. T. Chen, G.J. Dvorak, C.C. Yu, Int. J. Solids Struct. **44**(3–4), 941 (2007)
21. H.L. Duan, B.L. Karihaloo, J. Mech. Phys. Solids **55**(5), 1036 (2007)
22. H. Le Quang, Q.-C. He, J. Mech. Phys. Solids **55**, 1889 (2007)
23. H. Le Quang, Q.-C. He, Arch. Appl. Mech. **79**, 225 (2009)
24. A. Javili, P. Steinmann, Int. J. Solids Struct. **47**(24), 3245 (2010)
25. A. Javili, P. Steinmann, Comput. Methods Appl. Mech. Eng. **200**(21–22), 1963 (2011)
26. A. Javili, A. McBride, P. Steinmann, Appl. Mech. Rev. **65**(1), 010802 (2013)
27. A.V. Nasedkin, A.A. Nasedkina, A.S. Kornievsky, A.I.P. Conf, Proc. **1798**, 020110 (2017)
28. A.V. Nasedkin, A.A. Nasedkina, A.S. Kornievsky, in *Coupled Problems 2017—Proceedings of VII International Conference on Coupled Problems in Science and Engineering, 12-14 June 2017, Rhodes Island, Greece*. ed. by M. Papadrakakis, E. Oñate, B.A. Schreflers, CIMNE, vol. 1140, (Barcelona, Spain, 2017)
29. A. Nasedkin, A. Nasedkina, A. Rajagopal, in *Advanced Materials—Proceedings of International Conference on Physics and Mechanics of New Materials and Their Applications, PHENMA 2018*. Springer Proceedings in Physics, ed. by I.A. Parinov, S.-H. Chang, Y-H. Kim, vols. 224, 399, (Springer, Berlin, 2019)
30. A.A. Nasedkina, A. Rajagopal, Mater. Phys. Mech. **37**, 34 (2018)
31. A.B. Kudimova, I.V. Mikhayluts, D.K. Nadolin, A.V. Nasedkin, A.A. Nasedkina, P.A. Oganesyan, A.N. Soloviev, Procedia Struct. Integrity **6**, 301 (2017)
32. N.V. Kurbatova, D.K. Nadolin, A.V. Nasedkin, P.A. Oganesyan, A.N. Soloviev, in *Analysis and Modelling of Advanced Structures and Smart Systems*. *Advanced Structured Materials*, ed. by H. Altenbach, E. Carrera, G. Kulikov, vol. 81, (Springer, Berlin, 2018), p. 69
33. A.B. Kudimova, D.K. Nadolin, A.V. Nasedkin, P.A. Oganesyan, A.N. Soloviev, Mater. Phys. Mech. **37**(1), 25 (2018)
34. H.L. Duan, J. Wang, B.L. Karihaloo, Z.P. Huang, Acta Mater. **54**, 2983 (2006)
35. V. Eremeyev, N. Morozov, Dokl. Phys. **55**(6), 279 (2010)
36. A.V. Nasedkin, A.S. Kornievsky, Comput. Continuum Mech. **10**, 375 (2017). (In Russian)
37. A.V. Nasedkin, A.S. Kornievsky, in *Wave Dynamics and Composite Mechanics for Microstructured Materials and Metamaterials*. *Advanced Structured Materials*, ed. by M.A. Sumbatyan, vol. 59, 107, (Springer, Berlin, 2017)

Chapter 28
Investigation of Initial Stresses' Influence on Surface Wave Field in Bulk Metallic Glass Layer

T. I. Belyankova, E. I. Vorovich, V. V. Kalinchuk, and O. M. Tukodova

Abstract The role of elastic moduli of the fourth order in the investigation of the dynamic characteristics of prestressed bodies made of materials that allow large static deformations is studied. The studies were carried out in the Lagrange coordinate system. Linearized defining relations and equations of motion of a prestressed medium are used, which allow us to consider nonlinear effects of the "second" and "third" orders. On the example of the problem of the propagation of shear harmonic oscillations, the influence of the initial stresses on the propagation velocity of surface waves is studied. Two, five, and nine constant models of a prestressed layer made of palladium-based bulk metal glass are considered. The results obtained in the framework of various models are compared. The difference of the effect of initial stresses on the velocities and critical output frequencies of the higher modes of surface waves, calculated with and without higher order moduli, is shown. A significant effect of the magnitude of the initial stresses is established for uniaxial and biaxial initial stress states.

28.1 Introduction

The technological development of aircraft and cars building, devices making and electronics has led to the need to create new, high-tech, artificial materials that can retain their physical properties and unique qualities under any operating regime and conditions. The breadth and the variety of problems performed with the participation of new materials lead to the need for a detailed study of their physical properties, technological and strength characteristics. Carrying out such studies is associated with the need to solve complex applied problems of the theory of elasticity and to

T. I. Belyankova (✉) · V. V. Kalinchuk
Southern Scientific Center of Russian Academy of Sciences, Rostov-on-Don, Russia
e-mail: tbelen415@mail.ru

I. I. Vorovich Institute of Mathematics, Mechanics and Computer Science, Southern Federal University, Rostov-on-Don, Russia

E. I. Vorovich · O. M. Tukodova
Don State Technical University, Rostov-on-Don, Russia

I. A. Parinov et al. (eds.), *Advanced Materials*, Springer Proceedings in Materials 6, https://doi.org/10.1007/978-3-030-45120-2_28

attract mechanical models of a hyperelastic medium [1, 2], with varying degrees of accuracy, reflecting the processes occurring in the materials under study. For isotropic materials, the elastic potential is represented as the scalar function of the invariants of one of the tensors of the strain measure or the strain tensor [2–6]. For hard materials (rocks, metals, alloys, crystals, etc.), the representation of the elastic potential proposed by Murnaghan in the form of a cubic function of the invariants of the Cauchy—Green strain tensor [7] with III-order constants is widely used.

Due to theoretical and experimental studies, the values of constants of the third order are known for a wide range of metals, alloys, and various structural materials, crystals with various symmetry classes [6, 8–11], as well as for some rocks [12]. The use of models of hyperelastic material with moduli of elasticity of the third order made it possible to more accurately describe the properties of a prestressed medium: to study second-order effects [11, 12], to determine mechanical stresses [13, 14], to study the characteristics of the dynamics, propagation and localization of waves in prestressed media [15–26]. The review of works in this direction is presented in [15, 21].

In [15], a sequential linearization of the nonlinear equations of the mechanics of a solid elastic-deformable body was carried out in the Lagrange and Euler coordinate systems. Linearized defining relations and equations of motion of a prestressed medium are constructed in an arbitrary, generally curvilinear coordinate system. Expressions presented in a compact, convenient for research form were used in [15, 24–26] to solve a number of specific mixed problems of the dynamic theory of elasticity. In particular, for the model of an initially isotropic hyperelastic material with a potential in the Murnagan form, the influence of the nature of the initial mechanical influences on the formation, propagation, and localization of wave fields in both homogeneous and inhomogeneous prestressed media were studied [24–26].

Recently, a number of new materials, promising in practical applications and possessing unique physical properties has appeared. In particular, these materials are able to withstand a very high level of elastic deformation, at which the nonlinearity of the elastic properties becomes very significant. In [27–31], the results of studies to determine the elastic moduli of the third and fourth order for bulk metal glasses based on zirconium (Zr) and palladium (Pd) are presented. The study of the dynamics of structures involving such materials requires an improvement in the theory of linearized contact for prestressed bodies. In [32], a sequential linearization of the nonlinear equations of mechanics of an initially isotropic elastic body in the vicinity of a certain initial stress state was carried out. The linearization was carried out in the framework of the theory of small strains superimposed on a final one in the Lagrange coordinate system. The representation of the specific strain energy in terms of the algebraic invariants of the Green-Lagrange strain tensor is used as the elastic potential for an initially isotropic body. Linearized defining relations and equations of motion of a prestressed medium are obtained, allowing to consider the nonlinear effects of initial deformation on the elastic properties of an initially isotropic body. In this paper, we propose an approach to study the dynamics of prestressed initially isotropic elastic bodies with allowance for IV modules. Using the example of the problem of excitation of shear harmonic oscillations in a layer by a point surface

source, the effect of higher-order moduli on the propagation velocity of surface waves is studied. Two-, five-, and nine-constant models are considered, as well as a model of linear approximation in deformations. The effect of prestresses on the velocities and critical output frequencies of new modes is investigated.

28.2 Formulation of the Problem

Consider the boundary-value problem of vibrations of a prestressed layer caused by the action of a surface load $\boldsymbol{q} = \{q_1, q_2, q_3\}e^{-i\omega t}$, distributed in a certain region Ω. Outside this region, the surface of the medium is free of stresses. The lower edge of the layer $|x_1|, |x_2| \leq \infty$, $0 \leq x_3 \leq h$ is rigidly bonded to a non-deformable base. The layer material is assumed to be compressible, initially isotropic, having an elastic potential

$$\chi = -pI_1 + \frac{1}{2}\lambda I_1^2 + \mu I_2 + \frac{1}{6}\nu_1 I_1^3 + \nu_2 I_1 I_2 + \frac{4}{3}\nu_3 I_3 + \frac{1}{24}\gamma_1 I_1^4 + \frac{1}{2}\gamma_2 I_1^2 I_2 + \frac{4}{3}\gamma_3 I_1 I_3 + \frac{1}{2}\gamma_4 I_2^2. \tag{28.1}$$

Here $I_k = \mathrm{tr}(\mathbf{S}^k)$, $(k = 1, 2, 3)$ are the algebraic invariants of the Cauchy-Green strain tensor $\mathbf{S}$; λ, μ are elastic moduli of the second order; ν_1, ν_2, ν_3 and γ_1, γ_2, γ_3, γ_4 are elastic moduli of the third and fourth orders, respectively. We assume that the state $\mathbf{S} = 0$ is a state with minimal free energy, i.e. $p = 0$, the initial stress state is determined by a uniform initial deformation [3, 15, 32]:

$$\mathbf{R} = \mathbf{r} \cdot \mathbf{\Lambda}, \mathbf{\Lambda} = \delta_{km} v_k \mathbf{i}_k \mathbf{i}_m; \; v_k = \mathrm{const}, k = 1, 2, 3 \tag{28.2}$$

here $\mathbf{R}, \mathbf{r}$ are the radius vectors of a point of the medium in the initial deformed and natural state (NS), respectively, $v_i = 1 + \delta_i$, δ_i are the relative elongations of the fibers directed in a natural configuration along the axes coinciding with the Cartesian coordinates, δ_{ij} is the Kronecker symbol. The studies are carried out in the Lagrangian coordinate system, which coincides with a rectangular Cartesian system, the oscillation mode is assumed to be steady, the time factor is omitted.

Further, in the work we use dimensionless parameters: linear parameters are assigned to the layer thickness, density—to the density in the natural state, elastic parameters—to the shear modulus in the NS. As a dimensionless frequency, the parameter $\kappa_2 = \omega h / V_S^0$ is used, where $V_S^0 = \sqrt{\mu_0/\rho_0}$ is the shear wave velocity in the NS; ω is the angular frequency.

Within the framework of the accepted assumptions, the boundary-value problem of the oscillations of the prestressed layer in the Lagrange coordinates is described by the linearized equations of motion [15, 32]:

$$\nabla_0 \cdot \mathbf{\Theta} = \rho_0 \frac{\partial^2 \mathbf{u}}{\partial t^2} \tag{28.3}$$

and linearized boundary conditions on the surface $o = o_1 + o_2$:

$$o_1 : \ \mathbf{n} \cdot \mathbf{\Theta} = \mathbf{q}, o_2 : \ \mathbf{u} = \mathbf{u}^* \tag{28.4}$$

here ∇_0 is the Hamilton operator, $\mathbf{u} = \{u_1, u_2, u_3\}$ is the displacement vector, $\mathbf{n}$ is the vector of the external normal to the surface of the medium, defined in the coordinate system associated with the NS; ρ_0 is the density of the material in the NS; $\mathbf{\Theta}$ is the linearized Piola stress tensor, whose components are representable in the form [2–4, 15, 32]:

$$\Theta_{ij} = C^*_{ijkl} \frac{\partial u_k}{\partial x_l}, \ \ i, j = 1, 2, 3. \tag{28.5}$$

The coefficients C^*_{ijkl} determine the properties of a prestressed body and, in accordance with [32] have the form:

$$\begin{gathered} C^*_{iiii} = v_i^2 \xi_{ii} + 2v_i^2(\psi_1 + 3\psi_2 S_i) + P_i, C^*_{iijj} = v_i v_j \xi_{ij}, i \neq j, \\ C^*_{ijij} = v_j v_i \left(\psi_1 + \frac{3}{2}\psi_2 (S_i + S_j) \right), C^*_{ijji} = v_j^2 \left(\psi_1 + \frac{3}{2}\psi_2 (S_i + S_j) \right) + P_i \\ \xi_{kn} = \psi_{01} + 2\psi_{02} S_n + 3\psi_{03} S_n^2 + 2(\psi_{11} + 2\psi_{12} S_n) S_k + 4\psi_{21} S_k^2, k, n = 1, 2, 3 \end{gathered} \tag{28.6}$$

other coefficients C^*_{ijkl} are zero. According to [32], taking into account (28.1), (28.2) for the components S_k and P_k following relations are valid:

$$S_k = \frac{1}{2}(v_k^2 - 1), \ \ P_k = \psi_0 + 2\psi_1 S_k + 3\psi_2 S_k^2, \ \ k = 1, 2, 3. \tag{28.7}$$

$$\begin{gathered} \psi_{01} = \lambda + \nu_1 I_1 + \frac{1}{2}\gamma_1 I_1^2 + \gamma_2 I_2, \quad \psi_{02} = \psi_{11} = \nu_2 + \gamma_2 I_1, \\ \psi_{03} = \psi_{21} = \frac{4}{3}\gamma_3, \quad \psi_{12} = \gamma_4, \quad \psi_{13} = \psi_{22} = \psi_{23} = 0, \\ I_m = S_1^m + S_2^m + S_3^m, \quad m = 1, 2, 3. \end{gathered} \tag{28.8}$$

$$\begin{gathered} \psi_0 = \lambda I_1 + \frac{1}{2}\nu_1 I_1^2 + \nu_2 I_2 + \frac{1}{6}\gamma_1 I_1^3 + \gamma_2 I_1 I_2 + \frac{4}{3}\gamma_3 I_3, \\ \psi_1 = \mu + \nu_2 I_1 + \gamma_2 I_1^2/2 + \gamma_4 I_2, \ \ \psi_2 = \frac{4}{3}(\nu_3 + \gamma_3 I_1). \end{gathered} \tag{28.9}$$

In the absence of initial stresses ($\nu_1 = \nu_2 = \nu_3 = 1$), taking into account (28.6)–(28.9), we obtain:

$$C^*_{iiii} = \lambda + 2\mu,\ C^*_{iijj} = \lambda,\ C^*_{ijij} = \mu,\ C^*_{ijji} = \mu.$$

Taking into account representations (28.5), (28.6), we write the boundary-value problem (28.3), (28.4) in the form [15, 32]:

$$C^*_{ijkl}\frac{\partial^2 u_k}{\partial x_l \partial x_i} = \rho_0 \frac{\partial^2 u_j}{\partial t^2}, \quad j = 1, 2, 3 \tag{28.10}$$

with the boundary conditions:

$$\begin{aligned} x_3 = h\text{: } C^*_{3113}\frac{\partial u_1}{\partial x_3} + C^*_{1313}\frac{\partial u_3}{\partial x_1} &= q_1, \\ C^*_{3223}\frac{\partial u_2}{\partial x_3} + C^*_{2323}\frac{\partial u_3}{\partial x_2} &= q_2, \\ C^*_{3333}\frac{\partial u_3}{\partial x_3} + C^*_{1133}\frac{\partial u_1}{\partial x_1} + C^*_{2233}\frac{\partial u_2}{\partial x_2} &= q_3 \\ x_3 = 0\text{: } u_k = 0, k = 1, 2, 3 & \end{aligned} \tag{28.11}$$

28.3 Solution of the Problem

To solve the boundary value problem (28.10), (28.11), the approach [15] is used: the solution is constructed in Fourier images in the form of an expansions:

$$\begin{aligned} U_p &= \sum_{k=1}^{3} f_{pk}(c_{k1}\mathrm{sh}\,\sigma_k x_3 + c_{k2} ch\,\sigma_k x_3),\ p = 1, 2, \\ U_3 &= \sum_{k=1}^{3} c_{k1}\mathrm{ch}\,\sigma_k x_3 + c_{k2} sh\,\sigma_k x_3. \end{aligned} \tag{28.12}$$

Here U_k are the Fourier transforms of the component of the displacement vector; f_{ik} are coefficients selected from the condition when the solution (28.12) is satisfied to the equations of motion; c_{ik} are coefficients are determined by substituting (28.12) into the boundary conditions; σ_k are the values of the characteristic equation [15]. Using the inverse Fourier transform, the solution of the original boundary value problem (28.10), (28.11) is represented by the expressions (α_1, α_2 are the Fourier transform parameters in coordinates x_1, x_2):

$$\mathbf{u} = \frac{1}{4\pi^2}\iint\limits_{\Omega} \mathbf{k}(x_1 - \xi, x_2 - \eta, x_3, \kappa_2)\,\mathbf{q}(\xi, \eta)\,d\xi\,d\eta$$

$$\mathbf{k}(s,t,x_3,\kappa_2)=\int\limits_{\Gamma_1}\int\limits_{\Gamma_2}\mathbf{K}(\alpha_1,\alpha_2,x_3,\kappa_2)e^{-i(\alpha_1 s+\alpha_2 t)}d\alpha_1 d\alpha_2 \tag{28.13}$$

The form of the matrix—functions elements $\mathbf{K}(\alpha_1,\alpha_2,x_3,\kappa_2)$ in the representation (28.13) essentially depends on the nature of the initial stress state of the medium.

28.3.1 Shear Layer Vibrations

In the study of shear oscillations of a prestressed layer under the action of a surface source distributed in the region $\{\Omega(x_1,x_2,x_3)\colon |x_1|\le 1, |x_2|<\infty, x_3=h\}$, in the boundary value problem (28.3), (28.4), it is necessary to take into account the conditions:

$$u_2=u_2(x_1,x_3),\ u_1=u_3=0,\ \frac{\partial}{\partial x_2}=0. \tag{28.14}$$

Taking into account conditions (28.14), solution (28.13) looks like:

$$u_2(x_1,x_3)=\frac{1}{2\pi}\int\limits_{-1}^{1}k_{22}(x_1-\xi,x_3,\kappa_2)q(\xi)\,d\xi, \tag{28.15}$$

$$k_{22}(s,x_3,\kappa_2)=\int\limits_{\Gamma}K_{22}(\alpha,x_3,\kappa_2)\,e^{-i\alpha s}d\alpha,\ K_{22}(\alpha,x_3,\kappa_2)=\mathrm{sh}(\sigma_2 x_3)\Delta^{-1},$$
$$\sigma_2=\left(\alpha^2 C^*_{1221}-\kappa_2^2\right)(C^*_{3223})^{-1},\ \Delta=C^*_{3223}\sigma_2\mathrm{ch}(\sigma_2 h) \tag{28.16}$$

Contour Γ is selected according to the radiation conditions.

Representation (28.15) determines the displacement of an arbitrary point of the layer. In the case of a point source of oscillation $\mathbf{q}(x_1)=\{0,\ \delta(x_1),\ 0\}$ (here $\delta(x_1)$ is the Dirac function) for the displacement in the layer, the following expression is valid:

$$u_2(x_1,x_3,\kappa_2)=\frac{1}{2\pi}\int\limits_{\Gamma}K_{22}(\alpha,x_3,\kappa_2)e^{-i\alpha x_1}d\alpha. \tag{28.17}$$

It can be seen from representations (28.16), (28.17) that in this case the influence of the initial stresses on the displacements in the layer, is associated with changes in two coefficients C^*_{1221} and C^*_{3223}.

28.4 Determination of Initial Stress State

The state of a prestressed body is described by the Kirchhoff tensor, which in the case of a uniform initial deformation (28.2) is defined in (28.7) with coefficients (28.9). Grouping the terms by the degrees of the strain tensor **S**, for the components of the Kirchhoff tensor, we get:

$$\begin{aligned} P_1 &= (\lambda + 2\mu)S_1 + \lambda S_2 + \lambda S_3 + H_1^2 + H_1^3, \\ P_2 &= \lambda S_1 + (\lambda + 2\mu)S_2 + \lambda S_3 + H_2^2 + H_2^3, \\ P_3 &= \lambda S_1 + \lambda S_2 + (\lambda + 2\mu)S_3 + H_3^2 + H_3^3. \end{aligned} \tag{28.18}$$

Following [32], we consider four models:

Model I. In elastic potential (28.1), only terms with second-order modules are stored; coefficients ψ_k $(k = 1, 2, 3)$ (28.9) are determined by the expressions:

$$\psi_0 = \lambda I_1, \quad \psi_1 = \mu, \quad \psi_2 = 0, \quad H_k^2 = H_k^3 = 0.$$

The components of the Kirchhoff tensor in this case are linearly related to the components of the strain tensor.

Model II. The linear approximation for invariants of the strain measure is used:

$$v_k = 1 + \delta_k, \quad v_k^2 = 1 + 2\delta_k, \quad v_k v_i = 1 + \delta_k + \delta_i, \quad i, k = 1, 2, 3, \quad i \neq k$$

$$S_k = \delta_k, \quad I_1 = \theta = \delta_1 + \delta_2 + \delta_3, \quad I_2 = I_3 = 0,$$

The components of the Kirchhoff tensor (28.18) are expressed by the formulas:

$$P_k = \lambda\theta + 2\mu\delta_k, k = 1, 2, 3.$$

The coefficients C^*_{ijkl} from the representation (28.6) in this case can be expressed as

$$\begin{aligned} C^*_{iiii} &= P_i + (\lambda + 2\mu) + \nu_1\theta + 2(\lambda + 2\mu + 2\nu_2)\delta_i, \\ C^*_{iijj} &= \lambda + \nu_1\theta + (\lambda + 2\nu_2)\big(\delta_i + \delta_j\big), \\ C^*_{ijij} &= \mu + (\mu + 2\nu_3)\big(\delta_i + \delta_j\big), C^*_{ijji} = P_i + \mu + 2\mu\delta_j + 2\nu_3\big(\delta_i + \delta_j\big), \\ & i, j = 1, 2, 3, i \neq j. \end{aligned}$$

Model III. In the representation (28.1), only terms with elastic moduli of the second and third orders, for ψ_k $(k = 1, 2, 3)$ are saved;

$$\psi_0 = \lambda I_1 + \frac{1}{2}\nu_1 I_1^2 + \nu_2 I_2, \psi_1 = \mu + \nu_2 I_1, \psi_2 = \frac{4}{3}\nu_3,$$

in view (28.18) $H_k^2 \neq 0$ и $H_k^3 = 0$.

Model IV. In (28.1), modules of the third and fourth orders are taken into account. In the representation of the components of the Kirchhoff tensor (28.18), $H_k^2 \neq 0$ and $H_k^3 \neq 0$, $(k = 1, 2, 3)$, which allows us to take into account the influence of the second and third degrees of initial deformation. The form H_k^2 and H_k^3 is given in [32].

Relations (28.18) are the system of three, generally non-linear, equations for three unknowns: S_1, S_2, S_3, P_1, P_2, P_3 or their combinations, depending on the method of setting the initial stress-strain state. In the combined setting of the initial state, it is assumed that deformation along one axis (for example, v_1) and two stress conditions are known. Deformations and stresses along other axes are determined from system (28.18).

Further, the influence of the magnitude of the initial stresses under uniaxial $1x_1$ ($P_1 = P$, $P_2 = P_3 = 0$) and biaxial $2x_1$ ($P_1 = 0$, $P_2 = P_3 = P$) initial stress states is investigated.

28.5 Numerical Analysis

The material used was $Pd_{40}Cu_{30}Ni_{10}P_{20}$ metal glass based on palladium (Pd) with the following parameters [29]:

$$\rho = 9300\,\text{kg m}^{-3},\ \lambda = 1.453 \times 10^{11}\ \text{Pa},\ \mu = 0.358 \times 10^{11}\ \text{Pa},$$
$$\nu_1 = -2.27 \times 10^{11}\ \text{Pa},\ \nu_2 = -2.34 \times 10^{11}\ \text{Pa},\ \nu_3 = -0.818 \times 10^{11}\ \text{Pa},$$
$$\gamma_1 = -105.828 \times 10^{12}\ \text{Pa},\ \gamma_2 = 15.556 \times 10^{11}\ \text{Pa},\ \gamma_3 = 1.81 \times 10^{11}\ \text{Pa},$$
$$\gamma_4 = -2.98 \cdot 10^{11}\ \text{Pa}.$$

As noted, in the case of shear vibrations of a prestressed layer with a clamped lower face, it follows from (28.16), (28.17) that the influence of the initial stresses on the displacements is associated with changes in the two coefficients C^*_{1221} and C^*_{3223}. In Fig. 28.1a, b the dependence of the coefficients C^*_{1221} and C^*_{3223} on the magnitude of the initial strains v_1, acting along the axis x_1, is presented for uniaxial $1x_1$ and biaxial $2x_1$ initial stress states. The numbers 1, 2, 3, 4 mark the curves corresponding to changes C^*_{1221} within the framework of the four models under consideration, curves $1'$, $2'$, $3'$, $4'$ correspond to the changes of C^*_{3223}. Dotted lines (curves 1) correspond to coefficients calculated without taking into account higher order modules [***model I***, $H_k^2 = H_k^3 = 0$ in (28.18)], dashed lines (curves 3)—taking into account modules of the third order $H_k^2 \neq 0$, $H_k^3 = 0$), solid lines (curves 4)—taking into account modules of the III and IV orders (***model IV***, $H_k^2 \neq 0$, $H_k^3 \neq 0$). The dash-dotted lines (curves 2) correspond to a linear respect to deformations approximation (***model II***).

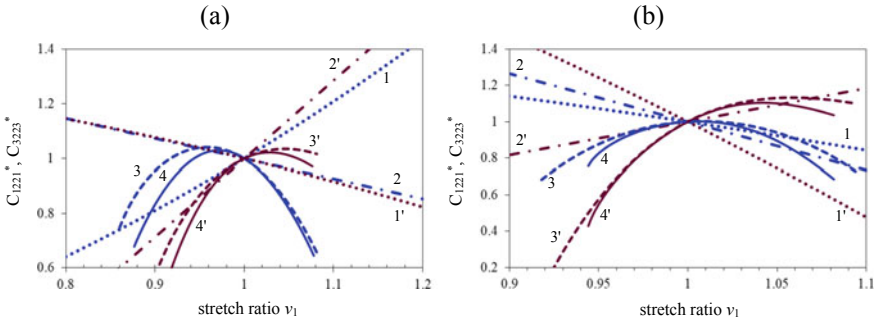

Fig. 28.1 Influence of the initial strain on the coefficients C^*_{1221} and C^*_{3223} of uniaxial $1x_1$ **a** and biaxial $2x_1$ **b** initial stress states

As follows from the graphs, the inclusion of higher order modules leads to significant nonlinearity in the behavior of the coefficients, the region of one-to-one correspondence, which determines the internal stability of the material, has significantly decreased. Taking into account IV constants to a greater extent narrows the range of elongations at which the material remains stable. It should be noted that, unlike model I, for the other three models there is a small region of small deformations in which the values of the coefficients are close.

28.5.1 Influence of Initial Stresses on Dispersion Properties of Layer

An analysis of the solutions of dispersion equation $\Delta(\alpha, \kappa_2) = 0$ (28.16) showed that the form of the initial stress state and the magnitude of the stresses that significantly affect the behavior of the coefficients C^*_{1221} and C^*_{3223} lead to significant changes of the dispersion properties of the layer material. This is manifested in a shift of the critical frequencies of the appearance of surface wave modes upwards and in a change of the angle of the dispersion curves inclination. In Fig. 28.1a–d on the example of the 5th mode, fragments of dispersion curves are shown for ***I*** (Fig. 28.2a), ***II*** (Fig. 28.2b), and ***III*** (Fig. 28.2d) ***models*** in case of initial stress state $1x_1$. Figure 28.2d shows a fragment for the initial stress state $2x_1$. Curves 1, 2, 3, 4 in the Figures correspond to tensions $v_1 = 1.01, 1.02, 1.03, 1.04$, curve 0 corresponds to the dispersion curve in the NS.

It can be seen from the Fig. 28.2 that when using ***model I***, the shift of the values of the critical frequencies occurs downward. For ***models II***, ***III***, and ***IV***, the action of initial stresses leads to a shift of the critical frequencies upward; their values depend on the type of model, the type and magnitude of the initial stress state.

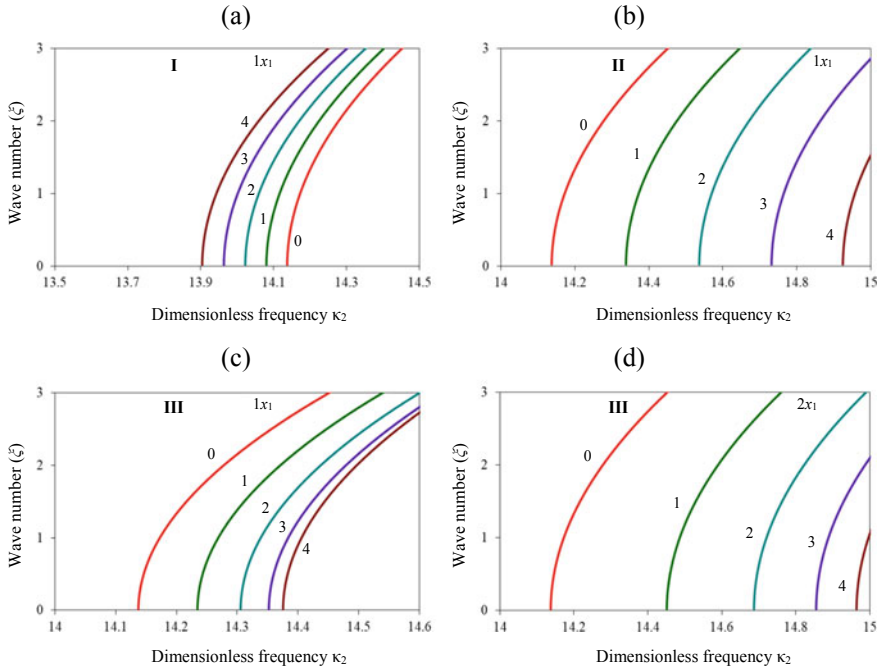

Fig. 28.2 Fragment of the 5th mode of dispersion curves for ***models I*** (**a**), ***II*** (**b**) and ***III*** (**c**) in the case of uniaxial tension $1x_1$, **d** fragment of the 5th mode for ***model III***, stress state $2x_1$

28.5.2 *Influence of Initial Stresses Magnitude on Surface Waves Velocity*

Figure 28.3a–d show the effect of the initial strains magnitude by the initial state $1x_1$ on the frequency distribution of the phase velocities of surface waves V_F^σ / V_S^0 [$V_F^\sigma = \omega / \xi$, ξ is the solution of dispersion (28.16)] for the models under consideration. As before, curves 1, 2, 3, 4 correspond to stretches $v_1 = 1.01, 1.02, 1.03, 1.04$, the number 0 marks the curves for the NS.

As follows from the figures, in ***models I***, ***III***, and ***IV***, the initial stress mainly affects the asymptotic values of the velocities. In ***model I***, this effect is directly proportional to the magnitude of the initial stresses, in ***models III*** and **IV**, it is inversely proportional. In ***model II***, the initial influence is mainly influenced by the shift of critical frequencies; the effect on the asymptotic values of the velocities is negligible.

A more visual representation of the influence of initial stresses on various modes of surface waves is given by the deviation and relative deviation of their phase velocities with respect to phase velocity in the NS:

$$D = \left(V_F^0 - V_F^\sigma\right) / V_S^0, \delta = \left(V_F^0 - V_F^\sigma\right) / V_F^0. \tag{28.19}$$

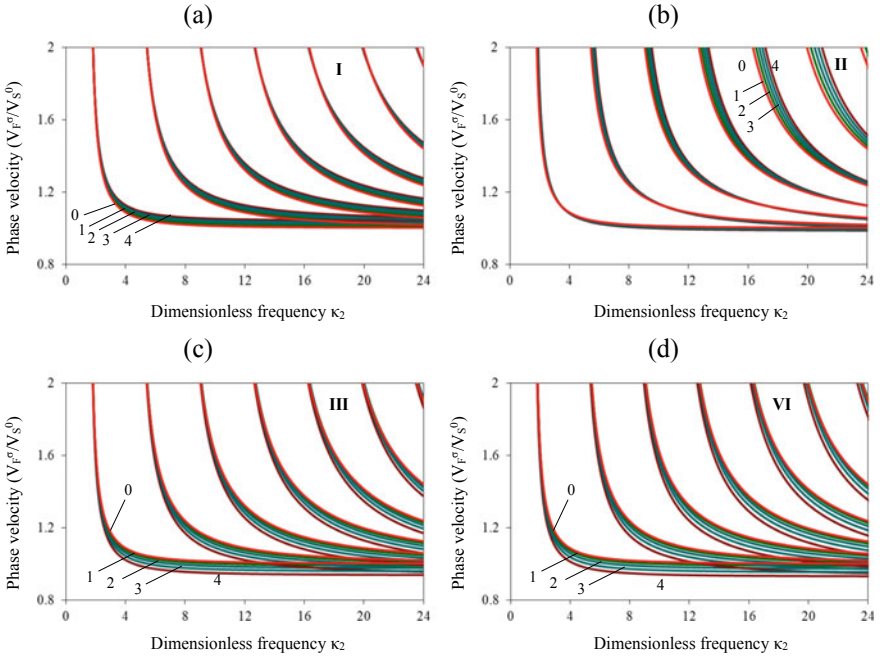

Fig. 28.3 Effect of the initial deformation on the velosity of surface waves for ***models I*** (**a**), ***II*** (**b**), ***III*** (**c**) and ***IV*** (**d**)

Figure 28.4a–d show the graphs of deviation D (28.19) for odd velocity modes of surface waves. Curves 1, 2, 3, 4 correspond to tension 1.01, 1.02, 1.03, 1.04 by a uniaxial initial stress state of $1x_1$.

The graphs in Fig. 28.4 illustrate the dependence of the asymptotic values of the phase velocities of surface waves on the initial deformation for various models. It can be seen from the Figures that the maximum influence of v_1 takes place in ***model IV***. The shift of the critical frequencies is insignificant in all models except for II, in which this shift is directly proportional to the tension v_1 and increases with increasing mode number.

Figure 28.5a–d show the graphs of relative deviation δ (28.19) for the first three modes of surface waves. The relative deviation, calculated in the framework of four models; in the case of a uniaxial $1x_1$ initial stress state for $v_1 = 1.01$ and 1.03, are given in Fig. 28.5a and b, respectively. For comparison, Fig. 28.5c, d show the graphs δ for the first three modes of ***model III*** in the case of uniaxial $1x_1$ and biaxial $2x_1$ tension $v_1 = 1.01$ and 1.03.

It can be seen from Fig. 28.5a, b that the maximum influence of the initial $1x_1$ strain on the phase velocities of surface waves occurs in ***models III*** and ***IV***. A somewhat smaller, but qualitatively opposite in character, effect of the initial deformation on surface waves is observed in ***model II***. The second factor in the influence of the initial deformation on surface waves is the shift of critical frequencies. For the initial

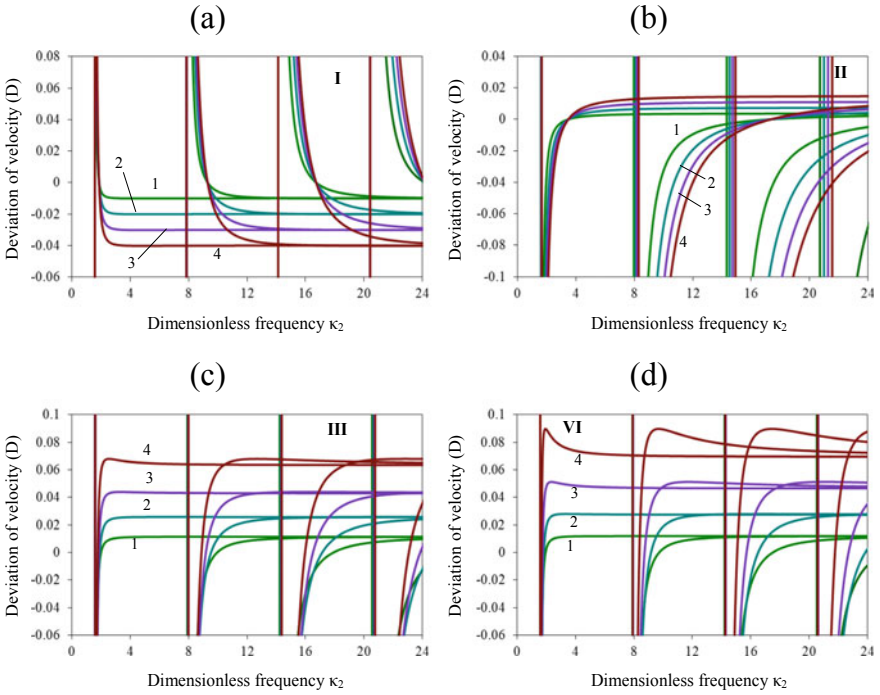

Fig. 28.4 The phase velocity deviation of the odd modes for ***models I*** (**a**), ***II*** (**b**), ***III*** (**c**) and ***IV*** (**d**)

deformation of the $1x_1$ species, it is pronounced in ***model II***; in ***models I***, ***III***, and ***IV***, it is insignificant.

From Fig. 28.5c, d it can be seen that a change in the form of the initial stress state leads to qualitatively different results. The determining factor of influence in ***model III*** for the initial $1x_1$ state is phase velocity. For the initial $2x_1$ state, the decisive factor in the effect is the shift in the value of the critical frequency. Comparing Fig. 28.5b and d it is easy to see that this shift in ***model III*** for the same values of v_1 exceeds the shift in ***model II***.

28.6 Conclusions

An approach is proposed to study the dynamic characteristics of a prestressed layer under the influence of large initial stresses made of a material that allows significant static deformations. The studies were carried out in the Lagrange coordinate system using various theories of dynamics of prestressed bodies. Two-, five-, and nine-constant models are considered. Linearized defining relations and equations of motion of a prestressed medium are used, which allow one to take into account the

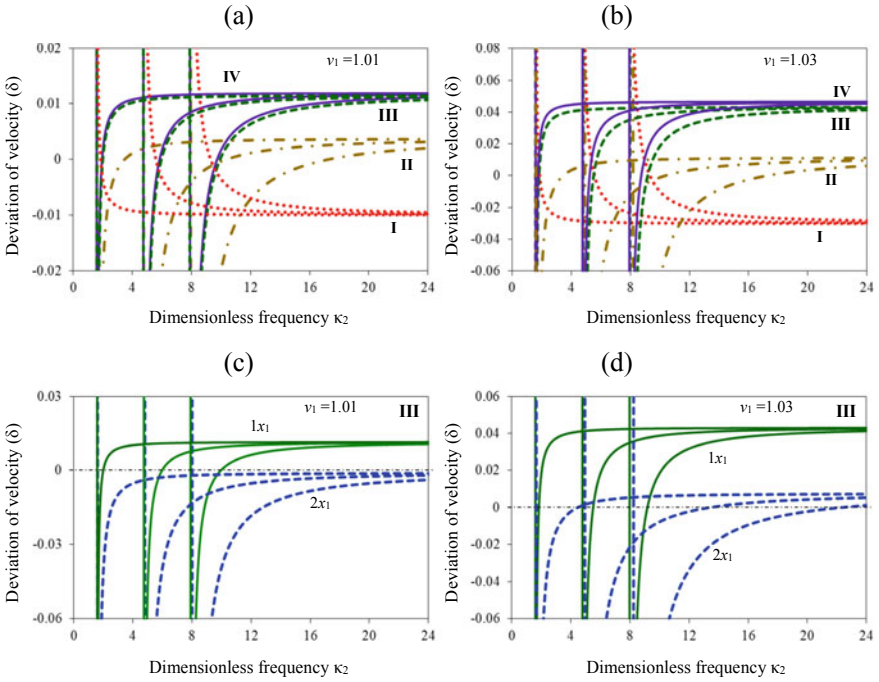

Fig. 28.5 The relative deviation of the phase velocities of the first three modes: **a**, **b** comparison of models under initial stress state $1x_1$; **c**, **d** comparison of the influence of the initial states $1x_1$ and $2x_1$, ***model III***

nonlinear effects of the "second" and "third" orders of influence of mechanical strains on the elastic properties of the starting material. Using the example of the problem of shear harmonic oscillations in a layer, we studied the influence of the magnitude and type of initial stresses on the structure of the surface field and the propagation velocity of surface waves. The results obtained in the framework of various models are compared. The effect of taking into account higher order moduli on the surface wave velocities at various values of the initial strains is shown. The influence of the type and magnitude of the initial uniaxial and biaxial effects on the transformation of the phase velocities of surface waves is established. It is shown that the decisive factor in the influence of the initial deformation on surface waves for some models may be the value of the phase velocity, for other models, the values of the critical frequencies of the appearance of surface wave modes. Which of the factors is decisive may depend on the type of initial stress state.

Acknowledgements The work was prepared during the competitive part of the state assignment of the Russian Ministry of Education and Science under project No. 9.1001.2017/4.6 with partial financial support from the Russian Foundation for Basic Research (projects 19-08-01051, 19-48-230042, 19-01-00719 and 18-08-01012).

References

1. C. Truesdell, *A First Course in Rational Continuum Mechanics* (Academic, New York, 1977)
2. G.A. Maugin, *Continuum Mechanics of Electromagnetic Solids* (Elsevier Science Publishers, Amsterdam, 1968)
3. A.I. Lurie, *Non-linear Theory of Elasticity* (North-Holland, Amsterdam, 1990)
4. V.A. Krasil'nikov, V.V. Krylov, *Introduction to Physical Acoustics* (Nauka, Moscow, 1984). (In Russian)
5. M. Shams, M. Destrade, R.W, Wave Motion **48**(7), 552 (2011)
6. M. Destrade, R.W. Ogden, J. Acoust. Soc. Am. **128**(6), 3334 (2010)
7. F.D. Murnaghan, Am. J. of Math **59**(2), 235 (1937)
8. R.N. Thurston, K. Brugger, Phys. Rev. **133**(6A), A1604 (1964)
9. R.T. Smith, R. Stern, R.W.B. Stephens, J. Acoust. Soc. Amer **40**(5), 1002 (1966)
10. S.S. Sekoyan. Akust. Zh **16**(3), 453 (1970). (In Russian)
11. D.S. Hughes, J.L. Kelly, Phys. Rev. **92**(5), 1145 (1953)
12. V.N. Bakulin, A.G. Protosenya, Dokl. Akad. Nauk SSSR **263**(2), 314 (1982)
13. V. Erofeev, V.A. Zaznobin, R.V. Samokhvalov, Acoust. Phys. **53**(5), 546 (2007)
14. N.Y. Nikitina, A.V. Kamyshev, S.V. Kazachek Russ. J. Nondestruct. Test **51**(3),171 (2015)
15. V.V. Kalinchuk, T.I. Belyankova, *Dynamic Contact Problems for Prestressed Bodies* (Fizmatlit, Moscow, 2002). (In Russian)
16. M. Hayes, R.S. Rivlin, Arch. Ration. Mech. and Anal. **8**(1), 15 (1961)
17. V.V. Kalinchuk, I.B. Polyakova, Int. Appl. Mech **18**(6), 504 (1982)
18. V.V. Kalinchuk, I.B. Poliakova, J. of Appl. Math. Mech. **44**(2), 224 (1980)
19. V.V. Kalinchuk, T.I. Belyankova, Izv. AN. MTT [Mechanics of Solids] **2**, 89 (1998)
20. A.N. Guz, *Elastic Waves in Initially Stressed Bodies. Vol. 1. General Aspects* (Naukova Dumka, Kiev, 1986). (In Russian)
21. A.N. Guz, *Elastic Waves in Initially Stressed Bodies. Vol. 2. Propagation Laws* (Kiev, Naukova Dumka, 1986). (In Russian)
22. T.I. Belyankova, V.V. Kalinchuk, J. Appl. Math. Mech. **57**(4), 713–724 (1993)
23. A.N. Guz, Int. Appl. Mech. **38**(1), 23 (2002)
24. V.V. Kalinchuk, T.I. Belyankova, *Dynamics of the Surface of Inhomogeneous Media* (Fizmatlit, Moscow, 2009). (In Russian)
25. T.I. Belyankova, V.V. Kalinchuk, Mater. Phys. Mech. **23**(1), 25 (2015)
26. T.I. Belyankova, V.V. Kalinchuk, Acoust. Phys. **63**(3), 245 (2017)
27. N.P. Kobelev, E.L. Kolyvanov, V.A. Khonik, Phys. Solid State **49**(7), 1209 (2007)
28. N.P. Kobelev, V.A. Khonik, A.S. Makarov, G.V. Afonin, YuP Mitrofanov, J. Appl. Phys. **115**(3), 033513 (2004)
29. N.P. Kobelev, E.L. Kolyvanov, V.A. Khonik, Phys. Solid State **57**(8), 1483 (2015)
30. H. Wang, M. Li, J. Appl. Phys. **113**, 213515 (2013)
31. Z. Zhou, H. Wang, M. Li, J. Appl. Phys. **126**, 145901 (2019)
32. T.I. Belyankova, V.V. Kalinchuk, D.N. Sheydakov, Mater. Phys. and Mech **40**(2), 187 (2018)

Chapter 29
Comparison of Two Numerical Inverse Laplace Transform Methods with Application for Problem of Surface Waves Propagation in an Anisotropic Elastic Half-Space

Ivan Markov and Leonid Igumnov

Abstract The propagation of the surface waves in elastic media has been extensively studied and is very important in many fields. The Laplace domain Boundary Element Method (BEM) is powerful and accurate numerical method that can be employed for treating such problems. Since anisotropic elastic problems is very computationally challenging for any BEM formulation, the choice of particular numerical Laplace inversion algorithm is crucial for efficient anisotropic elastodynamic Laplace domain boundary element analysis. In this investigation, for a specific problem of anisotropic linearly elastic half space subjected to transient loading, we examine two different methods for numerical inversion of Laplace transforms. The first method we test is the renowned Durbin's method which is based on a Fourier series expansion. The second method is the convolution quadrature method which is reformulated as a numerical Laplace transform inversion routine. Methods are compared in the context of their application in the framework of Laplace domain collocation boundary element formulation.

29.1 Introduction

The propagation of the surface waves in elastic media has been extensively studied and is very important in the fields of dynamic soil-structure interaction analysis, seismology, earthquake engineering, etc. Among other powerful numerical methods Boundary Element Method (BEM) is particularly well-suited for modelling elastic wave propagation in infinite and semi-infinite domains. There are different BEM formulations that can be used for treating such problems and Laplace domain direct BEM approach is one of most well-studied and frequently employed. In case of linear anisotropic elasticity BEM can be implemented very efficiently. However,

I. Markov (✉) · L. Igumnov
Research Institute for Mechanics, National Research Lobachevsky State University of Nizhny Novgorod, Nizhny Novgorod, Russia
e-mail: teanku@gmail.com

I. A. Parinov et al. (eds.), *Advanced Materials*, Springer Proceedings in Materials 6, https://doi.org/10.1007/978-3-030-45120-2_29

when anisotropic elastic materials are considered, implementation of any BEM that utilizes anisotropic elastic dynamic fundamental solutions gets complicated due to an issue with their efficient evaluation. As presented by Wang and Achenbach [1, 2], regular parts of three-dimensional anisotropic elastic fundamental solutions can be expressed as integrals over the surface of a half of a unit sphere. These integrals must be calculated using numerical quadrature which can be quite time consuming. Thus, a proper choice of a numerical inversion method can considerably boost the performance of frequency or Laplace domain BEM for linear anisotropic elastic materials.

Durbin's method [3] for numerical inversion of Laplace transforms is based on a Fourier series expansion and is a popular option for transient wave propagation problems. There is a number of works (e.g. [4–7]) that are dedicated to improvements of Durbin's method, including, among other aspects, convergence acceleration of the Fourier series, reduction of error, choice of free parameters.

Convolution Quadrature Method (CQM) is a relatively recent method originally developed by Lubich [8, 9] as a quadrature rule for convolution integrals. CQM can be reformulated as a numerical inversion procedure for Laplace transforms, and Schanz [10] stated that for a short time periods CQM is superior to other inversion methods.

Pekeris [11] presented analytical solutions for horizontal and vertical displacements of the free surface of a homogeneous isotropic linearly elastic half-space due to a surface impulse loading. Eskandari-Ghadi and Sattar [12] derived analytical expressions for the surface and internal displacements of a transversely isotropic half-space under axisymmetric surface point loading.

In the present chapter we present and discuss the comparison of the Durbin's method and the CQM in the context of their application in the framework of Laplace domain collocation BEM formulation for transient surface waves propagation in anisotropic linearly elastic half-space. Test functions are the horizontal and vertical displacements of the surface of a transversely isotropic half-space subjected to Heaviside-type surface point load.

29.2 Preliminary Considerations and Test Functions

The Laplace transform and its inversion are defined by the following relationships

$$F(s) = L\{f(t)\} = \int_0^{+\infty} \mathrm{e}^{-st} f(t)\mathrm{d}t,\ s = \alpha + i\omega, \tag{29.1}$$

$$f(t) = L^{-1}\{F(s)\} = \frac{1}{2\pi i} \int_{\alpha - i\infty}^{\alpha + i\infty} e^{st} F(s) ds, \tag{29.2}$$

with $f(t) = 0$ for $t < 0$, α is arbitrary real number greater than the real parts of all the singularities of $F(s)$.

Application of Laplace domain BEM for elastodynamic problems usually consists of obtaining Laplace domain responses for a set of sampling complex frequencies s_l, $l = \overline{1, N_s}$, and then obtaining time-domain solutions via numerical inversion method. It is expected that the Laplace domain BEM is mesh sensitive, meaning that the spatial discretization and the frequency discretization are related and not independent. In other words, a certain minimum number of boundary elements per wavelength are required for a reliable dynamic boundary element analysis. Even more intricate this issue becomes for anisotropic elastic media since the wave velocities are dependent on direction. Additionally, integrals in the expressions of anisotropic elastic dynamic fundamental solutions can become highly oscillatory for high frequencies. From the practical point of view it means, that before starting Laplace domain boundary element calculations, we need to somehow determine maximum allowable value $\omega_{\max}$ of imaginary part of complex Laplace transform parameter s. For all these reasons, further in our investigation we will assume, that in application of both considered numerical Laplace inversion methods, we are restricted by a certain value $\omega_{\max}$.

For the original function in time-domain denoted as $f(t)$ and approximation of $f(t)$ obtained with a numerical inversion routine from its Laplace transform as $\tilde{f}(t)$ we define relative error R_{err} and pointwise absolute error $A_{err}(t_k)$ as follows

$$R_{err} = \sqrt{\left(\frac{\sum_{k=0}^{N_t} \left(f(t_k) - \tilde{f}(t_k) \right)^2}{\sum_{k=0}^{N_t} f(t_k)^2} \right)}, \; A_{err}(t_k) = \left| f(t_k) - \tilde{f}(t_k) \right|, \; t_k = k \frac{t_{\max}}{N_t}, \tag{29.3}$$

where $t_{\max}$ is the largest value in the time range over which $\tilde{f}(t)$ is obtained.

As the test functions we use radial and vertical displacements of the free surface of transversely isotropic half-space under Heaviside-type surface point load. Transversely isotropic material of the half-space is characterized by mass density ρ and the elasticity tensor C_{ijkl}. In the cylindrical coordinates radial displacements $u(r, z = 0, t)$ and vertical displacements $w(r, z = 0, t)$ are given as follows [12]

$$u(r, z = 0, t) = -\frac{\alpha_3 P_{\max} t^2}{\pi^2 r^3} \mathrm{Im} \int_0^{\pi/2} \frac{a_{22}\beta_1 - a_{21}\beta_2}{f} \cos\theta d\theta, \tag{29.4}$$

$$w(r, z = 0, t) = \\ - \frac{P_{\max} t}{\pi^2 r^2} \mathrm{Im} \int_0^{\pi/2} \frac{\left((1 + \alpha_1)\psi^2 - \rho_0\right)(a_{22} - a_{21}) + \alpha_2 \left(a_{22}\beta_1^2 - a_{21}\beta_2^2\right)}{f} \cos\theta d\theta \tag{29.5}$$

$$\psi(r,t,\theta)=\frac{t\cos\theta}{r},\ f=a_{11}a_{22}-a_{12}a_{21}, \tag{29.6}$$

$$\alpha_1=\frac{C_{1212}+C_{1122}}{C_{1212}},\ \alpha_2=\frac{C_{1313}}{C_{1212}},\ \alpha_3=\frac{C_{1133}+C_{1313}}{C_{1212}},\ \rho_0=\frac{\rho}{C_{1212}}, \tag{29.7}$$

$$\beta_1=\sqrt{-k_1\psi^2+k_2+\frac{1}{2}\sqrt{k_3\psi^4-k_4\psi^2+k_5}},$$
$$\beta_2=\sqrt{-k_1\psi^2+k_2-\frac{1}{2}\sqrt{k_3\psi^4-k_4\psi^2+k_5}}, \tag{29.8}$$

$$a_{11}=\left(-\alpha_3C_{1133}+(1+\alpha_1)C_{3333}\psi^2-\rho_0C_{3333}\right)\beta_1+\alpha_2C_{3333}\beta_1^3, \tag{29.9}$$

$$a_{12}=\left(-\alpha_3C_{1133}+(1+\alpha_1)C_{3333}\psi^2-\rho_0C_{3333}\right)\beta_2+\alpha_2C_{3333}\beta_2^3, \tag{29.10}$$

$$a_{21}=\left(-(1+\alpha_1)C_{3333}\psi^2+\rho_0\right)i\psi+(\alpha_3-\alpha_2)i\psi\beta_1^2, \tag{29.11}$$

$$a_{22}=\left(-(1+\alpha_1)C_{3333}\psi^2+\rho_0\right)i\psi+(\alpha_3-\alpha_2)i\psi\beta_2^2, \tag{29.12}$$

$$k_1=\frac{\left(h_1^2+h_2^2\right)}{2},\ k_2=\frac{1}{2}\rho\left(\frac{1}{C_{3333}}+\frac{1}{C_{1313}}\right),\ k_3=\left(h_2^2-h_1^2\right)^2, \tag{29.13}$$

$$k_4=2\rho\left(\left(\frac{1}{C_{3333}}+\frac{1}{C_{1313}}\right)\left(h_1^2+h_2^2\right)-2\frac{C_{1111}}{C_{3333}}\left(\frac{1}{C_{1111}}+\frac{1}{C_{1313}}\right)\right),$$
$$k_5=\rho^2\left(\frac{1}{C_{3333}}-\frac{1}{C_{1313}}\right)^2, \tag{29.14}$$

where $P_{\max}$ is the amplitude of the load, h_1^2 and h_2^2 are the roots of the following equation

$$C_{3333}C_{1313}h^4-\left(C_{1111}C_{3333}-C_{1133}^2-2C_{1133}C_{1313}\right)h^2+C_{1111}C_{1313}=0. \tag{29.15}$$

For our investigation we chose $P_{\max}=1$ Pa, observation point is located at the distance $r=1$m, the mass density of transversely isotropic material is $\rho=2000\,\mathrm{kg/m^3}$ and the elasticity tensor C_{ijkl} are given in the Voigt notation as follows

$$\mathbf{C}^{TI}=\begin{bmatrix}5.82 & 2.11 & 1.44 & 0 & 0 & 0\\ & 5.82 & 1.44 & 0 & 0 & 0\\ & & 4.1 & 0 & 0 & 0\\ & & & 1.25 & 0 & 0\\ & \text{symm.} & & & 1.25 & 0\\ & & & & & 1.855\end{bmatrix}\times 10^8\ \text{Pa}. \tag{29.16}$$

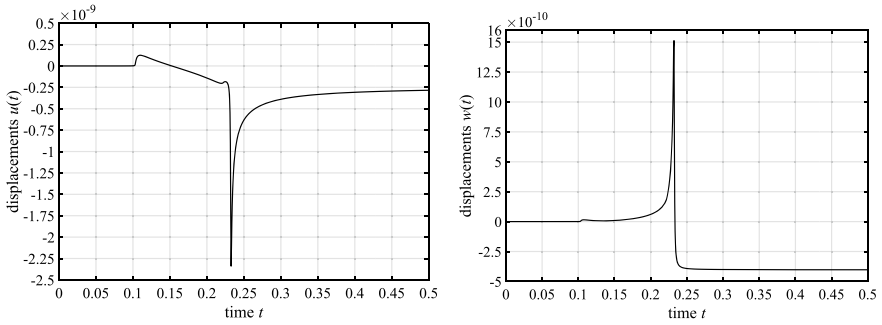

Fig. 29.1 Test functions **a** $u(t)$, **b** $w(t)$

For convenience we work with dimensionless variables and quantities

$$\mathbf{C}^{TI} = \mathbf{C}^{TI} p_2 p_1^2 / p_3,\ \rho = \rho p_2^3 / p_3,\ P_{\max} = P_{\max} p_1^2 (p_2 p_3),\ r = r/p_2,\ t = t/p_1, \tag{29.17}$$

$$p_1 = 0.018 \text{ s},\ p_2 = 1 \text{ m},\ p_3 = 1 \text{ kg}. \tag{29.18}$$

To avoid complicated procedure associated with dealing with the singularities of integrands [13] and to get meaningful error estimation around Rayleigh pole we introduce a small artificial damping into the elasticity tensor of the material as

$$\mathbf{C} = \mathbf{C}^{TI}(1 + 0.005i). \tag{29.19}$$

Under these considerations test functions $u(t)$ and $w(t)$ are depicted in Fig. 29.1.

29.3 Durbin's Method

We start with rewriting (29.1) as

$$F(s) = \int_0^{+\infty} e^{-st} f(t)dt = \int_0^{+\infty} e^{-(\alpha+i\omega)t} f(t)dt = \int_0^{+\infty} e^{-\alpha t}(\cos(\omega t) - \sin(\omega t)) f(t)dt$$
$$= \int_0^{+\infty} e^{-\alpha t} f(t)\cos(\omega t)dt + i\left(-\int_0^{+\infty} e^{-\alpha t} f(t)\sin(\omega t)dt\right) = \text{Re}(F(s)) + i\text{Im}(F(s)), \tag{29.20}$$

$$\text{Re}(F(s)) = \text{Re}(F(\alpha + i\omega)) = \int_0^{+\infty} e^{-\alpha t} f(t)\cos(\omega t)dt, \tag{29.21}$$

$$\mathrm{Im}(F(s)) = \mathrm{Im}(F(\alpha + i\omega)) = -\int\limits_0^{+\infty} \mathrm{e}^{-\alpha t} f(t) \sin(\omega t)\mathrm{d}t. \tag{29.22}$$

Recalling

$$\begin{aligned}\mathrm{Re}(F(\alpha - i\omega)) &= \int\limits_0^{+\infty} e^{-\alpha t} f(t) \cos(-\omega t)dt = \int\limits_0^{+\infty} e^{-\alpha t} f(t) \cos(\omega t)dt \\ &= \mathrm{Re}(F(\alpha + i\omega)),\end{aligned} \tag{29.23}$$

$$\begin{aligned}\mathrm{Im}(F(\alpha - i\omega)) &= -\int\limits_0^{+\infty} e^{-\alpha t} f(t) \sin(-\omega t)\mathrm{d}t = \int\limits_0^{+\infty} e^{-\alpha t} f(t) \sin(\omega t)dt \\ &= -\mathrm{Im}(F(\alpha + i\omega)).\end{aligned} \tag{29.24}$$

Rewriting (29.2)

$$\begin{aligned}f(t) &= \frac{1}{2\pi i}\int\limits_{\alpha - i\infty}^{\alpha + i\infty} e^{st} F(s)ds = \frac{1}{2\pi i}\int\limits_{-\infty}^{+\infty} e^{(\alpha + i\omega)t} F(s)id\omega \\ &= \frac{1}{2\pi i}\int\limits_{-\infty}^{+\infty} e^{\alpha t}(\cos(\omega t) + i\sin(\omega t))F(s)id\omega \\ &= \frac{e^{\alpha t}}{2\pi}\int\limits_{-\infty}^{+\infty} (\cos(\omega t) + i\sin(\omega t))F(s)d\omega \\ &= \frac{e^{\alpha t}}{2\pi}\int\limits_{-\infty}^{+\infty} (\cos(\omega t) + i\sin(\omega t))[\mathrm{Re}(F(s)) + i\mathrm{Im}(F(s))]d\omega \\ &= \frac{e^{\alpha t}}{2\pi}\int\limits_{-\infty}^{+\infty} [\mathrm{Re}(F(s))\cos(\omega t) - \mathrm{Im}(F(s))\sin(\omega t)]d\omega \\ &+ i\frac{e^{\alpha t}}{2\pi}\int\limits_{-\infty}^{+\infty} [\mathrm{Re}(F(s))\sin(\omega t) + \mathrm{Im}(F(s))\cos(\omega t)]d\omega.\end{aligned} \tag{29.25}$$

Expanding imaginary part in (29.25)

$$\begin{aligned}
&\int_{-\infty}^{+\infty} [\mathrm{Re}(F(s))\sin(\omega t) + \mathrm{Im}(F(s))\cos(\omega t)]d\omega \\
&= \int_{-\infty}^{0} [\mathrm{Re}(F(s))\sin(\omega t) + \mathrm{Im}(F(s))\cos(\omega t)]d\omega \\
&\quad + \int_{0}^{+\infty} [\mathrm{Re}(F(s))\sin(\omega t) + \mathrm{Im}(F(s))\cos(\omega t)]d\omega,
\end{aligned} \tag{29.26}$$

and now using (29.21) and (29.22) we get for the first integral in (29.26)

$$\begin{aligned}
&\int_{-\infty}^{0} [\mathrm{Re}(F(s))\sin(\omega t) + \mathrm{Im}(F(s))\cos(\omega t)]d\omega \\
&= \int_{+\infty}^{0} [\mathrm{Re}(F(\alpha + i(-\omega)))\sin(-\omega t) + \mathrm{Im}(F(\alpha + i(-\omega)))\cos(-\omega t)](-d\omega) \\
&= \int_{+\infty}^{0} [\mathrm{Re}(F(\alpha + i\omega))(-\sin(\omega t)) - \mathrm{Im}(F(\alpha + i\omega))\cos(\omega t)](-d\omega) \\
&\quad - \int_{+\infty}^{0} [\mathrm{Re}(F(\alpha + i\omega))\sin(\omega t) + \mathrm{Im}(F(\alpha + i\omega))\cos(\omega t)](-d\omega) \\
&= \int_{+\infty}^{0} [\mathrm{Re}(F(\alpha + i\omega))\sin(\omega t) + \mathrm{Im}(F(\alpha + i\omega))\cos(\omega t)]d\omega \\
&= -\int_{0}^{+\infty} [\mathrm{Re}(F(s))\sin(\omega t) + \mathrm{Im}(F(s))\cos(\omega t)]d\omega.
\end{aligned} \tag{29.27}$$

It follows from (29.26) and (29.27) that the imaginary part in (29.25) is zero. Applying (29.21) and (29.22) to the real part in (29.25) we get the equivalent representation of (29.2):

$$f(t) = \frac{e^{\alpha t}}{\pi} \int_{0}^{+\infty} [\mathrm{Re}(F(\alpha + i\omega))\cos(\omega t) - \mathrm{Im}(F(\alpha + i\omega))\sin(\omega t)]d\omega, \; t \geq 0. \tag{29.28}$$

Durbin's method (or sometimes also called the Fourier Series Method) consists of representing $f(t)$ as

$$\begin{aligned}
f(t) = \frac{e^{\alpha t}}{T}\Bigg[&-\frac{1}{2}\mathrm{Re}(F(\alpha)) + \sum_{k=1}^{\infty} \mathrm{Re}\Big(F\Big(\alpha + i\frac{k\pi}{T}\Big)\Big)\cos\Big(\frac{k\pi}{T}t\Big) \\
&- \sum_{k=0}^{\infty} \mathrm{Im}\Big(F\Big(\alpha + i\frac{k\pi}{T}\Big)\Big)\sin\Big(\frac{k\pi}{T}t\Big)\Bigg] - D_{err}, \; 0 < t < 2T,
\end{aligned} \tag{29.29}$$

where D_{err} is the discretization error due to approximation of the integral by the Fourier series. Since infinite series in (29.29) can only be summed up to a finite number N_{sum} of terms, the approximating formula for $f(t)$ is

$$f(t) \approx \tilde{f}(t) = \frac{e^{\alpha t}}{T}\Big[-\frac{1}{2}\mathrm{Re}(F(\alpha)) + \sum_{k=0}^{N_{\mathrm{sum}}} \Big\{\mathrm{Re}\Big(F\Big(\alpha + i\frac{k\pi}{T}\Big)\Big)\cos\Big(\frac{k\pi}{T}t\Big) - \mathrm{Im}\Big(F\Big(\alpha + i\frac{k\pi}{T}\Big)\Big)\sin\Big(\frac{k\pi}{T}t\Big)\Big\}\Big], \tag{29.30}$$

for $0 < t < 2T$.

Durbin derived formula (29.29) using a Fourier series expansion of $e^{-\alpha t} f(t)$ on the time interval $[0, 2T]$, which is formally equivalent to the application of the trapezoidal rule to (29.28) with the integration step size equal π/T. Aside from roundoff and discretization error in Durbin's formula (29.30), there is the truncation error since the series is not summed up to infinity. When the maximum of imaginary parts of complex frequencies is given as $\omega_{\max}$, the N_{sum} is then determined as

$$N_{\mathrm{sum}} = \left[\frac{\omega_{\max} T}{\pi}\right]. \tag{29.31}$$

Assuming that $t_{\max}$ is the largest value of time range over which $\tilde{f}(t)$ is obtained, then T is chosen so that $2T > t_{\max}$ or

$$T = T^* t_{\max},\ T^* > 0.5. \tag{29.32}$$

Slightly modifying the idea of Crump [4], α is chosen from the following relation

$$\alpha = \frac{\kappa \ln 10}{T} = \frac{\kappa \ln 10}{T^* t_{\max}}. \tag{29.33}$$

With (29.32) and (29.33) the input parameters in Durbin's method are $\omega_{\max}$ and $t_{\max}$, the free parameters are κ and T^*.

We start with presenting in Figs. 29.2, 29.3, 29.4 and 29.5 contour plots of $R_{err}(\kappa, T^*)$ for inverted vertical displacements $\tilde{w}(t)$ for two values of dimensionless time $t_{\max} = 0.5$ and $t_{\max} = 1.0$ and four different values of $\omega_{\max}$: 500, 2000, 4000, 15000. Vertical displacements are chosen since they seem to

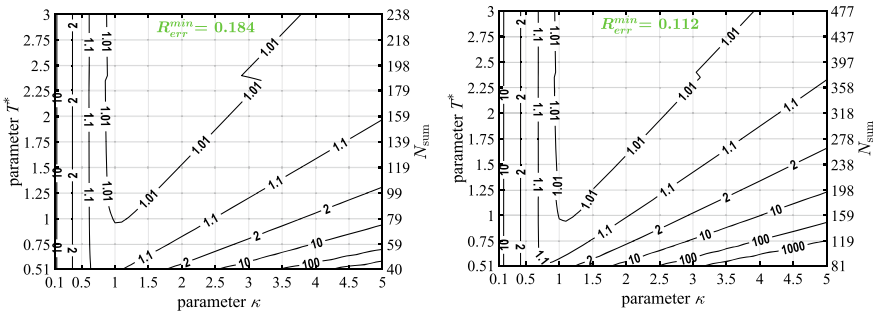

Fig. 29.2 Contour plots of $R_{err}(\kappa, T^*)$ for $\tilde{w}(t)$, $\omega_{\max} = 500$ and **a** $t_{\max} = 0.5$, **b** $t_{\max} = 1.0$

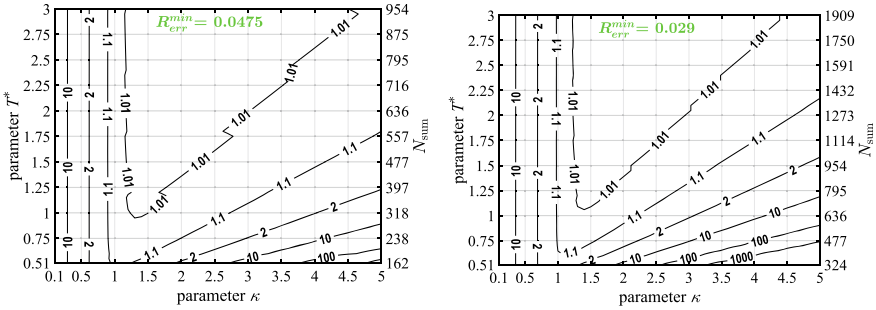

Fig. 29.3 Contour plots of $R_{err}(\kappa, T^*)$ for $\tilde{w}(t)$, $\omega_{\max} = 2000$ and **a** $t_{\max} = 0.5$, **b** $t_{\max} = 1.0$

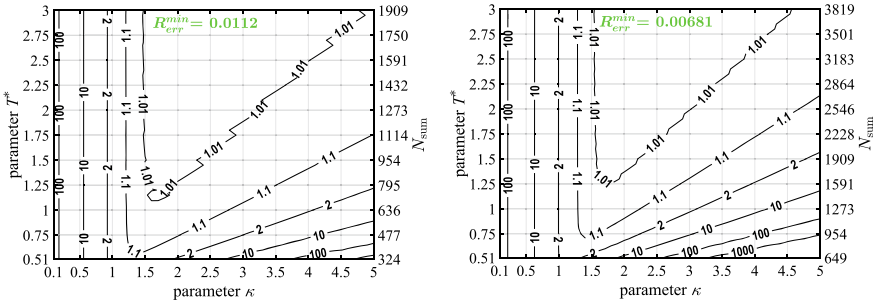

Fig. 29.4 Contour plots of $R_{err}(\kappa, T^*)$ for $\tilde{w}(t)$, $\omega_{\max} = 4000$ and **a** $t_{\max} = 0.5$, **b** $t_{\max} = 1.0$

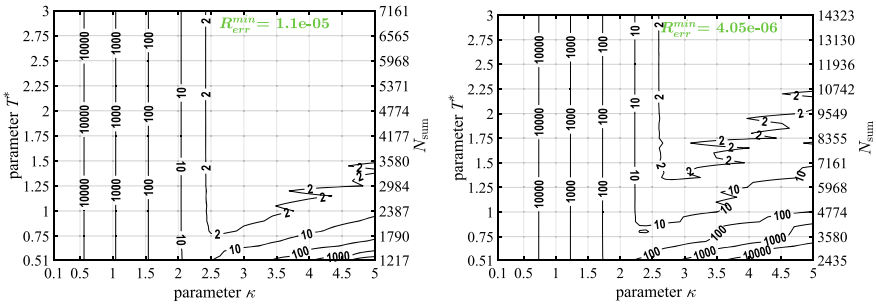

Fig. 29.5 Contour plots of $R_{err}(\kappa, T^*)$ for $\tilde{w}(t)$, $\omega_{\max} = 15000$ and **a** $t_{\max} = 0.5$, **b** $t_{\max} = 1.0$

present stricter error bounds than $\tilde{u}(t)$. Numbers along the contour lines mean how many times the error $R_{err}(\kappa, T^*)$ along each line is greater than minimal value $R_{err}^{\min}$ obtained for a given range of parameters κ and T^*.

General observations following from Figs. 29.2, 29.3, 29.4 and 29.5 are that for each $t_{\max}$ there is a different $\kappa_{\min}(\omega_{\max})$ that for all $\kappa < \kappa_{\min}$ Durbin's method produce exponentially growing error R_{err} regardless of T^* and therefore of sampling points count N_{sum}. Value of $\kappa_{\min}$ increases with increasing maximum value $\omega_{\max}$ of

imaginary parts of complex frequencies. For the values $\kappa > \kappa_{\min}$ levels of R_{err} roughly correspond to the straight lines $T^*(\kappa)$ defined for a fixed values of α. It is impossible to formulate universal relationship $R_{err}(\kappa, T^*)$ for all possible values of $\omega_{\max}$ and $t_{\max}$. Frequently employed rule of a thumb is to choose κ in the range $2 \leq \kappa \leq 3$ and it seem to provide adequate balance between accuracy and number of sampling points for $T^* \geq 0.75$. It should be emphasized, that for increasing value of κ, value of T^* should also increase for a given accuracy, which corresponds to the error analysis presented by Durbin in [3]. This is demonstrated in Fig. 29.6 for $t_{\max} = 0.5$, $T^* = 1.0$ and $\kappa = 2.0$, 2.5, 3.0 and 4.0. For the fixed T^*, starting from a certain value of κ, increasing it, and therefore α, leads to the rapid deterioration of the error R_{err} with increasing of $\omega_{\max}$ since roundoff and truncation errors are amplified by the $e^{\alpha t}/T$.

In Fig. 29.7 inverted solutions $\tilde{u}(t)$ and $\tilde{w}(t)$, obtained by Durbin's method with parameters $t_{\max} = 0.5$, $\omega_{\max} = 2000$, $T^* = 1.0$, $\kappa = 2.0$, ($N_{\text{sum}} = 319$, $\alpha \approx 9.21$), are compared with the reference solutions $u(t)$ and $w(t)$. Corresponding pointwise absolute errors A_{err} are depicted in Fig. 29.8. As it can be expected, points near the Rayleigh peak have the most deviation from the reference solutions. Gibb's oscillations are present due to the truncation of integration range and usually are suppressed

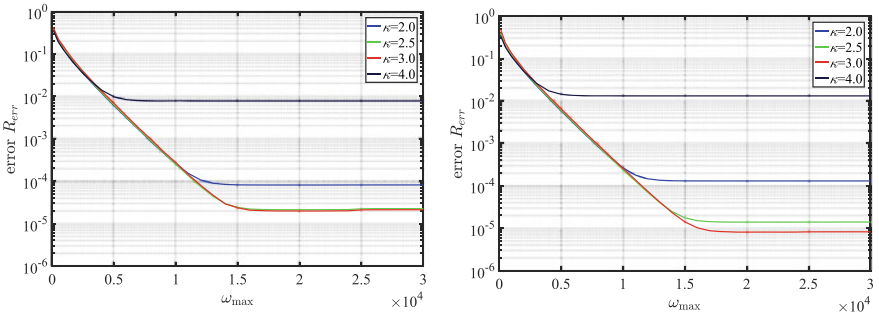

Fig. 29.6 Error R_{err} with $T^* = 1.0$ and $t_{\max} = 0.5$ for **a** $\tilde{u}(t)$, **b** $\tilde{w}(t)$

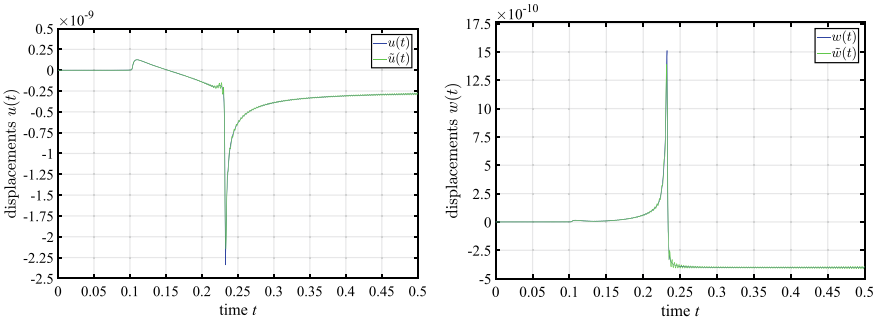

Fig. 29.7 Comparison between reference and inverted solutions for **a** $u(t)$, **b** $w(t)$

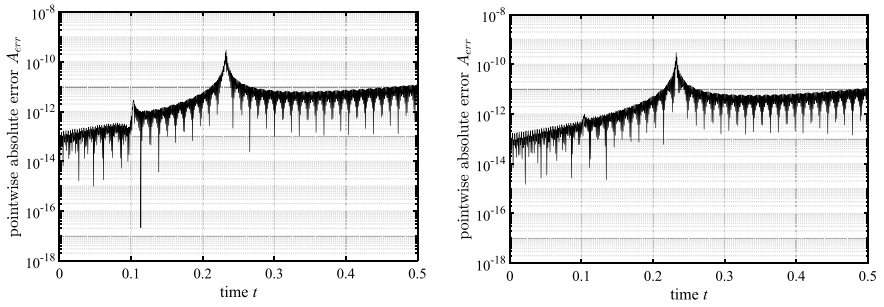

Fig. 29.8 Pointwise absolute error A_{err} for **a** $u(t)$, **b** $w(t)$

using a data windowing technique [14, 15]. But in course of our experiments we tried several window functions (Blackman, Hanning, Lanczos and Riesz) and found that application of a data filter leads to severe undershooting around Rayleigh peak. Additionally we have tried to use Wynn's epsilon method [4–6, 16] to accelerate the convergence of the series in Durbin's method and found that for complicated functions like $u(t)$ and $w(t)$, performance of the epsilon algorithm heavily depends on a proper choice of $\omega_{\max}$, which is impossible to make beforehand.

29.4 Convolution Quadrature Method

CQM was originally developed [8, 9] to numerically approximate convolution integrals

$$f(t) = y(t) * g(t) = \int_0^t y(t-\tau)g(\tau)d\tau, \tag{29.34}$$

as follows [10]

$$f(n\Delta t) = \sum_{k=0}^{n} \psi_{n-k}(\bar{y})g(k\Delta t),\ n = \overline{0, N_t}, \tag{29.35}$$

where $\bar{y}$ is the Laplace transform of $y(t)$, Δt is the time step, N_t is the number of time steps.

Now let $F(s)$ denote the Laplace transform of $f(t)$ with $f(t) = 0$ for $t < 0$. Consider the following convolution integral

$$f(t) = L^{-1}\{F(s)\} = L^{-1}\left\{sF(s)\frac{1}{s}\right\} = L^{-1}\{sF(s)\} * L^{-1}\left\{\frac{1}{s}\right\}$$

$$= L^{-1}\{sF(s)\} * H(t), \tag{29.36}$$

where $H(t)$ is the Heaviside step function.

Employing Backward Differential Formula of order two as an underlying time stepping method, we present slightly modified CQM to approximate convolution integral (29.36)

$$f(m\Delta t) \approx \tilde{f}(m\Delta t) = \sum_{k=0}^{n} \psi_{n-k}(sF(s))H(k\psi) = \sum_{k=0}^{n} \psi_k(sF(s)), \tag{29.37}$$

$$m = \overline{0, N_t},\ \Delta t = \frac{t_{\max}}{N_t}, n = \left[\frac{m\Delta t N_\psi}{t_{\max}}\right],\ N_\psi \geq N_t, \tag{29.38}$$

$$\psi_k(sF(s)) = \frac{R^{-k}}{2\pi}\int_0^{2\pi} s(\phi)F(s(\phi))e^{-ik\phi}\mathrm{d}\phi = \mathrm{Re}\left[\frac{R^{-k}}{\pi}\int_0^{\pi} s(\phi)F(s(\phi))\mathrm{e}^{-ik\phi}d\phi\right], \tag{29.39}$$

$$s(\phi) = \frac{\gamma\left(\mathrm{Re}^{i\phi}\right)N_\psi}{t_{\max}},\ \gamma\left(\mathrm{Re}^{i\phi}\right) = \frac{3}{2} - 2\mathrm{Re}^{i\phi} + \frac{\left(\mathrm{Re}^{i\phi}\right)^2}{2}, \tag{29.40}$$

where $0 < R < 1$ is the free parameter of the method, $t_{\max}$ is the largest value of time range over which $\tilde{f}(t)$ is to be obtained, N_ψ is also the free parameter of the method.

Suppose we are restricted by the maximum value $\omega_{\max} > 0$ of the imaginary parts of sampling frequencies $s(\phi)$. To determine value $\phi_{\max}$ corresponding to value $\omega_{\max}$, so that $|\mathrm{Im}(s(\phi_{\max}))| = \omega_{\max}$, we first solve the following the equation

$$\frac{\partial \mathrm{Im}\left(\gamma\left(\mathrm{Re}^{i\phi}\right)\right)}{\partial\phi} = 0, \tag{29.41}$$

to establish maximum value of $|\mathrm{Im}(s(\phi))|$ and compare it to $\omega_{\max}$ since imaginary part of the characteristic function $\gamma\left(\mathrm{Re}^{i\phi}\right)$ has only one local extremum in $[0, \pi]$. Expanding (29.41) we get

$$\frac{\partial \mathrm{Im}\left(\gamma\left(\mathrm{Re}^{i\phi}\right)\right)}{\partial\phi} = -2R\cos(\phi) + R^2 cos(2\phi) = 2R^2(cos(\phi))^2 - 2R\cos(\phi) - R^2 = 0, \tag{29.42}$$

$$\phi = \phi^* = \arccos\left(\frac{1 - \sqrt{2R^2 + 1}}{2R}\right). \tag{29.43}$$

If $|\mathrm{Im}(s(\phi^*))| > \omega_{\max}$ then we solve the following equation for the value $\phi_{\max}$

$$\mathrm{Im}(s(\phi_{\max})) = -\omega_{\max} \text{ or } \mathrm{Im}\left(\gamma\left(Re^{i\phi_{\max}}\right)\right) = -\frac{t_{\max}\omega_{\max}}{N_\psi} \text{ or} \tag{29.44}$$

$$-2R\sin(\phi_{\max}) + \frac{1}{2}R^2\sin(2\phi_{\max}) = -\frac{t_{\max}\omega_{\max}}{N_\psi},\ 0 < \phi_{\max} < \phi^* < \pi, \tag{29.45}$$

which we can solve using any suitable numerical root-finding method.

If $|\mathrm{Im}(s(\phi^*))| \le \omega_{\max}$ then we set $\phi_{\max} = \pi$. To evaluate integral in (29.39), we discard the part of the integral where $\phi > \phi_{\max}$

$$\begin{aligned}\psi_k(sF(s)) &= \frac{R^{-k}}{2\pi}\int_0^{\phi_{\max}} s(\phi)F(s(\phi))e^{-ik\phi}d\phi \\ &= \mathrm{Re}\left[\frac{R^{-k}}{\pi}\int_0^{\phi_{\max}} s(\phi)F(s(\phi))e^{-ik\phi}d\phi\right],\end{aligned} \tag{29.46}$$

and use trapezoidal rule with L equal subintervals $\phi_{\max}/L$ for the rest

$$\begin{aligned}\psi_k(sF(s)) = \frac{\phi_{\max}R^{-k}}{\pi L}\mathrm{Re}\Bigg[\Bigg(\sum_{p=0}^{L} s\left(\phi_p\right)F\left(s\left(\phi_p\right)\right)\mathrm{e}^{-ik\phi_p} \\ - \frac{s(0)F(s(0))+s(\phi_{\max})F(s(\phi_{\max}))e^{-ik\phi_{\max}}}{2}\Bigg)\Bigg],\end{aligned} \tag{29.47}$$

with $\phi_p = \phi_{\max}p/L$.

To make comparison with Durbin's method easier we require that L satisfies the same relationship as N_{sum}

$$L = \left[\frac{\omega_{\max}T}{\pi}\right] = \left[\frac{\omega_{\max}T^*t_{\max}}{\pi}\right], \tag{29.48}$$

where $T^* > 0$ is the free parameter.

Following [10], R can be determined from the relation

$$R = \varepsilon^{\frac{1}{2(N_\psi+1)}}, \tag{29.49}$$

where ε is problem dependent and usually $10^{-20} < \varepsilon < 10^{-1}$.

With (29.48) and (29.49) the input parameters in the CQM are same as in Durbin's method, namely $\omega_{\max}$ and $t_{\max}$, the free parameters are N_ψ, T^* and ε. Because of higher number of free parameters and the intertwined nature of their relationships in the CQM, it is difficult to produce explicit recommendations for choosing optimal values of the free parameters even for this particular problem. We performed a considerable number of numerical experiments and there are our general observations. For a fixed value of T^* the relative error R_{err} significantly depends on N_ψ and less on

ε. For the problem under consideration choosing $10^{-8} < \varepsilon < 10^{-2}$ yields acceptable results for a large range of $\omega_{\max}$ and $t_{\max}$. For a fixed value of ε again the relative error greatly depends on N_ψ, which in turn depends on $\omega_{\max}$. The relationship seems to be similar to dependence of κ on $\omega_{\max}$ in Durbin's method – the greater $\omega_{\max}$ the bigger N_ψ should be. Error depends on value of T^* much less. Basically, values of T^* greater than 0.75 do not noticeably improve accuracy. For the large values of N_ψ and therefore small value of $\phi_{\max}$, taking $\varepsilon = 10^{-2\kappa}$, where κ is the free parameter of Durbin's method, leads to the sampling frequencies defined in (29.40) with real parts roughly the same as defined in (29.33). Overall, largest pointwise absolute errors are located around peaks.

In Fig. 29.9 and 29.10 we present solutions $\tilde{u}(t)$ and $\tilde{w}(t)$ inverted with CQM with parameters $t_{\max} = 0.5$, $\omega_{\max} = 2000$, $T^* = 1.0$, $\varepsilon = 10^{-4}$, $N_\psi = 5 \cdot 10^5$ ($L = 319$, $\mathrm{Re}(s(\phi)) \approx 9.21$) and corresponding pointwise absolute errors A_{err}.

Results obtained with the CQM and depicted in Figs. 29.9 and 29.10 are very close to the results obtained with Durbin's method. In Fig. 29.11 we compare the errors R_{err} obtained with the CQM and Durbin's method for $500 \le \omega_{\max} \le 30{,}000$. The shared free parameters are $t_{\max} = 0.5$ and $T^* = 1.0$, also $\kappa = 3.0$ for Durbin's method and $\varepsilon = 10^{-2\kappa} = 10^{-6}$, $N_\psi = 1 \cdot 10^6$ for the CQM. With this choice of

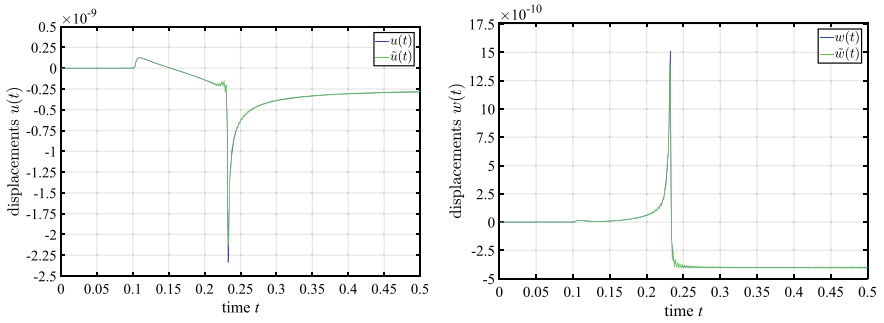

Fig. 29.9 Comparison of CQM inverted solutions and reference solutions for **a** $u(t)$, **b** $w(t)$

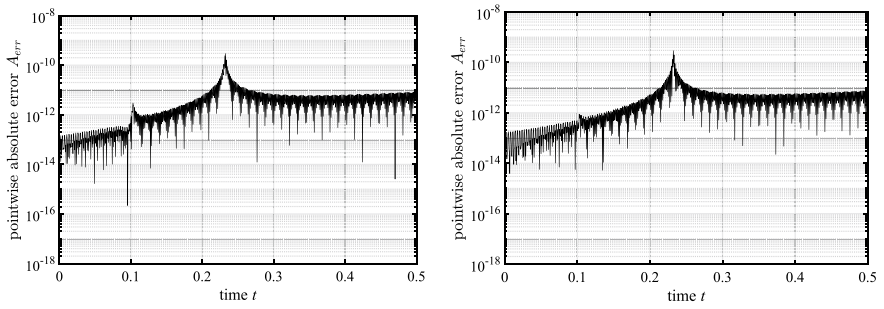

Fig. 29.10 Pointwise absolute error A_{err} with CQM for **a** $u(t)$, **b** $w(t)$

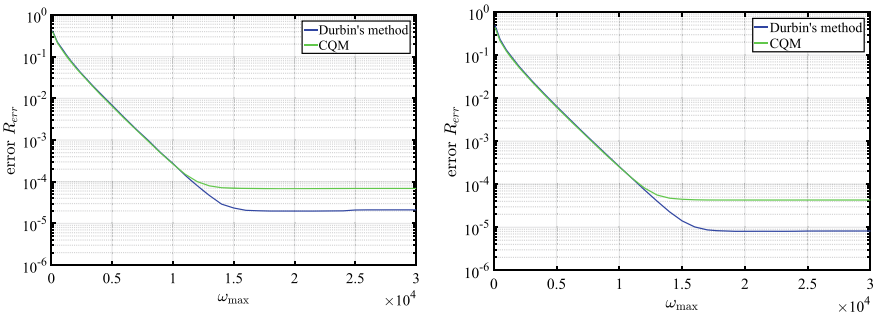

Fig. 29.11 Comparison of Durbin's method and CQM for **a** $\tilde{u}(t)$, **b** $\tilde{w}(t)$

parameters both methods produce the same number of sampling frequencies for each $\omega_{\max}$. Until $\omega_{\max} \approx 11{,}000$ both methods demonstrate very close accuracy.

29.5 Conclusions

Both considered methods for numerical inversion of Laplace transforms are almost identical accuracy-wise with a right choice of free parameters. The Durbin's method have only two free parameters and choosing their values is much more straightforward, while CQM have three free parameters and choosing their optimal values can be rather complicated. Overall CQM does not seem to provide any special features or present any apparent advantages over Durbin's method in the problems such as considered.

Acknowledgements The work is financially supported by the Russian Science Foundation under grant No. 18-79-00082.

References

1. C.Y. Wang, J.D. Achenbach, Elastodynamic fundamental solutions for anisotropic solids. Geophys. J. Int. **118**(2), 384 (1994)
2. C.Y. Wang, J.D. Achenbach, Three-dimensional time-harmonic elastodynamic Green's functions for anisotropic solids. Proc. R. Soc. A **449**(1937), 441 (1995)
3. F. Durbin, Numerical inversion of Laplace transforms: An efficient improvement to Dubner and Abate's method. Comput. J. **17**(4), 371 (1974)
4. K.S. Crump, Numerical inversion of Laplace transforms using a Fourier series approximation. J. ACM **23**(1), 89 (1976)
5. F. de Hoog, J. Knight, A. Stokes, An improved method for numerical inversion of Laplace transforms. SIAM J. Sci. Stat. Comput. **3**(3), 357 (1982)
6. G. Honig, U. Hirdes, A method for the numerical inversion of Laplace transforms. J. Comput. Appl. Math. **10**(1), 113 (1984)

7. X. Zhao, An efficient approach for the numerical inversion of Laplace transform and its application in dynamic fracture analysis of a piezoelectric laminate. Int. J. Solids Struct. **41**(13), 3653 (2004)
8. C. Lubich, Convolution quadrature and discretized operational calculus. I. Numer. Math. **52**(2), 129 (1988)
9. C. Lubich, Convolution quadrature and discretized operational calculus. II. Numer. Math. **52**(4), 413 (1988)
10. M. Schanz, *Wave Propagation in Viscoelastic and Poroelastic Continua: A Boundary Element Approach* (Springer, Berlin, Heidelberg, 2001), 170p
11. C.L. Pekeris, The seismic surface pulse. Proc. Natl. Acad. Sci. **41**(7), 469 (1955)
12. M. Eskandari-Ghadi, S. Sattar, Axisymmetric transient waves in transversely isotropic half-space. Soil Dyn. Earthq. Eng. **29**(2), 347 (2009)
13. H.G. Georgiadis, D. Vamvatsikos, I. Vardoulakis, Numerical implementation of the integral-transform solution to Lamb's point-load problem. Comput. Mech. **24**(2), 90 (1999)
14. J. Xiao, W. Ye, L. Wen, Efficiency improvement of the frequency-domain BEM for rapid transient elastodynamic analysis. Comput. Mech. **52**(4), 903 (2013)
15. M. Schanz, W. Ye, J. Xiao, Comparison of the convolution quadrature method and enhanced inverse FFT with application in elastodynamic boundary element method. Comput. Mech. **57**(4), 523 (2016)
16. P. Wynn, On a device for computing the em(Sn) transformation. Math. Tables Other Aids Comput. **10**(54), 91 (1956)

Chapter 30
Twofold Re-reflections of Ultrasonic Waves from Obstacles in a Two-Dimensional Elastic Material, Taking into Account Any Laws of Their Reflections and Transformations

Nikolay V. Boyev

Abstract In this chapter, the problem of the diffraction of ultrasonic waves by cavity obstacles in an infinite two-dimensional elastic medium with double reflections is studied. A short pulse is introduced into the elastic medium with tonal filling with several periods of a plane high-frequency, monochromatic longitudinal or transverse elastic wave. Double re-reflections of waves with any possible reflections (longitudinal wave to longitudinal, transverse to transverse waves) and transformations (longitudinal waves to transverse, transverse waves to longitudinal) are considered. The integral representations of the displacements in the reflected waves are written out on the basis of the physical theory of Kirchhoff diffraction. An asymptotic estimate of multiple diffraction integrals using the multidimensional stationary phase method gives an explicit form of the geometrical optical approximation of displacements in doubly reflected and transformed waves.

30.1 Introduction

High-frequency waves are used in ultrasonic testing of elastic materials to detect possible accumulations of cavity defects, solid and elastic inclusions, and also to study the properties of metamaterials. In the propagation of high-frequency waves in clusters of obstacles, both multiple re-reflections of waves and their transformation on the boundary contours of obstacles are possible. A numerical study of the problems of short-wavelength diffraction of elastic waves is significantly complicated if the wavelength is much less than the average size of the obstacle. In connection with this circumstance, obtaining and applying explicit analytical expressions for the characteristics of the wave field in the framework of the geometric theory of diffraction (GTD) is an urgent task. The filtration properties of the metamaterial, which is an elastic matrix of hardened epoxy resin and containing a three-period system of

N. V. Boyev (✉)
Southern Federal University, 105/42 Bolshaya Sadovaya Str., Rostov-on-Don, Russia 344006
e-mail: boyev@math.rsu.ru

I. A. Parinov et al. (eds.), *Advanced Materials*, Springer Proceedings in Materials 6, https://doi.org/10.1007/978-3-030-45120-2_30

hard balls, were studied experimentally [1] in a wide frequency range. A theoretical justification of these properties was obtained [2] in the acoustic approximation. The study of single and double scattering of short acoustic waves is the subject of [3–5]. A complete study of the features of the passage of high-frequency waves through clusters of obstacles in elastic media can be carried out on the basis of GTD methods taking into account all kinds of multiple reflections and transformations of elastic waves. In this paper, we consider all the laws of double reflections and transformations of short waves in a two-dimensional elastic medium containing obstacles in the form of cavities.

30.2 Problem Statement

In an infinite two-dimensional elastic medium there is a cluster of cavity obstacles. An unsteady short pulse of a special structure propagating in an elastic medium was chosen as a dynamic effect on the accumulation of defects. The pulse is filled with 6–12 periods of a plane high-frequency monochromatic elastic wave. The diffracted waves that passed through with any possible reflections and transformations can be received in any region of the elastic medium.

The task consists in a complete analytical study in the framework of GTD of all possible sequences of double reflections and transformations of elastic waves at the boundary contours of obstacles due to the fact that they form the basis for obtaining explicit expressions of the characteristics of the wave field for any laws of multiple reflections and wave transformations.

30.3 Solution Method

The tonal filling of the short pulse introduced into the obstacle cluster with a sufficient number of periods (6–12 periods) of the monochromatic wave allows us to study the task in the mode of harmonic oscillations. In this case, the incident wave is a superposition of point sources of circular waves. During discretization, each circular wave is replaced by a system of radial propagation rays of the elastic wave and only those rays that are directed toward the obstacles and interact with them are taken into account. Thus, the problem reduces to solving the problem of short-wavelength diffraction of elastic waves, taking into account their re-reflections and transformations in a local setting.

30.4 Study of the Problem in a Local Formulation

At point $\tilde{x}_0$ of an infinite elastic two-dimensional medium, there is a pulsating point source of a circular monochromatic wave generated by a concentrated force $\mathbf{Q}e^{-i\omega t}$, where ω is the oscillation frequency. We consider the directions $\mathbf{q}$ of wave propagation oriented on the boundary contour l of an obstacle or an accumulation of obstacles located in the elastic plane. In this case, the displacements at the point $\tilde{y}$ of the elastic plane caused by the point source are determined by the Kupradze matrix [6].

The goal is to study the amplitude characteristics of the scattered field at the contours of obstacles, taking into account all possible options for twofold reflections and transformations of elastic waves.

In the directions $\mathbf{q}$ and $\mathbf{q_1}$ at $\tilde{y}$, we have asymptotic representations of the amplitudes of displacements in the incident wave:

$$\mathbf{u}_{\mathbf{q}}^{(p)}(y) = \frac{Q_{\mathbf{q}}}{4\mu}\mathbf{q}i\frac{k_p^2}{k_s^2}\sqrt{\frac{2}{\pi k_p}}e^{-i\frac{\pi}{4}}\frac{e^{ik_pR_0}}{\sqrt{R_0}}\left[1+\mathrm{O}\left(\left(\frac{1}{k_pR_0}\right)\right)\right],\ Q_{\mathbf{q}} = (\mathrm{Q},\mathrm{q}), \quad (30.1)$$

$$\mathbf{u}_{\mathbf{q_1}}^{(s)}(y) = \frac{Q_{\mathbf{q}_1}}{4\mu}\mathbf{q}_1 i\sqrt{\frac{2}{\pi k_s}}e^{-i\frac{\pi}{4}}\frac{e^{ik_sR_0}}{\sqrt{R_0}}\left[1+\mathrm{O}\left(\frac{1}{k_sR_0}\right)\right],\ Q_{\mathbf{q}_1} = \left(\mathrm{Q},\mathrm{q}_1\right). \quad (30.2)$$

Here, the tangential direction $\mathbf{q_1}$ is perpendicular to the direction of wave $\mathbf{q}$ propagation. $Q_{\mathbf{q}}$ and $Q_{\mathbf{q}_1}$ are projections of the force $\mathbf{Q}$ on the directions $\mathbf{q_1}$ and $\mathbf{q}$. In Formulae (30.1), (30.2) and below, ρ is the density, λ, μ are the Lame coefficients, $k_p = \omega/c_p$, $k_s = \omega/c_s$, c_p and c_S are the wave numbers and velocities of the longitudinal and transverse waves. The components of the displacement vector of a wave reflected once from a free boundary contour at a point $\tilde{x}$ of the elastic plane are determined by the following integral [7]:

$$u_k(\tilde{x}) = \int_l \mathbf{T}_y[\mathbf{U}^{(k)}(\tilde{y},\tilde{x})]\cdot\mathbf{u}(\tilde{y})dl,\ k = 1,2, \quad (30.3)$$

$$\mathbf{T}_y\left[\mathbf{U}^{(k)}(\tilde{y},\tilde{x})\right] = 2\mu\frac{\partial\mathbf{U}^{(k)}}{\partial n} + \lambda\mathbf{n}\,\mathrm{div}\left(\mathbf{U}^{(k)}\right) + \mu\left(\mathbf{n}\times\mathrm{rot}\left(\mathbf{U}^{(k)}\right)\right), \quad (30.4)$$

where the Kupradze matrix $\mathbf{U}^{(k)}(\tilde{y},\tilde{x})$ is obtained from the matrix $\mathbf{U}^{(k)}(\tilde{y},\tilde{x}_0)$ by replacing $\tilde{x}_0$ by $\tilde{x}$ and R_0 by $R = |\tilde{y}-\tilde{x}|$; $\mathbf{T}_y$ is the force vector at the point $\tilde{y}$; $\mathbf{u}(\tilde{y})$ is the vector of the total displacement field on the boundary surface; $\mathbf{n}$ is the external normal to the contour l directed toward the elastic medium.

In the vectors of total elastic displacement on the boundary contour and in the vector $\mathbf{T}_y$ at the point $\tilde{y}$, we select the terms determined by the longitudinal (p-wave) and transverse (s-wave) waves.

$$u_k(\tilde{x}) = \int\limits_l \left\{ \mathbf{T}_y[\mathbf{U}_p^{(k)}(\tilde{y}, \tilde{x})] + \mathbf{T}_y[\mathbf{U}_s^{(k)}(\tilde{y}, \tilde{x})] \right\} \cdot \left[\mathbf{u}(\tilde{y};\, p) + \mathbf{u}(\tilde{y};\, s) \right] dl_y \quad (30.5)$$

$$u_k(\tilde{x}) = \int\limits_l \mathbf{T}_y[\mathbf{U}_p^{(k)}(\tilde{y}, \tilde{x})] \cdot \mathbf{u}(\tilde{y};\, p) dl_y + \int\limits_l \mathbf{T}_y[\mathbf{U}_s^{(k)}(\tilde{y}, \tilde{x})] \cdot \mathbf{u}(\tilde{y};\, p) dl_y$$
$$+ \int\limits_l \mathbf{T}_y[\mathbf{U}_p^{(k)}(\tilde{y}, \tilde{x})] \cdot \mathbf{u}(\tilde{y};\, s) dl_y + \int\limits_l \mathbf{T}_y[\mathbf{U}_s^{(k)}(\tilde{y}, \tilde{x})] \cdot \mathbf{u}(\tilde{y};\, s) dl_y \quad (30.6)$$

The first and last terms in Formula (30.6) describe the *p–p* and *s–s* reflections, and the second and third terms *p–s* and *s–p* of the transformation.

Direct use of the integral representation of displacements (30.3) over the entire "light" zone for an obstacle in the form of a cavity describes only once-reflected waves.

In [3–5], for a two-dimensional and three-dimensional problems in the case of a single reflection, an asymptotic solution is constructed that is local in nature and gives a geometrical optical approximation of the diffracted field amplitude in a small neighborhood of any ray emerging from a point $\tilde{x}_0$ reflected from the boundary contour of an obstacle at a point $\tilde{y}^*$ and arriving at the point $\tilde{x}$ of reception of the elastic medium.

30.5 Double Re-reflection of Elastic Waves from the Plane Contours of Obstacles, Taking into Account Possible Transformations

Double reflection of the wave can occur both from the contour of one non-convex obstacle, and from two obstacles, including a non-convex shape. Obtaining explicit expressions of the displacement amplitude in re-reflected and transformed waves based on the use of geometric considerations and Keller GTD divergence coefficients [8]. In the short-wavelength diffraction problem, taking into account multiple reflections and transformations on obstacles in an elastic medium, it is more convenient, in our opinion, to proceed from integral representations of the Kirchhoff physical theory of diffraction [8]. For the asymptotic estimation of the arising diffraction multiple integrals of rapidly oscillating functions, it is possible to use the multidimensional stationary phase method.

Note that the integral Formula (30.3) gives only a once reflected wave. For repeatedly reflected waves, the application of the integral representation (30.3) is possible only in the modification [9]. Following this modification, doubly reflected and transformed waves at the receiving point will be found by repeated integration of the rays successively over the neighborhoods l_1^* and l_2^* of the mirror reflection points $\tilde{y}_1^*$ and $\tilde{y}_2^*$, respectively. The applied modification [9] of the integral representation (30.3) means that when finding the leading term of the asymptotics of the double diffraction

integral, we will be in the framework of calculating the displacement amplitude in the wave twice reflected with possible transformations according to the GTD.

We consider the re-reflection of a high-frequency wave using the example of re-reflection of a ray $\tilde{x}_0 - \tilde{y}_1^* - \tilde{y}_2^* - \tilde{x}_3$ emitted from a point $\tilde{x}_0$ [p-wave (30.1)] and received at a point $\tilde{x}_3$ with a possible twofold transformation p–s–p.

The components of the p-wave displacement vector at the receiving point $\tilde{x}_3$ are given by the following formula:

$$u_k^{(p)}(\tilde{x}_3) = \int\limits_{l_2^*} \mathbf{T}_{y_2}\left[\mathbf{U}_p^{(k)}(\tilde{y}_2, \tilde{x}_3)\right] \cdot \mathbf{u}(\tilde{y}_2; s) dl_2. \tag{30.7}$$

Here $\mathbf{u}(\tilde{y}_2)$ is the vector of complete displacement at the point $\tilde{y}_2 \in l_2^*$ of the neighborhood of the point $\tilde{y}_2^*$, which is determined after the first p–s transformation on the neighborhood l_1^* of the reflection point $\tilde{y}_1^*$.

In the asymptotic estimate of the Kirchhoff integral in (30.7), the components of the vector of the total displacement field $u_k(\tilde{y}_2)$, $k = 1, 2$ under the sign of the integral should be chosen as a solution to the local diffraction problem of reflection of a plane incident s-wave [10], formed with p–s transformation on the neighborhood l_1^* of the reflection point $\tilde{y}_1^*$.

$$\begin{aligned} u_1(\tilde{y}_2; s) &= \left(V_{ss}(\tilde{y}_2) - 1 - tg\gamma_1 V_{sp}(\tilde{y}_2)\right) u_1^{(s)}(\tilde{y}_2), \\ u_2(\tilde{y}_2; s) &= \left(V_{ss}(\tilde{y}_2) + 1 + \frac{k_p}{k_s \sin\gamma_1}\sqrt{1 - \frac{k_s^2}{k_p^2}\sin^2\gamma_1} V_{sp}(\tilde{y}_2)\right) u_2^{(s)}(\tilde{y}_2), \end{aligned} \tag{30.8}$$

where $V_{ss}(\tilde{y}_2)$ and $V_{sp}(\tilde{y}_2)$ are the reflection coefficients s–s and s–p of the transformation [11].

At the same time, the components of the displacement vector $u_k^{(s)}(\tilde{y}_2)$, $k = 1, 2$ in Formula (30.8) themselves are expressed by a similar formula:

$$u_k^{(s)}(\tilde{y}_2) = \int\limits_{l_1^*} \mathbf{T}_{y_1}\left[\mathbf{U}_s^{(k)}(\tilde{y}_1, \tilde{y}_2)\right] \cdot \mathbf{u}(\tilde{y}_1; p) dl_1, \tag{30.9}$$

where the vector of the total displacement field $\mathbf{u}(\tilde{y}_1; p)$ (30.9) at points $\tilde{y}_1 \in l_1^*$ of the neighborhood of $\tilde{y}_1^*$ should be chosen as a solution to the local diffraction problem of reflection of a plane incident $p-$ wave (30.1) [10]:

$$\begin{aligned} u_1(\tilde{y}; p) &= \left(1 + V_{pp}(\tilde{y}) - \frac{k_s}{k_p \sin\gamma}\sqrt{1 - \frac{k_p^2}{k_s^2}\sin^2\gamma} V_{ps}(\tilde{y})\right) u_{1q}^{(p)}(\tilde{y}), \\ u_2(\tilde{y}; p) &= \left(1 - V_{pp}(\tilde{y}) - tg\gamma V_{ps}(\tilde{y})\right) u_{2q}^{(p)}(\tilde{y}), \end{aligned} \tag{30.10}$$

where V_{pp} and V_{ps} are the reflection coefficients p–p and p–s of the transformation [10], and $u_{1q}^{(p)}(\tilde{y})$ and $u_{2q}^{(p)}(\tilde{y})$ are the components of the displacement vector $\mathbf{u}_q^{(p)}(\tilde{y})$

in the incident p-wave (30.1). After substituting (30.10) in (30.9) and (30.9) in (30.8) and (30.8) in (30.7) and moving to the local polar coordinate system r, θ at the specular reflection point $\tilde{y}_2^*$, we arrive at the components of radial displacement at the point $\tilde{x}_3$:

$$u_r^{(p)}(\tilde{x}_3) = -\frac{Q_{\mathfrak{q}}}{4\pi\mu}\left(\frac{k_p}{k_s}\right)^2 2k_s\sqrt{\frac{2}{\pi k_s}}\frac{k_p}{2k_s}\left(-\frac{k_p}{2k_s}\right)e^{-i\frac{\pi}{4}}\frac{\cos\gamma_1\cos\gamma_3}{\sqrt{L_0L_1L_2}} \times V_{ps}(\tilde{y}_1^*)V_{sp}(\tilde{y}_2^*)\int\limits_{l_2^*}\int\limits_{l_1^*} e^{ik_p\phi_{psp}}dl_1dl_2, \tag{30.11}$$

$$u_\theta^{(p)}(\tilde{x}_3) = 0,$$
$$\phi_{psp} = |\tilde{x}_0 - \tilde{y}_1| + \frac{k_s}{k_p}|\tilde{y}_1 - \tilde{y}_2| + |\tilde{y}_2 - \tilde{x}_3|, \tag{30.12}$$
$$L_0 = |\tilde{x}_0 - \tilde{y}_1^*|,\ L_1 = |\tilde{y}_1^* - \tilde{y}_2^*|,\ L_2 = |\tilde{y}_2^* - \tilde{x}_3|.$$

At points of direct specular reflection $\tilde{y}_1^* \in l_1^*$ and $\tilde{y}_2^* \in l_2^*$, we assign the neighborhoods of these points to Cartesian coordinate systems $O_1X_1^{(1)}X_2^{(1)}$ and $O_2X_1^{(2)}X_2^{(2)}$ defined by the normals $\mathbf{n}_1 = O_1X_2^{(1)}$, $\mathbf{n}_2 = O_2X_2^{(2)}$ and tangent to the contour of the obstacle. Along the contours from the points $\tilde{y}_1^*$ and $\tilde{y}_2^*$, we count the lengths of the arcs Δs_1 in the vicinity of l_1^* and Δs_2 in the vicinity of l_2^*. For small Δs_1 and Δs_2 up to small second-order inclusive expressions for the first and third terms in phase φ_{psp} have the following form:

$$|\tilde{x}_0 - \tilde{y}_1| = L_0 + \Delta s_1 \sin\gamma_1^{(p)} + \frac{1}{2}\left(L_0^{-1}\cos^2\gamma_1^{(p)} + \frac{\cos\gamma_1^{(p)}}{\rho_1}\right)(\Delta s_1)^2, \tag{30.13}$$

$$|\tilde{y}_2 - \tilde{x}_3| = L_2 - \Delta s_2 \sin\gamma_2^{(p)} + \frac{1}{2}\left(L_2^{-1}\cos^2\gamma_2^{(p)} + \frac{\cos\gamma_2^{(p)}}{\rho_2}\right)(\Delta s_2)^2. \tag{30.14}$$

For p–s–p transformation, $\left\{-\sin\gamma_1^{(p)}, -\cos\gamma_1^{(p)}\right\}$ is the vector which determines the direction of the p-wave (30.1), and $\left\{-\sin\gamma_1^{(s)}, \cos\gamma_1^{(s)}\right\}$ is the direction of the reflected wave relatively the coordinate system $O_1X_1^{(1)}X_2^{(1)}$ at the point y_1^*, and $\left\{-\sin\gamma_2^{(s)}, -\cos\gamma_2^{(s)}\right\}$ is the vector determining the direction of incidence of the s-wave reflected at point y_1^* with respect to the coordinate system $O_2X_1^{(2)}X_2^{(2)}$ at the point $\tilde{y}_2^*$; while $\left\{-\sin\gamma_2^{(p)}, \cos\gamma_2^{(p)}\right\}$ is the direction of the reflected p-wave at the point $\tilde{y}_2^*$.

Let us find the term $|\tilde{y}_1 - \tilde{y}_2| = |\tilde{\mathbf{y}}_2\tilde{\mathbf{y}}_1|$ in the phase ϕ_{psp} (30.12). The points $\tilde{y}_1 \in l_1^*$ and $\tilde{y}_2 \in l_2^*$ in the local Cartesian coordinate systems $O_1X_1^{(1)}X_2^{(1)}$ and $O_2X_1^{(2)}X_2^{(2)}$ have the coordinates $\tilde{y}_1\left(-\Delta s_1, -\frac{(\Delta s_1)^2}{2\rho_1}\right)$ and $\tilde{y}_2\left(-\Delta s_2, -\frac{(\Delta s_2)^2}{2\rho_2}\right)$, where ρ_i are the radii of curvature of the boundary contours l_1 and l_2 of the two obstacles, respectively, at points $\tilde{y}_1^*$ and $\tilde{y}_2^*$. The distance $|\tilde{y}_1 - \tilde{y}_2|$ is considered in the coordinate

system $O_2X_1^{(2)}X_2^{(2)}$. In this coordinate system we denote the coordinates of the points $\tilde{y}_1(\xi_1, \eta_1)$, $\tilde{y}_2(\xi_2, \eta_2)$, $\tilde{y}_1^*\left(\xi_1^0, \eta_1^0\right)$. Taking this into account, we represent the vector $\tilde{\mathbf{y}}_2\tilde{\mathbf{y}}_1$ in the form:

$$\begin{gathered}\tilde{\mathbf{y}}_2\tilde{\mathbf{y}}_1 = \tilde{\mathbf{y}}_2^*\tilde{\mathbf{y}}_1^* + \mathbf{A}\tilde{\mathbf{y}}_1^*\tilde{\mathbf{y}}_1 - \tilde{\mathbf{y}}_2^*\tilde{\mathbf{y}}_2, \\ \tilde{\mathbf{y}}_2\tilde{\mathbf{y}}_1 = \{\xi_1 - \xi_2,\ \eta_1 - \eta_2\}, \tilde{\mathbf{y}}_2^*\tilde{\mathbf{y}}_1^* = \left\{\xi_1^0,\ \eta_1^0\right\}.\end{gathered} \tag{30.15}$$

Here $\mathbf{A} = \left(a_{ij}\right), i, j = 1, 2$ is the orthogonal transition matrix from the basis of the Cartesian coordinate system $O_2X_1^{(2)}X_2^{(2)}$ at the point $\tilde{y}_2^*$ to the basis of the Cartesian coordinate system $O_1X_1^{(1)}X_2^{(1)}$ at the point $\tilde{y}_1^*$. The matrix $\mathbf{A}$ has the form:

$$\mathbf{A} = \begin{pmatrix} \cos\alpha & -\sin\alpha \\ \sin\alpha & \cos\alpha \end{pmatrix}. \tag{30.16}$$

In the local coordinate systems, the vectors $\tilde{\mathbf{y}}_1^*\tilde{\mathbf{y}}_1$ and $\tilde{\mathbf{y}}_2^*\tilde{\mathbf{y}}_2$ have coordinates $\tilde{\mathbf{y}}_i^*\tilde{\mathbf{y}}_i\left(-\Delta s_i, -\frac{(\Delta s_i)^2}{2\rho_i}\right)$. Substituting the coordinates of all the vectors in relation (30.15), one obtains:

$$\begin{aligned}|\tilde{y}_1 - \tilde{y}_2| &= \left[(\xi_1 - \xi_2)^2 + (\eta_1 - \eta_2)^2\right]^{1/2} \\ &= \left[\left(\xi_1^0 - \Delta s_1\cos\alpha + \frac{(\Delta s_1)^2}{2\rho_1} + \Delta s_2\right)^2\right. \\ &\left. + \left(\eta_1^0 - \Delta s_1\sin\alpha - \frac{(\Delta s_1)^2}{2\rho_1}\cos\alpha + \frac{(\Delta s_2)^2}{2\rho_2}\right)^{1/2}\right.\end{aligned} \tag{30.17}$$

Expanding the square root in powers of Δs_1 and Δs_2 on the right-hand side of (30.17), we obtain the following asymptotic representation of the distance up to small second-order inclusive:

$$\begin{aligned}|\tilde{y}_1 - \tilde{y}_2| &= L_1 - \Delta s_1\sin\gamma_1^{(s)} + \Delta s_2\sin\gamma_2^{(s)} \\ &+ \frac{1}{2}\left(L_1^{-1}\cos^2\gamma_1^{(s)} + \frac{\cos\gamma_1^{(s)}}{\rho_1}\right)(\Delta s_1)^2 \\ &+ \frac{1}{2}\left(L_1^{-1}\cos^2\gamma_2^{(s)} + \frac{\cos\gamma_2^{(s)}}{\rho_2}\right)(\Delta s_2)^2 \\ &+ L_1^{-1}\Delta s_1\Delta s_2\cos\gamma_1^{(s)}\cos\gamma_2^{(s)}.\end{aligned} \tag{30.18}$$

Summing up the expressions $|x_0 - y_1|$, $\frac{k_s}{k_p}|y_1 - y_2|$, $|y_2 - x_3|$ and using Snell's law $k_p\sin\gamma_1^{(p)} = k_s\sin\gamma_1^{(s)}$, $k_s\sin\gamma_2^{(s)} = k_p\sin\gamma_2^{(p)}$, we write out the relation for phase φ_{psp} (30.12):

$$\phi_{psp} = L_0 + \frac{k_s}{k_p} L_1 + L_2 + \frac{1}{2}\left(\frac{\cos^2 \gamma_1^{(p)}}{L_0} + \frac{k_s \cos^2 \gamma_1^{(s)}}{k_p L_1} + \frac{\cos \gamma_1^{(p)}}{\rho_1} + \frac{k_s \cos \gamma_1^{(s)}}{k_p \rho_1} \right) (\Delta s_1)^2 + \frac{\cos \gamma_1^{(s)} \cos \gamma_2^{(p)}}{L_1} + \frac{1}{2}\left(\frac{k_s \cos^2 \gamma_2^{(s)}}{k_p L_1} + \frac{\cos^2 \gamma_2^{(p)}}{L_2} + \frac{k_s \cos \gamma_2^{(s)}}{k_p \rho_2} + \frac{\cos \gamma_2^{(p)}}{\rho_2} \right) (\Delta s_2)^2.$$

Phase φ_{psp} does not contain terms with the first powers Δs_1 and Δs_2. This suggests that the specular reflection points are stationary for phase φ_{psp}.

The leading term in the asymptotic behavior of the diffraction double integral (30.11) can be obtained using the two-dimensional stationary phase method [11]:

$$u_r^{(p)}(\tilde{x}_3) = -\frac{Q_{\mathbf{q}}}{\mu} \frac{k_p}{k_s} \sqrt{\frac{2}{\pi k_s}} e^{-i\frac{\pi}{4}} \frac{\cos \gamma_1 \cos \gamma_3}{\sqrt{L_0 L_1 L_2}} \times V_{ps}\left(\tilde{y}^*\right) V_{sp}\left(\tilde{y}^*\right) \times \frac{\exp\left\{ i\left[k_p L_0 + k_s L_1 + k_p L_2 + \frac{\pi}{4}\left(\delta_2^{(psp)} - 2 \right) \right] \right\}}{\sqrt{\left| \det D_2^{(psp)} \right|}} \tag{30.19}$$

Here $D_2^{(psp)}$ is the Hessian matrix:

$$D_2^{(psp)} = \begin{pmatrix} \dfrac{\cos^2 \gamma_1^{(p)}}{L_0} + \dfrac{k_s \cos^2 \gamma_1^{(s)}}{k_p L_1} + \dfrac{\cos \gamma_1^{(p)}}{\rho_1} + \dfrac{k_s \cos \gamma_1^{(s)}}{k_p \rho_1} & \dfrac{\cos \gamma_1^{(s)} \cos \gamma_2^{(p)}}{L_1} \\ \dfrac{\cos \gamma_1^{(s)} \cos \gamma_2^{(p)}}{L_1} & \dfrac{k_s \cos^2 \gamma_2^{(s)}}{k_p L_1} + \dfrac{\cos^2 \gamma_2^{(p)}}{L_2} + \dfrac{k_s \cos \gamma_2^{(s)}}{k_p \rho_2} + \dfrac{\cos \gamma_2^{(p)}}{\rho_2} \end{pmatrix},$$

and $\delta_2^{(psp)} = \operatorname{sign} D_2^{(psp)} = \nu^+ - \nu^-$ is the difference between the number of positive ν^+ and negative ν^- eigenvalues of the Hessian matrix $D_2^{(psp)}$.

Thus, in this subsection we obtain the leading term of the asymptotics (30.19) of the displacement amplitude $u_r^{(p)}(\tilde{x}_3)$ in the reflected high-frequency longitudinal wave during *p-s-p* transformation from the surfaces of one or two obstacles located in an elastic medium in the two-dimensional case.

Explicit expressions of the main terms of displacements in doubly re-reflected waves along the ray $\tilde{x}_0 - \tilde{y}_1^* - \tilde{y}_2^* - \tilde{x}_3$ in the remaining seven cases of various possible

reflections and transformations of elastic waves, namely: *p-p-p*, *p-p-s*, *p-s-s*, *s-s-s*, *s-s-p*, *s-p-s*, *s-p-p* were obtained by the method described above.

30.5.1 Case of p-p-p Transformation

$$u_r^{(p)}(\tilde{x}) = M^{(ppp)} \frac{\exp\left\{i\left[k_p(L_0+L_1+L_2)+\frac{\pi}{4}\left(\delta_2^{(ppp)}-2\right)\right]\right\}}{\sqrt{L_0L_1L_2}\sqrt{\left|\det\left(D_2^{(ppp)}\right)\right|}},$$

$$u_\theta^{(p)}(\tilde{x}) = 0,\ M^{(ppp)} = \prod_{n=1}^{2} V_{pp}\left(\tilde{y}_n^*\right)\cos\gamma_n^{(p)},\ \delta_2^{(ppp)} = \operatorname{sign}\left(D_2^{(ppp)}\right)$$

$$D_2^{(ppp)} = \begin{pmatrix} \cos^2\gamma_1^{(p)}\left(\frac{1}{L_0}+\frac{1}{L_1}\right)+\frac{2\cos\gamma_1^{(p)}}{\rho_1} & \frac{\cos\gamma_1^{(p)}\cos\gamma_2^{(p)}}{L_1} \\ \frac{\cos\gamma_1^{(p)}\cos\gamma_2^{(p)}}{L_1} & \cos^2\gamma_2^{(p)}\left(\frac{1}{L_1}+\frac{1}{L_2}\right)+\frac{2\cos\gamma_2^{(p)}}{\rho_2} \end{pmatrix}. \tag{30.20}$$

30.5.2 Case of p-p-s Transformation

$$u_\theta^{(s)}(\tilde{x}) = M^{pps} \frac{\exp\left\{i\left[k_pL_0+k_pL_1+k_sL_2+\frac{\pi}{4}\left(\delta_2^{(pps)}-2\right)\right]\right\}}{\sqrt{L_0L_1L_2}\sqrt{\left|\det\left(D_2^{(pps)}\right)\right|}},$$

$$u_r^{(s)}(\tilde{x}) = 0,\ M^{(pps)} = \frac{k_p}{k_s}V_{pp}\left(\tilde{y}_1^*\right)V_{ps}\left(\tilde{y}_2^*\right)\cos\gamma_1^{(p)}\cos\gamma_2^{(s)},\ \delta_2^{(pps)} = \operatorname{sign}\left(D_2^{(pps)}\right),$$

$$D_2^{(pps)} = \begin{pmatrix} \cos^2\gamma_1^{(p)}\left(\frac{1}{L_0}+\frac{1}{L_1}\right)-\frac{2\cos\gamma_1^{(p)}}{\rho_1} & \frac{\cos\gamma_1^{(p)}\cos\gamma_2^{(s)}}{L_1} \\ \frac{\cos\gamma_1^{(p)}\cos\gamma_2^{(s)}}{L_1} & \frac{\cos^2\gamma_2^{(p)}}{L_1}+\frac{k_s\cos^2\gamma_2^{(s)}}{k_pL_2}+\frac{\cos\gamma_2^{(p)}}{\rho_2}+\frac{k_s\cos\gamma_2^{(s)}}{k_p\rho_2} \end{pmatrix}. \tag{30.21}$$

30.5.3 Case of p-s-p Transformation

This case was considered in detail above in the text.

30.5.4 *Case of* p-s-s *Transformation*

$$u_\theta^{(s)}(\tilde{x}) = M^{pss}\frac{\exp\left\{i\left[k_pL_0 + k_sL_1 + k_sL_2 + \frac{\pi}{4}\left(\delta_2^{(pss)} - 2\right)\right]\right\}}{\sqrt{L_0L_1L_2}\sqrt{\left|\det\left(D_2^{(pss)}\right)\right|}},$$

$$u_r^{(s)}(\tilde{x}) = 0,\ M^{(pss)} = \frac{k_p}{k_s}V_{ps}\left(\tilde{y}_1^*\right)V_{ss}\left(\tilde{y}_2^*\right)\cos\gamma_1^{(s)}\cos\gamma_2^{(s)},\ \delta_2^{(pss)} = \operatorname{sign}\left(D_2^{(pss)}\right),$$

$$D_2^{(pss)} = \begin{pmatrix} \dfrac{\cos^2\gamma_1^{(p)}}{L_0} + \dfrac{k_s\cos^2\gamma_1^{(s)}}{L_1} & \dfrac{\cos\gamma_1^{(s)}\cos\gamma_2^{(s)}}{L_1} \\ + \dfrac{\cos\gamma_1^{(p)}}{\rho_1} + \dfrac{k_s\cos\gamma_1^{(s)}}{\rho_2} & \\ \dfrac{\cos\gamma_1^{(s)}\cos\gamma_2^{(s)}}{L_1} & \cos^2\gamma_2^{(s)}\left(\frac{1}{L_1} + \frac{1}{L_2}\right) - \dfrac{2\cos\gamma_2^{(s)}}{\rho_2} \end{pmatrix}. \quad (30.22)$$

30.5.5 *Case of* s-s-s *Transformation*

$$u_\theta^{(s)}(\tilde{x}) = M^{(sss)}\frac{\exp\left\{i\left[k_s(L_0 + L_1 + L_2) + \frac{\pi}{4}\left(\delta_2^{(sss)} - 2\right)\right]\right\}}{\sqrt{L_0L_1L_2}\sqrt{\left|\det\left(D_2^{(sss)}\right)\right|}},$$

$$u_r^{(s)}(\tilde{x}) = 0,\ M^{(sss)} = \prod_{n=1}^{2}V_{ss}\left(\tilde{y}_n^*\right)\cos\gamma_n^{(s)},\ \delta_2^{(\mathrm{sss})} = \operatorname{sign}\left(D_2^{(\mathrm{sss})}\right),$$

$$D_2^{(\mathrm{sss})} = \begin{pmatrix} \cos^2\gamma_1^{(s)}\left(\frac{1}{L_0} + \frac{1}{L_1}\right) + \frac{2}{\cos\gamma_1^{(s)}} & \dfrac{\cos\gamma_1^{(s)}\cos\gamma_2^{(s)}}{L_1} \\ \dfrac{\cos\gamma_1^{(s)}\cos\gamma_2^{(s)}}{L_1} & \cos^2\gamma_2^{(s)}\left(\frac{1}{L_1} + \frac{1}{L_2}\right) + \dfrac{2\cos\gamma_2^{(s)}}{\rho_2} \end{pmatrix} \quad (30.23)$$

30.5.6 *Case of* s-s-p *Transformation*

$$u_r^{(p)}(\tilde{x}) = M^{(ssp)} \frac{\exp\left\{i\left[k_s(L_0+L_1)+k_pL_2+\frac{\pi}{4}\left(\delta_2^{(ssp)}-2\right)\right]\right\}}{\sqrt{L_0L_1L_2}\sqrt{\left|\det\left(D_2^{(ssp)}\right)\right|}}$$

$$u_\theta^{(s)}(\tilde{x}) = 0,\ M^{(ssp)} = \frac{k_p}{k_s} V_{ss}\left(\tilde{y}_1^*\right) V_{sp}\left(\tilde{y}_2^*\right) \cos\gamma_1^{(s)} \cos\gamma_2^{(p)},\ \delta_2^{(ssp)} = \operatorname{sign}\left(D_2^{(ssp)}\right),$$

$$D_2^{(ssp)} = \begin{pmatrix} \cos^2\gamma_1^{(s)}\left(\frac{1}{L_0}+\frac{1}{L_1}\right)+\frac{2\cos\gamma_1^{(s)}}{\rho_1} & \frac{\cos\gamma_1^{(s)}\cos\gamma_2^{(p)}}{L_1} \\ \frac{\cos\gamma_1^{(s)}\cos\gamma_2^{(p)}}{L_1} & \frac{\cos^2\gamma_2^{(s)}}{L_1}+\frac{k_s\cos^2\gamma_2^{(p)}}{k_sL_2}+\frac{\cos\gamma_2^{(s)}}{\rho_2}+\frac{k_p\cos\gamma_2^{(p)}}{\rho_2} \end{pmatrix}. \tag{30.24}$$

30.5.7 *Case of* s-p-s *Transformation*

$$u_\theta^{(s)}(\tilde{x}) = M^{(sps)} \frac{\exp\left\{i\left[k_sL_0+k_pL_1+k_sL_2+\frac{\pi}{4}\left(\delta_2^{(sps)}-2\right)\right]\right\}}{\sqrt{L_0L_1L_2}\sqrt{\left|\det\left(D_2^{(sps)}\right)\right|}},$$

$$u_r^{(s)}(\tilde{x}) = 0,\ M^{(sps)} = \frac{k_p}{k_s} V_{sp}\left(\tilde{y}_1^*\right) V_{ps}\left(\tilde{y}_2^*\right) \cos\gamma_1^{(p)} \cos\gamma_2^{(s)},\ \delta_2^{(sps)} = \operatorname{sign}\left(D_2^{(sps)}\right),$$

$$D_2^{(sps)} = \begin{pmatrix} \frac{\cos^2\gamma_1^{(s)}}{L_0}+\frac{k_p\cos^2\gamma_1^{(p)}}{L_1}+\frac{\cos\gamma_1^{(s)}}{\rho_1}+\frac{k_p\cos\gamma_1^{(p)}}{k_s\rho_1} & \frac{\cos\gamma_1^{(p)}\cos\gamma_2^{(s)}}{L_1} \\ \frac{\cos\gamma_1^{(p)}\cos\gamma_2^{(s)}}{L_1} & \frac{k_p\cos^2\gamma_2^{(p)}}{k_sL_1}+\frac{\cos^2\gamma_2^{(p)}}{L_2}+\frac{k_p\cos\gamma_2^{(p)}}{k_s\rho_2}+\frac{\cos\gamma_2^{(s)}}{\rho_2} \end{pmatrix} \tag{30.25}$$

30.5.8 *Case of* s-p-p *Transformation*

$$u_r^{(p)}(\tilde{x}) = M^{(spp)} \frac{\exp\left\{i\left[k_s L_0 + k_p(L_1+L_2) + \frac{\pi}{4}\left(\delta_2^{(spp)} - 2\right)\right]\right\}}{\sqrt{L_0 L_1 L_2}\sqrt{\left|\det\left(D_2^{(spp)}\right)\right|}},$$

$$u_\theta^{(p)}(\tilde{x}) = 0,\ M^{(spp)} = \frac{k_p}{k_s} V_{sp}\left(\tilde{y}_1^*\right) V_{pp}\left(\tilde{y}_2^*\right) \cos\gamma_1^{(p)} \cos\gamma_2^{(p)},\ \delta_2^{(spp)} = \operatorname{sign}\left(D_2^{(spp)}\right)$$

$$D_2^{(spp)} = \begin{pmatrix} \frac{\cos^2\gamma_1^{(s)}}{L_0} + \frac{k_p \cos^2\gamma_1^{(p)}}{L_1} + \frac{\cos\gamma_1^{(s)}}{\rho_1} + \frac{k_p \cos\gamma_1^{(p)}}{k_s \rho_1} & \frac{\cos\gamma_1^{(p)} \cos\gamma_2^{(p)}}{L_1} \\ \frac{\cos\gamma_1^{(p)} \cos\gamma_2^{(p)}}{L_1} & \cos^2\gamma_2^{(p)}\left(\frac{1}{L_1} + \frac{1}{L_2}\right) - \frac{2\cos\gamma_2^{(p)}}{\rho_2} \end{pmatrix} \tag{30.26}$$

30.6 Conclusion

Thus, the main term of the asymptotics (30.19)–(30.26) of the displacement amplitude in a high-frequency longitudinal or transverse wave twice reflected along the $\tilde{x}_0 - \tilde{y}_1^* - \tilde{y}_2^* - \tilde{x}_3$ ray for an arbitrary sequence of reflections and transformations from one or two obstacles in an elastic medium in the two-dimensional case is obtained in the work. The amplitude of movement in the reflected elastic wave (30.19)–(30.26) is determined by the distances from the wave source to the first point $\tilde{y}_1^*$ of the specular reflection L_0, from the second point of the specular reflection $\tilde{y}_2^*$ to the receiving point L_2, and the distance L_1 between points $\tilde{y}_1^*$ and $\tilde{y}_2^*$. Points $\tilde{y}_1^*$ and $\tilde{y}_2^*$ can belong both to the boundaries of two isolated obstacles and to the boundary l of one obstacle of complex non-convex shape. The main term of the asymptotics of displacement also explicitly contains the radii of curvature ρ_i of the boundary contours l_1 and l_2 of two obstacles, respectively, at points $\tilde{y}_1^*$ and $\tilde{y}_2^*$ of the direction of incident and reflected waves at points of specular reflection and coefficients of reflection and transformation. The phase of the reflected wave (30.19)–(30.26) is determined by the distances L_0, L_1, L_2, wave numbers k_p and k_s, the sign of the Hessian matrix, and also the number of points of specular reflection.

References

1. Z. Liu, X. Zhang, Y. Mao, Y. Zhu, Z. Yang, C.T. Chan, P. Sheng, Science **289**, 1734 (2000)
2. N.V. Boyev, M.A. Sumbatyan, in *Wave Dynamics and Composite Mechanics for Microstructured Materials and Metamaterials*, vol. 59, ed. by M.A. Sumbatyan (Springer, Heidelberg, 2017), p. 173
3. V.M. Babich, V.S. Buldyrev, *Asymptotic Methods in Short-Wavelength Diffraction Theory* (Alpha Science, New York, 2008)

4. N.V. Boyev, in *Wave Dynamics and Composite Mechanics for Microstructured Materials and Metamaterials*, vol. 59, ed. by M.A. Sumbatyan (Springer, Heidelberg, 2017), p. 91
5. M.A. Sumbatyan, N.V. Boyev, J. Acoust. Soc. Am. **95**(5), 2347 (1994)
6. V.D. Kupradze, *Potential Methods in the Theory of Elasticity* (Israel Program for Scientific Translations, Jerusalem, 1965)
7. V. Novatsky, *Theory of Elasticity* (Mir, Moscow, 1975). (in Russian)
8. H. Hyunl, A. Maue, K. Westpfal, *Theory of Diffraction* (Mir, Moscow, 1964). (in Russian)
9. V.A. Borovikov, B.Y. Kinber, *Geometrical Theory of Diffraction* (The Institution of Electrical Engineers, London, 1994)
10. L. Brekhovskikh, *Waves in Layered Media* (Academic Press, New York, 2012)
11. M.V. Fedorjuk, *Saddle Point Method* (Nauka, Moscow, 1977). (in Russian)

Chapter 31
On the Use of Models of the Tymoshenko Type in the Analysis of Wave Processes in Wedge-Shaped Waveguides

Aleksandr Vatulyan and Lyubov Parinova

Abstract Wave processes in topographic waveguides are studied. A wedge-shaped waveguide with a triple cross-section is considered. Hypotheses for variable stiffness plates are taken into account. Dispersion dependencies for two orthotropic materials for a model of the Timoshenko type using the variational Hamilton-Ostrogradsky principle and the Ritz approximate calculation method are constructed. The results are compared with those obtained in the study of the Kirchhoff model. A mathematical software Maple was used for computational experiments.

31.1 Introduction

The solution of the problems on the propagation of elastic waves traveling along the edge of a topographic waveguide is relevant in seismology, microelectronics, flaw detection and acoustics. The study of the kinematics of such waves can be used to develop new non-destructive testing methods and to create effective delay lines and filters.

For the first time, wave processes in wedge-shaped topographic waveguides were studied in the 1970–80s in [1, 2]. The finite element method was used to study wave processes in a wedge-shaped waveguide at an arbitrary opening angle. In the same period the conditions for the existence of symmetric and antisymmetric vibration modes in a wedge-shaped waveguide were found using the generalized variational principle [3]. In the twenty-first century, the existence of wedge waves was rigorously proved in [4, 5]. The existence of waves in some types of topographic waveguides was proved in [6]. The most interesting case is a waveguide with a small aperture angle. While the use of approximate models based on models of oscillations of plates of variable stiffness is very fruitful. Approximate models were constructed in [7–10] and antisymmetric vibration modes in topographic waveguides for orthotropic materials were studied taking into account the properties of the Kirchhoff model.

A. Vatulyan · L. Parinova (✉)
I. I. Vorovich Mathematics, Mechanics and Computer Sciences Institute,
Southern Federal University, Rostov-on-Don, Russia
e-mail: parinovali@mail.ru

I. A. Parinov et al. (eds.), *Advanced Materials*, Springer Proceedings
in Materials 6, https://doi.org/10.1007/978-3-030-45120-2_31

The purpose of this work is to study the propagation features of wave processes in wedge-shaped topographic waveguides of finite height based on more complex models of plates of variable stiffness, for example, the model of the Tymoshenko type, to obtain dispersion relations, to compare the results with the dependences obtained previously.

31.2 Formulation of Problem

The natural vibrations of an orthotropic topographic waveguide with a cross-section in the form of a triangle with a small angle 2α at the apex of height h are considered. An elastic wave propagating along the edge of a wedge-shaped structure is studied.

We assume that a Cartesian coordinate system $Ox_1x_2x_3$ is connected with the waveguide. The x_3-axis is directed perpendicular to the plane of the section S and passes through the apex of the angle of an isosceles triangle, not lying at the base. The base of the waveguide $x_1 = h$ is pinched. The remaining faces of the waveguide are free of loads.

The solution to the problem for a topographic wedge-shaped waveguide is sought in the form of traveling waves:

$$u_1(x_1, x_2, x_3, t) = U_1(x_1, x_2)\cos(\gamma x_3 - \omega t)$$
$$u_2(x_1, x_2, x_3, t) = U_2(x_1, x_2)\cos(\gamma x_3 - \omega t)$$
$$u_3(x_1, x_2, x_3, t) = U_3(x_1, x_2)\sin(\gamma x_3 - \omega t)$$

where γ is a wave number, ω is the oscillation frequency, $U_m(x_1, x_2)$, $m = 1, 2, 3$ are amplitudes of propagating waves.

Next, dimensionless parameters are entered:

$$\gamma_1 = \frac{C_{11}}{C_{55}}, \gamma_2 = \frac{C_{22}}{C_{55}}, \gamma_3 = \frac{C_{33}}{C_{55}}, \gamma_4 = \frac{C_{44}}{C_{55}}, \gamma_5 = \frac{C_{12}}{C_{55}},$$
$$\gamma_6 = \frac{C_{66}}{C_{55}}, \gamma_7 = \frac{C_{23}}{C_{55}}, \gamma_8 = \frac{C_{13}}{C_{55}}, \frac{\rho\omega^2 h^2}{C_{55}} = \beta, \gamma^2 h^2 = \mu,$$

where C_{ij} are elastic moduli of an orthotropic medium, ρ is density. As in [7–10], the problem of the propagation of an elastic wave along the edge of a wedge-shaped waveguide is reduced to finding the stationary value of some quadratic functional M:

$$M[U_i] = \int_S M_0 \mathrm{d}S \tag{31.1}$$

where the integrand has the form:

$$M_0 = (\gamma_1 U_{1,1} + \gamma_5 U_{2,2} + \gamma_8 U_{3,3})U_{1,1} + (\gamma_5 U_{1,1} + \gamma_2 U_{2,2} + \gamma_7 U_{3,3})U_{2,2} + (\gamma_8 U_{1,1} + \gamma_7 U_{2,2} + \gamma_3 U_{3,3})U_{3,3} + \gamma_6 (U_{1,2} + U_{2,1})^2 + (U_{1,3} + U_{3,1})^2 + \gamma_4 (U_{2,3} + U_{3,2})^2 - \beta\,(U_1^2 + U_2^2 + U_3^2)$$

The condition of stationarity of the functional $\delta M[U_i] = 0$ leads to the solution of a homogeneous boundary-value problem with two parameters. We find such a relationship between these parameters μ and β, for which the variational equation has a nontrivial solution.

31.3 The Model of the Timoshenko Type Plate

Oscillations of a symmetric region are divided into two problems, such as symmetric and antisymmetric oscillations. The studied types of motions are usually absent for the symmetric case. Therefore, to find a solution to the problem, the antisymmetric case is considered. It is assumed that the components of the displacement amplitudes $U_i(x_1, x_2)$ satisfy the following relation parity and oddness coordinate relations x_2:

$$U_1(x_1, -x_2) = -U_1(x_1, x_2)$$
$$U_2(x_1, -x_2) = U_2(x_1, x_2)$$
$$U_3(x_1, -x_2) = -U_3(x_1, x_2)$$

Generalized hypotheses are introduced due to the small opening angle α. These hypotheses are similar for the model of the Timoshenko type [11]:

$$U_1 = x_2 W_1(x_1) \tag{31.2}$$

$$U_2 = h W_2(x_1) \tag{31.3}$$

$$U_3 = \gamma x_2 h W_3(x_1) \tag{31.4}$$

Integration over x_2 is made in the presentation of functional (1). New dimensionless variable: $z = \frac{x_1}{h}$ is introduced. A simplified value of functional (1) is found taking into account hypotheses (2–4). Thus, the task of studying localized waves for topographic wedge-shaped waveguides is reduced to the problem of finding the stationary value of the functional M:

$$M[W] = \int_0^1 M_0^* \mathrm{d}z \tag{31.5}$$

here

$$M_0^* = ht\left(\begin{array}{l}\frac{1}{3}z^3t^2\Big(\Big(\gamma_1 W_1'^2 + 2\mu\gamma_8 W_1' W_3 + \mu^2\gamma_3 W_3^2 + \mu\big(-W_1 + W_3'\big)^2\Big) + \\ -\beta\big(W_1^2 + \mu W_3^2\big)\Big) + z\Big(\gamma_6\big(W_1 + W_2'\big)^2 + \gamma_4\mu(-W_2 + W_3)^2 - \beta W_2^2\Big)\end{array}\right)$$

where $t = tg\alpha$.

The stationary value of the functional $M[W]$ is found by the approximate method. This method is based on the Ritz method. The solution $W(z)$ is selected taking into account the requirements for coordinate functions from the class of functions bounded and satisfying the boundary conditions of rigid pinching at $z = 1$.

We shall look for a solution in the form:

$$W_1 = (z-1)^2 \sum_{n=1}^{N} a_n \varphi_n(z)$$

$$W_2 = (z-1)^2 \sum_{n=1}^{N} b_n \varphi_n(z)$$

$$W_3 = (z-1)^2 \sum_{n=1}^{N} c_n \varphi_n(z)$$

A system of functions $\phi_n(z) = z^{n-1}$, $n = 1, 2, \ldots$ is selected as coordinate functions. Then functional (5) takes a quadratic form of $3N$ variables:

$$M(a_1, b_1, c_1, a_2, b_2, c_2, \ldots a_N, b_N, c_N) = \int_0^1 M_1 \mathrm{d}z \tag{31.6}$$

where $M_1 = M_1(a_1, b_1, c_1, a_2, b_2, c_2, \ldots a_N, b_N, c_N)$.

As an example, we consider a special case for $N = 2$. After integrating (6) over z the functional transforms into a quadratic form of 6 variables:

$$\begin{aligned} M(a_1, b_1, c_1, a_2, b_2, c_2) &= k_{11}a_1^2 + k_{12}a_1b_1 + k_{13}a_1c_1 + k_{14}a_1a_2 \\ &+ k_{15}a_1b_2 + k_{16}a_1c_2 + k_{22}b_1^2 + k_{23}b_1c_1 + k_{24}b_1a_2 + k_{25}b_1b_2 \\ &+ k_{26}b_1c_2 + k_{33}c_1^2 + k_{34}c_1a_2 + k_{35}c_1b_2 + k_{36}c_1c_2 + k_{44}a_2^2 \\ &+ k_{45}a_2b_2 + k_{46}a_2c_2 + k_{55}b_2^2 + k_{56}b_2c_2 + k_{66}a_6^2 \end{aligned}$$

where $k_{ij} = k_{ij}(\beta, \mu)$, $i, j = 1 - 6$ due to bulkiness are not given, for example:

$$k_{11} = \frac{1}{30}\gamma_6 + \frac{1}{45}\gamma_1 t^2 - \frac{1}{840}\beta t^2 + \frac{1}{840}\mu t^2,$$

A linear homogeneous system is formed with respect to the coefficients a_k, b_k, $c_k, k = 1, 2, \ldots, N$, according to the condition of stationarity of the functional. The

determinant of the obtained system of linear equations is equal to zero. It turns out an approximate dispersion, namely algebraic equation that relates β and μ.

31.4 Computational Experiments

When finding dispersion dependences, the convergence of the Ritz method was studied depending on the number of coordinate functions. Calculations are performed for barite materials with parameters [12]:

$$\gamma_1 = 3.154,\ \gamma_2 = 2.799,\ \gamma_3 = 3.720,\ \gamma_4 = 0.419,$$
$$\gamma_5 = 1.710,\ \gamma_6 = 3.154,\ \gamma_7 = 1.036,\ \gamma_8 = 0.964$$

and austenitic steel with parameters [12]:

$$\gamma_1 = 2.036,\ \gamma_2 = 2.036,\ \gamma_3 = 1.674,\ \gamma_4 = 1.000,$$
$$\gamma_5 = 0.761,\ \gamma_6 = 2.036,\ \gamma_7 = 1.124,\ \gamma_8 = 1.124$$

The graphs of dispersion dependencies were constructed in respect to the relative dependencies $\mu(\beta)$ for these materials (see Fig. 31.1).

Dispersion dependencies are shown by red and blue colors for the cases $N = 3$ and $N = 8$, respectively.

Table 31.1 shows the values μ for different values of the frequency parameter for different values of frequency parameter β for various number of coordinate functions.

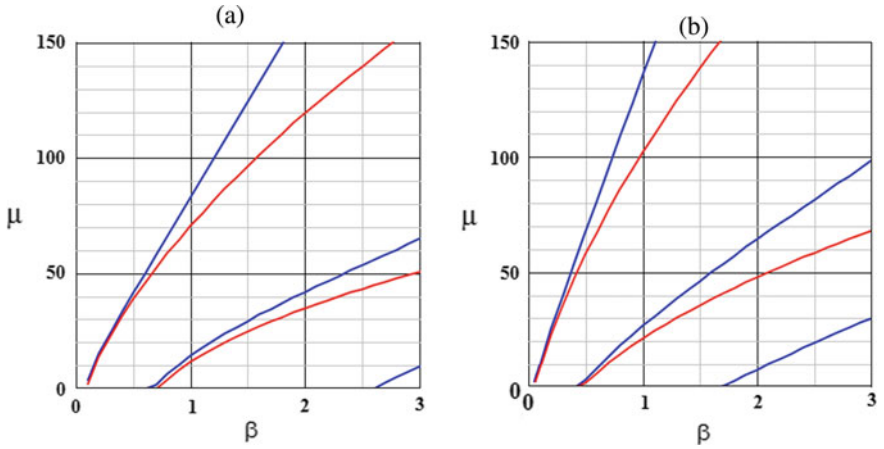

Fig. 31.1 Plots of parametric dependences for barite (**a**) and austenitic steel (**b**) materials for the opening angle $\alpha = 3°$

Table 31.1 Values of μ for barite for wedge at $\alpha = 3°$ and $N = 8$

Mode No.	β	Number of coordinate functions			
		$N = 5$	$N = 6$	$N = 7$	$N = 8$
First mode	1	82.191	82.819	82.894	82.902
	2	157.664	163.749	165.441	165.759
	3	223.703	239.666	246.317	248.241
	4	282.151	309.584	324.084	329.673
	5	334.870	373.974	398.009	409.315
	6	383.178	433.645	467.983	486.616
Second mode	1	13.557	13.789	14.052	14.149
	2	41.518	41.696	41.875	41.906
	3	63.365	64.410	64.787	64.805
	4	82.696	85.710	86.661	86.777
	5	100.622	106.112	108.122	108.511
	6	117.379	125.676	128.219	130.127
Third mode	3	5.714	8.879	9.184	9.590
	4	23.282	27.845	28.029	28.417
	5	36.946	42.730	43.103	43.534
	6	48.532	55.434	56.220	56.751

The monotonic growth of the sought values is characteristic for the implementation of the Ritz method. For $N = 8$, stabilization of values is achieved at the calculating the parameter μ for the first three propagating modes. The relative difference in the values μ corresponding to $N = 7$ and $N = 8$ does not exceed 5%.

The comparison of the results of the dependence μ on the parameter β for the model of the Timoshenko type and the previously studied Kirchhoff model [8, 9] is made for $N = 4$. Graphs of dispersion dependencies are shown in Fig. 31.2.

The digits 1, 2, 3 show in Fig. 31.2 first, second, and third modes, respectively. The dots illustrate the results of calculations for the Kirchhoff model. The solid cirves show the results of calculations for the model of the Timoshenko type. We can note that the dispersion dependences for both models practically coincide for the first mode. The discrepancy is slightly larger for the second and third modes.

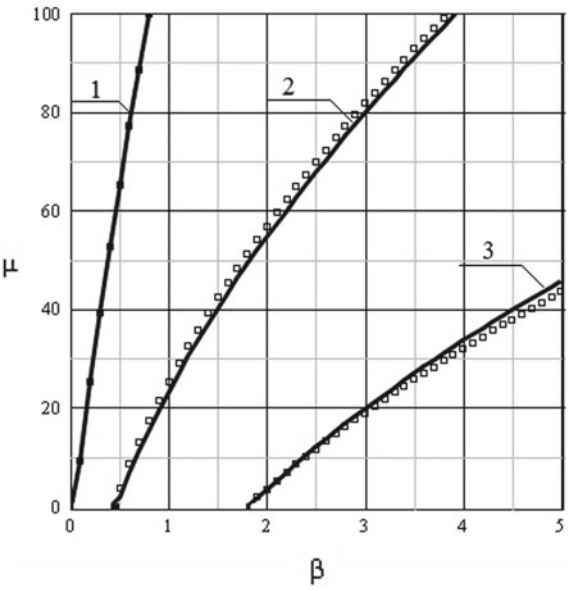

Fig. 31.2 Plots of dispersion dependencies for the Kirchhoff model and the model of Timoshenko type

Acknowledgements The performed study was funded by RFBR, project No. 19-31-90079.

References

1. E.A. Ash, R.M.D.L. Rue, R.F. Humphryes, IEEE Trans. Microw. Theory Tech. **17**(11), 882 (1969)
2. P.E. Lagasse, I. M. Mason, E.A. Ash, IEEE Trans. Microwave Theory Tech. **MTT-21**, 225 (1973)
3. H.F. Tiersten, D. Rubin, in *Proceedings of the IEEE Ultrasonics Symposium*, 117 (1974)
4. G.L. Zavorohin, A.I. Nazarov, Notes Sci. LOMI **380**, 45 (2010). (in Russian)
5. I.V. Kamockij, Algebra Anal. **20**(1), 86 (2008) (in Russian)
6. V.M. Babich, Algebra Anal. **22**(1), 98 (2010) (in Russian)
7. A.O. Vatulyan, L.I. Parinova, Vestn. DGTU **5**(4), 491 (2005) (in Russian)
8. A.O. Vatulyan, L.I. Parinova, in *Advanced Materials—Techniques, Physics, Mechanics and Applications*, ed. by I.A. Parinov, S.-H. Chang, M.A. Jani, Springer Proceedings in Physics, vol. 193 (Springer Cham, Heidelberg, 2017), 309
9. A.O. Vatulyan, L.I. Parinova, Univ News North-Caucasus Reg Nat Sci **3**, 10 (2018). (in Russian)
10. L.I. Parinova, in *Advanced Materials Proceedings of the International Conference on "Physics and Mechanics of New Materials and Their Applications", PHENMA 2018,* ed. by I.A. Parinov, S.-H. Chang, Y.-H. Kim, Springer Proceeding in Physics vol. 224 (2019), 487
11. R.D. Nedin, A.O. Vatulyan, I.V. Bogachev, Math. Methods Appl. Sci. **41**(4), 1600 (2018)
12. V.S. Blistanov, V.S. Bondarenko, N.V. Peremolova et al., in: *Acoustic Crystals*, ed. by M.P. Shaskol'skaya (Nauka, Moscow, 1982), 632 p. (in Russian)

Chapter 32
Construction of the Mechanical Model of Keratoprosthesis of the Ocular Cornea

Arkadiy Soloviev, Nadegda Glushko, Alexander Epikhin and Michael Swain

Abstract By developing ocular prostheses, a number of problems arise, one of which is the design of the connection between the rigid optical part and the soft tissue of the cornea; their Young's modules can differ by three orders of magnitude. In this case, the problem arises of creating some intermediate layer, possibly with gradient properties, the purpose of which is to exclude injury to soft biological tissues. An analytical and finite element modeling of the interaction of a cylindrical optical prosthesis, an intermediate heterogeneous layer and the cornea, in the framework of elastic media, in two versions: (i) without taking into account curvature (round plate) and (ii) taking into account curvature (spherical dome or shell), was performed. In a simplified model, the intermediate layer is represented as a spring layer, the determination of the rigidity of which will allow one to create an original design. Based on the proposed models, the stress-strain state of soft biological tissues was calculated.

32.1 Introduction

A keratoprosthesis is a cell-free artificial implant consisting of central optics held in a cylindrical frame. Keratoprosthesis replaces the removed part of the cornea. When developing keratoprostheses, scientists faced many difficulties, and many of the early corneal transplants had high rates of infection and rejection. In the late 1980s, a "core-and-skirt" device in which a bio-integrated "skirt" surrounds central optics became the most common design. Important parameters were not only the size, but also the location of the pores in the porous skirt. Keratoprostheses, such as AlphaCor,

A. Soloviev (✉) · N. Glushko
Department of Theoretical and Applied Mechanics, Don State Technical University, Rostov-on-Don, Russia
e-mail: solovievarc@gmail.com

A. Epikhin
Don State Medical University, Rostov-on-Don, Russia

M. Swain
Sydney University, Sydney, Australia

I. A. Parinov et al. (eds.), *Advanced Materials*, Springer Proceedings in Materials 6, https://doi.org/10.1007/978-3-030-45120-2_32

formerly known as Chirila keratoprostheses, were a polymethylmethacrylate device with a central optical region fused to the surrounding spongy skirt.

Modern keratoprostheses consist of an optical element and a support plate. The optical element is mainly in the form of a cylinder or lens, consists of an optically transparent material. The base plate connected to the optical element may have various forms: the shape of a ring with holes or a "wheel with spokes", can be made in the form of "ears" or "amoeba-shaped legs". The book [1] provides descriptions of various types and forms of both mounts and keratoprostheses themselves. The main complication after keratoprosthetics is aseptic necrosis of the cornea that occurs in front of the implant support. It is a complication that quite often leads to rejection of the keratoprosthesis [1]. The main reason for the occurrence of aseptic necrosis is the blocking of the flow of vital substances into the layers of the cornea, which are located above the keratoprosthesis support. In this regard, for the manufacture of a support plate, it is necessary to use a biocompatible material that would allow corneal tissue to grow through the support mount.

The patent [2] describes a microporous keratoprosthesis base plate made of stretched polytetrafluoroethylene (PTFE), the structure of which has a configuration in the form of polymer nodes that are connected by fibrils with a length of 7–8 μm. Based on the data, PTFE with a fibrillar structure has too small pores, which does not allow corneal tissue to grow. Therefore, it is necessary to additionally penetrate it with pores perpendicular to the surfaces of the support plate with a diameter of 20–150 μm and preferably 50 μm. The thickness of the base plate should be about 0.2 μm, but not more than 0.3 μm.

In patent [3] a keratoprosthesis is described, consisting of an optical element and a support fixture made in the form of a ring. The optical element is made of an optically transparent substance, such as polymethylmethacrylate (PMMA), and the support mount is made of a hydrophilic porous material having a fibrous structure that can grow through the corneal tissues. A support plate with a thickness of 0.15–0.30 μm is formed from said fiber; with an outer diameter of the ring of about 9.5 mm, is worn on an optical element, the front of which is made in the form of a cylinder. The part directed inside the eye has the shape of a truncated cone, a larger section of which is directed inward. The backing plate has "elastic characteristics necessary to prevent keratoprosthesis rejection and necrosis resulting from pressure from surrounding eye tissue.

In patent [4], the keratoprosthesis support plate is made in the form of two parallel shells spaced 0.4–0.7 μm apart. The optimal distance is 0.3 ± 0.02 mm; the shells are slightly conical in shape and are attached to the cylindrical optical element. The material of the support plates should be "bio-populated", therefore, it is assumed that the shells should be made of a material with a porosity of 50% and higher, the pores should be open and their diameter should be about 20–100 μm.

The patent [5] describes a keratoprosthesis (Fig. 32.1), consisting of a support plate and an optical element. The base plate is made in the form of a convex-concave lens with a radius of curvature of 7–10 mm In each individual case, the radius of curvature of the base plate is selected in accordance with the radius of curvature of the cornea of the patient, which is determined using hard contact lenses or in another

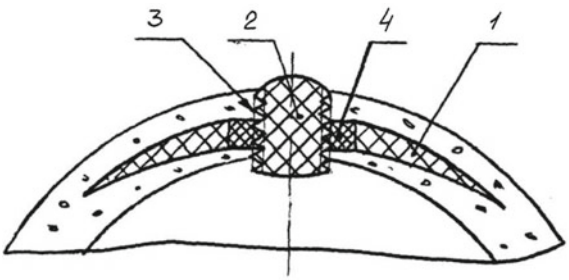

Fig. 32.1 Scheme of keratoprosthesis [5]

way. In the part adjacent to the optical element, the support plate has a thickness of 0.3–0.7 mm, tapering at the edges to a thickness of about 0.01 mm. The outer diameter of the support plate can be 7–12 mm, depending on the individual diameter of the cornea of the patient's eye. In the center, the support plate has a cylindrical hole necessary for attaching the optical element. The optical element is in the form of a cylinder, the outer end (directed from the eye) of which is always convex, and the inner end, depending on how many diopters the optical element is designed for, can be flat or slightly convex. The optical element is made of polymethyl methacrylate or polycarbonate. It is possible to perform optical elements in 40–60 diopters. Also, the optical element of the keratoprosthesis under consideration can be collapsible. In this case, a screw thread is applied along the lateral surface of the cylinder. The prosthesis is additionally equipped with a washer having an internal screw thread. The washer is connected (glued) with its outer side to the inner surface of the cylindrical hole of the base plate. A keratoprosthesis can be implanted into the intralamellar pocket of the cornea, while the support plate is located inside the cornea of the eye, and the optical element penetrates all layers of the cornea.

The patent [6] describes an implant for strengthening the cornea, which is made in the form of a round or oval plate having the shape of a trefoil, chamomile, or in the form of a convex-concave lens, which has a radius of curvature of 7–10 mm. The lens may have a cylindrical hole in the center, which can be used for subsequent keratoprosthetics. The structure of the material from which the implant is made has a volume fraction of void space of 15–40%, a specific surface space of voids of 0.25–0.55 $\mu m^2/\mu m^3$, an average distance between voids of 25–50 μm, and an average volume chord of 8–25 μm. The inventive implant is a convex-concave lens having a radius of curvature corresponding to the radius of curvature of the cornea of the patient. In the central part, the implant has a thickness of 0.3–0.7 mm, descending along the edges to 0.01 mm.

The patent [7] describes the effectiveness of treatment using the method of surgical treatment of cataracts using keratoprosthetics as an implant with a support base of permeable-porous titanium nickelide, which copies the curvature of the eye and supports a cylindrical optical element located in its central hole. The support base is mounted on the surface of the cornea and is retentively fixed by the scleral allograft, which is superimposed on top of the lamellar support base. The support base has the following parameters. The variable thickness of the plate support base with its

gradual increase to the hole located in the center, allows one to fix the optical element, made in the form of a cylinder, without an additional mounting sleeve, as well as a threaded connection, which is technically simple and operationally reliable. A simple and reliable way to fix the support base of the optical element in the hole is a tight fit. It is possible to produce it with a negative difference between the diameters of the hole and the actual bore diameter of the optical cylinder. A tight fit (the nature of the connection of parts) in the "hole-shaft" system is carried out in metals due to the elastic deformation of the material. Titanium nickelide is subject to deformation according to the law of elastic deformation, which is several times larger than the elastic deformation of metals. This is what makes it possible to insert a keratoprosthesis (a lightweight and precision construction) with the least mechanical effort, which reduces the possibility of technological defects and errors. The rough surface of the hole in the slice of the porous material prevents the migration of the optical element in the absence of additional fixing elements. The reliability of the fastening of the optical element is also enhanced by a decrease in porosity, as well as a predominant pore size near the hole, in the result of an increase in the mechanical strength of the material in the central part of the base, which carries the main load. The absolute values of pore size and porosity are selected taking into account the conditions for the optimal integration of porous titanium nickelide and body tissues: such as the cornea of the eye, on the one hand, and the allograft, on the other hand. Fast and successful integration of a porous implant (basis) with surrounding tissues, mechanically strong fixation of the optical element, i.e. a reduction in the risk of keratoprosthesis reposition is regarded as an increase in effectiveness in treating a cataract.

In patent [8], attention is drawn to the fact that the support part of the implant in shape and area should provide maximum resistance to the buoyant effect of intraocular fluid pressure on the optical part of the keratoprosthesis, while minimizing the deformation of the proper tissue. The material of the supporting part should not only be biocompatible, but also structured in such a way that to be able to ensure fusion of the above and the underlying layers of the cornea, which are separated during the keratoprosthesis implantation. The author notes that keratoprostheses are known, including an optical element made of an optically transparent substance, for example, PMMA, and a ring-shaped support plate made of a hydrophilic porous material of polytetrafluoroethylene or polyethylene [3, 4], whose merit is the possibility of fusion over and supporting layers of the cornea due to the high porosity of the material from 50% and above, and pore diameters up to 100 μm. The main drawback of the designs is excessive flexibility and low mechanical strength. These characteristics do not allow for a long time to reliably hold and fix the installed keratoprosthesis with large optics. The combined keratoprosthesis described in the patent consists of an optical part, which is made of a transparent solid or elastic polymer saturated with ultraviolet adsorbent. It is a removable bolt with a diameter of 5–6 mm, having a mushroom-shaped front end and spherical and/or aspherical surfaces of the ends and a thread on the side surface of the haptic part, made in the form of a support disk with an outer diameter of 8–12 mm, the thickness of which can vary from 0.3 to 0.9 mm. It is made of porous and/or perforated solid and/or elastic reactive polymer

and/or metal with a volume fraction of void space no more than 50%. The haptic part includes two parts: (i) from the front, it consists of biological materials; (ii) from the back, it includes artificial biocompatible materials. The supporting disk of the rear part is made plane and connected perpendicularly to the centrally located supporting hollow cylinder by means of a groove and/or flange formed on the outer rear part of the cylinder. The cylinder is equipped with an internal thread, which corresponds to the profile and diameter of the thread of the optical bolt. In this case, the support disk can pass into the cover sleeve, which wraps around the support cylinder from the outside. The support plate in front is connected to a round bio-disk, which is cut from freshly taken or preserved sterile biological materials of different layered combinations of biological tissues. For this, parts of the keratoprosthesis are sterilized before joining. The connection is carried out under sterile conditions, immediately before the implantation of a keratoprosthesis or in advance with subsequent storage before surgery. The external diameter of the bio-disk is made larger than the external diameter of the supporting disk by 0.3–1 mm, a coaxial hole is made in the center of the bio-disk, the diameter of which must correspond to the outer diameter of the cover sleeve or supporting cylinder.

In this work, we consider a keratoprosthesis, which has an optical element (*first area* is white) of a cylindrical shape and there is a certain intermediate layer on the cylindrical surface with mechanical properties inhomogeneous in radius. Semi-axial sections of the keratoprosthesis are shown in Fig. 32.2, (a) without taking into account the curvature and (b) taking into account the curvature of the cornea, a layer with functionally gradient properties is highlighted in gray (*second area*) and the cornea (*third area*—is the region with points). This layer is designed to provide non-traumatic contact of optics with soft tissues of the cornea. Analytical and numerical models of keratoprosthesis implantation into the cornea based on FEM are constructed. The stress-strain state of the cornea in the contact area was investigated.

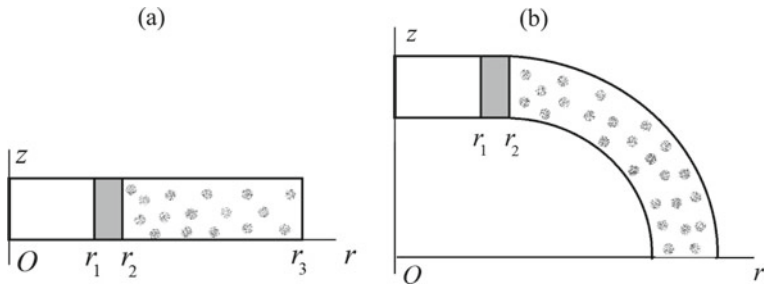

Fig. 32.2 Semi-axial section, plate model (**a**), domes (**b**)

32.1.1 Research Purpose

The stress-strain state of the cornea is studied in the vicinity of the contact with the keratoprosthesis, the outer layer of which is a certain structure that allows one to reduce soft tissue injury. This intermediate (interface) layer is modeled by a hollow cylinder with functionally gradient mechanical properties.

32.1.2 Research Scope

At this study, we consider the following frameworks of the problem:

(i) an analytical model of an implanted prosthesis based on the bending a composite circular plate;
(ii) FEM model of an implanted prosthesis based on a composite circular plate;
(iii) FEM model of an implanted prosthesis based on a composite spherical dome;
(iv) FEM model of the cornea based on a circular plate, in which the interface layer is replaced by the spring type conditions for joining with an absolutely rigid optical part;
(v) FEM model of the cornea based on a spherical dome, in which the interface layer is replaced by the spring type conditions for joining with an absolutely rigid optical part.

32.2 Research Method

32.2.1 Continuous Formulation of the Problem

The general mathematical formulation of the problem under study consists of the boundary-value problem of the theory of elasticity for a composite isotropic body, two of which are homogeneous cylindrical optical prostheses and corneas, with elastic moduli Er_1 and Er_3, and the interface layer has a functionally gradient elastic modulus $Er_2 = Er_2(r)$. The right side is fixed on the left side, symmetry conditions are set, a uniformly distributed pressure acts on the lower border, which corresponds to an excess intraocular pressure compared to atmospheric pressure, continuity conditions are set at the interface. The system of differential equations for unknown components of the displacement vector $\vec{u} = (u_1, u_2, u_3)$ is presented as [9]

$$\sigma_{ij,j} = 0, \quad \sigma_{ij} = c_{ijkl}\,\varepsilon_{kl} - \alpha\, p\, \delta_{ij}, \quad \varepsilon_{kl} = \frac{1}{2}\left(u_{k,l} + u_{l,k}\right) \tag{32.1}$$

where σ_{ij}, c_{ijkl}, ε_{kl} are the components of the tensors of stresses, elastic constants, deformations, respectively.

The boundary conditions are set for the displacement and stress vectors on the corresponding surfaces S_u and S_t:

$$u_i|_{S_u} = u_i^0(\overline{x}, t), \quad \overline{x} \in S_u \tag{32.2}$$

$$t_i|_{S_t} = \sigma_{ij} n_j|_{S_t} = q(\overline{x}, t), \quad \overline{x} \in S_t \tag{32.3}$$

where n_j are the coordinates of the unit vector of external normal.

In the case of modeling the second section by spring boundary conditions at the interface boundary S_{int} with continuous displacements, the condition is the set $\sigma_n = -k\,u_n$, where k is a certain stiffness coefficient, characterizing the elastic properties of the second section.

To study model (i), boundary-value problem (1–3) reduces to a system of ordinary differential equations (4–6) for the first, second, and third sections, respectively, relatively to $\theta(r)$ being the angle of rotation of the unit vector of normal with a power law of changing the elastic modulus of the second section along radius [10]:

$$\left(\frac{\mathrm{d}^2}{\mathrm{d}r^2}\theta_1(r)\right)r^2 + \left(\frac{\mathrm{d}}{\mathrm{d}r}\theta_1(r)\right)r - \theta_1(r) = \frac{1}{2}K_1 l q r^3 \tag{32.4}$$

$$\left(\frac{\mathrm{d}^2}{\mathrm{d}r^2}\theta_2(r)\right)r^2 + a\left(\frac{\mathrm{d}}{\mathrm{d}r}\theta_2(r)\right)r + a\vartheta_2\theta_2(r) + \left(\frac{\mathrm{d}}{\mathrm{d}r}\theta_2(r)\right)r - \theta_2(r) = \frac{1}{2}\frac{K_2 q\left(r^2 - r_1^2\right)r^{2-a}}{r} \tag{32.5}$$

$$\left(\frac{\mathrm{d}^2}{\mathrm{d}r^2}\theta_3(r)\right)r^2 + \left(\frac{\mathrm{d}}{\mathrm{d}r}\theta_3(r)\right)r - \theta_3(r) = \frac{1}{2}K_3 3q\left(r^2 - r_2^2\right)r \tag{32.6}$$

where $K_i = 1/D_i$, D_i is the cylindrical stiffness $i = 1, 2, 3$.

The general solution of the system of (4–6) is constructed

$$\text{at first section: } \theta_1(r) = rC_2 + \frac{1}{16}K_1 l q r^3 + \frac{C_1}{r}$$

$$\text{at second section: } \theta_2(r) = r^{-\frac{1}{2}a+\frac{1}{2}\sqrt{a^2-4a\vartheta_2+4}}C_4 + r^{-\frac{1}{2}a+\frac{1}{2}\sqrt{a^2-4a\vartheta_2+4}}C_3 + \frac{1}{2}\frac{K_2 q r^{1-a}\left(\left(\left(r^2 - r_1^2\right)\vartheta_2 - r^2 + 3rl^2\right)a - 8rl^2\right)}{(8 + (\vartheta_2 - 3)a)a(\vartheta_2 - 1)}$$

$$\text{at third section: } \theta_3(r) = \frac{C_5}{r} + rC_6 - \frac{1}{16}K_3 3q\left(4\ln(r)r_2^2 - r^2\right)r \tag{32.7}$$

where

$$\mathrm{Er}_2 = \mathrm{Er}_1\left(\frac{r_1}{r}\right)^a, \quad D_i = \frac{\mathrm{Er}_i h_i^3}{12\left(1-\vartheta_i^2\right)}, \quad \mathrm{Er}_2 = \mathrm{Er}_1\left(\frac{r_1}{r}\right)^{\frac{\ln\left(\frac{Er_1}{Er_3}\right)}{\ln\left(\frac{r_2}{r_1}\right)}}$$

Arbitrary constants C_i are determined from the boundary conditions at the right end and the matching conditions, moreover $C_1 = 0$.

32.3 Results and Discussion

Numerical modeling was carried out in the finite element software ACELAN [11, 12], the components of the stress-strain state in problem (ii) are presented in Figs. 32.3, 32.4, 32.5 and 32.6.

The Characteristics of the stress-strain state in problem (iv) are presented in Figs. 32.7 and 32.8.

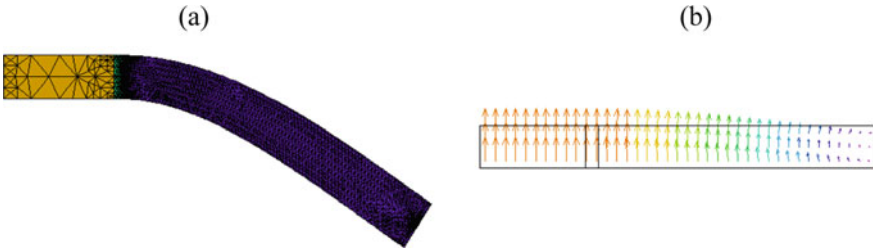

Fig. 32.3 Finite element grid (**a**), displacement vector distribution (**b**)

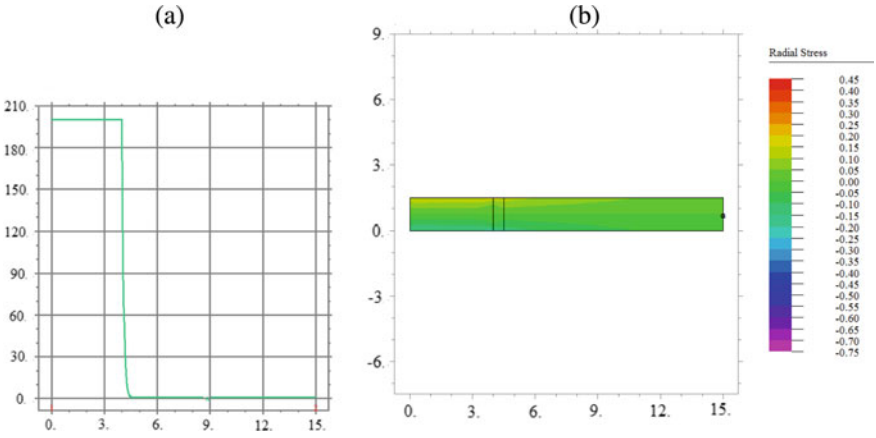

Fig. 32.4 Dependence of elastic modulus on radius (**a**), distribution of radial stresses (**b**)

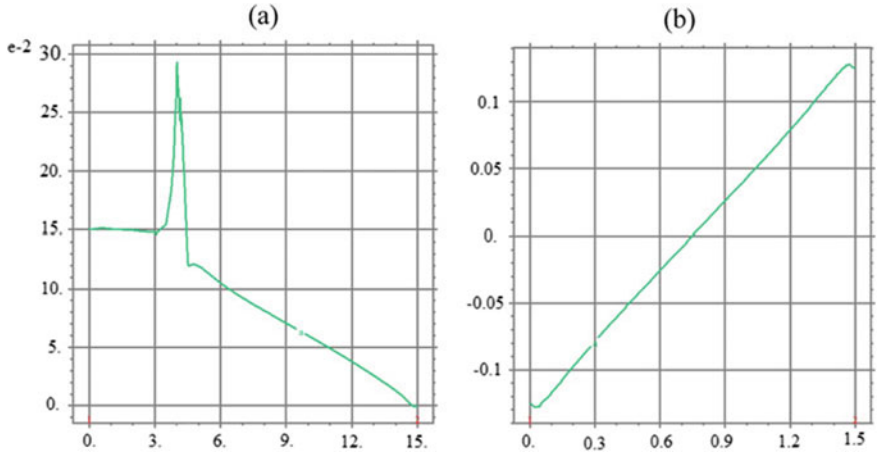

Fig. 32.5 Dependence of radial stresses on radius on the upper border (**a**), and on the interface with cornea (**b**)

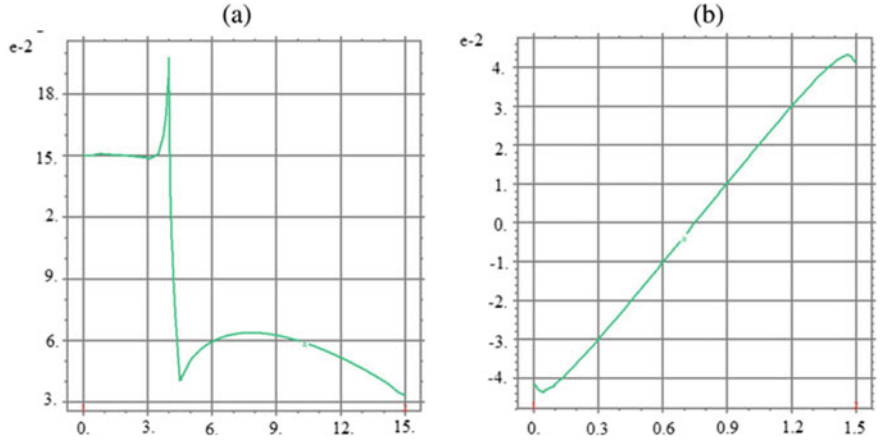

Fig. 32.6 Dependence of angular stresses on radius on the upper border (**a**), and on the interface with cornea (**b**)

The characteristics of the stress-strain state in problem (iii) are presented in Figs. 32.9, 32.10, 32.11 and 32.12.

The characteristics of the stress-strain state in problem (v) are presented in Figs. 32.13, 32.14 and 32.15.

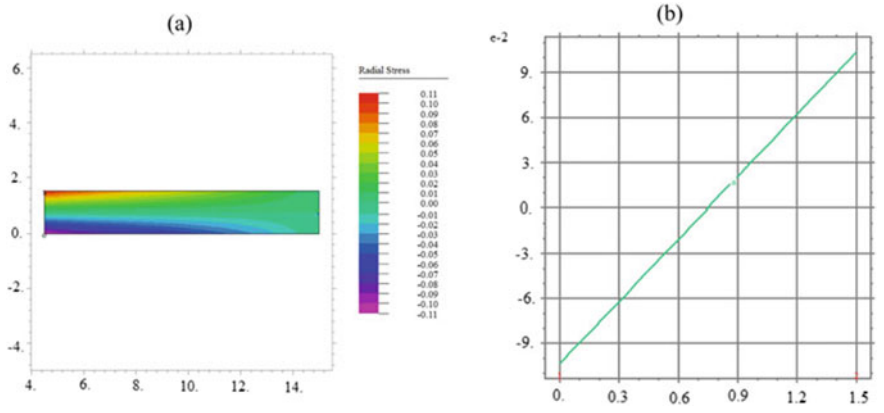

Fig. 32.7 Distribution of radial stresses along radius (**a**), dependence of radial stresses on radius on left boundary (**b**)

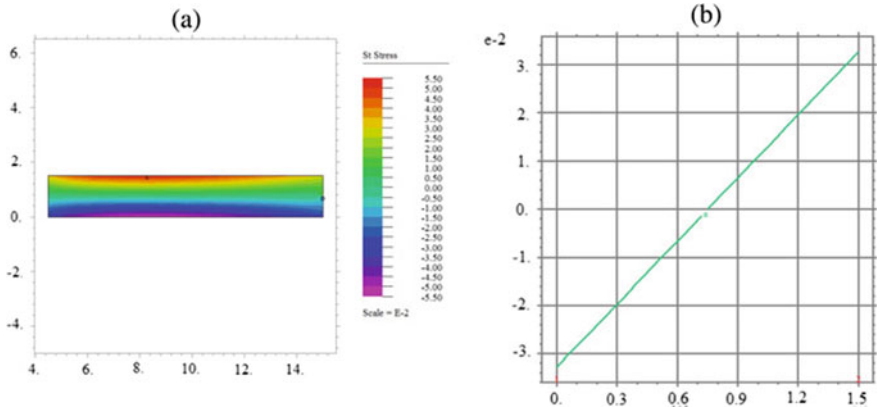

Fig. 32.8 Distribution of angular stresses (**a**), dependence of angular stresses on the left boundary (**b**)

32.4 Conclusion

The keratoprosthesis models are considered, the feature of which is the presence of an intermediate layer between a rigid optical prosthesis and the soft tissues of cornea. This intermediate layer may provide non-traumatic contact. Several models (analytical and finite element) of a prosthesis implanted in the cornea were built. The components of a stress-strain cornea at the contact region are calculated. The present analysis of the stress results will determine the stiffness of the intermediate layer and, in accordance with this, propose its design.

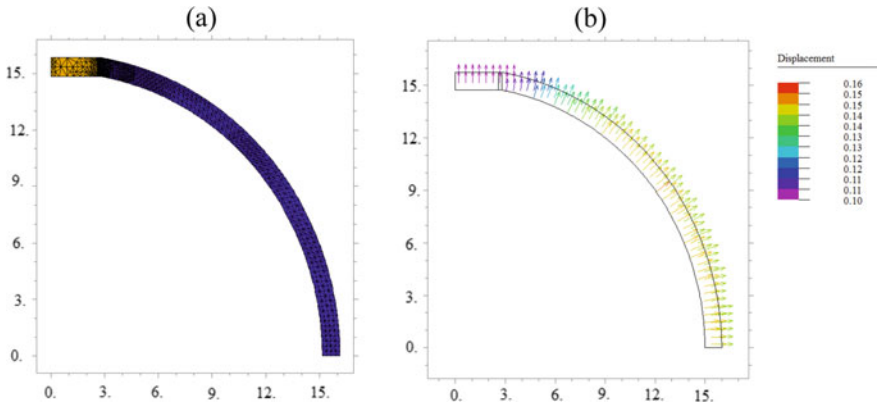

Fig. 32.9 Finite element grid (**a**), displacement vector distribution (**b**)

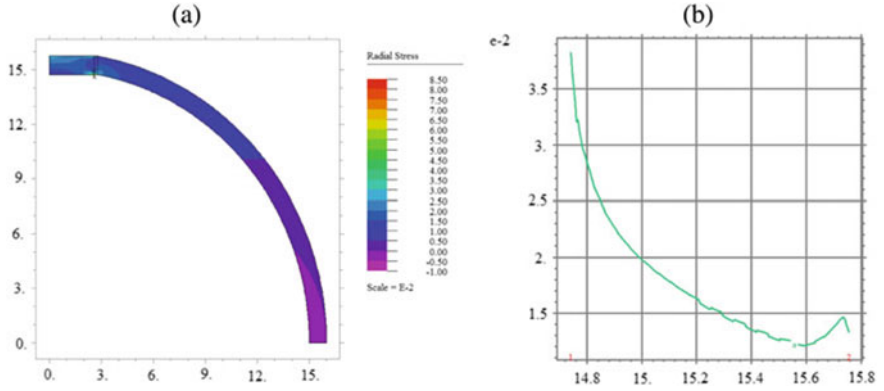

Fig. 32.10 Distribution of radial stresses in the region (**a**), at the interface with cornea (**b**)

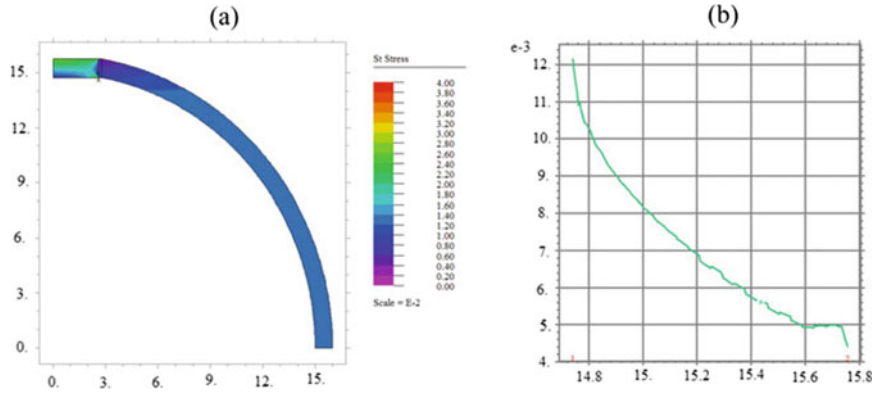

Fig. 32.11 Distribution of angular stresses in the region (**a**), at the interface with cornea (**b**)

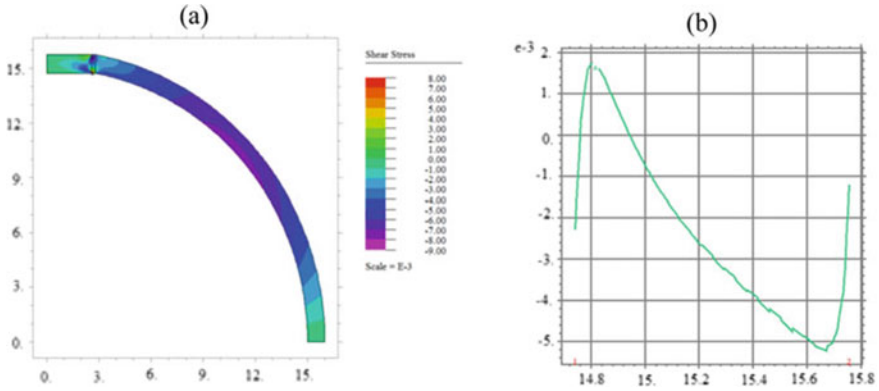

Fig. 32.12 Distribution of shear stresses in the region (**a**), at the interface with cornea (**b**)

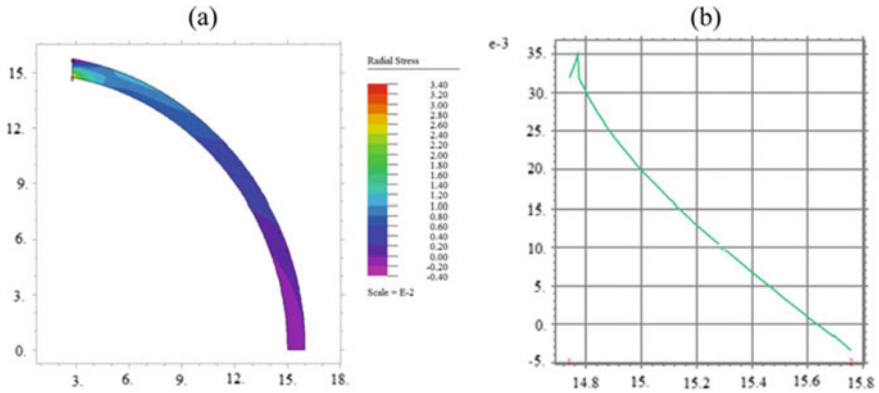

Fig. 32.13 Distribution of radial stresses in the region (**a**), at the interface with cornea (**b**)

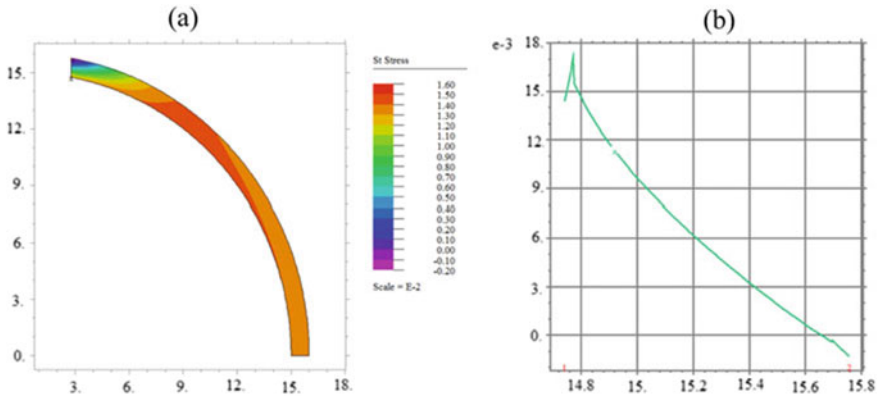

Fig. 32.14 Distribution of angular stresses in the region (**a**), at the interface with cornea (**b**)

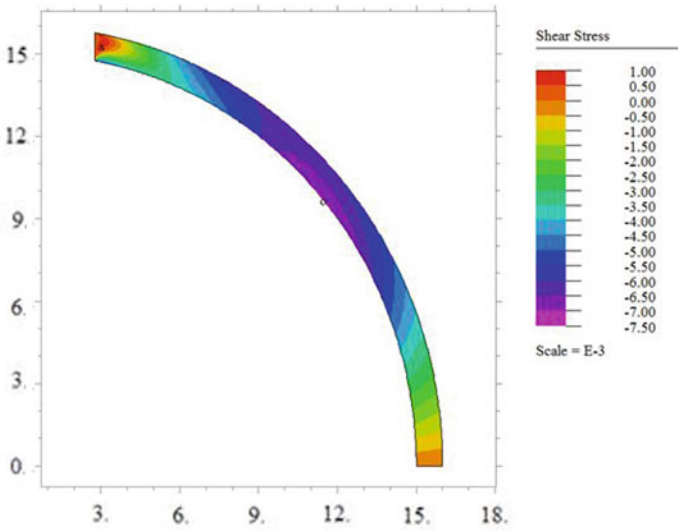

Fig. 32.15 Distribution of shear stresses in the region

Acknowledgements This research was supported by the Government of Russian Federation (grant no. 14.Z50.31.0046).

References

1. S.N. Fedorov, Z.I. Moroz, V.K. Zuev, *Keratoprosthetics*. Moscow, Medicine, 144 p. (1982) (in Russian)
2. *Patent US 5713956 A*, IPC A61F2/14 (1998)
3. *Patent US 5489301*, IPC A61F2/14 (1996)
4. *Patent US 6106552*, IPC A61F2/14 (2000)
5. V.E. D'yakov, Y.S. Astahov, R.T. Hapchaev, Y.A. Kortunov, L.M. Fedotova, *Keratoprosthesis*. Patent RU2270643C1 IPC A61F2/14 A61L27/56 (2006) (in Russian)
6. V.E. D'yakov, Y.S. Astahov, E.V. Bojko, N.A. Ushakov, R.T. Hapchaev, Y.A. Kortunov, L.M. Fedotova, *The implant to strengthen the cornea*, RU2270642C1 IPC A61F2/14 A61L27/56 (2006) (in Russian)
7. A.A. Berezovskaya, V.N. Hodorenko, I.V. Zapuskalov, V.E. Gyunter, *Keratoprosthesis and method of surgical treatment of cataracts with its help*, RU2367379C1 IPC A61F2/14 A61F9/07 (2009) (in Russian)
8. A.N. Epihin. *Combined keratoprosthesis*, RU2707646C1 IPC A61F9/07 A61F2/16 (2019) (In Russian)
9. V. Novackij, *Theory of Elasticity*. Moscow, Mir, 864 p. (1975) (in Russian)
10. S.V. Boyarshinov, *Machine-Building Mechanics*. Moscow, Mashinostroenie. 456 p. (1973) (in Russian)
11. A.V. Belokon, V.A. Eremeyev, A.V. Nasedkin, A.N. Solov'yev, J. Appl. Math. Mech. **64**(3), 367 (2000)
12. A.V. Belokon, A.V. Nasedkin, A.N. Solov'yev. J. Appl. Math. Mech. **66**(3), 481 (2002)

Chapter 33
Simulation of the Stress-Strain State of the Spline Joint of the Helicopter Tail Transmission

M. I. Chebakov, S. A. Danilchenko, and E. M. Kolosova

Abstract In the present work, frictional contact interaction between the tip and the shaft of the tail transmission of the MI-26 helicopter is considered in the framework of the linear theory of elasticity. The geometrical dimensions of the joint elements are taken from the design documentation. To set the profile of the tooth section, the necessary parametric equations were derived. To solve the tasks set, the finite element method and the ANSYS software were used. The main attention in the calculations was paid to the study of contact pressure q and effective (equivalent) stresses σ_e on the tip teeth surfaces that are in direct contact with the teeth of the cup. In accordance with one of the proposed ways to increase the operational life of the node under study, a thin coating with mechanical characteristics different from the teeth original material was designed placed on the contacting surface of the tip tooth. The stress-strain state of the node has been calculated for various geometrical and mechanical parameters of the coating.

33.1 Introduction

There are some parts in mechanisms that operational life is sufficiently less than for others. Limited resource items primarily include the most loaded joints. Technological units, mentioned above, are braking systems, where due to the large magnitude of the friction forces work, to the presence of high sliding speeds of the contact surfaces and their significant heating, intensive wear of the brake pads occurs; helicopter tail transmission, in the shaft joints of which involute tooth gears are used. Such gears fail mainly due to crushing and wear of the working surfaces of the teeth. The interaction processes in the frictional contact area of the helicopter's spline joint of the tail transmission are characterized by small amplitude relative vibrations and significant dynamic loads occurring in junction under operating conditions.

M. I. Chebakov (✉) · S. A. Danilchenko · E. M. Kolosova
Southern Federal University, Rostov-on-Don, Russia
e-mail: michebakov@yandex.ru

M. I. Chebakov · S. A. Danilchenko
Rostov State Transport University, Rostov-on-Don, Russia

I. A. Parinov et al. (eds.), *Advanced Materials*, Springer Proceedings in Materials 6, https://doi.org/10.1007/978-3-030-45120-2_33

Currently, various methods are used to reduce the wear of rubbing parts [1]. For example, the usage of lubricants and anti-friction materials that reduce friction [2–4]. Also, one of the effective ways to increase the durability of working junctions is to modify the surfaces of the tribocontact including by hardening and coating them [5–8]. According to such approach the main difficulty is to obtain the optimal surface modification parameters for each particular joint.

One way to solve this problem may be to assess the effect of various modification parameters on the stress-strain state of the joint. In theoretical terms, the problem of evaluating the stress-strain state of a heavily loaded tribo-conjugate assembly is reduced to solve the contact problem of the deformable solid mechanics. In spite of considerable advance in this field of knowledge, in practice, such problems require studying novel contact problems with complicated physical and mechanical properties in the contact area, calling in contemporary numerical-analytic and numerical only methods, integrated calculation and design methodology using finite element technologies, including the steps of creating finite element models, performing calculations and results estimation.

33.2 Formulation of the Transmission Spline Junction Contact Interaction Problem

In the framework of linear theory of elasticity frictional contact interaction between the tip and the shaft of the tail transmission of the MI-26 helicopter is considered. The geometric dimensions of the connected elements are taken from the design documentation. To set the tooth cross-section profile, the necessary parametric equations were derived. To derive formulas the following involute parameters were used: m = 3 mm—engagement module, $z = 27$—number of gear teeth, $\alpha = 20°$—profile angle of the original contour, $h_a^* = 1$—the height of the tooth head of the original contour, $x^* = 0$—displacement of the initial contour (worm cutter) when cutting a tooth, $c^* = 0.25$—gear radial clearance, $r_i^* = 0.38$—the radius of the fillet of the tooth of the original contour (Fig. 33.1). An asterisk indicates the assignment of this linear quantity to the engagement modulus.

Based on these data, auxiliary values were calculated: the radius of the pitch circle $r = 0.5mz$, tooth projections circle radius $r_a = r + m(x^* + h_a^*)$, depressions teeth radius circle $r_f = r - m(x^* + h_a^* + c^*)$; $\mu = \arcsin[r\sin(\pi/2 + \alpha)/r_a]$, $\beta = \pi/2 - (\alpha + \mu)$, $n = r\sin\beta/\sin\mu$, $k = m[h_a^* + c^* - r_i^*(1 - \sin\alpha)]$.

As a result, we obtain parametric equations for the involute portion of the tooth $(a - b)$

$$\begin{cases} x_э = A_э \sin\varphi_э - B_э \cos\varphi_э; \\ y_э = A_э \cos\varphi_э + B_э \sin\varphi_э - r, \end{cases}$$

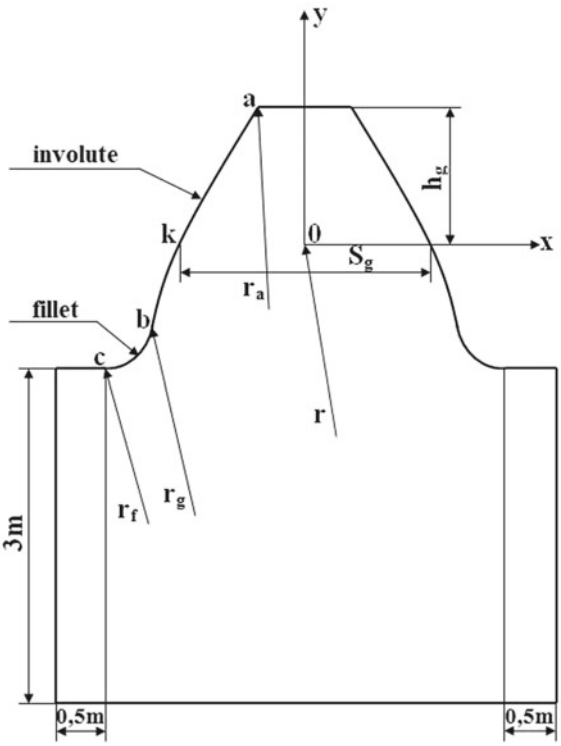

Fig. 33.1 Cross-section tooth profile

where $A_э = mx^* - k + U\cos\alpha + r$, $B_э = (mx^* - k + U\cos\alpha)ctg\alpha$, $\varphi_Э = [U/\sin\alpha - \pi m/4 - k(tg\alpha + ctg\alpha) + mx^* ctg\alpha]/r$. Linear parameter U is varying from $U_{\min} = 0$ (in point b), to $U_{\max} = ntg\alpha + (k - mx^*)/\cos\alpha$(in point a)

We also obtain the parametric equations of the tooth fillet portion ($b - c$):

$$\begin{cases} x_г = A_г \sin\varphi_г - B_г \cos\varphi_г; \\ y_г = A_г \cos\varphi_г + B_г \sin\varphi_г - r, \end{cases}$$

where $A_г = m[x^* - k^* + \rho_i^*(\sin\alpha - \sin\vartheta) + 0.5z\ ]$,
$B_г = m[x^* - k^* + \rho_i^*(\sin\alpha - \sin\vartheta)]ctg\vartheta$,
$\varphi_г = -m[\pi/4 + k^* tg\alpha + \rho_i^*\cos\alpha - (x^* - k^* + \rho_i^*\sin\alpha)ctg\vartheta]/r$.

Angle parameter ϑ varies from $\vartheta_{\min} = \alpha$ (in point b) to $\vartheta_{\max} = \pi/2$(in point c). At the final step of calculation, the following checks were made: (1) at point a, $(r + y_Э)^2 + x_Э^2 = r_a^2$; (2) at point b, $x_Э = x_г$ and $y_Э = y_г$; 3) at point c, $(r + y_г)^2 + x_г^2 = r_f^2$. The right side of the tooth profile is symmetrical to the left about the axis Oy, i.e. $x_{прав.} = -x_{лев.}$ and $y_{прав.} = y_{лев.}$

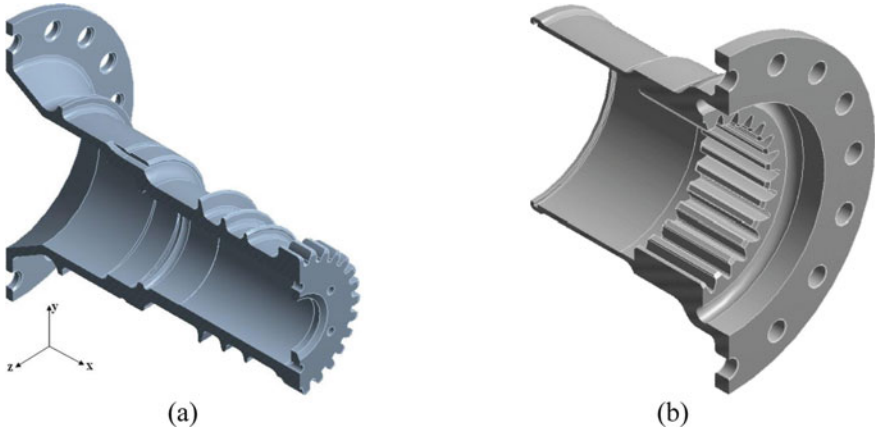

Fig. 33.2 Solid models of tip (**a**) and shaft (**b**) (axial section)

It is assumed that the shaft and tip are in perfect coaxial position. The end face of the shaft in the wider part is fixed in all directions, and a load in the form of the moment M is applied to the end face of the tip in the wider part, which causes rotation around its axis. Between the contacting surfaces of the teeth of the tip and the shaft, Coulomb friction with a coefficient k is set. Solid-state models of junction elements are shown in Fig. 33.2.

33.3 Finite-Element Simulation of Contact Interaction in Transmission Spline Junction

To solve this problem, the finite element method and the ANSYS software package were used. To construct the finite element mesh, a ten-node tetrahedral elastic element SOLID187 was used. For better convergence and increased accuracy of calculations in accordance with the methodology for solving contact problems on the surfaces of the teeth of the shaft and tip, directly contacting each other, condensing of the finite element meshing was applied. To simulate contact interaction, the surfaces of the teeth of the tip and the shaft were coated with CONTA174 and TARGE170, respectively. The constructed finite element model of the junction is shown in Figs. 33.3 and 33.4.

33.4 Results

To conduct numerical calculations, the following values of the mechanical characteristics of the materials were applied: for the tip—a material with Young's modulus

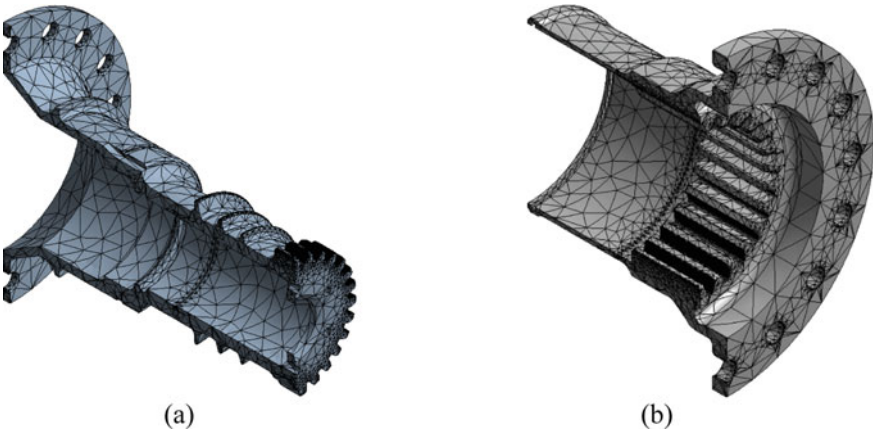

Fig. 33.3 Finite-element models of tip (**a**) and shaft (**b**) (axial section)

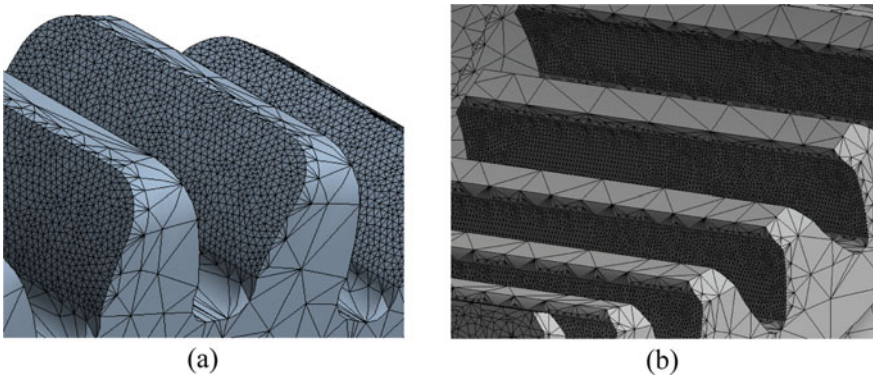

Fig. 33.4 Finite-element meshing of the tip (**a**) and shaft (**b**) surfaces

$E_1 = 2 \times 10^5$ MPa, Poisson's ratio $\upsilon_1 = 0.3$, density $\rho_1 = 7850$ kg/m^3; for the shaft—a material with Young's modulus $E_2 = 3 \times 10^5$ MPa, Poisson's ratio $\upsilon_2 = 0.28$ and density $\rho_2 = 7850$ kg/m^3. The moment M applied to the tip was set to 5×10^4 N/m, the friction coefficient between the contacting teeth surfaces $k = 0.15$.

The main attention in the calculations was given to the study of contact pressure q and effective (equivalent) stresses σ_e on the surfaces of the teeth of the tip directly at contact with the teeth of the shaft. The results are given for one of the contacting surfaces, since with perfect alignment on all the teeth of the tip due to the uniformity of their geometry and the applied load, the results coincide.

In a real junction, due to the volumetric design of the tail transmission and the complex connection scheme of its individual components during operation, it is not possible to achieve ideal alignment of the mating elements. In the individual transmission shafts, the axis of the tip and the cup deviate by an angle within 7 min

(0.01°). To assess the effect of the misaligned arrangement of the spline joint elements on the stress-strain state, calculations were performed for cases when the axis of the cup has a horizontal deviation (rotation about the *Oy*-axis in Fig. 33.2a) or vertical (rotation about the *Oz*-axis in Fig. 33.2a) relative to the tip axis.

Calculations show that the deviation of the axis of the shaft in the horizontal plane leads to a shift of the contact spot in the corresponding direction, while the contact pressure values change by no more than 4%, effective stresses by no more than 9% compared to those with the coaxial position. When the axis of the shaft deviates in the vertical plane, stress concentrators appear. The values of contact pressure and effective stresses in these spots increase by 42% and 25%, respectively.

Further, in accordance with one of the proposed methods for increasing the service life of the test site on the contact surface of the tip tooth, a thin coating was modeled with mechanical characteristics different from the initial tooth material. It is assumed that the coating and tooth surface are rigidly joined. When setting the mechanical characteristics of the coating, the following condition was fulfilled: the elastic modulus of the E_3 coating should be higher than that of the material of the teeth of the tip, but not exceed the corresponding value for the teeth of the shaft. In order to estimate the effect of the elastic modulus and Poisson's ratio for a coating with a thickness of 40 μm, contact pressure and effective stresses were calculated for various values of these characteristics. The results are shown in Table 33.1.

It follows from the table that an increase in the elastic modulus and Poisson's ratio leads to an increase in contact pressure and effective stresses on the surface of the coating, while the effective stresses on the boundary between the coating and the tooth edge practically do not change. It should be noted that a change in the

Table 33.1 Maximum values of contact pressure and effective stress on the surface of the coating, as well as the effective stress at the interface between the coating and the tooth tip edge for various values of the elastic modulus and Poisson's ratio of the coating

Young's modulus and Poisson's ratio values of coating	Maximum contact pressure on the surface of the coating q, MPa	Maximum effective stress on the surface of the coating σ_{emax}, MPa	Maximum effective stress in the interface of the coating and tooth σ_{emax}, MPa
$E_3 = 2.5 \times 10^5$ MPa, $\upsilon_3 = 0.25$	533	936	205
$E_3 = 2.5 \times 10^5$ MPa, $\upsilon_3 = 0.3$	535	944	206
$E_3 = 2.5 \times 10^5$ MPa, $\upsilon_3 = 0.35$	537	956	207
$E_3 = 3 \times 10^5$ MPa, $\upsilon_3 = 0.25$	558	1066	206
$E_3 = 3 \times 10^5$ MPa, $\upsilon_3 = 0.3$	559	1092	206
$E_3 = 3 \times 10^5$ MPa, $\upsilon_3 = 0.35$	564	1095	207

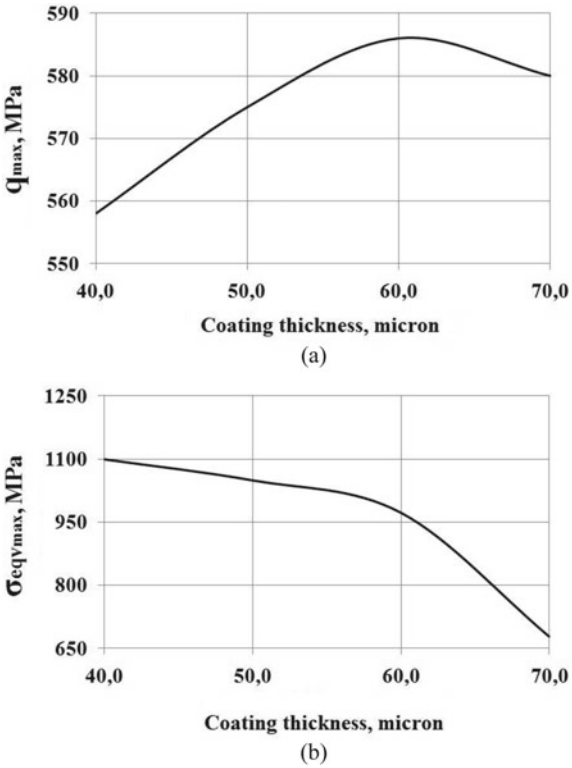

Fig. 33.5 Dependences of maximum contact pressure (**a**) and effective stresses (**b**) on coating thickness of the coating surface

elastic modulus has a greater effect on the values of the calculated stresses than the Poisson's ratio.

To study the effect of the coating thickness on the stress-strain state, the contact pressure distributions and the effective stresses on the coating surface were compared, as well as the effective stresses at the interface between the coating and the tooth face on which it was applied.

Using the obtained data, we plotted the dependence of the maximum contact pressure and effective stress on the coating surface, as well as the effective stress at the interface between the coating and the tooth edge (which is coated), from the coating thickness (Figs. 33.5, 33.6). The coating characteristics are given as following: $E_3 = 3 \times 10^5$ MPa, $\upsilon_3 = 0.3$, $\rho_3 = 7850$ kg/m^3.

33.5 Conclusions

From the analysis of the results obtained, it follows that with perfect alignment of the shaft and tip and a large load, as well as taking into account the shape of the teeth, contact occurs in the middle of the surface of the tip tooth. In this case, the

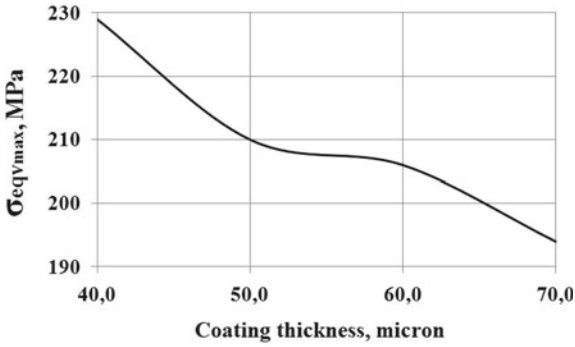

Fig. 33.6 Dependence of maximum effective stress σ_e on coating thickness at the interface of coating and tooth

maximum values of contact pressure and effective stresses are reached at the point of intersection of the involute with the fillet, since this point is irregular. After estimation of the misaligned arrangement effect of the spline junction elements on the stress-strain state, it was found that deviation from the coaxial position in the vertical plane has a greater effect on the contact pressure and effective stresses on the tip tooth surface than the deviation in the horizontal plane.

The study of the coating influence on the stress-strain state showed that with an increase in the elastic characteristics of the coating material, an increase in the contact pressure and effective stresses on the coating surface is observed. This is due to a decrease in contact area. The effective stresses at the boundary between the coating and the face of the tip tooth on which it is applied are practically unchanged.

After assessing the thickness influence of the coating, it was found that with an increase in this parameter, a more uniform distribution of stresses occurs in the coating. Furthermore, this leads to a decrease in effective stresses both on the surface of the coating and on the boundary between the coating and the tooth edge, but the contact pressure increases in this case. Probably, this may be connected with a decrease in the influence of the material of the tip tooth, for which the value of the elastic modulus was set lower than that of the coating.

The refinement of the developed model will allow us to solve contact problems for the components of the spline junction, taking into account the presence of coating on interacting surfaces. Based on the data obtained by such calculations, recommendations can be made on the choice of coating thickness for specific values of their physical and mechanical characteristics in order to optimize the stress-strain state of the assembly.

Acknowledgements The research is carried out in accordance with the Federal Target Program "*Research and Development in the Priority Areas of Development of the Russian Scientific and Technological Complex* for 2014–2020" *and* is supported by the Government of the Russian Federation represented by the Ministry of Higher Education and Science of Russia (Agreement No. 14.607.21.0203, Project identifier RFMEFI60718X0203).

References

1. D.K. Dwivedi, *Surface Engineering: Enhancing Life of Tribological Components* (Springer, New Delhi, 2018), p. 224
2. B.N.J. Persson, *Sliding Friction. Physical Principles and Applications* (Springer, Berlin, 2000), p. 513
3. V.A. Levchenko, I.A. Buyanovsky, V.N. Matveenko, J. Mater. Sci. Chem. Eng. **5**(1), 175 (2017)
4. L.R. Rudnick (ed.), *Lubricant Additives Chemistry and Applications*, 2nd ed. (CRC Press, New York, 2009), p. 778
5. L.H. Baldaev, *Renovation and Hardening of Machine Parts Using Thermal Spraying Methods* (KHT, Moscow, 2004), p. 134 (in Russian)
6. S. Armadar, R. Schmid, S. Equey, I. Fagoaga, N. Espallargas, J. Therm. Spray Technol. **22**(1), 10 (2013)
7. D.V. Shtansky, A.N. Sheveiko, M.J. Petrzhik, E.E. Levashov, A. Leyland, A.L. Yerokhin, D. Mathews, Surf. Coat. Technol. **200**(1–4), 208 (2005)
8. A.A. Voevodin, D.V. Shtansky, E.A. Levashov, J.J. Moore (ed.), *Nanostructured Thin Films and Nanodispersion Strengthened Coatings* (Springer Science & Business Media, 2004), p. 322

Chapter 34
Shell with Auxetic Properties in the Model Taking into Account the Transverse Shear

Anatoly S. Yudin

Abstract The Tymoshenko type model of constructively anisotropic shell with auxetic properties is considered. Forced oscillations in the frequency range including the first resonances are analyzed. The internal scattering of vibrational energy is taken into account. The influence of the transverse shear on the amplitude-frequency characteristics (AFCs) of the input malleability is investigated. It is compared with the frequency response obtained from the equations of the theory of Kirchhoff-Love.

34.1 Introduction

The intention to increase the level of operational properties of materials creates new areas of research. In particular, the direction of search for structures that have anomalous properties is developing. They include materials with a negative Poisson's ratio, which can expand in a direction perpendicular to the direction of stretching (auxetics). Data on such materials, natural and artificial, are collected in the detailed review [1], in which typical structures are considered and their classification is given. The history of search of natural materials, experimental observations and development of mechanical models with properties of auxetics is also briefly presented.

One of the methods for creating auxetic materials is the technology of composite materials. The possibilities of obtaining inexpensive quasi-isotropic auxetic materials in the form of two-phase composites, one of the phases of which are auxetic particles, are analyzed. The particles can have different shapes: spherical, ellipsoidal, disk, blade and needle. Auxetic composites, the matrix phase and the filler which are not authenticate, are also considered. Several approaches differ in the level of detail of the environment and scale levels. There are three levels:

1. *macroscopic level*, when the occurrence of a negative Poisson's ratio is explained on the basis of the relations of the theory of elasticity of anisotropic bodies;

A. S. Yudin (✉)
I. I. Vorovich Institute of Mathematics, Mechanics and Computer Sciences, Southern Federal University, Rostov-on-Don, Russia
e-mail: ayudin@sfedu.ru

I. A. Parinov et al. (eds.), *Advanced Materials*, Springer Proceedings in Materials 6, https://doi.org/10.1007/978-3-030-45120-2_34

macroscopic analysis covers, for example, composites formed by oblique-angle reinforcement of an elastic matrix;
2. *mesoscopic level*, when the auxetic properties are due to the form of structural units at the scale of cells, pores, inclusions, etc.; periodic inhomogeneities of the meso-level have foam, granular materials and some others;
3. *microscopic level*, when, the features of elastic behavior are explained by intra- and intermolecular interaction, which is typical for many single crystals and some other materials [1].

Composites are characterized by properties associated with a decrease in shear stiffness. Therefore, in the case of shells, there is a need to apply refined models. Previously, the Kirchhoff-Love type theory was used in the trial analysis [2]. The calculations showed a noticeable effect of the negative Poisson's ratio on the reduction of the amplitudes of forced vibrations. Here the effect of the transverse shift is estimated using the equations of the Tymoshenko-type theory in combination with the auxetic properties. The method of complex amplitudes and semi-analytical method of solution construction are used. In the case of a cylindrical shell freely supported at the ends, Fourier series in two coordinates are used. The problem of forced oscillations is solved by decomposition of the displacement amplitudes in the eigenforms of oscillations. This provides a separation of equations to determine the coefficients of the harmonic numbers. The algorithm on this basis allows one to build the amplitude-frequency characteristics necessary for analysis quickly, taking into account the losses in the material.

34.2 Basic Equations

Let us consider the shell of rotation in a system of curvilinear orthogonal coordinates which lines coincide with the lines of the principal curvatures. According to the hypothesis of a direct non-orthogonal material normal, the displacements of shell points are defined as follows:

$$\begin{aligned} &U(\alpha_1,\ \alpha_2,\ z) = u(\alpha_1,\ \alpha_2) + z\varphi_1(\alpha_1,\ \alpha_2),\ V(\alpha_1,\ \alpha_2,\ z) = v(\alpha_1,\ \alpha_2) + z\varphi_2(\alpha_1,\ \alpha_2) \\ &W(\alpha_1,\ \alpha_2,\ z) = w(\alpha_1,\ \alpha_2), \end{aligned} \tag{34.1}$$

where u, v, w are the components of displacements of points of the middle surface of the shell; φ_1, φ_2 are angles of rotation normal to the middle surface. The number of degrees of freedom of the material here is five.

In this case, the linear deformation relations have the form:

$$\begin{aligned} &\varepsilon_{11}(\alpha_1,\ \alpha_2,\ z) = E_{11}(\alpha_1,\ \alpha_2) + zK_{11}(\alpha_1,\ \alpha_2),\ \varepsilon_{13}(\alpha_1,\ \alpha_2,\ z) = E_{13}(\alpha_1,\ \alpha_2),\ (1 \leftrightarrow 2), \\ &\varepsilon_{12}(\alpha_1,\ \alpha_2,\ z) = E_{12}(\alpha_1,\ \alpha_2) + zK_{12}(\alpha_1,\ \alpha_2), \varepsilon_{33}(\alpha_1,\ \alpha_2,\ z) = 0. \end{aligned} \tag{34.2}$$

Here E_{jj}, E_{12}, E_{j3}, K_j, K_{12}, (j = 1, 2) are the tensile-compression deformation, tangential and transverse shear, curvature changes, torsion of the middle surface of the shell, respectively. They are associated with the components of displacements and angles of rotation for normal formulae:

$$\begin{aligned}
E_{11} &= \frac{1}{A_1}\frac{\partial u}{\partial \alpha_1} + \frac{1}{A_1 A_2}\frac{\partial A_1}{\partial \alpha_2} v + k_1 w, E_{13} = \varphi_1 - \vartheta_1, (1 \leftrightarrow 2),\\
E_{12} &= \frac{1}{A_1}\frac{\partial v}{\partial \alpha_1} - \frac{1}{A_1 A_2}\frac{\partial A_1}{\partial \alpha_2} u + \frac{1}{A_2}\frac{\partial u}{\partial \alpha_2} - \frac{1}{A_1 A_2}\frac{\partial A_2}{\partial \alpha_1} v,\\
K_{11} &= \frac{1}{A_1}\frac{\partial \phi_1}{\partial \alpha_1} + \frac{1}{A_1 A_2}\frac{\partial A_1}{\partial \alpha_2}\varphi_2, (1 \leftrightarrow 2),\\
K_{12} &= \left(\frac{1}{A_1}\frac{\partial \varphi_2}{\partial \alpha_1} - \frac{1}{A_1 A_2}\frac{\partial A_1}{\partial \alpha_2}\varphi_1\right) + \left(\frac{1}{A_2}\frac{\partial \varphi_1}{\partial \alpha_2} - \frac{1}{A_1 A_2}\frac{\partial A_2}{\partial \alpha_1}\varphi_2\right),\\
\vartheta_1 &= k_1 u - \frac{1}{A_1}\frac{\partial w}{\partial \alpha_1}, \vartheta_2 = k_2 v - \frac{1}{A_2}\frac{\partial w}{\partial \alpha_2},
\end{aligned} \tag{34.3}$$

where: A_1, A_2 are the Lame coefficients; k_1, k_2 are the main curvatures of the middle surface of the shell.

For rotation shells, the kinematic relations (34.3) can be written as follows:

$$\begin{aligned}
&E_{11} = u' + k_1 w, E_{22} = v^{\bullet} + \psi u + k_2 w, E_{12} = v' + u^{\bullet} - \psi v,\\
&K_{11} = \varphi_1', K_{22} = \varphi_2^{\bullet} + \psi \varphi_1, K_{12} = \varphi_2' + \varphi_1^{\bullet} - \psi \varphi_2,\\
&E_{13} = \varphi_1 - \vartheta_1, E_{23} = \varphi_2 - \vartheta_2, \vartheta_1 = k_1 u - w', \vartheta_2 = k_2 v - w^{\bullet},\\
&(\cdot)' = \frac{1}{A_1}\frac{\partial ()}{\partial \alpha_1}, (\cdot)^{\bullet} = \frac{1}{A_2}\frac{\partial ()}{\partial \alpha_2}, \psi = \frac{1}{A_1 A_2}\frac{\partial A_2}{\partial \alpha_1}.
\end{aligned} \tag{34.4}$$

In the cylindrical shell version: $k_1 = 0$, $k_2 = 1/R_c$, $\psi = 0$, $A_2 = R_c$,

$$\begin{aligned}
&E_{11} = u', E_{22} = v^{\bullet} + k_2 w, E_{12} = v' + u^{\bullet},\\
&K_{11} = \varphi_1', K_{22} = \varphi_2^{\bullet}, K_{12} = \varphi_2' + \varphi_1^{\bullet},\\
&E_{13} = \varphi_1 - \vartheta_1, E_{23} = \varphi_2 - \vartheta_2, \vartheta_1 = -w', \vartheta_2 = k_2 v - w^{\bullet}.
\end{aligned} \tag{34.5}$$

Equations of motion of the envelope follow the principle of Hamilton: $\int_0^t (\delta K - \delta U + \delta A)dt = 0$, in which the integrand is formed by the algebraic sum of the variations of the kinetic energy δK, the potential energy δU, and the elementary work of the external forces δA:

$$\begin{aligned}
\delta U = \iint_S &(T_{11}\delta E_{11} + T_{22}\delta E_{22} + S\delta E_{12} + Q_{11}\delta E_{13} + Q_{22}\delta E_{23} + M_{11}\delta K_{11} + M_{22}\delta K_{22}\\
&+ 2H\delta K_{12})A_1 A_2 d\alpha_1 d\alpha_2,
\end{aligned}$$

$$\delta K = \iint\limits_{s} \{b(u_{,t}\,\delta u_{,t} + v_{,t}\,\delta v_{,t} + w_{,t}\,\delta w_{,t}) + c(u_{,t}\,\delta\varphi_{1,t} + v_{,t}\,\delta\varphi_{2,t} + \varphi_{1,t}\,\delta u_{,t} + \varphi_{2,t}\,\delta v_{,t}) + d(\phi_{1,t}\,\delta\varphi_{1,t} + \varphi_{2,t}\,\delta\varphi_{2,t})\}A_1A_2 d\alpha_1 d\alpha_2,$$

$$\delta A = \iint\limits_{s} (q_1\delta u + q_2\delta v + q_3\delta w)A_1A_2\, d\alpha_1 d\alpha_2. \tag{34.6}$$

Here

$$T_{jj} = \int\limits_{h} \sigma_{jj} dz,\ Q_{jj} = \int\limits_{h} \sigma_{j3} dz,\ H = \int\limits_{h} \sigma_{12} z dz,\ S = \int\limits_{h} \sigma_{12} dz\ ,\ M_{jj} = \int\limits_{h} \sigma_{jj} z dz,\ j = 1, 2 \tag{34.7}$$

are the internal forces and moments, given to the main surface, respectively;

$$b = \int\limits_{h} \rho\, dz\ ,\ c = \int\limits_{h} \rho z dz\ ,\ d = \int\limits_{h} \rho z^2 dz \tag{34.8}$$

are the inertia coefficients; ρ is the density of the shell material.

In the future, the established forced oscillations of the shell with the dependence of the values on time t of the form are considered: $F(\alpha_1, \alpha_2, t) = F_a(\alpha_1, \alpha_2)e^{-i\omega t}$, where F_a is the complex amplitude of the harmonic quantities included in the equation, ω is the circular frequency of the driving load.

After substitution of expressions (34.6) for variations, execution of the procedure for transferring derivatives, separation of the time parameter and assembling the coefficients with independent variations δu, δv, δw, $\delta\varphi_1$, $\delta\varphi_2$, the equations of harmonic stationary oscillations for complex amplitudes are obtained from the Hamilton principle. They have the form in the embodiment of the shells of rotation:

$$\begin{aligned}
&T'_{11} + \psi(T_{11} - T_{22}) + S^{\bullet} + k_1 Q_{11} + \omega^2(bu + c\varphi_1) + q_1 = 0,\\
&S' + 2\psi S + T^{\bullet}_{22} + k_2 Q_{22} + \omega^2(bv + c\varphi_2) + q_2 = 0,\\
&Q'_{11} + \psi Q_{11} + Q^{\bullet}_{22} - k_1 T_{11} - k_2 T_{22} + \omega^2 bw + q_3 = 0,\\
&M'_{11} + \psi(M_{11} - M_{22}) + H^{\bullet} - Q_{11} + \omega^2(cu + d\varphi_1) = 0,\\
&H' + 2\psi H + M^{\bullet}_{22} - Q_{22} + \omega^2(cv + d\varphi_2) = 0.
\end{aligned} \tag{34.9}$$

For a cylindrical shell we have:

$$\begin{aligned}
&T'_{11} + S^{\bullet} + \omega^2(bu + c\varphi_1) + q_1 = 0,\ S' + T^{\bullet}_{22} + k_2 Q_{22} + \omega^2(bv + c\varphi_2) + q_2 = 0,\\
&Q'_{11} + Q^{\bullet}_{22} - k_2 T_{22} + \omega^2 bw + q_3 = 0,\ M'_{11} + H^{\bullet} - Q_{11} + \omega^2(cu + d\varphi_1) = 0,\\
&H' + M^{\bullet}_{22} - Q_{22} + \omega^2(cv + d\varphi_2) = 0,
\end{aligned} \tag{34.10}$$

where for complex amplitudes the designations of the initial values are left. The elasticity relations are taken in the form of constructive orthotropy:

$$\begin{gathered}
T_{11} = B_{11}E_{11} + B_{12}E_{22} + A_{11}K_{11} + A_{12}K_{22}, T_{22} = B_{12}E_{11} + B_{22}E_{22} + A_{12}K_{11} + A_{22}K_{22}, \\
M_{11} = A_{11}E_{11} + A_{12}E_{22} + D_{11}K_{11} + D_{12}K_{22}, M_{22} = A_{12}E_{11} + A_{22}E_{22} + D_{12}K_{11} + D_{22}K_{22}, \\
S = B_{33}E_{12} + A_{33} \cdot 2K_{12}, H = A_{33}E_{12} + D_{33} \cdot 2K_{12}, Q_{11} = G_{13}E_{13}, \;\; Q_{22} = G_{23}E_{23};
\end{gathered} \tag{34.11}$$

$$\begin{gathered}
B_{11} = \sum_{\lambda=1}^{\Lambda} B_{1(\lambda)} + B_{p1}, \;\; B_{22} = \sum_{\lambda=1}^{\Lambda} B_{2(\lambda)} + B_{p2}, \\
B_{12} = B_{21} = \sum_{\lambda=1}^{\Lambda} B_{1(\lambda)}\nu_{2(\lambda)} = \sum_{\lambda=1}^{\Lambda} B_{2(\lambda)}\nu_{1(\lambda)}, B_{33} = \sum_{\lambda=1}^{\Lambda} \bar{G}_{(\lambda)}, \\
D_{11} = \sum_{\lambda=1}^{\Lambda} (D_{1(\lambda)} + z_{(\lambda)}^2 B_{1(\lambda)}) + D_{p1}, D_{12} = \sum_{\lambda=1}^{\Lambda} (D_{1(\lambda)} + z_{(\lambda)}^2 B_{1(\lambda)})\nu_{2(\lambda)}, \\
D_{22} = \sum_{\lambda=1}^{\Lambda} (D_{2(\lambda)} + z_{(\lambda)}^2 B_{2(\lambda)}) + D_{p2}, A_{11} = \sum_{\lambda=1}^{\Lambda} B_{1(\lambda)}z_{(\lambda)} + B_{p1}z_{p1}, \\
A_{22} = \sum_{\lambda=1}^{\Lambda} B_{2(\lambda)}z_{(\lambda)} + B_{p2}z_{p2}, A_{12} = \sum_{\lambda=1}^{\Lambda} B_{1(\lambda)}z_{(\lambda)}\nu_{2(\lambda)}, A_{33} = \sum_{\lambda=1}^{\Lambda} \bar{G}_{(\lambda)}z_{(\lambda)}, \\
B_{11} = \sum_{\lambda=1}^{\Lambda} B_{1(\lambda)} + B_{p1}, \;\; B_{22} = \sum_{\lambda=1}^{\Lambda} B_{2(\lambda)} + B_{p2}, B_{12} = B_{21} = \sum_{\lambda=1}^{\Lambda} B_{1(\lambda)}\nu_{2(\lambda)} = \sum_{\lambda=1}^{\Lambda} B_{2(\lambda)}\nu_{1(\lambda)}, \\
B_{33} = \sum_{\lambda=1}^{\Lambda} \bar{G}_{(\lambda)}, D_{11} = \sum_{\lambda=1}^{\Lambda} (D_{1(\lambda)} + z_{(\lambda)}^2 B_{1(\lambda)}) + D_{p1}, D_{12} = \sum_{\lambda=1}^{\Lambda} (D_{1(\lambda)} + z_{(\lambda)}^2 B_{1(\lambda)})\nu_{2(\lambda)}, \\
D_{22} = \sum_{\lambda=1}^{\Lambda} (D_{2(\lambda)} + z_{(\lambda)}^2 B_{2(\lambda)}) + D_{p2}, D_{33} = \sum_{\lambda=1}^{\Lambda} (\tilde{G}_{(\lambda)} + z_{(\lambda)}^2 \bar{G}_{(\lambda)}) + \tilde{G}_{p1} + \tilde{G}_{p2}, \\
A_{11} = \sum_{\lambda=1}^{\Lambda} B_{1(\lambda)}z_{(\lambda)} + B_{p1}z_{p1}, A_{22} = \sum_{\lambda=1}^{\Lambda} B_{2(\lambda)}z_{(\lambda)} + B_{p2}z_{p2}, \\
A_{12} = \sum_{\lambda=1}^{\Lambda} B_{1(\lambda)}z_{(\lambda)}\nu_{2(\lambda)}, A_{33} = \sum_{\lambda=1}^{\Lambda} \bar{G}_{(\lambda)}z_{(\lambda)};
\end{gathered} \tag{34.12}$$

$$\begin{gathered}
B_{1(\lambda)} = E_{1(\lambda)}h_{(\lambda)}/\bar{\nu}_{(\lambda)}, \; B_{2(\lambda)} = E_{2(\lambda)}h_{(\lambda)}/\bar{\nu}_{(\lambda)}, \\
D_{1(\lambda)} = E_{1(\lambda)}h_{(\lambda)}^3/(12\bar{\nu}_{(\lambda)}), \; D_{2(\lambda)} = E_{2(\lambda)}h_{(\lambda)}^3/(12\bar{\nu}_{(\lambda)}), \\
\bar{G}_{(\lambda)} = G_{(\lambda)}h_{(\lambda)}\bar{\nu}_*, \; \tilde{G}_{(\lambda)} = G_{(\lambda)}h_{(\lambda)}^3\bar{\nu}_*/12, \;\; \bar{\nu}_* = 1 - \nu_*^2, \; \bar{\nu}_{(\lambda)} = (1 - \nu_{1(\lambda)}\nu_{2(\lambda)})/\bar{\nu}_*, \\
\tilde{G}_{p1} = G_{p1}J_{p1}/l_{p1}, \; \tilde{G}_{p2} = G_{p2}J_{p2}/l_{p2}, \;\; B_{p1} = E_{p1}F_{p1}/l_{p1}, \; B_{p2} = E_{p2}F_{p2}/l_{p2}, \\
D_{p1} = E_{p1}I_{p1}^{o}/l_{p1}, \; D_{p2} = E_{p2}I_{p2}^{o}/l_{p2}, \;\; I_{p1}^{o} = I_{p1} + z_{p1}^2F_{p1}, \; I_{p2}^{o} = I_{p2} + z_{p2}^2F_{p2}.
\end{gathered} \tag{34.13}$$

Here $E_{k(\lambda)}$ are elastic constants of layers (k = 1, 2); $h_{(\lambda)}$ is the thicknesses; $z_{(\lambda)}$ are the eccentricities (normal coordinates of the middle surface of the λ-th layer); l_{pk} is the distance between the ribs; E_{pk}, G_{pk} are the Young's moduli and shear of the material of the ribs; F_{pk} is the cross-section area (CSA) of ribs; I_{pk} are the moments of inertia CSA of the ribs relative to the axes passing through the center of gravity CSA of the ribs parallel to the tangent to the coordinate lines of the reference surface; I_k^o is the moment of inertia of the ribs CSA relative to the tangent of the k-th coordinate line; J_{pk} are the moments of inertia of the ribs in torsion; $B_{k(\lambda)}$, $D_{k(\lambda)}$, $G_{(\lambda)}$, $\tilde{G}_{(\lambda)}$, are

the effective tensile stiffness of the λ-th layer-compression, bending, shear, torsion, respectively; G_{13}, G_{23} are induced shear stiffness of the shell: B_{pk}, $D_{pk,}$ $\tilde{G}_k$ are the stiffness of the ribs in tension-compression, bending, torsion, respectively.

The inertial characteristics of the shell (mass per unit area) are determined by the parameters:

$$\rho_{1j} = \rho_1 + \Delta_j, j = 1,\ 2,\ 3, \rho_1 = \sum_{\lambda=1}^{\Lambda} \rho_{(\lambda)} h_{(\lambda)} + \sum_{k=1}^{2} [\rho_{pk} F_{pk}/(\bar{\nu}_* \int_{pk})]. \quad (34.14)$$

Here ρ_1 is the specific mass of the actually reinforced shell, $\rho_{(\lambda)}$ is the density of the materials of the layers, ρ_{pk} is the density of the materials of the ribs; Δ_j are the inertial components of the masses modeling the useful filling of the shell. These masses can be involved in various ways in oscillations in different coordinate directions. Their accounting can be carried out in different ways depending on the number of the circumferential harmonic. Input design information can be entered in both dimensional and dimensionless form. In the dimensional version should be put $\bar{\nu}_* = 1$.

34.3 Method of Solution

Since we consider axisymmetric constructions, it is possible to separate the circumferential coordinate α_2 in the above equations. Let us limit the normal load q_3, symmetrically located relative to the origin of the circumferential coordinate. Then the decomposition in Fourier series can be performed either in cosines or in sines. For example:

$$w = \sum_{n=0}^{\infty} w_n \cos n\alpha_2,\ v = \sum_{n=0}^{\infty} v_n \sin n\alpha_2, T_{11} = \sum_{n=0}^{\infty} {}_{11n} \cos n\alpha_2,$$
$$q_3 = \sum_{n=0}^{\infty} q_{3n} \cos n\alpha_2, \quad (34.15)$$

and so on. The components of the stress-strain state are decomposed by cosines u, w, φ_1, ϑ_1, E_{11}, E_{22}, E_{12}, E_{13}, E_{23}, K_{11}, K_{22}, K_{12}, T_{11}, T_{22}, M_{11}, M_{22}, Q_{11}, by sine – v, φ_2, ϑ_2, E_{12}, K_{12}, S, H, Q_{22}.

Let us proceed in the basic relations and equations to dimensionless quantities, using the basic normalizing parameters E_*, ν_*, R_*, h_*, ρ_*. They make sense and dimension of the characteristic, respectively, Young's modulus, Poisson's ratio, radius of curvature or linear size (large), thickness (small size), density of the material. Combinations of divisors having the dimension of normalized quantities are formed from the main normalizing parameters.

Symbols are entered: $\varepsilon_* = h_*/R_*$ is the thin-walled parameter; $\bar{\nu}_* = 1 - \nu_*^2$; $B_* = E_* h_*/\bar{\nu}_*$, $A_* = E_* h_*^2/\bar{\nu}_*$, $D_* = E_* h_*^3/\bar{\nu}_*$ are the normalizing values for the coefficients of reduced stiffness in the elasticity relations; $c_* = \sqrt{E_*/(\rho_* \bar{\nu}_*)}$ is the characteristic speed of sound in the shell material; $F_* = R_* h_*/\bar{\nu}_*$, $S_* = R_* h_*^2/\bar{\nu}_*$ $J_* = R_* h_*^3/\bar{\nu}_*$ are the values for normalization of the cross-section parameters of edges (areas and moments of inertia). We also introduce a dimensionless frequency parameter, related to the circular frequency $\omega = 2\pi f$, where f is the frequency in hertz, by the formula: $\Omega = \omega R_*/c_*$.

The formulae of transition to dimensionless quantities have the form [3]:

$$
\begin{aligned}
&\{U, V, W, u, v, w\}_L = \{...\}_D / h_*, \quad \{A_1, A_2\}_L = \{...\}_D / R_*,\\
&\{k_1, k_2, \psi; \tau_1, \tau_2; K_{11}, K_{22}, K_{12}\}_L = \{...\}_D \cdot R_*,\\
&\{\vartheta_1, \vartheta_2, \varphi_1, \varphi_2; \varepsilon_{11}, \varepsilon_{22}, \varepsilon_{12}; \Omega_1, \Omega_2; E_{11}, E_{22}, E_{12}\}_L = \{...\}_D / \varepsilon_*,\\
&\{M_{11}, M_{22}, H\}_L = \{...\}_D R_* / D_*, \quad \{T_{11}, T_{22}, S; Q_{11}, Q_{22}\}_L = \{...\}_D R_* / A_*,\\
&\{q_1, q_2, q_3\}_L = \{...\}_D R_*^2 / A_*, \quad \{\rho_1, \rho_{1j}, \Delta_j\}_L = \{...\}_D / (\rho_* h_*),\\
&\{\rho_{(\lambda)}, \rho_{pj}\}_L = \{...\}_D / \rho_*, \quad \{B_{jk}, B_{j(\lambda)}, B_{pj}, \overline{G}_{(\lambda)}, G_{13}, G_{23}\}_L = \{...\}_D / B_*,\\
&\{A_{jk}\}_L = \{...\}_D / A_*, \quad \{D_{jk}\}_L = \{...\}_D / D_*, \quad \{E_{(\lambda)}, G_{(\lambda)}, E_{pj}, G_{pj}\}_L = \{...\}_D / E_*,\\
&\{J_{pj}, I_{pj}, I^o_{pj}\}_L = \{...\}_D / J_*, \quad \{F_{pj}\}_L = \{...\}_D / F_*, \quad j, k = 1, 2, 3.
\end{aligned}
\tag{34.16}
$$

In Formulae (34.16), dimensionless quantities are grouped by braces with the index "L" in the left parts of the equations. Their dimensional (normalized) analogs are implied in brackets with the index "D" in the right parts of the formulae.

As a test design, we consider a circular cylindrical shell supported by the edges of the longitudinal and circumferential directions. The construction was analyzed in [2] by Kirchhoff-Love theory, so a comparison of mathematical models can be made. The main surface of the shell has a radius R. We assume $R^* = R$, then $A_1 = 1$, $A_2 = 1$, $k_2 = 1$.

We apply the method of complex amplitudes to the equations for the cylindrical shell and separate the n-th circumferential mode. After the transition to dimensionless quantities, kinematic relations are reduced to the form:

$$
\begin{aligned}
&E_{11n} = u_n', E_{22n} = nv_n + w_n, E_{12n} = v_n' - nu_n,\\
&K_{11n} = \varepsilon_* \varphi_{1n}', K_{22n} = \varepsilon_* n\varphi_{2n}, K_{12n} = \varepsilon_*(\varphi_{2n}' - n\varphi_{1n}),\\
&E_{13n} = \varphi_{1n} - \vartheta_{1n}, E_{23n} = \varphi_{2n} - \vartheta_{2n}, \vartheta_{1n} = -w_n', \vartheta_{2n} = v_n + nw_n;
\end{aligned}
\tag{34.17}
$$

The simplest analytical solution is constructed for the free support: $v = 0$, $M_{11} = 0$, $T_{11} = 0$, $w = 0$, $Q_{11} = 0$, $\varphi_2 = 0$. These conditions and homogeneous ($q_{3n} = 0$) Eqs. (34.1)–(34.3) satisfy the following forms of natural oscillations:

$$u_n(x) = u_{nk} \cos(mx), \quad v_n(x) = v_{nk} \sin(mx), \quad w_n(x) = w_{nk} \sin(mx),$$

$$\varphi_{1n}(x) = \varphi_{1nk}\cos(mx), \quad \varphi_{2n}(x) = \varphi_{2nk}\sin(mx), \tag{34.18}$$

where $m = k\pi/L$, k is a number of longitudinal half-waves, $x = \alpha_1$ is the longitudinal coordinate. We will also denote the circumferential coordinate as $\theta = \alpha_2$.

The problems of forced oscillations can be solved by decomposition of the displacement amplitudes in the eigenforms of oscillations (34.17), i.e. in the Fourier series and along the longitudinal coordinate. This provides a separation of equations to determine the coefficients by mode numbers.

In the circumferential coordinate θ, cosine and sine series expansions are performed in rows in the interval $(0, 2\pi)$ due to the symmetry of the load in the diametrical plane (DP), which is assumed. In the longitudinal direction, the solutions on the interval (0, L) are also represented by rows of sines and cosines. Restrictions on the load coordinates along the length of the shell are not imposed. Here we perform the decomposition of even and odd functions on the interval (−L, L), which are formally considered as a continuation of the solution to the interval (−L, 0) in an even or odd way. We are only interested in the part on the interval (0, L) of the shell. Therefore, the number n is the number of waves in the circumferential direction, and k is the number of half-waves on the generator of the shell.

The series solution for displacement and rotation angles as functions of coordinates and frequency is

$$\begin{aligned}
u(x,\ \theta,\ \Omega) &= \sum_{k=1}^{M} u_{0k}(\Omega)\cos[(k\pi/L)x] + \sum_{k=1}^{M}\sum_{n=1}^{N} u_{nk}(\Omega)\cos[(k\pi/L)x]\cos(n\theta),\\
v(x,\ \theta,\ \Omega) &= \sum_{k=1}^{M}\sum_{n=1}^{N} v_{nk}(\Omega)\sin[(k\pi/L)x]\sin(n\theta),\\
w(x,\ \theta,\ \Omega) &= \sum_{k=1}^{M} w_{0k}(\Omega)\sin[(k\pi/L)x] + \sum_{k=1}^{M}\sum_{n=1}^{N} w_{nk}(\Omega)\sin[(k\pi/L)x]\cos(n\theta),\\
\varphi_1(x,\ \theta,\ \Omega) &= \sum_{k=1}^{M} \varphi_{10k}(\Omega)\cos[(k\pi/L)x] + \sum_{k=1}^{M}\sum_{n=1}^{N} \varphi_{1nk}(\Omega)\cos[(k\pi/L)x]\cos(n\theta),\\
\varphi_2(x,\ \theta,\ \Omega) &= \sum_{k=1}^{M}\sum_{n=1}^{N} \varphi_{2nk}(\Omega)\sin[(k\pi/L)x]\sin(n\theta).
\end{aligned} \tag{34.19}$$

Using expansions of this type in all relations and equations, we obtain for the coefficients of trigonometric series:

$$\begin{aligned}
&E_{11nk} = -mu_{nk}, \quad E_{22nk} = nv_{nk} + w_{nk}, , E_{12nk} = mv_{nk} - nu_{nk},\\
&K_{11nk} = -\varepsilon_* m\varphi_{1nk}, \quad K_{12nk} = \varepsilon_* n\varphi_{2nk},\ K_{12n} = \varepsilon_*(m\varphi_{2nk} - n\varphi_{1nk}),\\
&E_{13nk} = \varphi_{1nk} + \vartheta_{1nk}, \quad E_{23nk} = \varphi_{2nk} + \vartheta_{2nk},\\
&\vartheta_{1nk} = -mw_{nk}, \quad \vartheta_{2nk} = v_{nk} + nw_{nk}, \vartheta_{2n} = v_n + nw_n;
\end{aligned} \tag{34.20}$$

$$\begin{aligned}
T_{11nk} &= B_{11}E_{11nk} + B_{12}E_{22nk} + A_{11}K_{11nk} + A_{12}K_{22nk},\\
T_{22nk} &= B_{12}E_{11nk} + B_{22}E_{22nk} + A_{12}K_{11nk} + A_{22}K_{22nk},\\
M_{11nk} &= A_{11}E_{11nk} + A_{12}E_{22nk} + D_{11}K_{11nk} + D_{12}K_{22nk},
\end{aligned}$$

$$
\begin{aligned}
&M_{22nk} = A_{12}E_{11nk} + A_{22}E_{22nk} + D_{12}K_{11nk} + D_{22}K_{22nk},\\
&S_{nk} = B_{33}E_{12nk} + 2A_{33}K_{12nk},\\
&H_{nk} = A_{33}E_{12nk} + 2D_{33}K_{12nk},\\
&Q_{11nk} = G_{13}E_{13nk},\ \ Q_{22nk} = G_{23}E_{23nk};
\end{aligned}
\tag{34.21}
$$

$$
\begin{aligned}
&mT_{11nk} + nS_{nk} + \Omega^2(bu_{nk}+\varepsilon_* c\varphi_{1nk}) = 0,\\
&-mS_{nk} - nT_{22nk} + Q_{22nk} + \Omega^2(bv_{nk} + \varepsilon_* c\varphi_{2nk}) = 0,\\
&-mQ_{11nk} + nQ_{22nk} - T_{22nk} + \Omega^2 bw_{nk} + q_{3nk} = 0,\\
&mM_{11nk} + nH_{nk} - Q_{11nk}/\varepsilon_* + \Omega^2(cu_{nk} + \varepsilon_* d\varphi_{1nk}) = 0,\\
&-mH_{nk} - nM_{22nk} - Q_{22nk}/\varepsilon_* + \Omega^2(cv_{nk} + \varepsilon_* d\varphi_{2nk}) = 0.
\end{aligned}
\tag{34.22}
$$

We consider the load acting on the normal to the shell and equivalent to the concentrated force Q_3. Let l is the length of the platform along the longitudinal coordinate, δ_1 is the length of a segment of its midline (like a trapezoid); 2δ is the angle of coverage along the circumferential coordinate; x_1, θ_1 are the longitudinal and angular coordinates of the center of the site, $S = l\delta_1$ is the area of application of the load.

Let us move on to dimensionless quantities by formulae:

$$
\{l,\ \delta_1\}_L = \{l,\ \delta_1\}_D/R_*,\ \ \{Q_3\}_L = \{Q_3\}_D(1-\nu_*^2)/E_*h_*^2,\ \ \{q_3\}_L = \{q_3\}_D(1-\nu_*^2)R_*^2/E_*h_*^2. \tag{34.23}
$$

Further (in a dimensionless form), the concentrated force is "smeared" across the site into the normal intensity load $q_{3a} = Q_3/(l\delta_1)$ distributed over the surface within the platform. In the domain of curvilinear coordinates $\{x\in(0, L);\ \theta\in(0, 2\pi)\}$, corresponding to the shell under consideration, the distributed load can be specified using Heviside step function $h(x)$, which is 0 at $x < 0$ and 1 at $x \geq 0$.

Then in the field of definition $q_3(x, \theta) = q_{3a}\Phi_1(x)\Phi_2(\theta)$, where

$$
\begin{aligned}
&\Phi_1(x) = [H(x - (x_1 - l/2)) - H(x - (x_1 + l/2))],\\
&\Phi_2(\theta) = [H(\theta - (\theta_1 - \delta)) - H(\theta - (\theta_1 + \delta))].
\end{aligned}
\tag{34.24}
$$

The decomposition of the even function $\Phi_2(\theta)$ into cosines has the form:

$$\Phi_2(\theta) = \delta/\pi + \sum_{n=1}^{N} [2/(n\pi)] \sin(n\delta) \cos(n\theta_1) \cos(n\theta). \tag{34.25}$$

Let us continue $\Phi_1(x)$ on the interval (-L, 0) in an odd way. The corresponding expansion in the interval (-L, L) by sine has the form:

$$\Phi_1(x) = \sum_{k=1}^{M} [4/(k\pi)] \sin[(k\pi/L)l/2)] \sin[(k\pi/L)x_1] \sin[(k\pi/L)x)]. \tag{34.26}$$

Thus, the normal load $q_3(x, \theta)$ is approximated by a double row:

$$q(x, \theta) = \frac{a_{\theta 0}}{2} \sum_{k=1}^{M} a_{xk} \sin[(k\pi/L)x] + \sum_{n=1}^{N} \sum_{k=1}^{M} a_{\theta n} a_{xk} \sin[(k\pi/L)x] \cos(n\theta), \tag{34.27}$$

where

$$\begin{aligned} a_{\theta 0} &= q_{3a} 2l/L, \; a_{\theta n} = q_{3a}[2/(n\pi)] \sin(n\delta) \cos(n\theta_1), \\ a_{xk} &= q_{3a}[4/(k\pi)] \sin[(k\pi/L)l/2] \sin(mx_1). \end{aligned} \tag{34.28}$$

or

$$q(x, \theta) = \sum_{n=0}^{N} \sum_{k=1}^{M} q_{nk} \sin[(k\pi/L)x] \cos(n\theta), \; q_{k0} = a_{\theta 0} a_{xk}/2, \; q_{kn} = a_{\theta n} a_{xk}. \tag{34.29}$$

Let us substitute (34.20) into (34.21) and then into (34.22). Collecting the coefficients at u_{nk}, v_{nk}, w_{nk}, φ_{1nk}, φ_{2nk}, we obtain algebraic system of equations of the fifth order to determine the coefficients of the series (34.19) when $n > 0$: $KX = B$. Here $K = [K_{\lambda\mu}]$, $\lambda, \mu = 1, \ldots, 5$ is the matrix of the system; X is the column with unknown elements: $X_1 = u_{nk}$, $X_2 = v_{nk}$, $X_3 = w_{nk}$, $X_4 = \varphi_{1nk}$, $X_5 = \varphi_{2nk}$; B is the right part, dependent on the load ratios:

$$K = \begin{bmatrix} K_{11} & K_{12} & K_{13} & K_{14} & K_{15} \\ K_{21} & K_{22} & K_{23} & K_{24} & K_{25} \\ K_{31} & K_{32} & K_{33} & K_{34} & K_{35} \\ K_{41} & K_{42} & K_{43} & K_{44} & K_{45} \\ K_{51} & K_{52} & K_{53} & K_{54} & K_{55} \end{bmatrix}, X = \begin{bmatrix} X_1 \\ X_2 \\ X_3 \\ X_4 \\ X_5 \end{bmatrix}, \quad B = \begin{bmatrix} 0 \\ 0 \\ q_{nk} \\ 0 \\ 0 \end{bmatrix}. \tag{34.30}$$

The elements of the matrix K are defined by formulae:

$$K_{11} = b\Omega^2 - B_{11}m^2 - B_{33}n^2, K_{12} = mn(B_{12} + B_{33}), K_{13} = B_{12}m,$$
$$K_{14} = \varepsilon_*(c\Omega^2 - A_{11}m^2 - 2A_{33}n^2), K_{15} = \varepsilon_* m(A_{12}m + 2A_{33}n);$$
$$K_{21} = mn(B_{12} + B_{33}), K_{22} = b\Omega^2 - B_{33}m^2 - B_{22}n^2 - G_{23}, K_{23} = -n(B_{22} + G_{23});$$
$$K_{24} = \varepsilon_* mn(A_{12} + 2A_{33}), K_{25} = \varepsilon_*(c\Omega^2 - 2A_{33}m^2 - A_{22}n^2) + G_{23};$$
$$K_{31} = B_{12}m, K_{32} = -n(B_{22} + G_{23}), K_{33} = b\Omega^2 - G_{13}m^2 - G_{23}n^2 - B_{22},$$
$$K_{34} = \varepsilon_*(A_{12}m + A_{22}n) - G_{13}m, K_{35} = n(G_{23} - \varepsilon_* A_{22});$$
$$K_{41} = -(A_{11}m^2 + A_{33}n^2), K_{42} = mn(A_{12} + A_{33}), K_{43} = m(A_{12} - G_{13}/\varepsilon_*),$$
$$K_{44} = \varepsilon_*(d\Omega^2 - D_{11}m^2 - 2D_{33}n^2) - G_{13}/\varepsilon_*, K_{45} = \varepsilon_* mn(D_{12} + 2D_{33});$$
$$K_{51} = mn(A_{12} + A_{33}), K_{52} = c\Omega^2 - A_{22}n^2 - A_{33}m^2 + G_{23}/\varepsilon_*, K_{53} = n(G_{23}/\varepsilon_* - A_{22}),$$
$$K_{54} = \varepsilon_* mn(D_{12} + 2D_{33}), K_{55} = \varepsilon_*(d\Omega^2 - 2D_{33}m^2 - D_{22}n^2) - G_{23}/\varepsilon_*. \quad (34.31)$$

The equations for determining the coefficients of the zero circumferential mode are processed separately. The problem is reduced to a system of three algebraic equations: PY = C with respect to $Y_1 = u_{0k}$, $Y_2 = w_{0k}$, $Y_3 = \varphi_{10k}$, where

$$P = \begin{bmatrix} P_{11} & P_{12} & P_{13} \\ P_{21} & P_{22} & P_{23} \\ P_{31} & P_{32} & P_{33} \end{bmatrix}, Y = \begin{bmatrix} Y_1 \\ Y_2 \\ Y_3 \end{bmatrix}, \quad C = \begin{bmatrix} 0 \\ q_{0k} \\ 0 \end{bmatrix}, \quad (34.32)$$

$$P_{11} = b\Omega^2 - B_{11}m^2, P_{12} = B_{12}m, P_{13} = \varepsilon_*(c\Omega^2 - A_{11}m^2);$$
$$P_{21} = B_{12}m, P_{22} = b\Omega^2 - G_{13}m^2 - B_{22}, P_{23} = \varepsilon_* mA_{12} - G_{13}m;$$
$$P_{31} = c\Omega^2 - A_{11}m^2, P_{32} = m(A_{12} - G_{13}/\varepsilon_*), P_{33} = \varepsilon_*(d\Omega^2 - D_{11}m^2) - G_{23}/\varepsilon_*. \quad (34.33)$$

34.4 Calculations and Analysis

The shell was considered as the initial one, the rigidity of the constructive anisotropy of which is similar to that considered in [2]. Loss factor $\eta = 0.03$, dimensionless length $L = \pi$. The driving harmonic force is applied in the middle of the length.

Let us consider the comparison of models for orthogonal (theory of Kirchhoff—Love—K) and slope normal (the theory of Timoshenko type—T), first. Model K corresponds to the dashed curves, model T—to the continuous ones. The results for the second model have lower vibration amplitudes and strongly depend on the values of the transverse shear modules G_{13} and G_{23}. It was assumed in the calculations $G_{13} = G_{23}$. It is possible both to coincide with the main resonance (mode n = 3, Fig. 34.1), and to leave this resonance to other frequencies (Fig. 34.2). At the same time, close

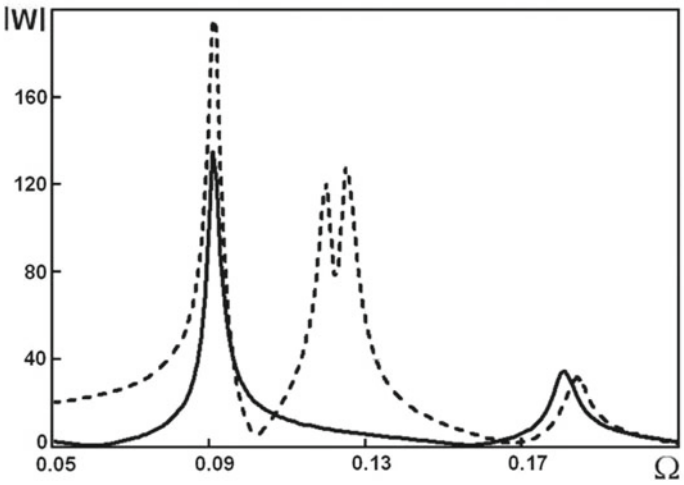

Fig. 34.1 $\nu = 0.3$, $G_{13} = 0.000087B_{33}$

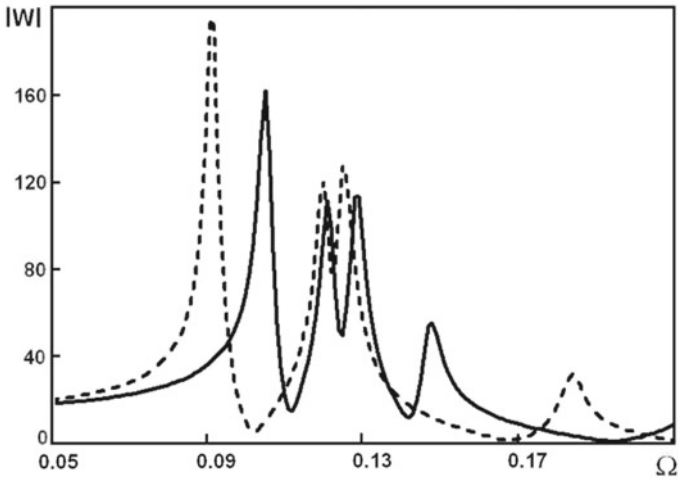

Fig. 34.2 $\nu = 0.3$, $G_{13} = 0.005B_{33}$

in frequency resonance modes n = 2 and n = 4 can be cut off. The resonance of the n = 5 mode can also be shifted.

Let us try to explain the difference between the theories of K and T. We turn to the equations of oscillations (34.9), (34.10). It is necessary to remove the terms associated with the inertia of turns in variant K in the fourth and fifth equations. There are no elasticity relations for shear forces here, since transverse deformations are considered to be zero. The transverse forces are determined from the last two equations through bending and torques and are substituted into the second and third equations.

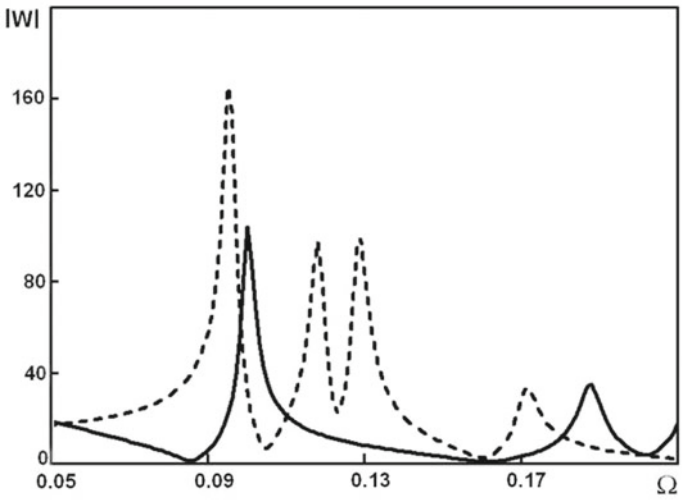

Fig. 34.3 $\nu = -0.5$, $G_{13} = 0.0001B_{33}$

Accordingly, these values are affected by the flexural and torsional stiffness of the shell. In theory of T, the shearing forces become independent stress state components affecting four of the five equations. Therefore, the transverse shear strains and transverse shear modules become decisive here, by varying which it is possible to more flexibly control the amplitude-frequency characteristics.

Let us consider the influence of the Poisson's ratio ν on the amplitude-frequency characteristics in the model of T. The coefficient ν was set equal to -0.5 and -0.3 in the auxetic version. In general, the influence of the negative Poisson's ratio has a positive effect on vibration damping. Here, both the suppression of the resonances $n = 2$ and $n = 4$ (Fig. 34.3), and their preservation (Fig. 34.4) are also observed.

Model variation of material parameters was performed here. It is necessary to set the properties of the material based on the analysis of its structure and mechanical test data to calculate specific products.

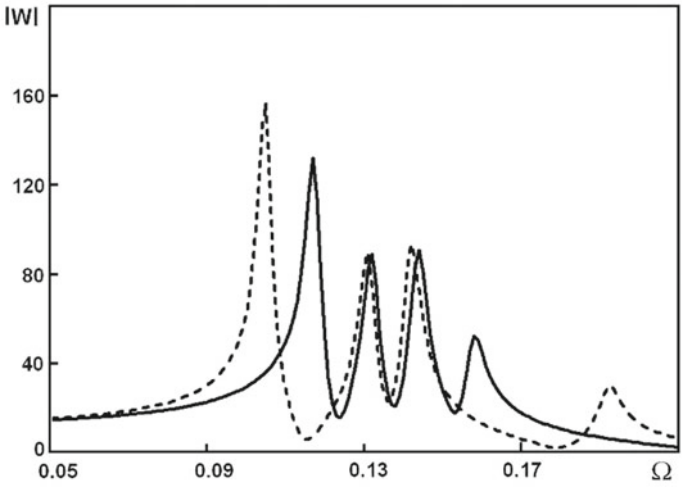

Fig. 34.4 $\nu = -0.3$, $G_{13} = 0.0036B_{33}$

Acknowledgements Research was financially supported by Southern Federal University, 2020 (Ministry of Science and Higher Education of the Russian Federation).

References

1. D.A. Konjok, K.W. Wojciechowski, Y.M. Pleskachevsky, S.V. Shilko, *Mechanics of Composite Materials and Structures (Moscow)*, vol. 10, no. 1 (2004), pp. 35–69
2. A.S. Yudin, S.A. Yudin. in *Proceedings of the 2015 International Conference on Physics and Mechanics of New Materials and Their Applications, devoted to 100th Anniversary of the Southern Federal University*, ed. by I.A. Parinov, S.-H. Chang, V.Y. Topolov (Nova Science Publishers, New York, 2016), pp. 447–452
3. A.S. Yudin, *Stability and Oscillations of Structurally Anisotropic and Articulated Shells of Rotation* (Southern Federal University Press, Rostov-on-Don, 2011), 362 p. (In Russian)

Chapter 35
Coupled Problem of Thermoviscoelasticity for Composite Polymer Shell of Revolution

V. G. Safronenko

Abstract The problem of connectedness of mechanical and thermal fields has acquired great practical importance in the mechanics of shells made of polymer composite materials. A number of specific properties of polymers, such as low thermal conductivity, high sensitivity to temperature change, large hysteresis losses, lead to harmonic loading under the effect of heat generation in the body of the shell, namely dissipative heating. To solve the problem of forced vibrations of polymer composite shells, taking into account thermomechanical connectivity, along with effective thermal-viscoelastic characteristics, it is necessary to specify effective thermal characteristics (thermal conductivity, thermal expansion, and specific heat). A complete system of relations is presented, including the equations of forced oscillations of polymer-based composite shells of revolution, heat conduction equations taking into account the effect of heat generation, the constitutive equations of thermoviscoelasticity with the corresponding boundary conditions. As an example, we consider forced axisymmetric vibrations of a fibrous-layered cylindrical shell. In the following, it is assumed that the hard fitting condition is satisfied at the ends of the shell and the temperature is kept constant.

35.1 Introduction

At the first stage, the solution of the heat generation problem is considered without taking into account the temperature dependences of the properties of the polymer (the so-called weakly coupled problem). Numerical calculations are made for three variants of reinforcement. The amplitude-frequency and temperature-frequency characteristics in the frequency range, including the first eigenfrequencies, are obtained. Further, the related problem of thermoviscoelasticity is considered for the case of axisymmetric forced vibrations. The problem is essentially non-linear in nature due

V. G. Safronenko (✉)
I. I. Vorovich Mathematics, Mechanics and Computer Sciences Institute, Southern Federal University, Rostov-on-Don, Russia
e-mail: safron@math.sfedu.ru; ya.safronenko2014@yandex.ru

I. A. Parinov et al. (eds.), *Advanced Materials*, Springer Proceedings in Materials 6, https://doi.org/10.1007/978-3-030-45120-2_35

to the dependence of polymer properties on temperature and the presence of a dissipative function in the heat equation. Therefore, in solving a system of differential equations, in addition to the orthogonal sweep method, an iterative method was implemented with a given accuracy. The calculations indicate a significant discrepancy between the amplitudes and heat generation temperature in the vicinity of the resonant frequencies. In this case, the solution of the problem, which does not take into account the effect of temperature on the properties of the polymer, yields substantially underestimated values both in the calculation of the amplitude-frequency and temperature-frequency characteristics. Outside the resonance regions, the solutions of both problems are fairly close.

35.2 Methods

The complete system of equations describing the related problem of thermoviscoelasticity for the shell of revolution has the following form in common notations:

$$\begin{aligned}
\frac{1}{A_1}\frac{\mathrm{d}y_1^*}{\mathrm{d}\alpha_1} &= \psi(T_{22} - y_1) - k_1 y_3 - \rho_{11}\Omega^2 y_4 - q_1,\\
\frac{1}{A_1}\frac{\mathrm{d}y_2^*}{\mathrm{d}\alpha_1} &= \psi\big(M_{22)} - y_2\big) + \frac{1}{\varepsilon_1} y_3 - \varepsilon_1\rho_{12}\Omega^2 y_5,\\
\frac{1}{A_1}\frac{\mathrm{d}y_3^*}{\mathrm{d}\alpha_1} &= -\psi y_3 + k_1 y_1 + k_2 T_{22} - \rho_{11}\Omega^2 y_6 - q_3,\\
\frac{1}{A_1}\frac{\mathrm{d}y_4^*}{\mathrm{d}\alpha_1} &= E_{11} - k_1 y_6,\\
\frac{1}{A_1}\frac{\mathrm{d}y_5^*}{\mathrm{d}\alpha_1} &= K_{11},\\
\frac{1}{A_1}\frac{\mathrm{d}y_6^*}{\mathrm{d}\alpha_1} &= k_1 y_4 - \theta_1,\\
\frac{1}{A_1}\frac{\mathrm{d}y_7}{\mathrm{d}\alpha_1} &= \Theta - C_1(y_8 - T_{\mathrm{cp}}) - \psi y_7,\\
\frac{1}{A_1}\frac{\mathrm{d}y_8}{\mathrm{d}\alpha_1} &= -C_2\mu_{11} y_7
\end{aligned} \tag{35.1}$$

In the case of axisymmetric loading the resolving functions are [1]:

$$\begin{aligned}
&y_1^* = T_{11}; \quad y_2^* = M_{11}; \quad y_3^* = Q_{11}; \quad y_4^* = u;\\
&y_5^* = \varphi_1; \quad y_6^* = w; \quad y_7 = q_1; \quad y_8 = T.\\
&y_i^* = y_i^R + i y_i^I
\end{aligned} \tag{35.2}$$

To solve the problem of forced oscillations of polymer composite shells taking into account thermomechanical coupling, along with effective viscoelastic characteristics, it is necessary to set effective thermal characteristics (coefficients of thermal conductivity, thermal expansion and specific heat capacity). For a polydisperse medium with cylindrical inclusions corresponding to a fibrous composite, the effective thermal conductivity coefficients are given in [2]. Due to the transversal isotropy of the medium, only two components of the tensor of the effective thermal conductivity coefficients are independent, and Fourier's law is written as

$$\begin{bmatrix} q_1 \\ q_2 \\ q_3 \end{bmatrix} = \begin{bmatrix} -\lambda_{11} & 0 & 0 \\ 0 & -\lambda_{22} & 0 \\ 0 & 0 & -\lambda_{22} \end{bmatrix} \begin{bmatrix} \nabla_1 T \\ \nabla_2 T \\ \nabla_3 T \end{bmatrix} \tag{35.3}$$

In the coordinate axes (α_1, α_2, z) entered on the median surface of the shell of revolution, respectively:

$$\nabla_1 T = \frac{1}{A_1}\frac{\partial T}{\partial \alpha_1}; \quad \nabla_2 T = \frac{1}{A_2}\frac{\partial T}{\partial \alpha_2}; \quad \nabla_1 T = \frac{\partial T}{\partial z} \tag{35.4}$$

In this case, the effective coefficient in the axial direction (along the fiber) is determined by the rule of mixtures. For a two-phase medium, we obtain:

$$\lambda_{11} = V_\mathrm{f}\lambda_\mathrm{f} + V_\mathrm{m}\lambda_\mathrm{m}. \tag{35.5}$$

where λ_m, λ_f are thermal conductivity coefficients of isotropic matrix and fiber materials. The effective coefficient λ_{22} can be found by the formula:

$$\lambda_{22} = \lambda_\mathrm{m}\left[1 + \frac{V_\mathrm{f}}{\frac{\lambda_\mathrm{m}}{\lambda_\mathrm{f}-\lambda_\mathrm{m}} + \frac{1-V_\mathrm{f}}{2}}\right] \tag{35.6}$$

We assume that the temperature gradient over the thickness of the thin shell is zero. In this case, the matrix of effective thermal conductivity coefficients in the axes of symmetry has the form:

$$\Lambda = \begin{bmatrix} -\lambda_{11} & 0 \\ 0 & -\lambda_{22} \end{bmatrix} \tag{35.7}$$

Consider the case, where a new coordinate system $(\alpha_1', \alpha_2', z)$ is derived from the system (α_1, α_2, z) by rotating by some angle β. We introduce a transition matrix B, which has the form:

$$B = \begin{bmatrix} \cos\beta & -\sin\beta \\ \sin\beta & \cos\beta \end{bmatrix} \tag{35.8}$$

The thermal conductivity matrix in the new coordinate system will look like this:

$$\Lambda' = B^{-1}\Lambda B$$

$$\Lambda' = \begin{bmatrix} -(\lambda_{11}\cos^2\beta + \lambda_{22}\sin^2\beta) & \sin\beta\cos\beta(\lambda_{11} - \lambda_{22}) \\ \sin\beta\cos\beta(\lambda_{11} - \lambda_{22}) & -(\lambda_{11}\sin^2\beta + \lambda_{22}\cos^2\beta) \end{bmatrix} \tag{35.9}$$

The matrix of thermal resistance, inverse Λ' has the form:

$$\begin{aligned} \mathrm{M} &= \begin{bmatrix} -\mu_{11} & -\mu_{12} \\ -\mu_{21} & -\mu_{22} \end{bmatrix} = (\Lambda')^{-1} \\ &= \begin{bmatrix} -\frac{(\lambda_{11}\sin^2\beta + \lambda_{22}\cos^2\beta)}{\lambda_{11}\lambda_{22}} & -\frac{\sin\beta\cos\beta(\lambda_{11} - \lambda_{22})}{\lambda_{11}\lambda_{22}} \\ -\frac{\sin\beta\cos\beta(\lambda_{11} - \lambda_{22})}{\lambda_{11}\lambda_{22}} & -\frac{(\lambda_{11}\cos^2\beta + \lambda_{22}\sin^2\beta)}{\lambda_{11}\lambda_{22}} \end{bmatrix} \end{aligned} \tag{35.10}$$

In the case of an axisymmetric problem for an arbitrary shell, the Fourier equation can be written as

$$\frac{\mathrm{d}T}{A_1\mathrm{d}\alpha_1} = -\mu_{11}q_1. \tag{35.11}$$

The energy equation, composed taking into account the convective heat transfer on the front surface of the shell, will be written as

$$\frac{\mathrm{d}q_1}{A_1\mathrm{d}\alpha_1} + \psi q_1 = \frac{1}{h}\Theta - \frac{2\alpha}{h}\big(T - T_{\mathrm{cp}}\big), \tag{35.12}$$

where λ is the effective coefficient of thermal conductivity; α is the coefficient of heat transfer from the shell surface.

The boundary conditions for the energy equation under conditions of preservation at the ends of the shell of a constant temperature T_0, and the absence of heat flow, have the form:

$$\begin{cases} T|_{\alpha_1=0} = T_0 & T|_{\alpha_1=L} = T_0 \\ q_1|_{\alpha_1=0} = 0 & q_1|_{\alpha_1=L} = 0 \end{cases}. \tag{35.13}$$

Taking into account the expression of the dissipative function, we give the equation of thermal conductivity to the dimensionless form.

$$\begin{aligned} \Theta = \frac{\omega}{2}\Bigg(& \frac{E_* h_*^2}{R_*} \hat{T}_{11}^{R} \frac{h_*}{R_*} \hat{E}_{11}^{I} - \frac{E_* h_*^2}{R_*} \hat{T}_{11}^{I} \frac{h_*}{R_*} \hat{E}_{11}^{R} + \cdots \\ & + \frac{E_* h_*^3}{R_*} \hat{M}_{11}^{R} \frac{h_*}{R_*^2} \hat{K}_{11}^{I} - \frac{E_* h_*^3}{R_*} \hat{M}_{11}^{I} \frac{h_*}{R_*^2} \hat{K}_{11}^{R} + \cdots \end{aligned}$$

$$+\frac{E_* h_*^2}{R_*}\tilde{Q}_{23}^R\frac{h_*}{R_*}\hat{E}_{23}^I-\frac{E_* h_*^2}{R_*}\hat{Q}_{23}^I\frac{h_*}{R_*}\hat{E}_{23}^R\Big)$$
$$=\frac{\Omega}{2}\sqrt{\frac{E_*}{R_*^2\rho_*}}\frac{E_* h_*^3}{R_*^2}(\hat{T}_{11}^R\hat{E}_{11}^I+\cdots+\varepsilon_1\hat{M}_{11}^R\hat{K}_{11}^I+\cdots$$
$$+\hat{Q}_{23}^R\hat{E}_{23}^I). \tag{35.14}$$

We obtain the following dimensionless quantities:

$$\hat{\Theta}=\sqrt{\frac{\rho_*}{E_*}}\frac{R_*^3}{E_* h_*^3}\Theta,\quad \hat{T}=\frac{T}{T_*},\quad \hat{h}=\frac{h}{h_*} \tag{35.15}$$

$$\frac{\mathrm{d}\hat{q}_1}{R_*\hat{A}_1\mathrm{d}\alpha_1}=\sqrt{\frac{E_*}{\rho_*}}\frac{E_* h_*^3}{R_*^3}\hat{\Theta}\frac{1}{h_*\hat{h}}-\frac{2\alpha}{h_*\hat{h}}(\hat{T}-\hat{T}_{\mathrm{cp}})T_*-\frac{1}{R_*}\hat{\psi}\hat{q}_1,$$
$$\frac{T_*\mathrm{d}\hat{T}}{R_*\hat{A}_1\mathrm{d}\alpha_1}=-K\mu_{11}\hat{q}_1 \tag{35.16}$$

Write down finally (35.12) as

$$\frac{\mathrm{d}\hat{q}_1}{\hat{A}_1\mathrm{d}\alpha_1}=\hat{\Theta}\frac{1}{\hat{h}}-C_1(\hat{T}-\hat{T}_{\mathrm{cp}})-\hat{\psi}\hat{q}_1,$$
$$\text{where } C_1=\frac{2\alpha T_*}{h_* K},\ \hat{q}_1=\frac{1}{R_* K}q_1,\ \frac{\mathrm{d}\hat{T}}{\hat{A}_1\mathrm{d}\alpha_1}=-C_2\mu_{11}\hat{q}_1 \tag{35.17}$$

where $C_2=\frac{R_*^2 K}{T_*}$, $K=\sqrt{\frac{E_*}{\rho_*}}\frac{E_* h_*^2}{R_*^3}$.

In the future, it is assumed that at the ends of the shell, the condition of anchorage is fulfilled and a constant temperature is maintained:

$$y_4^*=0,\ y_5^*=0,\ y_6^*=0,\ y_7=0,\ y_8=T_{\mathrm{cp}}\text{ at }a_1=0,\ L \tag{35.18}$$

35.3 Numerical Experiment

Let us consider the forced axisymmetric oscillations of the fibrous-layered cylindrical shell, taking into account the thermomechanical coupling. The physical and mechanical characteristics of the polymer matrix correspond to the dependencies [3]. Let the multilayer cylindrical shell be exposed to an external load with an intensity of $p_3 = 5$ kPa. The load is distributed over a ring of width R. The shell consists of five layers, while the physical and mechanical characteristics of the reinforcing

fibers correspond to carbon fiber with mechanical properties: $E_f = 186$ GPA; $\nu_f = 0.3$; $\rho_f = 1730$ kg/m^3; $\lambda_f = 20$ W/(m deg). Characteristics of the polymer matrix: $\rho_m = 1214$ kg/m^3; $\lambda_m = 0.15$ W/(m deg). Medium temperature $T_0 = 293$ K.

Let us consider at the first stage the solution of the problem of heat formation without taking into account the dependence of the properties of the polymer on temperature (the so-called loosely coupled problem).

Numerical calculations are made for three variants of reinforcement. The specific content of fibers in the composite $V_f = 0.7$. Figure 35.1 presents the amplitude-frequency characteristics of the shell in the frequency range, including the first resonances and Table 35.1 shows values of the first three resonant frequencies and their oscillation amplitudes.

Figure 35.2 presents the temperature-frequency dependences for these three reinforcement options and Table 35.2 shows values of the self-heating temperature at first three resonant frequencies.

Next, we consider the related thermoviscoelasticity problem for the case of axisymmetric forced oscillations. The problem is essentially nonlinear due to the dependence of the polymer properties on temperature and the presence of a dissipative function in the energy equation. Therefore, by solving the system of differential

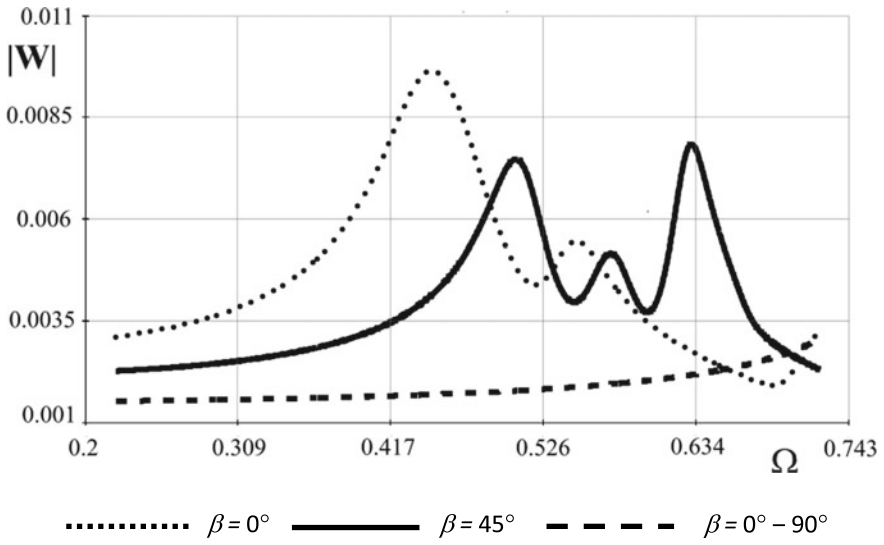

Fig. 35.1 Amplitude-frequency characteristics for the three variants of reinforcement

Table 35.1 Values of the first three resonant frequencies and their oscillation amplitudes

	Ω_1	$\|W_1\|$	Ω_2	$\|W_2\|$	Ω_3	$\|W_3\|$
$\beta = 0°$	0.477	0.01	0.549	0.005	–	–
$\beta = 45°$	0.507	0.008	0.574	0.005	0.631	0.0084

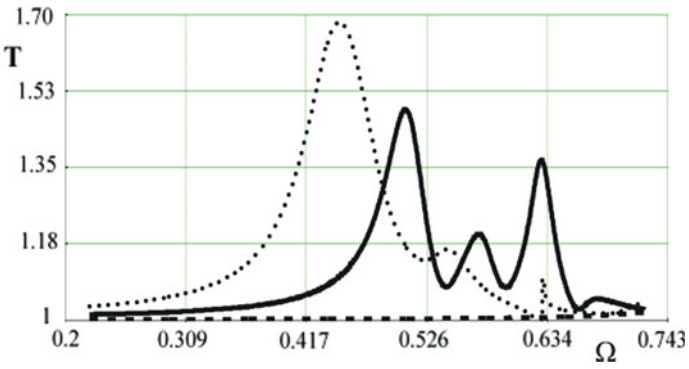

Fig. 35.2 Self-heating temperature

Table 35.2 Values of the self-heating temperature at first three resonant frequencies

	T_1	T_2	T_3
$\beta = 0°$	1.62	1.15	–
$\beta = 45°$	1.46	1.21	1.37

equations, in addition to the orthogonal run method, an iterative method with a given accuracy was implemented. The results of amplitude-frequency characteristics calculations corresponding to the coupled and weakly coupled formulation of the problem are present in Fig. 35.3a and b, respectively. The coupled problem is understood here as a problem in which the physical and mechanical properties of the polymer depend only on the initial temperature of the shell equal to T_0. The corresponding temperature-frequency characteristics are shown in Fig. 35.4a and b. The frequency ranges including the first resonances are considered, where there is a gap in the solution of the related problem at the intervals $\Omega_1 = [0.415–0.485]$ and $\Omega_2 = [0.623–0.634]$. In this frequency range, the convergence of the solution is violated, and the accumulation of the critical error is achieved at the first iterations. By solving a weakly coupled problem, stationary vibrational and temperature regimes exist for all taken values of the frequency parameter. The calculations indicate a significant discrepancy between the amplitudes and temperature of heat formation in the vicinity of resonance frequencies. In this case, the solution of the problem, which does not take into account the influence of temperature on the properties of the polymer, gives significantly underestimated values both in the calculation of amplitude-frequency and temperature-frequency characteristics. Outside the resonant regions, the solutions of both problems are quite close.

Figure 35.5a and b present typical distributions of transverse deflection and temperature along the length of the shell in the vicinity of the first resonance at a frequency $\Omega = 0.4$.

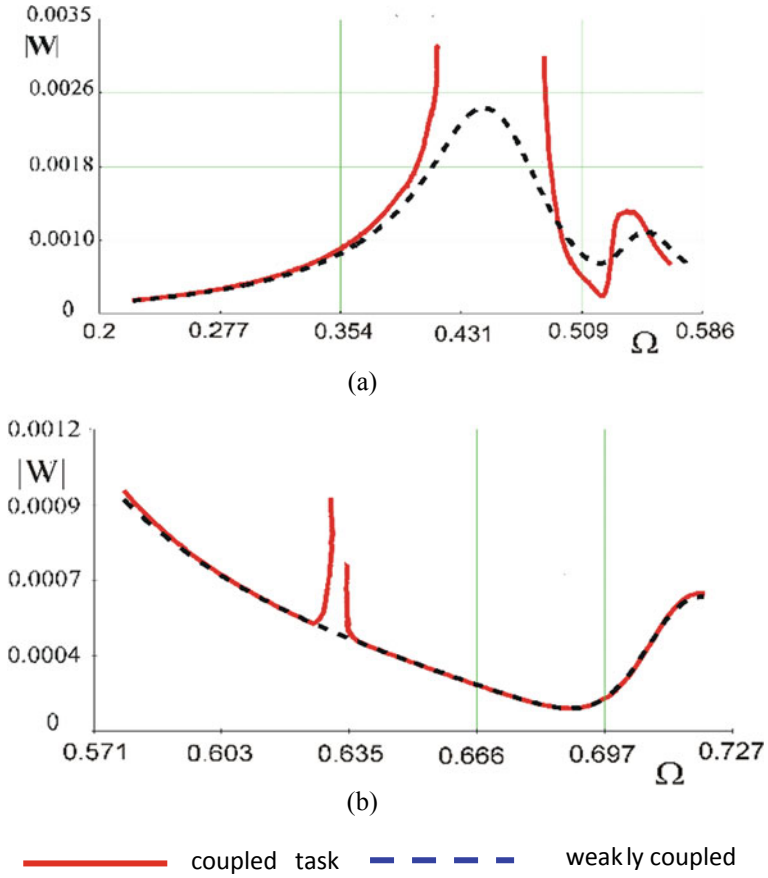

Fig. 35.3 Amplitude–frequency characteristics

35.4 Conclusion

The forced oscillations of the composite polymer shell of revolution are considered taking into account the thermomechanical coupling. The related problem of thermo-viscoelasticity for a fibrous-layered cylindrical shell is investigated numerically in an axisymmetric formulation. The problem of heat formation with and without taking into account the dependence of the properties of the polymer matrix on temperature is considered.

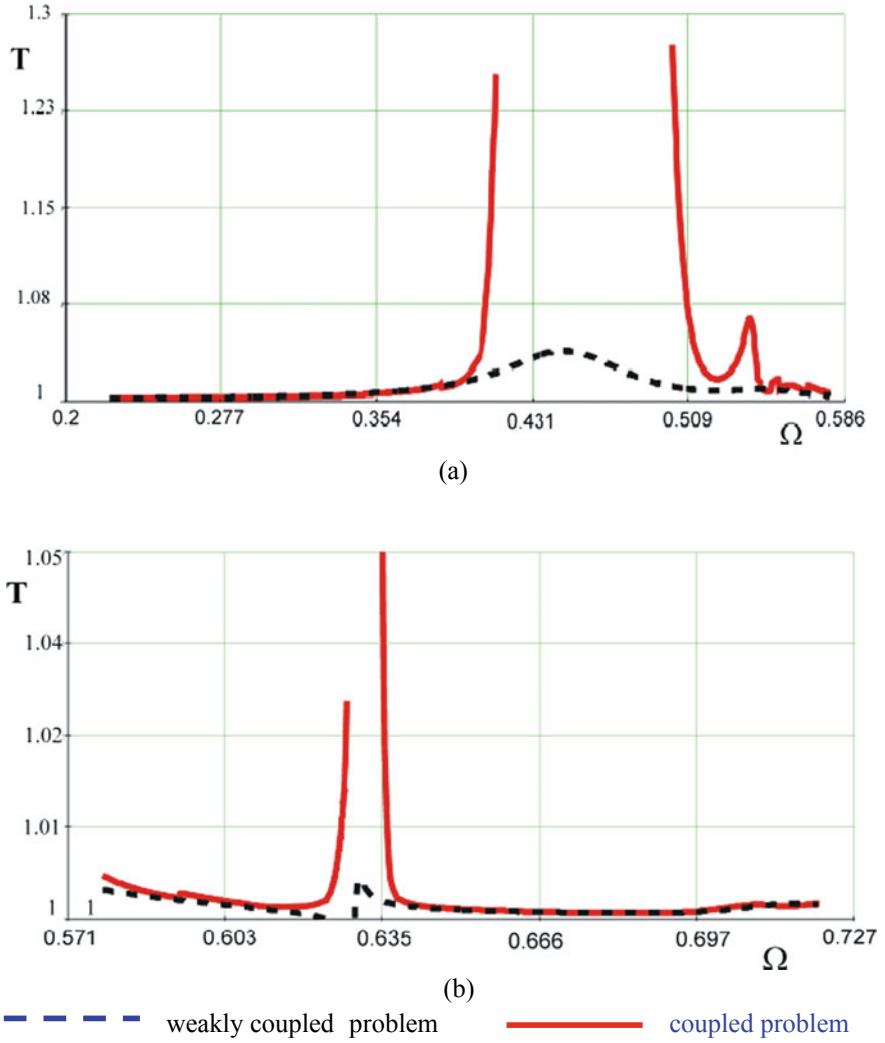

Fig. 35.4 Temperature–frequency characteristics

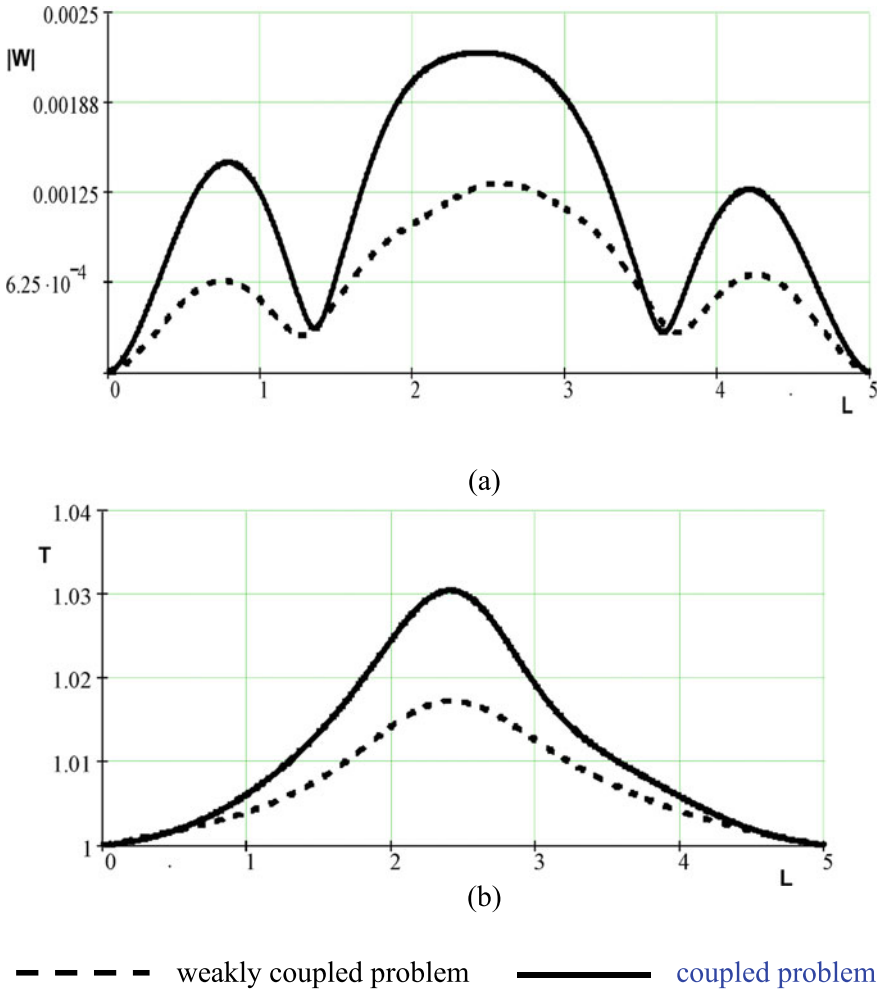

Fig. 35.5 Distributions of transverse deflection and temperature along shell length

References

1. E.I. Grigolyuk, G.M. Kulikov, *Multilayer Reinforced Shell* (Mashinostroenie, Moscow, 1988), 288 p. (in Russian)
2. R.M. Cristensen, *Mechanics of Composite Materials* (Mir, Moscow, 1982), 336 p. (in Russian)
3. Y.P. Stepanenko, K.V. Isaev, A.D. Azarov, In: *Proceedings of II International Conference "Modern Problems of Continuum Mechanics*, Rostov-on-Don, vol. 1, 118 (1996) (in Russian)

Chapter 36
The Study of Stratification of Multilayer Structures Based on Finite Element Modeling and Neural Network Technologies

A. V. Cherpakov, P. V. Vasiliev, A. N. Soloviev, I. A. Parinov and B. V. Sobol

Abstract An approach to solving the problem of identifying the thickness of the layers of a multilayer structure using the combination of the finite element method and artificial neural networks (ANNs) is presented. The simulation of a multilayer structure in the ANSYS finite element software is presented. The construction model consists of 4 layers, each of which has certain properties. The model is an imitation of the soil foundation of the road surface. Simulation in the form of a simplified, plane statement of the problem is considered. The analysis of surface waves, excited during the simulation of impact loading. The wave field of displacements in a given section of the structure is analyzed. Based on a numerical experiment, an approach is constructed to estimate the thickness of one of the layers of the structure. The application of ANN to restore information about the thickness of one of the layers is considered. As a result of the study, a method for identifying the thickness of the layers of a multilayer structure was developed, based on a combination of the finite element method and ANN.

36.1 Introduction

The reconstruction of properties and defects, the restoration of the homogeneity of the structure of materials in layered structures, for example, such as pavements and various soil bases, is an important technical problem. Solving the reconstruction problem will allow us to evaluate the current state of the structure of the studied

A. V. Cherpakov (✉) · A. N. Soloviev
Department of Theoretical and Applied Mechanics, Don State Technical University, 1, Gagarin Square, Rostov-on-Don, Russia 344010
e-mail: alex837@yandex.ru

A. V. Cherpakov · A. N. Soloviev · I. A. Parinov
Institute of Mathematics, Mechanics and Computer Sciences, Southern Federal University, 8a, Milchakov Str., Rostov-on-Don, Russia 344000

P. V. Vasiliev · B. V. Sobol
Department of Information Technologies, Don State Technical University, 1, Gagarin Square, Rostov-on-Don, Russia 344010

I. A. Parinov et al. (eds.), *Advanced Materials*, Springer Proceedings in Materials 6, https://doi.org/10.1007/978-3-030-45120-2_36

layered structure. The task of restoring information about stratification of layered structures is especially relevant for monitoring and comparative analysis of structural changes from mechanical action on layers in a certain area of the structure.

Such identification can be carried out using instruments (laser displacement sensors, cycle meters, accelerometers, etc.), which are located along the investigated surface of the structure and monitor it [1]. A more attractive detection method is the use of acoustic sensors and receivers mounted on the external surface and detecting various zones of structural heterogeneity (defects, inclusions, voids, etc.) based on the reflected signals from the defects. Such a system should be equipped with software, allowing the analysis of the reflected signal to identify a defective area of the structure. Corresponding software can be developed based on the use of an artificial neural network (ANN) [2]. The use of ANN in reconstruction of the damaged state of structural elements is described in [3–12]. The use of various architectures and algorithms of ANN is described in [3–7]. Defining defects in anisotropic plates using ANN is the subject of [8]. In [9], the authors pointed out the advantages of identification methods that do not require the preliminary construction of a mathematical model of the object of study.

In this chapter, we develop a method for reconstructing the depth of one of the layers of a layered structure using pavement as an example. Mathematically, the problem is reduced to the inverse geometric problem of the theory of elasticity [13]. The structure is loaded in the form of a pulsed impact effect at a certain distance from the studied zone; a series of sensors recording vibrations is located in a certain sequence in the linear direction of the study zone. The transverse and longitudinal vibrations are measured during the time when the waves reflected from the ends of the simulated section of the structure have not time to reach the sensor. In this way, real conditions for studying the layered structure of the soil base are simulated. Analysis of the measured amplitude-time characteristics (ATCs) shows the possibility of their use in inverse problems of defect recovery.

An ANN is used as a tool for solving the inverse problem of reconstruction of defect parameters. The popularity of using ANNs is due to the fact that they were originally designed to solve just such problems, to find nonlinear dependencies in multidimensional data arrays. ANN, unlike other algorithmic constructions, are not programmed, but trained on a multitude of data for various studied design parameters. Training samples are built by solving direct problems in the finite element (FE) software ANSYS. The trained network, having received new, previously unknown analysis results, is able to correctly recognize the defect parameters.

The use of FE modeling is rather effectively shown in [14–20]. We study the parameters of the natural modes of vibration, as well as their angular values of the forms of the vibration curves, showing fairly good correlation data with the magnitude of the defect in the structural element.

The aim of the work is to build a FE model in the ANSYS software and develop principles for solving the problem of identifying layer parameters, using the example of restoring information about the second layer for given parameters of the structure properties, in a multilayer structure with pulsed excitation based on a combination of numerical experimental analysis and the use of neural network technologies.

36.2 Statement of the Problem

The problem is solved in a plane formulation using the finite element method (FEM). In this work, linear equations of the theory of elasticity are used taking into account the energy dissipation adopted in the ANSYS package [21, 22].

For an elastic medium, we have:

$$\rho\ddot{u}_i + \alpha\rho\dot{u}_i - \sigma_{ij,j} = f_i;$$
$$\sigma_{ij} = c_{ijkl}(\varepsilon_{kl} + \beta\dot{\varepsilon}_{kl});$$
$$\varepsilon_{kl} = \left(u_{k,l} + u_{l,k}\right)/2;$$

where ρ is the density of material; u_i are the components of the vector function of displacements; $\sigma_{i,j}$ are the components of the tensor of mechanical stresses; f_i are the components of the vector of the density of mass forces; ε_{kl} components of the strain tensor; c_{ijkl} components of the fourth-rank tensor of elastic moduli; α non-negative damping coefficients (in ANSYS).

Let us consider in more detail the mechanical boundary conditions. When determining the mechanical boundary conditions, the body boundary is represented as a union of disjoint regions $S = S_u S_t S_{ut}$ on which the following conditions are specified:

(i) is the condition for fixing the border or given movements

$$u_i|_{S_u} = u_i^0$$

(ii) is the condition of the force action under which the components of the vector of mechanical stresses are specified

$$t_i = \sigma_{ij} n_j\big|_{S_t} = p_i$$

(iii) is the condition for smooth contact with an absolutely rigid body—equality to zero of normal displacements and tangential stresses:

$$u_n = u_i n_i|_{S_{ut}} = 0, t_i^{(k)} = \sigma_{ij} n_j \tau_i^{(k)}\Big|_{S_{ut}} = 0$$

36.3 FE Modeling

We consider the problem in a flat setting. As a simulated structure, an element of a multilayer structure, including 4 layers, was selected. Figure 36.1 shows an example of the physical structure of the "base" system "road construction—soil". The numbers in the figure indicate the numbers of layers of the structure, the physical and geometric characteristics of which are given in Table 36.1.

All layers are rigidly coupled with each other and with the underlying half-space (Fig. 36.1). As input parameters, the surface displacement field is considered as a result of short-term pulsed exposure. Parameters of layer properties are known. The thickness of the second layer d_2 is considered as the investigated variable parameter. The magnitude of the variation of the 2nd layer lies in the range of $d_2 = 0$–1.1 m. It is assumed that under dynamic loading of the structure, the dependences of the thickness variations of the second layer d_2 on the magnitude of the vibration responses measured at certain points of the structure will be found.

An impulse in the form of a force P_t of a conditional unit amplitude is applied at point 1 (Fig. 36.2b). Pulse loading has a linear character with respect to the time of application of the load in the form of force (Fig. 36.2a). The load application time is $\tau = 0.003$ s, which corresponds to the parameters of real impact loading. The displacement of wave field is analyzed in the area adjacent to the point of influence on the surface of layer 1. The characteristics of the waves propagating in the layered structure are studied based on the implementation of the FEM using the ANSYS complex.

In the result of impulse loading, transverse and longitudinal waves of displacements of points arise both on the surface of the structure and throughout its volume.

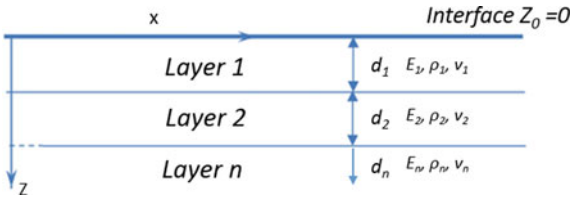

Fig. 36.1 Notation for layered soil structure with horizontal interfaces

Table 36.1 Parameters of the layers

Layer No.	Elements	Thickness (m)	E (GPa)	ρ (kg/m^3)	ν	Damping factor
1	Asphalt-concrete	0.1	4	2000	0.33	0.001
2	Disconnected layers	0–1.1	0.1	2000	0.33	0.001
3	Underlying layer	0.1	2	2000	0.33	0.001
4	Underlying half-space	5	0.1	2000	0.33	0.001

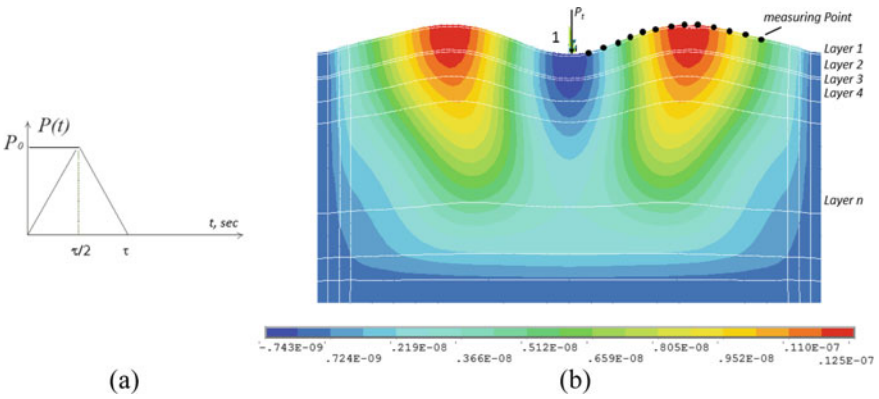

Fig. 36.2 **a** Diagram of the impulse load from the force P_t, applied at point 1 of the structure; an example of the result of transverse vibrations at a certain point at time $t = 0.02$ s, by modeling structural vibrations

An example of the implementation of the calculation results is a graph of the shape of transverse vibrations at time $t = 0.02$ s, when modeling structural vibrations (Fig. 36.2b). Control points are located on the surface at a distance of 0.1 m from each other. The first point is located at a distance of 0.1 m from the place of impact. Data is collected at 60 points. Figure 36.3 shows the results of numerical calculations of transverse displacements at various points on the surface. In the process of solving

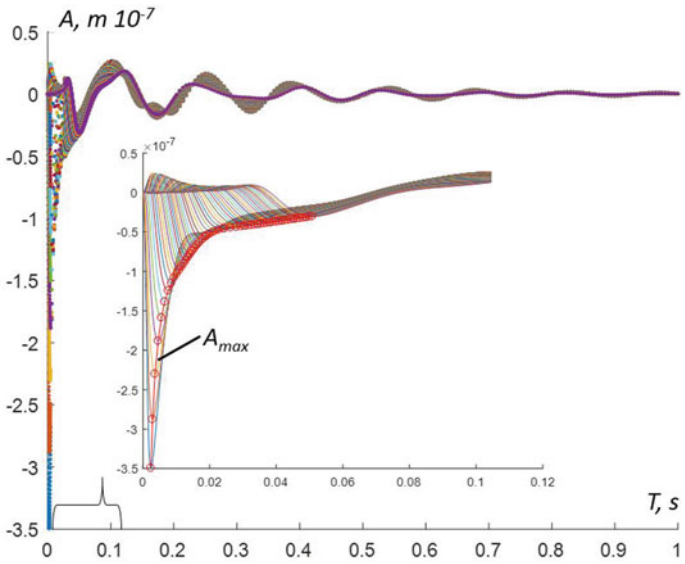

Fig. 36.3 Amplitudes of the displacements of the traveling shear wave at the studied points on the surface at different points in time

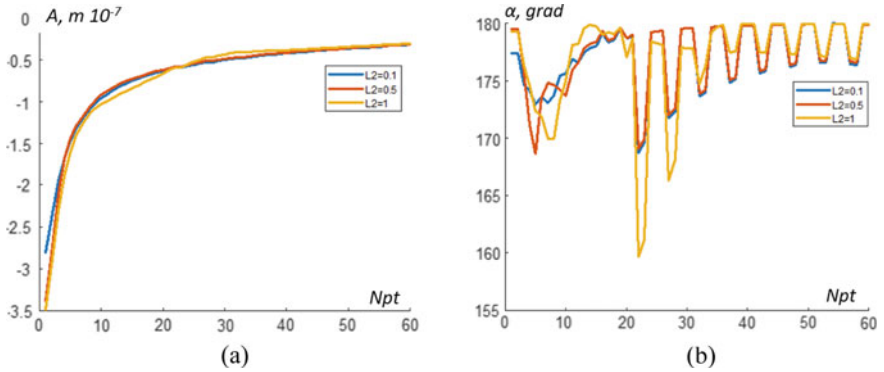

Fig. 36.4 **a** Plots of the maximum amplitudes of transverse vibrations; **b** bending angles of curves of maximum amplitudes at the corresponding points *Npt* on the surface of the structure

the problem, the transverse displacements are calculated at the control points of the structure in the time range of $t = 0-1$ s. Of particular interest is the displacement field of the points of the surface layer in the time range of $t = 0-0.12$ s. This range is characterized by the fact that the primary form of deflections of the layered structure is formed and there are no vibration responses from the excitation of the outer layers of the structure. The oscillation amplitudes have maximum values of deflections at the corresponding points.

The maximum oscillation amplitudes in a given time interval are measured. The curves of transverse deflections are constructed and the bending angles of these curves are calculated depending on the time of registration and the number of the studied point for each value from the varied parameters of thickness d_2 of the second layer. Figure 36.4a shows the peak values of the oscillations for a thickness of the second layer $d_2 = 0.1$ m, 0.5 m, 1 m; graphs of the bending angles of the curves at the corresponding measurement points are also presented (Fig. 36.4b). The initial analysis shows that the oscillation amplitudes have a non-linear logarithmic trend of change depending on the registration point. Nonlinearity of the trend is shown by the angles of the deflection of the curve of maximum amplitudes for various values of the depth of layer 2, which has certain pronounced inflection points. Data are collected on the deflection curves of non-stationary oscillations for all variations of the d_2 layer.

36.4 Application of Neural Network Technologies in the Task of Identifying the Thickness of Hidden Layer of Structure

Artificial neural networks are computer systems that take the basics in biological neural networks that make up the brain of animals. Such systems are "learned" to perform tasks based on prepared examples. This is a nonlinear modeling tool. They are typically used to model complex relationships between inputs and outputs to find patterns in large amounts of data.

In the framework of this task, it is necessary to establish a relationship between the amplitudes of oscillations propagating in the multilayer structure, as well as the angles of the deflection of the curve of maximum amplitudes with a layer thickness d_2 (Fig. 36.2b). Based on the data obtained, at the stage of FE modeling, it is possible to form a training set and conduct training on the constructed neural network model.

In the result of the numerical solution of direct problems by using the FE software package ANSYS, data were obtained at 60 points, located on the surface of the multilayer structure. For each set of 60 values, a specific layer height d_2 was set. Training vectors have been prepared that contain the amplitudes of oscillations and the angles of deflection of the maxima of the amplitudes as input values, and the thickness of the layer under study as output values. A total of 100 numerical experiments were conducted. Thus, the training and test samples consist of 50 vectors. All data used in training the neural network are normalized and are on the interval [0, 1].

In order to solve the problem of identifying a parameter-value of the layer thickness, it is most rational, in this case, to apply a fully-connected multilayer ANN model. The proposed neural network model consists of 60 input neurons. The first hidden layer contains 32 neurons. The second hidden layer contains 8 neurons. As an activation function, the Rectified Linear Unit (ReLU) was selected. Sigmoid is set as the output activation function. For training, the Adam optimization method (Method for Stochastic Optimization) [23] is used. The root mean square error (MSE) was chosen as the loss function. It has been established that 4000 epochs of training are sufficient to achieve the required level of quality of ANN work, if amplitude values are used in the training set. In Fig. 36.5, the process of training a neural network model based on various data obtained during FE modeling is shown. The analysis shows that when reaching more than 1000 epochs, the mean-square error changes insignificantly.

36.5 Conclusion

The problem of unsteady oscillations under pulsed loading of a layered structure is considered. The results of transverse displacements at the control points of the structure during the propagation of the wave from pulse excitation at a certain point are presented. During the simulation, the time interval in which the effects of the

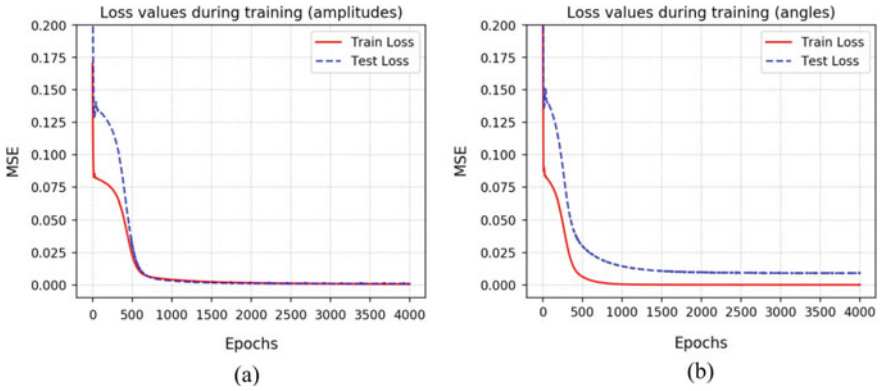

Fig. 36.5 Change in the error value (MSE) of the neural network during its training based on the values of amplitudes (**a**), based on the values of the deflection angles of the curve of maximum amplitudes (**b**)

backward passage of the wave are not taken into account is considered as the analyzed one. Using optimization in the ANSYS complex allowed us to accelerate the process of solving the problem.

In the result of the study, an approach was developed to identify the thickness of layers of a multilayer structure, based on a combination of the finite element method and ANN. The most successful configuration of the neural network architecture was established, namely: 60 input neurons, 32 neurons on the first hidden layer, 8 neurons on the second hidden layer and 1 output neuron.

The study showed that the prepared volume of the data set is sufficient for the successful training of the constructed model and identification of the thickness of the hidden layer of the structure. In this case, the relative accuracy of determining the layer thickness in the case of applying the values of the amplitudes of the oscillations is 97%, and in the case of applying the values of the inflection angles of the curves of maximum amplitudes 91%.

Based on the foregoing, we conclude that ANN algorithms can be successfully used to evaluate the stratification of multilayer structures using acoustic sounding from the far zone.

Acknowledgements Research was financially supported by Southern Federal University, 2020 grant number VnGr/2020-04-IM (Ministry of Science and Higher Education of the Russian Federation).

References

1. C.B. Park, R.D. Miller, J. Environ. Eng. Geophys. **13**(1) (2008)
2. S. Haykin, *Neural Networks—A Comprehensive Foundation* (Prentice Hall, 1998), 842 p
3. A.A. Krasnoshchekov, B.V. Sobol, A.N. Solov'ev, A.V. Cherpakov, Russian J. Nondestruct. Test. **47**(6) (2011)
4. Z. Waszczyszyn, L. Ziemianski, Comput. Struct. **22**(79) (2001)
5. A.N. Solov'ev, P.S. Kurbatova, N.I. Saprunov, S.N. Shevcov, in *Proceedings of 10-th International Conference "Modern Problems of Continuum Mechanics",* Rostov-on-Don (2006) (in Russian)
6. S.W. Liu, J.H. Huang, J.C. Sung, C.C. Lee, Comput. Methods Appl. Mech. Eng. **191** (2002)
7. V. Khandetsky, I. Antonyuk, NDT&E Int. **7**(35) (2002)
8. Y.G. Xu, G.R. Liu, Z.P. Wu, X.M. Huang, Int. J. Solids Struct. **38** (2001)
9. X. Fang, H. Luo, J. Tang, Comput. Struct. **85** (2005)
10. A.N. Solov'ev, B.V. Sobol', P.V. Vasil'ev, Russian J. Nondestruct. Test. **52**(3) (2016)
11. A. Soloviev, B. Sobol, P. Vasiliev, in *Advanced Materials—Proceedings of the International Conference on "Physics and Mechanics of New Materials and Their Applications", PHENMA 2018*, ed. by I.A. Parinov, S.-H. Chang, Y.-H. Kim, Springer Proceedings in Physics, vol. 224 (Springer Nature, Cham, Switzerland, 2019), 615–626
12. D.A. Pozharskii, B.V. Sobol, P.V Vasiliev, Mech. Adv. Mater. Struct. (18 May 2018)
13. A.O. Vatul'jan, *Inverse Problems in Solid Mechanics* (Moscow, Fizmatlit, 2007), 224 p (in Russian)
14. A.V. Cherpakov, A.N. Soloviev, V.V. Gricenko, O.U. Goncharov, Def. Sci. J. **66**(1) (2016)
15. V.A. Akopyan, A.N. Solov'ev, A.V. Cherpakov, S.N. Shevtsov, Russian J. Nondestruct. Test. **49**(10) (2013)
16. A.V. Cherpakov, O.V. Shilyaeva, M.N. Grigoryan, T.V. Polyakova, IOP Conf. Ser.Mater. Sci. Eng. **698**, 066021 (2019)
17. A.V. Cherpakov, E.A. Shlyakhova, I.O. Egorochkina, Y.A. Kokareva, Mater. Sci. Forum **931** (2018)
18. A.N. Soloviev, I.A. Parinov, A.V. Cherpakov, Y.A. Chaika, E.V. Rozhkov, Mater. Phys. Mech. **37**(2) (2018)
19. A. Cherpakov, I. Egorochkina, E. Shlyakhova, A. Kharitonov, A. Zarovny, S. Dobrohodskaya, in *MATEC Web of Conferences*, vol. 106, 04009. (2017)
20. S.N. Shevtsov, A.N. Soloviev, I.A. Parinov, A.V. Cherpakov, V.A. Chebanenko, *Piezoelectric Actuators and Generators for Energy Harvesting—Research and Development* (Springer Cham, Switzerland, 2018), 182 p
21. A.V. Nasedkin, DrSc Thesis (Phys.-Math. Sciences). Rostov State University, Rostov-on-Don, 271 p. (2001) (in Russian)
22. V.A. Krasil'nikov, V.V. Krylov, *Introduction to Physical Acoustics* (Moscow, Nauka, 1984), 400 p (in Russian)
23. D. Kingma, J. Ba, in *International Conference on Learning Representations.* arXiv:1412.6980 (2014)

Chapter 37
The Structural Correlation and Mechanical Properties in Amorphous Hafnium Oxide Under Pressure

Nguyen-Hoang Thoan, Nguyen-Trung Do, Nguyen-Ngoc Trung, and Le-Van Vinh

Abstract In this chapter, the classical molecular dynamics technique was used to investigate the atomistic structure of amorphous hafnium oxide (HfO_2) under pressure. The local atomic structure and the liquid-solid transition of HfO_2 were analyzed the pair radical distribution functions, bond angle distributions, coordination number and the void distribution. The simulation reveals that although the fractions of structural units HfO_x and OHf_y strongly change with the density, the partial bond angle distributions of these structural units are identical for all constructed models. This result has enabled us to establish a relationship between the bond angle distributions and the fractions of structural units. From deformation of samples, elastic moduli and Poisson ratio were determined. The Young's modulus and yield stress increase with the increasing density. The strain hardening becomes more pronounced as the density increases.

37.1 Introduction

Hafnium oxide, HfO_2, has been extensively studied for use as silicon dioxide replacements in the gate oxide insulating layer in complementary metal oxide semiconductor (CMOS) devices and resistive RAM devices [1–4]. This oxide has high electric constant (high-κ) of about 25–30 depending on fabrication process conditions. In addition, it has a wide band gap, relatively high refractive index, high thermal and chemical stability, high melting point, excellent compression performance and low thermal expansion coefficient. Solid HfO_2 can be formed at different phases including amorphous, monoclinic, tetragonal and cubic. However, HfO_2 often deposits as an amorphous phase by CVD or ALD fabrication processes. Many comprehensive studies of the structure and thermodynamics of the HfO_2 crystal and amorphous phases

N.-H. Thoan · N.-T. Do · N.-N. Trung (✉)
School of Engineering Physics, Hanoi University of Science and Technology, Hanoi, Vietnam
e-mail: trung.nguyenngoc@hust.edu.vn

L.-V. Vinh
Phenikaa University, Hanoi, Vietnam

I. A. Parinov et al. (eds.), *Advanced Materials*, Springer Proceedings in Materials 6, https://doi.org/10.1007/978-3-030-45120-2_37

have been investigated intensively by both experiments and simulations in recent years [5–9]. Recently, we investigated MD simulation results on liquid-amorphous transition of HfO_2 undercooling process [10]. Tapily et al. demonstrated that the initial low temperature ALD deposited HfO_2 in its amorphous state is harder and stiffer than the polycrystalline form of HfO_2 [11]. Therefore, this has motivated us to carry out this study. Therefore, in this study, we report on the results of density and the structural evolution of a-HfO_2 under compression, and discuss the unit structure HfO_x and mechanical behavior of these systems.

37.2 Computational Procedures

The MD simulation has been performed using an initial configuration containing 6000 atoms (2000 hafnium and 4000 oxygen ones) in a cube under periodic boundary conditions. We apply the Morse-KBS combined potential:

$$\varphi_{ij} = \frac{q_i q_j e^2}{r_{ij}} + D_{ij}\left\{\left[1 - \exp\left[-a_{ij}\left(r_{ij} - r_0\right)\right]\right] - 1\right\} + \frac{C_{ij}}{r_{ij}^{12}} \tag{37.1}$$

where, r_{ij} is the distance between an ion of type i and an ion of type j (i, j = Hf, O), e is the elementary charge, and $q_{\mathrm{Hf}} = 2.4$ and $q_{\mathrm{O}} = -1.2$ are partial charges of hafnium and oxygen respectively; D_{ij}, a_{ij} and r_0 are Morse potential parameters (listed in [12]); and C/r^{12} is the repulsive contribution. The cation-cation interactions are assumed to be purely coulombic.

The long-range Coulomb interactions were calculated with the Ewald summation technique, which is applied to three-dimensional periodic boundary conditions [13]. The Verlet algorithm with a time step of 1.5 fs is adopted and the simulation was executed at a constant pressure (the ensemble NPT). Classical MD simulation and the Verlet algorithm can be seen in detail elsewhere [14, 15]. The scaling method was adopted during the simulation to control the system temperature. The pressure is defined in terms of the virial expression [16]. The initial configuration was randomly generated all atoms in the simulation box corresponding to the density of 10.2 g cm^{-3} with condition that no two atoms be closer than 1.0 Å. The initial configuration was then equilibrated for 50,000 static relaxation (SR) steps. In the SR method the system is at absolute zero due to no kinetic energy, and the atoms are displaced in the direction in which the resultant force acts. The displacement step (SR step) is proportional to the resultant force. In the next step, this configuration had been equilibrated by MD method at temperature of 5000 K for over 50,000 time steps. Then, the samples were cooled down to 300 K within 470,000 time steps (with the cooling rate of 66.67 K/ps) without and with applying an pressure during cooling process ($P = 0$–100 GPa). After reaching 300 K, samples are relaxed for 50,000 time steps to get a stable state.

To determine the coordination number, bond angle distribution (BAD), the structural unit HfO_x and OHf_y linkages, we used the cutoff distance $R_{c(\mathrm{Hf–O})} = 2.57$ Å,

which is a cutoff radius as the first minimum after peak of Hf–O PRDF for 300 K-samples. The radius distributions of voids were calculated following the procedure which was described elsewhere [17]. If every atom is considered as a sphere, then there is a part of the system in which no atomic sphere exists. The radius of Hf and O atoms are 1.55 and 0.73 Å, respectively. The void is defined as a sphere that can be inserted in contact with four atoms and do not intersect with any atom. The volume of voids (V_{void}) is calculated by randomly generating 300,000 points in the simulation box containing the voids inside. Then, the number of points (n_{void}) located in the voids is determined. V is defined as the volume of sample. The V_{void} is evaluated by $V_{void} = V \times n_{void}/300{,}000$. Strain-stress simulations with a strain rate of 2×10^{11} s^{-1} were calculated following the computational procedures which were described in detail elsewhere [18].

37.3 Results and Discussion

Figure 37.1 presents potential energy (PE) per atom of different samples as function of cooling temperature. For all samples, the PEs change continuously so that the liquid-solid phase transition is continuous as other glass transition [19]. The liquid-to-solid transition temperatures of HfO_2 systems are determined by extrapolation of the low temperature and high temperature dependence of PE. We found out that the transition temperature increases with increasing pressure, and in the range of 2550–3000 K.

Figure 37.2 shows snapshots of samples at 300 K after cooling from 5000 K without and with pressure $P = 50$ GPa. We can see the more condense when applying a pressure on the sample.

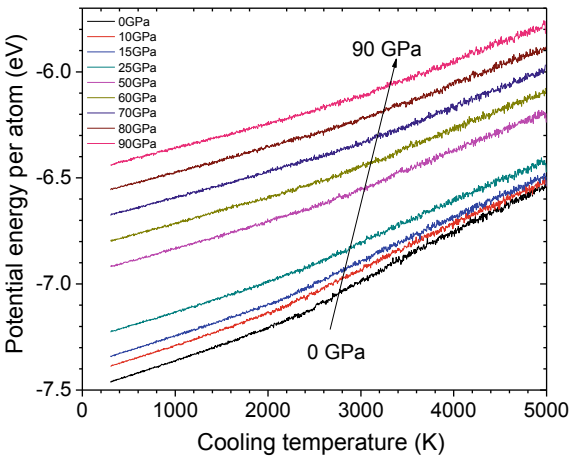

Fig. 37.1 Potential energy per atom of different samples as function of cooling temperature

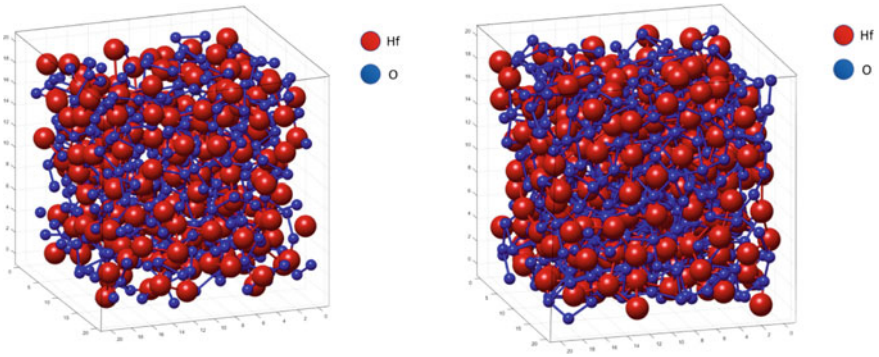

Fig. 37.2 Snap shots of samples at 300 K after cooling from 5000 K without and with pressure $P = 50$ GPa

In order to investigate the effect of pressure on structural parameters, the volume per atom and density dependence of the pressure up to 100 GPa is calculated and presented in Fig. 37.3. We can see that the volume decreases gradually with increasing pressure from 0 to 100 GPa. This result is logical because upon compression, the material is compressed and the atoms move closer each other decreasing the unit cell volume. This *P*-*V* isotherm shows that no discontinuous change. Although there is no experiment of the pressure-induced structural transformation in a-HfO_2, however, both experiment [20] and first-principles computations [21] show that the transformation from monoclinic to orthorhombic hafnia at 7–17 GPa occurs with the increase of density ~20%. Using first-principles computations on pressure-volume isotherms of amorphous and cubic HfO_2. Hoat et al. [22] proved that with increasing pressure up to 30 GPa. On experimental study by Rathak et al., the volume of monoclinic hafnia varies faster than that of orthorhombic [20]. There is not experimental results with pressure larger than 30 GPa.

Figure 37.4 presents the partial and total PRDF $g(r)$ of a-HfO_2 samples at different pressures. For the total RDFs $g_N(r)$ exhibiting the short order structure of amorphous phase (see Fig. 37.4a), the first peak is almost unchanged, while the second peak shifts to the left from 2.83 to 2.55 Å with increasing pressure. At 0 GPa (no pressure) the $g_N(r)$ of the model is good agreement with the experimental data [23]. The first peak of the $g_N(r)$ is contributed from the pair RDF $g_{\text{Hf–O}}(r)$ and the second and third peaks are contributed from the pair RDFs $g_{\text{O–O}}(r)$ and $g_{\text{Hf–Hf}}(r)$. All $g_{\text{Hf–O}}(r)$ functions of all samples exhibit a solid state with disorder structure (amorphous phase), indicating that no pressure-induced phase transformation occurs in a-HfO_2 systems. For the $g_{\text{Hf–O}}(r)$ exhibiting the Hf–O bond distance (see Fig. 37.4b), the shape and peak position are almost unchanged except the height of the first peak with increasing pressure. Hf–O bond distance is almost unchanged at $r = 2.07 \pm 0.02$ Å, which is shorter than the average value of 2.14 Å in the monoclinic crystal [9]. The $g_{\text{Hf-Hf}}(r)$ in Fig. 37.4c present a dual peak between 3 and 4 Å. The first one slightly shifts to the

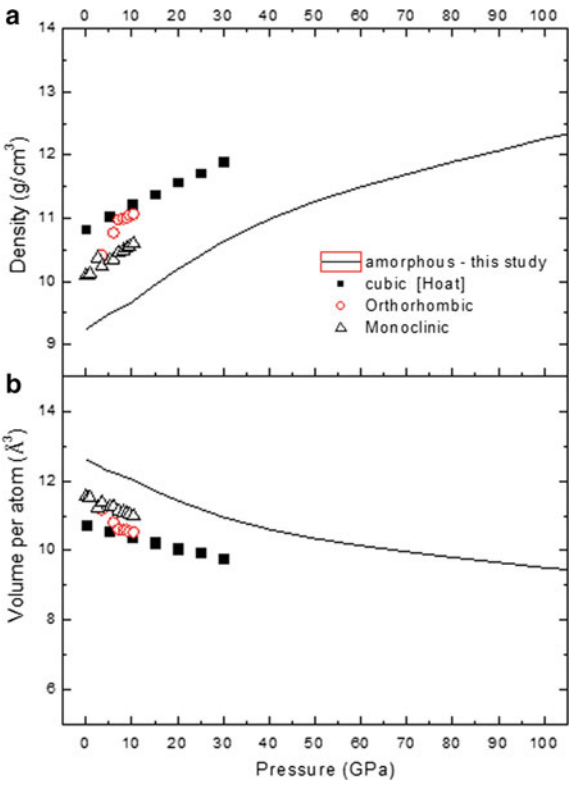

Fig. 37.3 **a** Density dependence of the pressure of and **b** pressure-volume isotherms of a-HfO_2 systems at the temperature of 300 K

left from 3.26 to 3.20 Å; while the second one at ~3.80 Å decrease its intensity with increasing pressure. In Fig. 37.4d, the first peak of the gO–O(r) (see Fig. 37.4d) also shifts to the left from 2.77 to 2.51 Å upon compression, and the second from 4.12 to 3.94 Å. These results are close to that in previous simulation and experimental studies [23–26].

The network structure of a-HfO_2 samples consists of HfO_x ($x = 5, 6, 7, 8$) units and OHf_y ($y = 2, 3, 4$) linkages as presented in Fig. 37.5. Here one can see that HfO_6 units and OHf_3 linkages are dominant for samples at 0 GPa. However, the increasing of pressure induces in amorphous hafnium a change in the Hf coordination number, which passes on average from six to eight. Fraction of HfO_6 units decreases drastically from 78.7% at $P = 0$ GPa to 1.77% at $P = 100$ GPa. While, fraction of HfO_8 units increases drastically from 0.35% at $P = 0$ GPa to 60.2% at $P = 100$ GPa. On average, the Hf–O coordination number ranges from 6.14 to 7.58 as shown in Fig. 37.5c.

The same trend has been observed also for the average oxygen coordination number. As shown in Fig. 37.5b, fraction of OHf_3 units decreases continuously from 63.6% at $P = 0$ GPa to 20.4% at $P = 100$ GPa. While, fraction of OHf_4 units

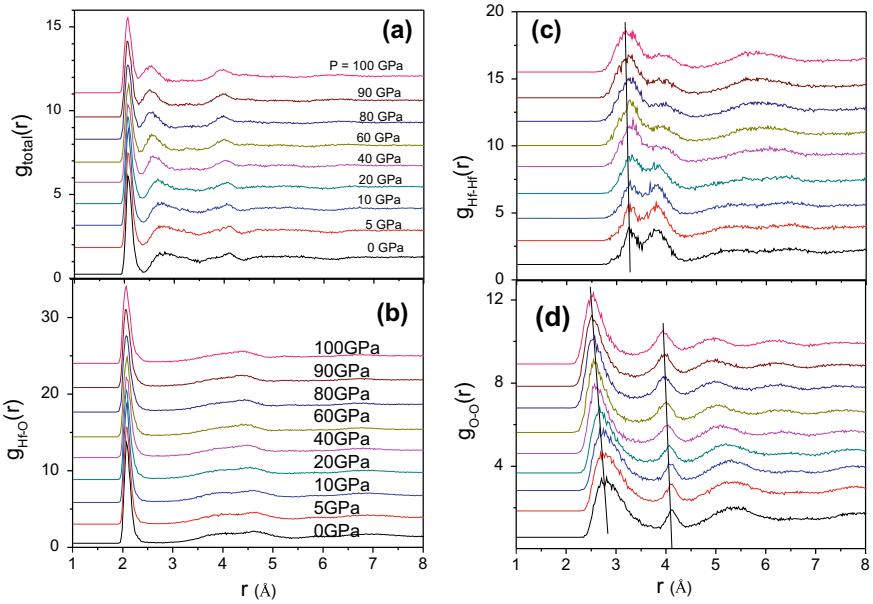

Fig. 37.4 Total (**a**) and partial (**b**–**d**) radical distribution functions of amorphous HfO_2 with different pressures; the straight lines are to guide the eyes

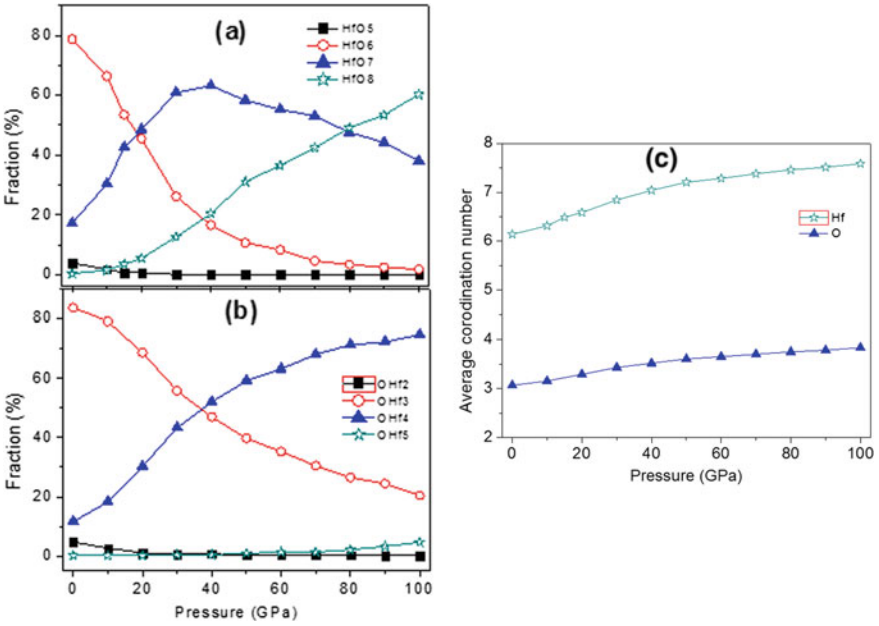

Fig. 37.5 Fractions of **a** HfO_x ($x = 5$, 6, 7 or 8) units; **b** OHf_y ($y = 2$, 3, 4) linkages, and **c** the average co-ordination number of Hf (surrounding by O) and of O (surrounding by Hf)

increases continuously from 11.6% at $P = 0$ GPa to 74.8% at $P = 100$ GPa. On average, the O–Hf coordination number ranges from 3.07 to 3.84 as shown in Fig. 37.5c. Cressoli et al. simulated amorphous HfO_2 and also found a prevalence of six- and seven-fold coordinated Hf and three- and four-fold coordinated oxygen atoms [27]. However, there is a large variation in the predicted packing between the polyhedra in the different models. A study combining both classical MD and DFT calculations found domination of six-fold Hf atoms and three-fold O atoms led to significantly more corner-sharing polyhedral than edge sharing [26]. According to Gallington et al., corner and edge shared HfO_7 polyhedra present in the monoclinic phase compared to the solely edge shared HfO_8 polyhedra that comprise the cubic phase [23]. In the monoclinic phase, Hf atoms are surrounded by seven oxygen atoms, with an asymmetric arrangement of Hf–O bond distances in the range 2.03 to 2.25 Å, corresponding to a mixture of seven-edge shared polyhedra and four-corner shared polyhedra in the unit cell [28]. In monoclinic HfO_2, 50% of the O atoms have a coordination number equal to three and 50% have a coordination number equal to four. Gallington found essentially the same numbers are observed both in the melt (O–Hf CN = 3.5) and the amorphous solid (O–Hf CN = 3.4); likewise, the distribution of bond lengths is highly asymmetric, with ~30% of the atoms involved in extended O–Hf bonds [23]. This behavior might be associated with a more compact structure, which is promoted by the higher density, being related to the smaller volume available for the system to relax.

More details about the local atomic structures can be inferred from bond angle distributions (BAD). In Fig. 37.6, O–Hf–O BAD describes the topology inside the structural units, and the Hf–O–Hf one gives the connectivity between them. The O–Hf–O BADs, shown in Fig. 37.6, have two peaks. The positions of both two peaks shift to the left upon compression up to 40 GPa: the main one shifts from 78° to 73°, and the other from 160° to ~136°. In addition, the height of both two peaks increase with increasing pressure up to 40 GPa. These results may be related to changing of main structure units from HfO_6 to HfO_7 when increasing pressure. When increasing pressure from 40 to 100 GPa, the position of both two peaks and the height of the main peak are almost unchanged; while the height of the second minor peak increase slightly. Broglia et al. also showed that Hf–O–Hf angles are insensitive to density, and the Hf–O coordination number is most affected by density [12]. In this study, changing of pressure results in change of sample's density, so our results agree with Broglia's [12].

Figure 37.7 presents Hf–O–Hf BADs of samples with different pressure. Compared the results in Fig. 37.5, the Hf–O–Hf BAD at $P = 0$ GPa is contributed mainly from the Hf–O–Hf bond angles of OHf_3 linkages, at which a main peak locates at 99°, and a small peak at 126°. These bond angles have been also observed in [12] with difference of 2°. Upon increasing pressure, positions of both two peaks shift slightly to the right, the intensity of the first peak slightly reduces, and the second peak's intensity reduces stronger. At $P = 100$ GPa, the Hf–O–Hf BAD is contributed mainly from the Hf–O–Hf bond angles of the HfO_4 linkages.

Our recent study, [10], reported that the almost corner-sharing bond appears in the HfO_5–HfO_5 connectivity whereas three types (corner-, edge- and face-) of sharing

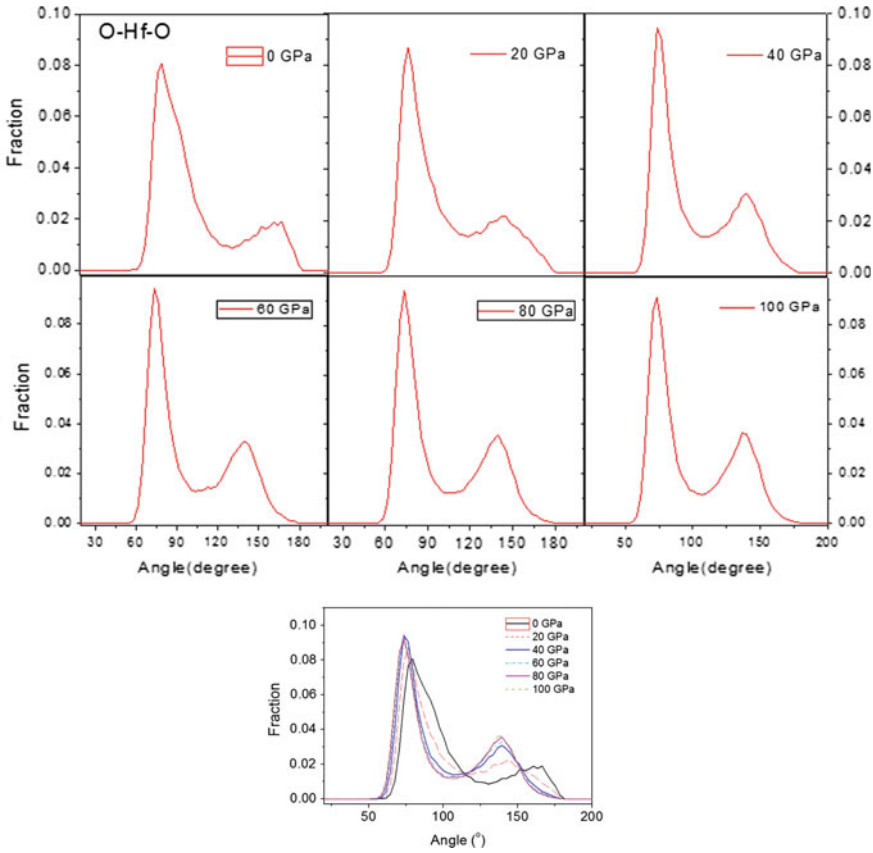

Fig. 37.6 O–Hf–O BADs for samples with different pressure

bonds appear in the HfO_6–HfO_6 and HfO_7–HfO_7 connections. For HfO_5–HfO_6 and HfO_5–HfO_7 connection, corner-sharing bonds account for dominant bonds whereas edge-sharing bonds account for minor bonds and face-sharing bonds do not appear. For HfO_5–HfO_7 connections, edge- and face-sharing bonds are the predominant part whereas small amounts of face-sharing bonds appear. The strong shift of main structure units from HfO_6 to HfO_7 upon compression results in deduce of HfO_5- and HfO_6-related connectivity and increase of HfO_7-related connectivity. These also affects the BADs, because each connectivity has its own bond angle.

Figure 37.8a shows the radial distribution of voids for a-HfO_2 samples with difference pressure. It is clear that, the peak shift to the left. This indicates decrease of void's dimension upon compression. Figure 37.8b indicates the volume of voids decreases with increasing pressure.

We also investigate the mechanical behavior of a-HfO_2 sample upon compression. The Young's modulus was determined by extended the sample uniformly in the *x*-, *y*-, and *z*-directions and uniaxial deformation along the *z*-direction. Figure 37.9a present

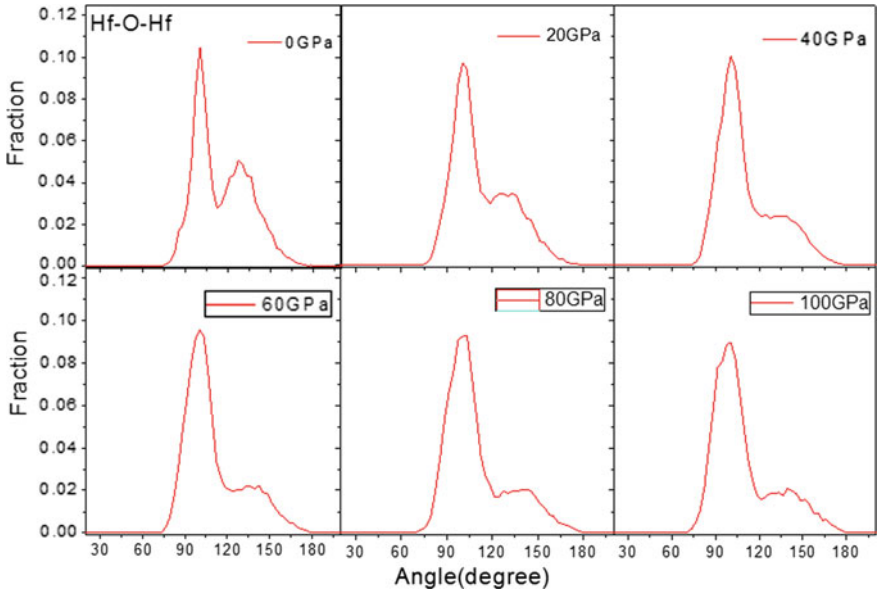

Fig. 37.7 Hf–O–Hf BADs for samples with different pressure

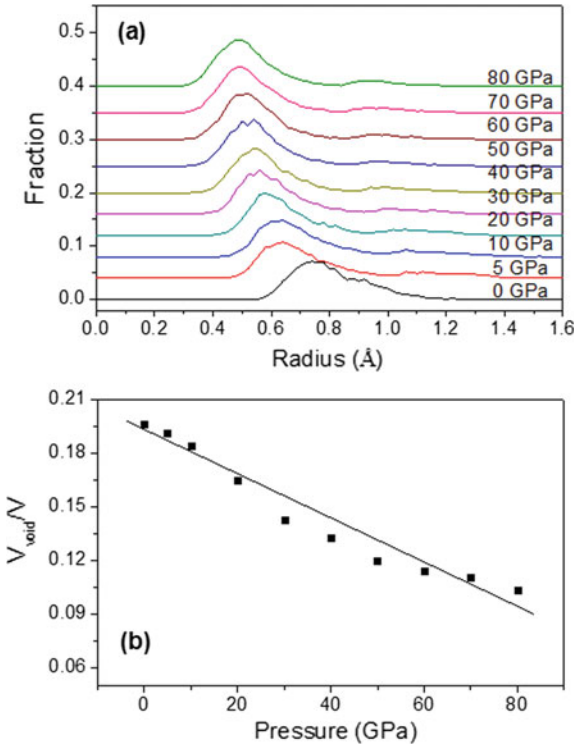

Fig. 37.8 **a** Radial distribution of voids for a-HfO_2 samples with difference pressure and **b** dependence of the ratio V_{void}/V on the pressure

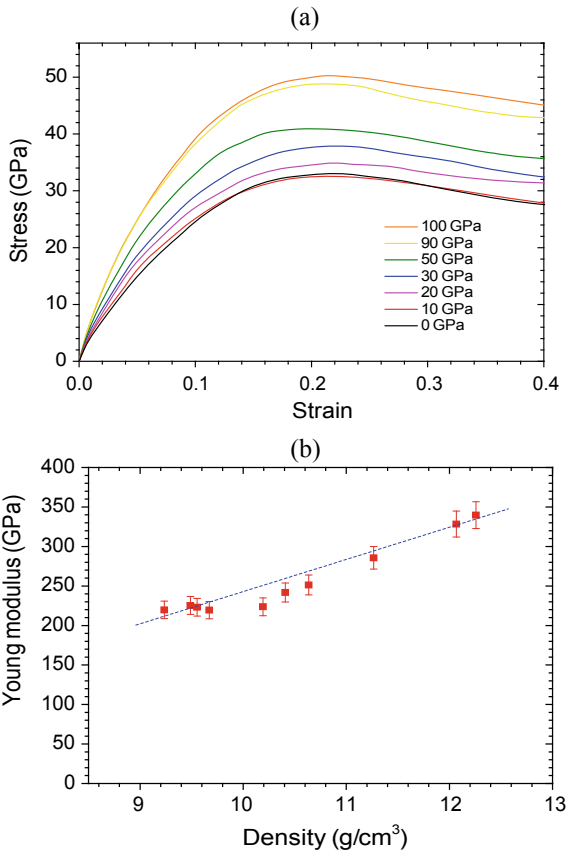

Fig. 37.9 **a** Stress-strain curves for a-HfO_2 samples upon compression; **b** Young's modulus of a-HfO_2 systems as a function of the density of the sample; the line is to guide the eyes

stress-strain curves for a-HfO_2 samples upon compression. The Young's modulus is estimated by the slope of the stress-strain curves in the linear regions. The calculated Young's modulus is comparable with experimental one for amorphous HfO_2. The Young's modulus increases with increasing density due to the increasing fraction of high coordination number.

37.4 Conclusion

MD has been used to investigate the atomic structural characteristics and mechanical behavior of a-HfO_2 system upon compression. Under pressure, the transition of HfO_x units and OHf_y linkages occurs from low to higher coordination numbers. The number of small voids increases and big voids decreases, simultaneously. The Young modulus increase upon compression due to the increasing fraction of high coordination number and the decrease of the volume of voids.

Acknowledgements This research is funded by Vietnam National Foundation for Science and Technology Development (NAFOSTED) under grant number 103.02-2015.31. The first author would like to acknowledge Prof. Chua Soo Jin and Dr. Nguyen Xuan Sang, (RMIT, Singapore) for their valuable advices and discussions.

References

1. J. Robertson, Rep. Prog. Phys. **69**(2), 327 (2006)
2. G.D. Wilk, R.M. Wallace, J.M. Anthony, J. Appl. Phys. **89**(10), 5243 (2001)
3. R. Mitsuhashi, K. Yamamoto, S. Hayashi, A. Rothschild, S. Kubicek, A. Veloso, S. Van Elshocht, M. Jurczak, S. De Gendt, S. Biesemans, M. Niwa, Microelectron. Eng. **80**, 7 (2005)
4. Intel, *Introducing the 45 nm Next-Generation Intel® Core™ Microarchitecture* (2007)
5. A.A. Demkov, A. Navrotsky, *Materials Fundamentals of Gate Dielectrics* (Springer, Berlin, 2005)
6. E.K. Evangelou, M.S. Rahman, I.I. Androulidakis, A. Dimoulas, G. Mavrou, K.P. Giannakopoulos, D.F. Anagnostopoulos, R. Valicu, G.L. Borchert, Thin Solid Films **518**(14), 3964 (2010)
7. C.-H. Chang, Y.-K. Chiou, Y.-C. Chang, K.-Y. Lee, T.-D. Lin, T.-B. Wu, M. Hong, J. Kwo, Appl. Phys. Lett. **89**, 242911 (2006)
8. Y. Wang, F. Zahid, J. Wang, H. Guo, Phys. Rev. B Condens. Matter **85**(22), 1–5 (2013)
9. W.L. Scopel, A.J.R. da Silva, A. Fazzio, Phys. Rev. B **77**(17), 172101 (2008)
10. T.H. Nguyen, V.V. Le, T.N. Nguyen, Vacuum **161**, 251–258 (2019)
11. K. Tapily, N. News, J.E. Jakes, D. Gu, H. Baumgart, Int. J. Surf. Sci. Eng. **5**, 193 (2011)
12. G. Broglia, G. Ori, L. Larcher, M. Montorsi, Model. Simul. Mater. Sci. Eng. **22**, 065006 (2014)
13. P.P. Ewald, Ann. Phys. **369**(3), 253 (1921)
14. S. Yip, *Handbook of Materials Modeling* (Springer, Dordrecht, 2005)
15. J.M. Haile, *Molecular Dynamics Simulation: Elementary Methods* (Wiley, New York, 1997)
16. J.-P. Hansen, I.R. McDonald, *Theory of Simple Liquids*, 4th edn. (Academic Press, London, 2013)
17. P.K. Hung, H.V. Hue, L.T. Vinh, J. Non. Cryst. Solids **352**(30–31), 3332 (2006)
18. V.-V. Le, V.-H. Nguyen, V.-H. Nguyen, K.-H. Pham, Comput. Mater. Sci. **79**, 110–117 (2013)
19. P.G. Debenedetti, H. Stillinger Frank, *Nature* **410**(6825), 259–267 (2001)
20. S. Pathak, G. Mandal, P. Das, AIP Conf. Proc. **1942**(1), 030027 (2018)
21. J. Zhang, A. R. Oganov, X. Li, K.-H. Xue, Z. Wang, and H. Dong, Phys. Rev. B **92**, 184104 (2015).
22. D.M. Hoat, J.F.R. Silva, A.M. Blas, Phys. B. Phys. Condens. Matter (2018)
23. L.C. Gallington, Y. Ghadar, L.B. Skinner, J.K.R. Weber, S.V Ushakov, A. Navrotsky, A. Vazquez-mayagoitia, J.C. Neuefeind, M. Stan, J.J. Low, C.J. Benmore, Materials **10**, E1290 (2017)
24. T.-J. Chen, C.-L. Kuo, J. Appl. Phys. **110**(6), 064105 (2011)
25. J.P. Trinastic, R. Hamdan, Y. Wu, L. Zhang, H. Cheng, J. Chem. Phys. **139**, 154506 (2013)
26. Y. Wang, F. Zahid, J. Wang, H. Guo, Phys. Rev. B **85**, 224110 (2012)
27. D. Ceresoli, D. Vanderbilt, Phys. Rev. B **74**(12), 5 (2006)
28. C. Wang, M. Zinkevich, F. Aldinger, J. Am. Ceram. Soc. **89**, 3751–3758 (2006)

Chapter 38
A Comparison Study of a DIC and Extensometer on Stress-Strain Curve for AL5052 Aluminum Sheets and Its FEM Applications

Ngoc-Duc Do, Van-Thuong Nguyen, and Duc-Toan Nguyen

Abstract The digital image correlation (DIC) method is an advanced technical method to measure material strain by comparing several captured figures during deformation. DIC provides full-field displacements and full-field strains in recorded images. In fact, there is much software using the DIC algorithm. However, a commercial DIC system requires a high initial investment. In this study, the DIC algorithm was built based on the open-source of Matlab software, temporarily called NCORR DIC. A DIC system was built including a computer system, extensometer, tensile testing machine, high-resolution camera, NCORR DIC software and applied for AL5052 sheet metal test sample. After obtaining the images from the tensile test, the entire image will be included in the NCORR DIC software for processing. To check the accuracy of the DIC system, the results of the stress-strain curve of NCORR software were compared with the standard test method using extensometer. The obtained results measured from NCORR DIC software were imported into a finite element method (FEM) software to check the accuracy of this method. Moreover, the hardening model (Voce, Swift, Kim-Tuan) provides empirical evidence and prerequisite conditions for the development of new fracture criteria to describe behavior fractures.

38.1 Introduction

Today, in the field of scientific research, there are many methods for measuring displacement and strain fields. Among them are the methods that require relatively high trade. Along with the development of today's modern digital image processing technology, digital image correlation techniques for full-field strain measurement [1] have researched by many other researchers. To optimize the design and shorten the production time, measure detailed properties of important materials such as deformation limits, Poison coefficients, elastic modules, etc. The most commonly used

N.-D. Do · V.-T. Nguyen · D.-T. Nguyen (✉)
School of Mechanical Engineering, Hanoi University of Science and Technology, 1A-Dai Co Viet Street, Hai Ba Trung District, Hanoi City, Vietnam
e-mail: toan.nguyenduc@hust.edu.vn

I. A. Parinov et al. (eds.), *Advanced Materials*, Springer Proceedings in Materials 6, https://doi.org/10.1007/978-3-030-45120-2_38

method to search for material properties is to test the tensile strength with a compression tractor. However, this method only provides an average displacement-strain field over the length according to the specified standard. The DIC method [2] is a method that uses image tracking and analysis techniques to accurately measure changes of images. It has the advantage of being highly accurate and full-field displacement and strain measurements on each pixel.

The 2D-DIC system used the Ncorr software [3] developed based on Matlab's open-source to measure the full-field strain distribution. Significant progress has been made in recent decades in both the development of DIC measurement methods and in enhancing the performance of related computational algorithms. To achieve these advances, not to mention the flexible, high-quality Ncorr software. It has an easy-to-access and intuitive user interface dialog box, using many new DIC 2D algorithms, completely contained in Matlab software and contains drawing tools to create images. The idea is to provide users of a DIC program that is easy to use, efficient and flexible. The material used in this study is AL5052. All recorded images will be included in the Ncorr software for processing. To check the accuracy of the DIC system, the results of the stress-strain curve of NCORR software for AL5052 were compared with the standard test method using an extensometer. The obtained results measured from NCORR DIC software were imported into a finite element method (FEM) [4] software to check the accuracy of this method. Furthermore, this study monitors the flow curve and ductile failure of AL5052 materials based on the DIC method. Therefore, the Bao and Wierzbicki criterion [5] is presented in conjunction with three hardening models (Voce, Swift, Kim-Tuan) [6–8] to achieve fracture profiles. It provides empirical evidence and prerequisite conditions for the development of new fracture criteria to describe behavior fractures in a large range of triaxiality stress. The software used the finite element method (FEM) in this study is Abaqus [9]. Simulation software is easy to use and highly accurate.

In this chapter, thanks to the accurate measurement results of the DIC method for the ductile damage model, various hardening models have made the same prediction for the force-displacement scheme before achieving maximum drag. Moreover, comparing the simulation results based on various hardening models with the experimental data of the tensile test shows the effect of the post-necking prediction of the hardening model on the simulation results of the tensile test. Through this simulation, the accuracy of the post-necking prediction of the Kim-Tuan, Swift and Voce models has been confirmed.

38.2 Development of 2D-DIC System and Its Application

38.2.1 The 2D-DIC System in House [10]

Figure 38.1 shows the in-house 2D-DIC system developed in this study. There are three steps to implementing this method: (i) spray paint on the surface of materials to

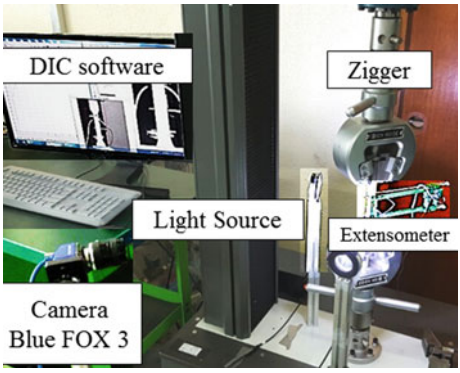

Fig. 38.1 In-house 2D-DIC system

distribute gray intensity; (ii) record the deformation process images of the material; (iii) apply DIC software to obtain full displacement-strain. In addition, during loading, the specimen surface is also strictly required in the same plane that is parallel to the sensor plane of the camera.

38.2.1.1 Basic Principle and Concept

Digital use measurement (DIC) is an optical method that uses image tracking and analysis techniques to accurately measure changes of 2D images. This method is often used to measure full-fields displacement-strain, and it is widely applied in many fields of science and engineering.

The overall objective of the DIC measurement method is to obtain displacement and distortion data in the region of interest (ROI) for a sample of material undergoing deformation. Basically, the image of a sample is taken when it is deformed. These images are used as inputs for the DIC program. The idea is to somehow get the one-to-one correspondence between the points in the original undeformed image and the subsequent deformed image.

38.2.1.2 Displacement Mapping Function

Figure 38.2 shows the Basic principle of the DIC method. For distortion mapping, the mapping function associated with the image can be obtained from comparing a set of sub-pairs of waves across the entire image. The coordinates or grid points F(x, y) and G(x^*, y^*) are related by the translations that occur between the two images. If the distortion is small and perpendicular to the optical axis of the camera, then the relationship between F(x, y) and G(x^*, y^*) can be approximated by 2D affine transformations such as [see (38.1) and (38.2)]:

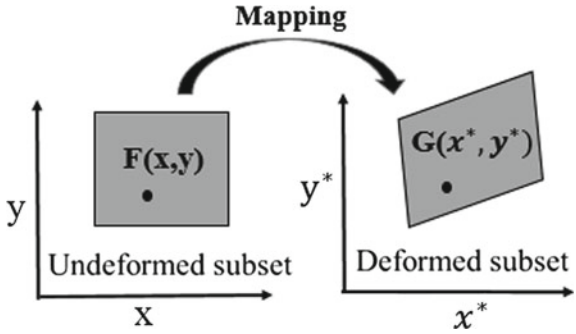

Fig. 38.2 Basic principle of DIC method

$$x^* = x + u + \frac{\partial_u}{\partial_x}\Delta_x + \frac{\partial_u}{\partial_y}\Delta_y \tag{38.1}$$

$$y^* = y + v + \frac{\partial_v}{\partial_x}\Delta_x + \frac{\partial_v}{\partial_y}\Delta_y \tag{38.2}$$

Here u and v are translations of the center of the sub-image in the X and Y directions respectively. The distances from the center of the sub-image to the point (x, y) are denoted by Δ_x and Δ_y, displacement gradient: $\frac{\partial_u}{\partial_x}$, $\frac{\partial_u}{\partial_y}$, $\frac{\partial_v}{\partial_x}$, $\frac{\partial_v}{\partial_y}$.

38.2.1.3 Correlation Criterion

Before the correlation analysis process, a correlation criterion is selected to assess the similarity degree between the reference and deformed subsets. Moreover, the DIC algorithms find the extremum of a correlation cost function to find the deformation of the subset. Hence, the zero-normalized sum of squared differences (ZNSSD) [11] is one of these functions at the integer location, which can be written as follows:

$$C_{ZNSSD} = \sum_{i=-M}^{M}\sum_{j=-M}^{M}\left[\frac{f(x_i, y_j) - f_m}{\Delta f} - \frac{g\left(x_i^*, y_j^*\right) - g_m}{\Delta g}\right]^2 \tag{38.3}$$

where f and g are the functions of the reference and the current image grayscale intensity at a point location (x, y), respectively. f_m, g_m, Δf and Δg are determined by using the following functions:

$$f_m = \frac{1}{(2M+1)^2}\sum_{i=-M}^{M}\sum_{j=-M}^{M} f(x_i, y_j) \tag{38.4}$$

$$g_m = \frac{1}{(2M+1)^2}\sum_{i=-M}^{M}\sum_{j=-M}^{M} g\left(x_i^*, y_j^*\right) \tag{38.5}$$

$$\Delta f = \sqrt{\sum_{i=-M}^{M}\sum_{j=-M}^{M}\left[f\left(x_i, y_j\right) - f_m\right]^2} \tag{38.6}$$

$$\Delta g = \sqrt{\sum_{i=-M}^{M}\sum_{j=-M}^{M}\left[g\left(x_i^*, y_j^*\right) - g_m\right]^2} \tag{38.7}$$

38.2.1.4 Calculation of Strain

From the displacement gradient, Lagrangian strains are calculated by:

$$E_{xx} = \frac{1}{2}\left[2\frac{\partial_u}{\partial_x} + \left(\frac{\partial_u}{\partial_x}\right)^2 + \left(\frac{\partial_v}{\partial_x}\right)^2\right] \tag{38.8}$$

$$E_{xy} = \frac{1}{2}\left(\frac{\partial_u}{\partial_y} + \frac{\partial_v}{\partial_x} + \frac{\partial_u}{\partial_x}\frac{\partial_u}{\partial_y} + \frac{\partial_v}{\partial_x}\frac{\partial_v}{\partial_y}\right) \tag{38.9}$$

$$E_{yy} = \frac{1}{2}\left[2\frac{\partial_v}{\partial_y} + \left(\frac{\partial_u}{\partial_y}\right)^2 + \left(\frac{\partial_v}{\partial_y}\right)^2\right] \tag{38.10}$$

Engineering strain and true strain are calculated by the way used strain contour maps computed by DIC method:

$$\varepsilon_{eng} = -1 + \sqrt{2 * E_{Lag} + 1} \tag{38.11}$$

$$\varepsilon_{true} = \ln\left(1 + \varepsilon_{eng}\right) \tag{38.12}$$

Here the subscripts “eng”, “Lag”, “true” mean engineering, Lagrangian, true, respectively.

Thus, the average true strain (ε_{ave}) is calculated as follows:

$$\varepsilon_{ave} = \frac{1}{M\ X\ N}\sum_{1}^{N}\sum_{1}^{M}\varepsilon(i, j) \tag{38.13}$$

where M and N are the total number of the DIC grid points along the tensile axis and its perpendicular axis in the region of interest (ROI), respectively; $\varepsilon_{(i, j)}$ is the local true strain at grid point (i, j) and ε_{ave} is the average true strain calculated over the entire gauge section (region of interest).

38.2.2 Experiment System

Figure 38.3 shows a schematic drawing of a 2D-DIC system. To eliminate disruption from ambient light, a strong white LED light source is used to illuminate the sample and a corresponding filter is used to illuminate to produce the sharpest image for analysis. The camera is perpendicular to the position of the subject, the images taken will be digitized before being included in the computer software. Standard tensile tests according to ASTM-8 are performed for AL5052-O sheets with a thickness of 1 mm at a constant tensile speed of 5 mm/min. For measuring the normal tension curve, an extensometer with a gauge length of 50 mm is attached to the back.

The camera is perpendicular to the position of the subject, the images taken will be digitized before being included in the computer software. The camera used in this study is a Blue FOX 3 camera with CMOS sensor technology, full resolution of 1936 $\times$ 1216 pixels and a frame rate of 41. The distance from the image to the sample is 450 mm. Camera parameters will be maintained during the test, so it will not affect the deformation measurement. The projects of the DIC method in the DIC software can be shown in Table 38.1.

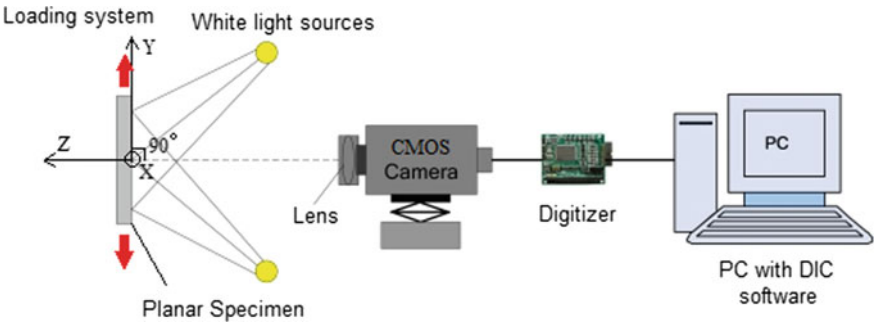

Fig. 38.3 Schematic figure of the 2D-DIC system

Table 38.1 Project of DIC method

Material	Subset size (Pixels)	Step size (Pixels)	Speckle size (mm)
AL5052	20	2	0.3
1 pixel $\approx$ 0.15 m			

38.3 Experiment and Simulation of Tensile Test

38.3.1 Flow Curve

Furthermore, Young's modulus (E), tensile yield strength YS (σ), and Poisson's ratio (υ) were also calculated from the DIC results. The mechanical properties for AL5052 are determined as shown in Table 38.2.

During tensile testing, the stress is calculated by various methods (using a contact extensometer in the conventional method and a non-contact optical extensometer in the DIC method). At the same time, stress evolution can be estimated based on measured axial force data. The formula for calculating stress is expressed as

$$\sigma_{\text{true}} = \sigma_{\text{eng}}\left(1 + \varepsilon_{\text{eng}}\right) \tag{38.14}$$

As can be seen in Fig. 38.4, it shows that the measurement results from the DIC method are relatively accurate compared to traditional methods using extensometer. Furthermore, to confirm again the proposed method, the results measured from the DIC are input to a simulation program in the next section.

Table 38.2 Mechanical properties for AL5052

Material	r_0	σ_{YS} (MPa)	E (Gpa)	ϑ
AL5052	0.763	209.71	72.3	0.32

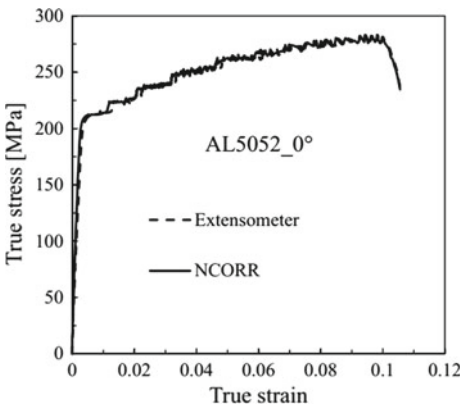

Fig. 38.4 Comparison True Strain-Stress DIC method and method using an extensometer

38.3.2 FEM Model

The purpose of this section is to check the accuracy of the material parameters being the input of a simulation program. A FEM model simulating a tensile test [12] for the AL5052 sheet is carried out by using the ABAQUS/EXPLICIT version 6.14. To determine the exact value of $\overline{\varepsilon_f}$, a finer mesh of 0.3 mm has been applied. The finite element mesh of the numerical tensile test is shown in Fig. 38.5. In addition, to simulate the tensile test, the left end is fixed and the displacement condition is applied to the right end. The Swift, Voce and Kim-Tuan hardening models have been widely applied to describe the flow curves of sheet metal needed. In this study, three hardening models were used to verify the effect of the hardening model on the simulation results of the tensile test on AL5052 materials, see (38.15)–(38.17).

(i) Swift Equation:

$$\sigma = K(\varepsilon_0 + \varepsilon)^n \tag{38.15}$$

(ii) Voce Equation:

$$\sigma = \sigma_0 + A\left(1 - \exp^{-b\varepsilon}\right) \tag{38.16}$$

(iii) Kim-Tuan Equation:

$$\sigma = \sigma_0 + T(\varepsilon + \varepsilon_0)^m\left(1 - \exp^{-c\varepsilon}\right) \tag{38.17}$$

Figure 38.6 shows a comparison between the applications of the three hardening models above depicting the post-necking of the AL5052 sheet. The parameters of the different hardening models are summarized in Table 38.3. It is clear that all hardening models are very well suited to the empirical data of the flow curve in the range of uniform elongation. Among the three models, the Kim-Tuan equation gives

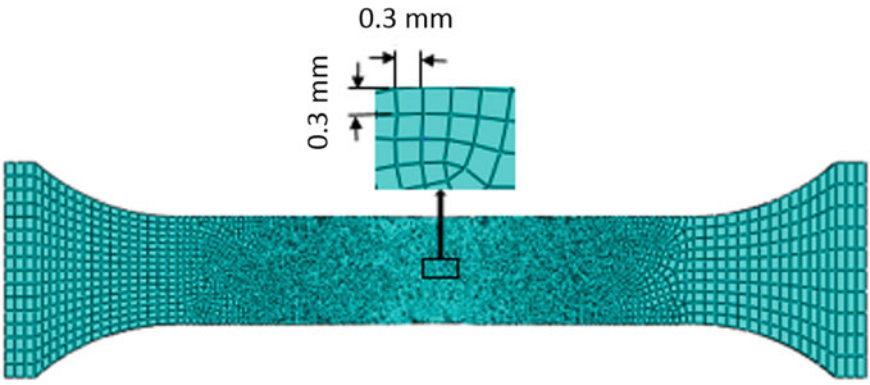

Fig. 38.5 FEM model

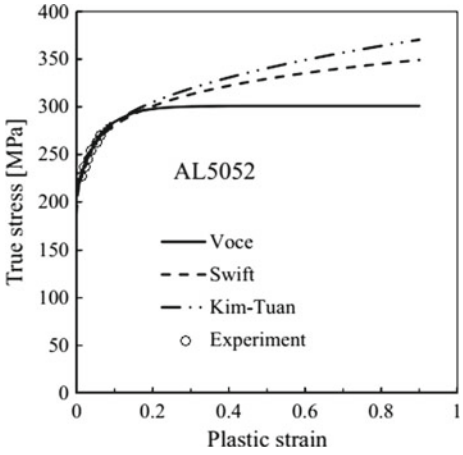

Fig. 38.6 Hardening models and the results from DIC measurement method

Table 38.3 Parameters of hardening models for flow curve of AL5052 sheet

Initial yield stress		Swift		Voce		Kim-Tuan		
ε_0	σ_0 (MPa)	K (MPa)	n	A (MPa)	B	T (MPa)	m	c
0.002	209.715	355.54	0.1	93.97	16.12	172.61	0.36	44.1

the highest result of flow stress within a large strain range, while the Voce equation results are the lowest. This shows the effect of the post-neck prediction of stiffening model on tensile test simulation results.

38.3.3 Ductile Damage Model

The ductile criterion describes the evolution of damage in a material when a critical value is reached. Moreover, this leads to the onset of a macro fracture. The ductile criteria at piles are taken according to:

$$D = \int_0^{\overline{\varepsilon_f}} \left(\frac{1}{\overline{\varepsilon_f}(\eta)} \right) d\varepsilon_f \tag{38.18}$$

where D is a state variable of plasticity damage, denoting the onset of fractures when D reaches unity; $\overline{\varepsilon_f}$ is the equivalent plastic strain at the onset of fracture and η is the stress triaxiality.

Concerning these models, the ductile damage model proposed by Bao and Wierzbicki has been widely applied by many researchers. In this model, $\overline{\varepsilon_f}$ evolution can be approximated by the following equation:

$$\overline{\varepsilon_f} = \begin{cases} \infty, & \eta \le -1/3 \\ C_2/(1+3\eta), & -1/3 < \eta \le 0 \\ C_1 + (C_2 - C_1)(\eta/\eta_0)^2, & 0 < \eta \le \eta_0 \\ C_2\eta/\eta_0, & \eta \ge \eta_0 \end{cases} \tag{38.19}$$

where η_0 is the average value of the stress triaxiality in unilateral tension; C_2 is equal to the maximum equivalent plastic strain observed during the uniaxial tension test. In addition, regarding the hypothesis of maximum shear stress, $C_1 = \left(\sqrt{3}/2\right)^{1/n}$ with n is the hardening exponent of the material. According to this expression, three material constants including η_0, C_2 and n are determined based on DIC measurement results.

The first, from (38.19), stress triaxiality is given as the ratio of mean stress (σ_m) to the equivalent stress (σ_e). This ratio can be calculated as follows:

$$\eta = \frac{\sigma_m}{\sigma_e} = \frac{(\sigma_1 + \sigma_2 + \sigma_3)/3}{\frac{1}{\sqrt{2}}\sqrt{(\sigma_1 - \sigma_2)^2 + (\sigma_2 - \sigma_3)^2 + (\sigma_3 - \sigma_1)^2}} \tag{38.20}$$

where σ_i are the principal stresses.

The stress triaxiality also can be determined in the plane-stress condition by:

$$\eta = \frac{(\sigma_1 + \sigma_2)/3}{\sqrt{\sigma_1^2 + \sigma_2^2 - \sigma_1\sigma_2}} \tag{38.21}$$

We have a relationship using the laws of flow:

$$\frac{d\varepsilon_2}{d\varepsilon_1} = \frac{2\sigma_2 - \sigma_1}{2\sigma_1 - \sigma_2} \tag{38.22}$$

If the strain path is ratio during the tensile test, we can get the regarding relationship:

$$\frac{d\varepsilon_2}{d\varepsilon_1} \approx \frac{\varepsilon_2}{\varepsilon_1} \tag{38.23}$$

Therefore, the relationship between σ_1 and σ_2 can be approximated by:

$$\sigma_2 \approx \frac{2\varepsilon_2 + \varepsilon_1}{2\varepsilon_1 + \varepsilon_2}\sigma_1 \tag{38.24}$$

According to this relationship, the evolution of a stress triaxiality is calculated for a local element located in the necking region for the AL5052-sheet. Mean of stress triaxiality (η_0) is determined by 0.39.

Figure 38.7 shows the good agreement with those of the extrapolation data from the DIC measurement. To clarify the damage model for the tested material, the

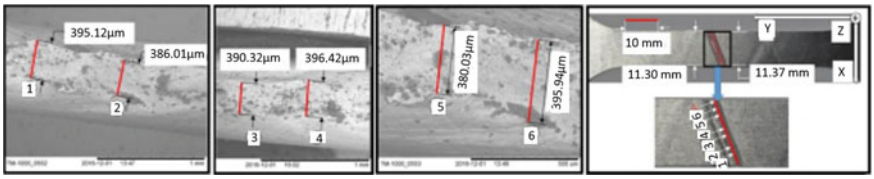

Fig. 38.7 SEM observations of the thickness of AL5052-O sheet under tension

Table 38.4 Material parameters of the Bao and Wierzbicki criterion for AL5052

σ_0 (MPa)	σ^* (MPa)	C_1	C_2	η_0
209.72	257.57	0.13	1.12	0.39

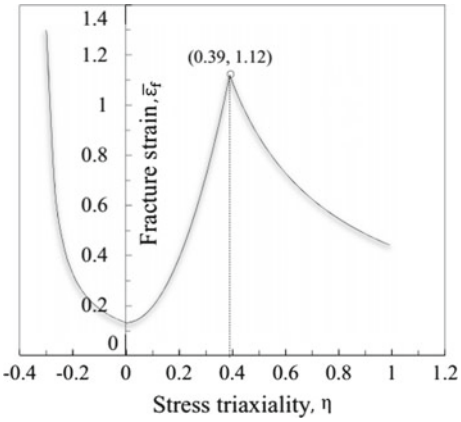

Fig. 38.8 Fracture strain and stress triaxiality for AL5052 sheet from (38.19) based on Bao and Wierzbicki criterion

processing of the AL5052 sheet was looked over by a scanning electron microscopy (SEM) machine [13]. This supports the use of the ductile damage model for the Al5052 sheet in this study. C_2 in (38.19) is determined as 1.12 by SEM.

Finally, the hardening exponent of the tested material can be found by simply fitting the stress-strain data obtained from the tensile test with a hardening model, such as Hollomon or Swift. Therefore, all parameters of the ductile damage model C_1, C_2, and η_0 are identified (can be seen in Table 38.4). These parameters to the evolution of strain to fracture in the space of $(\eta, \overline{\varepsilon_f})$ presented in Fig. 38.8.

38.3.4 Relationship Between Ductile Damage Parameters for Kim-Tuan Hardening Model

From the mathematical equation of the Kim-Tuan model, it is not possible to indicate the hardening exponent of the material tested. Fortunately, the value of the parameter

m of the Kim-Tuan model can be calculated based on the measured data of the maximum tensile force point (MTFP):

$$\mathrm{m} = \varepsilon^* \frac{\sigma^*}{\sigma^* - \sigma_0} \tag{38.25}$$

According to the diffuse necking criterion, the hardening exponent at MTFP is equal to the deformation at this time. Therefore, the relationship between parameter m (in Kim-Tuan hardening model) and parameter n (in ductile damage model) can be expressed as follows:

$$\mathrm{n} = \mathrm{m} \frac{\sigma^* - \sigma_0}{\sigma^*} \tag{38.26}$$

Therefore, C_1 in (38.19) can be calculated as follows:

$$\mathrm{C}_1 = \mathrm{C}_2 \left(\sqrt{3}/2\right)^{\sigma^*/(\mathrm{m}(\sigma^* - \sigma_0))} \tag{38.27}$$

38.4 Comparison Results

Figure 38.9 shows a comparison of simulation and experimental results on the angle of fracture observed on the specimen surface. The post-necking of the hardening model strongly affects the angle of fracture. Compared to the experimental results, the Voce model, with a prediction of saturation stress at the initial value of strain, produced the most misleading prediction of the fracture profiles. Meanwhile, Swift and Kim-Tuan hardening models provide better prediction for the fracture profile of the AL5052 model. Therein, the Swift and Kim-Tuan models provided a better prediction about fracture profiles of the AL5052 model.

Figure 38.10 shows the thickness measurement from the simulation result by

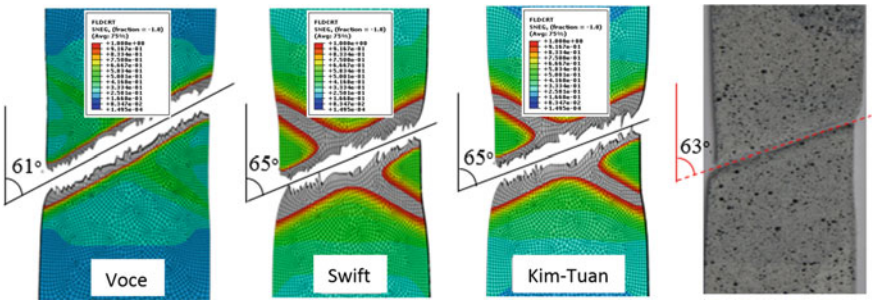

Fig. 38.9 Fracture profile of AL5052 sheet from simulations and experiment

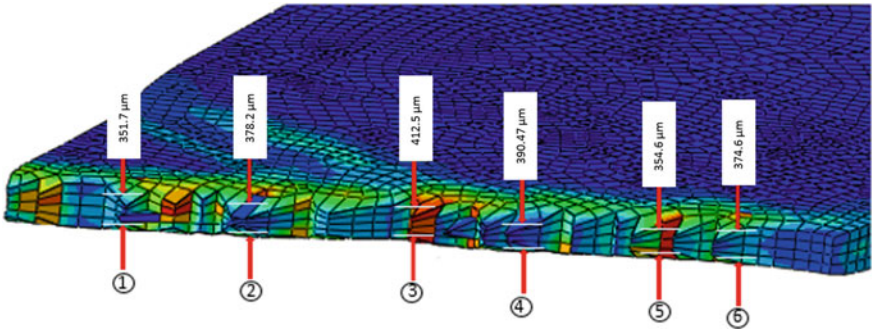

Fig. 38.10 Thickness measurement at the fracture region in the simulation by applying Kim-Tuan hardening model

applying the Kim-Tuan hardening model. Obviously, the thickness of the material under test is greatly reduced when the necking occurs. Furthermore, this figure depicts the 6 points corresponding to the points of the test in Fig. 38.7 to measure thickness in the fracture area. Therefore, it is part of the simulation results to confirm the accuracy of the proposed method.

Figure 38.11 shows the result of force and displacement obtained from the tensile test and the maximum tensile force. For comparison, force-displacement data based on FEM simulations are also plotted in this figure. These consistent results testify to the accuracy of the material properties outlined in previous sections of the current study. However, from another perspective, the hardened models studied have provided different results on force-displacement after the MTFP. This demonstrates the influence of the post-necking prediction of the flow curve on the accuracy of the FEM models for tensile test simulation. The Voce hardening model with saturated stress predicts that failure will occur as soon as the maximum force is reached, while

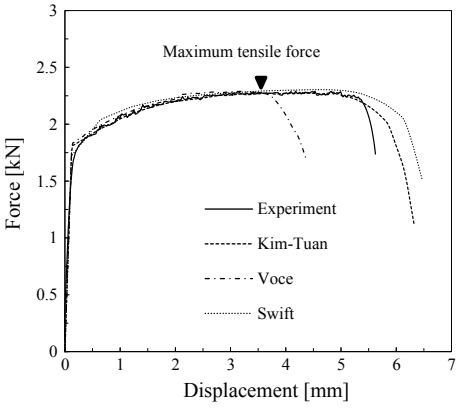

Fig. 38.11 Results of force-displacement for AL5052 sheet experiment and simulation

the Swift hardening model overestimates the elongation of the test piece. The advantage of Kim-Tuan hardening model is that it makes an accurate prediction for the force-displacement diagram (see Fig. 38.11).

38.5 Conclusion

The developed internal DIC 2D system provides an accurate measurement of full-field displacement and strain compared to traditional measuring methods using extensometers. The comparison results show the relative accuracy of the DIC method with the traditional measurement method using an extensometer. Therefore, from these measurement results, the material parameters AL5052 sheet were found. Moreover, using the DIC measurement method, this study identifies the flow curve and ductile damage model for an aluminum sheet with high accuracy. The idea of extrapolating the measured data from the last image before the fracture is proposed. This procedure can be effectively applied to other sheet metal materials.

Moreover, the advantage of the DIC measurement method to evaluate ductile fracture through simulation. The results show this provides a better prediction for the fracture profile of the AL5052 model, determines the maximum tensile force, force-displacement data based on FEM simulations. The thickness of the material under the test is greatly reduced when the occurrence of necking occurs.

Acknowledgements This research is funded by University Project at Hanoi University of Science and Technology under grant number "T2018-TĐ-204".

References

1. O.H. Kwon, S.T. Kim, J.W. Kang, J. Korean Soc. Saf. **28**(4), 26–32 (2013)
2. B. Pan, K. Qian, H. Xie, A. Asundi, Measur. Sci. Tech. **20**(6), 1–17 (2009)
3. J. Blaber, B. Adair, A. Antoniou, Exp. Mech. **55**, 1105–1122 (2015)
4. J.N. Reddy, *An Introduction to the Finite Element Method* (McGraw-Hill Book Company, New York, NY, 1984), 495 p.
5. Y. Lou, H. Huh, S. Lim, K. Pack, Int. J. Solids Struct. 49 (2012)
6. T.Q. Pham, B.-H. Lee, K.-C. Park, Y.-S. Kim, Int. J. Mech. Sci. 140 (2018)
7. H.W. Swift, J. Mech. Phys. Solids **1**(1), 1–18 (1952)
8. J.-H. Kim, A. Serpantié, F. Barlat, F. Pierron, M.-G. Lee, Int. J. Solids Struct. **50**(24), 3829–3842 (2013)
9. ABAQUS user's manual version 6.12 (Hibbitt, Karlsson & Sorensen Inc., 2012)
10. M.A. Sutton, J.H. Yan, V. Tiwari, H.W. Schreier, J.J. Orteu, Opt. Lasers Eng. **46**(10), 746–757 (2008)
11. B. Pan, H. Xie, Z. Wang, Appl. Opt. **49**(28), 5501–5509 (2010)
12. C.-S. Oh, N.-H. Kim, Y.-J. Kim, J.-H. Baek, Y.-P. Kim, W.-S. Kim, Eng. Fract. Mech. **78**(1), 124–137 (2011)
13. H. Jin, W.-Y. Lu, J. Kornelis, J. Strain Anal. Eng. Des. (2008)

Part IV
Applications of Advanced Materials

Chapter 39
An Analytical Model for AlGaN/GaN MOS-HEMT for High Power Applications

Nguyen-Trung Do, Nguyen-Hoang Thoan, Tran Minh Quang, Dao Anh Tuan, and Nguyen-Ngoc Trung

Abstract We develop a physics based analytical model for AlGaN/GaN high electron mobility transistors (HEMT and MOS-HEMT) to study the *I-V* characteristics, current transfer characteristics, transconductance and drain-conductance. The model is modified from a model first presented by Chang and Fetterman for AlGaAs/GaAs HEMT (Chang and Fetterman in Solid-State Electron 30(5), 1987 [1], IEEE Trans Electron Dev Ed-34(I), 1987 [2]) The linear and non-linear drain currents have been separately calculated and merged them in order to evaluate the *I-V* characteristics. The threshold voltage has been evaluated from current transfer characteristics plot and verified from the transconductance parameter. We also consider the effect of polarization on threshold voltage of the devices. Moreover, to prove the exactness of our model, we compare our data with our experiment data for common HEMT, Hasan's MOS-HEMT and Yoon's HEMT with short channel.

39.1 Introduction

Nowadays, the development of power devices and modern applications such as smart phone, electric converter is helping our life became more convenience. The classic Si-based devices has reached limitation so it's difficult to create new one with better performances. GaN-based high electron mobility Transistors (HEMTs) are emerging as great candidates for high-temperature, high-power and radio-frequency (RF) electronics due to their unique capabilities of achieving higher current density, higher breakdown voltage, higher operating temperatures and higher cut-off frequencies compared to silicon (Si) [3]. Due to higher breakdown voltage, up to 2×10^6 V/cm, GaN MOSFET and GaN/AlGaN HEMT can operate at higher temperature and power than that of Si MOSFET and GaAs HEMT [3, 4]. Moreover, GaN is more chemical stable and environmentally friendly than GaAs. GaN-based HEMT has a current flow which is controlled by a metal Schottky-gate leads to a MOS structure on the top of HEMT, which decreases gate leakage current in Schottky-gate devices and the

N.-T. Do · N.-H. Thoan · T. M. Quang · D. A. Tuan · N.-N. Trung (✉)
School of Engineering Physics, Hanoi University of Science and Technology, Hanoi, Vietnam
e-mail: trung.nguyenngoc@hust.edu.vn

I. A. Parinov et al. (eds.), *Advanced Materials*, Springer Proceedings in Materials 6, https://doi.org/10.1007/978-3-030-45120-2_39

current collapse occurs in unpassivated devices due to traps existing between gate and drain. However, there are so many difficulties to manufacture a good HEMT; simulation theory model on computer before manufacturing experimental HEMT is a method focused by many researchers.

In this study, we built up an analytical model to simulate electrical characteristics of Gate first process flow HEMT (use n^+-GaN capping layer to form better ohmic contact) and MOS-HEMT based on AlGaN/GaN hetero structure. Our model is based on the model proposed by Chang and Fetterman for AlGaAs/GaAs HEMT [1, 2] and it is extended for both kinds of HEMTs with long and short channel. Moreover, we also compare the simulation data with results obtained from experiment such as $I_d - V_d$ characteristics, value of I_{dsat} corresponds to different gate voltages, V_g then calculates some other characteristics of HEMT like pinch-off voltage, $V_{pinch\text{-}off}$, transconductance, G_m. All of them are prove that our model could be used to simulation for conventional and Gate first process flow HEMT. In addition, we use this model to simulate MOS-HEMT of Hasan and HEMT of Yoon with short channel. Our simulation data has a strong coincidence with experiment data which Hasan and Yoon showed in their research.

39.2 Simulation Procedure and Experimental

The AlGaN/GaN epi-layers structure and HEMT design, used in this study, is present in Fig. 39.1. It consists of, starting from the bottom, a thick buffer C-doped layer grown on substrate, an undoped GaN, followed by donor layer doped with Si, an undoped AlGaN channel layer, GaN cap layer and finally a very thin oxide layer. The aluminum mole of AlGaN is variable. For this simulation, the effects of drain, source parasitic resistances, thickness of each layer and doping concentration are considered. The effect of cap and oxide layers is included in the capacitance calculation. However, mobility variation and voltage dependence of the Fermi level have not been included.

Here, the threshold voltage expression for an *n*-channel device has been derived considering the effect of the oxide layer and polarization [5]:

$$V_{th} = \theta_b - \Delta E_c - \frac{qN_D d_d^2}{2\varepsilon_0 \varepsilon_b} - \frac{\sigma_p d}{\varepsilon_0 \varepsilon_b} - \frac{Q_{ox}}{2C_{ox}} - \frac{\sigma_p}{C_{ox}} \tag{39.1}$$

where σ_p is the polarization charge density, θ_b is the metal-semiconductor Schottky barrier height, d is the overall AlGaN upper layer thickness, d_d is the doped AlGaN layer thickness, ε_0 is a vacuum permittivity, ε_b is an AlGaN barrier layer relative permittivity, N_D is the barrier layer doping concentration in the doped-AlGaN, C_{ox} is the gate oxide capacitance, ΔE_c is the conduction band discontinuity/offset ($\Delta E_c = 0$ at 300 K), Q_{ox} is the fixed oxide charge.

Spontaneous polarization and electric polarization, combined with the difference of bandgap between substrate GaN and AlGaN barrier layer, forms a two dimensions electron gas (2DEG) near the GaN/AlGaN boundary. Polarization charge density is

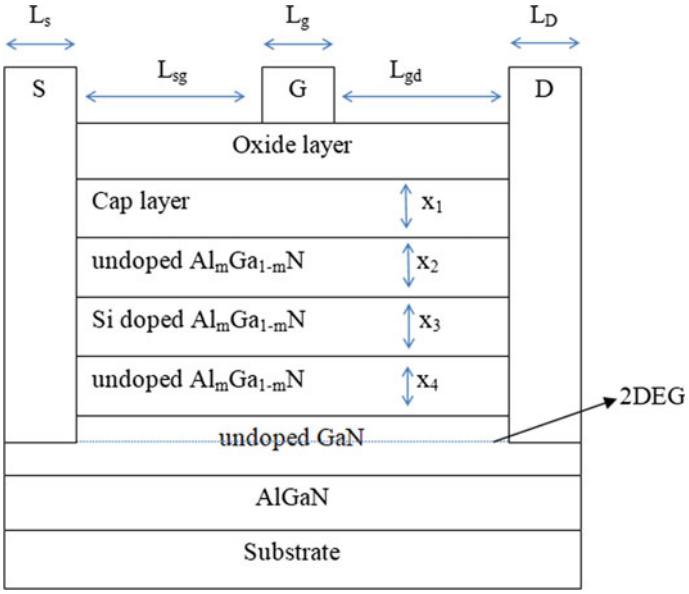

Fig. 39.1 Schematic diagram of the studied AlGaN/GaN MOS-HEMTs

a parameter dependent on the concentration of Al in $Al_mGa_{1-m}N$ [5]:

$$\sigma_p = -0.52m + 2\frac{a(GaN) - a0(m)}{a0(m)}\left[e31(m) - e_{33}(m)\frac{C_{31}(m)}{C_{33}(m)}\right] \tag{39.2}$$

where, a(GaN) and a_0 are lattice constant of GaN and AlGaN, respectively; e_{31} and e_{33} are piezoelectric coefficients; C_{31} and C_{33} are elastic stiffness constants. This study used the relation of molar ratio and some parameters of MOS-HEMT SiO_2/AlGaN/GaN as reported in [5].

39.2.1 Simulation Model

Our simulation model could be used in general case; it means this model can be applied for both HEMT and MOS-HEMT with long and short channels. The 2DEG channel is divided into two regions: low-field region $0 \leq x \leq L_1$, and the high-field region, $L_1 \leq x \leq L_2$, as shown in Fig. 39.2.

In this proposed model, the drain resistance is considered constant in the whole region. The drain current is given as [1, 2]

$$I_{DS} = qn_s(x)Zv(x) \tag{39.3}$$

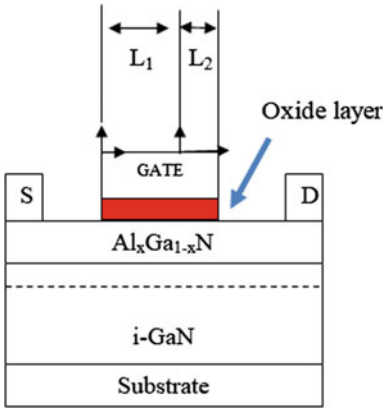

Fig. 39.2 Simulation of HEMT structure

where Z is the gate width and $v(x)$ is the electron drift velocity. The Gaussian Standing Wave (GSW) equation for velocity-field dependence is

$$v(x) = v_s\left(1 - e^{-\xi(x)/\xi_c}\right) \tag{39.4}$$

where v_S is the saturation drift velocity, $\xi_c = v_S/\mu$, μ is the low-field mobility.

The potential at $x = L_1$ is:

$$V_{L1} = V_G - V_{TO} - \frac{I_C}{G_0}$$

where I_c is the current in the 2DEG channel. So, the channel current–voltage relation in the low-field region is given as

$$L_1 = \frac{I_c C_2(t_0)}{\xi_c G_0}$$

For the high-field region, $0 \leq x' \leq L_2$, one needs to solve the two-dimensional Poisson equation:

$$\frac{\partial^2 V(x', y)}{\partial x'^2} + \frac{\partial^2 V(x', y)}{\partial y^2} = -\frac{q N_D(y)}{\epsilon_2} \tag{39.5}$$

The equation is subjected to the following boundary conditions:

$$(a)\quad V(0, y) = V_G + \frac{q}{\epsilon_2}\left(\int_0^d N_D(y)dy - \frac{I_c}{qZv_s}\right)y - \frac{q}{\epsilon_2}\int_0^d\int_0^d N_D(y)dydy$$

$$(b)\quad \frac{\partial V}{\partial x'}(0, d) = \xi_0$$

$$(c)\quad V(x', 0) = V_g$$

$$(d)\quad \frac{\partial V}{\partial y}(x', d) = -\frac{I_c}{qZv_s}$$

Boundary condition (*a*) ensures the continuity of the potential across the interface of the two regions. In the low field region, $x \leq L_1$, it is assumed that in the depletion region the x component of the electric field is a slow-varying function and hence $\partial^2 V/\partial x^2 \approx 0$, giving condition (*a*). One needs to assume that $\xi = \xi_0$ at condition (*b*) for the 2DEG channel. The electron drift velocity at $x' = 0$ is v_S and ξ_0 is infinite. However, it is physically not possible. For practical purpose, it is assumed that ξ_0 is the electric field at which the electron velocity v reaches the value $0.99v_S$ in the high-field region. For condition (*c*), the metal gate is treated as an equipotential plane. Condition (*d*) shows that *y*-component of the electric field is discontinuous at the hetero-interface due to 2DEG.

39.2.2 Fabrication Procedure

The main steps involved in the process flow of fabricating the AlGaN/GaN HEMTs are sample cleaning and preparation, photolithography (ohmic and gate), metallization (ohmic and gate metals), ohmic contacts annealing, dielectric deposition (for the MOS-HEM), and dry etching of dielectric.

The 4-in. AlGaN/GaN on Si substrate epi-layers wafer used in this study was grown by NTT-AT Corporation. The parameters of wafer are following: sheet resistance is 300–400 Ω/sq. 2; sheet carrier density is about 10^{13} cm^{-2}; electron mobility is ~2000 cm^2/V s; and breakdown voltage is ~1000 V.

The MASK's set for photolithography is designed by using CleWin 4 software and manufactured by the Formosa Microsemi Co., LTD.

The fabrication processes of conventional HEMT started with the mesa isolation etching in the ICP chamber. We used a RIE power of 400 W and an ICP power of 250 W. These values have been chosen in view that mesa structures require an etching depth of at least 1.2 μm so as to prevent leakage current between adjacent devices. Hence, a high RIE power of 400 W has been chosen as it produces ions with higher energy for bombardment so as to achieve a higher etch rate. The gas mixture used in the etching was Cl_2/Ar (20/5 sccm) and the HEMT epi-layer structure was etched for 6 min. An average etch depth of 1.3 μm was attained. Ohmic contacts were then formed using e-beam evaporation with Ti/Al/Pd/Au (20 nm/200 nm/60 nm/100 nm) metallization scheme. This was followed by rapid thermal annealing at 650 °C for 1 min. Prior to the metal evaporation, the samples were subjected to an etching procedure down to a depth of approximately 17–20 nm from the surface where the *n*-doped AlGaN donor layer is located. Gate contacts of Pd/Au (50 nm/150 nm) were patterned using optical lithography. The gate length was 2 μm and the width was 100 μm. The drain-source separation was about 4 μm and the gate-drain distance was about 1 μm.

39.3 Results and Discussion

39.3.1 Comparing Simulation and Experiment Results of Conventional HEMT

Figure 39.3 indicates $I_{ds} - V_{ds}$ of the fabricated conventional AlGaN/GaN HEMT and compares it with simulation data, corresponding to different V_g. The obtained value of saturation current is about 79.5 mA (corresponding to 795 mA/mm) at a gate bias of $V_g = 2$ V, and the $I_d - V_d$ characteristic curve has a knee voltage of about 6 V. This indicates the processing procedures developed in the formation of good ohmic and Schottky contact, as described in the previous sections, have enabled the successful fabrication of the AlGaN/GaN HEMT.

The pinch-off voltage determines from intersection of I_{dsat} and $I_{ds} - V_{ds}$ curves, which correspond to different gate voltage and the value of pinch-off voltage, as shown the parabolic-like orange curve in Fig. 39.3.

The obtained simulation value of $V_{pinch\text{-}off}$ at $V_g = 2$ V has not big difference when compare to the experimental value, $V_{pinch\text{-}off\ experiment} \sim 5$ V. As we can see from Fig. 39.3, the data obtained from $I_{ds} - V_{ds}$ curves using our model are in excellent agreement with the data obtained from experiment.

Figure 39.4 shows transconductance, G_m, and saturation current, I_d, depends on gate voltage, V_g (at drain voltage of 10 V), of conventional AlGaN/GaN HEMT with 5 μm channel length and 2 μm gate length. From the graph, the peak transconductance is found to be approximately 165 mS/mm. Our model can simulate the upward region of G_m curve and the value of G_m from simulation data also reaches peak at about ~160 mS/mm.

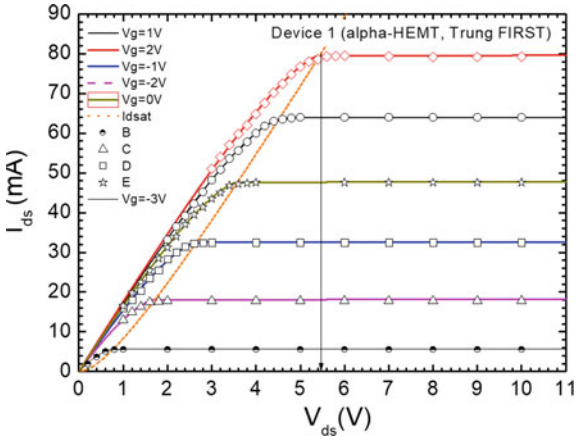

Fig. 39.3 $I_d - V_d$ characteristic of conventional AlGaN/GaN HEMT in comparison with simulation; solid line—this model, open symbols—experimental data

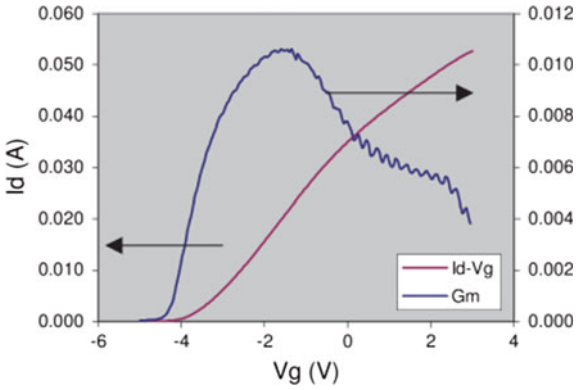

Fig. 39.4 Transconductance and saturation current depend on gate voltage (at drain voltage of 10 V) of conventional AlGaN/GaN HEMT with 5 μm channel length and 2 μm gate length

39.3.2 Comparing Simulation and Experiment Results of MOS-HEMT with Long Channel

We also compared results obtained from our model with Hasan's experimental devices. Simulated MOS-HEMT devices is traditional $Al_mGa_{1-m}N$/GaN device with Al mol concentration $m = 0.2$ mol with oxide layer SiO_2 below gate. Width and length of gate also was chosen with the same size as Hasan device for comparing easily, gate length and width are $L_g = 40$ μm, $W_g = 153$ μm, respectively, and thickness of oxide layer is $t_{ox} = 10$ nm. Moreover, to unified with Hasan research, chosen electron mobility is 2200 cm^2/V s.

Figure 39.5 shows $I_{ds} - V_{ds}$ curves calculated from MOS-HEMT simulation and compares them with Hasan et al. experiment data, corresponding to different V_g. We can see that I_{ds} reaches the maximum value of 33 mA/mm at $V_g = 0$ V. This is sensible with results obtained from Hasan report [6]. The open symbols are the

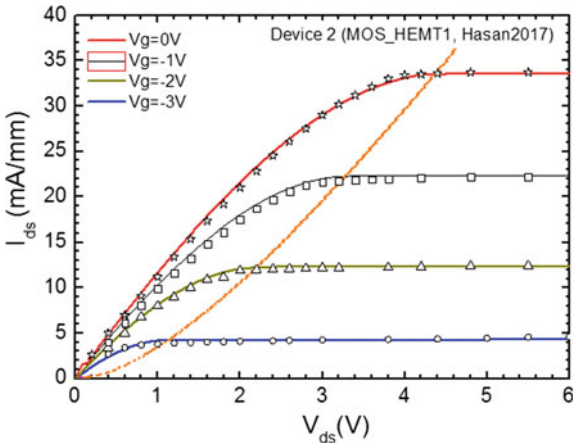

Fig. 39.5 $I_d - V_d$ characteristics of MOS HEMT in comparison with simulation: solid line—simulation; open symbol—experimental data of [6]

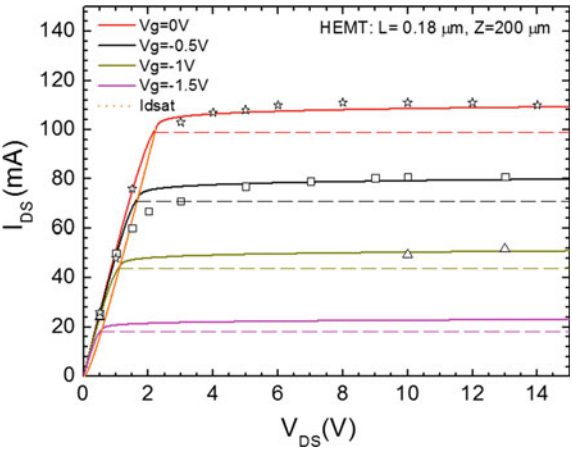

Fig. 39.6 $I_d - V_d$ characteristics of Yoon's MOS HEMT in comparison with simulation: solid line—simulation; open symbol—experimental data of [6]

experimental data; the solid lines represent the calculated curves. As we can see from this figure, the curves using the extended model are in excellent agreement with the experimental data, so our model is good for simulate MOS-HEMT with long channel.

39.3.3 Comparing Simulation and Experiment Results of HEMT with Short Channel

In this section, we compare simulation results obtained from our model and data from Yoon's experimental research with short-channel HEMT.

Transistor model used to simulate is an $Al_mGa_{1-m}N/GaN$ device with Al mol concentration, $m = 0.25$ with a 20 nm $Al_{0.25}Ga_{0.75}N$ layer above a 2 μm GaN layer and no oxide layer. Metal gate has width, $W_g = 200$ μm and length, $L_g = 0.18$ μm.

Figure 39.6 shows the simulation $I_{ds} - V_{ds}$ characteristic curves and experimental results of Yoon-HEMT with short channel, corresponding to changing gate voltage, $V_g = -1, -0.5$ and 0 V. We note that, all given experimental values relatively close to the simulation results. Moreover, the value of saturation drain current from simulation data at $V_g = 0$ V is 112 mA. This is sensible with results obtained from Yoon's report [6].

A comparison between simulated from our model and measured $I_d - V_d$ characteristic of short-channel HEMT from Yoon's research, proves that our model is not only good fit for HEMT with long channel but also could be used for HEMT with short channel and the MOS-HEMT.

39.4 Conclusion

Due to its excellent material properties, GaN-based technology is set to become the dominant semiconductor in high-power and high-speed electronics. In conclusion, this research has been successful in building a suitable model to simulate common HEMT and MOS-HEMT. The data obtained from simulation methods are compared with result from Hasan's long channel, Yoon's short channel and our experiment designed HEMT. This comparison of the simulations and measured $I_d - V_d$ characteristics proves the exactness and correctness of our analytical model.

So, we can use this model to estimate and consider HEMT performances with different input parameters. This allows us to design a MOS-HEMT structure for manufacturing products to get better HEMTs for high power applications.

Acknowledgements This research was supported by Vietnam Ministry of Science and Technology and World Bank through Project "Fostering Innovation through Research, Science and Technology (FIRST), Grants No 01/FIRST/1.a/HUST. We gratefully acknowledge Prof. Chua Soo Jin (Department of Electrical and Computer Engineering, National University of Singapore) for the Project cooperation.

References

1. C.-S. Chang, H. I. Fetterman, Solid-State Electron. **30**(5) (1987)
2. C.-S. Chang, H. I. Fetterman, IEEE Trans. Electron Dev. **Ed-34**(I) (1987)
3. E.A. Jones, F. Wang, D. Costinett, IEEE J. Emerg. Sel. Top. Power Electron. (JESTPE-2016-01-0036.R1). https://doi.org/10.1109/jestpe.2016.2582685
4. S. Taking, *AlN/GaN MOS-HEMTs Technology*. A thesis submitted in fullfillment for the degree of Doctor of Philosophy (2012)
5. M.R. Hasan, A. Motayed, M.S. Fahad, M.V. Rao, J. Vac. Sci. Technol. **B35**, 052202 (2017)
6. H.S. Yoon, B.-G. Min, J.M. Lee, D.M. Kang, H.K. Ahn, K.-J. Cho, J.-W. Do, M.J. Shin, H.-W. Jung, S.I. Kim, H.C. Kim, J.W. Lim, J. Korean Phys. Soc. **17**(6), 360–364 (2017)

Chapter 40
Structural Scheme of Electroelastic Actuator for Nanomechatronics

Sergey M. Afonin

Abstract Structural scheme of the electroelastic actuator for nanomechatronics and its transfer functions was obtained. Changes in the elastic compliance and stiffness of the piezoactuator, accounting for the type of control, were found. The transfer functions of the piezoactuator for nanomechatronics with transverse, longitudinal, and shear piezoeffects and voltage or current control were also obtained. Electroelastic actuator based on electroelasticity with piezoelectric or electrostriction effects is used for nanomechatronics. The structural scheme of the piezoactuator obtained in this work reflects the transformation of electrical energy into mechanical energy, in contrast to Cady's and Mason's electrical equivalent circuits of piezotransducer. The study explains the direct piezoeffect on the acting voltage of the piezoactuator. Changes in elastic compliance due to the direct piezoeffect determine the structural scheme of the piezoactuator with feedback for nanomechatronics systems. For the structural scheme, we considered the inverse piezoeffect, the elastic flexibility of the variables, the stiffness of piezoactuator, the direct piezoeffects, and the counter electromotive force, depending on the speed of the movement of the piezoactuator face. To construct the structural scheme of the piezoactuator, we solved the inverse piezoeffect equation and the wave equation under appropriate boundary conditions for calculating the parameters of the nanomechatronics system with piezoactuator. Due to the reaction of the piezoactuator and considering the direct piezoeffect, the elastic compliance and rigidity of the piezoactuator are changed. The structural scheme of the piezoactuator is obtained, considering the inverse piezoelectric effect and the back electromotive force due to the direct piezoelectric effect. The transfer functions of the piezoactuators for nanomechatronics with the transverse, longitudinal, shear, generalized piezoeffects and with both voltage and current controls are obtained.

S. M. Afonin (✉)
Institute of Microdevices and Control Systems, National Research University of Electronic Technology (MIET), Moscow, Russia
e-mail: eduems@mail.ru

I. A. Parinov et al. (eds.), *Advanced Materials*, Springer Proceedings in Materials 6, https://doi.org/10.1007/978-3-030-45120-2_40

40.1 Introduction

Electroelastic actuators with piezoelectric or electrostriction effects are used in the nanomechatronics systems in nanotechnology, nanobiology, adaptive optics, microelectronics, and power engineering. The piezoactuators, based on the piezoelectric effect, are often used for nano- and microdisplacement in nanotechnology, microelectronics, nanobiology, energy, and astronomy. The piezoactuator is piezo mechanical device designed to actuate or control mechanisms and systems using the piezoelectric effect and to convert electrical energy into mechanical energy [1–9]. A cell structure combined with the piezoactuator is used in nanomechatronics systems. The nanometric accuracy of nano-mechatronic systems is provided by the piezoactuator. In nanotechnology, photonics, and adaptive optics, these piezoactuators are used for aligning the mirrors of laser ring gyroscopes, for combining and scanning in atomic-force microscopes, and in laser systems [10–23]. The structural scheme of the piezoactuator represents the system of Laplace transformation equations for the displacement of its ends due to the inverse piezoeffect, which, accounting for the electromechanical parameters of the piezoactuator, describes its structure, the conversion of electrical field energy into mechanical energy, the displacements and forces corresponding to the ends of the piezoactuator, and the appearance of the counter electromotive force due to the direct piezoelectric effect.

At this work, we obtained structural scheme of the piezoactuator obtained clearly and visually reflects the transformation of electrical energy into mechanical energy, in contrast to Cady's and Mason's electrical equivalent circuits of the piezotransducer [2, 3]. To construct the structural scheme of the piezoactuator, we solved the inverse piezoeffect equation and the wave equation under appropriate boundary conditions for calculating the parameters of the nanomechatronics system with the piezoactuator. Due to the reaction of the piezoactuator and considering the direct piezoeffect, the elastic compliance and rigidity of the piezoactuator are changed. The speed movement of the end the piezoactuator, considering the direct piezoeffect, affects the current through the piezoactuator and on the actual voltage on a piezoelectric actuator. The structural scheme of the piezoactuator is obtained, considering the inverse piezoelectric effect and the back electromotive force due to the direct piezoelectric effect. The elastic compliance and the stiffness of the piezoactuator are found for the transverse, longitudinal, shear, generalized piezoelectric effects and for the types of the voltage or current controls. The transfer functions of the piezoactuators for nanomechatronics with the transverse, longitudinal, shear piezoeffects and with voltage or current controls are obtained. The effects of the geometric and physical parameters of the electroelastic actuator and external load on its dynamic characteristics are determined. To calculate nanomechatronics systems with electroelastic actuator, its structural scheme and matrix transfer function are obtained.

We solve the inverse piezoeffect equation and the wave equation under appropriate boundary conditions for calculating the parameters of the nanomechatronics system with the piezoactuator. Due to the reaction of the piezoactuator and accounting for the direct piezoeffect, the elastic compliance and rigidity of the piezoactuator, which,

along with the piezomodule, are the main parameters of the piezoactuator, change depending on whether the control is by voltage or by current. The high-speed movement of the end of the piezoactuator, accounting for the direct piezoeffect, affects the current through the piezoactuator and on the actual voltage on the piezoactuator.

40.1.1 Research Purpose

The purpose of this paper is calculation of structural scheme of the electroelastic actuator for nanomechatronics.

40.1.2 Research Scope

At this work, we consider the following frameworks of the problem:

(i) Deformation of the electroelastic actuator for nanomechatronics;
(ii) Applied theory of the structural schemes of the electroelastic actuator for nanomechatronics;
(iii) Calculation of the structural-parametric model for the electroelastic actuator;
(iv) Determination of the transfer function for the electroelastic actuator;
(v) Numerical and analytical calculation of the static and dynamic characteristics of the piezoactuator.

40.2 Research Method

The method of mathematical physics is used to solve the wave equation with the Laplace transform to obtain the structural scheme and the structural-parametric model of the electroelastic actuator for nanomechatronics.

The problem of obtaining the structural scheme of the piezoactuator is solved using the method of mathematical physics. The solution of the wave equation is found, taking into account the boundary conditions. Using the Laplace transform, the problem of the wave equation with partial derivatives of the hyperbolic type is reduced to linear ordinary differential equation. The transfer functions of the piezoactuator are determined from its structural scheme. The structural scheme of the piezoactuator obtained in this work clearly reflects the transformation of electrical energy into mechanical energy, in contrast to the electrical equivalent circuit of the piezotransducer or the piezovibrator [2, 3]. The study accounts for the direct piezoeffect on the acting voltage on the piezoactuator. Changes in elastic compliance due to the direct piezoeffect determine the structural scheme of the piezoactuator with feedback for nanomechatronics. The paper presents the following options for constructing the

structural scheme of the piezoactuator: taking into account the reverse piezoeffect and constant elastic flexibility and stiffness of the piezoactuator; taking into account the inverse and direct piezoeffects and the variables of elastic flexibility and stiffness of the piezoactuator; taking into account the inverse and direct piezoeffects, the variables of elastic elasticity and stiffness of the piezoactuator, and the influence of the counter electromotive force, depending on the speed of the movement of piezoactuator end.

Consider the deformation of the piezoactuator for nanomechatronics, which corresponds to its stress state. If an electric field is created in the piezoactuator, then deformation and mechanical stress will occur. Accordingly, if mechanical stress is created in the piezoactuator, electric induction and electric charge will occur on the plates of the piezoactuator. The electroelasticity equations of the piezoactuator, in general form for the inverse and direct piezoeffects [3, 5, 6, 8, 10] have the form;

$$S_i = d_{mi} E_m + s_{ij}^E T_j, \tag{40.1}$$

$$D_m = d_{mi} T_i + \varepsilon_{mk}^E E_k, \tag{40.2}$$

where $i, \ j = 1, \ 2, \ldots, 6, \ m, \ k = 1, \ 2, \ 3$ are the indexes; $l = (\delta, h, b)$ are the working lengths of the piezoactuators with longitudinal, transverse, and shear piezoeffects along axis i; S_i is the relative displacement of the piezoactuator section along axis i; d_{mi} is the piezomodule; $E_m(t) = u(t)/\delta$ is the electric field strength along axis m; $u(t)$ is the voltage on the plates of the piezoactuator; s_{ij}^E is the elastic compliance at $E = \text{const}$; T_j is the mechanical stress along axis j; δ is the thickness of the piezoactuator; $D_m(t)$ is the electric induction along axis m; ε_{mk}^T is the dielectric permittivity at $T = \text{const}$.

From (40.1) in statics, we can obtain the steady-state movement ξ_0 of the piezoactuator for nanomechatronics:

$$\xi_0 = d_{mi}(l/\delta)u_0, \tag{40.3}$$

where u_0 is the voltage amplitude on the plates of the piezoactuator.

The equation of forces acting on the ends of the piezoactuator has the form

$$T S_0 = F + M \frac{\partial^2 \xi(x, t)}{\partial t^2},$$

where F is the external force applied to the piezoactuator and M is the moved mass.

Let us consider deformation of the electroelastic actuator for nanomechatronics. To compile the structural scheme of the piezoactuator for nanomechatronics with voltage control, we will jointly solve the wave equation, the equation for the inverse piezoeffect, and the force equation at its ends. Calculating the piezoactuator for nanomechatronics involves the wave equation, which describes wave propagation in the long line with attenuation and without distortion [3, 5, 7, 9, 16–18, 22]. Using

the Laplace transform, the initial problem for the hyperbolic-type partial differential equation reduces to the simple linear ordinary differential equation [5–9, 17, 18].

Applying the Laplace transform to the wave equation and setting the initial conditions to zero gives the second-order linear ordinary differential equation in the form

$$\frac{\mathrm{d}^2\Xi(x,\,p)}{\mathrm{d}x^2} - \gamma^2\Xi(x,\,p) = 0, \tag{40.4}$$

solution is the function

$$\Xi(x,\,p) = Ce^{-x\gamma} + Be^{x\gamma}, \tag{40.5}$$

where $\Xi(x,\,p)$ is the Laplace transform of the bias of the piezoactuator; x is the coordinate; p is the Laplace operator; $\gamma = p/c^E + \alpha$ is the wave propagation coefficient; c^E is the speed of sound in the piezoactuator at $E = \text{const}$; α is an attenuation coefficient, accounting for the damping of vibrations during wave propagation due to energy dissipation and heat loss.

We denote

$$\begin{aligned}\Xi(0,\,p) &= \Xi_1(p) \quad \text{for } x = 0;\\ \Xi(l,\,p) &= \Xi_2(p) \quad \text{for } x = l.\end{aligned}$$

Therefore, we get the coefficients C and B for solving linear ordinary differential equation in the form

$$C = (\Xi_1 e^{l\gamma} - \Xi_2)/[2\mathrm{sh}(l\gamma)], \quad B = (\Xi_2 - \Xi_1 e^{-l\gamma})/[2\mathrm{sh}(l\gamma)].$$

The solution of the linear ordinary differential equation is

$$\Xi(x,\,p) = \{\Xi_1(p)\mathrm{sh}[(l-x)\gamma] + \Xi_2(p)\mathrm{sh}(x\gamma)/\}\mathrm{sh}(l\gamma).$$

The equations for the forces acting on the ends the piezoactuator for nanomechatronics have the form

$$\begin{aligned}T_j(0,\,p)S_0 &= F_1(p) + M_1p^2\Xi_1(p) \quad \text{for } x = 0;\\ T_j(l,\,p)S_0 &= -F_2(p) - M_2p^2\Xi_2(p) \quad \text{for } x = l.\end{aligned} \tag{40.6}$$

We have the system of equations for mechanical stresses at the ends of the piezoactuator at $x = 0$ and $x = l$ in the form

$$\begin{aligned}T_j(0,\,p) &= \frac{1}{s_{ij}^E}\frac{\mathrm{d}\Xi(x,p)}{\mathrm{d}x}\bigg|_{x=0} - \frac{d_{mi}}{s_{ij}^E}E_m(p);\\ T_j(l,\,p) &= \frac{1}{s_{ij}^E}\frac{\mathrm{d}\Xi(x,p)}{\mathrm{d}x}\bigg|_{x=l} - \frac{d_{mi}}{s_{ij}^E}E_m(p).\end{aligned} \tag{40.7}$$

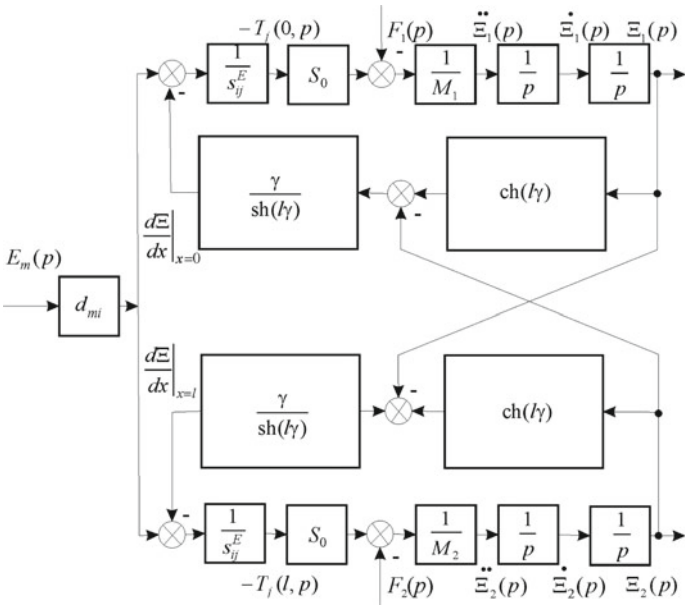

Fig. 40.1 Structural scheme of piezoactuator for nanomechatronics with voltage control at zero source resistance

System (40.7) gives the following system of equations for the structural-parametric model of the piezoactuator for nanomechatronics with voltage control at zero source resistance $R = 0$ and for the structural scheme in Fig. 40.1 of the piezoactuator for nanomechatronics

$$\begin{aligned}
\Xi_1(p) &= [1/(M_1 p^2)]\left\{\begin{array}{l} -F_1(p) + (1/\chi_{ij}^E) \\ \times[d_{mi} E_m(p) - [\gamma/\mathrm{sh}(l\gamma)][\mathrm{ch}(l\gamma)\Xi_1(p) - \Xi_2(p)]] \end{array}\right\}; \\
\Xi_2(p) &= [1/(M_2 p^2)]\left\{\begin{array}{l} -F_2(p) + (1/\chi_{ij}^E) \\ \times[d_{mi} E_m(p) - [\gamma/\mathrm{sh}(l\gamma)][\mathrm{ch}(l\gamma)\Xi_2(p) - \Xi_1(p)]] \end{array}\right\},
\end{aligned} \tag{40.8}$$

where $\chi_{ij}^E = s_{ij}^E / S_0$.

From the transformations, we obtain the system of equations of the structural-parametric model of the piezoactuator for nanomechatronics with voltage control:

$$\begin{aligned}\Xi_1(p) &= \left[1/\left(M_1 p^2\right)\right]\left\{\begin{array}{l}-F_1(p)+\left(1/\chi_{ij}^E\right)\\ \times\left[d_{mi}E_m(p)-\gamma\Xi_1(p)/\mathrm{th}(l\gamma)+\gamma\Xi_2(p)/\mathrm{sh}(l\gamma)\right]\end{array}\right\};\\ \Xi_2(p) &= \left[1/\left(M_2 p^2\right)\right]\left\{\begin{array}{l}-F_2(p)+\left(1/\chi_{ij}^E\right)\\ \times\left[d_{mi}E_m(p)-\gamma\Xi_2(p)/\mathrm{th}(l\gamma)+\gamma\Xi_1(p)/\mathrm{sh}(l\gamma)\right]\end{array}\right\}.\end{aligned} \tag{40.9}$$

Equation (40.8) for the structural-parametric model of the piezoactuator for nanomechatronics with voltage control convert to

$$\begin{aligned}\Xi_1(p) &= [1/(M_1 p^2)]\left\{\begin{array}{l}-F_1(p)+C_{ij}^E l\\ \times[d_{mi}E_m(p)-[\gamma/\mathrm{sh}(l\gamma)][\mathrm{ch}(l\gamma)\Xi_1(p)-\Xi_2(p)]]\end{array}\right\};\\ \Xi_2(p) &= [1/(M_2 p^2)]\left\{\begin{array}{l}-F_2(p)+C_{ij}^E l\\ \times[d_{mi}E_m(p)-[\gamma/\mathrm{sh}(l\gamma)][\mathrm{ch}(l\gamma)\Xi_2(p)-\Xi_1(p)]]\end{array}\right\},\end{aligned} \tag{40.10}$$

where $C_{ij}^E = S_0/(s_{ij}^E l) = 1/(\chi_{ij}^E l)$ is the stiffness of the piezoactuator with voltage control.

The structural-parametric model of the piezoactuator for nanomechatronics makes it possible to obtain its transfer functions. The joint solution of (40.10) for displacing two faces of the piezoactuator with voltage control gives the system

$$\begin{aligned}\Xi_1(p) &= W_{11}(p)E_m(p)+W_{12}(p)F_1(p)+W_{13}(p)F_2(p);\\ \Xi_2(p) &= W_{21}(p)E_m(p)+W_{22}(p)F_1(p)+W_{23}(p)F_2(p),\end{aligned} \tag{40.11}$$

and the matrix equation in the form

$$\begin{pmatrix}\Xi_1(p)\\ \Xi_2(p)\end{pmatrix} = \begin{pmatrix}W_{11}(p) & W_{12}(p) & W_{13}(p)\\ W_{21}(p) & W_{22}(p) & W_{23}(p)\end{pmatrix}\begin{pmatrix}E_m(p)\\ F_1(p)\\ F_2(p)\end{pmatrix}, \tag{40.12}$$

where the transfer functions are

$$\begin{aligned}W_{11}(p) &= \Xi_1(p)/E_m(p) = d_{mi}\left[M_2\chi_{ij}^E p^2+\gamma th(l\gamma/2)\right]/A_{ij};\ \chi_{ij}^E = s_{ij}^E/S_0;\\ A_{ij} &= M_1M_2\left(\chi_{ij}^E\right)^2p^4+\left\{(M_1+M_2)\chi_{ij}^E/\left[c^E\mathrm{th}(l\gamma)\right]\right\}p^3\\ &\quad+\left[(M_1+M_2)\chi_{ij}^E\alpha/th(l\gamma)+1/\left(c^E\right)^2\right]p^2+2\alpha p/c^E+\alpha^2\\ W_{21}(p) &= \Xi_2(p)/E_m(p) = d_{mi}\left[M_1\chi_{ij}^E p^2+\gamma th(l\gamma/2)\right]/A_{ij};\\ W_{12}(p) &= \Xi_1(p)/F_1(p) = -\chi_{ij}^E\left[M_2\chi_{ij}^E p^2+\gamma/th(l\gamma)\right]/A_{ij};\\ W_{13}(p) &= \Xi_1(p)/F_2(p);\\ W_{22}(p) &= \Xi_2(p)/F_1(p) = \left[\chi_{ij}^E\gamma/sh(l\gamma)\right]/A_{ij};\end{aligned}$$

$$W_{23}(p) = \Xi_2(p)/F_2(p) = -\chi_{ij}^E\left[M_1\chi_{ij}^E p^2 + \gamma/th(l\gamma)\right]/A_{ij}.$$

Equation (40.12) for voltage control at zero source resistance $R = 0$ gives the transfer function of the piezoactuator for the transverse piezoelectric effect, with resonance conditions at $M_1 = 0$ and $M_2 = 0$, in the form

$$\mathrm{tg}(kh/2) = \infty, \tag{40.13}$$

where $k = \omega/c^E$ is frequency coefficient; ω is circular frequency.

This is because

$$k_i h = \pi(2i - 1), \tag{40.14}$$

where index $i = 1,\ 2,\ 3, \ldots$.

Therefore, for $i = 1$, the piezoactuator is the half-wave vibrator with resonance frequency

$$f_1 = c^E/(2h). \tag{40.15}$$

For the piezoactuator from piezoceramics PZT under the transverse piezoeffect at $c^E = 3 \times 10^3$ m/s and $h = 2.5 \times 10^{-2}$ m, the resonance frequency is $f_1 = 60$ kHz.

Consider the influence of the reaction of the piezoactuator for nanomechatronics due to the creation of an anti-electromotive force by the piezoactuator due to the direct piezoeffect during its static deformation.

The maximum force $F_{\max}$ and mechanical stress $T_{j\max}$ developed by the piezoactuator with the inverse piezoelectric effect when powered from the voltage source are

$$F_{\max} = \frac{U}{\delta} d_{mi} \frac{S_0}{s_{ij}^E}, \quad \frac{F_{\max}}{S_0} s_{ij}^E = E_m d_{mi}, \quad T_{j\max} s_{ij}^E = E_m d_{mi}. \tag{40.16}$$

Consequently,

$$T_{j\max} = E_m d_{mi}/s_{ij}^E, \quad F_{\max} = E_m d_{mi} S_0/s_{ij}^E. \tag{40.17}$$

We estimate the maximum force $F_{\max}$ and the maximum mechanical stress $T_{j\max}$ developed by the piezoactuator for nanomechatronics when powered from the current source.

Let us consider static characteristic piezoactuator with one fixed for the longitudinal piezoeffect with the voltage control. We have in Fig. 40.2 maximum displacement ξ_{2m} for $F_2 = 0$ and maximum force F_{2m} for $\xi_2 = 0$ in the form

$$\xi_{2m} = d_{33} U_m, \tag{40.18}$$

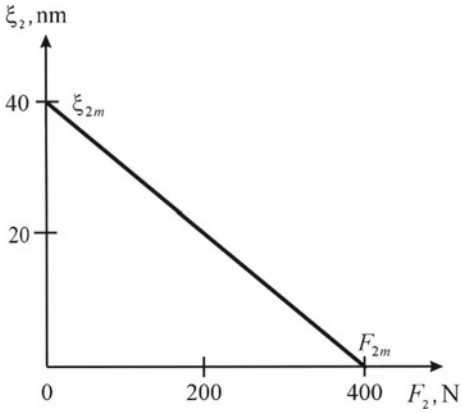

Fig. 40.2 Static characteristic piezoactuator for longitudinal piezoeffect

$$F_{2m} = \frac{d_{33} U_m S_0}{s_{33}^E \delta}. \tag{40.19}$$

For the voltage-controlled piezoactuator for nanomechatronics at the longitudinal piezoeffect from piezoceramics PZT with one fixed face at zero source resistance $R = 0$ for $d_{33} = 4 \times 10^{-10}$ m/V, $\delta = 6 \times 10^{-4}$ m, $S_0 = 1.8 \times 10^{-4}$ m^2, $s_{33}^E = 3 \times 10^{-11}$ m^2/N, $U_m = 100$ V we obtain in Fig. 40.2 values of maximum displacement $\xi_{2m} = 40$ nm, maximum force $F_{2m} = 400$ N. The measurements were made on UMM-5 press. The discrepancy between the experimental data and the calculation results is 5%.

We consider the direct piezoeffect, accounting for the positive force feedback due to the direct piezoeffect, for the maximum force in the following form

$$F_{\max} = \frac{U}{\delta} d_{mi} \frac{S_0}{s_{ij}^E} + \frac{F_{\max}}{S_0} d_{mi} S_p \frac{1}{\varepsilon_{mk}^T S_p / \delta} \frac{1}{\delta} d_{mi} \frac{S_0}{s_{ij}^E}, \tag{40.20}$$

from which

$$\frac{F_{\max}}{S_0} s_{ij}^E \left(1 - \frac{d_{mi}^2}{\varepsilon_{mk}^T s_{ij}^E}\right) = E_m d_{mi} \tag{40.21}$$

we have

$$T_{j\max}(1 - k_{mi}^2) s_{ij}^E = E_m d_{mi}, \; k_{mi} = d_{mi} / \sqrt{s_{ij}^E \varepsilon_{mk}^T} \tag{40.22}$$

where k_{mi} is the electromechanical coupling coefficient.

Consequently,

$$T_{j\max} s_{ij}^D = E_m d_{mi}; \tag{40.23}$$

$$s_{ij}^D = (1 - k_{mi}^2)s_{ij}^E = k_s s_{ij}^E, \quad k_s = 1 - k_{mi}^2 = s_{ij}^D / s_{ij}^E, \quad k_s > 0,$$

where k_s is the coefficient of the change of elastic compliance.

Moreover, we have

$$F_{\max} = E_m d_{mi} S_0 / (s_{ij}^E k_s) = E_m d_{mi} S_0 / s_{ij}^D. \tag{40.24}$$

Consequently,

$$T_{j\max} = E_m d_{mi} / s_{ij}^D. \tag{40.25}$$

The elastic compliance s_{ij} of the piezoactuator takes the form $s_{ij}^E > s_{ij} > s_{ij}^D$, where $s_{ij}^E / s_{ij}^D \le 1.2$. $C_{ij}^E = S_0 (s_{ij}^E l)$ is the stiffness of the piezoactuator with voltage control and $C_{ij}^D = S_0 / (s_{ij}^D l)$ is the stiffness of the piezoactuator with current control. Consequently, $C_{ij}^E < C_{ij} < C_{ij}^D$, $C_{ij} = S_0 / (s_{ij} l)$ is the stiffness of the piezoactuator. When the electrodes are open, the stiffness of the piezoactuator increases when compared with closed electrodes. Increasing the resistance of the power supply and matching circuits decreases the elastic compliance and increases the rigidity of the piezoactuator. When controlling the piezoactuator from the power source with finite source resistance and accounting for positive force feedback due to the direct piezoeffect, we get the maximum force of the piezoactuator as

$$F_{\max} = \frac{U}{\delta} d_{mi} \frac{S_0}{s_{ij}^E} + \frac{F_{\max}}{S_0} d_{mi} S_p \frac{1}{\varepsilon_{mk}^T S_p / \delta} k_u \frac{1}{\delta} d_{mi} \frac{S_0}{s_{ij}^E}, \tag{40.26}$$

which gives

$$\begin{aligned} &\frac{F_{\max}}{S_0} s_{ij}^E \left(1 - \frac{d_{mi}^2 k_u}{\varepsilon_{mk}^T s_{ij}^E}\right) = E_m d_{mi}, \quad k_{mi} = d_{mi} / \sqrt{s_{ij}^E \varepsilon_{mk}^T}; \\ &T_{j\max} \left(1 - k_{mi}^2 k_u\right) s_{ij}^E = E_m d_{mi}, \quad 0 \le k_u \le 1, \end{aligned} \tag{40.27}$$

where k_u is the coefficient of control from the electric power source.

When controlling the piezoactuator from the current source, we have $k_u|_{R\to\infty} = 1$; when controlling the piezoactuator from the voltage source, we have $k_u|_{R\to 0} = 0$; with elastic compliance, we have

$$\begin{aligned} &s_{ij} = (1 - k_{mi}^2 k_u) s_{ij}^E = k_s s_{ij}^E, \quad k_s = 1 - k_{mi}^2 k_u, \quad k_s > 0, \\ &(1 - k_{mi}^2)|_{R\to\infty} \le k_s \le 1|_{R\to 0}, \quad k_s|_{R\to\infty} = 1 - k_{mi}^2, \quad k_s|_{R\to 0} = 1, \end{aligned} \tag{40.28}$$

where k_s is the coefficient of change of the elastic compliance.

Controlling the piezoactuator from the power source with the finite source resistance gives expressions for positive force feedback in Fig. 40.3 in the structural-

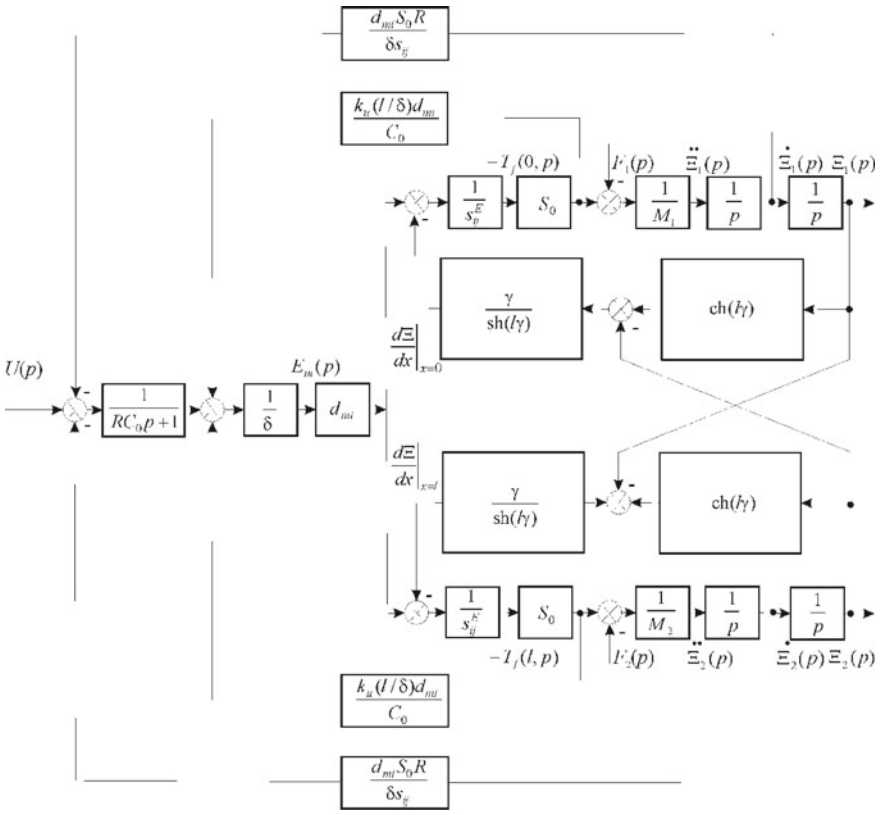

Fig. 40.3 Structural scheme of electroelastic actuator for nanomechatronics with voltage control and finite source resistance

parametric model of piezoactuator for nanomechatronics

$$U_{F\alpha}(p) = \frac{k_u(l/\delta)d_{mi}}{C_0} F_\alpha(p), \quad \alpha = 1,\ 2. \tag{40.29}$$

For controlling current from the source with infinitely large resistance gives $k_u|_{R\to\infty} = 1$.

After transformations, we obtain the structural-parametric model of the piezoactuator for nanomechatronics with the current control and its transfer functions.

Therefore, the system of equations for the structural-parametric model and the structural scheme of the electroelastic actuator for nanomechatronics in Fig. 40.3 have the form

$$\Xi_1(p) = [1/(M_1 p^2)]\left\{\begin{array}{l} -F_1(p) + (1/\chi_{ij}^{\Psi}) \\ \times\left[d_{mi}\Psi_m(p) - [\gamma/\mathrm{sh}(l\gamma)][\mathrm{ch}(l\gamma)\Xi_1(p) - \Xi_2(p)]\right] \end{array}\right\}; \tag{40.30}$$

$$\Xi_2(p) = [1/(M_2 p^2)]\left\{\begin{array}{l} -F_2(p) + (1/\chi_{ij}^{\Psi}) \\ \times\left[d_{mi}\Psi_m(p) - [\gamma/\mathrm{sh}(l\gamma)][\mathrm{ch}(l\gamma)\Xi_2(p) - \Xi_1(p)]\right] \end{array}\right\},$$

where $\chi_{ij}^{\Psi} = s_{ij}^{\Psi}/S_0$, $v_{mi} = \left\{\begin{array}{l} d_{33}, d_{31}, d_{15} \\ g_{33}, g_{31}, g_{15} \end{array}\right.$, $\Psi_m = \left\{\begin{array}{l} E_3, E_1 \\ D_3, D \end{array}\right.$, $s_{ij}^{\Psi} = \left\{\begin{array}{l} s_{33}^{E}, s_{11}^{E}, s_{55}^{E} \\ s_{33}^{D}, s_{11}^{D}, s_{55}^{D} \end{array}\right.$,
$\gamma = \left\{\begin{array}{l} \gamma^E \\ \gamma^D \end{array}\right.$, $c^{\Psi} = \left\{\begin{array}{l} c^E \\ c^D \end{array}\right.$.

To account for the effect of the velocity of the ends of the piezoactuator in Fig. 40.3 due to the appearance of the counter electromotive force from the direct piezoeffect, the structural scheme of the piezoactuator is supplemented with negative feedback

$$U_{\dot{\Xi}\alpha}(p) = \frac{d_{mi} S_0 R}{\delta s_{ij}} \dot{\Xi}_{\alpha}(p), \ \alpha = 1, \ 2. \tag{40.31}$$

40.3 Results and Discussion

The structural-parametric model and the structural scheme of the piezoactuator for nanomechatronics with feedback of the piezoactuator reflect the conversion of the electrical energy into the mechanical energy. The structural-parametric model and structural scheme change depending on whether the piezoactuator is controlled by voltage or current.

We constructed the structural scheme and the matrix transfer function of the electroelastic actuator. We obtained the matrix transfer function of the electroelastic actuator [8, 18] from the structural-parametric model (40.30) in the form

$$\begin{aligned} &(\Xi(p)) = (W(p))\ (P(p)), \\ &(\Xi(p)) = \begin{pmatrix} \Xi_1(p) \\ \Xi_2(p) \end{pmatrix}, \quad (W(p)) = \begin{pmatrix} W_{11}(p) & W_{12}(p) & W_{13}(p) \\ W_{21}(p) & W_{22}(p) & W_{23}(p) \end{pmatrix}, \\ &(P(p)) = \begin{pmatrix} \Psi_m(p) \\ F_1(p) \\ F_2(p) \end{pmatrix}, \end{aligned} \tag{40.32}$$

where $(\Xi(p))$, $(W(p))$, $(P(p))$ are the matrices of Laplace transforms of the displacements for the faces, the transfer functions, the control parameters.

We find the displacement of both faces of the electroelastic actuator in the static regime for $\Psi_m(t) = \Psi_{m0} \cdot 1(t)$, $F_1(t) = F_2(t) = 0$ at the inertia load. From (40.32) the static displacements of both faces of the actuator at $m \ll M_1$ and $m \ll M_2$ and the inertial load are respectively

$$\xi_1(\infty) = \lim_{t\to\infty} \xi_1(t) = \nu_{mi} l \Psi_{m0} M_2/(M_1 + M_2), \tag{40.33}$$

$$\xi_2(\infty) = \lim_{t\to\infty} \xi_2(t) = \nu_{mi} l \Psi_{m0} M_1/(M_1 + M_2), \tag{40.34}$$

$$\xi_1(\infty) + \xi_2(\infty) = \lim_{t\to\infty} (\xi_1(t) + \xi_2(t)) = \nu_{mi} l \Psi_{m0}, \tag{40.35}$$

where m is the mass of the piezoactuator; M_1, M_2 are the load masses.

The static displacements of both faces of the piezoactuator for the longitudinal piezoeffect and the inertial load at $m \ll M_1$ and $m \ll M_2$ are respectively

$$\xi_1(\infty) = d_{33} U_0/(M_1 + M_2), \tag{40.36}$$

$$\xi_2(\infty) = d_{33} U_0 M_1/(M_1 + M_2). \tag{40.37}$$

We have the static characteristics of the piezoactuator from piezoceramics PZT for the longitudinal piezoeffect at $m \ll M_1$ and $m \ll M_2$. At $d_{33} = 4 \times 10^{-10}$m/V, $U_0 = 250$ V, $M_1 = 1$ kg, and $M_2 = 4$ kg, we obtain the static displacements of both faces of the piezoactuator as $\xi_1(\infty) = 80$ nm, $\xi_2(\infty) = 20$ mm, and $\xi_1(\infty) + \xi_2(\infty) = 100$ nm.

Consider the structural schemes of the piezoactuator with distributed and lumped parameters at one fixed face with elastic-inertial load, controlled by voltage with finite source resistance. From (40.29)–(40.31) for the piezoactuator with one rigidly fixed face at elastic-inertial load for $M_1 \to \infty$ we obtain structural scheme in Fig. 40.4 with distributed parameters.

After the structural transformations of the initial structural scheme seen in Fig. 40.4a we obtain the transformed structural scheme seen in Fig. 40.4b with elastic compliance $s_{ij} = (1 - k_{mi}^2 k_u) s_{ij}^E$. With replacing the hyperbolic cotangent on two members of the power series and using the structural scheme in Fig. 40.4b we have coefficient k_d of the direct piezoeffect and coefficient k_r of the reverse piezoeffect of the piezoactuator in the form

$$k_d = k_r = \frac{d_{mi} S_0}{\delta s_{ij}}. \tag{40.38}$$

We get the structural scheme of the piezoactuator with concentrated parameters for one rigidly fixed face under elastic-inertial load with $M_1 \to \infty$, as seen in Fig. 40.5.

For the structural scheme of the piezoactuator in Fig. 40.5 at $R = 0$, we define the following expression for its transfer function

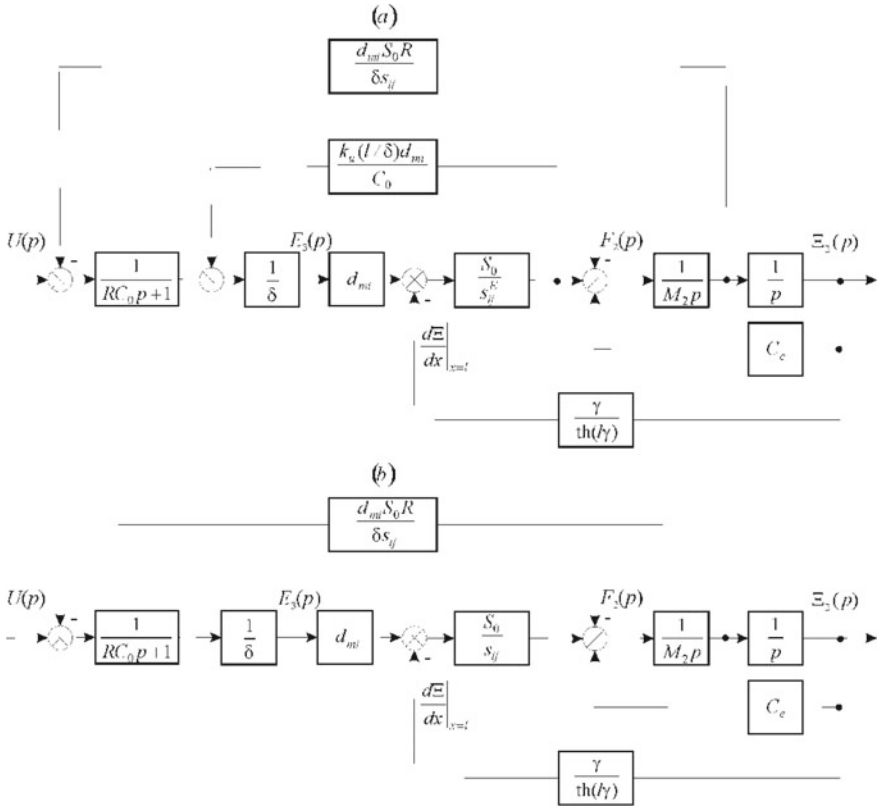

Fig. 40.4 Structural scheme with distributed parameters of piezoactuator, fixed at one face and voltage control at finite source resistance for **a** initial scheme and **b** transformed scheme

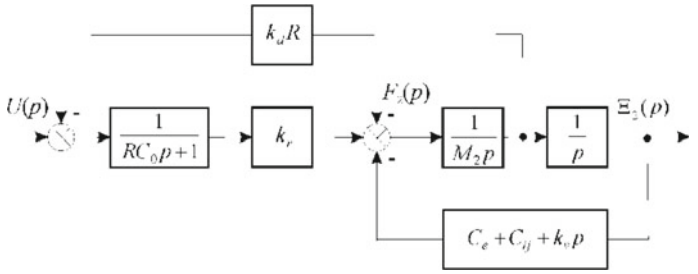

Fig. 40.5 Structural scheme with lumped parameters of piezoactuator, fixed at one face with elastic-inertial load and voltage control at finite source resistance

$$W(p) = \frac{\Xi_2(p)}{U(p)} = \frac{k_r}{M_2 p^2 + k_v p + C_{ij}^E + C_e}. \tag{40.39}$$

After transformations, we obtain the transfer function for the piezoactuator in the form

$$W(p) = \frac{\Xi_2(p)}{U(p)} = \frac{d_{mi}(l/\delta)}{(1 + C_e/C_{ij}^E)(T_t^2 p^2 + 2T_t \xi_t p + 1)}; \tag{40.40}$$

$$T_t = \sqrt{M_2/(C_{ij}^E + C_e)}, \quad \xi_t = k_v \Big/ \left(2(C_{ij}^E + C_e)\sqrt{M_2(C_{ij}^E + C_e)}\right),$$

$$C_{ij}^E = S_0/(s_{ij}^E l) = 1/(\chi_{ij}^E l).$$

Consequently, the transfer function of the piezoactuator with the transverse piezoelectric effect and voltage control at $R = 0$ has the form

$$W(p) = \frac{\Xi_2(p)}{U(p)} = \frac{d_{31} h/\delta}{(1 + C_e/C_{11}^E)(T_t^2 p^2 + 2T_t \xi_t p + 1)};$$

$$T_t = \sqrt{M_2/(C_e + C_{11}^E)}, \quad \xi_t = \alpha h^2 C_{11}^E \Big/ \left(3c^E \sqrt{M(C_e + C_{11}^E)}\right);$$

$$C_{11}^E = S_0/(s_{11}^E h) = 1/(\chi_{11}^E h),$$

where $\Xi_2(p)$ and $U(p)$ are the Laplace transformations of the displacement of the face and the voltage on the plates of the piezoactuator; δ is the thickness; h is the height; T_t and ξ_t are the time constant and the attenuation coefficient of the piezoactuator.

For the piezoactuator from PZT piezoceramics with the transverse piezoeffect and voltage control with one rigidly fixed face for $M_1 \to \infty$, $m \ll M_2$, and the step input voltage amplitude $U_0 = 200$ V at $d_{31} = 2.5 \times 10^{-10}$ m/V, $h/\delta = 20$, $M_2 = 1$ kg, $C_{11}^E = 2 \times 10^7$ N/m and $C_e = 0.5 \times 10^7$ N/m, we get $\xi_0 = 800$ nm and $T_t = 0.2 \times 10^{-3}$ s. The experimental and calculated values for the piezoactuator are in agreement up to an accuracy of 5%.

40.4 Conclusion

Applied theory of structural schemes of the electroelastic actuator for nanomechatronics is constructed. We determine structural-parametric model and transfer function for electroelastic actuator. We obtain numerical and analytical calculation of the static and dynamic characteristics of the piezoactuator from its transfer function. This work defines the structural-parametric model and structural scheme of the piezoactuator, taking into account the inverse piezoeffect and the back electromotive force due to the direct piezoeffect.

The structural-parametric model and structural scheme of the piezoactuator for nanomechatronics with feedback visually reflect the conversion of the piezoactuator the electrical energy into the mechanical energy. The structural-parametric model and structural scheme of the piezoactuator are shown to change depending on controlled by voltage or current. The maximum forces and mechanical stresses, which the piezoactuator develops for the transverse, longitudinal, shear piezoeffects, are determined.

The elastic compliances and the stiffness of the piezoactuators are found for the transverse, longitudinal, shear piezoeffects, depending from the type control by voltage or current. The transfer functions of the piezoactuators for nanomechatronics with the transverse, longitudinal, shear piezoeffects with voltage or current control are obtained.

References

1. J. Schultz, J. Ueda, H. Asada, *Cellular Actuators* (Butterworth-Heinemann Publisher, Oxford, 2017), 382 p
2. W.G. Cady, *Piezoelectricity*: *An Introduction to the Theory and Applications of Electromechanical Phenomena in Crystals* (McGraw-Hill Book Company, New York, London, 1946), 806 p
3. W. Mason (ed.), *Physical Acoustics: Principles and Methods, vol. 1. Part A. Methods and Devices* (Academic Press, New York, 1964), 515 p
4. K. Uchino, *Piezoelectric Actuators and Ultrasonic Motors* (Kluwer Academic Publisher, Boston, MA, 1997), 347 p
5. S.M. Afonin, Structural-parametric model and transfer functions of electroelastic actuator for nano- and microdisplacement, in *Piezoelectrics and Nanomaterials*: *Fundamentals, Developments and Applications*, ed. by I.A. Parinov (Nova Science Publishers Inc., New York, 2015), pp. 225–242
6. S.M. Afonin, A structural-parametric model of electroelastic actuator for nano- and microdisplacement of mechatronic system, in *Advances in Nanotechnology*, vol. 19, ed. by Z. Bartul, J. Trenor (Nova Science Publishers Inc., New York, 2017), pp. 259–284
7. D. Zwillinger, *Handbook of Differential Equations* (Academic Press, Boston, 1989), 673 p
8. S.M. Afonin, Doklady Math. **74**(3), 943 (2006)
9. S.M. Afonin, J. Comput. Syst. Sci. Int. **45**(2), 317 (2006)
10. S.M. Afonin, Dokl. Phys. **53**(3), 137 (2008)
11. S.M. Afonin, Doklady Math. **73**(2), 307 (2006)
12. S.M. Afonin, Russ. Eng. Res. **32**(7–8), 519 (2012)
13. S.M. Afonin, Russ. Eng. Res. **36**(6), 423 (2016)
14. S.M. Afonin, Mech. Solids **44**(6), 935 (2009)
15. S.M. Afonin, J. Comput. Syst. Sci. Int. **49**(1), 73 (2010)
16. S.M. Afonin, J. Comput. Syst. Sci. Int. **54**(3), 424 (2015)
17. S.M. Afonin, Int. J. Phys. **5**(1), 9 (2017)
18. S.M. Afonin, Actuators **7**(1), 1 (2018)
19. S.M. Afonin, Actuators **8**(3), 1 (2019)
20. S.M. Afonin, Mech. Solids **49**(2), 196 (2014)
21. S.M. Afonin, Int. J. Phys. **7**(2), 50 (2019)
22. S.M. Afonin, MOJ Ecol. Environ. Sci. **3**(5), 306 (2018)
23. H.S. Nalwa (ed.), *Encyclopedia of Nanoscience and Nanotechnology*, vol. 10 (American Scientific Publishers, Los Angeles, 2004)

Chapter 41
On Extraction of Energy from Rotating Objects

Tejkaran Narolia, Vijay K. Gupta, and Ivan A. Parinov

Abstract In the recent years, researchers are trying to make devices self-powered. For this purpose, energy is converted from the ambient vibrations generated by the device or some other internal source. In this chapter, it is proposed to extract energy from the rotating objects to self-power small sensors. For this purpose, a stator and rotor of parallel plates are mounted on the coaxial shaft. The stator plate has a series of isolated piezoelectric patches of rectangular shape mounted on inner surface. The surface of the piezoelectric patches is covered by the magnetic slab of same size. The upper rotator plate is made of aluminum with inner surface having the series of magnetic slabs of same size and shape. Due to rotation of the rotating plate, periodic compressive magnetic force will be applied on the piezoelectric patches resulting in generation of electric charge. It is observed that output power of the order of 1.3572 W can be obtained from 11 mm radius plate harvester. The effects of rotating speed, piezoelectric patch dimension and magnet dimension on the generated root mean square electric power has been discussed in this paper.

41.1 Introduction

Replacement of batteries in small-power consuming wireless sensors, implantable medical devices, and structural health monitoring are the tedious tasks. Researchers are trying to use energy harvesting methods in place of these batteries. Mechanical energy is one of the most abandoned energy that can be harvest from surroundings. There are various sources of mechanical energy such as vibrating structure, a moving object, and vibration induced by flowing air or water.

Piezolectric materials (for example, PZT) are one of the medium to convert mechanical energy into electrical energy [1]. Piezoelectric materials have been used in transducers to change mechanical motion or force into electrical energy or vice

T. Narolia (✉) · V. K. Gupta
PDPM IIITDM Jabalpur, Jabalpur 482005, India
e-mail: tejkarannarolia@gmail.com

I. A. Parinov
Southern Federal University, Rostov-on-Don, Russia 344090

I. A. Parinov et al. (eds.), *Advanced Materials*, Springer Proceedings in Materials 6, https://doi.org/10.1007/978-3-030-45120-2_41

versa [2]. Umeda et al. [3] proposed an electrical equivalent model for mechanical model consisting of lumped mass, spring and damper to convert mechanical impact energy into electrical energy using piezoelectric material. Roundy et al. [4–6] showed a slightly distinct perspective, using electrical equivalent circuit to explain the PZT bender, which minimize the gap between theoretical and experimental results. Sirohi et al. [7] developed an energy-harvesting device based on piezoelectric material using galloping cantilever beam. Rezaei-Hosseinabadi et al. [8] presented a topology for PZT energy harvesting made of a lift-based wind turbine and a PZT beam without contact vibration mechanism. They showed that 2 mW/cm^3 power density can be achieved at 3.8 V with wind speed of 0.9 m/s. Kishore et al. [9] designed a wind-mill having horizontal axis wind turbine with 12 magnets of alternating polarity around its periphery and a $60 \times 20 \times 0.7$ mm^3 PZT bimorph element having a magnet at its tip. They reported that 450-μW peak electric power at the rated speed of 4.2 mph of wind can be achieved. Wu et al. [10] developed a cantilever harvester for cross-wind, which was able to generate 2 W power at resonance frequency. Tao et al. [11] used a scotch yoke mechanism for converting the rotational motion into linear vibrations of two piezoelectricity-levers through springs. They reported that power of the order of 150 W can be harvested for a piezoelectric wind turbine with a radius of blades of 1 m at the wind speed of 7.2 m/s, and the designed angular velocity of 50 rad/s. Xie et al. [12] presented a ring PZT harvester, which was excited by repulsive magnetic forces at high excitation frequencies. They reported that 5274.8 W of power can be harvested using their mechanism. Most of the literature discussions use piezoelectrics in d_{31} mode for energy harvesting.

In this chapter, a simple configuration of piezoelectric energy harvester with parallel coaxial plates is presented. A mathematical model has been developed for RMS power generation and effect of various design parameters on energy harvesting has been studied.

41.2 Configuration of Piezoelectric Energy Harvester with Parallel Coaxial Plates

For extracting the energy from the rotating object, harvester with parallel coaxial plates is proposed. The harvester consists of a rotor plate, stator plate, piezoelectric patches and magnetic slabs shown in Fig. 41.1. Relative angular motion between the stator and rotor generates periodic magnetic repulsive force between the magnet slabs. This repulsive force produces compression in the piezoelectric patches resulting to generation of electric charge on the PZT surface.

Considering, r as radius of the stator and rotator plate; d as space between the stator plate and the rotator plate; l as the length of the piezoelectric patches and magnetic slabs; w as the width of the piezoelectric patches and magnetic slabs; t_p and t_m as the thickness of the piezoelectric patches and magnetic slabs, respectively, the repelling force F_M between two permanent magnets of thickness t_m can be expressed as [13, 14].

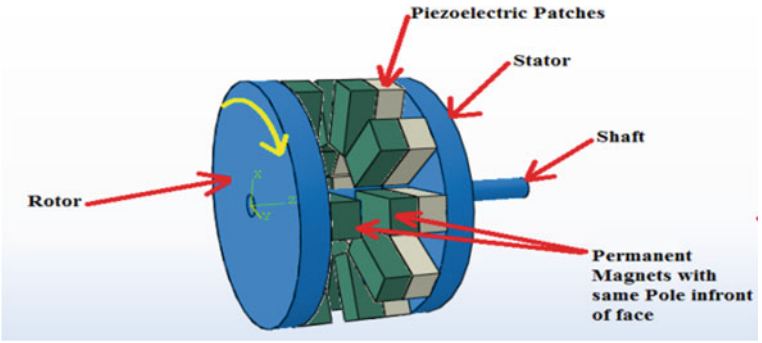

Fig. 41.1 Simple configuration of the piezoelectric energy harvester

$$F_M = lwt_m^{1/3} B_r |B(d)| f(d) \tag{41.1}$$

where B_r is the residual flux density of the magnet, $B(d)$ is the magnitude of the magnetic flux density field, and $f(d)$ is an empirical function representing the decay of the repelling force between two magnets.

For a rectangular magnet, the relation for calculation of $B(d)$ and $f(d)$ can be expressed as [14]

$$B(d) = \frac{B_r}{\pi}\left[\tan^{-1}\left\{\frac{lw}{2d\sqrt{4d^2+l^2+w^2}}\right\} - \tan^{-1}\left\{\frac{lw}{2(t_m+d)\sqrt{4(t_m+d)^2+l^2+w^2}}\right\}\right] \tag{41.2}$$

$$f(d) = \left[1.749 + 1.145e^{\left(-\frac{d}{d_0}\right)}\right] \times 10^6\left(NT^{-2}m^{\left(-\frac{7}{3}\right)}\right) \tag{41.3}$$

where $d_0 = 1$ mm.

Due to this repulsive force, the induced compression on PZT patches can be obtained using the fundamental relationship of the PZT material in the poling direction [15]:

$$D_3 = d_{33}\, T_3 \tag{41.4}$$

where D_3 is the density of surface charge displacement on the surface of the piezoelectric patches; d_{33} and T_3 are the piezoelectric strain coefficient and the normal stress applied in the poling direction of the piezoelectric material. The surface charge Q_g^i and voltage V_g^i on the ith piezoelectric patch at time t are given as

$$Q_g^i(t) = D_{3i}A = D_{3i}lw = d_{33}T_{3i}(t)lw \tag{41.5}$$

$$V_g^i(t) = D_{33}A/C_v = Q_g^i(t)/C_v = d_{33}T_{3i}(t)lw/C_v \tag{41.6}$$

where A is the surface area of the PZT patch.

Capacitance of the PZT patch can be estimated as

$$C_v = C_v' \times l \times w \times 0.0001/\left(0.01 \times 0.01 \times t_p\right) \tag{41.7}$$

where, C_v' is the unit capacitance of the PZT patch and $w = 0.01$ m, $l = 0.01$ m, $t_p = 0.0001$ m are sizes of the piezoelectric patch.

The periodic normal stress induced into the piezoelectric patch can be written as

$$T_{3i}(\mathrm{t}) = \left| \frac{F_M \sin(\mathrm{n}_1 \mathrm{n}_2 \pi t)}{lw} \right| \tag{41.8}$$

where n_1 is the excitation frequency in cycles per second; n_2 is the number of magnetic slabs mounted on the outer face of the rotator plate; $1 \leq i \leq 2n_2$ and $2n_2$ is the number of the PZT patches bonded on the inner surface of the stator plate. It can be seen that a decrease in the width of the magnetic slabs leads to increase in the value of the n_2 and hence to an increase in the excitation frequency on the piezoelectric patches.

The generated periodic charge and voltage on the ith PZT patch can then be deduced as

$$Q_g^i(t) = D_{33}\mathrm{F_M}|\sin(n_1 n_2 \pi t)|, \tag{41.9}$$

$$V_g^i(t) = D_{33}\mathrm{F_M}|\sin(n_1 n_2 \pi t)|/C_v. \tag{41.10}$$

The generated power in the form of RMS at the time, T, is given as

$$p_e^{rms} = \sqrt{\left(\frac{1}{T} \int_0^T [p_e(t)]^2 dt \right)} \tag{41.11}$$

where $p_e(t)$ is the total generated power by all the PZT patches on the stator plate at time t $(0 < t < T)$, which is provided as

$$p_e(t) = \sum_{i=1}^{2n_2} \frac{d\,Q_g^i(t)}{dt} V_g^i(t) = \sum_{i=1}^{2n_2} d_{33}^2 n_1 n_2 \pi F_M^2 |\sin(n_1 n_2 \pi t) \cos(n_1 n_2 \pi t)|/C_v \tag{41.12}$$

To calculate the RMS power, the period, T, can be divided into j time steps with a sufficiently short time interval, Δt. A discrete form of the expression in (41.11) can be written as [15]

$$p_e^{rms} = \sqrt{\frac{\Delta t}{2(T-\Delta t)} \sum_{i=2}^{j} \left([p_e(t_i)]^2 + [p_e(t_{i-1})]^2 \right)} \tag{41.13}$$

41.3 Results and Discussion

After deriving the relation of RMS power due to rotation, effect of rotating speed of the rotor, piezoelectric patch and magnetic slab sizes (length, width and thicknesses), space between the stator plate and the rotator plate, and residual flux density of the magnet on the generated power have been studied. The properties of material and sizes of the energy harvester used in the simulations are summarized in Tables 41.1 and 41.2. It is assumed that the piezoelectric patches, magnets and rotor-stator plates are made of PZT-4 (lead zirconate titanate), N5311 (neodymium iron boron) and aluminum, respectively.

In this study, five different values of the thickness of piezoelectric patches are considered. Analysis is carried out using the following parameters of the energy harvester: $l_m = 6$ mm, $w = 3$ mm, $t_m = 5$ mm $d = 0.5$ mm and $B_r = 1.48$ T, at rotating speed of the rotor plate of $n_1 = 1600$ c/s.

Effect of thickness of the magnet on the RMS power is plotted in Fig. 41.2. It can be observed that as the thickness of the magnetic slab increases, RMS power increases nonlinearly. Maximum RMS power obtained is 0.714 W at the magnet thickness of $t_p = t_m = 5$ mm.

Effect of width of PZT patch on RMS of the generated electric power is shown in Fig. 41.3 corresponding to 5 mm thickness of the magnet. It can be observed that after 1.2 mm width of the piezo, there is drastic reduction in power. This is due to the fact that the number of patches reduces as width increases. Highest RMS output power of 1.07 W is obtained at a width of 1.2 mm.

Figure 41.4 depicts the variation of RMS output power with length of the piezoelectric patch. The width in this case is considered as $w = 1.2$ mm and thickness of

Table 41.1 Material properties and dimensions of piezoelectric patches (PZT-4)

K_{33}	d_{33} (C/N)	$c^E(\mathrm{N}/m^2)$	l (m)	w (mm)	t_p (mm)
0.70	2.89e−10	1.1541e11	1–6	0.8–3.2	2–5
C_v'	0.375 for the piezoelectric patch with the geometry of $w = 0.01$ m, $l = 0.01$ m, $t_p = 0.0001$ m [14]				

Table 41.2 Material properties and sizes of plates (Al) and magnets (neodymium iron boron)

r (mm)	d	B_r	n	l (mm)	w (mm)	t_m (mm)
11	0.5–1.1	0.9–1.5	1/3	1–6	0.8–3.2	2–5

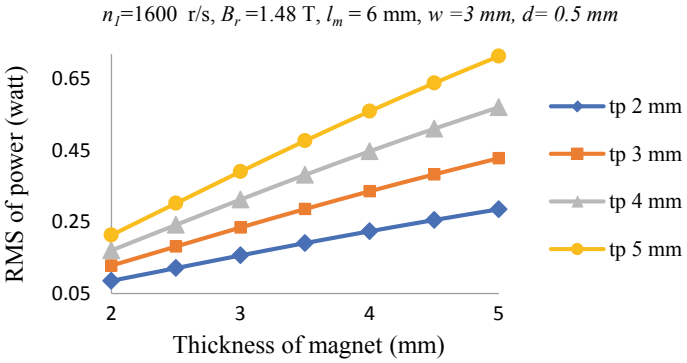

Fig. 41.2 Effect of magnet thickness on RMS of output power

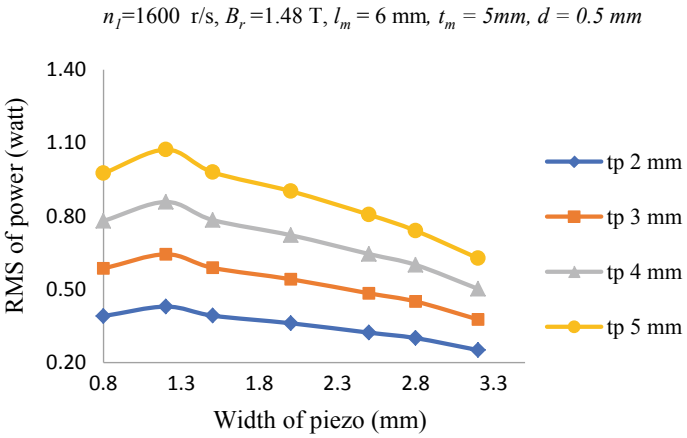

Fig. 41.3 Effect of width of piezo on RMS of output power

magnet t_m as 5 mm. It can be observed that RMS power increases with the length of the piezoelectric patch up to a maximum value of 4 mm and then decreases. The maximum RMS of power is 1.36 W for piezo thickness of 5 mm and 4 mm length.

Figure 41.5 shows the effect of space between the stator plate and the rotator plate, d on the RMS power. It can be observed that RMS power decreases nonlinearly with an increase in the space between the stator plate and the rotator plate.

Figure 41.6 shows the effect of residual flux density on RMS power. It can be observed that that RMS power nonlinearly increases with an increase in the residual flux density of the magnet. It is seen that that the RMS power is exponentially proportional to the residual flux density of the magnet with a power of 4 as shown in (41.1), (41.2), and (41.12). Thus, slight increase in the residual flux density of magnets leads to a remarkable increase in the RMS power.

Figure 41.7 shows variation of rotator speed on the RMS power. It is observed

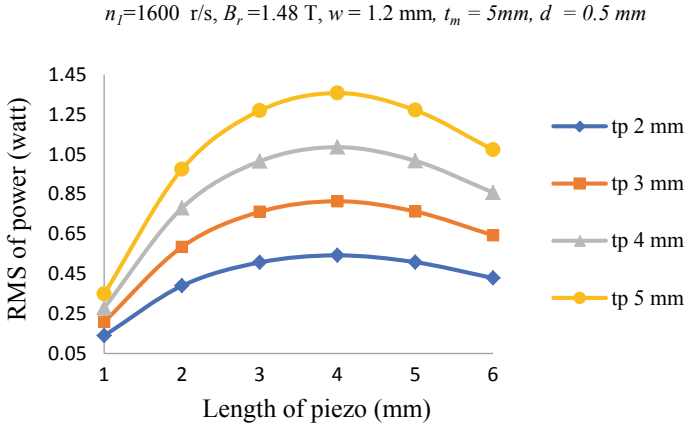

Fig. 41.4 Effect of length of piezo on RMS of output power

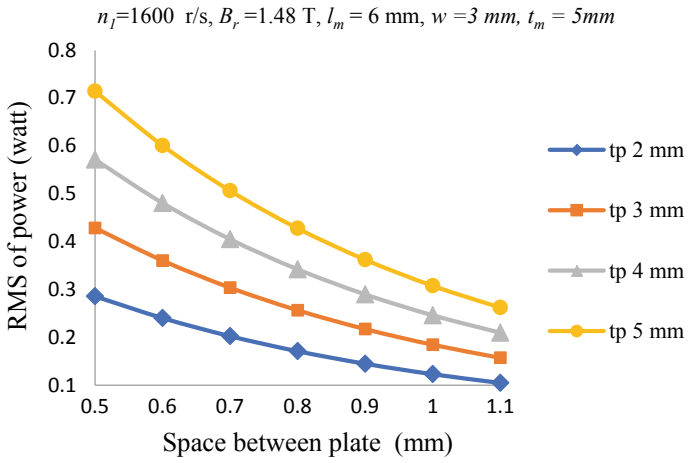

Fig. 41.5 Effect of space between plates on RMS of output power

that with increase in speed of rotator, RMS power increases. There is increase from 0.446 to 0.714 W as the rotating speed changes from 1000 to 1600 c/s with a 5 mm thick piezoelectric patch.

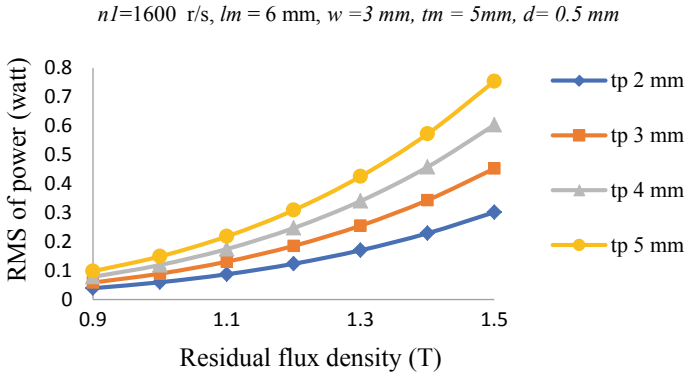

Fig. 41.6 Effect of residual flux density on output power (rms)

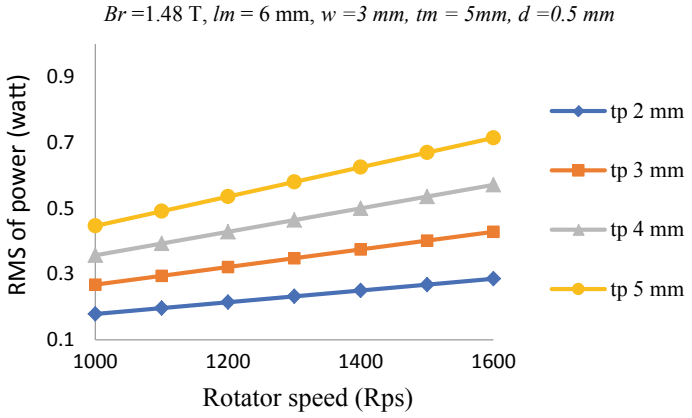

Fig. 41.7 Effect of rotator speed on output power (rms)

41.4 Conclusion

In this chapter a simple configuration using parallel plate piezoelectric energy harvester for extracting energy from rotating object has been proposed. Mathematical relation for the RMS power for piezoelectric based energy harvester is derived. Effect of various parameters such as dimensions of the magnetic slab and piezoelectric patch, magnetic flux density and rotation speed has been analyzed. The results show that the RMS power increases with increase in the length and thicknesses of both the piezoelectric patch and magnetic slab. RMS power also increases with increase in the rotating speed of the rotor plate and the residual flux density of the magnet. Decrease in space between the stator plate and the rotor plate and the width of the

piezoelectric patch and magnetic slab results in increase of RMS power. In this case, maximum power of 1.3572 W is obtained for geometric parameters of $l = 4$ mm, $w = 1.2$ mm, $t_m = t_p = 5$ mm, $n_1 = 1600$ c/s, $d = 0.5$ mm, $r = 11$ mm and magnetic field intensity B_r of 1.48 T.

Acknowledgements The work was supported by the grant of Russian Foundation for Basic Research, No. 19-08-00365.

References

1. T. Eggborn, *Analytical Models to Predict Power Harvesting with Piezoelectric Materials*. Dissertação de Mestrado, Virginia Polytechnic Institute and State University, 2003
2. J. Ajitsaria, S.Y. Choe, D. Shen, D.J. Kim, Smart Mater. Struct. **16**, 447–454 (2007)
3. M. Umeda, K. Nakamura, S. Ueha, Japan. J. Appl. Phys. **35**, 3267–3273 (1996)
4. S. Roundy, P.K. Wright, Smart Mater. Struct. **13**, 1131–1142 (2004)
5. S. Roundy, J. Intell. Mater. Syst. Struct. **16**, 809–823 (2005)
6. S. Roundy, E.S. Leland, J. Baker, E. Carleton, E. Reilly, E. Lai, B. Otis, J.M. Rabaey, P.K. Wright, V. Sundararajan, I.E.E.E. Trans, Pervasive Comput. **4**, 28–36 (2005)
7. J. Sirohi, R. Mahadik, J. Vib. Acoust. **134**(1), 011009 (2012)
8. N. Rezaei-Hosseinabadi, A. Tabesh, R. Dehghani, A. Aghili, IEEE Trans. Industr. Electron. **62**(6), 3576–3583 (2015)
9. R.A. Kishore, D. Vučković, S. Priya, Ferroelectrics **460**(1), 98–107 (2014)
10. N. Wu, Q. Wang, X. Xie, Smart Mater. Struct. **22**(9), 095023 (2013)
11. J.X. Tao, N.V. Viet, A. Carpinteri, Q. Wang, Eng. Struct. **133**, 74–80 (2017)
12. X.D. Xie, Q. Wang, N. Wu, Int. J. Eng. Sci. **77**, 71–78 (2014)
13. *The original K&J magnet calculator*. www.kjmagnetics.com/calculator.asp
14. W. Al-Ashtari, M. Hunstig, T. Hemsel, W. Sextro, Smart Mater. Struct. **21**, 035019 (2012)
15. D. Damjanovic, Rep. Prog. Phys. **61**, 1267–1324 (1998)

Chapter 42
Computer Modeling and Experimental Research of Component Processing Procedure in the Centrifugal-Rotary Equipment

Nguyen Van Tho, A. N. Soloviev, M. A. Tamarkin, and I. A. Panfilov

Abstract In this paper, the work is dedicated to modeling and analysis of the distribution characteristics of stress-strain state and temperature in the vicinity of the contact region, analysis of the removal of metal during centrifugal-rotary processing (CRO) detail in abrasive discrete environment. Examines the interplay of a single abrasive particle with workpiece surface. The study is meant to explore the stress-strain state and temperature in the vicinity of the contact region, removal of metal from workpiece surface depending on the parameters of contact interaction (pressure force, processing time, sliding speed) which are associated with the process. The problem is addressed to the finite element method. Simultaneously with numerical modeling, experiments were conducted on centrifugal-rotary setup and the dependence removal of metal on the processing technological parameters was investigated.

42.1 Introduction

The centrifugal-rotary processing method occupies a special position in the known workpiece processing methods by surface plastic deformation because it achieves the highest productivity of machining process, many times higher than the productivity of other method [1, 2]. This is one of the best surface finishing methods to achieve the best productivity, surface quality. Process optimization requires the development of models that improve friction interactions between abrasive particles and the workpiece surface.

N. Van Tho · A. N. Soloviev (✉) · I. A. Panfilov
Department of Theoretical and Applied Mechanics, Don State Technical University, Rostov-on-Don, Russia
e-mail: solovievarc@gmail.com

N. Van Tho · M. A. Tamarkin
Department of Mechanical Engineering, Don State Technical University, Rostov-on-Don, Russia
e-mail: tehn_rostov@mail.ru

N. Van Tho
Faculty of Mechanical Engineering, Hai Phong University, Hai Phong City, Vietnam
e-mail: thonv@dhhp.edu.vn

I. A. Parinov et al. (eds.), *Advanced Materials*, Springer Proceedings in Materials 6, https://doi.org/10.1007/978-3-030-45120-2_42

Fig. 42.1 Model of abrasive particles and workpiece

In this research, the interaction process of an abrasive particle with workpiece surface is considered with a three-dimensional formula in the dynamic framework of thermoplastic theory in a static formula, taking into account the internal heating contact area. So, Li et al. [3] used structural thermal analysis, and a prediction of the wear and tear of the seal element was made. Tran et al. [4] dedicated to creating an effective machine learning framework for local predictions of surface erosion through Gaussian processes. The results of real-time experimental measurements on metal removal due to sliding aluminum oxide particles are presented by Gee et al. [5].

The operation of a abrasive cone in the form of a conical cone is modeled by a circle of a smaller diameter in contact with workpiece, taking into account dry friction and removal of metal from workpiece surface (Fig. 42.1). It depends on the parameters of technological process, namely size of abrasive particles, volume of abrasive medium, rotational speed of centrifuge and interaction force are considered. Two problems are considered, in the first problem, research of the stress distribution and temperature characteristics in the vicinity of the contact region when particles slide at a constant speed. In the second task, the rate of the removal of metal from workpiece surface when sliding an abrasive particle depends on the theoretical and experimental technological parameters.

In this research, we use the following models and methods:

(i) the interaction of abrasive particles with the workpiece surface is considered within the dynamic problem of thermoplastic contact theory, taking into account the Coulomb friction and heating the surface in the contact region;
(ii) Archard model is used to model material removal process in a dynamic contact problem;
(iii) theoretical problems are solved by finite element method in FlexPDE and ANSYS;
(iv) Experimental research of processing in centrifugal-rotary setup.

42.2 Problem Formulation

It is thought that the surface of abrasive particles has an irregular shape in the form of truncated cones on the surface. The diagram of building a three-dimensional model of

the abrasive contact interaction with workpiece is shown in Fig. 42.1. The interaction of a single abrasive particle with workpiece surface is considered. The problem is formed in the framework of the dynamic contact problem of elastic theory, taking into account dry friction and metal removal in the contact region. The abrasive particles are modeled by a truncated cone, in a smaller base in contact with workpiece surface. The abrasive particle is pressed onto workpiece surface by a vertical force and slides with a constant speed, modeled by a parallel rectangle that is much larger than the diameter of the contact point.

Friction and removal of metals have been studied for a long time and their base is presented in [6]. The processing in the rotating chamber is described in the works of M. A. Tamarkin et al. and research on the features of this process are present in [7, 8]. The process of interaction takes place resulting in wear and heating of workpiece surface. Experiments and calculations are presented in [9], it is known that the temperature in the processing area is not high and does not lead to changes in the surface layer structure of workpiece surface. In this chapter, we study the contact interaction of a abrasive particle sliding on workpiece surface.

42.2.1 Problem Formulation of Abrasive Particle Movement Taking into Account Friction and Heat Release

In the first problem, the process of releasing heat due to friction is considered. Tangential stresses on the contact surface are related to normal stresses according to Coulomb's law with a friction coefficient f. It is thought that friction coefficient may depend on the surface temperature T at the points of contact $f = f(T)$. Assuming a weak connection and a quasarized formula without mass and volumetric heat sources in a moving coordinate system (Fig. 42.2), wherein $x_1 \to x_1 - vt, x_i \to x_i,\ i = 2, 3$ the complete equations have the following forms:

$$\mu u_{i,kk} + (\lambda + \mu) u_{k,ki} - (3\lambda + 2\mu)\alpha_T \theta_{,i} - v^2 \rho u_i = 0 \tag{42.1}$$

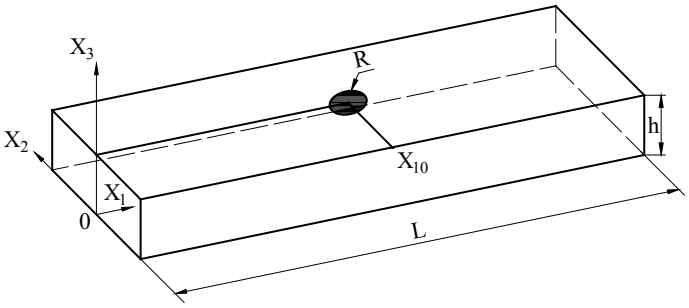

Fig. 42.2 Diagram workpiece and flat round stamp

$$\lambda_q T_{,u} + c_\varepsilon \theta = 0 \tag{42.2}$$

where $\Theta = T - T_0$, $T_0 = 273\ ^\circ\mathrm{C}$, λ, μ are the Lame coefficients, α_T is the coefficient of linear expansion, λ_q is the thermal conductivity coefficient, c_ε is the specific heat.

The boundary conditions are divided in mechanical and temperature conditions:
at $x_3 = 0$

$$\text{hard clutch:} \quad u_k = 0 \tag{42.3}$$

$$\text{or smooth base:} \quad u_3 = 0, t_i = \sigma_{ij} n_j = 0, \quad i = 1, 2 \tag{42.4}$$

$$\text{thermal insulated surface:} \quad \frac{\partial T}{\partial n} = 0 \tag{42.5}$$

$$\text{or heat interchange:} \quad \frac{\partial T}{\partial n} = \frac{h_1}{\lambda_q}(T_1 - T) \tag{42.6}$$

$$\text{or prespecified temperature:} \quad T = T_1 \tag{42.7}$$

at $x_3 = h$ the stamp takes into account ultimate friction force:

$$u_3 = -\delta, t_1 = -f\, t_3, (x_1 - x_{10})^2 + x_2^2 \le R^2 \tag{42.8}$$

$$\text{heat dissipation under stamp:} \quad \frac{\partial T}{\partial n} = \frac{Q}{\lambda_\mathrm{q}}, \quad Q = vt_1, (x_1 - x_{10})^2 + x_2^2 \le R^2 \tag{42.9}$$

$$\text{free surface:} \quad t_i = \sigma_{ij} n_j = 0, (x_1 - x_{10})^2 + x_2^2 > R^2 \tag{42.10}$$

$$\text{heat interchange:} \quad \frac{\partial T}{\partial n} = \frac{h_2}{\lambda_q}(T_2 - T), (x_1 - x_{10})^2 + x_2^2 > R^2 \tag{42.11}$$

$$\text{or prespecified temperature:} \quad T = T_2, (x_1 - x_{10})^2 + x_2^2 > R^2 \tag{42.12}$$

where h_1, T_1 and h_2, T_2 are the heat transfer coefficient and medium temperature below and above the strip.

In a numerical solution, for example, by the finite element method of a boundary value problem (42.1), (42.2) a selected set of boundary conditions (42.3)–(42.12), introduce fictitious borders: $x_1 = 0$ and $x_1 = L$ if $L \gg \max(2R, h)$, on which we set the following boundary conditions:
at $x_1 = 0, L$

$$u_1 = 0,\ t_k = 0,\ k = 2, 3 \tag{42.13}$$

$$\frac{\partial T}{\partial n} = \frac{h_3}{\lambda_q}(T_3 - T) \tag{42.14}$$

$$\text{or } T = T_3 \tag{42.15}$$

where h_3, T_3 are the heat transfer coefficient and initial temperature of the strip.

42.2.2 Problem Formulation of Material Removal

The value of force of a abrasive particles on workpiece of the sliding process is related to the rotation speed of the setup ω and is determined as follows:

$$F = m\omega^2 R \tag{42.16}$$

where m is the mass of abrasive particle, R is the machining radius (distance from the axis of rotation to the workpiece).

The problem is reduced to motion of a circular cone with constant speed $v > 0$ in positive direction of x_1-axis, taking into account the friction forces arising under it. Due to this interaction, the strip material is removed, the Archard model is used [10]:

$$w = \frac{K}{H}\sigma_n^b v_{rel}^q \tag{42.17}$$

where w is the displacement of contact surface points in the direction removal of metal; K is the metal removal coefficient; H is the material hardness; σ_n is the contact pressure; v is the relative sliding speed; b, q are some parameters characterizing the power dependence of the quantity.

The boundary conditions correspond to the effect of uniform pressure distribution P on the round surface of the abrasive particle (Fig. 42.3), cone and workpiece are in friction contact, the lower plane of the part is fixed, the remaining surfaces have no stress.

Table 42.1 presents the parameters of the abrasive particles and workpiece.

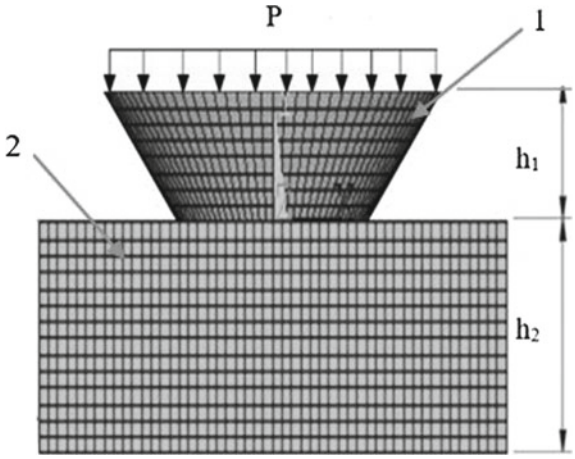

Fig. 42.3 Design contact interaction of the abrasive particles and workpiece

Table 42.1 Model parameters of abrasive particles and workpiece

No.	Characteristic	Material model	
		Workpiece (Steel)	Abrasive particles (Corundum)
1	Young's modulus (MPa)	2×10^5	2×10^9
2	Poisson's ratio	0.28	0.3
3	Material hardness (HB)	190	20,600
4	Density (kg/m^3)	7850	4000

42.3 Finite Element Modeling

42.3.1 Distribution of Stress-Strain State and Temperature Characteristics

The solution of boundary value problem, described in Sect. 42.2.1, was obtained by using the finite element method in the FlexPDE. The simplification of the finite element model is shown in Fig. 42.4. Since the elastic modulus and hardness of abrasive particles is much greater than workpiece, then its action is replaced by a hard stamp (Scheme 3 in Fig. 42.4). The finite element grid is shown in scheme 4 of Fig. 42.4 and has a thickening in the vicinity of the contact region.

42.3.2 Value of Removed Metal from Workpiece Surface

Method for solving the second boundary value problem (Sect. 42.2.2), finite element method and ANSYS software are used, which implements the Archard metal removal

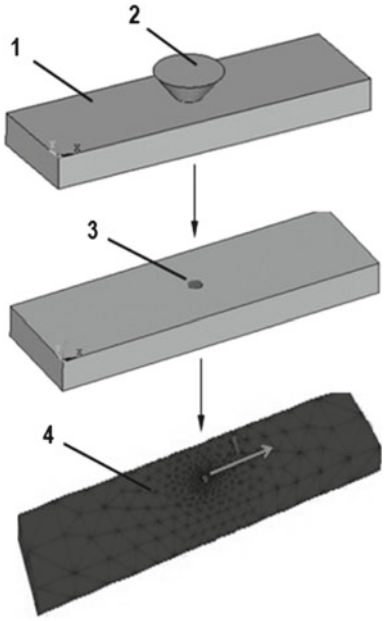

Fig. 42.4 Diagram contact interaction: 1 workpiece; 2 abrasive particle; 3 flat round stamp abrasive particle; 4 finite element mesh

model. Figure 42.5 shows the finite element mesh of a three-dimensional model of workpiece and abrasive particle; in the contact area, the mesh is thickened. The final elements SOLID185, CONTA174 and TARG169 are used for contact surfaces.

Both models are activated using the TB, WEAR command, and their binding to contact elements is carried out through 01 unique material identifier ID. Activation of the generalized Archard wear model is carried in the formats: *TB*, *WEAR*, *MATID*, *ARCD*, where MATID is the identification of the material associated with contact elements.

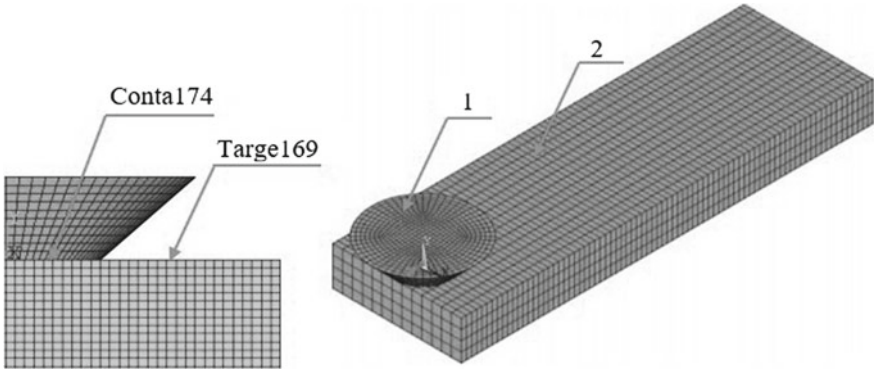

Fig. 42.5 Finite-element partitioning in contact problem: 1 abrasive particle, 2 workpiece abrasive particle 1, sliding with a constant speed v along the workpiece surface

42.4 Numerical Results

42.4.1 Calculation of Stress-Strain State and Temperature

In the first problem, finite element method was applied [11]. The mechanical properties and temperature specified in the SI system are used: Young's modulus $E = 2 \times 10^{11}$ Pa, Poisson's Ratio 0.3, coefficient of thermal expansion $\alpha_T = 11.9 \times 10^{-6}\,\kappa^{-1}$, density $\rho = 7.8 \times 10^3\,\mathrm{kg/m^3}$, thermal conductivity $\lambda_q = 52\,\mathrm{w/(m\,k)}$, thermal capacity $c_\varepsilon = 462\,\mathrm{J/k}$, heat transfer coefficient $h_1 = 1791.3\,\mathrm{w/(m^2\,\kappa)}$, $h_2 = 1791.3\,\mathrm{w/(m^2\,\kappa)}$, initial and external temperature $T_1 = T_2 = T_3 = 293\,\mathrm{k}$, strip length $b = 25\,\mathrm{h\,m}$, sliding speed $v = 0.2\,\mathrm{m/s}$, strip height $h = 0.04\,\mathrm{m}$, stamp width $2a = 0.02\,\mathrm{m}$, friction coefficient $f = 0.2$, penetration depth $\delta = 1.0 \times 10^{-4}\,\mathrm{m}$

Figure 42.6 shows the distribution characteristics in the stress-strain state and temperature of the strip.

Table 42.2 presents the relationship between the penetration depth of stamps and vertical component of contact interaction force F.

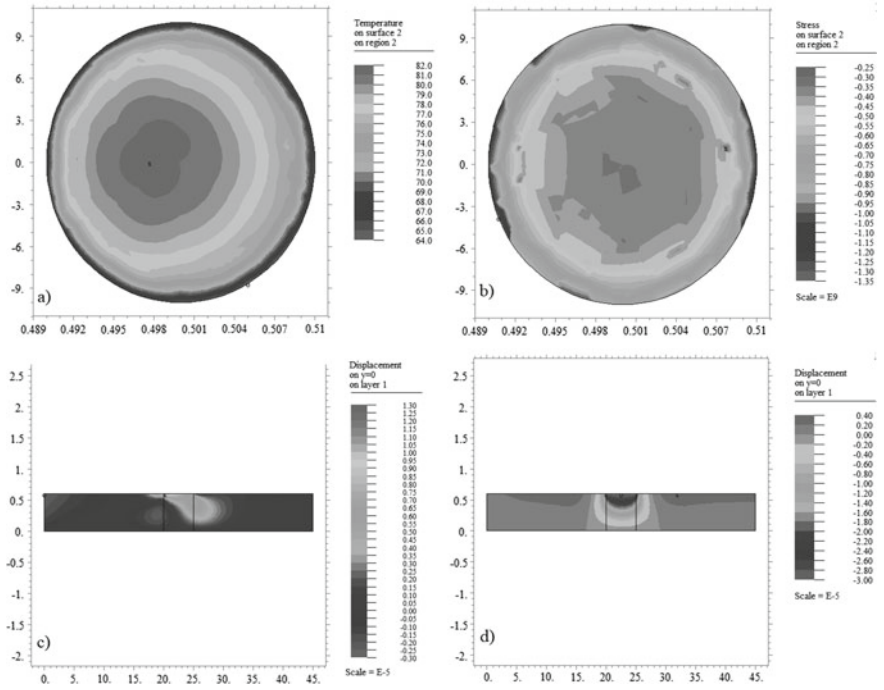

Fig. 42.6 Characteristics of the stress-strain state and temperature in the strip: **a** temperature under the stamp, **b** distribution of horizontal displacement, **c** distribution of vertical displacement, **d** voltage distribution in area under the stamp

Table 42.2 Relationship between contact force and penetration depth

Penetration depth (M)	1.0×10^{-5}	2.0×10^{-5}	3.0×10^{-5}	4.0×10^{-5}	5.0×10^{-5}
F(N)	55	96	138	180	221

The dependences of maximum temperature on speed, friction coefficient and penetration depth of the stamp are shown in Figs. 42.7, 42.8 and 42.9 in 3 cases:

(i) when friction coefficient $f = 0.2$; $\delta = 3.10^{-5}$ m and sliding speed change from $v = 0.1$ m/s to $v = 0.5$ m/s;
(ii) when $\delta = 3 \times 10^{-5}$ mm, sliding speed $v = 0.2$ m/s and friction coefficient f change from $f = 0.05$ to $f = 0.3$;

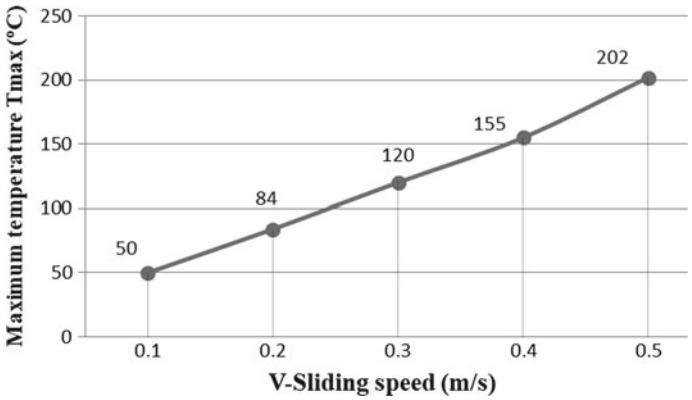

Fig. 42.7 Dependence of temperature on sliding speed

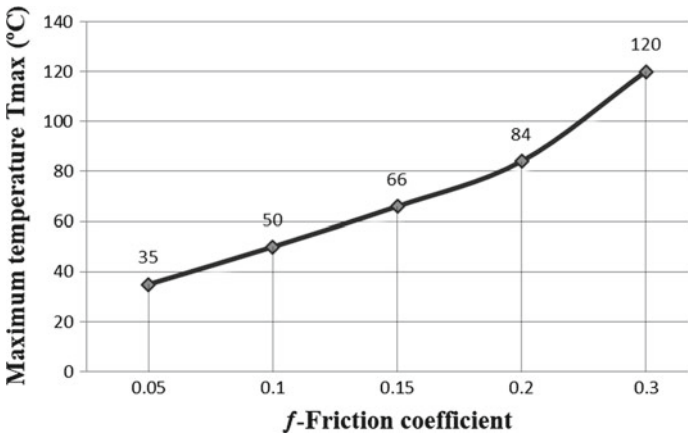

Fig. 42.8 Dependence of temperature on friction coefficient

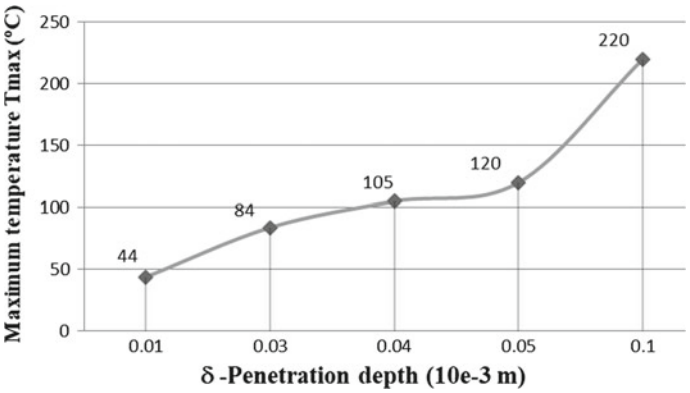

Fig. 42.9 Dependence of temperature on penetration depth

(iii) when sliding speed $v = 0.2$ m/s, friction coefficient $f = 0.2$ and penetration depth change from $\delta = 10^{-5}$ m to $\delta = 10^{-4}$ m.

42.4.2 Calculation of Removed Metal from Workpiece Surface

Calculations are made for an abrasive particle and workpiece, the material parameters are shown in Table 42.1. The following mechanical properties and geometric parameters are used: metal removal rate $K_d = 1.06793 \times 10^{-6}$; $b = q = 1.0$; radius of the truncated cone $R_1 = 2$ mm and $R_2 = 4$ mm, cone height $h_1 = 2$ mm; workpiece height $h_2 = 3$ mm, workpiece length $L = 30$ mm, workpiece width $D = 5$ mm; friction coefficient $f = 0.1$; step $t = 1\,s$.

Figure 42.10 shows the distribution of metal removal rate from workpiece surface when abrasive particles is pressed to workpiece by vertical pressure $P = 2.5\,\text{N/mm}^2$ and slide with constant speed $v = 30$ mm/s on workpiece surface.

Figure 42.11 shows the distributions of rates for metal removal from workpiece surface depending on rotation speed, for the values of rotation speed equal to 5, 12, 16 and 20 rp/s.

The dependence of maximum rate of removed metal from workpiece surface on the rotation speed of the setup is present in Fig. 42.12. It can be noted that metal removal rate increases linearly with the rotation speed of CRO.

Figure 42.13 shows the numerical results obtained by performing 4 different processing modes depending on the time. Note that curves 1 and 2 are smooth and increase over time. When machining in this mode, the workpiece surface provides the best of metal removal rate and surface roughness. Curves 3 and 4 show that metal removal values increase over time, but in these modes, instability has occurred,

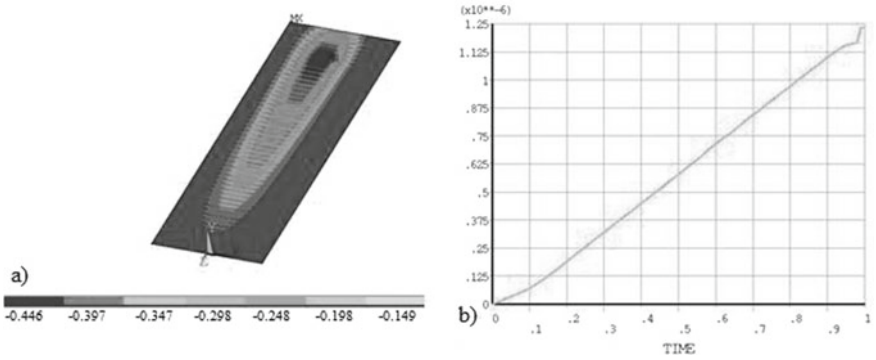

Fig. 42.10 Distribution of removed metal (mm x 10^{-6}): **a** distribution of rates for metal removal from workpiece surface, **b** dependence of maximum rate of metal removal on time

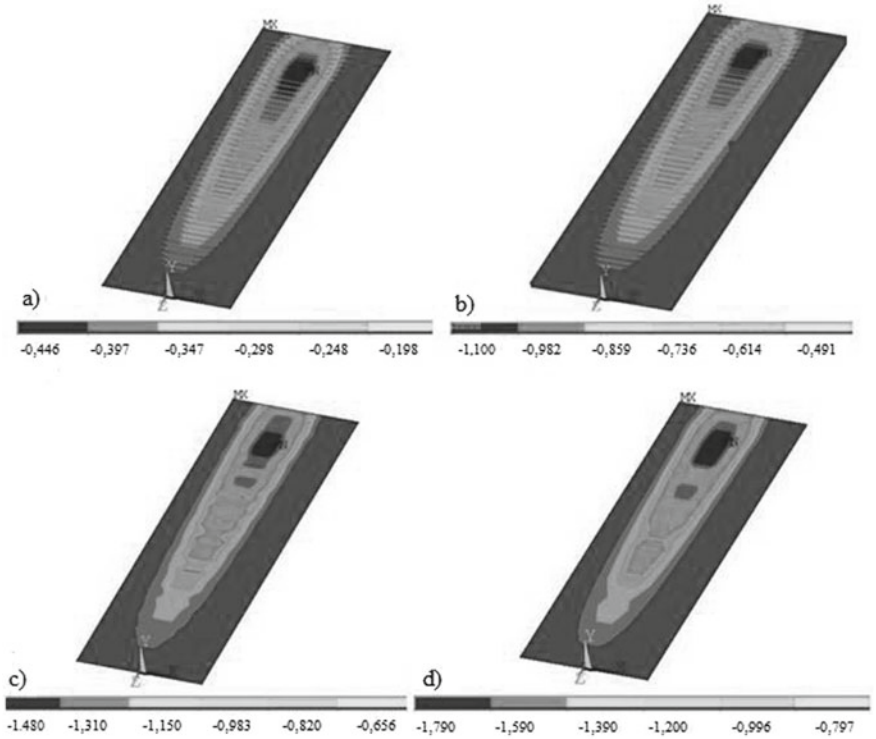

Fig. 42.11 Distribution of metal removal rate on rotation speed (mm x 10^{-6}): **a** 5 rp/s; **b** 12 rp/s; **c** 16 rp/s; **d** 20 rp/s

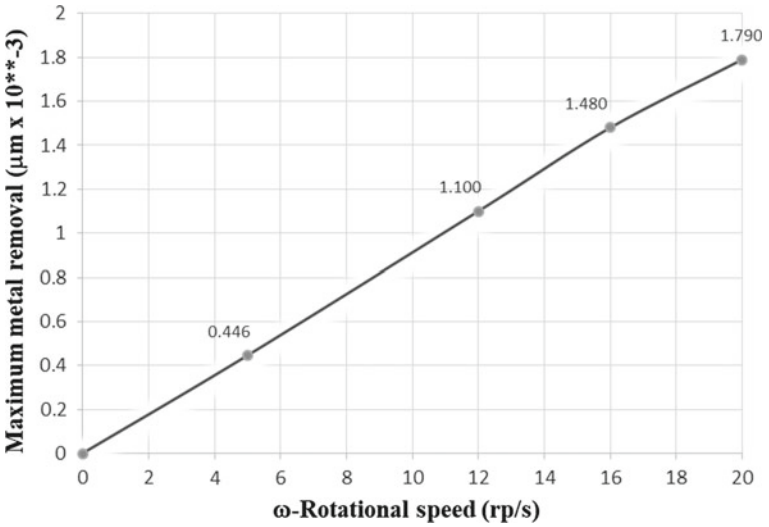

Fig. 42.12 Maximum of metal removal rate depending on rotation speed

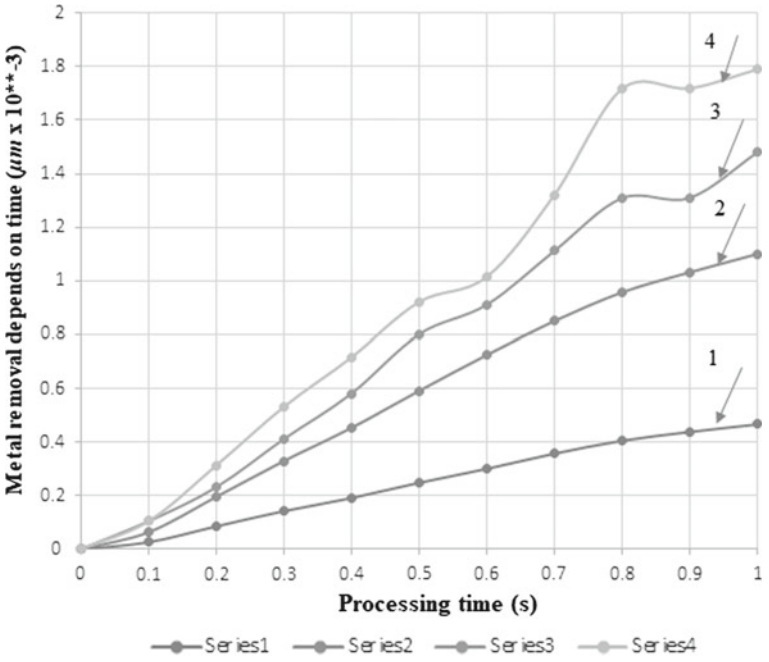

Fig. 42.13 Metal removal rate depending on time: (Series 1) 5 rp/s; (Series 2) 12 rp/s; (Series 3) 16 rp/s; (Series 4) 20 rp/s

Table 42.3 Dependence of metal removal due to vertical force

Vertical force F(N)	100	280	370	460
Removal of metal from the workpiece surface ($\mu m \times 10^{-3}$)	0.487	1.23	1.57	1.95

uncontrolled metal removal rate, causing high surface roughness, the authors of [12] noted similar results.

Table 42.3 shows the dependence metal removal rate from workpiece surface on the uniformly distributed pressure acting on the larger circle of the dead-end cone.

42.5 Experiments

42.5.1 Technology Equipment

Experimental research on the CRO process have been carried out on the CROS-7, including working chambers, process fluid delivery units and hydraulic installations that control the rotation of the work chamber.

The summary of the CRO method is that abrasive particles 3 and workpiece 4 (Fig. 42.14 [6]) are loaded into the working chamber and rotated about the vertical axis so that the entire mass of the load becomes a torus in which particles move along spiral paths. The toroidal helical flow is ensured through the design of the machine working chamber consisting of a fixed cylindrical ring 1 and a rotating bottom (rotor) 2 adjacent to it, having a common plate shape. Workpieces 4 are loaded into the working chamber with abrasive particles 3. To reduce wear, the inner surfaces of the bottom and the fixed part of the working chamber are coated with a wear-resistant material.

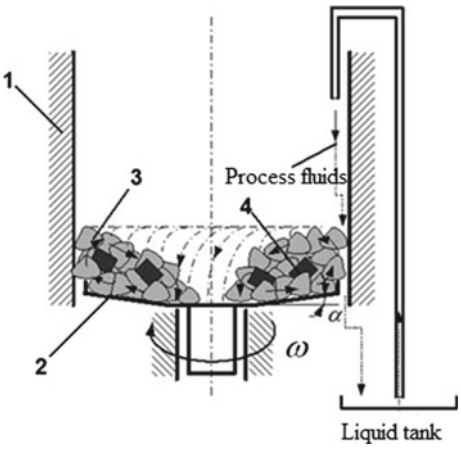

Fig. 42.14 Centrifugal-rotary processing CROS-7 in abrasive medium: 1 fixed cylindrical ring; 2 rotor; 3 abrasive particles; 4 workpieces

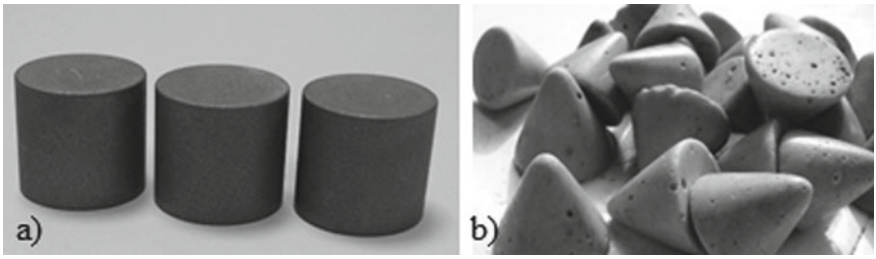

Fig. 42.15 **a** Workpiece and **b** abrasive particles in experiments

42.5.2 Experimental Research on the CROS-7

In order to investigate the process of metal removal from workpiece surface, we used steel 45 cylindrical samples of size Ø 20 × 20 mm (Fig. 42.15).

The parameters of abrasive particles and workpieces are shown in Table 42.1. Moreover, 3 samples were processed, every 30 min, the processing is stopped, the samples are taken out of the chamber, washed, dried and weighed on the analytical balance.

The following formula was used to perform comparison between the numerical results and experimental data:

$$m = V\rho \tag{42.18}$$

where m is the metal removal weight, V is the volume of lost metal after machining process, ρ is the density.

Figure 42.16 shows the comparison between numerical simulation results and experimental research metal removal rate of workpiece from the rotation speed.

It is obvious that, the data obtained in experimental research are well consistent with numerical simulation results.

42.6 Conclusion

In this work, we have developed a three-dimensional statement for contact interaction, considering the interaction process of an abrasive particle moving at a constant speed with the workpiece surface.

Finite element models of the abrasive particle and workpieces were constructed in the FlexPDE and ANSYS software.

When modeling the metal removal process, taking into account the removal of metal from workpiece surface, the abrasive particles had not wear. The calculation for metal removal were made with different technological process parameters: the dependences of metal removal rate on time were constructed with different values of

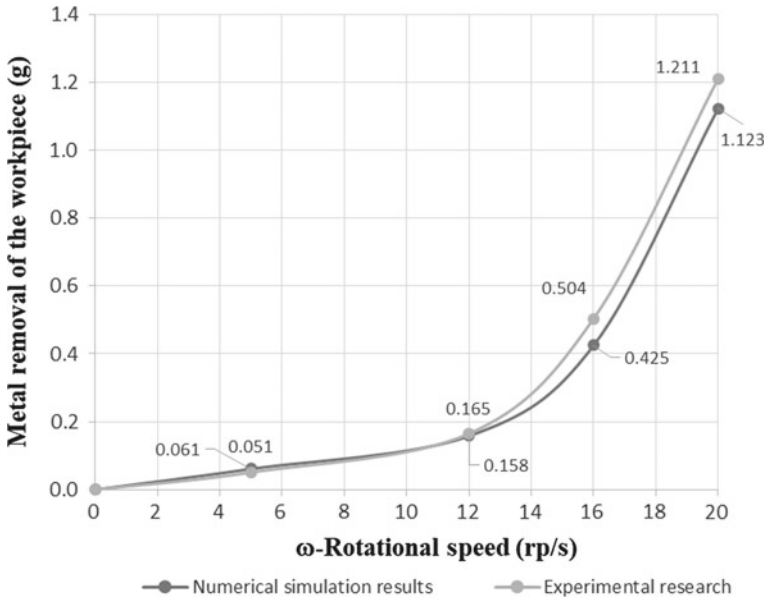

Fig. 42.16 Compared results of numerical modeling and experimental research

the CRO angular velocity, the dependence of maximum rate of metal removal on the rotation speed was constructed. The dependence of metal removal rate on the force acting on abrasive particles was investigated, too.

The studies of the stress-strain state on the surface and in the volume of workpiece were performed. The dependences of temperature, of the interaction force on penetration depth of the stamp, taking into account friction coefficient and slip speed of abrasive particles were constructed. In the consideration, the strength of the interaction depended on set of parameters, such as: rotational speed, type of abrasive particles, their total volume, and so on. The dependences constructed in the work allow determining the optimal values of the parameters of the CRO in workpiece machining.

References

1. M.A. Tamarkin, E.E. Tishchenko, O.A. Rozhnenko, in *Stin*. No. 2 (2009), pp. 26–30. (in Russian)
2. M.A. Tamarkin, E.E. Tishenko, V.V. Druppov, *Vestnik of Rybinsk State Aviation Technological Academy*, No. 11 (2007), pp. 169–186. (in Russian)
3. Li Xin, Peng Gaoliang, Li Zhe, Finite Elem. Anal. Des. **83**, 10–21 (2014)
4. Anh Tran, John M. Furlan, Krishnan V. Pagalthivarthi, Robert J. Visintainer, Int. J. Sci. Wear **422**, 9–26 (2019)
5. M. Gee, J. Nunn, Wear **376–377**, 1866–1876 (2017)

6. A.N. Soloviev, M.A. Tamarkin, N. Van Tho, Vestnik Don State Tech. Univ. **19**(3), 214–220 (2019). (in Russian)
7. I.V. Kragelsky, *Friction and Wear* (Mashinostroenie, Moscow, 1986), 480 p. (in Russian)
8. M.A. Tamarkin, O.A. Rozhnenko, E.E. Tishchenko, in *Strengthening Technologies and Coatings*, vol. 11 (2011). (in Russian)
9. A.N. Soloviev, M.A. Tamarkin, T.V. Nguen, in *Ecological Bulletin of Research Centers of the Black Sea Economic Cooperation*, No. 1 (2019), pp. 51–58
10. M.I. Chebakov, S.A. Danilchenko, A.A. Lyapin, News of North-Caucasus region. Nat. Sci. **2**, 32–37 (2017). (in Russian)
11. https://www.pdesolutions.com
12. R. Suresh, M. Prasanna Kumar, S. Basavarajappa, Int. J. Sci. Mater. Today Proc. **4**, 11218–11228 (2017)

Chapter 43
Optimization Design of a 2-DOF Compliant Parallel Mechanism Using NSGA-II Algorithm for Vibration-Assisted Milling

Huy-Tuan Pham, Van-Khien Nguyen, Khac-Huy Nguyen, Quang-Khoa Dang, Trung-Kien Hoang, and Son-Minh Pham

Abstract Compliant parallel mechanisms (CPMs) combining parallel mechanisms and compliant mechanisms exhibiting many advantages such as high stiffness, high load carrying capacity, and high accuracy are widely used in various precision engineering applications. This chapter proposes a new design of a CPM using hollow flexural hinges combined with semicircular hinges and leaf springs for a non-resonant vibration assisted milling application. The mechanism will be actuated by piezoelectric actuators. The dimensions of the mechanism are optimized using an FEA-based global search evolutionary optimization (NSGA-II) procedure, aiming to maximize the natural frequencies and decoupling between its two axes. The optimization procedure is programmed in MATLAB whereas the ANSYS Mechanical ADPL code is embedded to support and enhance the calculation process. Using the optimal parameters, the established model for the mechanical performance evaluation of the CPM is verified with the finite-element method. A prototype of the mechanism can be fabricated using wire EDM machining method and it will be incorporated into a CNC machining center to validate the performance of the established system.

43.1 Introduction

Vibration assisted machining (VAM) is a hybrid machining method which combines small amplitude vibration into either the conventional or non-conventional subtractive machining approaches to enhance the cutting performance and efficiency. Researches showed that with the integrated reciprocating motion to the tools or workpieces, tighter tolerance and higher quality surface finish could be obtained especially when hard, high brittleness and low fracture toughness materials are machined [1, 2]. Other reported benefits of VAM include reduction in machining forces, suppression of burr formation, reduction of tool wear and extension of tool life.

H.-T. Pham (✉) · V.-K. Nguyen · K.-H. Nguyen · Q.-K. Dang · T.-K. Hoang · S.-M. Pham
Faculty of Mechanical Engineering, Ho Chi Minh City University of Technology and Education, Ho Chi Minh City, Vietnam
e-mail: phtuan@hcmute.edu.vn

I. A. Parinov et al. (eds.), *Advanced Materials*, Springer Proceedings in Materials 6, https://doi.org/10.1007/978-3-030-45120-2_43

The purpose of integrating vibration into non-conventional machining methods such as EDM or wire-EDM is to enhance the cutting speed. For conventional machining methods, VAM has been applied to turning, milling, drilling, and grinding, for the processing of hard materials. While in VATurning the vibration can be easily applied to the tool since it is stationary, the integration of vibration in VAMilling is much more challenging [3].

Currently two vibration methods that are used in VAMilling are shown in Fig. 43.1.

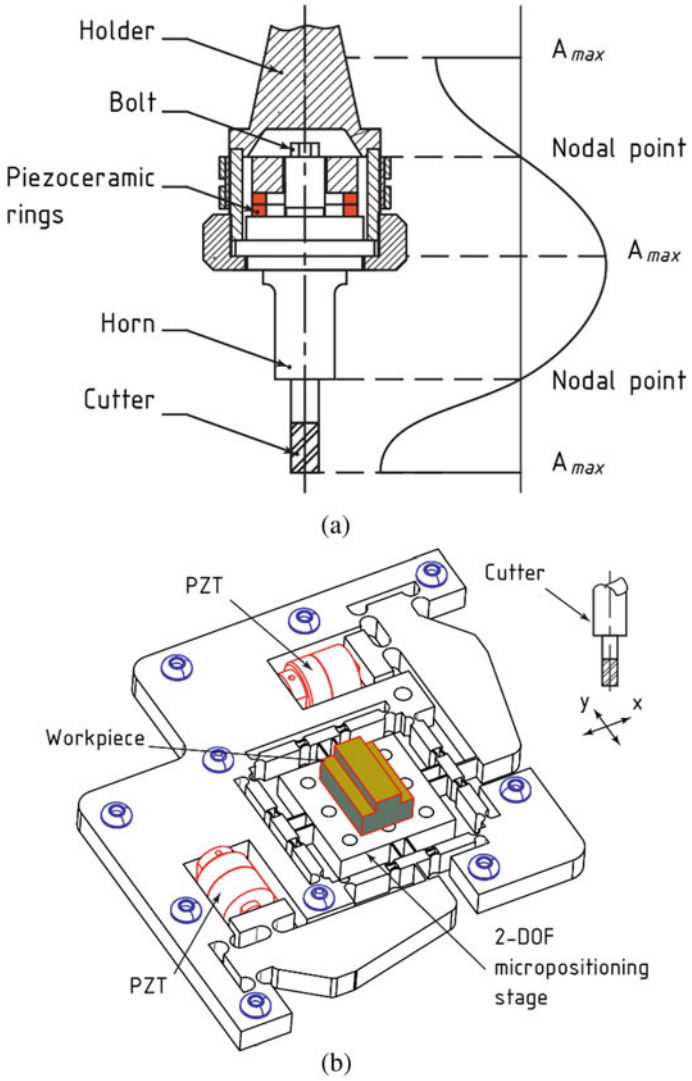

Fig. 43.1 Vibration-assisted machining principle: **a** resonant mode [6]; **b** non-resonant mode

In Fig. 43.1a, ultrasonic vibration is integrated into the holder of the tool and operated using resonant principle. A horn will transmit the mechanical vibration from the piezoceramic rings to the cutter and this amplitude can be magnified depending on the design of the horn. Horn design is a crucial but intricate task in this system and its natural frequencies must match the vibration frequency of the PZT [4–7]. Any mismatch of these frequencies would lead to catastrophic failures for the tool or the machining system. The other simpler method to feed the vibration into the machining system is to oscillate the workpiece as illustrated in Fig. 43.1b whereas the design of a 2-DOF micro-positioning stage using compliant mechanism is the heart of the system. This paper proposes a 2-DOF platform using a novel design of a hollow circular flexure hinge to optimize the static and dynamic performance of a high precision machining stage. The stage can be used to verify the efficiency of VAMilling in either macro or micro machining.

43.2 Problem Formulation

43.2.1 Design Concept

In this section, a 2-DOF micro-positioning platform is designed to integrate into a conventional CNC milling machine that could help to induce the vibration of the workpiece to enhance the machining efficiency. A new hollow flexural hinge in our previous research [8] is used in combination with the classical semicircular hinge and leaf spring to optimize the static and dynamic loading performance of the stage. Figure 43.2 is the design of the hollow hinge where the experimental results have shown that it could help to improve the stiffness and guiding accuracy.

The configuration of the 2-DOF micro-positioning platform is shown in Fig. 43.3.

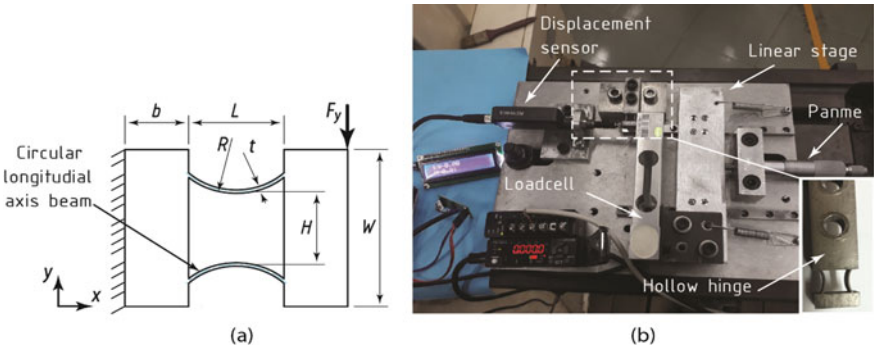

Fig. 43.2 New hollow flexural hinge for the 2-DOF positioning platform: **a** design parameters of the hinge, **b** experimental testing of a fabricated prototype

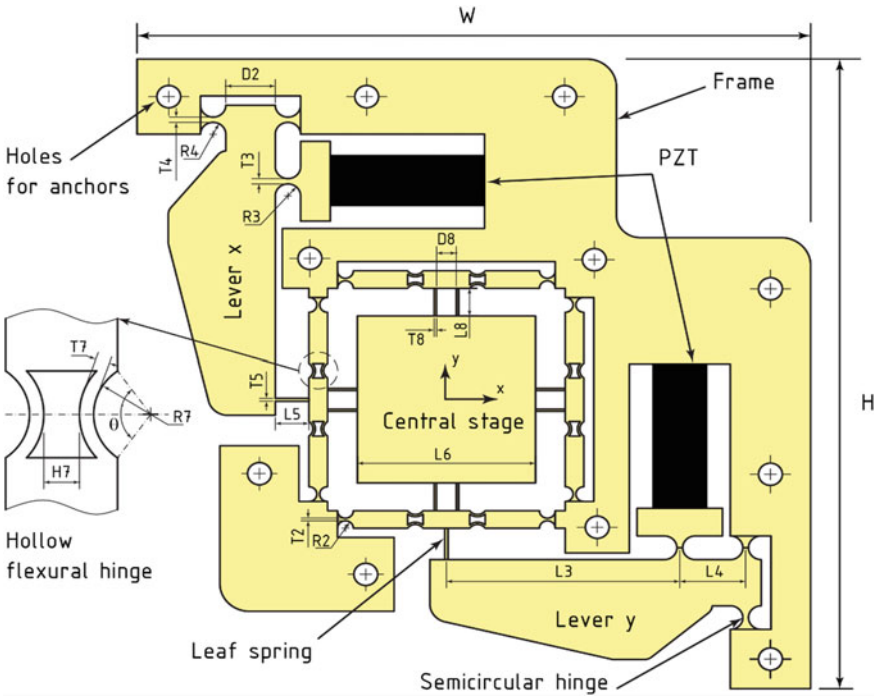

Fig. 43.3 Design parameters of a 2-DOF micro-positioning table for vibration-assisted machining

In this design the central stage is connected to the frame via compliant mechanisms including eight hollow hinges, eight semicircular hinges and eight leaf springs. This stage is vibrated by the vibration from the two PZT actuators that could drive the motion in either x- or y-direction. Two lever mechanisms are used to transfer the vibration and amplify the motion from the vibration sources. Thirteen design parameters are also shown in Fig. 43.3.

43.2.2 Design Concept

In order to independently vibrate workpiece in two perpendicular directions (x and y), two PZT actuators are used. This 2-DOF micro-positioning stage could separately and simultaneously activate the two vibration motions of the workpiece during the machining process. However, before one could use this stage for the best VAMilling performance, three objectives should be optimized by varying the above thirteen design variables. Firstly, since this machining method follows a non-resonant mode, resonant phenomenon must be mitigated. The natural frequency of the stage should be maximized to enlarge the processing vibration frequency range. Secondly, fatigue failure is also a crucial concern for all compliant mechanisms when they are operated

Table 43.1 Formulation of the design optimization problem

1. **Objectives**: • Minimize the maximum concentrated stress (σ_m) • Minimize the parasitic motion (δ_y) • Maximize the first-mode natural frequency (f_o)
2. **Design variables**: • Hollow hinges: T_7, R_7, θ • Lever circular hinges: T_3, R_3, T_4, R_4 • Leaf springs: T_5, L_5, T_8, L_8 • Table circular hinges: T_2, R_2
3. **Constraints**: i. (g_1): $1.0 \leq T_i \leq 4.0$ (mm), $(i = 2–8)$ ii. (g_2): $3.0 \leq R_i \leq 8.0$ (mm), $(i = 2–7)$ iii. Design space, (g_3): $W \times H = 340 \times 340$ (mm) iv. The maximum stress within the CPM (g_4): $\sigma_m < [\sigma_y]/SF$

in dynamic modes especially under high frequency. Therefore, the designing task should not only assure the maximum stress within the elastic range but it also should be small as possible to lengthen the lifetime of the mechanism. The last objective function is to minimize the parasitic motion of the CPM to reduce the decoupling between its two axes and enhance its driving accuracy. The optimization problem of the CPM is formulated in Table 43.1 with three objective functions, thirteen design variables and four constraint functions.

In order to optimize the shape and size of the CPM, an effective optimization procedure for the design of compliant mechanisms was developed [9] and it is used for the synthesis of the current mechanism (Fig. 43.4). The nondominated sorting genetic algorithm (GA) integrated with ANSYS Mechanical ADPL is applied. This algorithm was proved to be suitable for solving constrained nonlinear problems with multiple objective functions. In this analysis, both static and dynamic behaviors of the mechanism are investigated by using the finite element method.

Static analysis is used to calculate the amplification of the lever mechanisms where PZT input displacement is transmitted to the displacement of the central stage. Both maximum stress and parasitic motion are considered in this analysis type to evaluate the first two objective functions in Table 43.1. Figure 43.5a shows the FEM results for the displacement of the mechanism when PZT-X is activated and Fig. 43.5b illustrates the stress distribution among the flexural hinges.

Modal analysis of the mechanism is also implemented to investigate its dynamic behavior. The first three modes are presented as shown in Fig. 43.6. The first two modes are the translational motion of the stage in two main directions and their frequencies are quite close with each other. The third mode is the rotation motion of the central stage. During the operation of the stage, the machining frequency should be smaller than the first natural frequency of the mechanism to mitigate the resonant phenomenon.

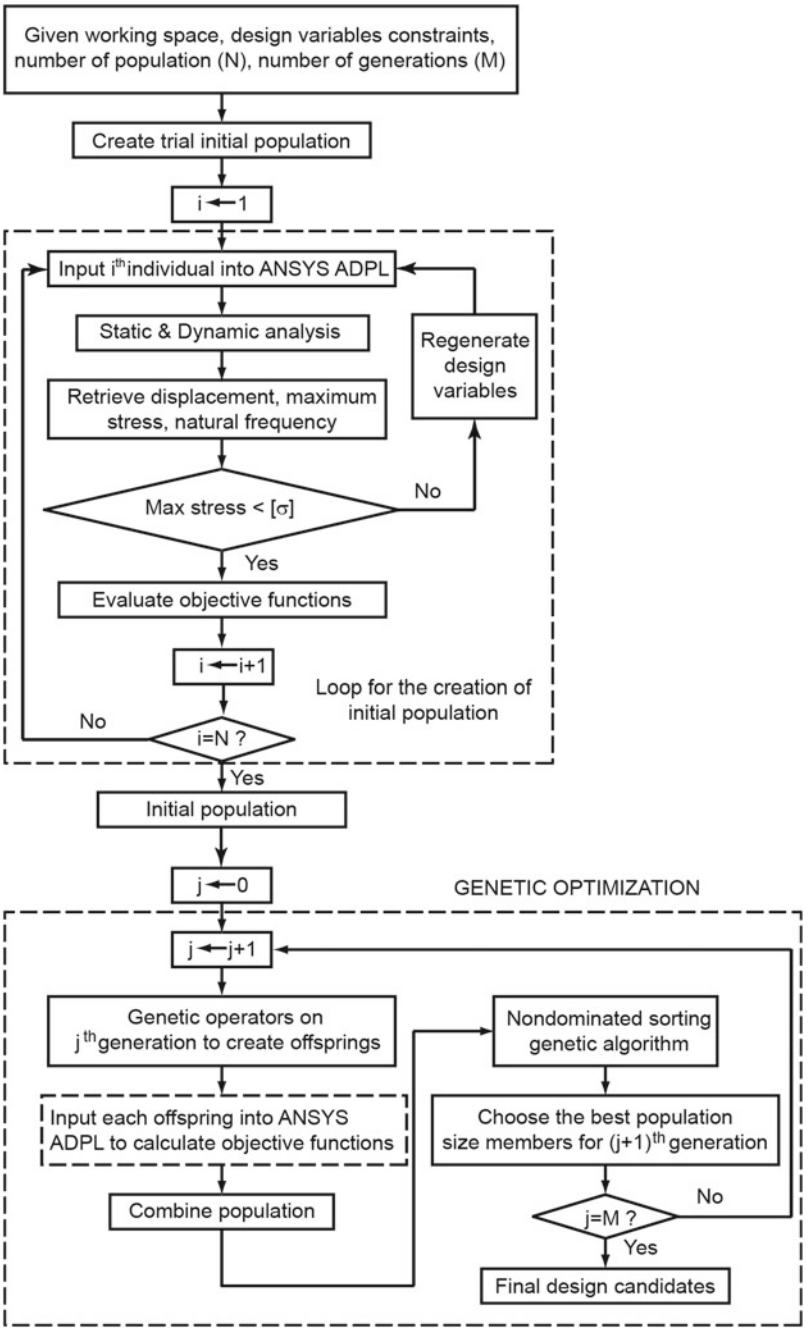

Fig. 43.4 Flowchart of the FEA-based genetic algorithm optimization procedure

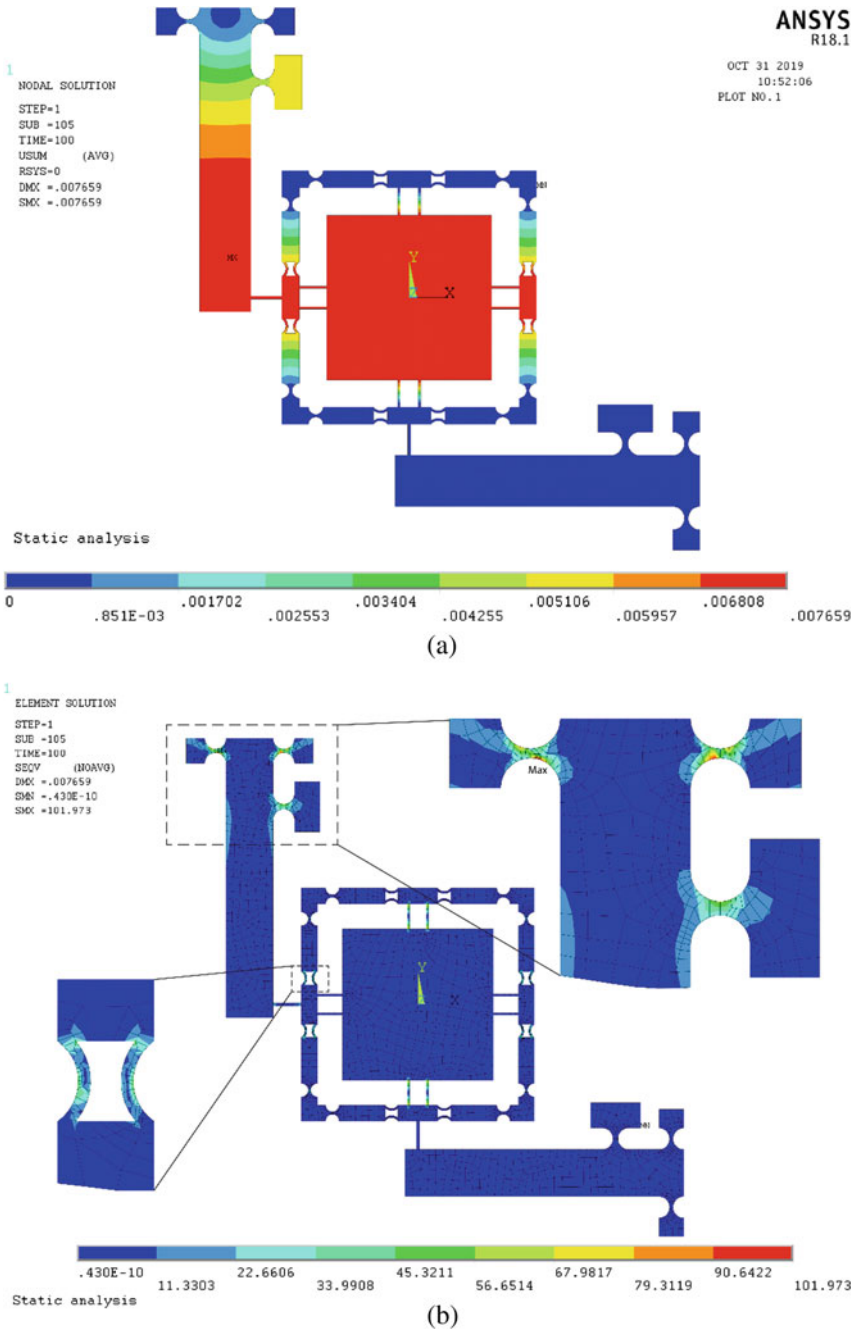

Fig. 43.5 Total displacement of the mechanism with x-input displacement (**a**); Von-Mises stress distribution (**b**)

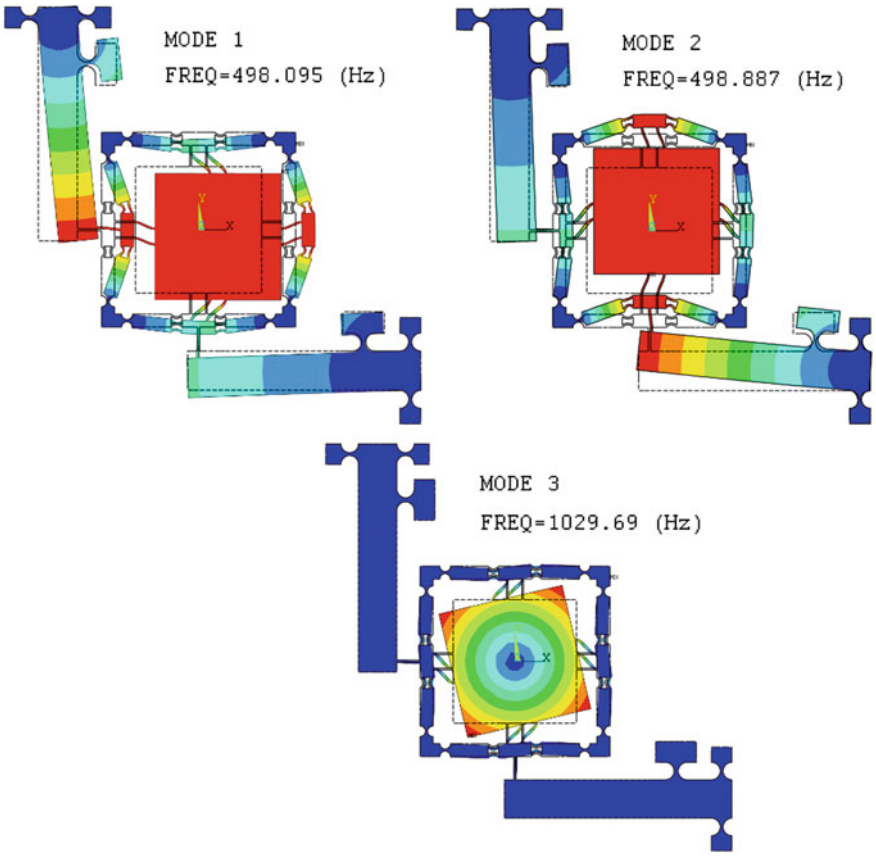

Fig. 43.6 Mode shape analysis

43.3 Results and Discussion

In the analysis, aluminum Al7075-T6 is used whose mechanical properties are Young's modulus ($E = 71.7\,\text{GPa}$), Poisson's ratio ($\vartheta = 0.33$), yield strength $\left(\sigma_y = 503\,\text{MPa}\right)$, and density $\left(\rho = 2810\,\text{kg/m}^3\right)$ and the out-of-plane thickness of the structure is 15.0 mm. By using the GA optimization method integrated with the ANSYS Mechanical ADPL and the number of generations is 60, the optimum results for the design variables of the CPM are presented in Table 43.2.

Physik Instrument piezoelectric actuators (model: P-225.10) with a maximum travel range of 15 μm and a maximum pushing force of 12,500 N will be used in this research. Figure 43.7 shows the displacement of the central table in both *x*- and *y*-directions when PZT-X is activated. An input displacement of 5 μm is applied and the obtained output motion in x-direction is 7 μm with the amplification of the lever mechanism is 1.4. This output motion can be optimized to make it bigger

Table 43.2 Optimum design variables of the CPM

Design variables	Values (mm)	Design variables	Values (mm)
T_2	1.4	R_2	4.0
T_3	2.9	R_3	6.4
T_4	2.9	R_4	6.4
T_5	1.6	L_5	17.0
T_7	1.2	R_7	4.8
T_8	1.2	L_8	15
θ	109°		

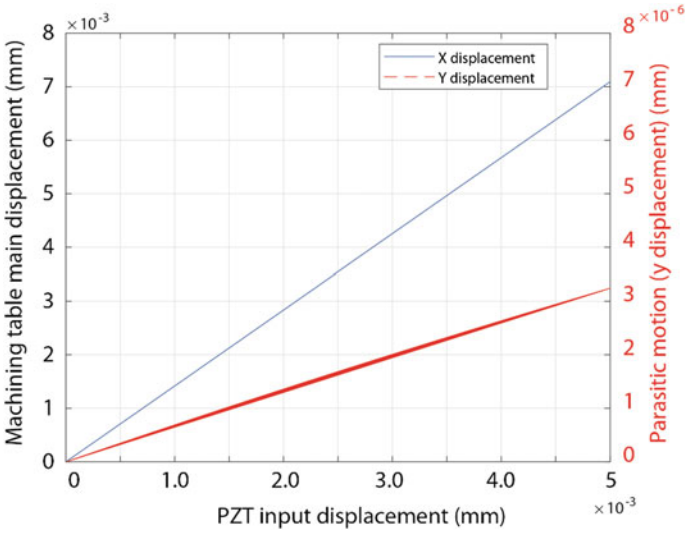

Fig. 43.7 Displacement simulation results

but since during the VAM process large vibration amplitude is not a key factor to affect the machining performance so it is not included into the objective functions of the optimization problem. With the optimum design, the parasitic motion of the stage in *y*-direction is thousand times smaller than the main motion. This shows a complete decoupling between two axes. In order to ensure for the best performance and mitigate the resonant phenomenon of the CPM, the natural frequency of the mechanism should be several times larger than the activation frequency of the PZT. When 5 μm excitation is expected from the PZT, the required working frequency is around 150 Hz. Figure 43.8 is the harmonic analysis result that shows the frequency response of the mechanism. The first natural frequency of the optimum design is 498 Hz that is high enough for embedding external vibration to the machining process.

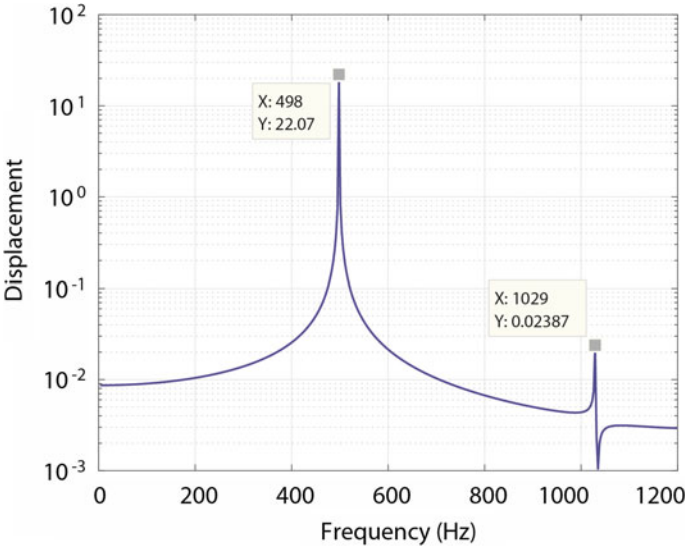

Fig. 43.8 Harmonic analysis of the CPM

43.4 Conclusion

Compliant parallel mechanisms were used in this research to design a micro-positioning stage for VAMilling. The highly precise vibration of the PZT actuators was transferred to the machining stage via the compliant mechanism combining different types of flexural hinges. In this chapter, hollow flexural hinges were integrated with semicircular hinges and leaf springs to construct the mechanism. Finite element method combined with multi-objective genetic algorithm was used to optimize the dimensions of the hinges. The simulated results show that the optimum design exhibits a first natural frequency that is three times larger than the excitation frequency of the PZT for 5 μm input driving. The maximum stress is 101.9 MPa that is equivalent to a safety factor of around 5.0 and a relatively small parasitic motion that ensures for a completely decoupling between two axes. This characteristic is favorable for any vibration-assisted machining processes. In the latter stage of this research, the designed mechanism will be fabricated using wire EDM and integrated into a CNC milling center to investigate the influence of the vibration effect to the machining performance.

Acknowledgements The authors are thankful for the financial support from the HCMC University of Technology and Education (HCMUTE), under Grant No. T2019-08TD.

References

1. Y. Gu, X. Chen, J. Lin, M. Lu, F. Lu, Z. Zhang, H. Yang, Micromachines **9**, 499 (2018)
2. W. Chen, D. Huo, Y. Shi, J.M. Hale, Int. J. Adv. Manuf. Technol. **97**, 2033–2049 (2018)
3. V.K. Nguyen, H.H. Pham, H.T. Pham, Mod. Environ. Sci. Eng. **4**(5), 469–475 (2018)
4. D.A. Wang, W.Y. Chuang, K. Hsu, H.T. Pham, Ultrasonics **51**, 148–156 (2011)
5. H.T. Pham, X.Q. Nguyen, N.P. Nguyen, J. Sci. Technol. Tech. Univ. **110**, 115–120 (2016)
6. Q.K. Dang, P.L. Chang, T.N. Dang, F. Weng, J.Y. Uan, D.A. Wang, J. Mater. Process. Technol. **266**, 208–216 (2019)
7. V. Ostasevicius et al., J. Mech. Eng. **59**(6), 351 (2013)
8. V.K. Nguyen, D.L. Tuong, H.T. Pham, H.H. Pham, Appl. Mech. Mater. **889**, 337–345 (2019)
9. H.T. Pham, D.A. Wang, Sens. Actuators A **167**, 438–448 (2011)

Chapter 44
Design and Analysis of a Compliant Constant-Torque Mechanism for Rehabilitation Devices

Thanh-Vu Phan, Huy-Tuan Pham, and Cong-Nam Truong

Abstract Medical or healthcare devices assisting the rehabilitation of human joints often rely on functional mechanisms that could provide stable output torque. To achieve this target, available equipment usually uses motorized mechanisms combined with complicated sensorized control system. This paper presents a novel design concept of a monolithic compliant constant-torque mechanism (CTM). It could produce an output torque that does not change in a prescribed input rotation. Thanks to the monolithic nature of the compliant mechanism, the device is more compact, lightweight and portable regardless of sensors or actuators. However, to be used in the rehabilitation equipment, the mechanism must produce a stable output torque in a sufficiently wide range of operation. The design methodology of this compliant CTM uses a genetic algorithm shape optimization. After obtaining the optimal configuration, finite element analysis is used to verify the design. This chapter also proposes a general design formulation to find the CTMs with a certain constant output torque in a specified input rotation range that can be used for human joint rehabilitative devices or human mobility-assisting devices.

44.1 Introduction

Constant-torque mechanism (CTM) is defined as a mechanism that could provide a stable output torque regardless of the variation of the rotation angle input. This mechanism can be found in many applications including technological or medical devices and daily life products [1, 2]. In order to maintain a stable output torque, some rehabilitation devices that are constructed from rigid mechanisms will use sensors and actuators and combine with complicated control systems [3–6]. Other passive devices such as the splint in [7] composed of the digit apparatuses and it is identified as a constant-torque spring. It is a combination from plenty of parts therefore it reduces the accuracy of the mechanism and makes a challenge in decreasing the size

T.-V. Phan · H.-T. Pham (✉) · C.-N. Truong
Faculty of Mechanical Engineering, HCMC University of Technology and Education, Ho Chi Minh City, Vietnam
e-mail: phtuan@hcmute.edu.vn

I. A. Parinov et al. (eds.), *Advanced Materials*, Springer Proceedings in Materials 6, https://doi.org/10.1007/978-3-030-45120-2_44

of mechanism. In comparison with the traditional rigid-body counterparts, the use of compliant mechanisms results in reduced wear, reduced need for lubrication, and a consistently high precision [8].

The compliant CTM is another variant of compliant constant-force mechanism in which the mechanism rotates around its axis. The constant-force mechanisms have been attracted by many researchers [9–13] while the CTMs did not receive an appropriate concerned. Hou et al. [2] proposed a compliant CTM as a function joint. Prakashah et al. [14] used variable width spline curves to synthesize a compliant CTM. A simpler compliant CTM by using the straight beams was proposed in [15]. However, it produces a shorter range of constant-torque in comparison with the curved beams.

The designing concept of the CTM in this paper follows the idea of regulating the torque—rotation curve of a bi-stable mechanism by converting the negative stiffness region into zero stiffness section. Using a similar concept, Wang et al. has designed a simple structure of a constant output torque by using the buckling phenomenon of a linear bi-stable beam that was arranged with an inclined angle [15]. With the purpose of lengthening the working range, this paper proposes the configuration of a CTM with the combination of three slender curve beams in different directions that is similar to the design of a constant-force mechanism [10].

44.2 Design

44.2.1 Operational Principle and Design Concept

Most ideal compliant mechanisms (CMs) will obey the Hooke's law when they are operated in the elastic regime. However, some special CMs such as the CTM will exhibit an irregular torque curve that differs from the purely elastic mechanism as shown in Fig. 44.1. It includes two regions: the pre-stress stage and the working

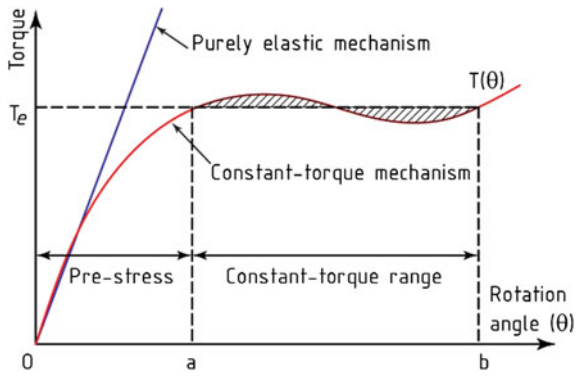

Fig. 44.1 Torque—rotation curve of a compliant CTM

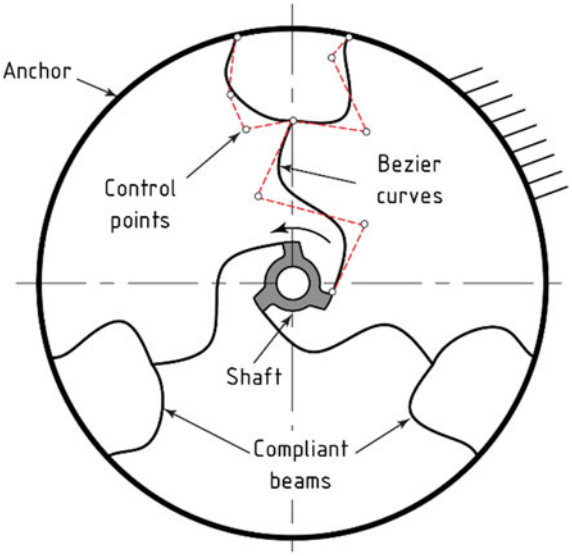

Fig. 44.2 Concept of the CTM

range. During the initial loading process, any elevation of the input rotation angle would lead to the increment of the reaction output torque. If a CTM is properly designed, after this stage, the torque will remain stable in a certain range despite of the increasing of the rotation angle. It is the working range of the CTM.

The proposed CTM in this research has three identical branches that are oriented symmetrically around the center of the mechanism. Each one includes three compliant beams that are parameterized using Bezier curves as shown Fig. 44.2. The outer ring is used to anchor two ends of each beam group. The whole mechanism can rotate around a shaft that is used to constraint the motion of the CTM in one degree-of-freedom.

44.2.2 Optimization Design of the CFM

Owing to the symmetry of the design, only one branch with three slender beams illustrated in Fig. 44.3 is analyzed. The design variables are coordinates of ten control points $C_i(x, y)(i = 0 - 9)$ that compose three 3rd-order Bezier curves and their width w. The control point C_3 is constrained in the vertical center line and it is the intersection of the three beams. In any design, the working space or the maximum boundary of mechanism is the first thing that needs to be concerned. Here, the outer ring that attaches to two points C_0 and C_6 is considered as a part of the boundary constraint. The area with radius R that attaches to point C_9 is a predefined parameter so that it could provide enough space to set up the shaft.

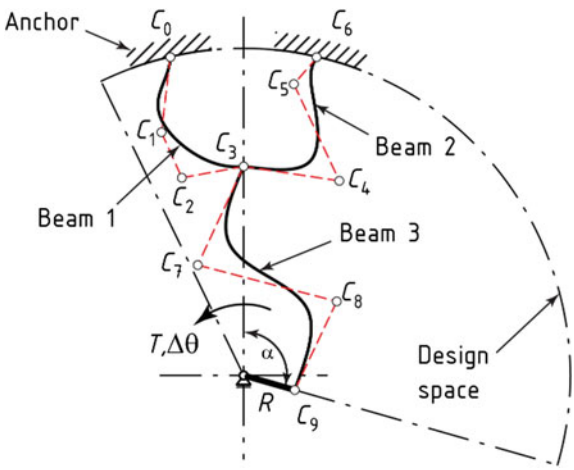

Fig. 44.3 Schematic of one branch of the CTM and the design variables of three Bezier curves

Based on the preliminary parameters, trial designs are randomly created by using MATLAB and finite element analysis by ABAQUS is applied to obtain the behavior between output torque and rotation angle. Simultaneously, the stress is also evaluated to assure the operation of the CTM within the elastic regime. The design variables are parameterized and optimized by genetic algorithm (GA) to attain the optimum shape and size of curved beams. The flowchart of this algorithm which was verified to be suitable for solving constrained nonlinear problems is given in Fig. 44.4. The optimization problem in this research is formulated in the following objective function:

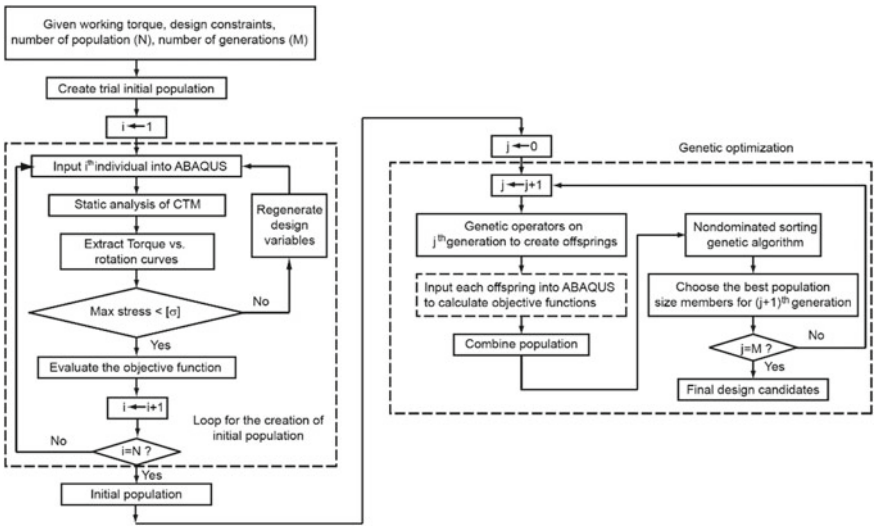

Fig. 44.4 Flowchart of the FEA-based genetic algorithm optimization procedure

Table 44.1 Formulation of compliant constant torque mechanism optimization

Objective: Minimize the variation of the torque following (44.1)
Design variables: Control points: $C_i(x, y)$ $(\mathrm{i} = 0 - 9)$ In-plane thickness: w
Constraints: $g_1 : C_i(x) < 0 (i = 0 - 2; 7); C_i(x) > 0 (i = 4 - 6; 8)$ $g_2 : 0.7 \leq w \leq 1.5$ (mm) The maximum stress within the CTM, $g_3 : \sigma_m < \sigma_y / SF$

$$\text{Min } f(\theta) = \int_a^b (T - T_e)^2 d\theta \tag{44.1}$$

This CTM has 20 designed variables including the (x, y) coordinates of ten Bezier control points in which the point C_3 just has one variable y coordinate and a uniform width (w) of the beams. The objective of this design is to minimize the variation of the torque function toward a constant torque regardless the rotation angle of the mechanism in the working range. The optimization formulation is described in Table 44.1. The radius R is prescribed as 15 mm. Three constraint functions with different purpose are embedded to govern the optimization process. The function g_1 is to prevent the curved beams from the intersection. The function g_2 defines the bound for the width of slender beams. The stress of the mechanism is required in the constraint g_3.

44.3 Results and Discussion

In the analysis, polyoxymethylene (POM) is considered being a high-performance engineering polymer with many applications in industry; it is used for the device. POM as well as other thermoplastic materials exhibit viscoelastic behavior and time-dependent properties. However, if the loading process is regarded as static, it can be assumed to be linear elastic and isotropic material [16]. In this model, the Young's modulus (E) of POM is taken as 2.6 GPa, the Poisson's ratio $\left(v_p\right)$ is taken as 0.25, and the out-of-plane thickness of the structure is 10 mm. By using the GA optimization method integrated with the FEM beam element model in Fig. 44.5 and the number of generation equal to 25, the optimum results for the design variables of the parameterized curves are presented in Table 44.2.

To verify for the nonlinear stiffness and structural integrity of the mechanism and improve the accuracy from the simulation to the practical device, a three-dimensional model of the obtained optimum beam-element design (Fig. 44.6) is built to analyze the behaviors of the CTM. The torque—rotation curves of the optimum mechanism are indicated in Fig. 44.7. The constant-torque value of 3D model is slightly higher

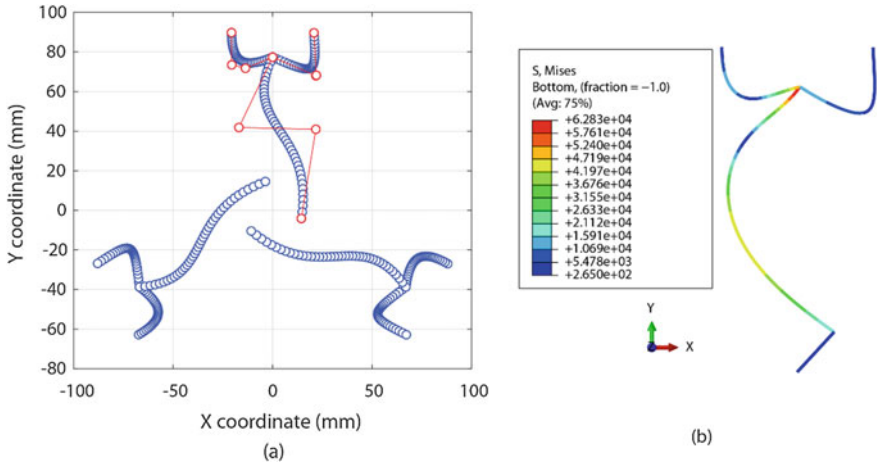

Fig. 44.5 FEM beam element model (**a**) and simulation results using Abaqus (**b**)

Table 44.2 Optimum design variables of the CTM

Design variables	Values (mm)	Design variables	Values (mm)
$C_0(x, y)$	(−20.69, 89.76)	$C_5(x, y)$	(21.99, 68.23)
$C_1(x, y)$	(−20.56, 73.49)	$C_6(x, y)$	(20.80, 89.64)
$C_2(x, y)$	(−13.68, 71.76)	$C_7(x, y)$	(−16.96, 41.85)
$C_3(x, y)$	(0.00, 77.37)	$C_8(x, y)$	(21.74, 40.95)
$C_4(x, y)$	(21.80, 68.00)	$C_9(x, y)$	(14.43, −4.10)
w	0.90		

than that of 2D model, but the stability is quite good for both cases. In the operational range, from 20º to 60º, the torque remains steady at 242 N mm and 247 N mm for 2D and 3D simulation, respectively. The torque can be adjusted to higher value by increasing the out-of-plane thickness without changing the flatness of the mechanism.

The designed CTM can find its applications in integration to a rehabilitative devices or human mobility-assisting devices. With this mechanism, sophisticated sensors and feedback control systems can be eliminated to maintain a constant output torque. One such prototype is shown in Fig. 44.8. It is an effectively supportive device for recovering in knee injuries or going up and down the stairs. Thanks to the monolithic nature of the compliant mechanism, the proposed CTM can be designed more compactly to adapt for ankle or elbow rehabilitation devices.

Fig. 44.6 3D model of the CTM

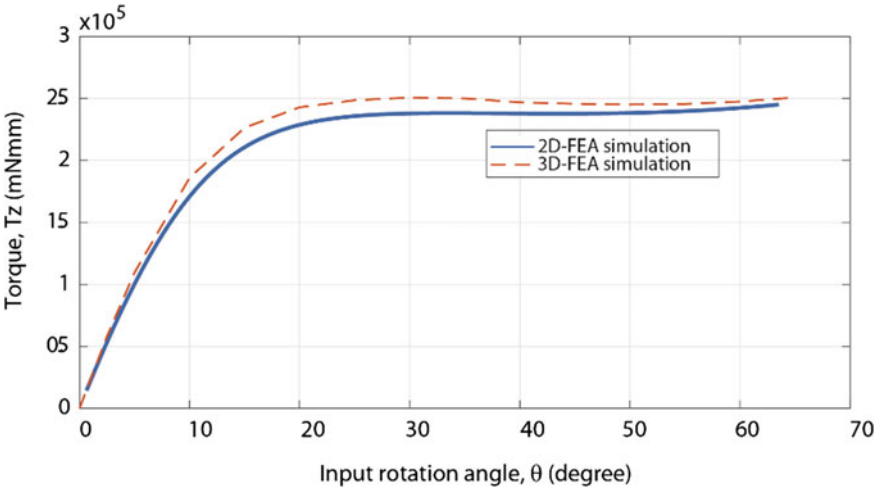

Fig. 44.7 Torque—rotation results using FEA simulation

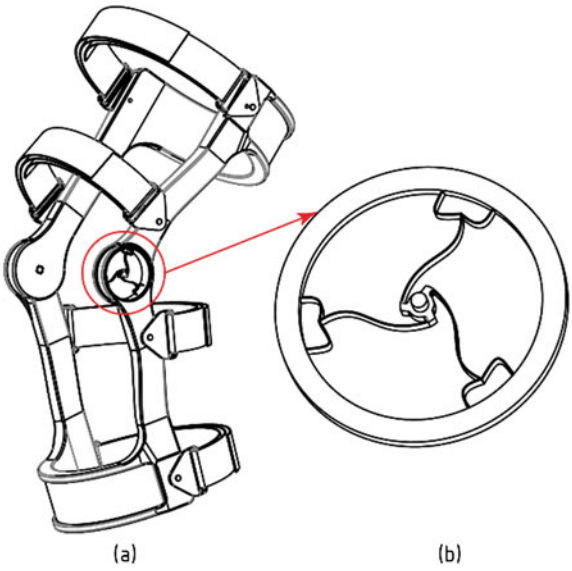

Fig. 44.8 Illustration of applying the CTM in the rehabilitation devices

44.4 Conclusions

In this research, a simple and efficient method for the design of a compliant CTM was proposed. Shape optimization coupled with genetic algorithm has been used during the design process. Taking full advantage of compliant mechanism s, without movable joints, the use of the designed device would result to reduced wear, reduced need for lubrication and increased performance by increasing precision. The feasibility of using the mechanism to achieve constant output torque is confirmed by finite element analyses. The proposed CTM can be used for human joint rehabilitative devices or human mobility-assisting devices. The design could be monolithically fabricated and miniaturized to use in another smaller devices.

References

1. J. McGuire, Ph.D. Dissertation, The University of Texas at Austin (1994)
2. C.W. Hou, C.C. Lan, Mech. Mach. Theory. **62**, 166–181 (2013)
3. H.A. Sierra et al., Adv. Mech. Eng. **7**(6), 1–13 (2015)
4. F. Sup et al., Int. J. Robot. Res. **27**, 263–273 (2008)
5. R.R. Torrealba et al., Mech. Mach. Theory. **116**, 248–261 (2017)
6. Q. Liu, et al., J. Healthc. Eng. 3867243 (2018)
7. A. Kipnis, et al., *United States Patent*, Patent No. 5,399,154 (1995)
8. L.L. Howell, *Compliant Mechanisms* (Wiley-Interscience, New York, 2001)
9. C. Boyle, L.L. Howell, S.P. Magleby, M.S. Evans, Mech. Mach. Theory **38**(12), 1469–1487 (2003)
10. H.T. Pham, D.A. Wang, Mech. Mach. Theory **46**, 899–909 (2011)

11. J.Y. Wang, C.C. Lan, J. Mech. Des. **136**(7), 071008 (2014)
12. H.T. Pham, N.H.N. Hieu, J. Sci. Technol. **115**, 063–068 (2016)
13. Q. Xu, J. Mech. Robot. **9**, 011006 (2017)
14. H.N. Prakashah, H. Zhou, J. Mech. Robot. **8**, 064503 (2016)
15. P. Wang, S. Yang, Q. Xu, Int. J. Precis. Eng. Manuf. **19**(12), 1–8 (2018)
16. H.T. Pham, D.A. Wang, Sens. Actuators A **167**, 438–448 (2011)

Chapter 45
Improve the Loading Capacity and Stiffness of Hydrostatic Spindle Medium Sized Circular Grinding Machines Based on Simulation and Geometric Parameters of the Bearing

Van-Hung Pham, Manh-Toan Nguyen, and Tuan-Anh Bui

Abstract Loading capacity and stiffness of spindle grinding machine are important features that determine the machining capability and precision of the machine. Characteristics of hydrostatic spindle bearing depend on geometric parameters, oil properties, temperature and oil chamber pressure. The hydrostatic spindle bearing with four high pressure chambers has been designed and manufactured for the 3K12 external circular grinding machine with bearing diameter and length corresponding to 70 mm and 56 mm, respectively. This chapter presents a simulation and experimental results to determine oil viscosity in accordance with the actual geometry bearing parameters in order to achieve the highest loading capacity and stiffness of the bearing. This is the base for determining the characteristics of lubricant oil under the specific machining process and working conditions of the hydrostatic spindle bearing.

45.1 Introduction

Hydrostatic bearing systems have been widely used in machine tools, because of their high stiffness. Many researches have been worked to improve the performance of a hydrostatic bearing. In order to improve the bearing performance many methods have been proposed such as: adding a membrane to a restrictor [1, 2] and changing the shape of a recess [3–5]. In addition, the hydrostatic bearings with a variable external flow restrictor have been also proposed as typical examples of the hydrostatic bearing with higher performance [6–9]. By using variable external flow restrictors, the static stiffness of a hydrostatic bearing can be improved significantly. However, such restrictors have a desirable problem which both dynamic stiffness and response are decreased. These studies almost focus on improving performance of hydrostatic

V.-H. Pham · M.-T. Nguyen · T.-A. Bui (✉)
School of Mechanical Engineering, Hanoi University of Science and Technology,
No.1 Dai Co Viet Rd, Hanoi, Vietnam
e-mail: anh.buituan@hust.edu.vn

I. A. Parinov et al. (eds.), *Advanced Materials*, Springer Proceedings
in Materials 6, https://doi.org/10.1007/978-3-030-45120-2_45

bearing by improve bearing design. However, with a designed hydrostatic bearing system, the performance of bearing is also strongly depended on its geometry data. On the other hand, with an existed hydrostatic bearing, there are many methods to improve bearing performance, working oil is an example [10–12]. These studies focuses on finding working oil pressure and viscosity to get the highest stiffness and loading capacity of hydrostatic spindle based on simulation. Furthermore, the performance evaluating experiments are also conducted to verify simulation results.

45.2 Loading Capacity and Stiffness Simulation

Hydrostatic journal bearing used in this study is hydrostatic spindle designed for medium sized circular grinding machine that is constructed of 4 recesses as shown in Fig. 45.1. The recess pressure is controlled by capillary restrictor, spindle diameter is $D = 70$ mm, bearing length is $L = 56$ mm, the eccentricity e of the bearing is 4.5 μm and bush case having no axial groove.

The eccentricity e and relative eccentricity ε of the grinding machine hydrostatic spindle are 4.5 μm and 0.3, respectively, land width of bush case are $a = 14$ mm and $b = 14$ mm. With mentioned geometry parameters, hydrostatic film stiffness can be calculated as [13].

$$J = \frac{p_s \,.\, L \,.\, D}{h_o} . J_n \tag{45.1}$$

where

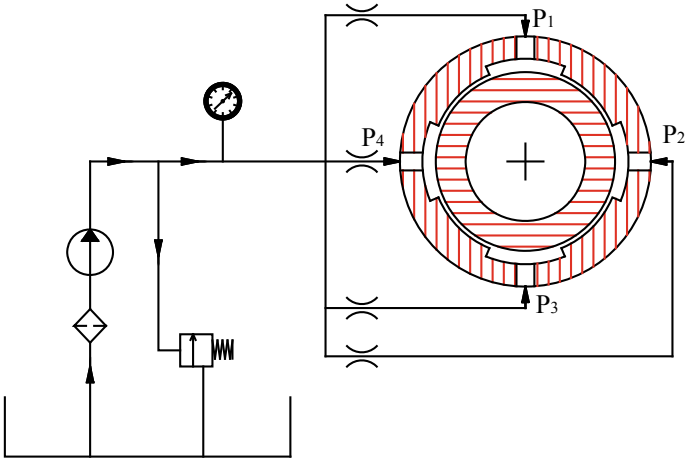

Fig. 45.1 Diagram structure of the hydrostatic spindle unit used for the medium-sized outer grinding machine

$J_n = \frac{3n^2}{2\pi}\frac{\beta\left(1-\frac{a}{L}\right)\sin^2\left(\frac{\pi}{n}\right)}{z+1+2\gamma\,.\,\sin^2\left(\frac{\pi}{n}\right)}$ is the dimensionless stiffness; $n = 4$ is the number of recesses; $\gamma = \frac{n\,.\,a\,.\,(L-a)}{\pi\,.\,D\,.\,b}$ is the circumferential flow factor; $z = \left[\frac{\beta}{1-\beta}\right]$ is used for capillary control; $\beta = \frac{p_r}{p_s}$; $h_o = \frac{e}{\varepsilon} = \frac{4.5}{0.3} = 15$ (μm).

Hence

$$\gamma = \frac{4 * 14 * (56 - 14)}{\pi * 70 * 14} = \frac{2.4}{\pi} \tag{45.2}$$

and

$$J_n = \frac{9 * \beta(1 - \beta)}{\pi + 2.4(1 - \beta)} \tag{45.3}$$

Therefore

$$J = \frac{p_s\,.\,L\,.\,D}{h_o}.\frac{9 * \beta(1 - \beta)}{\pi + 2.4(1 - \beta)} \tag{45.4}$$

On the other hand

$$S_h = \frac{\eta N}{P_s}\left(\frac{D}{2h_o}\right)^2 \tag{45.5}$$

Therefore

$$P_s = \frac{\eta N}{S_h}\left(\frac{D}{2h_o}\right)^2 \tag{45.6}$$

where N is the angular velocity of shaft (rad/s).

Then (45.4) can be rewritten as

$$J = \frac{\eta N\,.\,L\,.\,D^3}{4S_h h_o^3}\frac{9 * \beta(1 - \beta)}{\pi + 2.4(1 - \beta)} \tag{45.7}$$

The bearing stiffness is strongly depended on dynamic viscosity η. MATLAB software was used to simulate a relationship between bearing stiffness and pump pressure p_s, oil viscosity η. In general, viscosity of oil that used for hydrostatic lubrication is chosen low to achieve cooling effect of fluid flow. On the other hand, at low viscosity of oil, it is difficult to achieve very high pressure, in most of cases, pressure of oil is limited by a value no higher than 10 MN/m^2. Therefore, the simulation has been made with a range of viscosity: 0–3 mPa s and pressure: 0–10 MN/m^2. Figure 45.2 shows relationship between bearing stiffness J and oil viscosity, gauge pressure ratio β when diameter of spindle $D = 70$ mm and the fabricated bearing clearance $h_0 = 12$ μm. As it can be seen, stiffness proportional to oil viscosity, increasing in viscosity will result in increasing of bearing stiffness.

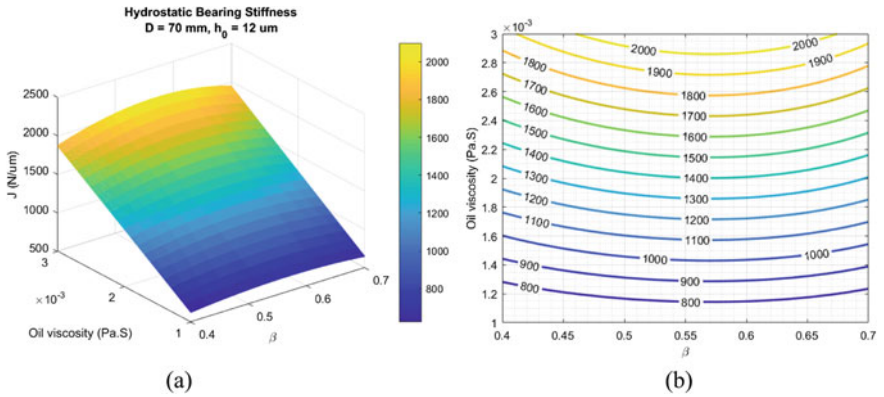

Fig. 45.2 Hydrostatic bearing stiffness with $D = 70$ mm, $h_0 = 12$ μm

Similarly, a relationship between stiffness of the hydrostatic bearing and pump pressure is also simulated to determine the most appropriate pressure value for the fabricated bearing, the simulation result is shown in Fig. 45.3. As it can be seen, the bearing stiffness increasing in proportion to the pump pressure in a range of 0 to 10 MPa. Calculation results show that the appropriate pressure range that satisfies the requires of the hydrostatic bearing applied in machine tools should be greater than 5 MPa. This is also the basis for selecting the oil supply system for the experiment system later.

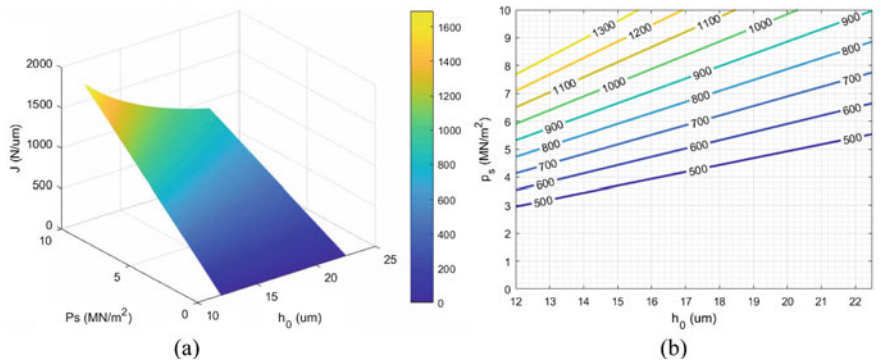

Fig. 45.3 Hydrostatic bearing stiffness with $D = 70$ mm and $\beta = 0.5$

45.3 Experimental Setup

In order to verify simulation results, a testing bench has been set up as shown in Figs. 45.4 and 45.5. There are 2 pneumatic cylinders used to apply load on spindle

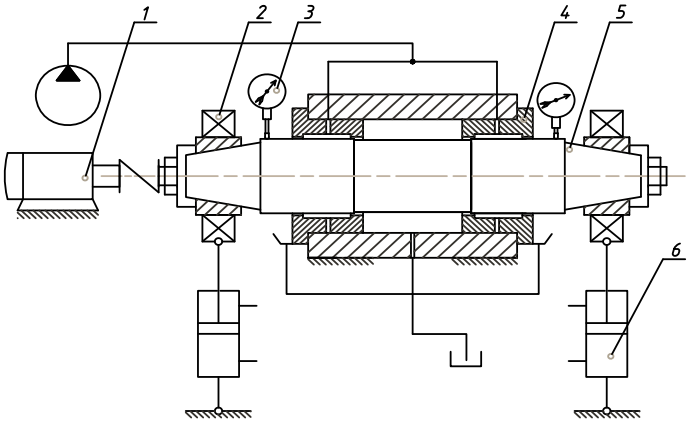

Fig. 45.4 Hydrostatic spindle testing bench layout: 1—motor; 2—journal bearing; 3—radial indicator; 4—bearing bush case; 5—spindle; 6—pneumatic cylinder

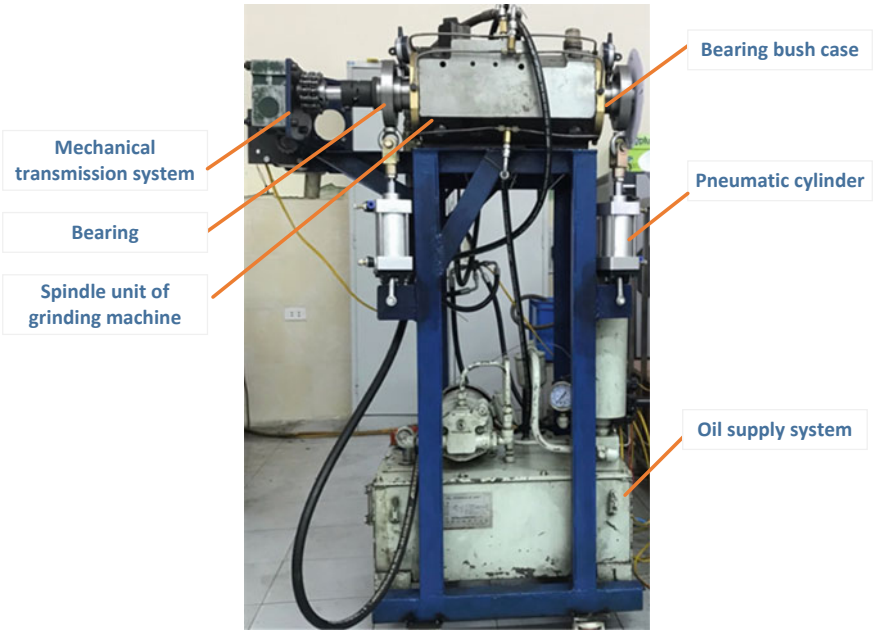

Fig. 45.5 Hydrostatic spindle testing bench

and displacement of spindle is monitored by 2 radial indicators. These pneumatic cylinders are supplied by three separated compressed air sources which are calibrated to corresponding to three designed loads applied to spindle: 500, 1000 and 1500 N. Values of viscosity of oils used in this experiment are equal to: 1, 1.5 and 2 mPa s; and oil pressure is 5 MN/m^2.

45.4 Results and Discussion

The experiment has been carried out step-by-step strictly follow procedure: (i) pumping hydrostatic pressure into bearing; (ii) wait for one minute to ensure stable of pressure oil inside system; (iii) applying load on spindle and see the displacements of spindle. With each load and oil experiment has been done five times and displacement of spindle was averaged on that five displacements. Experimental results are presented in Table 45.1.

Based on the displacement of spindle, experimental stiffness of hydrostatic bearing could be estimated as

$$\frac{1}{J_{\text{bearing}}} = \frac{1}{J} - \frac{1}{J_{\text{shaft}}} \tag{45.8}$$

where J is the stiffness of hydrostatic spindle (N/μm), J_{shaft} is the stiffness of shaft (N/μm), J_{bearing} is the stiffness of bearing (N/μm).

Spindle shaft made of 40XMH steel and stiffness of shaft is about of $J_{\text{shaft}} = 470$ (N/μm) therefore stiffness of hydrostatic bearing, which is obtained from experiment is shown in Table 45.2.

As it can be seen, for viscosity of oil in a range of 1–2 mPa s, stiffness of hydrostatic bearing obtained from simulation is about 700–1400 (N/μm). However, stiffness that obtained from experiment is smaller, it is in the range of 534.09–932.54 N/μm. The stiffness obtained from experiment smaller than that of simulation because of:

(i) In simulation process, spindle shaft and bush case are in ideal conditions: axis of shaft and that of bush cases are parallel. But in fact, in manufacturing and assembly process, these axes are non-parallel.

Table 45.1 Displacement of hydrostatic spindle under loading condition and spindle stiffness

Load (N)	Oil viscosity					
	Spindle displacement (μm)			Stiffness (N/μm)		
	1 mPa s	1.5 mPa s	2 mPa s	1 mPa s	1.5 mPa s	2 mPa s
500	2.0	1.8	1.6	250.0	277.8	312.5
1000	3.8	3.4	3.2	263.2	294.1	312.5
1500	5.8	5.6	5.0	258.6	267.9	300.0

Table 45.2 Experimental stiffness of hydrostatic bearing

Stiffness (N/μm)			
Load (N)	Oil viscosity		
	1 mPa s	1.5 mPa s	2 mPa s
500	534.091	679.191	932.540
1000	597.964	785.953	932.540
1500	575.041	622.792	829.412

(ii) This hydrostatic spindle is upgraded from hydrodynamic spindle of medium sized circular grinding. The bush case housing is original while bush cases are new designed, and they are elastic deformed in assembly process; this deformation is also non-regular deformation on circumference of bush case or bush case is not ideal cylindrical form as in simulation.
(iii) Under high pressure of oil, bush case made by copper bronze also is elastic deformed.
(iv) The deformation of bush case would result in changing of clearance, however this deformation of bush case, bearing, shaft, etc. have not been counted in simulation. Therefore, simulation bearing stiffness is higher than that obtained from experiments.

On the other hand, the experimental results also show that with a known viscosity and pressure, the hydrostatic bearing stiffness is not stable when load is changed. This instability arises since the radial indicators used in experiment have resolution of 1 μm while displacement of spindle is not more than 7 μm so incorrectness in measuring displacement of spindle may result in the stability of stiffness.

It also can be seen that either in simulation or experiment, the stiffness of hydrostatic bearing increase when viscosity of oil is increased. However, high viscosity reduces flow and hence pumping power; moreover, the spindle of grinding machine always works at high speed that leads to high power consumption and requires high flow to achieve cool running so viscosity of oil should not be high. The stiffness of the machine tool spindle is commonly into range of 250–500 N/μm. For medium-sized external cylindrical grinding machines, the total hydrostatic spindle unit stiffness J should reach of 300–500 N/μm [14]. Experiment results pointed out that, with viscosity of 2 mPas, the stiffness of a whole hydrostatic spindle is in a range of 300–500 N/μm. So, the oil viscosity of 2 mPas should be the most feasible for this application.

45.5 Conclusion

This chapter presents a study on numerical simulation and experimental study of hydrostatic bearing spindle stiffness of the medium-sized external cylindrical grinding machine. The simulation results are consisted with experimental results while there are some differences between them, however those differences are reasonable.

The hydrostatic bearing stiffness shows a difference between theoretical calculation and experimental results due to some reasons. Such as a high working pressure may cause an expansion of the copper bush case with a limited thickness, leading to increasing of the bearing clearance, which will increase the flow and reduce the experimental stiffness of the hydrostatic spindle bearing unit.

Both simulation and experiment also point out that the stiffness of a hydrostatic bearing strongly depends on viscosity and pressure of oil. Increasing of viscosity or pressure would result in increasing of stiffness. However, increase of viscosity or pressure will result in some draw back such as decreasing in cooling, pumping up power, etc. With a designed hydrostatic bearing there is a range of hydrostatic parameters that satisfy required stiffness. Therefore, there are always an optimum viscosity and pressure, at which hydrostatic bearing gets the best performance. For instant, with the hydrostatic spindle of medium-sized circular grinding machine, the oil viscosity of 2 mPa s should be the most feasible for the hydrostatic spindle of grinding machine.

References

1. N. Singh, S.C. Sharma, S.C. Jain, S.S. Reddy, Tribol. Int. **37**, 11–24 (2004)
2. Y. Kang, P.C. Shen, Y.P. Chang, H.H. Lee, C.P. Chiang, Tribol. Int. **40**, 1369–1380 (2007)
3. T.A. Osman, Z.S. Safar, M.O.A. Mokhtar, Tribol. Int. **24**(3), 137–141 (1991)
4. S.C. Sharma, S.C. Jain, D.K. Bharuka, Tribol. Int. **35**, 347–356 (2002)
5. S.C. Sharma, V.M. Phalle, S.C. Jain, Tribol. Int. **44**, 617–626 (2011)
6. J.E. Mayer, M.C. Shaw, J. Basic Eng. **85**(2), 291–296 (1963)
7. W.B. Rowe, J.P. O'Donoghue, Proc. Inst. Mech. Eng. **184**(3L), 1–9 (1969)
8. C.K. Singh, D.V. Singh, Wear **44**, 223–230 (1977)
9. X. Zuo, J. Wang, Z. Yin, S. Li, Tribol. Int. **66**, 83–92 (2013)
10. J. Wang, G. Gong, H. Yang, in *Proceedings of the 2008 IEEE/ASME International Conference on Advanced Intelligent Mechatronics* (2008), pp. 1390–1395
11. T. Tsubouchi, J. Shinoda, Tribol. Online. **5**(5), 230–234 (2010)
12. K. Kuze, H. Sawano, H. Yoshioka, H. Shinno, in *Emerging Technology in Precision Engineering XIV*. (2012), pp. 523–537
13. W. Brian Rowe et al., *Hydrostatic, Aerostatic, and Hybrid Bearing Design*, Elsevier (2012)
14. V.-H. Pham, T.-A. Bui, T.-D. Nguyen, J. Sci. Technol. **130**, 17–23 (2018)

Chapter 46
Inverse Method for Estimating the Convection Coefficient at Gap Inside Bearing Rig Test

Thi-Thao Ngo, Jin H. Huang, and Van-The Than

Abstract This paper presents an inverse method to estimate the convection coefficient in the gap of rig test for bearing by using two measured temperatures. The measurement temperatures are obtained by performing the test for different speeds. The temperature is then used as input data in the inverse algorithm. The method is constructed based on finite different thermal model and an optimization method—the conjugate gradient method. After acquiring the convection coefficients for various speeds, formulae of the convection coefficient of two bearing kinds are established. To validate the inverse results, a comparison of simulation and experimental temperatures has been carried out. The results show that the predicted temperatures are in good agreement with the measured temperatures.

46.1 Introduction

Bearing is one of the key components of almost rotating machinery. The bearing is designed to operate at demand speed and load-carrying capacity. In spite of different operational mechanisms and geometry configurations, the bearing is susceptible to a peculiar form of failure known as seizure whose root cause is thermal effects. In high speed machine tool, the bearings are usually used to support the rotation of shaft which connected to cutting tool. At beginning, to issue a new kind of the bearing, temperature characteristics usually considers through rig test model. Stein and Tu [1] applied thermal resistance to predict temperature of the rig test model and further resulting on thermal preload. Takabi and Khonsari [2] also used the thermal network to investigate the thermal induced preload. In their studies, the convection coefficient

T.-T. Ngo · V.-T. Than (✉)
Faculty of Mechanical Engineering, Hung Yen University of Technology and Education, Khoai Chau, Hung Yen, Vietnam
e-mail: thanthe.ck@gmail.com

J. H. Huang
Department of Mechanical and Computer-Aided Engineering, Feng Chia University, Taichung, Taiwan, ROC

I. A. Parinov et al. (eds.), *Advanced Materials*, Springer Proceedings in Materials 6, https://doi.org/10.1007/978-3-030-45120-2_46

inside system was calculated by using some theory and approximate empirical equations. However, these equations are usually established for simple and laboratory conditions. Therefore, determining the convection coefficients to construct an accurate thermal model for rig test is necessary task. Directly measurement the coefficient inside the rig test is very difficult due to complex structure and high-speed rotation. Fortunately, inverse method is an appropriate solution, which is widely utilized in science and engineering. The inverse method is applied to estimate temperature, heat generation, convection coefficients, parameters, etc. which are far from easy to directly measure or calculate. The inverse method has been successfully applied to estimate heat sources and convection coefficients in many researches [3–6]. In this chapter, the inverse method is used to estimate the convection coefficient inside gap of the rig test system. The coefficient is finally formed as a function of speed for convenience during creating the thermal model of various speeds.

46.2 Inverse Algorithm

Figure 46.1 shows the inverse schematic. It shows that the finite different (FD) thermal model is employed. Based on round symmetric property and ignored small structures, the Shaft-Bearing-Housing system is discretized into thirty-one elements and the center of each element is described as a location with average temperature. Heat from the center of one element to the centers of the adjacent elements is transfer through their contact areas.

In order to derive the FD equation for the model, the energy balance method, which enables analysis of many different phenomena, is applied. In the energy balance method, the FD equation for each node is obtained by applying conservation of energy to a control volume about the nodal region (Fig. 46.2) [7].

$$\sum_{n=1}^{4} \frac{T_n - T_i}{R_{in}} + q_i = m_i Cp_i \frac{\partial T_i}{\partial t} \tag{46.1}$$

where T_n is the temperature of the nth node which is related to the node i; T_i is the temperature of node i; R_{in} is the thermal resistance coefficient between nodes i and n; and q_i, m_i and C_i are the heat rate, mass, and thermal capacity of node i, respectively.

The bearing heat generation (q) is determined through the frictional torque of the bearing (M) and speed (n) [7] as following

$$q = 1.047 \times 10^{-4} nM \tag{46.2}$$

$$M = M_1 + M_v + M_s \tag{46.3}$$

$$M_1 = f_1 F_1 d_m \tag{46.4}$$

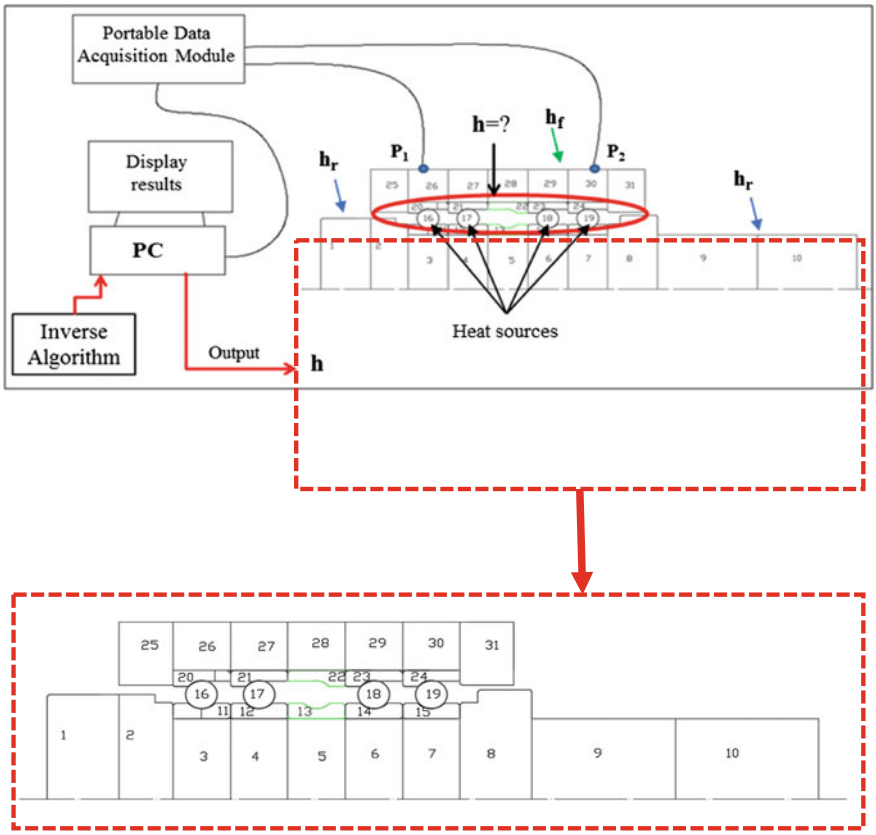

Fig. 46.1 Schematic of inverse method

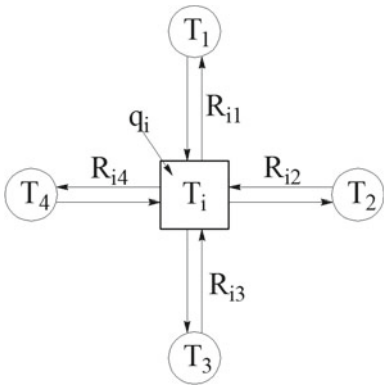

Fig. 46.2 A node with its adjoining nodes

$$M_v = \begin{cases} 10^{-7} \cdot (\nu_0 n)^{2/3} f_v d_m^3 & \text{if } \nu_0 n \geq 2000 \\ 10^{-7} \cdot 160 f_v d_m^3 & \text{if } \nu_0 n < 2000 \end{cases} \tag{46.5}$$

where M_1 and M_v are the friction torque of the bearing related to applied load and lubricant viscosity, respectively. In (46.4), f_1 is a factor related to the type of bearing and load; F_1 represents the static equivalent load; d_m is the pitch diameter. For (46.5), f_v is a factor dependent on the types of bearings and the lubrication method; and ν_0 stands for the kinematic viscosity of the lubricant.

The spinning friction moment can be carried out as

$$M_s = \frac{3\mu Q a E}{8} \tag{46.6}$$

where μ, Q, a, and E are the friction coefficient, normal contact force, semi-major axis of the contact ellipse, and the elliptical integral of the second kind, respectively.

The above equations reveal that the total heat generation is obviously a function of the bearing's parameters, lubricant kinematic viscosity, preload, and rotational speed.

For heat conduction, according to [8], the axial and radial thermal resistance coefficient can be obtained as

$$R_{axial} = \frac{\Delta x}{kA} \tag{46.7}$$

$$R_{radial} = \frac{\ln(r_o/r_i)}{2\pi kL} \tag{46.8}$$

in which Δx and A are the distance and contact area between two node, respectively; k stands the thermal conductivity. In (46.8), r_o, r_i and L denote the external, internal radius and length of element, respectively.

The heat transfer between ball and inner/outer ring is conducted by small ellipse area. The thermal contact resistance of ball and inner/outer ring can be obtained by [9]:

$$R_{br} = \frac{1}{2\pi a k_{ball}} K\left(e, \frac{\pi}{2}\right) + \frac{1}{2\pi a k_{ring}} K\left(e, \frac{\pi}{2}\right) \tag{46.9}$$

where a, b are the semi-axis of the elliptic contact area; $K\left(e, \pi/2\right)$ is the complete integral of the first kind. k_{ball}, k_{ring} are the thermal conductivity of the ball and rings, respectively.

Contact between the outer rings and housing is through a small air gap, so the thermal contact resistance coefficient is determined as [10]:

$$R_{hr} = \frac{h_{ring}}{k_{ring} S} + \frac{h_{gap} - (T_{ring} - T_{housing})\alpha r_{housing}}{k_{air} S} \tag{46.10}$$

where h_{ring}, h_{gap} are the thickness of outer ring and initial clearance of the assembly, respectively; $r_{housing}$ and S are the inside radius of the housing and contact surface area of the outer ring and housing, respectively; α stands for the thermal expansion coefficient.

The contact between inner ring and shaft is a joint under pressure. Therefore, the heat transfer in this contact is considered as smooth and no drop temperature in there.

The convective coefficient can be calculated as

$$h = \overline{Nu} k_{air} / d \tag{46.11}$$

where d is the equivalent diameter, k_{air} is the thermal conductivity of air, and $\overline{Nu}$ is the average Nusselt number. There are three kinds which are natural (h_f), force (h_r) and inside gap (h) convections; and the $\overline{Nu}$ of each kind is determined by:

$$\overline{Nu} = \left\{ 0.6 + 0.387 (Ra_D)^{1/6} \Big/ \left[1 + (0.559/\Pr)^{9/16} \right]^{8/27} \right\}^2 \tag{46.12}$$

$$\overline{Nu} = 0.6366 (\mathrm{Re}\,\Pr)^{1/2} \tag{46.13}$$

Equations (46.12) and (46.13) are applied for natural convection [8] and force convection around rotational shaft [9], respectively.

Most difficult is examination of convection in the gap. Because of the complex structure, the convection coefficient of inside gap cannot be obtained by regular theory. Instead of, an inverse method is applied to estimate the convection coefficient based on measurement temperature for this situation.

To obtain measured temperatures on housing surface, experiment has been performed. Table 46.1 characterizes bearing geometry and Fig. 46.3 shows the schematic of test system, which includes bearing test rig model, driver motor, speed control etc. The system will be controlled and recorded by the temperature results for different speeds.

Two kinds of bearings, 7010 and 7014, are used during the experiments. Table 46.2 characterizes materials of bearing parts and Fig. 46.4 presents structure of the bearing test model. Four bearings, shaft and housing are assembled and then fixed on frame.

Table 46.1 Bearing geometry

Characteristics	7010	7014
I.D (mm)	50	70
O.D (mm)	80	110
Ball diameter (mm)	8.731	11.906
Pitch diameter (mm)	65	90
Width (mm)	16	20
Number of balls	19	21
Nominal contact angle (°)	17	17

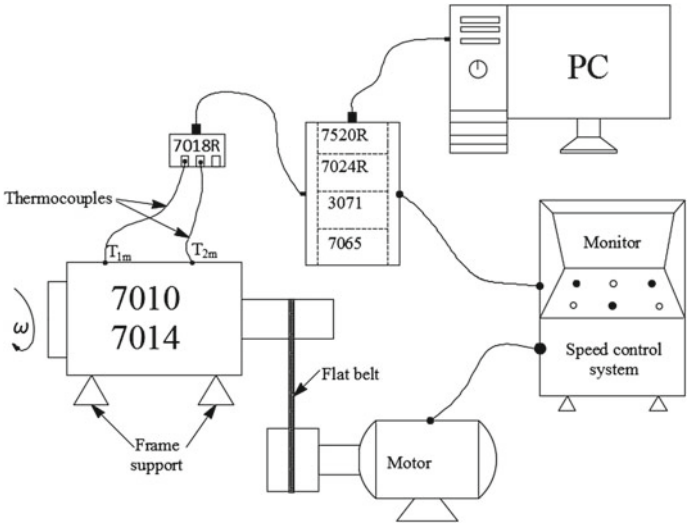

Fig. 46.3 Schematic of experiment

Table 46.2 Bearing parts' materials

	Ball	Rings
Density (kg/m^3)	3200	7830
Thermal conductivity (W/mK)	32.5	42.5
Specific heat (kJ/kg K)	850	470
Expansion coefficient (10^{-6}/K)	3.2	12
Poisson's ratio	0.26	0.3
Young's modulus (GPa)	300	208

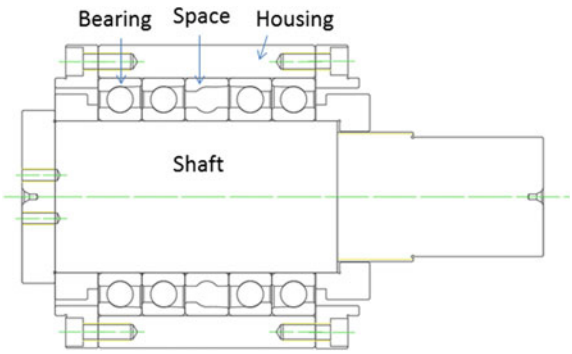

Fig. 46.4 Bearing test model

In the experiments, thermocouple K type with error of 0.10°C is chosen to measure temperature on housing surface. All thermocouples are collected by 7018 module and then transfer to computer for processing and displaying.

The inverse method combines the finite element (FE) thermal model and the conjugate gradient method (CGM). Based on two measured temperatures taken on spindle housing, the solution for the inverse problem is obtained when the objective function is minimized with respect to the unknown parameter h. The objective function has been defined by

$$J(h) = \sum_{j=1}^{M} \left[T_j - T_{jm}\right]^2 \tag{46.14}$$

where T_j and T_{jm} are the estimated and measurement temperatures at the measured points P_1 and P_2. $M = 2$ stands for number of measurement points. The iteration function of CGM is given as

$$h^{k+1} = h^k - \beta^k P^{k+1} \text{ with } k = 0, 1, 2 \ldots \tag{46.15}$$

$$\beta = \sum_{j=1}^{M} \left[T_j - T_{jm}\right] \Delta T \Big/ \sum_{j=1}^{M} [\Delta T]^2 \tag{46.16}$$

$$\Delta T = T(h + \delta h) - T(h) \tag{46.17}$$

where δh should be a real number and be smaller than estimation values. The direction of descent P can be expressed as

$$P^{k+1} = \nabla J^k + r^k P^k \tag{46.18}$$

$$\nabla J = \frac{\partial J}{\partial h} = \frac{J(h + dh) - J(h - dh)}{2dh} \tag{46.19}$$

where dh denotes a small perturbation of the unknown h; and r is the conjugation coefficient:

$$r^k = \sum_{j=1}^{M} \left[(\nabla J)^k \Big/ (\nabla J)^{k-1}\right]^2 \tag{46.20}$$

All above computation procedures is summarized and depicted in Fig. 46.5.

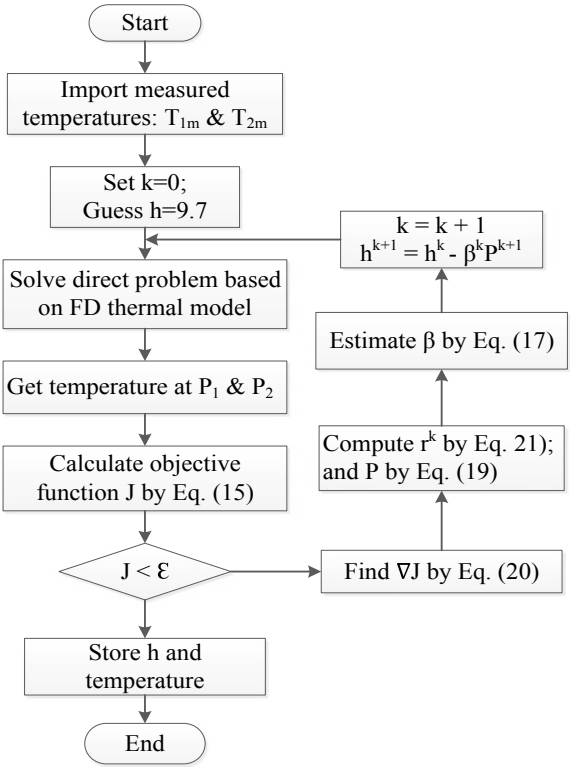

Fig. 46.5 Computation algorithm

46.3 Results and Discussion

46.3.1 Testing Results

The experiment has been performed by running from low to high speeds. Each speed is kept until reach steady-state temperatures; then the speed will be increased. The process is repeated for all demand speeds. Figure 46.6 shows the recorded the temperatures during testing 7010 and 7014 bearings. Temperature results are then listed in Table 46.3.

46.3.2 Inverse Value of h

Based on the experimental temperature, the magnitude of *h* at the gap for different speeds as well as bearing kinds is carried out by present inverse method. Then, 3rd-order polynomial is applied to acquire function for this situation, refer to Fig. 46.7. Equation (46.21a, 46.21b) gives explicit formulae of 7010 and 7014 bearings:

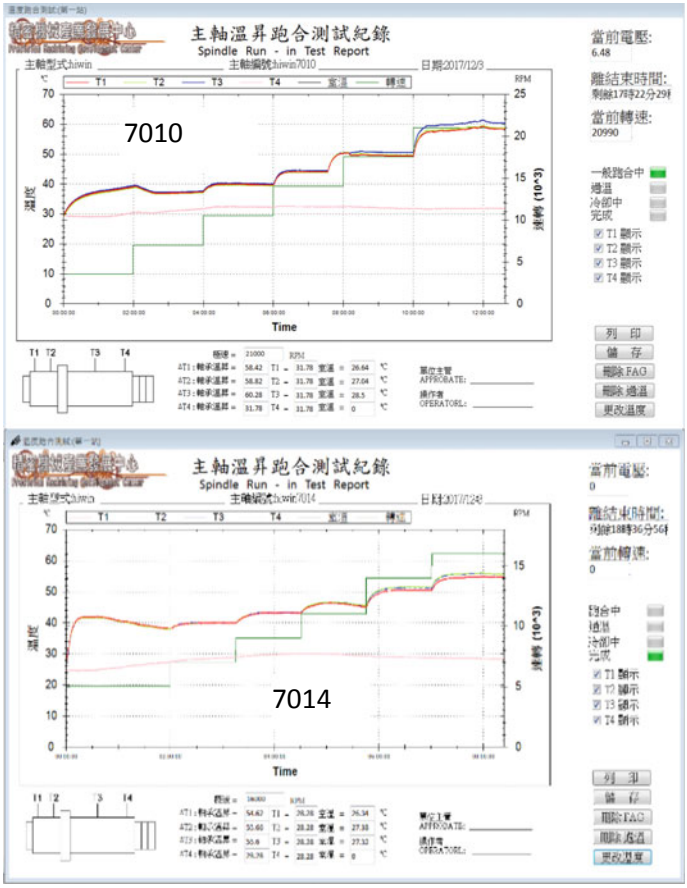

Fig. 46.6 Recorded measurement temperatures

$$h = 2.567 \times 10^{-11} n^3 - 1.512 \times 10^{-6} n^2 + 0.02567n - 36.72 \text{ for } 7014 \tag{46.21a}$$

$$h = a(2.567 \times 10^{-11} n^3 - 1.512 \times 10^{-6} n^2 + 0.02567n - 36.72) \text{ for } 7010 \tag{46.21b}$$

where $a = 1.044 \times 10^{-13} n^3 - 7.351 \times 10^{-9} n^2 + 1.002 \times 10^{-4} n + 1.357$

The formula of h indicates a convection in the gap as function of rotational speed. The magnitude of h is low at low speed and then increase to reach highest value around 12,000 rpm; after that it is decreased. The phenomenon appears due to change of air flow mode [11].

Table 46.3 Experimental temperature results

Speed (rpm)	T_1 (°C)	T_2 (°C)	T_{oo} (°C)
(a) For 7010 bearing			
7000	37	37	31
10,500	40	40	32
14,000	44	44	32
17,500	50	50	32
21,000	58	58	32
23,000	66	66	32
(b) For 7014 bearing			
5000	38	38	27
7000	40	40	29
9000	43	43	30
11,000	45	45	29
14,000	50	51	29
16,000	55	56	28

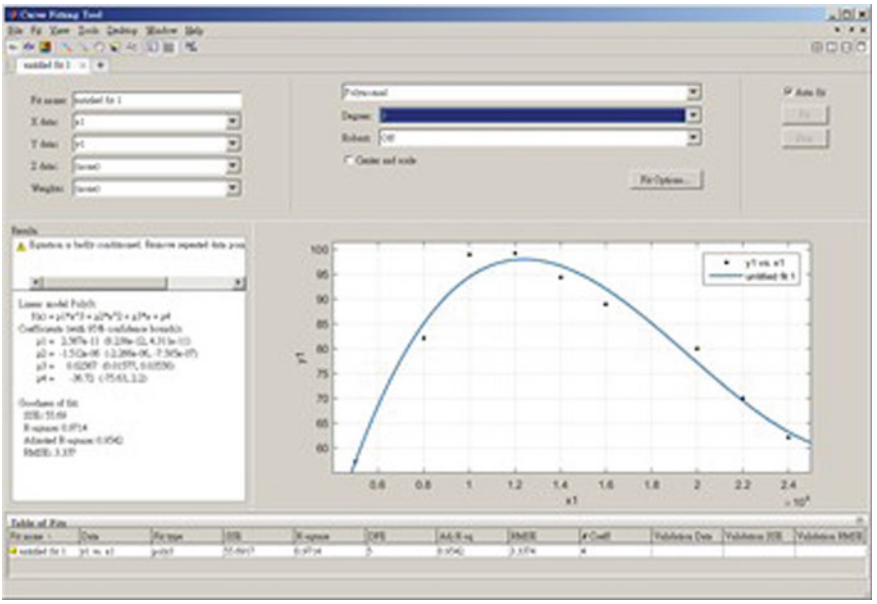

Fig. 46.7 Function of coefficient *h*

46.3.3 Comparison of the Temperature Results

After having the convection coefficients, the simulation temperature can be obtained based on above thermal model.

Figure 46.8 presents a comparison of simulated and measured temperatures. In these figures, T_{1m} and T_{2m} are the temperatures from experiment; and T_{1s} and T_{2s} are the temperatures from simulation. The results show that the simulation temperatures agree well with experimental temperatures. The percentage of different temperatures for all speeds are less than 6%, refer to Tables 46.4 and 46.5. Therefore, it can say that

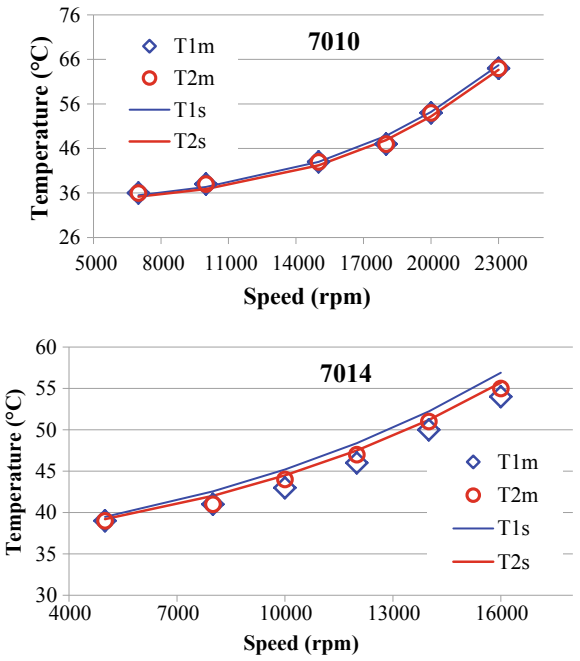

Fig. 46.8 Comparison of temperature results

Table 46.4 Difference of temperature results for 7010

Speed (rpm)	T_1 (°C)			T_2 (°C)		
	T_{1m}	T_{1s}	Error (%)	T_{2m}	T_{2s}	Error (%)
7000	36	35.5	−1.5	36	35.2	−2.3
10,000	38	37.3	−1.7	38	36.9	−3.0
15,000	43	43.0	−0.1	43	42.2	−1.9
18,000	47	48.8	3.9	47	47.9	1.9
20,000	54	54.2	0.4	54	53.2	−1.5
23,000	64	64.7	1.1	64	63.7	−0.5

Table 46.5 Difference of temperature results for 7014

Speed (rpm)	T_1 (°C)			T_2 (°C)		
	T_{1m}	T_{1s}	Error (%)	T_{2m}	T_{2s}	Error (%)
5000	39	39.5	1.2	39	39.2	0.5
8000	41	42.6	3.8	41	42.0	2.5
10,000	43	45.2	5.1	44	44.5	1.1
12,000	46	48.4	5.2	47	47.5	1.1
14,000	50	52.2	4.5	51	51.2	0.4
16,000	54	56.9	5.4	55	55.7	1.3

application of this inverse method to estimate the convection coefficients is accurate and appropriate for current study.

46.4 Conclusion

With steady-state temperature from measurement, the convection coefficient corresponding to each speed is determined by the inverse method. Therefore, the convection coefficient in the gap of bearing test rig structure as a function of rotational speed is issued. Based on the function, the temperature for different speeds are easily predicted. Results indicate that the simulation temperatures are close to the measurement temperatures. Moreover, the results also reveal that percentage errors for all speeds are less than 6%. Hence it can say that the present inverse method can accurately estimate the convection coefficient. The finding here will provide useful information during construct thermal model for similar bearing test system.

References

1. J.L. Stein, J.F. Tu, ASME Control Manuf. Proc. **28**, 31–44 (1991)
2. J. Takabi, M.M. Khonsari, Tribol. Int. **60**, 93–103 (2013)
3. T.-T. Ngo, J.-H. Huang, C.-C. Wang, Int. Commun. Heat Mass Transf. **69**, 66–75 (2015)
4. T.-T. Ngo, J.-H. Huang, C.-C. Wang, Int. Commun. Heat Mass Transf. **71**, 137–147 (2016)
5. Jin-Huang Huang et al., Appl. Therm. Eng. **105**, 65–76 (2016)
6. Van-The Than et al., Int. J. Therm. Sci. **111**, 50–65 (2017)
7. T.A. Harris, *Rolling Bearing Analysis*, 4th edn. (Wiley Inc., New York, 2001)
8. F.P. Incropera, D.P. Dewitt, *Fundamentals of Heat and Mass Transfer*, 7th edn. (Wiley, New York, 2011)
9. K. Nakajima, J. Thermophys. Heat Transf. **9**, 88–95 (1995)
10. B. Bossmanns, J.F. Tu, Int. J. Mach. Tools Manuf **39**, 1345–1366 (1999)
11. P.R.N. Childs, C.A. Long, J. Mech. Eng. Sci. **210**(2), 123–134 (1996)

Chapter 47
Combining the Kalman Filter and Particle Filter in Object Tracking to Avoid Occlusion Problems

Jen-Hong Lan, Ssu-Wei Chen, Chih-Hsueh Lin, Chin-Shiuh Shieh, Shyh-An Yeh, I-Hsing Tsai, Chao-Hong Liu, Chin-Dar Tseng, Hung-Yu Wang, Jia-Ming Wu, and Tsair-Fwu Lee

Abstract We propose a combination of algorithms called the Kalman particle filter (KPF) that overcomes the object tracking occlusion problem in image processing while also achieving a reasonable computation time. When object occlusion occurs while using a Kalman filter (KF), we switch to the particle filter (PF) to track the

J.-H. Lan · C.-H. Lin · C.-S. Shieh · S.-A. Yeh · I.-H. Tsai · C.-H. Liu · C.-D. Tseng · H.-Y. Wang · T.-F. Lee (✉)
Medical Physics & Informatics Lab., Department of Electronics Engineering, National Kaohsiung University of Science and Technology, Kaohsiung 809, Taiwan, ROC
e-mail: tflee@kuas.edu.tw

J.-H. Lan
e-mail: phy10779@gmail.com

C.-H. Lin
e-mail: y4509@yuanhosp.com.tw

C.-S. Shieh
e-mail: csshieh@gmail.com

S.-A. Yeh
e-mail: sayeh@outlook.com

I.-H. Tsai
e-mail: 1105405104@nkust.edu.tw

C.-H. Liu
e-mail: cslin@nkust.edu.tw

C.-D. Tseng
e-mail: 1102405111@gm.kuas.edu.tw

H.-Y. Wang
e-mail: lwan@ms36.hinet.net

J.-H. Lan
Medical Physics and Research Department, Hong Kong Sanatorium & Hospital, 2 Village Road, Happy Valley, Hong Kong, China

S.-W. Chen · T.-F. Lee
Department of Electrical Engineering, National Kaohsiung University of Science and Technology,

I. A. Parinov et al. (eds.), *Advanced Materials*, Springer Proceedings in Materials 6, https://doi.org/10.1007/978-3-030-45120-2_47

object until the system is stable, and then switch back to the KF. We compared the results of running each algorithm (KF, PF, and KPF), independently, executed 30 times; the tracking performance was evaluated using six different methods. We found that KPF successfully addressed the occlusion problem, providing accurate estimates using highly efficient operations.

47.1 Introduction

In recent years, image object tracking has become an important issue in the image processing and computer vision fields. Object tracking is used in many applications, including video surveillance [1, 2], medical electrocardiography [3], biotechnology [4], and vehicle tracking [5, 6]. Common object-tracking algorithms include mean shift [7], optical flow [8], the Kalman filter (KF) [9], and the particle filter (PF) [10]. Each has its advantages as well as its disadvantages. Mean shift has a quick computational speed and thus is useful for visual tracking, but if the camera lens or object being tracked is moving fast, this can lead to inaccurate results. The optical flow algorithm is good for motion detection and object expansion, but it is a large algorithm with a high computational cost; thus, it is better suited for more complex operations than background tracking. The KF algorithm is a fast and optimal recursive algorithm but it cannot be applied to a nonlinear system, leading to decreased accuracy. Finally, the PF algorithm is particularly useful for nonlinear and non-Gaussian estimation tracking [11], but decided that the number of particles is a difficult problem, which will affect the speed of the operation.

Here, we focus on the KF and PF algorithms. Wang et al. [12] used the KF algorithm to characterize moving objects using a red, green and blue color model (RGB) color-based approach, and then applied a threshold to measure the similarity between detected regions. Li et al. [13] used it to track multiple moving people in a room using cameras. Peterfreund [14] used the same algorithm to track contours of non-rigid objects and, in combination with optical-flow measurements, to detect objects.

There have also been a number of studies investigating tracking using the PF algorithm, which takes place in five steps: initialization, prediction, observation

Kaohsiung, Taiwan, ROC
e-mail: matias6933@gmail.com

C.-H. Lin · C.-S. Shieh · H.-Y. Wang · T.-F. Lee
Biomedical Engineering, Kaohsiung Medical University, Kaohsiung 80708, Taiwan, ROC

J.-M. Wu
Department of Biomedicine Engineering, Chengde Medical University, Chengde, Hebei, China
e-mail: jiaming.wu@chmsc.com

Department of Medical Physics, Chengde Medical University, Chengde, Hebei, China

Department of Radiation Oncology, Yee-Zen Hospital, Tao Yuan City 326, Taiwan, ROC

assessment, output, and re-sampling. There are more reports on the observation assessment and re-sampling steps. Based on the literature it can be concluded that a new observation model is needed in the assessment step to compare features and calculate similarities. In particular, the likelihood $p(z_k|x_k)$ distribution needs to be evaluated. To this end, particle likelihood based on color [15] and based on edges [16] have been used, and the two methods have been combined [17]. Regarding the re-sampling step, two classic algorithms have generally been used: sampling importance re-sampling (SIR) [18] and sequential important sampling re-sampling (SIS) [19]. However, some new methods have recently been proposed. For example, Fu et al. [20, 21] proposed the exquisite re-sampling (ER) algorithm. This method has improved accuracy because re-sampled particles reflect more of the probability density function (PDF) of the true state; this maintains the diversity of particles and thus avoids sample impoverishment during particle filtering. Bouaynaya et al. [22] applied a motion-based PF algorithm to track faces, relying on the characterization of the optimal density and Kullback-Leibler (KL) divergence as a similar measure. Abdel-Hadi [23] applied KPF to color-based tracking; it uses color histograms as features and requires a smaller number of particles to reduced computational time, but the image sequences size is big, the computational cost of tracking is increased. Chen et al. [24] applied the Gaussian particle filter (GPF) to track contours.

The remainder of this chapter is structured as follows. The next section presents background on each algorithm, and describes our proposed method, the Kalman particle filter (KPF), and the experimental conditions under which it was tested. Section 47.3 presents the results of the experiment and performance evaluation. Section 47.4 discusses the limitations of our method, suggests future directions for further research, and presents our conclusions.

47.2 Methods

47.2.1 KF

The typical KF process is guided by the following linear difference and measurement equations:

$$x_k = Ax_{k-1} + w_{k-1} \tag{47.1}$$

$$z_k = H_{xk} + v_k \tag{47.2}$$

where x_k and z_k indicate the state and the measurement at time K, A is the transition matrix, H is the measurement matrix, and w_{k-1} and v_k represent the Gaussian process noise and Gaussian measurement noise. The last two terms are normal probability distributions and independent of each other:

$$P(w) \sim N(0, Q) \tag{47.3}$$

$$P(v) \sim N(0, R) \tag{47.4}$$

The KF consists of two types of equations: time update and measurement update equations. The former is responsible for the prediction of the current state and error covariance for estimates to obtain a priori estimates for the next step:

$$\hat{x}_k^- = A\hat{x}_{k-1} + w_k \tag{47.5}$$

$$P_k^- = AP_{k-1}A^T + Q \tag{47.6}$$

Time update and measurement update equations need to form a feedback look for the system measurement update equations, as follows:

$$K_k = P_k^- H^T \left(HP_k^- H^T + R\right)^{-1} \tag{47.7}$$

$$\hat{x}_k = \hat{x}_k^- + K_k\left(z_k - H\hat{x}_k^-\right) \tag{47.8}$$

$$P_k = (I - K_k H)P_k^- \tag{47.9}$$

where K is Kalman gain and R is the measurement variance matrix.

47.2.2 PF

PF, also known as the sequential Monte Carlo or condensation method, uses a weighted sample to represent the PDF, and it can be applied to the state space of the model. It is based on Bayesian estimation, which consists of two important steps: predicting and updating. Given the state vector x_k and observation information $z_{1:k}$ at time k, suppose that the initial probability density $p(x_0)$ of the state variable is known. Then the posterior probability distribution $p\left(x_k|z_{1;k}\right)$ can be obtained by:

$$p(x_k|z_{1:k-1}) = \int p(x_k|x_{k-1})p(x_{k-1}|z_{1:k-1})dx_{k-1} \tag{47.10}$$

where $p(x_k|x_{k-1})$ is a dynamic model. The update step, using the new image z_k is carried out as

$$p(x_k|z_{1:k}) = \frac{p(z_k|x_k)p(x_k|z_{1:k-1})}{\int p(z_k|x_k)p(x_k|z_{1:k-1})} \tag{47.11}$$

where $p(x_k|x_{k-1})$ is the measurement likelihood function, which follows from the observation model, and $p(x_k|Z_{1:k})$ is the normalizing constant.

In PF, for a given proposal density $q\left(x_k|x_{k-1}^n, z_k\right)$, the support of which includes the support of the posterior, the new set of weighted particles at time k, $\left\{w_k^n, x_k^n\right\}_{n=1}^N$, is such that

$$p(x_k|z_{1:k}) \approx \sum_{n=1}^{N} w_k^n \delta\left(x - x_k^n\right) \tag{47.12}$$

where δ is the Dirac delta function, $w_k^i = \tilde{w}_k^n / \sum_{n=1}^N \tilde{w}_k^n$ is the normalized weight, and $\tilde{w}_k^n$ is given by

$$\tilde{w}_k^n = w_{k-1}^n \frac{p\left(x_k^n|x_{k-1}^n\right) p\left(z_k|x_k^n\right)}{q\left(x_k^n|x_{k-1}^n, z_k\right)} \tag{47.13}$$

Given a discrete approximation of the posterior distribution, the average state of all particles to update the target state is the state of the target at time k,

$$\hat{x}_k = \sum_{i=1}^{N} w_k^n x_k^n \tag{47.14}$$

47.2.3 KF and PF Flowchart

Figure 47.1 shows a flowchart of the two algorithms. The basic steps of KF are applied to the initial value, prediction, observation, and update steps. If the KF algorithm is able to track objects and estimate the location of an object or shape and size in the first frame, it will enter the update step and then complete a cycle. For the PF, the basic steps are initialization, prediction, observation, output, and re-sampling.

The initial value is defined as the number of particles with the initial state vector, and so on. The output of the predicted path is obtained through observation; then, the particle is assigned to the position of the greatest chance to complete a cycle.

47.2.4 KF System

The KF algorithm used for tracking is defined in terms of its state and motion model; x_k is a six-dimensional system state vector, which can be expressed as

$$x_k = \left[x_0, y_0, v_{x,k}, v_{y,k}, a_{x,k}, a_{y,k}\right] \tag{47.15}$$

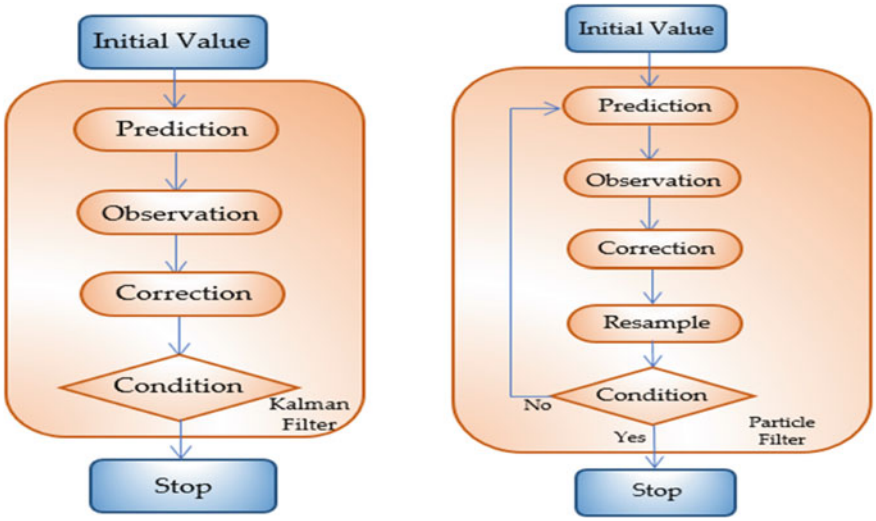

(a) Kalman filter (b) Particle filter

Fig. 47.1 Algorithm flowchart

where x_0 and y_0 represent horizontal and vertical centroid coordinates, $v_{x,k}$ and $v_{y,k}$ are the speeds, and $a_{x,k}$ and $a_{y,k}$ are the accelerations. Before starting the KF algorithm, we need to set the constant matrices A, B, H, Q, R, and I. These constants are set in advance; the more perfectly they are set, the more accurate the prediction and tracking will be, even if in the beginning, the estimate is not very accurate. Through constant corrections and cycles, good results can be obtained. Constant matrices A, B, and H provide important information describing the movement of objects and the observation of behavior, relatively speaking. Q and R, the process noise variance and measurement noise variance, respectively, are also critical in most applications. The initial values of A, Q, I, B, H, and R are as follows:

$$A = \begin{bmatrix} 1&0&1&0&0&0 \\ 0&1&0&1&0&0 \\ 0&0&1&0&1&0 \\ 0&0&0&1&0&1 \\ 0&0&0&0&1&0 \\ 0&0&0&0&0&1 \end{bmatrix} \quad Q = \begin{bmatrix} 200&0&1&0&0&0 \\ 0&200&0&1&0&0 \\ 0&0&20&0&1&0 \\ 0&0&0&20&0&1 \\ 0&0&0&0&20&0 \\ 0&0&0&0&0&20 \end{bmatrix} \quad I = \begin{bmatrix} 1&0&0&0&0&0 \\ 0&1&0&0&0&0 \\ 0&0&1&0&0&0 \\ 0&0&0&1&0&0 \\ 0&0&0&0&1&0 \\ 0&0&0&0&0&1 \end{bmatrix}$$

$$B = \begin{bmatrix} 0&0&0&0&0&0 \end{bmatrix} \quad H = \begin{bmatrix} 1&0&0&0&0&0 \\ 0&1&0&0&0&0 \end{bmatrix} \quad R = \begin{bmatrix} \left(\frac{2}{2.98}\right)^2 & 0 \\ 0 & \left(\frac{2}{2.98}\right)^2 \end{bmatrix}$$

If Q is estimated accurately, the estimated value of the confidence interval will be relatively small (see Fig. 47.2a). In contrast, if Q is estimated incorrectly, the

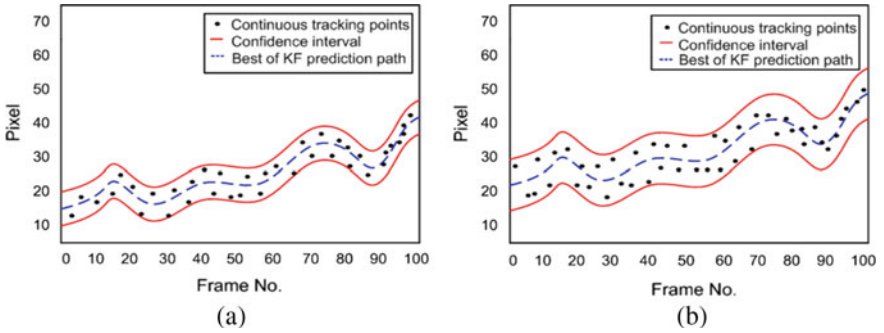

Fig. 47.2 Degree of influence of confidence interval: **a** narrow confidence interval; **b** wide confidence interval

estimated value of the confidence interval will be relatively high (see Fig. 47.2b). R affects the tracking rate; that is, it is the convergence rate.

Thus, we can almost determine the position at which the object will appear between the confidence intervals the next time. At the end of the initial steps, we continue to the next steps. According to (47.5) and (47.6), the new forecast range is calculated as follows:

$$x_s = \left[\hat{x}_k^-\right]_{1,1} - 1.97\sqrt{\left[\widehat{P}_k^-\right]_{1,1}} \rightarrow \left[\hat{x}_k^-\right]_{1,1} + 1.97\sqrt{\left[\widehat{P}_k^-\right]_{1,1}} \tag{47.16}$$

$$y_s = \left[\hat{x}_k^-\right]_{2,1} - 1.97\sqrt{\left[\widehat{P}_k^-\right]} \rightarrow \left[\hat{x}_k^-\right]_{2,1} + 1.97\sqrt{\left[\widehat{P}_k^-\right]_{2,1}} \tag{47.17}$$

In the predicted range of the target, we use a fast and simple method to set the color range of the characteristics of interest. We extract the f_r, f_g, and f_b color of the channel in the first frame, and then use the three-color channels to get a grayscale image, f_y:

$$f_y = (f_r \times 0.3) + \left(f_g \times 0.59\right) + (f_b \times 0.11) \tag{47.18}$$

$$f_{ra}(x, y) = \begin{cases} 255 & f_r(x_s, y_s) - f_{\mathrm{CROI}}(x_s, y_s) \leqq th' \\ 0 & \text{otherwise} \end{cases} \tag{47.19}$$

where f_{CROI} is the color range of the characteristics of interest, and must be a two-dimensional (2D) image, and th' is the threshold, used to remove the noise. Generally, if the KF algorithm does not find the target, it must search the whole image until the target is found again. In our proposed method, when this happens, we use the PF algorithm to track the object. However, before initiating the PF algorithm, we have to find the characteristic values of the target, and then calculate its similarity with the pre-set characteristic values.

47.2.5 PF System

To enhance the reliability of tracking, we use a novel color statistics method to track objects. First, we need to set the initial constants; these include the number of particles N and the color template q(u). Second, we need to spread the particles on the image and use the state transition matrix model to predict the state of each particle at the next time:

$$x_k = F x_{k-1} + w_{k-1} \tag{47.20}$$

where $F = \begin{bmatrix} 1\,0\,1\,0 \\ 0\,1\,0\,1 \\ 0\,0\,1\,0 \\ 0\,0\,0\,1 \end{bmatrix}$ defines the deterministic component of the model, and w_{k-1} is a multivariate Gaussian random variable.

In the general tracking approach, a similar measurement is used for the color histogram of the Bhattacharyya coefficient [25]; it is a representation of the distance. Assume that the color histogram $q = \{q(u)\}$ with for the target, and $p(x) = \{pu\,(x)\}$ with $\sum_{u=1}^{Na} q^{(u)} = 1$ for the candidate, where x is the center of the candidate location, and $u = 1,\ldots, Na$ denote the bins of the histogram, and the Bhattacharyya coefficient is:

$$D_{ba} = \sqrt{1 - \sum_{u=1}^{Na} \sqrt{p^{(u)}(x) - q^{(u)}}} \tag{47.21}$$

Because this method is a traditional PF algorithm, it is must compute the rectangular range of each particle, which requires a very large amount of computational resources. On the other hand, if the object is moving quickly, close to the lens or very far away from the lens, this will make it difficult to set the rectangle size, which will have an impact on the tracking effect.

In our approach, to improve the calculation time, we do not use the color histogram method. Instead, we use a new color statistical method, called the color block (CB) method. We have established a distance formula:

$$D[p(x), q] = \sqrt{1 - \sum_{u=1}^{Na} \left(p^{(u)}(x) - q^{(u)}\right)} \tag{47.22}$$

where x is the center of the candidate location, $u = 1,\ldots, Na$ indicates the RGB color vector, and $q(u)$ is the reference value of the original RGB color block. Then,

$$p^{(u)}(x) = \left(\sum_{i=1}^{m} \sum_{j=1}^{n} fr_k^{(ij)}, \sum_{i=1}^{m} \sum_{j=1}^{n} fg_k^{(ij)}, \sum_{i=1}^{m} \sum_{j=1}^{n} fb_k^{(ij)} \right)^{\mathrm{T}} \tag{47.23}$$

where $\sum_{i=1}^{m} \sum_{j=1}^{n} fr_k^{(i,j)}$, $\sum_{i=1}^{m} \sum_{j=1}^{n} fg_k^{(i,j)}$ and $\sum_{i=1}^{m} \sum_{j=1}^{n} fb_k^{(i,j)}$ are the totals of the RGB image of each particle block size.

To get the weight of each particle, we have to first calculate the color blocks from the substitution standard normal distribution and calculate their weight. The normal distribution of the probability density function of the mean variance is an instance of the Gaussian function:

$$f(x; \mu, \sigma) = \frac{1}{\sigma\sqrt{2\pi}} \exp\left(-\frac{(x-u)^2}{2\sigma^2} \right) \tag{47.24}$$

If there is a random variable subject to this distribution, we write. If $\mu = 0$ and $\sigma = 1$, this distribution is called a standard normal distribution, and this distribution can be simplified as

$$w_0(x) = \frac{1}{\sqrt{2\pi}\sigma} \exp\left(-\frac{(D[p(x), q])^2}{2\sigma^2} \right) \tag{47.25}$$

To obtain the state estimates, we use the following formula to calculate the a posteriori probability; it is the a priori probability multiplied by similarity, and then divided by the standardized similarity, to obtain the state estimate.

$$\hat{X}_K = \sum_{i=1}^{N} W_0^{(i)} X_k^{(i)} \tag{47.26}$$

$$W_0^{(i)} = \frac{W_0^{(i)}}{\sum_{i=1}^{N} W_0^{(i)}} \tag{47.27}$$

If after a few iterations, including the initialization, prediction, and updating steps, the particle degeneracy problem occurs, re-sampling is a common way to reduce the effects of degeneracy. In our proposed method, we use SIR, which is divided into the following three steps:

1. Calculation of the $N_{eff} = \frac{1}{\sum_{i=1}^{N} [0\tilde{w}_k^i]^2}$;
2. If $N_{eff} < N_{th}$, where N_{th} is preset threshold

$$\left\{ x_k^i, \frac{1}{N} \right\}_{i=1}^{N} = \text{Resampling}\left[\left\{ \tilde{x}_k^{(i)}, \tilde{w}_k^{(i)} \right\}_{i=1}^{N} \right]$$

3. Else

$$\left\{x_k^{(i)}, w_k^{(i)}\right\}_{i=1}^{N} = \left\{x_k^{(i)}, w_k^{(i)}\right\}_{i=1}^{N}$$

END

47.2.6 Combination of KF and PF

The combining of KF and PF would normally require excessive calculation. To get around this problem, we use an escape method. Specifically, when the KF operation encounters an object that is too fast or too sheltered, the method switches to a full-screen search using PF to enhance object tracking.

Figure 47.3 compares the KF and KPF methods. When the times from 0 to 19 are used with the KF algorithm, they estimate the confidence intervals p_k and the updated p_k^- and are able to find objects. When the time is 20, if the object is too fast, or encounters a shelter and escapes out of the confidence interval, the traditional KF algorithm searches the whole screen for the target, whereas the new algorithm uses PF to replace KF, until the system is stable, and then switches back to KF.

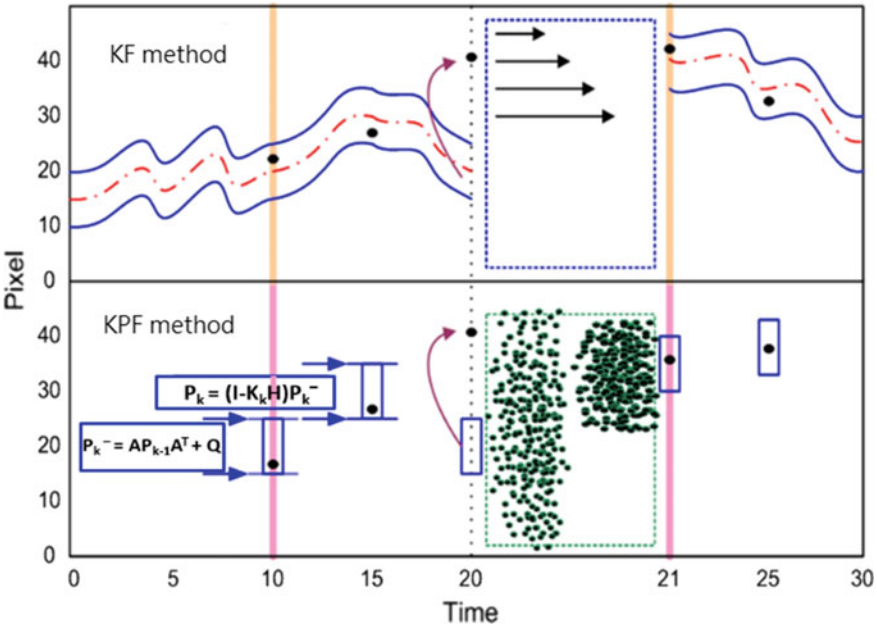

Fig. 47.3 Description of the algorithm process for the Kalman particle filter (KPF)

47.2.7 Performance Evaluation

To assess true path compared to an experimental path, several different methods have been developed, such as root mean square error (RMSE), mean square error (MSE), sum of squares due to error (SSE), mean absolute error (MAE), peak signal-to-noise ratio (PSNR), and Euclidean distance (ED).

The MSE [26] is defined between the parameters of tracked true path and the object bounding box path over all frames in a video as

$$\mathrm{MSE}_{\left(X_k^{(i)}, Y_k^{(j)}\right)} = \frac{1}{N_p}\sum_{i=1}^{N_p}\left(X_k^{(i)} - \hat{x}_k^{(i)}\right)^2 + \frac{1}{N_p}\sum_{j=1}^{N_p}\left(Y_k^{(j)} - \hat{Y}_k^{(j)}\right)^2 \tag{47.28}$$

where $X_k^{(i)}$ and $Y_k^{(j)}$ are true path centroids, $\widehat{X}_k^{(i)}$ and $\widehat{Y}_k^{(j)}$ are computed centroids, and N_p is the total number of frames in a video. The RMSE is the square root of the MSE; the formula is as follows:

$$\mathrm{RMSE}_{\left(X_k^{(i)}, N_k^{(j)}\right)} = \sqrt{\frac{1}{N_p}\sum_{i=1}^{N_p}\left(X_k^{(i)} - \hat{x}_k^{(i)}\right)^2 + \frac{1}{N_p}\sum_{j=1}^{N_p}\left(Y_k^{(j)} - \hat{Y}_k^{(j)}\right)^2} \tag{47.29}$$

The SSE and MSE are closely related, and the statistical parameter SSE is the sum of the squares for the real and object paths. The formula is as follows:

$$\mathrm{SSE}_{\left(X_k^{(i)}, Y_k^{(j)}\right)} = \sum_{i=1}^{N_p} X_k^{(i)} - \widehat{X}_k^{(i)} + \frac{1}{N_p}\sum_{j=1}^{N_p}\left(Y_k^{(i)} - \widehat{Y}_k^{(j)}\right) \tag{47.30}$$

With the MSE, RMSE, and SSE, smaller values indicate greater similarity. The PSNR [27] value is an extension of the MSE. Generally, the higher the value of PSNR, the better the quality. The formula is as follows:

$$\mathrm{PSNR}_{\left(X_k^{(i)}, Y_k^{(j)}\right)} = 10\log_{10}\frac{255^2}{\mathrm{MSE}_{\left(X_k^{(i)}, Y_k^{(j)}\right)}} \tag{47.31}$$

The main purpose of MAE is to assess the absolute gap between the real and the object path. It is similar to MSE, where smaller values indicate greater similarity:

$$\mathrm{MAE}_{\left(X_k^{(i)}, Y_k^{(j)}\right)} = \sum_{i=1}^{Np}\left|\left(X_k^{(i)} - \widehat{X}_k^{(i)}\right)\right| + \sum_{j=1}^{Np}\left|\left(Y_k^{(j)} - \widehat{Y}_k^{(j)}\right)\right. \tag{47.32}$$

ED is most readily understood as a distance calculation method, which estimates the similarity measure between different samples in classification. Generally,

it calculates the distance between the samples, the Euclidean distance between two n-dimensional vectors:

$$\mathrm{ED}_{\left(X_k^{(i)}, Y_k^{(j)}\right)} = \sqrt{\sum_{i=1}^{N_p}\left(X_k^{(i)} - \widehat{X}_k^{(i)}\right)^2 + \frac{1}{N_p}\sum_{j=1}^{N_p}\left(Y_k^{(j)} - \widehat{Y}_k^{(j)}\right)^2} \tag{47.33}$$

We used each of these six assessment tools to evaluate our algorithm and compare its performance to PF and KF. The mean values (standard deviation) of object tracking for 30 time paths were analyzed, with the exact t–test used to compare the difference between KPF and the other algorithms. A two–tailed value of $p < 0.05$ was deemed to indicate statistical significance.

47.3 Experimental Results

Figures 47.4, 47.5 and 47.6 show the experimental results of the KF, PF, and KPF algorithms, respectively. When using KF, the object became occluded at image frame 53 (Fig. 47.4). Because this algorithm cannot track objects in the prediction range, it must search the full screen until it finds objects. However, when searching the full screen, the detection of any other objects may cause the algorithm to begin to track those instead of the target, a major tracking error. This occurred from frame 53 until the end. PF showed good performance in response to occlusion (Fig. 47.5), but the number of particles (here, set to 2000) affected its speed. As shown in Fig. 47.6, our KPF method ran well when the object was not obscured or moved too fast, and

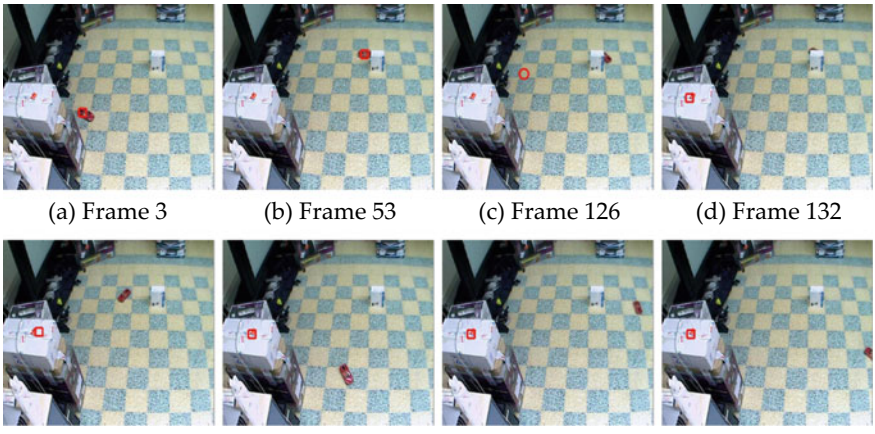

(a) Frame 3 (b) Frame 53 (c) Frame 126 (d) Frame 132

(e) Frame 147 (f) Frame 173 (g) Frame 222 (h) Frame 328

Fig. 47.4 Experimental results of the Kalman filter for remote control cars

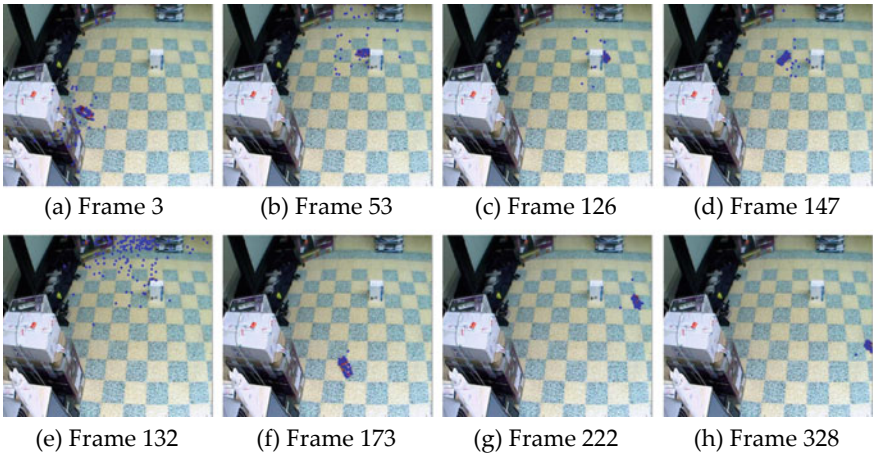

(a) Frame 3 (b) Frame 53 (c) Frame 126 (d) Frame 147

(e) Frame 132 (f) Frame 173 (g) Frame 222 (h) Frame 328

Fig. 47.5 Experimental results of the particle filter for remote control cars

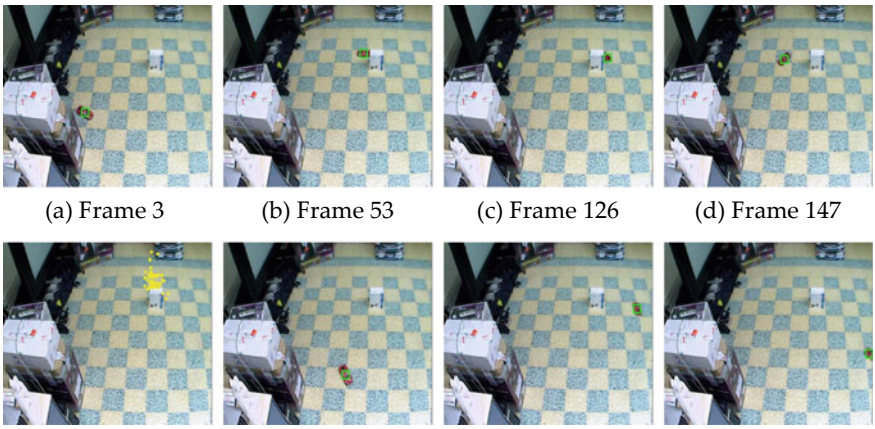

(a) Frame 3 (b) Frame 53 (c) Frame 126 (d) Frame 147

(e) Frame 132 (f) Frame 173 (g) Frame 222 (h) Frame 328

Fig. 47.6 Experimental results of the Kalman particle filter for remote control cars

showed faster computing speeds. When the object was obscured (frame 53), the algorithm automatically switched to PF, as shown in frame 132. Once the system stabilized, the algorithm returned to KF for accelerated operation, as shown in frames 147 until the end.

Table 47.1 shows the results of executing each algorithm 30 times. The computation speed of KPF was faster than the other algorithms. It also had a standard deviation near 0, indicating excellent accuracy. In contrast, in the other algorithms, execution paths tended to differ between runs. Figure 47.7 shows the average path

Table 47.1 Comparisons of the Kalman filter algorithm (KF), Particle filter algorithm (PF), Kalman particle filter algorithm (KPF) ($n = 30$)

Parameter	KF	PF	KPF	P1 value	P2 value
Elapsed time	7.88 ± 0.05	8.98 ± 0.057	7.4 ± 0.172	<0.001	<0.001
RMSE	6022.48 ± 3.70E−12	1886.17 ± 2.09E+03	910.03 ± 4.59E+02	<0.001	0.015
MSE	3.63E+0 ± 1.52E−08	7.80E+06 ± 1.41E+07	1.03E+06 ± 1.18E+06	<0.001	0.011
SSE	1.62E+10 ± 0.0	3.5E+09 ± 6.324E+09	4.63E+08 ± 5.30E+08	<0.001	0.011
MAE	5.06E+07 ± 0.0	1.22E+07 ± 1.92E+07	2.34E+06 ± 2.08E+06	<0.001	0.007
PSNR	−27.46 ± 1.81E−14	−11.04 ± 11.83	−10.1 ± 3.75	<0.001	0.708
EUD	7.22E+0 ± 1.85E−12	2.12E+03 ± 2.09E+03	1.28E+03 ± 4.59E+02	<0.001	0.035

Abbreviation: *RMSE* The Root Mean Square Error; *MSE* The Mean Square Error; *SSE* The Sum of Squares due to Error; *MAE* The Mean Absolute Error; *PSNR* The Peak Signal-to-Noise Ratio *EUD* The Euclidean Distance
P1 value: KPF algorithm compared with KF algorithm
P2 value: KPF algorithm compared with PF algorithm

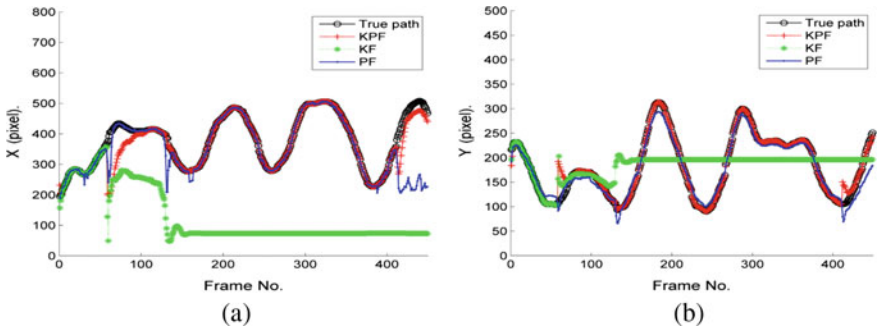

Fig. 47.7 Average path for tracking algorithms: **a** coordinates of X-direction; **b** coordinates of Y-direction

of each method for the 30 runs graphically. KPF provided good performance, both in terms of computing time and the performance evaluation.

47.4 Discussion

KPF can track an object in a sequence of images as well as in real-time situations, but in some cases the tracking is limited. For example, if the environment around the object is similar to the color, shape, or size of the target, it will likely cause tracking failure or a reduced accuracy rate. In addition, if there is a lack of light, too much light, or the object's speed is too fast, then the algorithms are not likely to be able to track objects.

The third issue is the number of particles; it is key to set the correct number of particles and to determine the size of the object being tracked. A new adaptive method for determining the quantity of particles is required. Chen et al. [24] proposed an adaptive GPF for comparing algorithms, such as the GPF mean shift, the PCA-based PF, and the adaptive template match. The adaptive GPF algorithm is highly accurate. Especially for contour tracking, the result is quite remarkable, but the Gaussian process is more sensitive to the background. If the background is fixed, the Gaussian PF shows good tracking. However, when the background moves, this may cause some noise, and this method loses its accuracy. However, there are many methods that can be used to remove noise. Bouaynaya et al. [22] proposed a motion-based PF algorithm for tracking target objects. It is fast and accurate, using a state vector as a differential between the average estimate and the previous average estimate, and characteristics of the KL divergence measure. However, because a complex environment for the divergence operation could cause a rupture of the image, this method is not suitable for use in complex environments. Hence, we proposed the KPF method, which shows improved performance whether in a simple or complex environment, even if the background is not fixed. Its speed is comparable to the adaptive GPF and MBPF methods.

KPF can be used in real-time systems, for example, for tracking traffic to reduce accident rates. In addition, because its resistance to obscured situations is good, it may be useful in biomedical and automotive applications, and could even be applied to near-field communications for remote control applications. These possibilities should be considered in future research.

In conclusion, our proposed KPF system can successfully track objects quickly and efficiently, even when target objects are periodically occluded.

Acknowledgements We thank Jia-Yu Chen and Jung-Ting Hsieh for editing technical supports. This study was supported financially, in part, by grant from MOST-107-2221-E-992-014-MY2.

References

1. Y.-L. Tian, M. Lu, A. Hampapur., in *2005 IEEE Computer Society Conference on Computer Vision and Pattern Recognition (CVPR'05)* (2005)
2. J. Zhu, Y. Lao, Y.F. Zheng, IEEE Trans. Circuits Syst. Video Technol. **20**(2), 223–235 (2009)
3. R. Vullings, B. De Vries, J.W. Bergmans, IEEE Trans. Biomed. Eng. **58**(4), 1094–1103 (2010)
4. E. Maggio, F. Smerladi, A. Cavallaro, IEEE Trans. Circuits Syst. Video Technol. **17**(10), 1348–1359 (2007)
5. A. Jazayeri et al., IEEE Trans. Intell. Transp. Syst. **12**(2), 583–595 (2011)
6. T. Xiong, C. Debrunner, IEEE Trans. Intell. Transp. Syst. **5**(4), 324–328 (2004)
7. D. Comaniciu, V. Ramesh, P. Meer., in *Proceedings IEEE Conference on Computer Vision and Pattern Recognition. CVPR 2000 (Cat. No. PR00662)* (2000)
8. J.L. Barron, D.J. Fleet, S.S. Beauchemin, Int. J. Comput. Vision **12**(1), 43–77 (1994)
9. A. Czyzewski, P. Dalka., in *2008 Ninth International Workshop on Image Analysis for Multimedia Interactive Services* (2008)
10. M.Z. Islam, C.-M. Oh, C.-W. Lee, Int. J. Signal Process., Image Process. Pattern, **2**(1) (2009)

11. T. Zhang, et al., in *2008 International Conference on Intelligent Computation Technology and Automation (ICICTA)* (2008)
12. J. Wang, et al., in *2010 2nd International Conference on Advanced Computer Control* (2010)
13. X. Li, et al., in *The 2010 IEEE International Conference on Information and Automation* (2010)
14. N. Peterfreund, IEEE Trans. Pattern Anal. Mach. Intell. **21**(6), 564–569 (1999)
15. Y. Wu, T.S. Huang, Int. J. Comput. Vision **58**(1), 55–71 (2004)
16. M. Isard, A. Blake, Int. J. Comput. Vision **29**(1), 5–28 (1998)
17. C. Yang, R. Duraiswami, L. Davis, in *Tenth IEEE International Conference on Computer Vision (ICCV'05)*, **1** (2005)
18. J.S. Liu, R. Chen, J. Am. Stat. Assoc. **93**(443), 1032–1044 (1998)
19. S. Maskell, N. Gordon, *Target Tracking*: *Algorithms and Applications* (Ref. No. 2001/174), IEE, **2**, 21–215 (2001)
20. X. Fu, Y. Jia, IEEE Trans. Signal Process. **58**(10), 5414–5420 (2010)
21. X. Fu, et al., in *Proceedings of the 2010 American Control Conference* (2010)
22. N. Bouaynaya, D. Schonfeld, IEEE Trans. Circuits Syst. Video Technol. **19**(7), 1068 (2009)
23. A. Abdel-Hadi, in *The 2010 International Conference on Computer Engineering and Systems* (2010)
24. P. Chen et al., IET Image Proc. **5**(5), 440–447 (2011)
25. T. Xiong, C. Debrunner., in *International Conference on Computer Analysis of Images and Patterns* (2003)
26. S. Nigam, A. Khare, IET Comput. Vision **6**(3), 231–251 (2012)
27. A. Ichigaya et al., IEEE Trans. Circuits Syst. Video Technol. **16**(2), 251–259 (2006)

Chapter 48
Generative Artificial Neural Network Model for Visualization of Internal Defects of Structural Elements

Arcady Soloviev, Boris Sobol, Pavel Vasiliev, and Alexander Senichev

Abstract This paper considers a simplified version of a deep generative convolutional neural network. The model is designed to generate images containing various forms of defects. Defects are presented as a simplified basic geometric primitive. At the network input, parameters are described that initiate the class of the figure and its geometric characteristics. The proposed model is designed to conduct research on the quality of image generation, the possibility of combining various types of defects, studying the influence of various parameters of the training set. Based on these studies, it is possible to build a more advanced generative model capable of restoring the shape of internal defects in structural elements based on ultrasonic non-destructive testing methods.

48.1 Introduction

Currently, artificial neural networks have found great application in the tasks of automatically extracting features from data. New models of neural networks are being developed that allow replacing manual data processing and at the same time increasing the complexity of the extracted features so that it will be difficult for a person to interpret them. Often, when training neural networks, it is difficult to understand what hidden features play a major role in the learning process.

A. Soloviev
Department of Theoretical and Applied Mechanics, Don State Technical University, Gagarin Square 1, Rostov-on-Don, Russia 344010

Institute of Mathematics, Mechanics and Computer Sciences, Southern Federal University, 8a Milchakova Str., Rostov-on-Don, Russia 344000

B. Sobol · P. Vasiliev (✉) · A. Senichev
Department of Information Technologies, Don State Technical University, Gagarin Square 1, Rostov-on-Don, Russia 344010
e-mail: lyftzeigen@mail.ru

I. A. Parinov et al. (eds.), *Advanced Materials*, Springer Proceedings in Materials 6, https://doi.org/10.1007/978-3-030-45120-2_48

When solving the inverse problems of mechanics, identification of defects, it is required to localize the defect and restore its geometric parameters. A wide range of approaches is used to solve such problems. Most of which are based on non-destructive testing methods. Also, recently, thanks to the development of neural network technologies, it has become possible to process large amounts of data in various representations.

Known works in which neural network methods are used in combination with the classical approaches of non-destructive ultrasonic testing [1]. As a result of finite element modeling, large amounts of data are collected, which can be interpreted and processed differently by neural networks. It can be fully connected, recurrent networks or convolutional neural networks.

48.2 Related Work

In recent years, many researchers have focused their efforts on the improvement of algorithms for detection of defects and the development of methods for automatic detection of cracks in the parts of structures and infrastructure. As practice has shown, the field of computer vision, aimed at detecting defects, is constantly evolving with steady progress in sensing technology, hardware and software. Despite this, there are still limitations to existing methods and approaches. In the field of detection of defects in structural elements, such restrictions may be, for example, the heterogeneity of the defects, a wide variety of surface types, the complexity of the background, various adjacencies, and more.

Convolutional neural network (CNN) is an architecture of artificial neural network, specially designed to work with images [2]. CNN is a multilayer neural network architecture that implements local receptive fields through convolutional layers and invariance of relatively small geometric deformations through a pooling layer.

This architecture shows outstanding results in the classical problem of recognition of handwritten digits [3], in recognition of the house numbers on the basis of the Google StreeView house number data set (SVHN) [4] and in the problem of recognition and classification of road signs [5].

Recent discoveries in the field of artificial convolutional neural networks have given researchers a unique tool and a number of advantages. With the increase of computing power of graphic processors, it became possible to apply deeper architectures of machine learning models [6]. Modern technology, such as increase of data, regularization, and others, were given the opportunity to avoid overfitting [7].

With the development of convolutional neural networks, it became possible to more effectively study and generalize the features of images. This has been applied to areas such as image classification [8], object search [9], vehicle detection [10].

In [11], the authors propose a neural network model that is capable of generating three-dimensional objects based on two-dimensional images or features of the generated object. The authors investigate the problem of direct generation of three-dimensional surface shapes of rigid and non-rigid forms using deep convolutional neural networks. The authors show that the network they developed studies the meaningful representation of form surfaces, allowing it to interpolate form orientations and poses, invent new form surfaces, and restore three-dimensional form surfaces from previously invisible images.

In [12], the authors examine the automatic detection of early visual concepts from raw data. The authors propose an uncontrolled approach to the study of untangled ideas about the main factors of variation. The paper discusses some aspects from the field of neurobiology and shows a model of a variational auto encoder capable of learning disentangled factors.

In [13], the authors developed a generative model of a deep convolution network that is capable of creating images based on given parameters. The authors show how the network is able to find features among various classes of objects under study. Also, the developed model can create new classes of generated objects by combining various input parameters.

48.3 Proposed Method

This chapter considers a simplified version of a deep generative convolutional neural network. The model is designed to generate images containing various forms of defects. Defects are presented in a simplified form in the form of basic geometric primitives. At the network input, parameters are described that initiate the class of the figure and its geometric characteristics.

The proposed model is designed to conduct research on the quality of image generation, the possibility of combining various types of defects, studying the influence of various parameters of the training set.

Based on these studies, it is possible to build a more advanced generative model capable of restoring the shape of internal defects in structural elements based on ultrasonic non-destructive testing methods.

48.4 Network Architecture

The deep convolutional generative network model consists of two separate inputs. The first input contains 4 parameters that correspond to four types of geometric primitives. The second input contains 5 parameters that describe the geometric features of each figure . Each of the two separated inputs is connected to its own fully con-

nected layer, consisting of 64 neurons. These fully connected layers combine together and transform into a two-dimensional representation. Next, using a combination of up-sampling and convolutional layers, image generation occurs. The batch normalization (BN) [14] is used. At the output of the neural network, an image of 128 × 128 pixels is obtained. The proposed model contains 1,969,665 training parameters.

48.5 Training Set Preparation

The training set is based on a combination of various types of primitives and their geometric features. Figure 48.1 shows the various geometric shapes used in the learning process of the model.

In the course of the study, it was found that in order to achieve the best quality of the generative model, it is necessary to balance the various classes of shapes imitating defects. For example, a relationship between the average value of the area of the figures and the quality of their generation is revealed. Figure 48.2 shows the average area of the figures of each class.

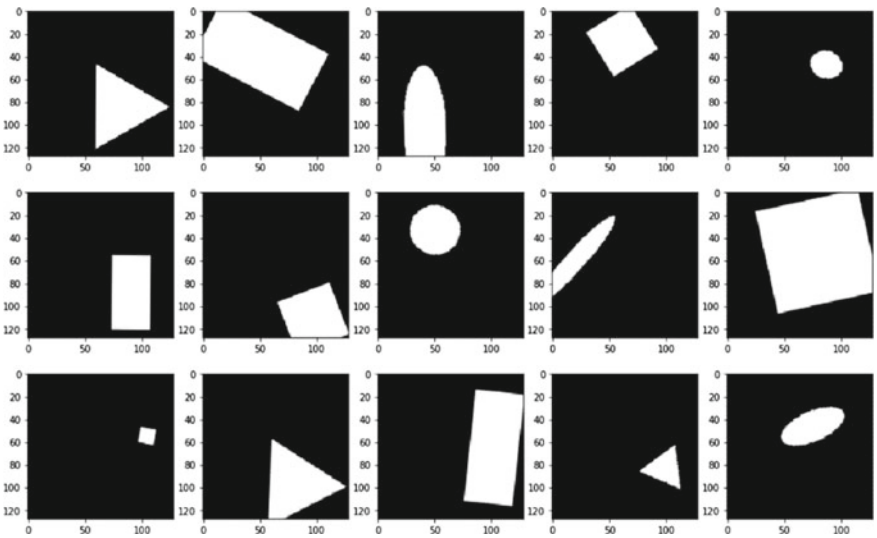

Fig. 48.1 Different figures types and its geometrical parameters are used in training set

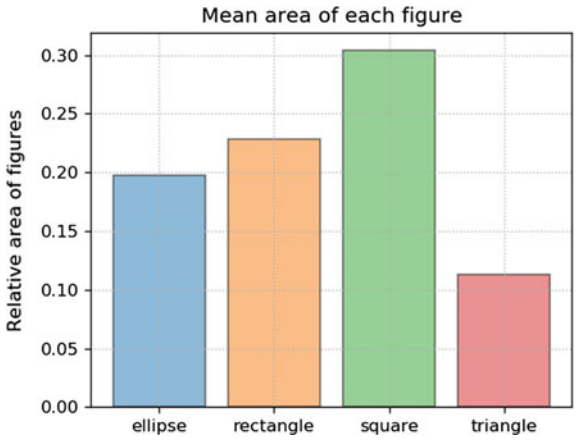

Fig. 48.2 Mean relative area of each type of figure

48.6 Neural Network Training

In connection with the specificity of the area under study, the intersection over union metrics (IoU, the Jacquard coefficient) and the equivalent binary measure of similarity (Dice, the Sørensen measure) are used to train and evaluate the performance of the neural network. As a loss function, the function $1 - J$ is used:

$$J(A, B) = \frac{|A \cap B|}{|A \cup B|}, S(A, B) = \frac{2|A \cap B|}{|A| + |B|}$$

Initialization of weights in the layers of the neural network is carried out using the Glorot method [15]. Batch normalization is performed to reduce the internal covariance shift by normalizing the input distributions of each layer. For training the Adam optimization algorithm (Method for Stochastic Optimization) is used [16].

The learning rate parameter changes with each epoch. Within the framework of the task, the optimal number of training epochs was established equal to 15. With more epochs, the accuracy of the neural network remained largely unchanged.

To implement the developed architecture, DCNN uses frameworks Keras and Tensorflow. Fine tuning of the neural network model was carried out and the optimal parameters of its structure were selected. The accuracy of neural networks with various configurations is shown in Fig. 48.3.

48.7 Results

After training the neural network, validation is performed on the prepared dataset. Each parameter set is fed to the input of the neural network, and the output is a generated binary mask with predicted figure. Figure 48.4 shows the results of the

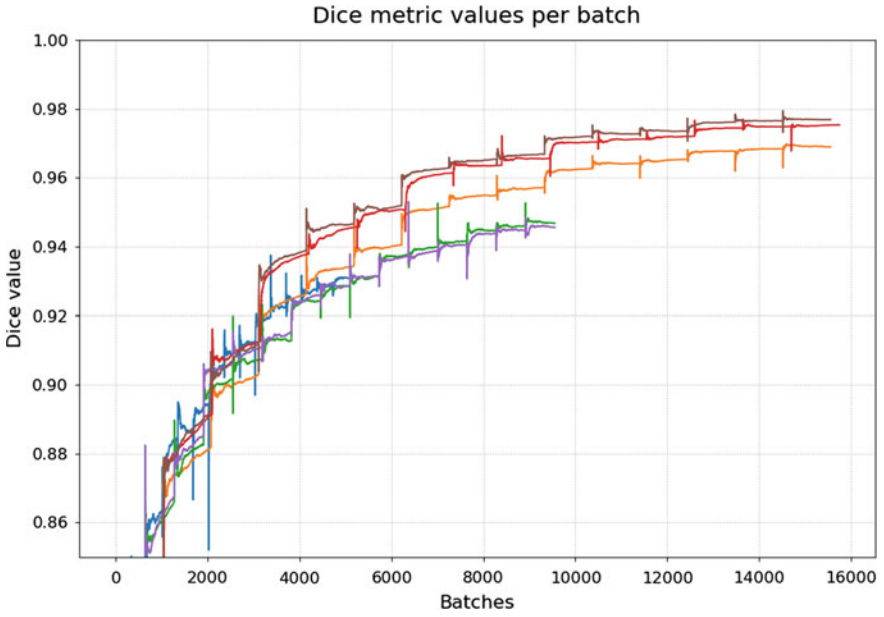

Fig. 48.3 Increasing model accuracy during learning process. Violet, blue and green plots—models are trained on small dataset contains 20,000 training samples. Orange plot—model is trained on large dataset contains 50,000 samples. Red plot—model used more convolutional layers (3 against 1). Brown plot—final fine-tuned model with separated inputs and rebalanced figures classes

trained network and their comparison with the true values from the test sample.

The quality of the prepared data set has a great influence on the training and the result of the neural network.

There are some most representative metrics. Based on this value we can perform fine tuning of the neural network. F1 is the same Dice value, the other metrics are well known and used in this type of problems. Figure 48.5 shows the average error for each geometrical figure.

48.8 Conclusion

As a result of the work done, a model of a generative deep convolutional neural network was developed. The main purpose of this model is the generation of various types of geometric shapes that simulate various internal defects in structural elements. Based on this model, the training process and fine-tuning are worked out. This will subsequently allow the use of models of a similar architecture in solving inverse problems of mechanics based on non-destructive testing methods.

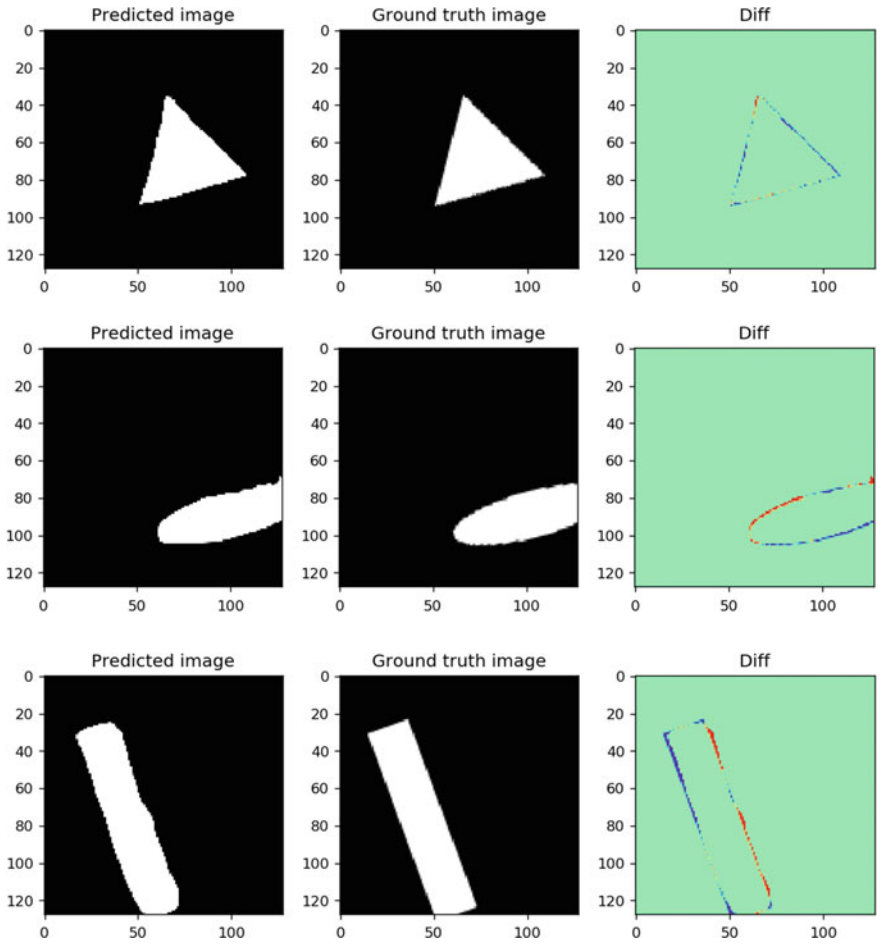

Fig. 48.4 Figures generated by neural network and its ground truth representation

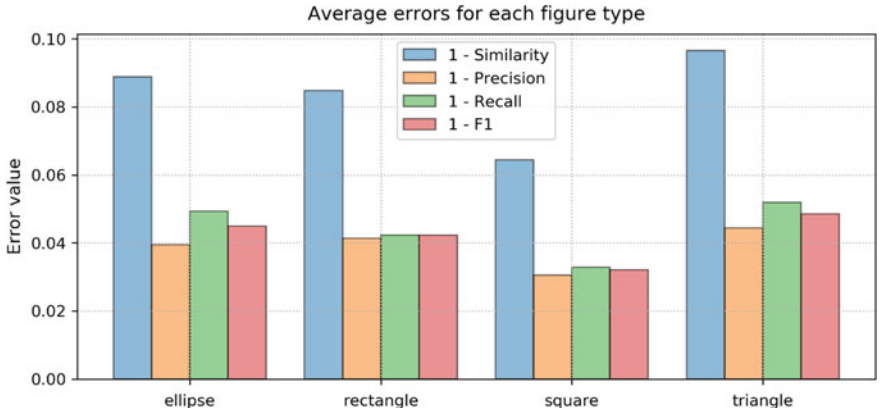

Fig. 48.5 Calculated metrics for each type of figure

Acknowledgements This research was performed into framework of financing RFBR grant number 19-08-00074.

References

1. B.V. Sobol, A.N. Soloviev, E.V. Rashidova, P.V. Vasiliev, PNRPU Mech. Bull. **4** (2019) https://doi.org/10.15593/perm.mech/2019.4.16
2. Y. LeCun, L. Bottou, Y. Bengio, P. Haffner, Proc. IEEE **86**(11), 2278–2324 (1998)
3. D. Ciresan, U. Meier, J. Schmidhuber, in *Proceedings. of Conference on Computer Vision and Pattern Recognition (CVPR)*, (2012) pp. 3642–3649
4. I.J. Goodfellow, Y. Bulatov, J. Ibarz, S. Arnoud, V. Shet, in *Proceedings of International Conference on Learning Representations (ICLR)*, (2014)
5. D. Ciresan, U. Meier, J. Masci, J. Schmidhuber, in *Proceedings of International Joint Conference on Neural Networks (IJCNN)*, (2011), pp. 1918–1921
6. I. Arel, D.C. Rose, T.P. Karnowski, IEEE Comput. Intell. Mag. **5**(4), 13–18 (2010)
7. P.Y. Simard, D. Steinkraus, J.C. Platt, in *Proceedings of International Conference on Document Analysis and Recognition (ICDAR)*, (2003), pp. 958–963
8. C. Szegedy et al. in *2015 IEEE Conference on Computer Vision and Pattern Recognition (CVPR)*, Boston, MA, (2015), pp. 1–9
9. R. Girshick, J. Donahue, T. Darrell, J. Malik, in *2014 IEEE Conference on Computer Vision and Pattern Recognition*, Columbus, OH, (2014), pp. 580–587
10. X. Chen, S. Xiang, C.L. Liu, C.H. Pan, IEEE Geosci. Remote Sens. Lett. **11**(10), 1797–1801 (2014)
11. A. Sinha, A. Unmesh, Q. Huang, K. Ramani, in *2017 IEEE Conference on Computer Vision and Pattern Recognition (CVPR)*, (2017), pp. 791–800
12. I. Higgins, L. Matthey, X. Glorot, A. Pal, B. Uria, C. Blundell, S. Mohamed, A. Lerchner, *ArXiv*, abs/1606.05579 (2016)
13. A. Dosovitskiy, J.T. Springenberg, T. Brox, in *2015 IEEE Conference on Computer Vision and Pattern Recognition (CVPR)*, Boston, MA, pp. 1538–1546 (2015)

14. S. Ioffe, C. Szegedy, *CoRR*, abs/1502.03167 (2015)
15. X. Glorot, Y. Bengio, in *AISTATS* (2010)
16. D. Kingma, J.B. Adam, in *International Conference on Learning Representations* (2014)

Chapter 49
Direct Mapping Based FBMC-LDPC Advanced Underwater Acoustic Transmission Scheme for Data Signals

Chin-Feng Lin, Tsung-Jen Su, Shun-Hsyung Chang, Ivan A. Parinov, and Sergey N. Shevtsov

Abstract This paper proposes a 2 × 2 direct mapping (DM) based of an underwater acoustic transmission (UAT) scheme for data signals based on filter bank multicarrier (FBMC)-low density parity check (LDPC). The 2 × 2 DM multiple-input multiple-output (MIMO) transmission mechanism, FBMC modulation, LDPC channel coding, adaptive binary phase shift keying (BPSK) modulation and four offset quadrature amplitude modulation (4-OQAM), and power assignment mechanism are integrated. The performances of bit error rates (BERs) and data error rates (DERs) of the proposed underwater data transmission scheme with perfect channel estimation (PCE) (0%), and the channel estimation errors(CEEs) of 5%, 10%, and 20% are investigated. The bit error rates (BERs) of data signals for underwater transmission must be less than 10^{-5}. The transmission power weightings and ratios of power saving (PS) for the proposed underwater acoustic transmission system are explored through simulations. From these simulation results, we evaluate the performances of the proposed advanced data UAT scheme.

C.-F. Lin (✉) · T.-J. Su
Department of Electrical Engineering, National Taiwan Ocean University, Kaohsiung, Taiwan, ROC
e-mail: lcf1024@mail.ntou.edu.tw

S.-H. Chang
Department of Microelectronic Engineering, National Kaohsiung University of Science and Technology, Kaohsiung, Taiwan, ROC

I. A. Parinov
I. I. Vorovich Mathematics, Mechanics, and Computer Science Institute, Southern Federal University, Rostov-on-Don, Russia

S. N. Shevtsov
South Center of Russian Academy of Science, Rostov-on-Don, Russia

I. A. Parinov et al. (eds.), *Advanced Materials*, Springer Proceedings in Materials 6, https://doi.org/10.1007/978-3-030-45120-2_49

49.1 Introduction

Underwater multimedia sensor networks (UMSNs) are a compelling interest of the research topic, and UMSNs can be applied to undersea monitoring, and advanced coastal surveillance. Sarisaray-Boluk et al. [1] adopt different combinations of multipath transport, watermarking-based error concealment, forward error correction, and adaptive retransmission mechanisms to achieve reliable and quality aware image transmission in underwater channel impairments. Singh et al. [2] propose a two-step preamble-based approach using a novel frame structure to estimate carrier frequency offset (CFO) and channel in multiple-input multiple-output (MIMO) filter bank multicarrier (FBMC) scheme with offset quadrature amplitude modulation (OQAM). At the first step, the coarse CFO estimator without channel information was developed, and the fine CFO can be draw on a constant carrier phase. At the second step, the minimum mean square error estimator is designed for effective channel estimation in time domains. Singh et al. [3] propose a post-processing signal-to-noise-plus-interference-ratio (PP-SNIR) method in a MIMO FMBC-OQAM scheme with imperfect channel state information, and PP-SNIR derived to calculate symbol error rate.

Amini et al. [4] investigated a FBMC transmission scheme in an underwater communication application, and Lin et al. [5] demonstrated a FBMC-based low density parity check (LDPC) code underwater acoustic transmission (UAT) scheme for voice and image signals. In previous study [6], the proposed direct mapping (DM) FBMC-based underwater transmission scheme (UTS) was demonstrated. The performances of transmission bit error rates (BERs) of the UTS, the mean square error (MSE) performances and the power saving ratios of the DM FBMC UTS scheme, for audio signals transmission with perfect channel estimation (PCE) were explored. The paper examines the BERs and data error rates (DERs) performances of the DM-based FBMC-LDPC UAT scheme. The power saving ratios of the DM-based FBMC-LDPC UAT scheme, and data signals received using BPSK modulation in the DM-based FBMC-LDPC UAT scheme, for a BER of 10^{-5}, were discussed.

49.2 Research Method

Figure 49.1 deplicts the proposed DM-based FBMC-LDPC UAT scheme for data signals. The transmission architecture has been demonstrated for voice signals [6], and the transmission performances of the proposed DM-based FBMC-LDPC UAT scheme is discussed for data signals. The underwater channel model with an underwater channel bandwidth of 3.9 kHz, a carrier central frequency of 11.5 kHz, and a transmission distance of 1 km was used [7]. The BER requirement of underwater transmission data signals is 10^{-5}, and the DER of the DM-based FBMC-LDPC UAT scheme with a BER of 10^{-5} is demonstrated. The DER is defined as follows:

$$\text{DER} = \frac{D_e}{D_t} \tag{1}$$

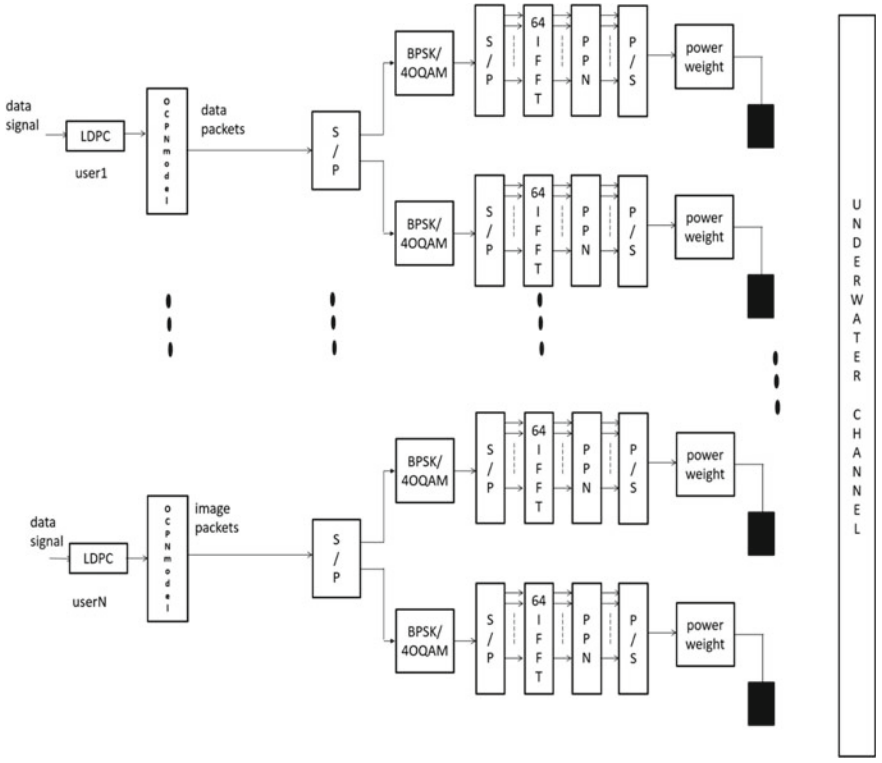

Fig. 49.1 Proposed the DM-based FBMC-LDPC UAT scheme for data signals

D_e and D_t denote the number of the transmission error data symbols, and the number of transmission data symbols, respectively. The performances of BERs and DERs of the proposed DM-based FBMC-LDPC UAT scheme with PCE) (0%) and CEEs of 5%, 10%, and 20% are investigated. With the CEEs increased, the BERs and DERs increased.

49.3 Simulation Results

Figure 49.2 shows that DER performances of the DM-based FBMC-LDPC UAT scheme, using BPSK modulation, with PCE (0%) and CEEs of 5%, 10%, and 20%, respectively. The 10^5 data symbols were simulated in the underwater data transmission. The colors 'black', 'red', 'blue', and 'purple', in Figs. 49.2 and 49.3, denote the DM-based FBMC-LDPC UAT scheme with a PCE, the DM-based FBMC-LDPC UAT scheme with a CEE of 5%, the DM FBMC UTS scheme with a CEE of 10%, and the DM-based FBMC-LDPC UAT scheme with a CEE of 20%, respectively. Using the BPSK modulation with a PCE, and CEEs of 5%, 10%, and 20%, respectively,

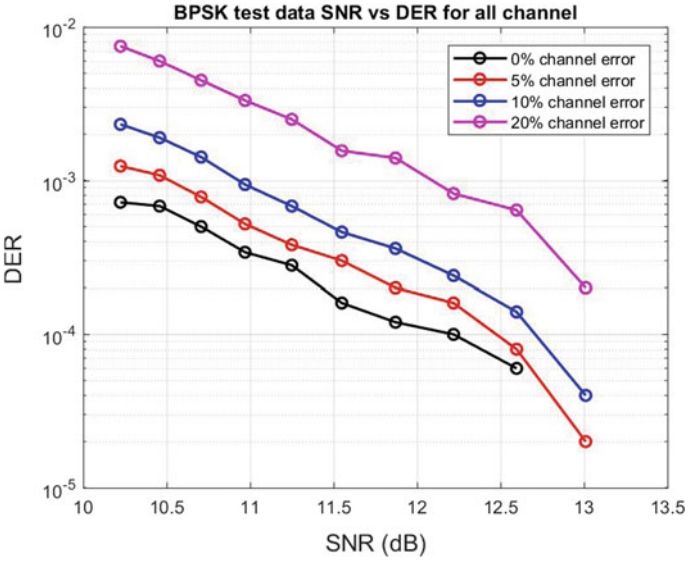

Fig. 49.2 DER performances of the DM-based FBMC-LDPC UAT scheme, using BPSK modulation, with PCE (0%) and CEEs of 5%, 10%, and 20%, respectively

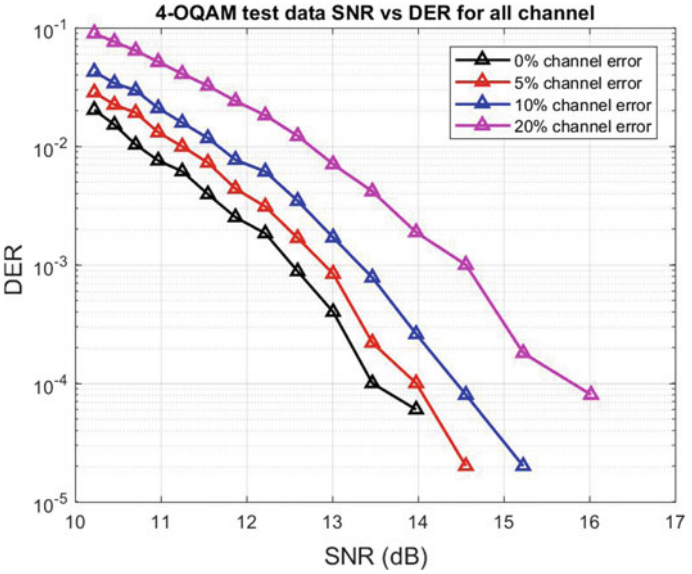

Fig. 49.3 DER performances of the DM-based FBMC-LDPC UAT scheme, using 4-OQAM modulation, with PCE (0%) and CEEs of 5%, 10%, and 20%, respectively

for signal to noise ratios (SNRs) of 12.59 dB, with the corresponding DERs of the received data signals were 6×10^{-5}, 8×10^{-5}, 1.4×10^{-4}, and 6.4×10^{-4}. Using the BPSK modulation with a PCE, and CEEs of 5%, 10%, and 20%, respectively, for SNRs of 12.59 dB, with the corresponding BERs of the received data signals were 2×10^{-6}, 2.67×10^{-6}, 4.67×10^{-6}, and 2.13×10^{-5}. With the CEEs increased, the BERs and DERs increased.

Figure 49.3 shows the DER performances of the DM-based FBMC-LDPC UAT scheme, using 4-OQAM modulation, with PCE (0%) and CEEs of 5%, 10%, and 20%, respectively. The data signals received using the 4-OQAM modulation with a PCE, and CEEs of 5%, 10%, and 20%, respectively, for signal to noise ratios (SNRs) of 12.59 dB, with the corresponding DERs of the received data signals were 8.8×10^{-4}, 1.68×10^{-3}, 3.46×10^{-3}, and 1.22×10^{-2}. Data signals were received using the 4-OQAM modulation with a PCE, and CEEs of 5%, 10%, and 20%, respectively, for signal to noise ratios (SNRs) of 12.59 dB, with the corresponding BERs of the received data signals 2.93×10^{-5}, 5.73×10^{-5}, 1.11×10^{-4}, and 4.1×10^{-4}. Simulation results show that the BERs and DERs performances of the DM-based FBMC-LDPC UAT scheme, using BPSK modulation, are better than that of the DM-based FBMC-LDPC UAT scheme, using 4-OQAM modulation.

Figure 49.4 demonstrates the power saving ratios of the DM-based FBMC-LDPC UAT scheme with a BER of 10^{-5}, for PCE. The maximum acceptable transmission

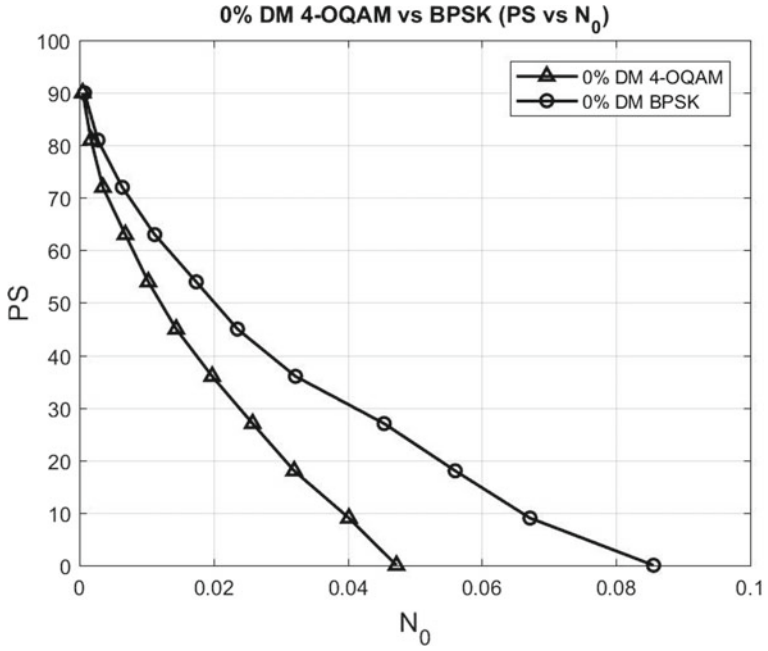

Fig. 49.4 Power saving ratios of the DM-based FBMC-LDPC UAT scheme with a BER of 10^{-5}, for PCE

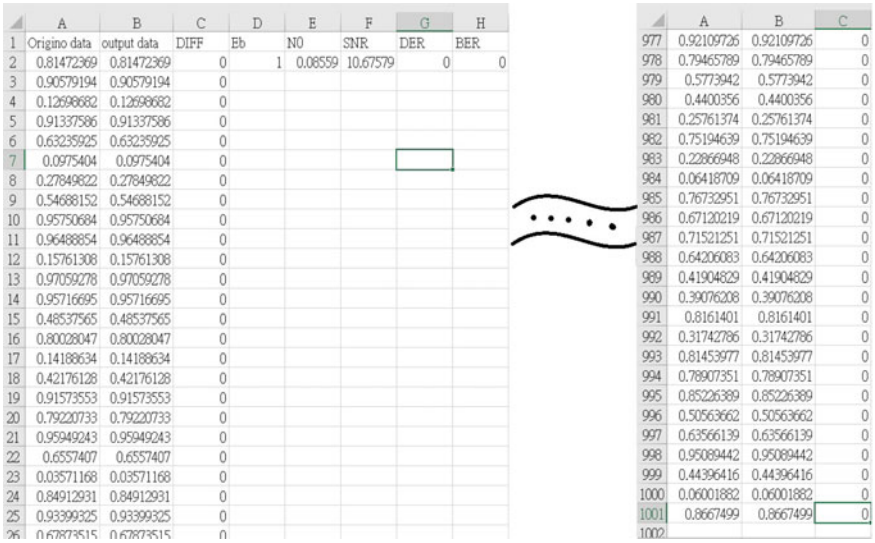

	A	B	C	D	E	F	G	H
1	Origino data	output data	DIFF	Eb	N0	SNR	DER	BER
2	0.81472369	0.81472369	0	1	0.08559	10.67579	0	0
3	0.90579194	0.90579194	0					
4	0.12698682	0.12698682	0					
5	0.91337586	0.91337586	0					
6	0.63235925	0.63235925	0					
7	0.0975404	0.0975404	0					
8	0.27849822	0.27849822	0					
9	0.54688152	0.54688152	0					
10	0.95750684	0.95750684	0					
11	0.96488854	0.96488854	0					
12	0.15761308	0.15761308	0					
13	0.97059278	0.97059278	0					
14	0.95716695	0.95716695	0					
15	0.48537565	0.48537565	0					
16	0.80028047	0.80028047	0					
17	0.14188634	0.14188634	0					
18	0.42176128	0.42176128	0					
19	0.91573553	0.91573553	0					
20	0.79220733	0.79220733	0					
21	0.95949243	0.95949243	0					
22	0.6557407	0.6557407	0					
23	0.03571168	0.03571168	0					
24	0.84912931	0.84912931	0					
25	0.93399325	0.93399325	0					
26	0.67873515	0.67873515	0					

	A	B	C
977	0.92109726	0.92109726	0
978	0.79465789	0.79465789	0
979	0.5773942	0.5773942	0
980	0.4400356	0.4400356	0
981	0.25761374	0.25761374	0
982	0.75194639	0.75194639	0
983	0.22866948	0.22866948	0
984	0.06418709	0.06418709	0
985	0.76732951	0.76732951	0
986	0.67120219	0.67120219	0
987	0.71521251	0.71521251	0
988	0.64206083	0.64206083	0
989	0.41904829	0.41904829	0
990	0.39076208	0.39076208	0
991	0.8161401	0.8161401	0
992	0.31742786	0.31742786	0
993	0.81453977	0.81453977	0
994	0.78907351	0.78907351	0
995	0.85226389	0.85226389	0
996	0.50563662	0.50563662	0
997	0.63566139	0.63566139	0
998	0.95089442	0.95089442	0
999	0.44396416	0.44396416	0
1000	0.06001882	0.06001882	0
1001	0.8667499	0.8667499	0
1002			

Fig. 49.5 Data signal received using BPSK modulation in the DM-based FBMC-LDPC UAT scheme with a BER and DER of zero, for PCE

BER value for the data signal is 10^{-5}. The data signals received using the BPSK modulation for the SNRs of 15.18 dB, 16.41 dB, and 18.40 dB, with the corresponding power saving ratios of 63%, 72%, and 81%, respectively. The data signals received using the 4-OQAM modulation for the SNRs of 17.33 dB, 19.04 dB, and 20.42 dB, with the corresponding power saving ratios of 63%, 72%, and 81%, respectively. At the same power saving ratio, the SNRs of the BPSK modulation are lower than that of 4-OQAM modulation. Figure 49.5 illustrates that the 1000 data symbols with EXCEL format received using the BPSK modulation in the DM-based FBMC-LDPC UAT scheme with a BER and DER of zero, for PCE. The received data signals are accurate, and the DM-based FBMC-LDPC UAT scheme can be applied to underwater data transmission.

49.4 Conclusion

In this paper, a DM-based FBMC-LDPC UAT scheme for data signals was dissicussed. The BERs and DERs performances of the DM-based FBMC-LDPC UAT scheme, using BPSK and 4-OQAM modulations, with PCE (0%) and CEEs of 5%, 10%, and 20%, respectively, were demonstrated. The BERs and DERs performances of the DM-based FBMC-LDPC UAT scheme using BPSK modulation is superior to the DM-based FBMC-LDPC UAT scheme using 4-OQAM modulation. With CEEs increased, the BERs and DERs performances decreased. Power saving ratios of the

DM-based FBMC-LDPC UAT scheme with a BER of 10^{-5}, for PCE, are explored. Simulation results show that the proposed DM-based FBMC-LDPC UAT scheme is suitable for underwater data transmission.

Acknowledgements The authors acknowledge the support of the grant from The Ministry of Science and Technology of Taiwan, under contract No. MOST 107-2221-E-992-027, MOST 105-2923-E-022-001-MY3, and the valuable comments of the reviewers.

References

1. P. Sarisaray-Boluk, V.C. Gungor, S. Baydere, A.E. Harmanci, Ad Hoc Netw. **9**, 1287 (2011)
2. P. Singh, E. Sharma, K. Vasudevan, R. Budhiraja, IEEE Wirel. Commun. Lett. **7**(5), 844 (2018)
3. P. Singh, R. Budhiraja, K. Vasudevan, IEEE Commun. Lett. **23**(2), 226 (2019)
4. P. Amini, R.R. Chen, B. Farhang-Boroujeny, IEEE J. Oceanic Eng. **40**(1), 115 (2015)
5. C.F. Lin, Y.T. Hung, H.W. Lu, S.H. Chang, I.A. Parinov, S.N. Shevtsov, J. Mar. Sci. Technol. **26**(3), 327 (2018)
6. C.F. Lin, C.K. Li, S.H. Chang, I.A. Parinov, S.N. Shevtsov, in *Advanced Materials—Proceedings of the International Conference on "Physics and Mechanics of New Materials and Their Applications", PHENMA 2018*, ed. by I.A. Parinov, S.-H. Chang, Y.-H. Kim. Springer Proceedings in Physics, vol. 224. (Springer Nature, Cham, Switzerland, 2019), pp. 651–659
7. J. Zhang, Y.R. Zheng, C. Xiao, in *Proceedings of the MIT/IEEE Ocean International Conference*, IEEE Publishers: USA (2008)

Chapter 50
Acquisition and Analysis of Endodontic Handpiece Vibration Signals

Ankit Nayak, P. K. Kankar, Prashant K. Jain, and Niharika Jain

Abstract The root canal treatment is the popular method for disinfection of infected teeth. Root canal treatment involves cavity preparation (root canal shaping), filling and sealing. The endodontic handpiece with endodontic files are used for the shaping of the root canals. In this process, the endodontic files dislodge material from the internal wall of the root canal. Material dislodging causes root canal shaping forces and vibration. Excessive forces and vibration may increase the chances of iatrogenic error like the instrument separation, root tooth fracture and root perforation. These errors can be predicted and eliminated by assessment of the vibration signals of endodontic handpiece. Endodontic handpiece composed of several parts like motor, transmission system and endodontic files and generate vibrations at different frequencies. The accelerometer is used for the vibration signal acquisition of the handpiece. The vibration signal quality is associated with the position of the accelerometer on the endodontic handpiece. This study is determining the suitable position of the accelerometer endodontic handpieces, for the better signal acquisition. The entire handpiece is divided into the segments of equal length. Then eight signals for each segment are recorded. For each position of the accelerometer, the root mean square of signals is compared, in order to accrue signals of higher amplitude. In this study, it has been found out that the amplitude of vibration is significantly varied along the length of the handpiece. On the base of this study, a suitable location for the accelerometer has been found out.

A. Nayak (✉) · P. K. Jain
CAD/CAM Lab, Mechanical Engineering Discipline, PDPM, Indian Institute of Information Technology, Design and Manufacturing Jabalpur, Jabalpur, Madhya Pradesh 482005, India
e-mail: ankitnayak@gmail.com

P. K. Kankar
Discipline of Mechanical Engineering, Indian Institute of Technology Indore, Indore, Madhya Pradesh 453331, India

N. Jain
Department of Conservative Dentistry and Endodontics, Triveni Institute of Dental Science, Hospital and Research Centre, Bilaspur, Chhattisgarh 495001, India

I. A. Parinov et al. (eds.), *Advanced Materials*, Springer Proceedings in Materials 6, https://doi.org/10.1007/978-3-030-45120-2_50

50.1 Introduction

The endodontic treatment process has evolved from the primitive tools to smart tools and it is continuously improving, to provide better treatment. In order to improve the RCT, several attempts has been reported in the literature. Endodontics has been benefited by the advancements in the field of technology; it includes sub areas of technology like material science, advanced fabrication techniques, computer programs, diagnosis techniques, fault detection and image analysis. Guided endodontics is the outcome of advanced diagnosis technique (CBCT) and precise fabrication technique of AM. Due to advancement in the metallurgy and material science, endodontics is benefited by the better alloy materials for the fabrication of endodontic files. Moreover, advanced endodontic sealers have been developed to seal the endodontic cavity. Nowadays, better endodontic instruments are used for the root canal access cavity preparation for improved outcome of the root canal treatment.

Literature reviled that the it was in the prehistoric age about 14,000 years ago [1] that a tooth was drilled in humanity's first root canal treatment. After that the historic root canal treatment was performed in 1938 by Edwin Maynard. Edwin Maynard was used a watch spring as the root canal shaping instrument [2]. After these trials several endodontic instruments were developed. These instruments were used in clinical practice. The consecutive development of endodontic instruments is shown Fig. 50.1.

Although Ni-Ti instruments are more flexible than stainless steel files [3], problems like screw in force [4, 5], stress accumulation [6] and root canal transportation

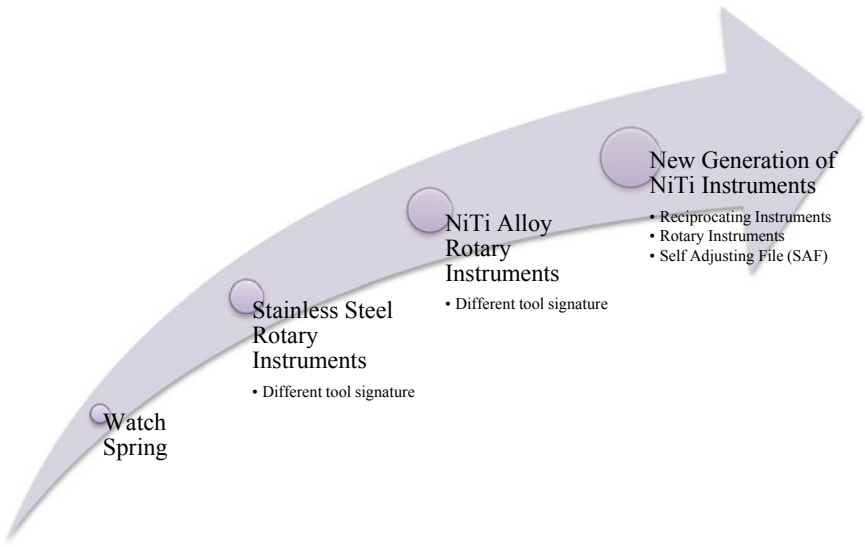

Fig. 50.1 Evolution in endodontic file design

[7] are still associated with the use of Ni-Ti rotary instruments. The kinematics of the rotary Ni-Ti instrument was later transformed into reciprocating motion because it was observed that reciprocating rotation increases the fracture resistance and extends the longevity of the instrument [8] as compared to continuous rotation. The reciprocating motion of the instrument also minimizes canal deformation and transportation [9].

In root canal shaping the material dislodging action causes the reaction forces on the endodontic instrument and the tooth [10]. These forces may lead to the fracture initiation in the dentine [11]. Due to the root canal shaping forces, stress is developed in the endodontic instruments. If the stress exceeds the ultimate torsional strength of the endodontic instruments then the instrument gets fractured [12]. Other than the shaping forces screw-in forces of the endodontic instruments are also the cause of the iatrogenic error [13].

Since the last few decades, researchers are investigating the root canal shaping force, their consequences on the dentine and endodontic instruments. Researchers have opted for different techniques for such investigations. In the area of biomedical engineering and medical science, it is the general concern that the availability of human body parts for the experimentation is very limited so to avoid such issues the analysis in a simulated environment is carry out. The simulated study helps to maintain the uniformity between the different populations of the samples.

Literature reveals that, researchers have been studied the effect of endodontic shaping forces and reaction torque on the root canal in the finite element analysis [14]. Finite element analysis was carried out to study the fracture of the endodontic instruments [15, 16]. Such studies helps to understand the stress distribution and fracture mechanics of the endodontic instruments. Few experimental studies were also carried out by researchers, to evaluate the shaping forces and their consequences of file separation. During the root canal shaping, the endodontic file adopts the curvilinear geometry of the root canal and keeps rotating in order to remove the dentine. In each rotation, a cyclic load is induced on the curvilinear portion of the file; this cyclic loading is caused fatigue failure of the endodontic file [17, 18]. These studies showing that the endodontic files may fractured during the root canal shaping, under certain conditions i.e. sharp curvature, excessive shaping forces [19] and torque [20]. However, few files show fewer chances of separation but still, it cannot be neglected. Existing literature does not suggest any approach to prevent the endodontic file separation during the root canal shaping. Prediction of file separation may help the endodontists to provide hassle free treatment procedure.

Other than the file separation, root canal shaping force also affects the shaping ability of the endodontic files. Excessive root canal shaping may cause the patent discomfort, root fracture and micro crack initiation.

Several studies have reported the crack initiation, vertical root fracture and craze lines in the root dentine after the endodontic shaping with NiTi instruments [21–24]. These cracks and lines may further propagate and resulted in tooth fracture. Few studies have been carried out by endodontists to determine the shaping force of different endodontic files and their consequences [25, 26].

Liu and Wu [27] measured root canal surface strain and canal transportation for three different files. They have fixed the strain gauges on the external surface of endodontic blocks to monitor the surface strain during the root canal shaping. Genovesi et al. 2016 [28] studied effect of 6 different files on dental crack formation. Few more studies [23] were carried out to compare the crack formation in different root canal instrumentation (shaping) techniques. They [23] were compared endodontic files of different kinematics and design. It was mentioned that the root canal shaping force and related stress are one of the major responsible factors for dentine cracks and root canal facture. From the literature, it can be concluded that the dentine cracks cannot be avoided in the case of root canal shaping with rotary or reciprocating instruments. These micro-cracks can be avoided by maintaining the root canal shaping force in the certain limit and assessment of the root canal shaping forces might be the solution for this problem.

Root canal shaping force affects the performance and life of the endodontic instruments. There are chances for breakage in NiTi instruments due several factors like torque generated, vertical load causing increase in torque, cyclic fatigue, instrument design and technique of instrumentation [29].

Improved design and kinematics of the instruments help to reduce the chances of the file separation. But still it cannot be avoided. Prediction of the file separation may help to avoid the instrument fracture during the root canal treatment.

The endodontic files apply root canal shaping force and vibrations on the tooth. The amplitude of the force and vibration may vary according to the design, material dislodging mechanism and kinematics of the endodontic file. The root canal shaping forces can be predicted by the vibration signature of the hand piece.

Vibrations signature analysis of the endodontic handpice may help to maintain the root canal shaping forces [30, 31] and vibration s in a certain limit. This helps to avoid the iatrogenic errors of the root canal treatment caused due to the excessive force and vibration. In this article the best suitable position for the accelerometer has been determined to acquire the maximum vibration signals of root canal shaping.

50.2 Material and Method

50.2.1 Endodontic Handpiece

The endodontic handpiece is used in mechanized or motorized root canal shaping. This handpiece provides the motion to the endodontic handpiece as per the specifications of the instruments. Endodontic handpiece assembly has several rotary parts like motor, coupling, bearings etc. which causes the vibrations. These vibrations may cause the crack initiation, crack propagation in the dentine or the vibration may also lead the hand-arm vibration syndrome in the endodontist's wrist.

For this study two endodontic handpiece i.e. Marathon and Micro-Mega MM control (Micro-Mega SA Besancon, France) were used for the vibration signature

Fig. 50.2 Different locations to mount the accelerometer for signal acquisition in **a** marathon and **b** MM control handpiece

acquisition. On Marathon and MM control handpiece 6 and 4 points, respectively, have been identified for the vibration signal acquisition as shown in Fig. 50.2.

50.2.2 Experimental Setup and Signal Analysis

The Dayton (3093B1) accelerometer with DEWESoft data acquisition system is used for the signal acquisition. The signals are logged by keeping the data acquisition frequency 51,200 Hz. The accelerometer is mounted with the help of a magnetic stud, on the outer periphery of the handpiece. Both handpices are operated at different RPM and the signals are logged in a dedicated computer. Vibration s signals are recorded for each pre defied pints of the handpiece. Vibration s signals of the different locations of the handpiece are analyzed in the MATLAB software. The root mean squire (RMS) value of each signal is calculated using (50.1) [30]. The RMS values of different groups are compared to know the difference between the RMS values of signals of different location.

$$AMS_{RMS} = \sqrt{\frac{1}{n}\left(Amp_1^2 + Amp_1^2 + Amp_1^2 + \cdots + Amp_n^2\right)} \tag{50.1}$$

50.3 Results and Discussion

The RMS values of vibration signature for the different sensor location is shown in the Table 50.1. The interval plot for this data is showing in the Fig. 50.3. From Table 50.1 and Fig. 50.3 it can be analyze that for Marathon hand piece the RMS value of the vibration signals is significantly high at location 6 while for MM control handpice the RMS value of the signature at location 2 is significantly more than the other 3 accelerometer locations.

The vibration signals may help to predict the fracture of endodontic file [32]. For signal analysis the strong signal is the favorable situation. Vibration signals are responsive to the changes in endodontic instrument structure like dull tool and instrument separation. The results of the present study are showing that the accelerometer location for maximum signal strength is not similar in each endodontic handpice. This might due to the kinematics and design of each instrument. MM-Control is the handpice of advanced generation than Marathon handpice. MM-control has less vibration than Marathon.

In any system, unbalanced rotary parts and/or hammering are the main causes of vibration. In root canal shaping, the primary causes of force or vibration are the motion of rotary parts [32] material dislodging, kinematics, geometry and cross-section of the endodontic file. Excessive vibration may further lead to minor or major crack initiations in the dentine, root fracture, or file fracture [33]. The endodontic motor, along with the contra-angle handpiece, is composed of many rotary parts: the rotor and shaft of the endodontic motor, the transmission shaft in the handpiece, gears, and the endodontic file. These parts may have some unbalanced mass and may generate vibrations at the frequency of the rotation and its harmonics [31].

50.4 Conclusion

The vibration signature acquisition of endodontic handpice has been presented in this article. From the experimental study it can be conclude that the intensity of the vibration signals is changed according through the handpice. For better outcome of the signal analysis the best suitable signal location for each handpice should be find out. Further it can also be conclude that the MM- control handpice has less vibrations than Marathon endodontic handpiece.

Table 50.1 The RMS value of vibration signatures for different accelerometer location

Accelerometer location	1	2	3	4	5	6
Marathon	1.08 ± 0.02	1.11 ± 0.02	2.29 ± 0.01	2.74 ± 0.01	3.43 ± 0.09	18.81 ± 0.78
MM-control	0.11 ± 0.001	0.13 ± 0.001	0.076 ± 0.006	0.078 ± 0.0008	–	–

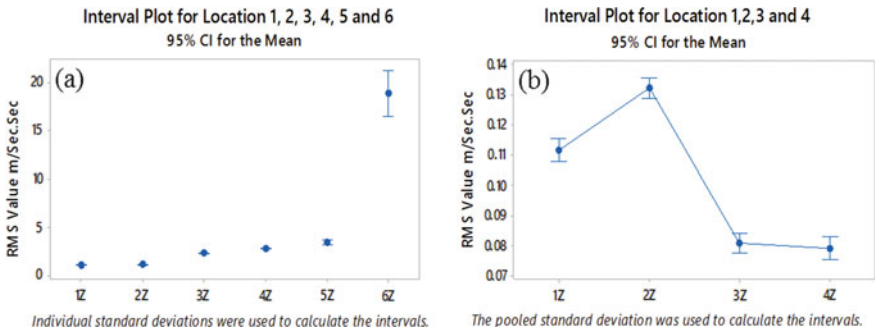

Fig. 50.3 Interval plot for different sensor location of **a** marathon and **b** MM-control handpiece

References

1. T.M. Smith, *The Tales Teeth Tell: Development, Evolution, Behavior* (The MIT Press, Cambridge, MA, 2018)
2. L.I. Grossman, J. Endod. **8**, S36–S40 (1982)
3. E. Schäfer, U. Schulz-Bongert, G. Tulus, J. Endod. **30**, 432–435 (2004)
4. A. Medha, *J. Clin. Diagnostic Res*. **2**, (2014)
5. S.Y. Sung, J.H. Ha, S.W. Kwak, R. El Abed, K. Byeon, H.C. Kim, Scanning. **36**, 500–506 (2014)
6. H.S. Topçuoğlu, S. Düzgün, A. Aktı, G. Topçuoğlu, Int. Endod. J. **50**, 713–717 (2017)
7. M. Alrahabi, M. Alkady, A. *Saudi*. J. Dent. Res. **8**, 1–4 (2017)
8. H.C. Kim, S.W. Kwak, G.S.P. Cheung, D.H. Ko, S.M. Chung, W. Lee, J. Endod. **38**, 541–544 (2012)
9. V. Tambe, P. Nagmode, S. Abraham, M. Patait, P. Lahoti, N. Jaju, J. Conserv. Dent. **17**, 561 (2014)
10. J.Y. Blum, P. Machtou, S. Esber, J.P. Micallef, Int. Endod. J. **30**, 386–396 (1997)
11. T. Özyürek, V. Tek, K. Yılmaz, G. Uslu, Restor. Dent. Endod. **42**, 332–341 (2017)
12. H.C. Kim, H.J. Kim, C.J. Lee, B.M. Kim, J.K. Park, A. Versluis, Int. Endod. J. **42**, 593–602 (2009)
13. J. Ha, W. Kwak, Korean Acad. Conserv Dent. **41**, 304–309 (2016)
14. G.M. Yared, G.K. Kulkarni, Int. Endod. J. **35**, 536–541 (2002)
15. S. Necchi, S. Taschieri, L. Petrini, F. Migliavacca, Int. Endod. J. **41**, 939–949 (2008)
16. A.M. Elnaghy, S.E. Elsaka, Int. Endod. J. **48**, 894–901 (2015)
17. E.C.P. Acosta, P.D. Resende, I.F. da C. Peixoto, É.S.J. Pereira, V.T.L. Buono, M.G. de A.Bahia, *J. Endod.*, **43**, 613–618 (2017)
18. M. Gündoğar, T. Özyürek, J. Endod. **43**, 1–5 (2017)
19. E. Pedullà, G. Plotino, N.M. Grande, A. Pappalardo, E. Rapisarda, Ann. Stomatol. (Roma) **3**, 59–63 (2012)
20. A. Arias et al., J. Endod. **43**, 1–5 (2017)
21. I.D. avu. Capar, H. Arslan, M. Akcay, B. Uysal, *J. Endod.* **40**, 1482–1484 (2014)
22. R. Liu, B.X. Hou, P.R. Wesselink, M.K. Wu, H. Shemesh, J. Endod. **39**, 1054–1056 (2013)
23. R.M. Gergi, N.E. Osta, A.S. Naaman, Eur. J. Dent. **9**, 508–512 (2015)
24. P.M. Venino, C.L. Citterio, A. Pellegatta, M. Ciccarelli, M. Maddalone, J. Endod. **43**, 1–5 (2016)
25. D. Tokita, A. Ebihara, M. Nishijo, K. Miyara, T. Okiji, J. Endod. **43**, 1706–1710 (2017)
26. A. Arias, R. Singh, O.A. Peters, J. Endod. **40**, 973–976 (2014)
27. W. Liu, B. Wu, J. Endod. **42**, 299–303 (2016)

28. F. Genovesi, S. Rapisarda, G.R.M. La Rosa, N.M. Grande, G. Plotino, C.G. Adorno, J. Endod. **43**, 1–6 (2017)
29. F.M. Da Silva, C. Kobayashi, H. Suda, Int. Endod. J. **38**, 17–21 (2005)
30. A. Nayak, P. Kankar, P.K. Jain, N. Jain, Proc. Inst. Mech. Eng. Part H J. Eng. Med. **233**, 839–848 (2019)
31. A. Nayak, P.K. Kankar, N. Jain, Jain, P.K. J. Dent. Sci. (2018)
32. A. Nayak, P.K. Kankar, P.K. Jain, N. Jain. in *Advanced Materials—Proceedings of the International Conference on "Physics and Mechanics of New Materials and Their Applications", PHENMA 2018*, ed. by I.A. Parinov, S.-H. Chang, Y.-H. Kim. Springer Proceedings in Physics, vol. 224. (Springer Nature, Cham, Switzerland, 2019), pp. 643–649
33. T. Özyürek, G. Uslu, K. Yilmaz, Saudi Endod. J. **7**, 151–155 (2017)

Index

I. A. Parinov et al. (eds.), *Advanced Materials*, Springer Proceedings in Materials 6, https://doi.org/10.1007/978-3-030-45120-2

D

E